AAAS

Science



EVOLVING IMMUNITY

SPECIAL ISSUE

7 AUGUST 2025

U.S. aid cuts put millions at risk from malaria **p. 560**

Improving brain delivery of Alzheimer's drugs **pp. 571 & 617**

Energy-efficient magnetic sensors **p. 623**

Check for updates

SPECIAL ISSUE

THE MULTIFUNCTIONAL IMMUNE SYSTEM

SARAH ROSS and CAROLINE ASH

The survival of single-celled and multicellular life requires immunity to pathogens. In humans, immune defenses are multilayered, combining molecules that sense and signal the presence of threats with a range of specialized cells that patrol the body. Although surveillance and defense are central to the purpose of the immune system, additional physiological roles have emerged alongside them.

This Special Issue explores the immune system at the molecular and cellular levels and how it has evolved to govern multiple facets of human health. Over millennia, pathogens have exerted evolutionary pressures that have diversified molecular defense mechanisms. Innate and adaptive immune cells cause damage as they eliminate infection, and the immune system itself can help to repair tissue. We now appreciate that some immune cells can reside within tissues, with their specialized roles in defense being harnessed to promote organ function in the absence of infection. Immune cells are influenced by reproductive biology, too, with immune cell networks exhibiting differences between females and males. These functionalities were established through the selection of beneficial genetic traits over countless generations. Yet the immune system also changes within a single human lifetime, from birth to adulthood and through older age, shaped by the environment, microbiomes, and the process of aging.

As we understand more about the integral role of the immune system in responding to pathogens and its broader role in tissue function, we must evolve how we think about its contribution to human health. Interdisciplinary research, which incorporates molecular and cellular immunology into the function of other physiological systems, is critical as we seek to advance therapeutics and achieve personalized health care. 10.1126/science.aea8294



ILLUSTRATION: RIOKA HAYAMA



This illustration depicts the broader role of the immune system and how it has formed a bidirectional and symbiotic relationship with other organ systems to regulate physiology. Although immune cells are exploratory, they can also become resident within organs, providing protection from pathogens and contributing to tissue homeostasis and function.

EVOLVING IMMUNITY

REVIEW

Evolution of antiviral host defenses against a backdrop of endogenous retroelements

George Kassiotis[1,2]* and Jonathan P. Stoye[1,2]*

Mammalian hosts deploy a multitude of germ line–encoded mechanisms to detect and restrict virus infection. These mechanisms must avoid pathological responses to endogenous retroviruses and other endogenous retrotransposable elements (RTEs)—viruses and viruslike genomic parasites that have invaded the host germ line and are passed down the generations as host genes. Although the location, specificity, and sensitivity of innate pattern recognition receptors and restriction factors are tuned to facilitate discrimination of infecting viruses from those that are part of self, immune cross-reactions do occur. The RTE viral heritage may, therefore, compromise the ability of the host to respond to virus infection without risking pathology. Nevertheless, RTEs have the potential to be co-opted as an alarm amplification system, to be repurposed as antiviral factors, and to contribute to the evolution of antiviral genes.

The evolutionary success of an organism is determined by replication of its genome in the face of exposure to a wide range of infectious parasites. All organisms have evolved defenses against infection (*1*). In mammals, distinct germ line–encoded defenses cell-autonomously sense and neutralize invading viruses and trigger signaling cascades alerting neighboring cells and the immune system to the presence of the invader. These defenses target evolutionarily conserved structures, all of which present patterns distinct from the host, such as viral capsids, which protect the invading genomes; viral envelope glycoproteins, which attach and fuse virus particles with the target cells; and viral genomes and their replication intermediates.

Restriction factors are germ line–encoded host defense molecules that can directly limit virus replication by interfering with one or more steps in virus replication or by restricting the availability of cellular resources. Pattern recognition receptors (PRRs) can sense virus-specific patterns and initiate a signaling cascade, leading to the production of interferons (IFNs) and induction of IFN-stimulated genes (ISGs) with antiviral activity. Although some restriction factors and PRRs are expressed constitutively, many are IFN-inducible, bolstering antiviral defenses upon virus sensing. Moreover, certain restriction factors may either directly initiate proinflammatory signaling cascades or indirectly facilitate sensing by dedicated PRRs, connecting the network of innate antiviral defenses.

However, these defenses cannot evolve to provide complete resistance—otherwise, there would be no selection pressure to maintain them in the absence of exposure (*1*). Rather, they provide sufficient resistance to ensure the survival of the host, so both host and virus species can survive. Moreover, these mechanisms can be potentially as damaging for the host as for the virus, and their deployment must be specific and proportionate to the risk of infection. During the ensuing arms race, viruses evolve countermeasures that allow them to evade or subvert host defenses and establish acute or chronic infection in somatic cells.

The situation becomes more complicated when considering retroviruses, viruses that must integrate into host DNA as part of their own replication cycle. Some can invade the host germ line, thus becoming endogenous and blurring the boundaries between host and virus. These elements, called endogenous retroviruses (ERVs), join other types of retrotransposable elements (RTEs) in the genome, with which they share a common ancestry (*2*) and the ability to amplify their DNA copies in the host germ line through the reverse transcription and reintegration of their RNA transcripts into DNA. There are now >4 million RTE integrations in the human genome—making up ~42% of our DNA—which belong to distinguishable groups (*2*, *3*), with distinct replication life cycles and with specific consequences for the host innate and adaptive immune systems (Fig. 1).

Through accumulated mutations and deletions, the vast majority of RTEs have lost the ability to replicate or retrotranspose. In addition, they are suppressed by epigenetic mechanisms developed in response to these genomic parasites. Nevertheless, some RTEs are still able to produce replication intermediates and proteins that can activate antiviral immunity. This creates a challenge for the host to discriminate between the few RTEs that retain pathogenic potential and those that no longer pose a threat or have even been co-opted in host physiology, while still maintaining sufficient responsiveness to exogenous virus infection. Here, we review how host antiviral defenses have evolved in the context of RTEs and discuss the surprising opportunities and ammunition against other infections that RTEs provide for their host.

Guarding against cellular entry and exit of viruses

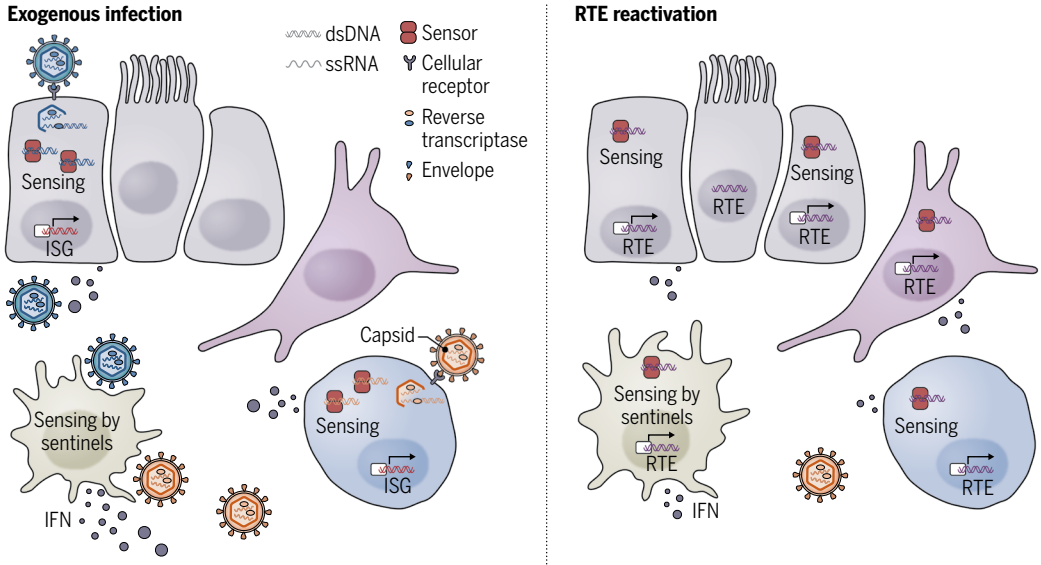
Perhaps the most effective defenses against infection are barriers to the ingress of the invader's genetic material through the membrane of the host cell. Entry of enveloped viruses requires attachment to cellular receptors and fusion of lipid membranes. Several host factors have evolved to block this step or reduce its efficiency. Where this defense succeeds, no further host action may be necessary. Processes required for virus entry are, therefore, frequently targeted by host restriction factors.

A recurring mechanism in host defense is the expression of intact or mutated envelope glycoproteins from ERVs, which blocks entry of exogenous viruses in a manner resembling viral superinfection resistance, whereby infection with a virus that uses a particular cellular entry receptor prevents entry of other viruses that use the same receptor. This mechanism has led to the convergence in evolution of exogenous retrovirus restriction in many species, including mice, cats, and sheep (Table 1) (*4*). A preserved copy of the human endogenous retrovirus (HERV)–T envelope glycoprotein that can bind its cognate receptor, MCT-1 (monocarboxylate transporter 1), without causing membrane fusion, may have led to the extinction of this family of exogenous retroviruses in our primate ancestors (*5*). Syncytin-1, derived from a HERV-W envelope glycoprotein and co-opted in human placentation, and the phylogenetically distant ERVH48-1 envelope glycoprotein (also known as suppressyn) bind to amino acid transporter ASCT2 as a receptor. ASCT2 acts as a cellular receptor for several other retroviruses, including currently circulating primate retroviruses, and syncytin-1 and ERVH48-1 binding to ASCT2 can, consequently, inhibit infection with diverse endogenous and exogenous retroviruses (*6*, *7*).

Efficient transmission of exogenous mouse mammary tumor viruses (MMTVs) relies on induction of T cell proliferation by virally encoded superantigens. Endogenous MMTV proviruses promote thymic deletion of superantigen-reactive T cells (*3*), thus providing relative resistance to exogenous MMTV infection through a distinct mechanism.

[1]The Francis Crick Institute, London, UK. [2]Department of Infectious Disease, Faculty of Medicine, Imperial College London, London, UK. ***Corresponding author. Email: george.kassiotis@crick.ac.uk (G.K.); jonathan.stoye@crick.ac.uk (J.P.S.)**

Fig. 1. Distinct immunogenic features of exogenous viruses and RTEs. Exogenous viruses typically target one or a few cell types, where they produce excessive amounts of viral nucleic acids, often with distinctive molecular patterns recognized by common or cell type–specific sensors. Their virions also access specialized sentinel cells, such as pDCs, which become the predominant sources of IFN. In contrast, RTEs are present and can be reactivated in every nucleated cell, but they are rarely transcribed at high levels and do not commonly produce specific molecular patterns and extracellular particles that would access pDCs.



- Cellular tropism; target selectivity
- Very high production of viral nucleic acids
- Creation of nonself patterns
- Virion access to sentinel immune cells
- Strong IFN response; few cells

- Present in every cell
- Relatively low level of transcription
- Patterns largely part of self
- Limited access to sentinel immune cells
- Weak IFN response; many cells

Table 1. RTE-related antiviral sensors and restriction factors. Only mammalian antiviral sensors and restriction factors that are directly derived or shaped by RTEs are included. The species in which they were first described is also indicated. eMLV, ecotropic MLV; enJSRV, endogenous JSRV; ERV-DC, feline endogenous gammaretrovirus of the domestic cat; FeLV, feline leukemia virus; MCF, mink cell focus-forming; MERV, murine endogenous retrovirus; Env, envelope.

Antiviral factor				Antiviral activity	
Gene	**Protein**	**Relation to RTEs**	**Ligand or target**	**RTEs**	**Exogenous viruses**
Fv4 (mouse)	Fv4	eMLV Env-derived	mCAT-1	eMLV	eMLV
Rmcf (mouse)	Rmcf	MCF virus Env-derived	XPR1	Nonecotropic MLV	Nonecotropic MLV
Refrex1 (cat)	Refrex-1	ERV-DC Env-derived	COPT1	ERV-DC	ERV-DC
Felix (cat)	FeLIX	FeLV-B Env-derived	PiT1	FeLV-B	FeLV-B
ERVS71-1 (human)	ENVT1	HERV-T Env-derived	MCT-1	HERV-T (defective)	HERV-T (extinct)
ERVH48-1 (human)	Suppressyn	ERVH48-1 Env-derived	ASCT2	ERVH48-1 (defective)	RD114/mammalian type D retroviruses
BST2 (human)	BST2; tetherin	Antagonized by HERV-K(HML-2) Env	Env, budding	ERVs, exosomes, LINEs	Retroviruses, enveloped viruses
Fv1 (mouse)	Fv1	MERV-L gag-derived	Capsid uncoating	MLV	MLV, diverse retroviruses
enJS56A1 (sheep)	enJS56A1	JSRV Gag-derived	Capsid assembly	enJSRV	JSRV
Apobec3 (mouse)	ABEC3	MLV insertion in the Rfv3 allele	DNA, RNA	ERVs, LINEs	MLV
APOBEC3B (human)	ABC3B	Regulation by nearby HERV-H	DNA, RNA	ERVs, LINEs	Retroviruses, hepadnaviruses
AIM2 (human)	AIM2	IFN inducibility by MER41	Cytoplasmic DNA	Untested	Diverse DNA and RNA viruses
IFI6 (human)	IFI6	IFN inducibility by MER41	Unclear	Untested	Diverse DNA and RNA viruses
GBP2 (human)	GBP2	Driven by ERV9 LTR12	Env processing	HERV-K(HML-2) pseudotypes	Diverse enveloped viruses
GBP5 (human)	GBP5	Driven by ERV9 LTR12	Env processing	HERV-K(HML-2) pseudotypes	Diverse enveloped viruses
TLR7 (human)	TLR7	Regulation by nearby HERV-H	Endosomal ssRNA	ERVs, LINEs, SINEs	Diverse ssRNA viruses
TLR8 (human)	TLR8	Regulation by nearby HERV-H	Endosomal ssRNA	ERVs, LINEs, SINEs	Diverse ssRNA viruses

CREDIT: ADAPTED BY K. HOLOSKI/*SCIENCE*

Viral egress also represents an important target for virus restriction where ERV products may play a role. ERV envelope glycoproteins can inhibit retroviruses that use unrelated receptors. For example, defective envelope glycoproteins from the most recently endogenized HERV-K(HML-2) family have been shown to limit production of HIV-1 in an incompletely understood manner (*8*). Tetherin [encoded by *BST2* (bone marrow stromal cell antigen 2)] is a restriction factor that prevents the release of enveloped virus particles from infected cells by physically tethering them to the plasma membrane of the producer cell. It is active against most tested viruses, including HERV-K(HML-2). In addition to this direct activity, virus assembly at the plasma membrane can be sensed as a molecular pattern by tetherin, triggering nuclear factor κB (NF-κB)–dependent proinflammatory responses, and tetherin-mediated accumulation of virus particles may also facilitate sensing by other receptors (*9*).

Several exogenous viruses can inactivate tetherin, albeit using different mechanisms. Such antagonistic activity seems to be retained by the envelope glycoprotein of some HERV-K(HML-2) proviruses, expression of which at the plasma membrane can inactivate tetherin (*10*), potentially facilitating instead of inhibiting exogenous virus release. As HERV-K(HML-2) envelope glycoproteins are variably expressed between individuals, and certain proviruses are insertionally polymorphic—present in some individuals but not others—they may differentially affect susceptibility to exogenous infection by disparate effects on tetherin (*10*).

The apparent success of restriction mechanisms blocking viral entry and exit may be responsible for the evolution of an RTE life cycle involving intracellular genome amplification without the need for cell-to-cell transmission or somatic cell infection (*11*). The evolution of such a life cycle further complicates the host's task in distinguishing endogenous from exogenous virus replication (*3*).

Targeting incoming viral genomes

If blocks at the cell membrane are circumvented, a second tier of defenses awaits. These secondary defenses include restriction factors that act to prevent the synthesis of complete cDNA copies of the viral genome or its access to the host genome for integration (*12*). A key target is the viral capsid protein that forms a shell enclosing the viral replication machinery and preventing sensing of viral nucleic acids. Examples of restriction factors that target the viral capsid include TRIM5α, a member of the large family of proteins bearing the tripartite motif, many of which contribute to antiviral immunity, and Fv1, which is derived from a murine endogenous retrovirus L family (MuERV-L) RTE and has followed an evolutionary pathway spawning variants with specific recognition properties for different retroviruses (*13*). TRIM5α appears to act by causing premature uncoating of the viral core inhibiting cDNA synthesis or exposing the viral nucleic acids to TREX1 (three-prime repair exonuclease 1), which digests cytosolic DNA and cDNA, whereas Fv1 most likely prevents core transit to the nucleus (*14*).

As with antiviral restriction factors targeting envelope glycoprotein–mediated virus entry and exit, those targeting the viral capsid can also act at multiple steps of the viral life cycle. For example, the Gag protein from an endogenous HERV-K(HML-2) provirus can poison HIV-1 core assembly (*15*), as does the Gag protein of endogenous Jaagsiekte sheep retrovirus (JSRV), which inhibits assembly of the cognate infectious retrovirus (*16*). These examples further underscore the repeated co-option of ERV proteins as restriction factors that provide genetic resistance to retroviral infection.

Triggering an IFN response

Successful entry of a virus particle into a host cell warrants a response proportional to the extent of subsequent virus replication. This requires fast and accurate detection of the invader, coupled to immediate block of both replication in the infected cell and virus spread to other cells. Detection is achieved by a battery of strategically placed PRRs, including Toll-like receptors (TLRs), retinoic acid–inducible gene I (RIG-I)–like receptors (RLRs), nucleotide-binding oligomerization domain (NOD)–like receptors (NLRs), and absent in melanoma 2 (AIM2)–like receptors (ALRs), that recognize diverse pathogen-associated molecular patterns (PAMPs) but may also bind ligands produced by the host cell. Several mechanisms have been described that maximize the ability of PRRs to sense infection, while limiting reactivity with self-generated ligands, including those from RTEs (*17*).

...discrimination between self- and virus-produced PRR ligands is not always possible, necessitating additional mechanisms of regulation.

PRRs can evolve specificity for structures that are produced exclusively or primarily during virus replication. They may also be expressed in a cell-specific manner or predominantly in specialized sentinels, such as plasmacytoid dendritic cells (pDCs) (Fig. 1). Nevertheless, discrimination between self- and virus-produced PRR ligands is not always possible, necessitating additional mechanisms of regulation.

Owing to 5′ capping and other modifications, polymerase II (Pol II)–transcribed host mRNAs are not sensed by RIG-I, which recognizes blunt-ended, double-stranded RNA (dsRNA), unmethylated at the 2′-O position, and with 5′ di- or triphosphates. However, Pol III–transcribed host RNAs, including 5*S* rRNA, and RTE RNAs, including the nonautonomous short interspersed nuclear elements (SINEs), lack 5′ capping and, instead, avoid sensing by RIG-I by forming complex secondary structures or by interacting with RNA binding proteins that shield them from detection (*18*). The dsRNA sensor MDA5, encoded by *IFIH1*, recognizes dsRNA longer than 300 base pairs (bp) produced during replication of certain viruses as well as by the host cell. Ancestrally derived from the 7SL RNA gene, the primate-specific Alu subfamily of SINEs have accumulated to >1 million copies in the human genome, thus increasing the probability that two or more Alu repeats may be present in the same RNA transcript. Inverted Alu repeats that are sufficiently similar and proximal can form intramolecular RNA hairpins for the entire length of the Alu sequence, which averages ~280 bp. This length, together with imperfect complementarity of the dsRNA region, further disrupted by ADAR (adenosine deaminase acting on RNA)–mediated editing, considerably reduces the ability of such hairpins to activate MDA5, suggesting that the length of the Alu sequence and tolerance of MDA5 to dsRNA mismatches are tuned to avoid this interaction (*19*). This balance is disrupted by gain-of-function *IFIH1* mutations or loss of ADAR activity, triggering spontaneous IFN production in immune disorders, including Aicardi-Goutières syndrome and systemic lupus erythematosus (*20*). Additional mechanisms that limit the availability of endogenous ligands for PRRs include nucleoside or nucleotide metabolizing enzymes such as SAMHD1, TREX1, and HELZ2, which digest highly structured RNAs (*21*).

When endogenous ligands cannot be efficiently modified or removed, their sensing can still be limited by regulated PRR expression and localization. Endosomal localization of the ligand-biding domains of dsRNA sensor TLR3, single-stranded RNA (ssRNA) sensors TLR7 and TLR8, and unmethylated CpG DNA sensor TLR9 also prevents detection of cytosolic ligands, and differences in intracellular localization also determine the targeting of host or virus RNA by zinc finger antiviral protein (ZAP) (*22*). Although several PRRs are constitutively expressed in anticipation of infection, several require IFN to induce their transcription, or a different isoform of the protein is induced after an IFN response.

For example, in response to IFN, the *ADAR* gene produces a larger isoform that, in addition to dsRNA binding domains, contains a domain (Zα) binding Z-form DNA or RNA. IFN signaling is a prerequisite for expression of the only other known mammalian protein with Zα domains, Z-DNA-binding protein 1 (ZBP1), which can sense Z-form DNA or RNA, leading to further IFN induction or necroptosis.

Certain PRRs, including those that are inducible by IFN, can regulate the IFN response at the resolution phase of an infection. The *ZC3HAV1* gene encodes two isoforms of the RNA binding protein ZAP that differ in length. Whereas the longer isoform is constitutively expressed and targets viral RNA, the expression of the shorter isoform requires IFN and targets the mRNA of *IFN* genes for degradation, thereby negatively regulating the IFN response (*22*). Therefore, the IFN response to exogenous virus infection appears to be finely tuned by coordinated regulation of sensing and signaling cascades as well as by negative feedback loops.

Innate sensing of RTEs

An evolutionary trade-off between prevention of overt PRR engagement by RTEs and the necessity of maintaining sensitivity to exogenous virus implies that RTE sensing may not be entirely avoided, particularly when homeostasis is disrupted. Moreover, as not all RTEs have been fully disarmed through evolution, the host must be prepared to sense their dysregulation to prevent further spread in the germ line and in somatic cells. Failure of such mechanisms is indicated by the frequent resurrection of ERVs in sensor- and immune-deficient mice (*23*, *24*).

At least three conditions contribute to RTE products being expressed and sensed by cells. First, epigenetic repression, which otherwise prevents RTE transcription, can be reversed during cellular infection, damage, or malignant transformation, leading to the production of excessive RTE nucleic acids and proteins. Indeed, several exogenous viruses can up-regulate RTE transcription, either through direct transactivation (*25*) or indirectly, in the case of SINEs, through elevated transcription by host Pol III (*18*). Exogenous viruses also induce proinflammatory mediators and target RTE repressors and restriction and other antiviral factors (*26*), all of which enhance RTE transcription indirectly. Infection with exogenous retroviruses, in particular, can complement replication defects in ERVs, leading to their mobilization. Second, IFN production during viral infection or other pathologies will additionally up-regulate PRR expression, which may facilitate detection of RTE products. And third, to complete their own replication, viruses may also counteract restriction factors and sensor regulators, such as SAMHD1, tetherin, PKR, and the APOBEC3 family, further enhancing the availability of RTE products for sensing.

The increased availability of RTE-derived ligands, coupled with increased PRR expression and reduced antiviral factor expression, now permits the sensing of RTEs, which can contribute to the overall antiviral response of the host (Fig. 2). Sensing of RTEs in the absence of infection or malignant transformation can directly cause or increase the risk of age-related inflammation, systemic autoimmunity, or severe interferonopathies (*3*). However, it may be less pathogenic during virus infection, which should independently trigger an antiviral response. Although certain viruses can benefit from the RTEs they induce (*27*), the contribution of induced RTEs to the antiviral response can enhance resistance to exogenous virus infection (*26*, *28*).

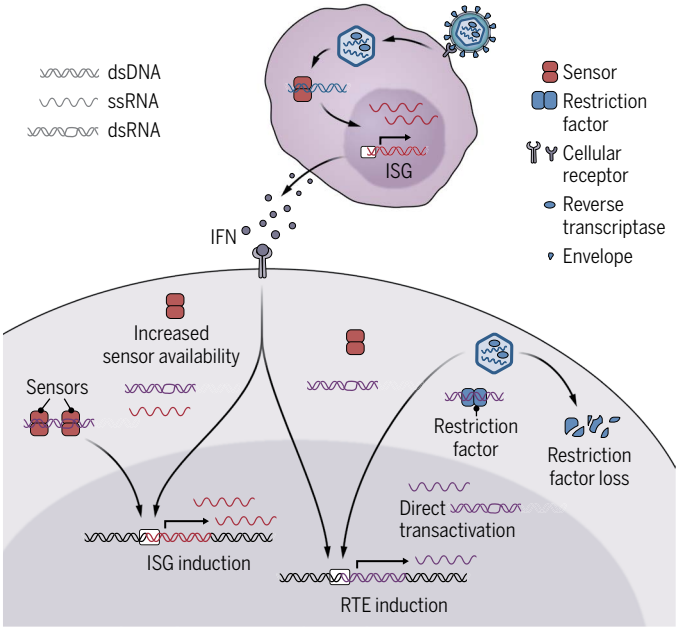


Fig. 2. RTE activation and sensing triggered by viral infection. Infection with exogenous viruses increases RTE transcription and availability either directly, through transactivation by viral transcription factors, or indirectly, through proinflammatory mediators or by inactivating repressor restriction and other antiviral factors that normally silence or control RTEs. In parallel, IFN production during viral infection up-regulates PRR expression. Increased RTE transcription and reduced control, combined with increased PRR availability, can initiate innate immune responses to RTEs, which, in turn, amplify responses to the exogenous infection.

CREDIT: ADAPTED BY K. HOLOSKI/*SCIENCE*

RTEs as regulators of adjacent innate immune gene function

Owing to their mutagenic potential and the regulatory sequences they carry, RTEs are a major force of host genome innovation. RTE integrations near or within genes can modify gene function on longer evolutionary timescales and with more profound consequences, and innate immune genes involved in sensing or restriction are no exception. RTE regulatory effects on genes that, in turn, affect resistance to infection or control RTE activity may have strong evolutionary effects.

For example, an intronic integration of a murine leukemia virus (MLV) long terminal repeat (LTR) in murine *Apobec3* enhances its expression and, consequently, its antiviral activity, thereby providing resistance to exogenous MLV infection (*29*). In human embryonic stem cells, a HERV-H integration has been co-opted as a functional enhancer of *APOBEC3G*, and genome-wide HERV-H transcriptional activity is positively correlated with expression of the entire *APOBEC3* locus as well as expression of the restriction factor *IFITM1* (*30*). A subfamily of murine B2 SINE repeats was found to contain signal transducers and activators of transcription 1 (STAT1)–binding sites and function as IFN-inducible enhancers (*31*), and MER41_BT and Bov-A2 repeats play a similar role in bovine cells (*32*). Human MER41 repeats provide IFN inducibility to several antiviral sensors and effectors (*33*), including *AIM2*, a cytosolic double-stranded DNA (dsDNA) sensor, and *IFI6*, which exhibits broad antiviral activity (*34*, *35*), but may also prevent RIG-I activation through competition for RNA ligands (*36*). Solitary *LTR12C*—single copies of the ERV9 subfamily LTR—also regulate expression and IFN inducibility of the downstream genes *GBP2* and *GBP5*, which inhibit the processing by the cellular protease furin of envelope glycoproteins of exogenous viruses, as well as of ERVs, such as HERV-K(HML-2) (*37*, *38*). An intronic *L1M2a* element has been co-opted as an enhancer of human *IFNAR1*, regulating both constitutive and IFN-inducible expression in B cells (*39*). Genetic loss of *TRIM28* in murine dendritic cells leads to the induction of proinflammatory and antiviral genes, including *Ifitm1* and *Gbp2b*, which has been attributed to regulatory control by adjacent derepressed RTEs (*40*). A copy of the Lx9c11 murine long interspersed nuclear element (LINE) subfamily has created the noncoding RNA *Lx9c11-RegoS*, which is indispensable in preventing lethal hyperinflammation during virus

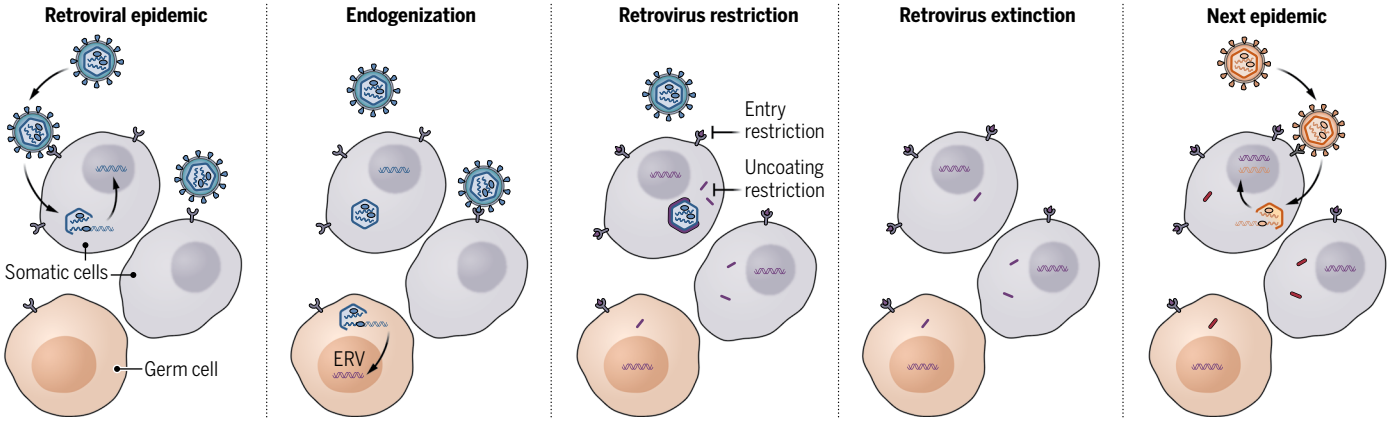


Fig. 3. A proposed cycle of retroviral epidemic and evolution of innate resistance. Infection with a new exogenous retrovirus may occasionally cause germline infection leading to endogenization of one or more proviral copies (ERV). With long evolutionary time, ERVs are co-opted to produce defective products that interfere and restrict infection with related retroviruses and achieve fixation in the host genome. When such restriction is efficient, it drives related exogenous viruses to extinction but may not necessarily protect against more-distant exogenous retroviruses, which can cause the next epidemic.

infection, through regulation of the genes encoding the Schlafen (SLFN) family of proteins (*41*).

Their cis-regulatory potential allows RTE integrations that are fixed in the genome to affect immune gene function negatively, too. Gene-dysregulating effects of RTEs are normally minimized by their epigenetic repression and suppression of their exonization but are particularly pronounced after malignant transformation, which is associated with RTE derepression, and may also manifest in other contexts. Transcriptional activation of a HERV-H provirus integrated downstream of the tandem *TLR7* and *TLR8* loci on human chromosome X initiates antisense transcription that is associated with loss of *TLR7* and *TLR8* transcription in several cancer types (*42*). Similarly, antisense transcription driven by a MER11C integration downstream of human *APOBEC3B* reduces its expression, without affecting expression of other APOBEC3 members on chromosome 22 in tumors of the male germ line (*42*). Moreover, hypoxia-driven transcriptional activation of an intronic HERV-E provirus reduces the expression of *RNGTT* (*42*), encoding an enzyme that initiates 5′ capping of newly synthesized mRNAs, a modification essential for mRNA stability, translation, and prevention of RIG-I sensing.

The cis-regulatory potential of germline RTEs may also modify the function of proteins involved in viral infection and concomitant innate immune response. Angiotensin-converting enzyme 2 (ACE2) is a major entry receptor for seasonal and pandemic human coronaviruses, such as human coronavirus NL63 (HCoV-NL63), severe acute respiratory syndrome coronavirus (SARS-CoV), and SARS-CoV-2; and higher-affinity ACE2 binding is a critical but readily acquired trait for animal coronavirus spillover to humans (*43*). Evolutionarily ancient intronic integrations of *MIRb* and *LTR16A1* repeats act as the promoter of an IFN-inducible truncated *ACE2* isoform, thus coupling the IFN response to the induction of an ACE2 protein form that cannot mediate virus entry (*44*). A primate-specific intronic *AluJr* repeat has been co-opted as an alternative terminal exon of *IFNAR2*, creating a nonfunctional decoy receptor for type I IFNs that lacks the intracellular domain responsible for downstream signaling, thereby regulating the antiviral response (*45*). These examples highlight the immense potential of RTEs to alter or tune the function and expression of innate immune genes, with direct consequences for resistance to viral infection.

The increased availability of RTE-derived ligands... can contribute to the overall antiviral response of the host.

Retention of viral heritage hinders co-option or causes pathology

Although RTEs are now part of the host genetic constitution and can be co-opted in essential host processes, this peaceful coexistence can sometimes be disrupted, causing such processes to fail. The fusogenic potential of ERV envelope glycoproteins has been recurrently co-opted by placental mammals, in the form of the syncytin genes, and these glycoproteins function during the formation of the syncytiotrophoblast, a multinucleated layer of cells covering the placenta (*46*). Syncytin-mediated fusion of trophoblast cells follows the same principles as fusion during virus entry and may be subject to restriction by the same factors that have evolved to prevent the latter. Indeed, syncytiotrophoblast formation can be adversely affected by IFN-induced transmembrane proteins (IFITMs) (*47*). These restriction factors inhibit the entry of several viruses by targeting envelope glycoproteins, and IFITM1 may also suppress several RTE families in human embryonic stem cells (*48*). Excessive activity of IFITMs induced by IFN or congenital infection can target syncytins, by virtue of their retroviral origin, ultimately leading to complications in pregnancy (*47*). Furthermore, the antiviral activity of GBP5 can also inhibit the processing and fusogenic function of syncytin-1 (*49*). These findings highlight a balance between the need to control potential pathogenic RTEs or exogenous viruses and the exapted function of syncytins at that stage of human embryo development.

Another example where host mechanisms that evolved to limit infection may affect the exapted function of RTEs is represented by the co-option of HERV LTRs as promoters and enhancers in the transcription and IFN inducibility of innate immune genes. RTEs are epigenetically repressed, in part by a multigene family of Krüppel-associated box–containing zinc finger proteins (KZNPs), which recruit the repressor TRIM28 (also known as KAP1) (*50*). Together with specialized mechanisms, such as PIWI-interacting RNAs, silencing RTEs specifically in the germ line (*51*), KZNP-mediated repression may reduce the immediate risk to adjacent genes posed by cis-regulatory activity of newly acquired RTEs, which can then be tested over longer evolutionary time for potentially beneficial activities through gradual or somatic cell type–specific release from KZNP control. However, excessive or persistent KZNP-mediated repression can restrict the evolutionary advantage that such cis-regulatory activity may provide. Indeed, reduced KZNP activity

in subsets of elite controllers of HIV-1 infection has been correlated with increased LTR-driven expression of key antiviral genes, including *GBP2* and *GBP5* (*52*), suggesting that KZNP targeting of proviral LTRs may modulate the ability of exapted cis-regulatory LTRs to drive or otherwise regulate antiviral genes.

Outlook

Although the interaction of RTEs with host innate immunity may be pathogenic when dysregulated or hinder the co-option of RTEs in physiological processes of the host, it also provides opportunities for the evolution of immune function. We propose that the current evidence supports a model whereby the transcriptional responsiveness of RTEs to viral infection or malignant transformation may provide an alarm amplification system for such types of danger. Exogenous viruses can outpace host innate immunity with faster evolution of countermeasures. In contrast, RTE integrations follow the much slower evolutionary pace of the host genome. This increased genetic stability, together with the presence of RTEs in every host cell, creates an ideal source of innate immune stimulation that can augment the immunogenicity of infected or transformed cells.

Inactivation of RTEs, either during the replication process or over evolutionary time, also offers the opportunity to repurpose their individual components in the antiviral response, as exemplified by the utilization of defective ERV envelope glycoproteins and capsids as restriction factors. This creates a cycle, initiated by widespread infection with an exogenous retrovirus, occasionally leading to its endogenization and eventual inactivation of endogenous copies through mutation (Fig. 3). Expression of defective components from the now-endogenous copies may block infection with the cognate circulating retrovirus, ultimately leading to its extinction, and endogenous copies become fixed in the host germ line (Fig. 3). Although the antiviral activities of defective ERVs might have been effective against ancient viral epidemics caused by their exogenous counterparts, they do not necessarily protect against modern-day or future viruses (*53*). The introduction of a retrovirus that bypasses existing ERV-derived antiviral activities initiates another cycle, until effective antiviral activities evolve further or are acquired de novo by the host.

In addition to their ability to trigger an IFN response and the co-option of their components as restriction factors, genomic RTE integrations that are eventually allowed by the host to function as regulatory sequences contribute to genomic innovation, including the control of innate immunity genes. Identification of such functions may not be trivial. RTEs in the genome can be recognized by homology with consensus sequences. However, high sequence similarity between copies of the same RTE family within the same genome, as well as sequence and insertional polymorphisms between genomes, complicate their analyses. Even more challenging is the annotation of transcripts that use or overlap with RTEs, particularly transcript isoforms that may characterize pathological conditions, such as malignant transformation (*54*, *55*), although it will be facilitated by more comprehensive annotation of the diversity and distribution of RTEs in the human reference genome (*56*) and by advances in long-read RNA sequencing methodologies. The IFN response is also associated with characteristic shifts in the transcriptome (*57*), and it would be important to characterize the contribution of RTEs in the creation of the IFN-inducible transcript isoforms. A potential contribution of RTEs is further supported by the association of their epigenetic state with interindividual variation in the innate immune response to HIV-1 (*52*) and influenza A (*58*). More-comprehensive genomic and transcriptomic analyses of RTEs, including their interindividual variation, will be an essential step toward understanding the evolutionary constraints our innate immune system faces in its fight against current and future exogenous viruses.

REFERENCES AND NOTES

1. M. Cohn, *Immunol. Rev.* **185**, 24–38 (2002).
2. J. N. Wells, C. Feschotte, *Annu. Rev. Genet.* **54**, 539–561 (2020).
3. G. Kassiotis, *Annu. Rev. Immunol.* **41**, 99–125 (2023).
4. R. Malfavon-Borja, C. Feschotte, *J. Virol.* **89**, 4047–4050 (2015).
5. D. Blanco-Melo, R. J. Gifford, P. D. Bieniasz, *eLife* **6**, e22519 (2017).
6. J. A. Frank *et al.*, *Science* **378**, 422–428 (2022).
7. S. Khare *et al.*, *Nat. Struct. Mol. Biol.* **31**, 1368–1376 (2024).
8. S. N. Terry *et al.*, *Virology* **509**, 52–59 (2017).
9. R. P. Galão, A. Le Tortorec, S. Pickering, T. Kueck, S. J. Neil, *Cell Host Microbe* **12**, 633–644 (2012).
10. C. Lemaître, F. Harper, G. Pierron, T. Heidmann, M. Dewannieux, *J. Virol.* **88**, 13626–13637 (2014).
11. R. Belshaw, A. Katzourakis, J. Paces, A. Burt, M. Tristem, *Mol. Biol. Evol.* **22**, 814–817 (2005).
12. M. H. Malim, P. D. Bieniasz, *Cold Spring Harb. Perspect. Med.* **2**, a006940 (2012).
13. M. W. Yap, G. R. Young, R. Varnaite, S. Morand, J. P. Stoye, *PLOS Genet.* **16**, e1008471 (2020).
14. D. Wolf, S. P. Goff, *Annu. Rev. Genet.* **42**, 143–163 (2008).
15. K. Monde *et al.*, *Retrovirology* **14**, 27 (2017).
16. M. Mura *et al.*, *Proc. Natl. Acad. Sci. U.S.A.* **101**, 11117–11122 (2004).
17. E. Bartok, G. Hartmann, *Immunity* **53**, 54–77 (2020).
18. L. Naesens, F. Haerynck, M. U. Gack, *Trends Immunol.* **44**, 435–449 (2023).
19. S. Ahmad *et al.*, *Cell* **172**, 797–810.e13 (2018).
20. C. G. Vinuesa, A. Grenov, G. Kassiotis, *Science* **380**, 478–484 (2023).
21. A. Luqman-Fatah, K. Nishimori, S. Amano, Y. Fumoto, T. Miyoshi, *RNA Biol.* **21**, 1048–1064 (2024).
22. J. Schwerk *et al.*, *Nat. Immunol.* **20**, 1610–1620 (2019).
23. G. R. Young *et al.*, *Nature* **491**, 774–778 (2012).
24. P. Yu *et al.*, *Immunity* **37**, 867–879 (2012).
25. E. F. Evans, A. Saraph, M. Tokuyama, *Viruses* **16**, 1649 (2024).
26. B. G. Hale, *Curr. Opin. Virol.* **52**, 211–216 (2022).
27. J. Karijolich, E. Abernathy, B. A. Glaunsinger, *PLOS Pathog.* **11**, e1005260 (2015).
28. D. C. Rookhuizen *et al.*, bioRxiv 2021.09.10.457789 [Preprint] (2021); https://doi.org/10.1101/2021.09.10.457789.
29. B. Sanville *et al.*, *PLOS Pathog.* **6**, e1000974 (2010).
30. M. Singh *et al.*, *PLOS Biol.* **21**, e3002162 (2023).
31. I. Horton, C. J. Kelly, A. Dziulko, D. M. Simpson, E. B. Chuong, *eLife* **12**, e82617 (2023).
32. C. J. Kelly, C. G. Chitko-McKown, E. B. Chuong, *Genome Res.* **32**, 1474–1486 (2022).
33. E. B. Chuong, N. C. Elde, C. Feschotte, *Science* **351**, 1083–1087 (2016).
34. J. Le Pen, C. M. Rice, *Curr. Opin. Immunol.* **87**, 102426 (2024).
35. R. B. Richardson *et al.*, *Nat. Microbiol.* **3**, 1214–1223 (2018).
36. L. Villamayor *et al.*, *Front. Immunol.* **14**, 1105309 (2023).
37. E. Braun *et al.*, *Cell Rep.* **27**, 2092–2104.e10 (2019).
38. S. Srinivasachar Badarinarayan *et al.*, *Nucleic Acids Res.* **48**, 10890–10908 (2020).
39. C. A. Buttler, D. Ramirez, R. D. Dowell, E. B. Chuong, *Mob. DNA* **14**, 20 (2023).
40. S. Chikuma *et al.*, *J. Immunol.* **206**, 1528–1539 (2021).
41. N. Bartonicek *et al.*, *Nature* **608**, 757–765 (2022).
42. J. Loong *et al.*, *Genome Med.* **17**, 48 (2025).
43. T. N. Starr *et al.*, *Nature* **603**, 913–918 (2022).
44. K. W. Ng *et al.*, *Nat. Genet.* **52**, 1294–1302 (2020).
45. G. I. M. Pasquesi *et al.*, *Cell* **187**, 7621–7636.e19 (2024).
46. C. Lavialle *et al.*, *Philos. Trans. R. Soc. London Ser. B* **368**, 20120507 (2013).
47. J. Buchrieser *et al.*, *Science* **365**, 176–180 (2019).
48. Y. Fu *et al.*, *FEBS Open Bio* **7**, 1102–1110 (2017).
49. V. Krchlikova *et al.*, *Sci. Adv.* **11**, eadt5388 (2025).
50. O. Rosspopoff, D. Trono, *Trends Genet.* **39**, 844–857 (2023).
51. M. Abajorga, L. Yurkovetskiy, J. Luban, *Viruses* **16**, 1756 (2024).
52. M. Singh *et al.*, *Genome Biol.* **26**, 28 (2025).
53. W. E. Johnson, *Nat. Rev. Microbiol.* **17**, 355–370 (2019).
54. J. Attig *et al.*, *Genome Res.* **29**, 1578–1590 (2019).
55. H. S. Jang *et al.*, *Nat. Genet.* **51**, 611–617 (2019).
56. S. J. Hoyt *et al.*, *Science* **376**, eabk3112 (2022).
57. M. T. Ueda *et al.*, *Cell Genom.* **4**, 100654 (2024).
58. X. Chen *et al.*, *Cell Genom.* **3**, 100292 (2023).

ACKNOWLEDGMENTS

Funding: This work was supported by the Francis Crick Institute (CC2088), which receives its core funding from Cancer Research UK, the UK Medical Research Council, and the Wellcome Trust. This project has received funding from the European Research Council (ERC) under the European Union's Horizon 2020 research and innovation program (grant 101018670).
Competing interests: G.K. is a scientific cofounder of EnaraBio and a member of its scientific advisory board. G.K. has consulted for EnaraBio, Repertoire Immune Medicines, ErVimmune, and AdBio Partners. The authors declare no other competing interests. **License information:** Copyright © 2025 the authors, some rights reserved; exclusive licensee American Association for the Advancement of Science. No claim to original US government works. https://www.science.org/about/science-licenses-journal-article-reuse

Submitted 2 April 2025; accepted 12 June 2025

10.1126/science.adx4379

EVOLVING IMMUNITY

REVIEW

Immune system influence on physiology

Matthias Nahrendorf[1,2,3,4,5], Florent Ginhoux[6,7,8,9], Filip K. Swirski[10,11,12]*

The immune system's central function is to maintain homeostasis by guarding the organism against dangerous external and internal stressors. Immunity's operational toolbox contains diverse processes, such as phagocytosis, antigen recognition, cell killing, and secretion of cytokines and antibodies. Although immune cells interact with each other, they also communicate with cells typically associated with other organ systems, including the nervous, circulatory, metabolic, musculoskeletal, endocrine, and hematopoietic. This abundant cross-talk shows that immunity transcends defense and homeostasis: It is a network that participates in many physiological processes necessary for life. By accessing the circulation and inhabiting every tissue, leukocytes sense, interpret, and regulate biological processes. In this Review, we highlight recent studies that illustrate the often bidirectional and symbiotic relationships through which the immune system regulates physiology.

Immune cells, or leukocytes, are obligate travelers that use the blood and lymph to access every tissue. Leukocytes are also highly specialized long-term tissue residents that form close niche circuits with noncirculating structural cells. Whether roaming or residing, immune cells are profoundly interactive, secreting and expressing ligands and receptors that facilitate abundant cell-to-cell cross-talk. Mostly studied for their propensity to respond to pathogens and injury, leukocytes are rightly understood as the central executors of the body's defense system. However, it is increasingly clear that leukocytes, and the stromal cells with which they interact, are integral constituents of physiological systems.

In this Review, we draw attention to studies that illuminate how the immune system modulates processes typically considered to be outside of immunology. We focus on immune partnerships with the nervous, cardiovascular and respiratory, gastrointestinal and metabolic, musculoskeletal, and endocrine systems. We conclude by discussing how the immune system interacts with the hematopoietic system and thus maintains itself by regulating its own development. We propose that leukocytes are not merely peripheral enablers of physiology: They are one of physiology's central protagonists, exercising their influence in every corner of mammalian life. Although their effects often use classical immune processes, such as phagocytosis or cytokine production, immune cells also exhibit nonclassical functions, masquerading as defining components of the allied system (Fig. 1).

The nervous system

The immune system, it has been proposed, represents a sixth sense, whereby antigen recognition extends the reach of the body's conventional senses—sight, sound, touch, taste, and smell (*1*). Although abundant work has shown that the immune system can influence behavior, often through the production of cytokines [reviewed in (*2*)], recent studies have underscored immune and sensory systems' shared evolutionary roots. Microglia, the brain's resident macrophages, are important in neuronal development, synaptic input balance, and repair. Microglia prune neurons by engulfing presynaptic elements of retinal ganglion cells during a period of robust pruning shortly after birth, as synaptic inputs from the eye compete for territory in the dorsal lateral geniculate nucleus of the thalamus (*3*). Microglia also mediate the balance between excitatory and inhibitory synaptic inputs, thus influencing memory, through mechanisms that engage interleukin-6 (IL-6) (*4*). Surveillance of nervous system integrity is active in tissue repair, during which a phenotypically and transcriptionally distinct subset of prenatally seeded dermal macrophages contributes to calcitonin gene–related peptide ($CGRP^+$) sensory nerve fiber regeneration after injury, possibly by clearing debris and secreting guidance cues and growth factors (*5*) (Fig. 2).

Although functions such as phagocytosis and cytokine production fall squarely within the conventional understanding of the immune system, they yield unexpected results when applied to the nervous system. During pregnancy, T cell–derived IL-17α promotes atypical, abnormal, and disorganized cortical development that propagates autism spectrum disorder abnormalities (*6*). Microglia-derived homeobox B8 (Hoxb8) stabilizes neural networks; mice deficient in Hoxb8 exhibit excessive, pathological grooming (*7*). That a microglial product helps regulate grooming is notable but perhaps understandable when considered from an evolutionary perspective: It may couple behavior that reduces pathogen count with the immune system, which controls and eliminates pathogens. Such neuroimmune symbiosis can also be found during exposure to allergens, which elicit avoidance behavior by activating areas in the brain involved in averse stimuli (*8*). The symbiosis may likewise apply to itch. When basophils, mast cells, and other immune cell–derived products, such as leukotrienes or cytokines, induce itch by interacting with sensory neurons in the skin, they incite scratching, which might represent a drive to either eliminate the itch-inducing agent or to stimulate an immune response against it (*9*, *10*).

A large and growing body of literature links inflammation with a variety of neurological and psychiatric conditions. The connection between inflammation and depression, for example, is well established [reviewed in (*11*)]. Depression risk alleles are associated with an immune response to infection—a link that raises the question of whether depressive symptoms, such as hyperthermia, reduced bodily iron stores, withdrawal behavior, hypervigilance, and decreased appetite, enhance pathogen defense. On one hand, immune cells located in the meninges can shape behavior, for example by producing anxiety-promoting IL-17 (*12*). On the other hand, circulating monocytes accumulating in various regions in the prefrontal cortex, amygdala, and hippocampus promote anxiety and social avoidance, possibly through IL-1 and IL-6, respectively (*13*). In response to social defeat stress, monocytes accumulate in reward-processing and stimuli-aversive brain regions, where they secrete matrix metalloproteinase 8 (MMP8), which regulates social avoidance by altering the extracellular space (*14*). In response to systemic immune challenge such as polyinosinic:polycytidylic acid [poly(I:C)], a mimic of viral infection, monocyte-derived tumor necrosis factor–α

[1]Center for Systems Biology, Massachusetts General Hospital and Harvard Medical School, Boston, MA, USA. [2]Department of Radiology, Massachusetts General Hospital and Harvard Medical School, Boston, MA, USA. [3]Gordon Center for Medical Imaging, Massachusetts General Hospital and Harvard Medical School, Boston, MA, USA. [4]Department of Internal Medicine I, University Hospital Wuerzburg, Wuerzburg, Germany. [5]Cardiovascular Research Center, Massachusetts General Hospital and Harvard Medical School, Boston, MA, USA. [6]Paris-Saclay University, Gustave Roussy, INSERM U1015, Villejuif, France. [7]Singapore Immunology Network (SIgN), A*STAR, Immunos Building, Singapore. [8]Shanghai Institute of Immunology, Shanghai Jiao Tong University School of Medicine, Shanghai, China. [9]Translational Immunology Institute, SingHealth Duke-NUS Academic Medical Centre, Singapore. [10]Cardiovascular Research Institute and the Department of Medicine, Icahn School of Medicine at Mount Sinai, New York, NY, USA. [11]The Friedman Brain Institute, Icahn School of Medicine at Mount Sinai, New York, NY, USA. [12]Marc and Jennifer Lipschultz Precision Immunology Institute, Icahn School of Medicine at Mount Sinai, New York, NY, USA. ***Corresponding author. Email: filip.swirski@mssm.edu**

(TNFα) impairs motor learning and learning-related dendritic spine plasticity (*15*).

Despite work showing that inflammation contributes to anxiety and depression, the immune system can also be protective regarding such conditions. In response to stress, T helper 17 cell (T_H17 cell)–derived IL-22 attenuates anxiety by directly suppressing neuronal activity in the septal area of the forebrain, a region known to regulate anxiety through projections to the hippocampus and hypothalamus (*16*). Immune cells can also defend in other ways. After myocardial infarction, monocytes migrate to the brain, where they increase slow wave sleep and abundance using TNFα, suppress the sympathetic nervous system, limit inflammation, and thus promote better healing (*17*).

Although immune cells can modify the nervous system through conventional immune processes and products, they can also synthesize neurotransmitters (*18*), respond to them (*19*), and modulate action potential (*20*). An early insight into immune-derived neurotransmitters stemmed from the observation that the spleen lacks cholinergic innervation, a finding that led to the identification of acetylcholine-producing T cells that limit TNFα production by splenic macrophages as part of the inflammatory reflex (*18*). Acetylcholine-producing T cells, it has subsequently been shown, control lymphocytic choriomeningitis virus infection (*21*) and are important in regulating blood pressure (*22*), whereas acetylcholine-producing B cells govern leukocyte production in the bone marrow (*23*). In the meninges, regulatory T cells (T_{reg} cells) produce the endogenous opioid enkephalin, which suppresses nociception (*24*), whereas in the liver, macrophages secrete growth and differentiation factor 15 (GDF15), which activates a circuit by which area postrema neurons induce sympathetic-dependent triglyceride production for tissue tolerance (*25*). Whether leukocytes function as interneurons or even impersonate neurons is debatable, but these insights do blur the boundary of where one system ends and another begins.

The cardiovascular and respiratory system

The lung, heart, blood, and lymphatic vessels collaborate to exchange and carry gases, nutrients, metabolites, cells, and signals to and from every location in the body. Many tightly regulated systems participate in seamless integration necessary to accomplish essential transportation tasks. Immune cells abundantly inhabit these tissues, where they perform jobs unrelated to pathogen surveillance that range from clearing surfactant in the lung (*26*) and controlling blood pressure in the vessel wall

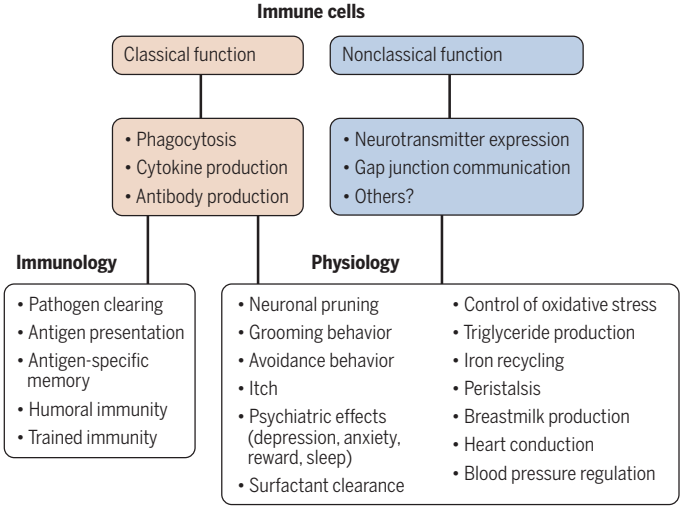


Fig. 1. Functions of immune cells that facilitate their roles in physiology. Classical functions of immune cells are integral to immunology. Immune cells modulate physiological processes through classical functions and nonclassical mechanisms typically associated with other cells and systems.

(*22*) to producing blood cells (*27*). These functions are vital, if only because oxygen transport disruption can be lethal within minutes—a clinically relevant example that frequently occurs in myocardial infarction and ischemic stroke (Fig. 2).

The primary engine of transport, the heart muscle, contracts ~100,000 times a day. Cardiomyocyte contractions require vast amounts of energy in the form of adenosine 5′-triphosphate (ATP), which is generated by mitochondria that, given their heavy metabolic burden, are frequently recycled. Cardiomyocytes shed spent mitochondria, along with other cell plasma–derived cargo, in exophers, which are membrane-wrapped microvesicles generated by cardiomyocyte autophagy machinery (*28*). Neighboring cardiac macrophages then ingest and eliminate the exophers. This process maintains cardiomyocyte integrity, allowing the heart to function efficiently. Disruptions to this process lead to impaired myocardial relaxation, a hallmark of heart failure with preserved ejection fraction (HFpEF)—a clinical condition that is often lethal. Like cardiomyocyte contraction, the underlying electrical de- and repolarizations also demand high amounts of energy and require efficient macrophage support to avert arrhythmia (*29*). Compelling evidence thus shows how immune cells, in this case resident cardiac macrophages, provide crucial metabolic support for cardiomyocytes and ensure healthy heart function.

Resident immune cells also participate in cardiac conduction, as shown in a study where depleting macrophages blocked atrioventricular conductance and lethally slowed heart rates in mice (*20*). Cellular imaging studies in mice and humans reveal more macrophages in the heart's conduction system, especially the sinus and atrioventricular nodes. These data are consistent with other studies indicating that resident leukocytes are nonhomogeneously distributed throughout organs. Cardiomyocytes and macrophages have been proposed to be connected by means of gap junctions, particularly connexin-43, and thus exchange ions to help cardiomyocytes repolarize more efficiently for more resilient conduction (*20*). However, the heart is also highly innervated by sympathetic, parasympathetic, and sensory fibers that support bidirectional communication between the heart and brain. Given that a subset of macrophages resides close to cardiac nerve fibers (*30*), it will be important to determine whether there is cross-talk between macrophages and nerves in the heart that may affect heart rhythm, contractile force, and perhaps even behavior (*31*).

The vascular wall contains numerous immune cells, including macrophages and T cells, which may inhibit the clotting system (*32*). A population of embryonic resident aortic intimal macrophages use long dendrites or cellular protrusions that twist between endothelial cells, reach the bloodstream, and inhibit fibrin and thrombin deposition in turbulent blood flow areas. When intimal macrophages are deleted, mice develop peripheral microembolisms. These findings demonstrate that immune cells, relying on phagocytosis and proteolytic enzymes, preserve a clot-repelling arterial intima—a prerequisite for the undisturbed transport of all blood components.

The gastrointestinal and metabolic system

The gastrointestinal (GI) and metabolic system plays a major role in how our body handles food, absorbs nutrients, and turns those nutrients into energy sources. The system maintains body temperature through thermogenesis in body fat, regulates blood sugar by partnering with the endocrine system in the pancreas, and detoxifies substances in the liver. Immune cells, whether resident or transient, are involved in all aspects of these processes (Fig. 2). One example involves the small intestine, which adapts to dietary changes, particularly carbohydrate availability, by modulating enzymes and transporters required for carbohydrate digestion and absorption. These responses depend on resident γδ T cells, which suppress IL-22 production from type 3 innate lymphoid cells (ILC3s) to regulate nutrient sensing (*33*). Notably, ILC3-derived IL-22 dampens epithelial lipid transport (*34*), a process that is regulated by neural-ILC3 circuits (*35*, *36*). In return, nutrient availability alters the tissue localization and transcriptome of the γδ T cells, a dynamic that highlights the constant cross-talk between the environment and immune-resident cells.

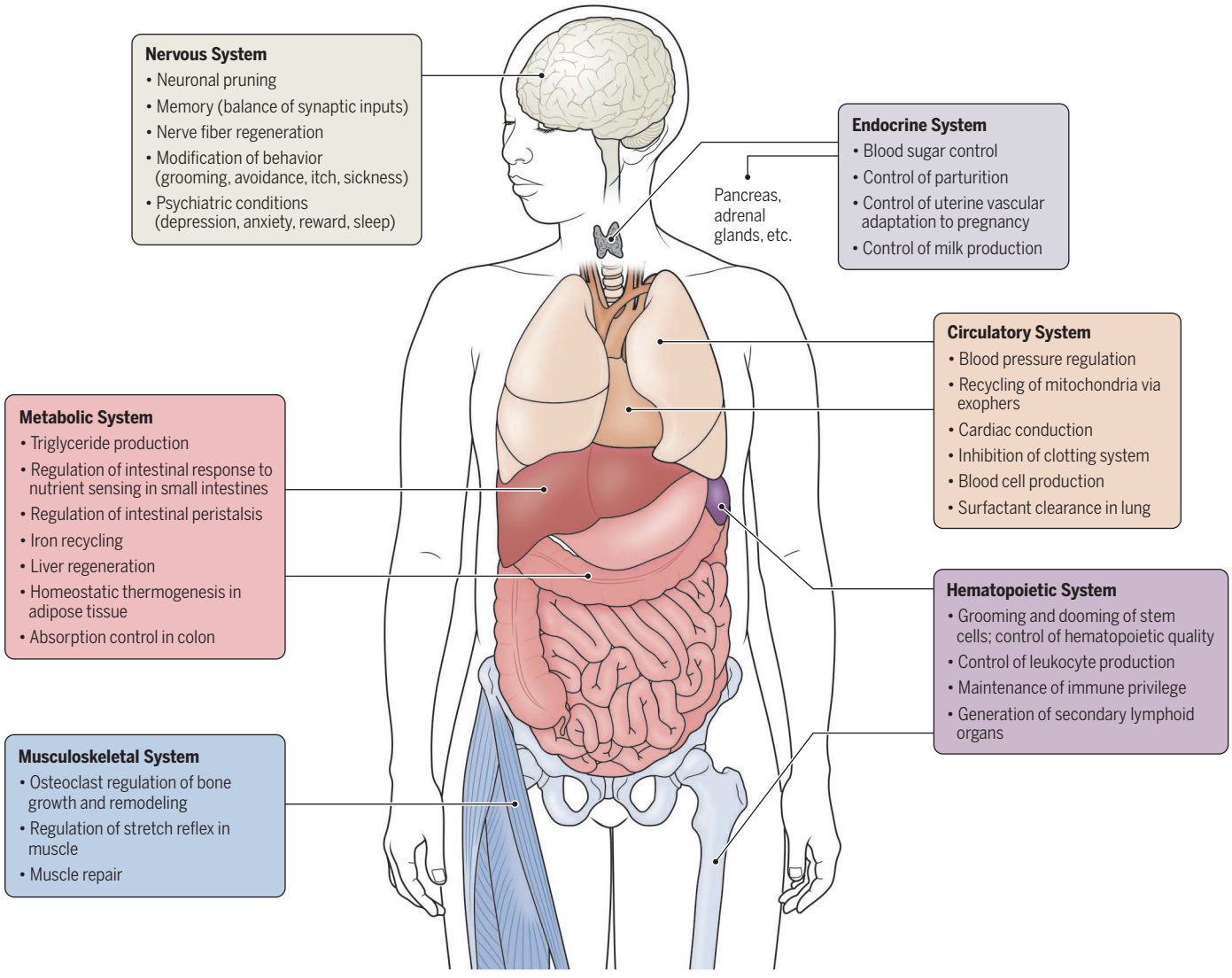


Fig. 2. The immune system's influence on physiology. Immune cells modulate physiology by interacting with various systems, including the nervous, metabolic, musculoskeletal, endocrine, circulatory, and hematopoietic. The figure, pointing to a relevant organ typically associated with a physiological system, identifies processes where immune cells have been implicated as important contributors.

Gut-resident macrophages are likewise involved in multiple specialized gut-modulating functions. Intestinal peristalsis, for instance, is influenced by dietary and microbial changes and is regulated by complex cellular interactions. A specific population of resident macrophages in the intestinal muscularis externa plays a key role in controlling colonic peristalsis (*37*). These macrophages secrete bone morphogenetic protein 2 (BMP2), which activates the receptor BMPR on enteric neurons. In response, enteric neurons produce colony-stimulating factor 1 (CSF-1), which is essential for macrophage maintenance. Microbial stimuli further regulate BMP2 and CSF-1 expression, exemplifying a dynamic, microbiota-driven interaction between muscularis macrophages and enteric neurons that governs GI motility.

Another notable example of immune participation in metabolism occurs in the colon, the tissue where the mucosa is responsible for absorbing fluids while preventing cell damage. The colon contains many fungi that produce potentially harmful metabolites during fluid absorption. It also contains a specialized group of macrophages that protect epithelial cells from these metabolites (*38*). These macrophages are equipped with balloon-like protrusions (BLPs) that extend into the epithelium to sample incoming fluids and act as quality-control agents that detect toxic substances and prevent their absorption. In the absence of such macrophages, colonocytes absorb harmful fungal products, which leads to cell death and intestinal barrier loss. These findings indicate that, in homeostasis, macrophages play a crucial sensory role in maintaining gut health and balance with the microbiota.

The liver processes nutrients; detoxifies harmful substances; and, along with the pancreas, manages blood sugar levels. Liver-resident immune cells, including macrophages named Kupffer cells (KCs), are involved in multiple aspects of liver physiology. The periportal vein (PV) zone, where blood from the gut drains to the liver, houses KCs expressing high levels of IL-10 and the scavenger receptor MARCO, which together neutralize inflammatory signals. Development of these $MARCO^+$ resident macrophages depend on gut microbiota, specifically the bacterial family *Odoribacteraceae*, which produces the postbiotic molecule isoallolithocholic acid. This gut-liver immune mechanism centered around resident PV $MARCO^+$ KCs is an important checkpoint that limits inflammation at the gateway of the liver (*39*).

Recruited immune cells can also contribute to liver physiology. One case in point is iron metabolism and erythrocyte recycling in

pathophysiological conditions, when compromised erythrocyte life span threatens the organism with anemia and iron toxicity. Recruited monocytes ingest stressed and senescent erythrocytes and differentiate into transient and damage-protective ferroportin 1 (FPN1; encoded by SLC40A1)–expressing macrophages that can deliver iron to hepatocytes (*40*). Such transient on-demand erythrocyte disposal and iron recycling protects the liver from damage. A second example involves recruited macrophages that undergo reprogramming by hepatocyte-derived glutamate during liver regeneration, leading to HIF1α stabilization and triggering WNT3 expression, which activates YAP1-driven hepatocyte proliferation (*41*). This cross-talk mechanism fine-tunes liver growth based on the body's needs and nutrient status.

Adipose tissue serves several important functions in the body, including energy storage, insulation, and temperature regulation. A specific *Cx3cr1*$^{+}$ macrophage subpopulation in brown adipose tissue (BAT) is crucial for maintaining homeostatic thermogenesis but not acute cold-induced thermogenesis (*42*). These macrophages regulate sympathetic innervation and norepinephrine levels, effects that illustrate macrophages' key role in regulating tissue innervation and metabolic balance. In white adipose tissue (WAT), resident lymphatic vessel endothelial receptor 1 (LYVE^{+}) macrophages coordinate vascular branching (*43*) and promote weight gain, glucose tolerance, and inflammation during high-fat diet (HFD). Adipose tissue–resident macrophages produce platelet-derived growth factor (PDGFcc) and control lipid storage in adipocytes in a leptin receptor– and C-C chemokine receptor type 2–independent manner (*44*). Thus, this tissue-resident macrophage population has key functions in regulating fat metabolism and metabolic syndrome.

Other tissue-resident immune cells linked to metabolic health and disease include invariant natural killer T (iNKT) cells, γδ T cells, and ILC2s. Two functional populations of iNKT cells control metabolic homeostasis in a nonredundant pathway involving IL-10 (*45*). Whereas NK1.1^{neg} cells almost exclusively produce IL-10 and other regulatory cytokines, NK1.1^{POS} iNKT cells predominantly produce interferon-γ (IFN-γ), which licenses natural killer cell–mediated macrophage killing to limit pathological macrophage expansion. Tissue-resident, IL-17–producing γδ T cells (γδ17 T cells), meanwhile, rely on the circadian clock to maintain adipose tissue homeostasis, exhibiting robust circadian rhythms that peak at night and that are essential for de novo lipogenesis in adipose tissue (*46*). Finally, IL-33–dependent WAT-resident ILC2s control adipocyte beiging by producing methionine-enkephalin peptides that augment Ucp1 (*47*). ILC2s, and particularly those residing in gonadal fat, are also dependent on sympathetic innervation that controls adipose mesenchymal cell production of glial-derived neurotrophic factor, thus illustrating yet another brain-body—and more specifically, brain-adipose—circuit (*48*).

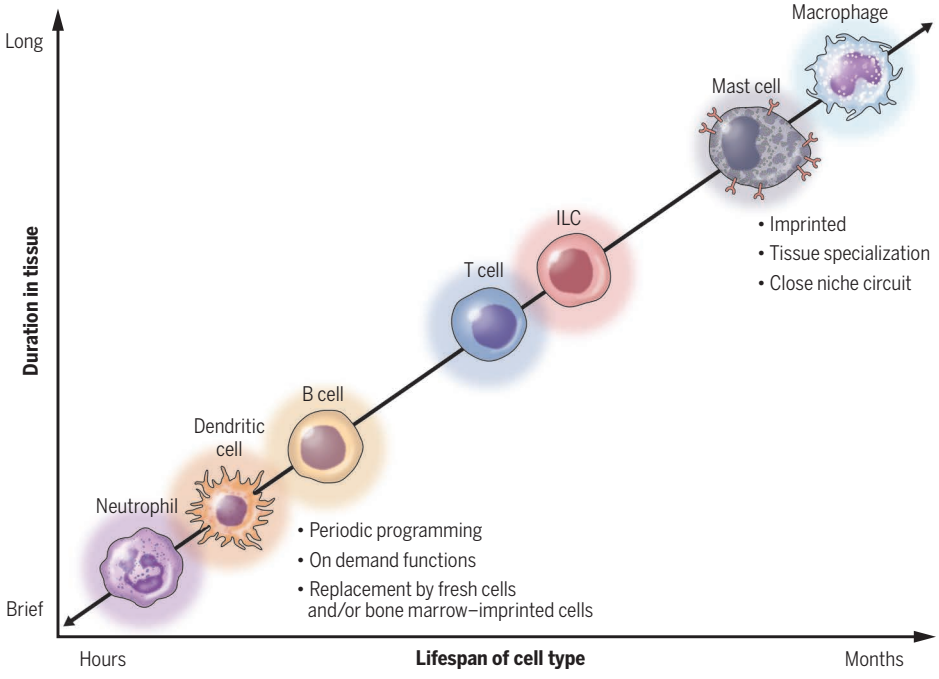


Fig. 3. Immune cell recruitment versus tissue residence. Immune cells' double property of tissue recruitment and residency endows them with the capacity to influence organ systems. Whereas some immune cells are short-lived, briefly residing in tissue, often for on-demand functions, others have very long lives, forming close niche circuits and participating in tissue specialization.

The musculoskeletal system

The musculoskeletal system, comprising bones, muscles, joints, cartilage, ligaments, and tendons, is essential for movement, support, and protection. Osteoclasts are large, multinucleated bone-resident macrophages that direct resorption of bone tissue by secreting acids and enzymes that dissolve the mineralized matrix and by breaking down collagen fibers. Osteoclasts work in concert with osteoblasts—which are cells responsible for forming new bone tissue—to keep bone structure in balance. Skeletal muscle also contains macrophage populations with diverse functions. Two recent discoveries highlight how these cells shape musculoskeletal physiology. One study, using a mouse model, described a specific population of macrophages within muscle with the ability to synthesize and release the neurotransmitter glutamate (*49*). These muscle spindle macrophages, named because of their proximity to muscle spindles and sensory proprioceptive afferents, directly modulate neural activity using glutamate and contribute to the stretch reflex, a fundamental neuromuscular circuit that coordinates motor function. A second study using zebrafish found that muscle-resident macrophages directly participate in muscle repair by interacting with satellite cells and form a transient but obligate niche necessary for stem cell proliferation. These muscle-dwelling macrophages secrete nicotinamide phosphoribosyltransferase (Nampt), which is necessary for muscle regeneration (*50*) (Fig. 2).

The endocrine system

Endocrine glands are located throughout the body and include the brain-dwelling pituitary and pineal glands as well as peripherally located glands, such as the thyroid, thymus, pancreas, adrenal, testes, and ovaries. The endocrine system is defined by its ability to produce hormones that communicate across long distances, participating in functions typically associated with the nervous system (pituitary, pineal, and adrenal), the reproductive or development and growth system (ovaries, testes, and thyroid), the metabolic system (pancreas), and the immune system (thymus). The endocrine system is therefore somewhat distinct because its defining feature is a mode of communication—hormone-dependent action at a distance—rather than an executive function, such as defense, energy processing, transportation, or motor control. That said, there are processes that fall squarely within the field of endocrinology involving recently identified immune contributions (Fig. 2).

CREDIT: K. HOLOSKI/*SCIENCE* ADAPTED FROM JILL GREGORY

One classical endocrine function is blood sugar control, which is known to be regulated by glucagon and insulin released by the pancreas. Intestine-dwelling ILC2s that express the adrenergic beta-2 receptor respond to sympathetic neural activity during fasting, which prompts their migration to the pancreas. In the pancreas, these ILCs produce IL-5 and IL-13, which stimulate α cells to secrete glucagon, thus increasing gluconeogenesis in the liver. This mechanism, whereby immune cells control a key endocrine function, also engages the nervous system, emphasizing how multiple systems commingle (*51*).

Another noteworthy context in which immune cells influence endocrine function is during and shortly after pregnancy. Birth is largely under endocrine control and involves progesterone, estrogen, oxytocin, prostaglandins, and cortisol, all of which derive from endocrine glands. Mice that are deficient in ILC2s experience severe parturition delays when luteolysis is circumvented. Parturition involves the cytokines IL-33 and IL-5 as well as eosinophils, which suggests that ILC2s contribute to the physiological processes required for giving birth (*52*). T_{reg} cells, which are essential for maternal immune tolerance of the fetus and placenta, appear to be vital upstream drivers of uterine vascular adaptation to pregnancy (*53*). During breastfeeding, intraepithelial lymphocytes (IELs) control milk production by favoring the differentiation and maturation of contractile and milk-secreting cells, thus promoting the fitness of offspring (*54*). These findings, again, illustrate how immune cells, most commonly understood as the first line against infection and injury, connect systems and influence physiology.

The hematopoietic system and immune system housekeeping

In addition to interacting with multiple other physiological systems, the immune system also interacts with, and regulates, itself. The development and maturation of immune cells begins in the bone marrow, where immune cells develop from hematopoietic stem cells. Recent work has shown that, in developing zebrafish and mice, macrophages enforce hematopoietic stem cell quality (*55*). During direct contact with blood stem cells, macrophage–stem cell interactions—described as grooming or dooming—have profound consequences for stem cell fate. Macrophages either ingest small parts of a stem cell, which then emerges unscathed and ready to divide, or engulf and kill the stem cell altogether if its surface expresses the "eat-me" molecule calreticulin, a sign of high reactive oxygen species content in the doomed cells. This stem cell selection by macrophages shapes the blood cell repertoire in adulthood (Fig. 2).

Immune cells often control hematopoietic output in collaboration with the nervous system. The bone marrow hematopoietic niche, which consists of various mesenchymal and stromal cells that integrate long-range signals from the body, shapes stem cell proliferative activity and lineage bias. B lymphocytes, for instance, produce the neurotransmitter acetylcholine in the bone marrow—which, like the spleen, may lack parasympathetic innervation—and curb inflammatory leukocyte production by acting on niche cells through the canonical hematopoietic factors CXCL12 and Angpt1 (*23*). B cell–specific deletion of choline acetyltransferase, an enzyme essential for acetylcholine synthesis, expands myeloid cells in steady state but also curbs emergency hematopoiesis after acute myocardial infarction, dampening cardiovascular inflammation. In agreement with these findings in mice, patients treated with donepezil, a drug that augments acetylcholine signaling, have lower blood leukocyte counts. A second example involves a strategically located preneutrophil that senses hypocretin (also known as orexin), a hypothalamic neuropeptide best known for promoting wakefulness (*19*). These preneutrophils, which reside in a hematopoietically proliferative medullary environment, are abundant sources of CSF-1, a cytokine required for monocyte production. During the active period when orexin levels are high, preneutrophil CSF-1 decreases, thus lowering monocyte production. This helps to explain why myelopoiesis follows a circadian rhythm but why, during sleep fragmentation when orexin levels decline, monocytosis ensues.

Outside of the bone marrow, there is evidence that immune cells participate in the formation of secondary lymphoid organs necessary for adaptive immune processes. For example, $ROR\gamma t^+$ lymphoid tissue inducer (LTi) cells, which are $CD4^+$ $CD3^-$ IL-7Rα^+ hematopoietic cells, are required for the development of lymph nodes and Peyer's patches (*56*). Generation of these LTi cells is controlled by maternal retinoid intake and fetal retinoid acid signaling, thus linking dietary intake during pregnancy with the ability of hematopoietic cells to control secondary lymphoid production and, by extension, immune fitness of the progeny (*57*).

Conclusions

This Review has explored how circulating and tissue-resident leukocytes contribute to various physiological systems. Although our discussion was not exhaustive—we have not specifically addressed the developmental or urinary systems, for example—our focus on the six included systems and their representative organs reveals that immune influence depends on at least three features of leukocyte biology. First, leukocytes are explorers, and unlike tourists, who are definitionally transient, explorers can colonize and establish settled populations. Other cells commit to one spatial fate: Erythrocytes only circulate, whereas endothelial cells, smooth muscle cells, and even neurons with long projections—as in the vagus and sciatic nerves—remain in one place. Leukocytes' ability to circulate or settle endows the immune system with exceptional resilience and rejuvenation capacity because long-lived tissue-resident cells damaged or rendered senescent within a particular organ can be replaced with bone marrow–derived circulating cells. Aging's effects on the bone marrow notwithstanding, this replenishment pipeline is a powerful component of leukocyte resilience (Fig. 3). Second, leukocytes are distinctive yet chameleonic. Leukocytes clearly have a core identity. But even though their operational range across organs includes classic functions, such as phagocytosis, leukocytes fulfill functions specifically tailored to the organ in which they reside and the system to which they contribute. Third, this is possible because, although leukocytes speak a core language, they are also polyglots capable of communicating across systems. As residents of nearly all tissues adapting to their adopted organs, leukocytes are notably interactive, communicating not only with each other but also with nearly every other circulating and structural cell. This connectivity allows immune cells to sense and influence processes far beyond their immediate sphere of influence. These tension-imbued leukocyte features—circulating and resident, individualistic yet changeable, and multilingual—render leukocytes exceedingly proficient system connectors. Leukocytes are, in a way, the lingua franca protagonists of the human body.

Leukocytes' ability to circulate or settle endows the immune system with exceptional resilience and rejuvenation capacity...

Along these lines, one could consider the immune system as the most ancient of systems, perhaps even older than the nervous system. Bacteria and sponges, whose evolutionary clades separated from that of humans 2 billion and 700 million years ago, respectively, have rudimentary immune systems but lack many others. The existence of an immune system across the domains of life may therefore explain why the immune system is so entangled with mammalian physiology and why it participates in virtually every disease. Pathologies accrue, especially aging-related diseases, such as cardiovascular and neurodegenerative, and the immune system, with its inflammatory arm, is a common denominator. Given these insights, it is more important than ever that therapeutic strategies targeting the immune system consider not only the effect that treatments will have on the focal

disease cluster but also their myriad consequential effects on various physiological systems.

REFERENCES AND NOTES

1. J. E. Blalock, E. M. Smith, *Brain Behav. Immun.* **21**, 23–33 (2007).
2. A. F. Salvador, K. A. de Lima, J. Kipnis, *Nat. Rev. Immunol.* **21**, 526–541 (2021).
3. D. P. Schafer *et al.*, *Neuron* **74**, 691–705 (2012).
4. K. Kim *et al.*, *Cell* **188**, 2705–2719.e23 (2025).
5. J. Kolter *et al.*, *Immunity* **50**, 1482–1497.e7 (2019).
6. G. B. Choi *et al.*, *Science* **351**, 933–939 (2016).
7. S.-K. Chen *et al.*, *Cell* **141**, 775–785 (2010).
8. E. B. Florsheim *et al.*, *Nature* **620**, 643–650 (2023).
9. F. Wang *et al.*, *Cell* **184**, 422–440.e17 (2021).
10. J. Meixiong *et al.*, *Immunity* **50**, 1163–1171.e5 (2019).
11. A. H. Miller, C. L. Raison, *Nat. Rev. Immunol.* **16**, 22–34 (2016).
12. K. Alves de Lima *et al.*, *Nat. Immunol.* **21**, 1421–1429 (2020).
13. D. B. McKim *et al.*, *Mol. Psychiatry* **23**, 1421–1431 (2018).
14. F. Cathomas *et al.*, *Nature* **626**, 1108–1115 (2024).
15. J. M. Garré, H. M. Silva, J. J. Lafaille, G. Yang, *Nat. Med.* **23**, 714–722 (2017).
16. M. Xia *et al.*, *Immunity* **58**, 218–231.e12 (2025).
17. P. Huynh *et al.*, *Nature* **635**, 168–177 (2024).
18. M. Rosas-Ballina *et al.*, *Science* **334**, 98–101 (2011).
19. C. S. McAlpine *et al.*, *Nature* **566**, 383–387 (2019).
20. M. Hulsmans *et al.*, *Cell* **169**, 510–522.e20 (2017).
21. M. A. Cox *et al.*, *Science* **363**, 639–644 (2019).
22. P. S. Olofsson *et al.*, *Nat. Biotechnol.* **34**, 1066–1071 (2016).
23. M. J. Schloss *et al.*, *Nat. Immunol.* **23**, 605–618 (2022).
24. É. Midavaine *et al.*, *Science* **388**, 96–104 (2025).
25. H. H. Luan *et al.*, *Cell* **178**, 1231–1244.e11 (2019).
26. B. C. Trapnell, J. A. Whitsett, *Annu. Rev. Physiol.* **64**, 775–802 (2002).
27. A. Chow *et al.*, *Nat. Med.* **19**, 429–436 (2013).
28. J. A. Nicolás-Ávila *et al.*, *Cell* **183**, 94–109.e23 (2020).
29. J. Grune *et al.*, *Nat. Cardiovasc. Res.* **1**, 649–664 (2022).
30. S. Chakarov *et al.*, *Science* **363**, eaau0964 (2019).
31. B. Hsueh *et al.*, *Nature* **615**, 292–299 (2023).
32. G. E. Hernandez *et al.*, *Nat. Cardiovasc. Res.* **1**, 67–84 (2022).
33. Z. A. Sullivan *et al.*, *Science* **371**, eaba8310 (2021).
34. K. Mao *et al.*, *Nature* **554**, 255–259 (2018).
35. C. Godinho-Silva *et al.*, *Nature* **574**, 254–258 (2019).
36. J. Talbot *et al.*, *Nature* **579**, 575–580 (2020).
37. P. A. Muller *et al.*, *Cell* **158**, 300–313 (2014).
38. A. S. Chikina *et al.*, *Cell* **183**, 411–428.e16 (2020).
39. Y. Miyamoto *et al.*, *Nature* **629**, 901–909 (2024).
40. I. Theurl *et al.*, *Nat. Med.* **22**, 945–951 (2016).
41. M. D. M. Rigual *et al.*, *Nature* **641**, 1005–1016 (2025).
42. Y. Wolf *et al.*, *Nat. Immunol.* **18**, 665–674 (2017).
43. H. Moura Silva *et al.*, *Sci. Immunol.* **6**, eabg7506 (2021).
44. N. Cox *et al.*, *Science* **373**, eabe9383 (2021).
45. N. M. LaMarche *et al.*, *Cell Metab.* **32**, 243–258.e6 (2020).
46. A. Douglas *et al.*, *Nature* **636**, 206–214 (2024).
47. J. R. Brestoff *et al.*, *Nature* **519**, 242–246 (2015).
48. F. Cardoso *et al.*, *Nature* **597**, 410–414 (2021).
49. Y. Yan *et al.*, *Nature* **637**, 698–707 (2025).
50. D. Ratnayake *et al.*, *Nature* **591**, 281–287 (2021).
51. M. Šestan *et al.*, *Science* **387**, eadi3624 (2025).
52. J. Siewiera *et al.*, *Immunity* **56**, 606–619.e7 (2023).
53. S. L. Hosking *et al.*, *JCI Insight* **10**, e169836 (2024).
54. D. Corral *et al.*, *Cell* **188**, 1662–1680.e24 (2025).
55. S. J. Wattrus *et al.*, *Science* **377**, 1413–1419 (2022).
56. G. Eberl *et al.*, *Nat. Immunol.* **5**, 64–73 (2004).
57. S. A. van de Pavert *et al.*, *Nature* **508**, 123–127 (2014).

ACKNOWLEDGMENTS

Illustrations were created by J. K. Gregory, MFA, at Mount Sinai. Editing was done by K. Joyes, PhD, at Mount Sinai. **Funding:** This review was funded by National Institutes of Health grants P01HL142494, R35HL176359, and R37NS136068 (to M.N.); National Institutes of Health grants P01HL142494 and P01 HL131478 (to F.K.S.); Fondation Leducq 24CVD01 (to M.N.); Fondation Leducq 20CVD01 (to F.K.S.); and Deutsche Forschungsgemeinschaft (DFG) no. 453989101 SFB 1525, Mercator fellow (to M.N.). **Author contributions:** M.N., F.G., and F.K.S. researched the literature and wrote the manuscript. **Competing interests:** The authors declare that they have no competing interests. **License information:** Copyright © 2025 the authors, some rights reserved; exclusive licensee American Association for the Advancement of Science. No claim to original US government works. https://www.science.org/about/science-licenses-journal-article-reuse

Submitted 24 April 2025; accepted 19 June 2025

10.1126/science.adx4380

EVOLVING IMMUNITY

REVIEW

Sex differences in tissue-specific immunity and immunology

Sonia Sharma[1,2]*, Alicia Gibbons[1,3], Erica Ollmann Saphire[1,3]

Biological sex exerts a substantial influence on the immune system and immune-related diseases. Males are more susceptible to the acute effects of viral disease and certain cancers, whereas females exhibit a more robust immune response that can make them prone to developing autoimmune complications. We reflect on the emerging appreciation of sex differences—governed by genetics, sex hormones, and environmental factors—in tissue immunity and immunology. Understanding these tissue context–dependent sex differences in the immune system is critical to deciphering the exact mechanisms that determine why women and men experience organ-specific infections, autoimmune or inflammatory diseases, and cancers differently. Only by parsing distinction at the tissue level can the development of personalized and precision immunotherapy approaches be conceived and then achieved.

Many sex-specific differences in immune responses have been observed. A plethora of evidence supports the central paradigm that infectious diseases disproportionally affect males in terms of susceptibility, severity and morbidity (*1*). Males suffer from increased severity and higher rates of death from acute viral and microbial infections and infection-associated cancers. Females generally fare better against infectious diseases, but their stronger overall immune response translates to greater susceptibility to autoimmune diseases and certain inflammatory conditions. Females are also more prone to long-term or chronic effects of infection, termed postacute sequelae, recognized as bona fide autoimmune or inflammatory-adjacent conditions (*2*), with symptoms including diffuse pain, joint pain, pulmonary fibrosis, and cognitive decline. These observations both demonstrate and establish clinically impactful sex differences in immune diseases and immunology. Understanding context- and tissue-dependent sex differences in the immune system is critical for advancing beyond the observation that males and females exhibit different immune responses to harnessing this information for better diagnosis, treatment, and prevention of disease.

Sex differences in immunity result from the contributions and interplay of genetics and hormonal and environmental factors. Immune cells reside in every organ and tissue, where they have distinct functions to shape cell-cell interactions, tissue development, homeostasis, and pathology; therefore, the function of each type of immune cell must be interpreted in its cell and tissue context. In this study, we consider the role that tissue-specific immunity plays in sex differences of the immune system, which is now being uncovered in immune-sentinel organs, such as the lung, fat, skin, intestine, and brain.

[1]La Jolla Institute for Immunology, La Jolla, CA, USA. [2]Laboratory for Inflammatory Immune Metabolism, RIKEN Center for Integrative Medical Sciences, Yokohama City, Kanagawa, Japan. [3]Department of Medicine, University of California San Diego, La Jolla, CA, USA. ***Corresponding author. Email: soniasharma@lji.org**

Genetic, hormonal, and environmental factors that impact immunity

The impact of biological sex on the immune system is defined by sex differences associated in both nonimmune and immune cells and further shaped by tissue-specific contexts (Fig. 1). Biological sex is defined by the classification of genotype XX as female and XY as male. Rarer genotype variations include individuals harboring XXY, XYY, or XO genotypes, which have been demonstrated to influence susceptibility to immune diseases (*3*). Autoimmune manifestations, such as systemic lupus erythematosus, Sjögren's syndrome, and scleroderma, are associated with increased X chromosome dosage and indicate a direct role for the X chromosome in modulating immunity.

The human X chromosome is approximately three times larger than the Y chromosome and carries ~800 more protein-coding genes enriched for immune function (*4*). To maintain X chromosome gene dosage equilibrium between XX females and XY males, in female cells, transcription from most genes is silenced from one of the two X chromosomes through a process called X chromosome inactivation. Approximately 23 to 30% of genes on that second inactive X (Xi) chromosome, however, actually escape inactivation. For some genes, escape from inactivation is tissue specific (*5*, *6*). Tissue-specific X chromosome escape genes include *ZBED2*, which encodes a transcription factor that regulates T cell exhaustion in tumors, and *USP11*, which regulates the activity of immune-suppressive regulatory T cells (T_{reg}). For other genes, escape from inactivation is constant; the second copy is never silenced. Some genes that always escape inactivation encode proteins that are involved in the activation of both the innate (early) and adaptive (later) immune responses. Some of the genes that always escape inactivation are present on both X and Y in homologous "pseudoautosomal" regions. For these genes, escape from inactivation prevents the haploinsufficiency of genes important for development and survival (*7*) that would otherwise occur with complete inactivation on an X. Other genes that escape inactivation may have a benefit to enhanced expression. *TLR7*, for example, an innate immune gene involved in recognizing microbial nucleic acids, is encoded only on the X but often escapes inactivation, providing females with two active copies (*8*).

In addition to X chromosome inactivation, many tissues, including the breast, subcutaneous fat, thyroid, skeletal muscle, and skin, display sex-specific differentially expressed genes (DEGs) and gene regulatory networks. These DEGs are derived from both the X chromosome and autosomal genes alike and have been functionally annotated across diverse biological processes, including the immune response. For example, all female tissues have universal enrichment in DNA- and RNA-binding proteins that recognize polypurine tracts. In the immune system, polypurine tracts are sequences involved in replication of human endogenous retroviruses (hERVs), remnants of ancient retroviruses that became integrated into the human genome during evolution and play a role in antimicrobial and antitumor innate immunity as well as in autoimmune disease (*9*). Female tissues have universal enrichment for genes encoding proteins involved in the innate immune antiviral response, including those involved in RNA processing in the innate immune system. Meanwhile, male tissues show sex-specific DEGs that denote universal deenrichment of T cell–mediated immunity (*10*). Xi escape and these sex-specific DEG patterns provide evidence for the role of the chromosomal complement in modulating immunity.

Sex hormones—estrogens, progesterones, and androgens—can influence how genes are regulated and expressed (*11*, *12*). Sex hormone levels differ between males and females and across varying life stages and, for females in particular, at different stages in the monthly menstrual cycle as well as with use of hormonal birth control and hormone replacement therapy. The changing influence of hormones is partly responsible for the plasticity of sex-based differences in immunity.

Both nonimmune and immune cells can respond to sex hormones. Cells of the peripheral and tissue-resident immune system express estrogen receptors (ERα and ERβ), androgen receptors (ARs), and progesterone receptors (PRs) and respond directly to sex hormone

signaling in a cell and tissue-specific manner. Cell-intrinsic responses of innate and adaptive immune cell populations to ER, AR, and PR signaling are well documented (Fig. 2) (*11*, *13*). In general, the immune-stimulatory effects of estrogen contrast with the immunosuppressive effects of testosterone, a finding that appears to hold true for both circulating and tissue-infiltrating immune cell populations.

More complex to understand is the potential impact of extrinsic environmental factors, including nutrition and behavior across the human life course, composition of the gut or skin microbiome, chemical exposures, and aging, all of which vary across individuals and may all impact immune diseases in a sexually divergent manner. Perhaps the best characterized environmental impact is that males and females have different steady-state gut microbiome compositions and that sex-specific differences in the microbiome influence the development of autoimmune disease in animal models (*14*). The skin microbiome also differs by sex in both composition and diversity (*15*).

Overall, sex biases in the function of the immune system are shaped by genetic, hormonal, and environmental influences that manifest in both immune and nonimmune cells.

Understanding context- and tissue-dependent sex differences in the immune system is critical for... better diagnosis, treatment, and prevention of disease.

Differences between immune cell subtypes in males and females

There is a clear sex bias in the composition and phenotypes of both circulating and tissue-resident immune cells. For example, the circulating T cell population in females exhibits a higher CD4:CD8 ratio compared with that in males (*16*), a skew that is associated with enhanced immune function and autoimmune disease (*16*, *17*). The lower CD4:CD8 ratio in males is also considered an immune risk phenotype, and within each sex, a lower CD4:CD8 ratio is associated with immune senescence. Accordingly, CD8+ T cells isolated from males have a less activated phenotype than those isolated from females ex vivo *(18)*.

These findings extend to long-lived CD8+ tissue resident memory T cells (Trm), which reside permanently in various tissues, providing first-line protection from infections and neoplasms at the barrier sites, and are more plentiful in the gut and skin of female mice than in that of male mice (*19*). Analysis of leukocyte distributions in the pleural and peritoneal cavities of mice also indicates that sex differences in T lymphocyte numbers may be less pronounced in the blood compared with other tissues (*20*).

Total B cell numbers are generally comparable between the sexes, but females tend to display increased numbers of class-switched and memory B cells, which are hyperefficient at producing antibodies. Therefore, females have the potential to mount a broader and more effective antibody response than males, particularly after reencountering a pathogen. This increased number of class-switched cells emerges in females between puberty and menopause, indicating a regulatory role for estrogen in B cell development (*21*).

Among innate immune cells, neutrophils, the most abundant proinflammatory cells in the blood, are slightly but significantly elevated in number in females (*22*). This effect is related to hormonal influences, as estrogen and testosterone levels demonstrate positive and negative correlation with neutrophil counts, respectively, and premenopausal women have higher blood neutrophil numbers compared with postmenopausal women. Neutrophils exposed to estradiol and progesterone are less apoptotic (*23*), and this phenotype is associated with longevity and tissue residency. Estrogen also appears to promote the effector functions of neutrophils, notably, their recruitment to sites of tissue inflammation. By contrast, nonclassical or "patrolling" monocytes, which can perform both anti- or proinflammatory functions depending on the particular disease context, are threefold more abundant in the blood of adult males (*24*). As in the adaptive immune system, higher numbers of innate cells do not necessarily confer augmented immune or antiviral activity, as increased numbers of circulating natural killer (NK) cells measured in male mice contrast with augmented NK cell activity in the females (*25*), which produced higher levels of the inflammatory antiviral cytokine interferon-γ (IFN-γ) after virus infection.

In mice, barrier tissue-resident group 2 innate lymphoid cells (ILC2s), which play important roles in parasitic infection and allergic inflammation, are negatively affected by androgen signaling and, as a result, ILC2 counts are lower in males and higher in females across multiple tissues (*26*). These innate lymphoid cells play key roles in cytokine secretion, infections, allergy, tissue homeostasis, and barrier functions. In the skin, the number and function of ILC2 are suppressed by androgen signaling, which in turn suppresses dendritic cell (DC) accumulation and activation (*27*). In the lung, adult female mice have higher ILC2 counts and phenotypically distinct ILC2 compared with adult male mice, and in humans, women with asthma have a higher number of ILC2 in the peripheral blood compared with men (*28*).

Plasmacytoid dendritic cells (pDCs) are key players in acute inflammation that produce high levels of antiviral type I IFN cytokines in response to infection. Type I IFN production occurs downstream of stimulation of the TLR7 receptor encoded by the Xi escape gene *TLR7*. Accordingly, female pDCs produce higher IFN-α across all life stages (*29*). Production of type I IFN is thought to be protective against COVID-19 pneumonia, which may partially explain its male bias in prevalence (*30*).

Sex differences vary by tissue, and indeed, a study of 11 murine immune cell types revealed that the greatest sex differences in transcriptomics or epigenetics occurred between the same cell type (i.e., macrophages) from different tissues rather than between different immune cell types from the same tissue. As the mice were housed under identical environmental conditions, these findings truly underscore sex dimorphism in the absence of sizable environmental differences (*31*). Furthermore, the sex biases in immune cell composition can vary by tissue: Adult female mice have higher counts of skin-resident T cells than males but not in the small intestine or the ear-draining lymph nodes (*27*).

Why are there sex differences in immune cell count and functionality, and why are these differences tissue-specific? Different tissues serve specialized immunological roles shaped by their anatomical location and biological function. Because different tissues are exposed to distinct pathogens and, in some cases, commensal microorganisms, they must be functionally adapted to meet those distinct immunological demands. Stronger antipathogen responses in females may protect them through their childbearing and -rearing years at the expense of autoimmune disease later in life, and functional adaptation to these local demands likely contributes to sex- and tissue-specific immune phenotypes.

Pathogen infection, control, and pathology in barrier tissues

Barrier tissues of the skin, respiratory tract, and gastrointestinal tracts are critical immunological frontlines that provide the first line of defense against invading pathogens. The mouse skin, lung, and intestine demonstrate sex-biased immune cell populations and phenotypes. In the skin and lung, the observed differences are sex hormone dependent (*27*) (*28*).

A recent example of sex bias in disease severity and outcome is in COVID-19, where males have both more severe disease and higher rates of death. A meta-analysis of single-cell RNA sequencing datasets derived from human lung biosamples demonstrated sex-, age-, and smoking-related biases in the expression levels of genes encoding the

severe acute respiratory syndrome coronavirus 2 (SARS-CoV-2) entry factors *ACE2*, *TMPRSS2*, and *CTSL*, which were elevated in males (*32*). In mice expressing the human variant of the SARS-CoV-2 viral entry receptor ACE2, after infection with the SARS-CoV-2 virus, male mice displayed higher expression of viral proteins in the lung tissue and demonstrated a more pronounced decline in body weight and higher lung injury scores compared with female mice (*33*). SARS-CoV-2 infection resulted in decreased ERα in the lung tissue of male mice, with levels of ERα restored after protective recombinant ACE2 inhalation, suggesting a sex hormone contribution to protection from SARS-CoV-2 downstream of ACE2 signaling.

Despite enhanced SARS-CoV-2 entry and replication in cells of male lung, the cellular innate immune antiviral response is blunted in this organ. A study of SARS-CoV-2 vaccine-naïve patients, sampled during the first wave of the COVID-19 pandemic, found lower expression and activity of adenosine deaminase 2 (ADA2) in female biosamples (*34*). ADA2, a conserved catabolic enzyme that inhibits the antimicrobial response, down-regulates expression of the antiviral cytokine type I IFN-β by inhibiting the expression of IFN-β–stimulating hERV transcripts (*35*). Bronchoalveolar lavage fluid–derived myeloid cells from female COVID-19 patients displayed lower *ADA2* transcripts compared with those from males (*34*) Accordingly, higher hERV and interferon-stimulated gene (ISG) expression was detectable in female lung epithelial cells. Despite higher ADA2 activity in the blood of males, sex-specific differences in hERVs were specific to lung tissue.

Impact of sex hormones on immune cell networks in tissues

Productive immune responses typically require the coordinated activity of immune cell networks. As such, sex differences observed in individual immune cell populations and functions are likely a consequence of broader, sex-based differences in immune networks. Transcriptomic analyses have revealed that specific gene set signatures are enriched between different sexes. Recent studies in specific tissues have begun to map these sex-based differences in immune cell networks, and sex-biased immune networks involving different immune cells as well as nonimmune immune interactions have been described (*36*).

In mice, the skin of adult females display higher numbers of classical T cell subsets and resident dendritic cell subsets (*27*). These sex differences in skin-associated T cells also occur in germ-free mice, suggesting that the sex bias in skin T cell numbers is independent of the presence or absence of a microbiome. The authors found that male sex hormones, through androgen receptor signaling, negatively regulate the innate lymphoid ILC2s abundant in skin, which suppress dendritic cell accumulation and activation, disrupt DC priming of T cells, and influence immune response in the skin (*27*). Although sex bias in T cell number also occurs in germ-free mice, it will influence bacterial colonization in conventionally raised mice; this study mechanistically demonstrates that sex hormone–based signaling can directly alter the host response to commensal and pathogenic microorganisms in mice.

Furthermore, biological sex can influence the interactions between immune and nonimmune cells (Fig. 2). Many nonimmune cells, including endothelial cells, adipocytes, fibroblasts, and keratinocytes, directly respond to sex hormones. The effects of sex hormone signaling in nonimmune cells can impact immune cells in multiple ways. For example, estrogen signaling in endothelial cells promotes vasodilation, which can influence immune cell trafficking, and reduces endothelial proinflammatory cytokine release, which can influence immune cell phenotype (*37*). Nonimmune sex hormone signaling can directly affect tissue immunity: upon knockdown of ERα in adipocytes, male but not female mice had increased expression of macrophage marker F4/80 in their adipose tissue, suggesting macrophage infiltration (*13*). This work demonstrates that sex biases in immunity can also be mediated by non-immune cells.

Sex differences in immune cell–mediated tissue homeostasis

Beyond response to external challenges, such as pathogens and commensal microbes, the immune system has critical roles in maintaining internal homeostasis. Here, we use the example of adipose tissue, which functions as a critical mediator of metabolic health, as well as an energy reservoir and an established immunological organ with a tissue-specific immune system. Adipose tissue is also well characterized as a sexually dimorphic tissue, with established differences in tissue distribution, immune makeup, inflammation, and metabolic signaling depending on sex (*38*). Adipocytes express ERα, ERβ, and AR, and sex hormone signaling through these receptors plays a key role in the phenotype and response to overnutrition-induced inflammation (*39*). Males and females accumulate excess energy into different adipose tissue deposits located at different sites of the body. For example, adult males tend to accrue more visceral adipose tissue (VAT) than adult females, a trend that is preserved in high-fat diet–fed diet-induced obesity C57BL/6J mice (*40*). Menopause in females, characterized by a decline in estrogen levels, is accompanied by a shift from predominantly subcutaneous adipose storage to visceral adipose storage and subsequent metabolic dysfunction in both depots. Whole-body ERα-knockout mice also have adipocyte hyperplasia and hypertrophy, insulin resistance, and glucose intolerance in both sexes in addition to increased VAT accumulation (*41*). Metabolic syndrome is more prevalent in males until the ages of 50 to 60. At the age of menopause, metabolic syndrome becomes more prevalent in females. Together, these studies underline an important role for estrogen signaling in protecting the deleterious effects of VAT storage.

Two distinct subpopulations of VAT T_{reg} cells have been described in mice: ST2+ and CXCR3+ (*42*). ST2+ T_{reg} cells are enriched in males and

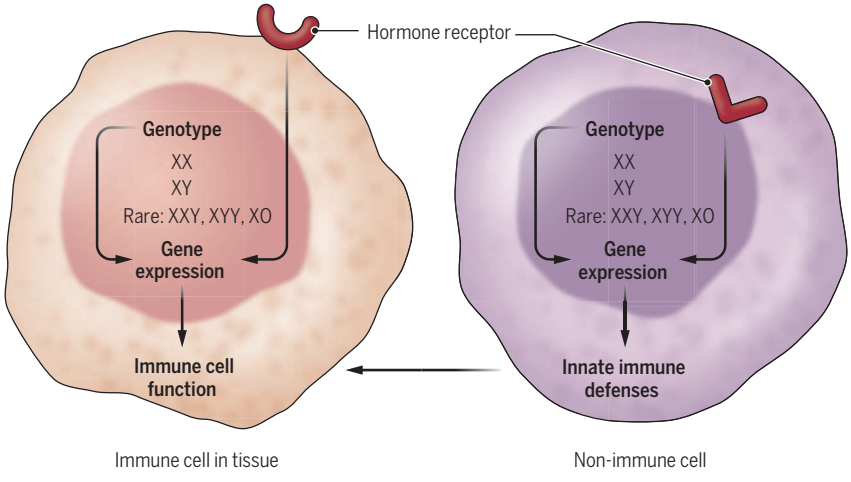


Fig. 1. The impact of sex on immune cells. The activities of both nonimmune and immune cells are influenced by hormones, sex chromosome genotype, and neighboring cells resident in the tissue. The overall impact on immune cell differentiation and function in tissues will reflect direct, cell-intrinsic effects on immune cells as well as indirect influences on immune cell function mediated by tissue-specific nonimmune cells.

are associated with glucose homeostasis, whereas CXCR3+ T_{reg} cells are enriched in females and are linked to inflammation control. Male ST2+ T_{reg} cells are present in higher numbers in lean male mice and transcriptionally distinct from those of female mice. Male ST2+ VAT T_{reg} number and profile are also dependent on androgen signaling, and, notably, knockout of ERα in female mice results in an increase in ST2+ VAT T_{reg} cells that display the phenotype of male VAT T_{reg} cells (*42*). In high-fat diet–fed obese mice, ST2+ VAT T_{reg} counts decrease in male mice and increase in female mice with no change in high-fat diet–fed ovariectomized female mice, suggesting a role for these T_{reg} cells in protecting female mice from obesity-induced VAT inflammation.

Balancing homeostasis with productive inflammation is a delicate act, and if dysregulated, autoimmunity and cancer can occur. In general, males exhibit higher rates and worse prognoses for nonreproductive cancers compared with females, with contributions from both sex and environmental factors. The tumor microenvironment is a distinct immunological niche with complex interactions between pro- and antitumor immune cells, stromal cells, and tumor cells. Sex hormone signaling is important in tumor development and cancer treatment efficacy in preclinical murine models. Estrogen signaling has been demonstrated to promote the actions of protumoral myeloid cells (*43*) and the depletion of antitumoral eosinophils (*44*). In males, androgen signaling promotes the transition of stemlike CD8+ T cells to terminally exhausted CD8+ T cells (*45*). There also exists an AR signaling–based male bias in the frequency of T progenitor exhausted cells, which are implicated in response to anti–PD-1 immune checkpoint blockade (*46*), perhaps explaining why males respond better to this therapy.

Developmental differences and their impact on tissue immunology

Sex-based differences in immunity might also stem from developmental processes that shape tissue structure and composition. In human lungs, sex-based differences in lung structure and respiratory function are observed as early as 16 to 24 weeks gestation and continue into adulthood (*47*). Prepubescent boys show increased prevalence and severity of asthma compared with that in age-matched girls, although, among adults, asthma afflicts adult females more frequently. Puberty introduces a range of sex-specific changes, including airway remodeling, shifts in sex hormone levels, and behavioral changes, all of which are implicated in adult asthma (*48*).

The brain is also a developmentally sexually dimorphic organ, with brain tissue or region size and composition differing by sex. Multiple cell types express sex hormone receptors, and sex hormones have effects on innate immune microglia cells in distinct regions of the brain (*49*). Microglia from the brains of healthy adult male and female mice have distinct transcriptional signatures at steady state, independent of estrogen (*49*). In this study, female murine microglia transplanted into microglia-depleted adult mouse male brains maintained a female-specific expression profile similar to that of control females 5 days after transplantation, suggesting a genetic or epigenetic basis of sex differences (*49*). Induction of murine middle cerebral artery occlusion in mice revealed higher damage in males at 24 and 48 hours. Transfer of female microglia into male brains, but not male microglia into female brains, reduced damage at both time points (*49*). Lipopolysaccharide-treated hippocampal microglia from adult mice also have sexually different gene signatures, perhaps owing to developmental differences (*50*). These studies demonstrate a role for both genetics and sex hormone signaling in sex-specific programming of microglia and brain development.

Conclusions

The impact of biological sex in the function of immune cells and the pathogenesis of immune diseases is complex. Understanding how sex differences impact the function of cells of the immune system is still at early stages, and understanding how that knowledge can be exploited and translated into therapeutic benefits remains to be realized. As immunotherapies move beyond standardized approaches and toward a realization that individuals respond differently to treatments, key factors, such as sex dimorphism, must guide decisions about

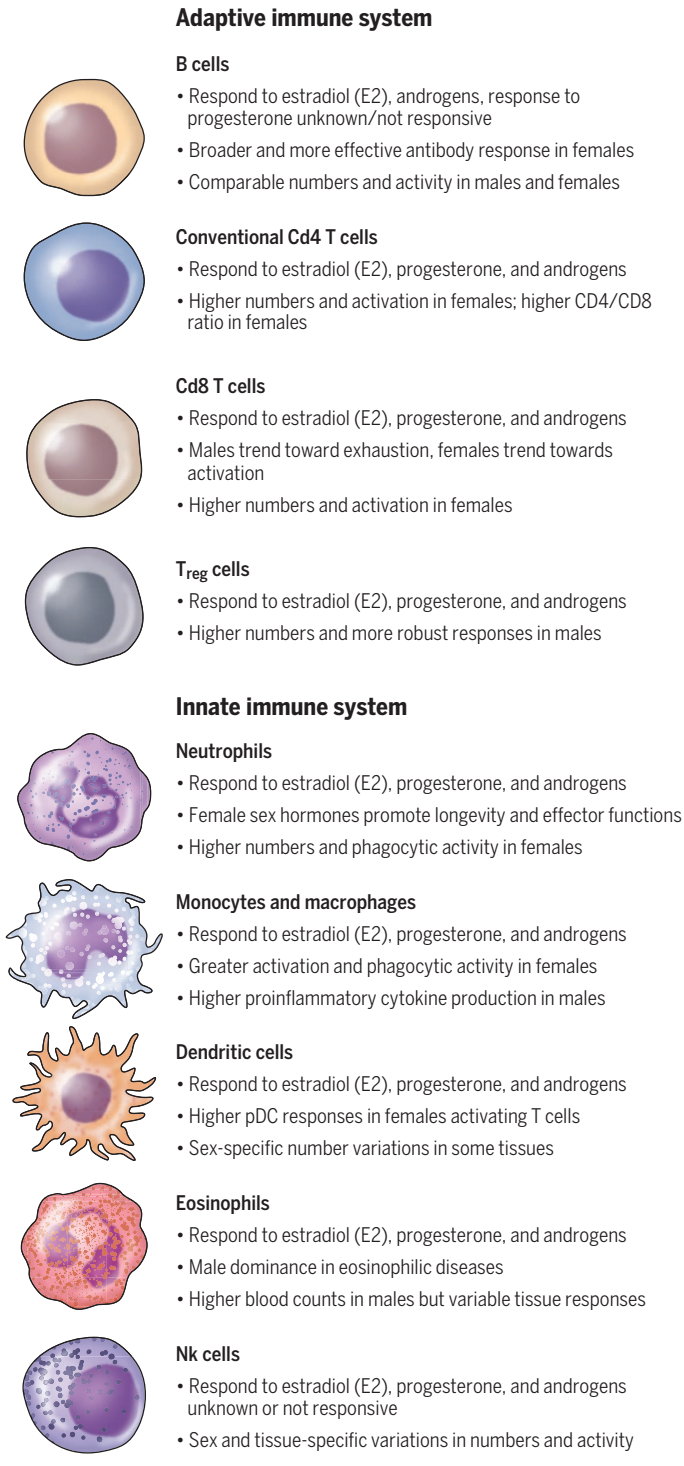


Fig. 2. Characteristics of human immune cells and their responsiveness to sex steroid hormones. Different types of immune cells of both the adaptive and innate branches of the immune system respond to sex hormones directly. Immune cell subtypes differ in number and activity between the sexes.

prevention, diagnosis, and treatment of immune diseases. Future studies must also consider the interplay of sex, race and ethnicity, age, and exogenous hormone supplementation, all of which may intersect to modulate immune function and treatment outcomes.

REFERENCES AND NOTES

1. S. L. Klein, K. L. Flanagan, *Nat. Rev. Immunol.* **16**, 626–638 (2016).
2. J. Silva, A. Iwasaki, *Sci. Transl. Med.* **16**, eado2102 (2024).
3. C.-H. Miquel, B. Faz-Lopez, J.-C. Guéry, *J. Autoimmun.* **137**, 102992 (2023).
4. K. S. Forsyth, N. Jiwrajka, C. D. Lovell, N. E. Toothacre, M. C. Anguera, *Nat. Rev. Immunol.* **24**, 487–502 (2024).
5. T. Tukiainen *et al.*, *Nature* **550**, 244–248 (2017).
6. J. B. Berletch *et al.*, *PLOS Genet.* **11**, e1005079 (2015).
7. J. B. Berletch, F. Yang, J. Xu, L. Carrel, C. M. Disteche, *Hum. Genet.* **130**, 237–245 (2011).
8. M. Souyris *et al.*, *Sci. Immunol.* **3**, eaap8855 (2018).
9. H. Katoh, T. Honda, *Biomolecules* **13**, 1706 (2023).
10. C. M. Lopes-Ramos *et al.*, *Cell Rep.* **31**, 107795 (2020).
11. J. P. Hoffmann, J. A. Liu, K. Seddu, S. L. Klein, *Immunity* **56**, 2472–2491 (2023).
12. F. Conforti *et al.*, *Cancer Cell* **43**, 343–360 (2025).
13. K. E. Davis *et al.*, *Mol. Metab.* **2**, 227–242 (2013).
14. J. G. M. Markle *et al.*, *Science* **339**, 1084–1088 (2013).
15. A. A. Ross, A. C. Doxey, J. D. Neufeld, *mSystems* **2**, e00043-17 (2017).
16. A. Amadori *et al.*, *Nat. Med.* **1**, 1279–1283 (1995).
17. K. C. Dodd, M. Menon, *Front. Immunol.* **13**, 945762 (2022).
18. M. Abdullah *et al.*, *Cell. Immunol.* **272**, 214–219 (2012).
19. M. Reina-Campos *et al.*, *Nature* **639**, 483–492 (2025).
20. R. S. Scotland, M. J. Stables, S. Madalli, P. Watson, D. W. Gilroy, *Blood* **118**, 5918–5927 (2011).
21. H. Peckham *et al.*, *J. Exp. Med.* **222**, e20241253 (2025).
22. B. J. Bain, J. M. England, *BMJ* **1**, 306–309 (1975).
23. E. J. Molloy *et al.*, *Blood* **102**, 2653–2659 (2003).
24. I. Heimbeck *et al.*, *Cytometry A* **77**, 823–830 (2010).
25. M. I. Cheng *et al.*, *Nat. Immunol.* **24**, 780–791 (2023).
26. F. Li *et al.*, *Nature* **629**, 193–200 (2024).
27. L. Chi *et al.*, *Science* **384**, eadk6200 (2024).
28. J.-Y. Cephus *et al.*, *Cell Rep.* **21**, 2487–2499 (2017).
29. S. H. Hagen *et al.*, *Cell Rep.* **33**, 108485 (2020).
30. Q. Zhang, P. Bastard, A. Cobat, J. L. Casanova; COVID Human Genetic Effort, *Nature* **603**, 587–598 (2022).
31. S. T. Gal-Oz *et al.*, *Nat. Commun.* **10**, 4295 (2019).
32. C. Muus *et al.*, *Nat. Med.* **27**, 546–559 (2021).
33. Y. Onodera *et al.*, *iScience* **26**, 107470 (2023).
34. P. Saminathan *et al.*, *iScience* **28**, 112418 (2025).
35. R. Dhanwani *et al.*, *Sci. Adv.* **6**, eaba3688 (2020).
36. A. M. Stranahan *et al.*, *Diabetes* **72**, 245–260 (2023).
37. J. Robert, *Atherosclerosis* **384**, 117278 (2023).
38. E. Gerdts, V. Regitz-Zagrosek, *Nat. Med.* **25**, 1657–1666 (2019).
39. J. Rizk, R. Sahu, D. Duteil, *Steroids* **199**, 109306 (2023).
40. N. M. Lainez *et al.*, *Front. Immunol.* **9**, 1992 (2018).
41. G. H. Goossens, J. W. E. Jocken, E. E. Blaak, *Nat. Rev. Endocrinol.* **17**, 47–66 (2021).
42. A. Vasanthakumar *et al.*, *Nature* **579**, 581–585 (2020).
43. B. Chakraborty *et al.*, *J. Clin. Invest.* **131**, e151347 (2021).
44. S. Artham *et al.*, *Sci. Adv.* **10**, eadp2442 (2024).
45. C. Yang *et al.*, *Immunity* **55**, 1268–1283.e9 (2022).
46. H. Kwon *et al.*, *Sci. Immunol.* **7**, eabq2630 (2022).
47. E. A. Townsend, V. M. Miller, Y. S. Prakash, *Endocr. Rev.* **33**, 1–47 (2012).
48. N. U. Chowdhury, V. P. Guntur, D. C. Newcomb, M. E. Wechsler, *Eur. Respir. Rev.* **30**, 210067 (2021).
49. A. Villa *et al.*, *Cell Rep.* **23**, 3501–3511 (2018).
50. R. Hanamsagar *et al.*, *Glia* **65**, 1504–1520 (2017).

ACKNOWLEDGMENTS

We thank J. Hambrick and G. Kirchweger for the preparation of Figs. 1 and 2. **Funding:** S.S. and A.G. were supported by National Institutes of Health (NIH) grant numbers U54AG065141, R01CA273230, and 1R01DK141162; E.O.S. was supported by institutional funds from La Jolla Institute for Immunology. **Author contributions:** S.S. and E.O.S. conceived the initial outline; A.G. and S.S. wrote the original draft; and A.G., S.S., and E.O.S. revised and edited the manuscript. **Competing interests:** The authors declare that they have no competing interests. **License information:** Copyright © 2025 the authors, some rights reserved; exclusive licensee American Association for the Advancement of Science. No claim to original US government works. https://www.science.org/about/science-licenses-journal-article-reuse

Submitted 19 May 2025; accepted 30 June 2025

10.1126/science.adx4381

EVOLVING IMMUNITY

REVIEW

Convergence and divergence of individual immune responses over the life course

C. Jessica E. Metcalf[1,2]*, Andrea L. Graham[1,3], Andrew J. Yates[4], Derek A. T. Cummings[5,6]

Three ingredients create the strikingly variable immune trajectories observed across human populations: (i) genetic variation, (ii) individual-scale generation of additional genetic diversity solely in lymphocytes, and (iii) collision of these processes with a changing environment through life, triggering plastic responses that can have lasting effects. We explore what generates or reduces immune variation, integrating recent empirical advances with potential overarching evolutionary principles. We posit that the multiple components of the immune system each present trade-offs (such as self-defense–self-harm, and investments in memory–retaining flexibility for future responses) that vary through life, and that variation in how immune components balance these trade-offs increases homeostasis to external and internal threats. Disentangling the mechanisms that shape immune diversity could inform effective strategies to manage microbial interactions and mitigate the burden of immune-mediated chronic diseases.

Even among genetically identical individuals, immune responses can differ markedly (*1*–*4*). Although age- or sex-matched individuals group along some immune axes, they can also diverge widely. For example, upon pathogen exposure, some individuals may escape infection altogether. For those who are infected, immediate symptoms can range from no effects to severe disease. Over the long term, post-acute infection syndromes such as autoimmune disorders and infection-associated cancers devastate some, whereas others are minimally affected. Understanding how these differences emerge requires disentangling how germline and somatic genetic and epigenetic factors interact with environmental influences over the life course.

In vertebrates, immune function emerges from the interlocking innate and adaptive immune systems, a dichotomy that has become blurred at the cellular level in recent years (*5*, *6*) but remains useful. Innate immunity is organized around often evolutionarily conserved, germline-encoded immune receptors capable of responding to conserved microbial features [microbe-associated molecular patterns (MAMPs)] or signs of damage [damage-associated molecular patterns (DAMPS)]. For example, in humans, the tightly evolutionarily constrained flagellin motor protein of bacteria (a MAMP) is recognized by an innate immune receptor, Toll-like-receptor 5 (TLR5), for which orthologs are recognizable across metazoan genomes. Similarly, double-stranded DNA in the cytosol (a DAMP) is recognized by the cyclic guanosine monophosphate–adenosine monophosphate (cGAMP) synthase (cGAS)–stimulator of inferon genes (STING) pathway in humans and across the tree of life (*7*).

By contrast, adaptive immunity derives from receptors constructed through stochastic processes, including recombination and somatic mutation. Cells that generate receptors that too strongly recognize "self" may be eliminated by apoptosis, which occurs in the thymus for T cells and in the bone marrow for B cells. Alternatively, they may be redirected into phenotypes promoting tolerance, such as regulatory T cells (T_{reg} cells) and B10 cells that produce the cytokine interleukin-10 (IL-10). This "central" tolerance is a stochastic process that is incomplete (*8*, *9*) and is reinforced by the subsequent deletion or modulation of self-reactive cells in the periphery (*10*). The remaining immune cells recognize a vast array of pathogen antigens and proliferate extensively upon binding them in an inflammatory context. B cell receptors (antibodies) also undergo affinity maturation to improve antigen recognition. Those that have increased affinity through mutation are selected in germinal centers (*11*). B and T cells responding to infections or vaccines typically go on to generate "memory" populations of varying degrees of persistence, allowing rapid and effective responses to pathogen reexposures.

The evolution of adaptive immunity (*12*) opened the way to somatic changes in hosts to allow control of pathogens within a generation (*13*) rather than requiring selection of genetic changes between host generations. The greater specificity of adaptive immunity was probably also selected for its contribution to managing the neutral and beneficial microbial diversity that lives in and on us (*14*) and for the control of neoplasms. The complex set of roles that includes managing the shifting ground of evolving pathogens, a changing microbiome, and the accumulating risk of cancer over the life course has selected for a complex, highly redundant, and context-specific immune system. Immunity is also profoundly programmable and reprogrammable, contingent on environmental changes both at the scale of individual cells [for example, chromatin remodeling (*15*) and epigenetically trained immunity (*16*)] and at the scale of cell populations (for example, amplification of specific lymphocyte clones, including those generated by somatic hypermutation), and at the scale of the host, in which preexisting immunity may modulate the success of new immune responses [for example, "original antigenic sin" (*17*)]. Such plasticity means that every exposure to a pathogen or other antigens has the potential to transform subsequent immune responses. These exposures in turn result in history-dependent dynamics and individual heterogeneity in immune outcomes that nevertheless, and despite the dangerous nature of many immune reactions (*18*), generally maintain homeostasis in the face of external and internal insults over a life course.

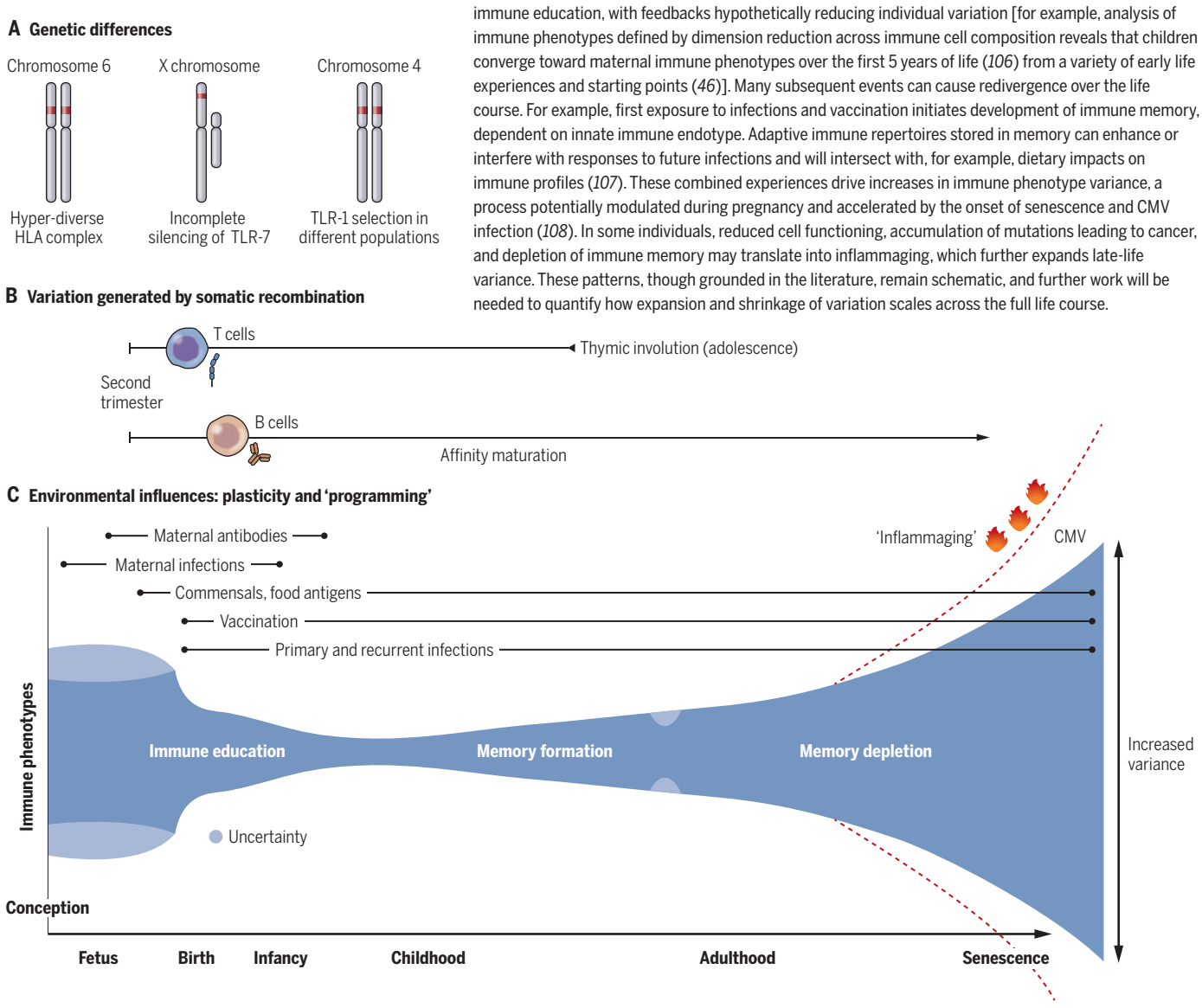
Inherent polymorphism and selection

Genetic differences can be pronounced; the short arm of chromosome 6 contains the most polymorphic gene cluster of the entire human genome, the major histocompatibility complex (MHC) (*19*), which presents antigenic peptides to T cell receptors. This diversity likely derives from heterozygote advantage (*20*) and/or frequency-dependent selection, in which rare MHC alleles confer protection against pathogen subversion or evasion of antigen presentation (*21*).

Varied and transient historical selection pressures have also shaped polymorphisms in innate immune receptors, including the Toll-like receptors, a family of surface proteins on macrophages, dendritic cells, and other immune cells that act as sentinels for pathogenic microorganisms. For example, TLR4 polymorphisms have been attributed to differences in exposure to pathogens such as the malaria parasite *Plasmodium* spp. (*22*). Similarly, the history of shared exposure to plague has led to convergence of TLR1 genes in European and Roma populations, presumably as a result of selection (*23*). Such polymorphisms can alter vulnerability to subsequent pandemics such as severe acute respiratory syndrome coronavirus 2 (SARS-CoV-2) (*24*).

[1]Department of Ecology and Evolutionary Biology, Princeton University, Princeton, NJ, USA. [2]Princeton School of Public and International Affairs, Princeton University, Princeton, NJ, USA. [3]Santa Fe Institute, Santa Fe, NM, USA. [4]Department of Pathology and Cell Biology, Columbia University Irving Medical Center, New York, NY, USA [5]Johns Hopkins Bloomberg School of Public Health, Johns Hopkins University, Baltimore, MD, USA. [6]Johns Hopkins Whiting School of Engineering, Johns Hopkins University, Baltimore, MD, USA. ***Corrresponding author. Email: cmetcalf@princeton.edu**

Fig. 1. Sources of immune variation across the human life course. (**A**) Genetic variation emerging from balancing selection (*19*), transient selection (*23*), or drift, or manifested through incomplete silencing on the X chromosome (*67*). (**B**) Somatic recombination of antigen receptors in B and T cells. (**C**) Abiotic or biotic environmental variation across the life course (*x* axis) triggering plastic responses of variable duration, which modulate the "immune phenotype" (*y* axis, reflecting multiple dimensions of immune variation, such as from cell population sizes to antigens recognized). (Left) Before birth, maternal infections and antibodies shape fetal immune development, and effects on variance are unclear. Circumstances of birth can amplify heterogeneity along a range of dimensions [for example, infants born pre-term or by cesarean sections may have varying abundances of cell populations or inflammatory profiles (*46*)]. Then, during early life, maternal antibodies, microbial communities, and early pathogens define immune education, with feedbacks hypothetically reducing individual variation [for example, analysis of immune phenotypes defined by dimension reduction across immune cell composition reveals that children converge toward maternal immune phenotypes over the first 5 years of life (*106*) from a variety of early life experiences and starting points (*46*)]. Many subsequent events can cause redivergence over the life course. For example, first exposure to infections and vaccination initiates development of immune memory, dependent on innate immune endotype. Adaptive immune repertoires stored in memory can enhance or interfere with responses to future infections and will intersect with, for example, dietary impacts on immune profiles (*107*). These combined experiences drive increases in immune phenotype variance, a process potentially modulated during pregnancy and accelerated by the onset of senescence and CMV infection (*108*). In some individuals, reduced cell functioning, accumulation of mutations leading to cancer, and depletion of immune memory may translate into inflammaging, which further expands late-life variance. These patterns, though grounded in the literature, remain schematic, and further work will be needed to quantify how expansion and shrinkage of variation scales across the full life course.



Autoimmune diseases often share genetic features (*25*) that align with evidence of positive selection, suggesting that these mutations historically played a role in pathogen defense (*26*). Autoimmune diseases are on the rise, and one possible explanation is that although mutations associated with autoimmunity might have been beneficial in historic pathogen-rich environments, in contemporary "hygienic" urban environments, they might tilt the immune "rheostat" that calibrates the balance between attack, restraint, and repair toward immunopathology (*18*). The mechanisms underlying this tilt remain to be determined. Relatively recent reductions of exposure to immunomodulatory pathogens and/or symbionts may be contributing to increases in immunopathology (*18*).

Understanding how diverse human immune trajectories emerge requires cataloging these genetic differences—a task that is underway, although gaps remain (*27*). It also requires translating how genetic differences map onto function and then titrating how heterogeneity narrows and builds over the life course of genetic differences, immune plasticity, and programming in response to environmental experience (Fig. 1).

The order of events

Two features provide some structure for building expectations for the diversity of human immune trajectories in the face of this complexity. First, time dependency means that the ordering of events matters, and we have some knowledge as to the timing of core immune events. Some immune processes are defined by age, such as the maturation of M cells during infant immune development (*28*), and the progressive reduction in thymic output from adolescence onward (*29*). Other processes reflect immune responses to insults that increase in prevalence with the passage of time, such as cancers or mutations that impair cell function. Infections will come and go, sometimes at predictable ages; for example, endemic immunizing infections such as measles tend to occur within a narrow age range, or sometimes repeatedly, as in the case

CREDIT: ADAPTED BY K. HOLOSKI/SCIENCE

of recurrent seasonal influenza. Age-dependent or predictable events may lead to convergence in immune responses, whereas stochastic differences in the timing and ordering of exposures will contribute to diverging immune responses between individuals (*30*).

Second, a blend of drift and selection over our evolutionary history has sculpted immune trajectories over age in the context of these time-varying processes, contingent on the as yet uncertain mapping between underlying immune trade-offs (Fig. 2) and larger life history trade-offs, including between survival and fertility, or current and future survival. Immune trade-offs can be organized around whether a response is triggered (a sensitivity–specificity trade-off) (Fig. 2A) (*31*), the appropriate scale of response (a self-harm–self-defense trade-off) (Fig. 2B) (*18*), and how the response modulates future responses (investments in specific responses that may take longer to mount and possibly restrict future responses, or investments in fast, less specific responses) (Fig. 2C) (*32*). This picture is further complicated by selection for redundancy in immune pathways, which provides robustness against hijacking by pathogens and appears to be most prevalent within the components of the innate immune system (*33*, *34*).

In this Review, we frame recent advances in understanding immune heterogeneity from early life and childhood to adulthood, including pregnancy and senescence (Fig. 1), in the context of hypothesized trade-offs under which the immune system has evolved (Fig. 2) and with an eye to applications, from therapeutics to vaccination. Our exploration of immune trajectories leans on a scale of abstraction because approaches to measurement vary across the literature. Throughout, we specify evidence for similarity among individuals in immune response (convergence) or differences (divergence) across the life course.

Early life

In the first months of life, mortality rates caused by infection can be higher than at any stage of life other than extreme old age (*35*). During this time, infants are also establishing the foundations for immune "tolerance" (*36*), an important component of successful immune functioning. Achieving tolerance requires balancing across trade-offs involving whether to respond to a given stimulus (Fig. 2A) and the magnitude of the response (Fig. 2B). Recent work indicates that mutual imprinting of the immune system and commensal microbes is central to "immune education." For example, on the skin, competitive recruitment of tolerizing mucosal-associated invariant T (MAIT) cells by vitamin B–producing microbes in turn favors these microbes' persistence (*37*). In the gut, maternal antibodies modulate how the developing infant immune system "sees" different antigens and develops neutralizing or "tolerizing" titers to them (*36*, *38*, *39*), establishing a transgenerational footprint of immune priming that extends into adult life (*40*, *41*). The selective pressures that shape this process likely emerge from the fact that information from the developing infant's environment, including maternal immunity, identifies an inflammatory baseline suitable for anticipated future environments (*42*). Mismatches between prediction and occurrence could result in inflammatory diseases. Recently, cesarean sections, use of antibiotics, and increased hygiene have all vastly improved human health; however, they have also reduced microbial diversity early in life, potentially disrupting longer-term immune function. The outcomes—including autoimmunity (*43*), inflammatory bowel disease (*44*), and allergies (*45*)—may be difficult to reverse.

Explanations for immune education often invoke feedback between the developing infant's immune state and its microbial communities. For example, MAIT cell recruitment is driven by but also modulates bacterial recruitment (*37*), alongside information derived from maternal immunity (*2*, *39*). Such feedbacks, or circular chains of cause and effect linking different actors within the system, can result in homeostasis in which changes to one actor propagate through the chain to mitigate the original change. Longitudinal measurement of immune cell populations over the first few weeks of life indicate that considerable initial diversity in the blood is swiftly canalized across children with diverse birth experiences (*46*). After 2 years, in unrelated children, the pattern of immunoglobulin A (IgA) antibody binding to bacterial taxa in the gut converges, is relatively independent of diet, and resembles that of their mothers (*2*). The resulting homeostasis between commensal microbes, particularly of the gut, and the infant's immune system sets the stage for tolerance to microbes appropriate to the environment as informed by both the mother's immune system and the infant's early experience (*38*).

The repeatability of such convergence and the range of measures and functions by which it might be characterized warrant further investigation. For example, in one study, the probability of primary measles vaccine failure was found to increase in children born by cesarean section (*47*), suggesting a disruptive effect of altered early-life microbial exposure. Yet these children displayed a robust response to the second vaccine dose, converging to a typical measles antigen response trajectory. However, lasting perturbations are also possible and across a range of scales. For example, early cessation of breastfeeding alters microbial colonization of nasal and gut niches, with effects on later-life respiratory syndromes, including asthma (*48*).

Expanding the evidence base for immune convergence in early life (Fig. 1C) and identifying the underlying mechanisms remain important open problems. It is also unclear whether and when convergence informed by maternal phenotypes might mitigate outcomes associated with "evolutionary mismatch," such as depleted early-life microbes that leave individuals vulnerable to immunopathologies later in life. Although explicitly considering the landscape of natural selection can provide a powerful lens for viewing the complex processes of immunity, balancing adaptive explanations against possible neutral alternatives is likely to be the most fruitful path to disentangling mechanisms.

Childhood

The immune system continues to develop throughout childhood (*49*) but remains distinct in many ways from adults. Challenges faced during childhood are different from later in life: Because most pathogens will be experienced for the first time, responses cannot rely on adaptive memory and must be swift and efficient. Children are potentially better equipped to deal with associated immunopathology of a rapid immune response (the costs of "self defense") (Fig. 2B) (*50*, *51*). Children have different immune cell populations relative to adults beyond a higher abundance of naïve (antigen-inexperienced) B and T cells because they have experienced less accumulated pathogen exposure (*52*). They also have, for example, considerable enrichment of a recently recognized cytotoxic B cell subset (*53*), which is in line with the tendency toward a more effector, less memory-oriented immunity (*54*), potentially reflecting greater response probability even at the cost of "false positives" (Fig. 2A). A handoff to a more adult immune system potentially requires navigating a trade-off between current and future responses (Fig. 2C), in which inexperienced cells must protect the host but also allow for the development of more specific adaptive responses. Rates of handover, and potentially divergence, can vary across tissues, with for example more rapid maturation of tissue resident memory T cells at mucosal sites relative to blood and lymphoid sites (*52*).

Adaptive immunity to primary exposures can develop by paths that are shared across individuals (T cell or B cell receptors recognizing "public" epitopes) or not (recognition of "private" epitopes). Public epitopes can emerge from germline-encoded shared biases in the generation process of receptors (*55*) but also from convergent functional selection (*56*), which has the potential to reduce individual heterogeneity in immune trajectories. Titrating the relative frequency of public versus private epitopes, and the contexts that lead to either, is an exciting direction for future research that has relevance for vaccine design (*57*) and may even shed light on ways in which in turn viral evolution might be constrained (*58*).

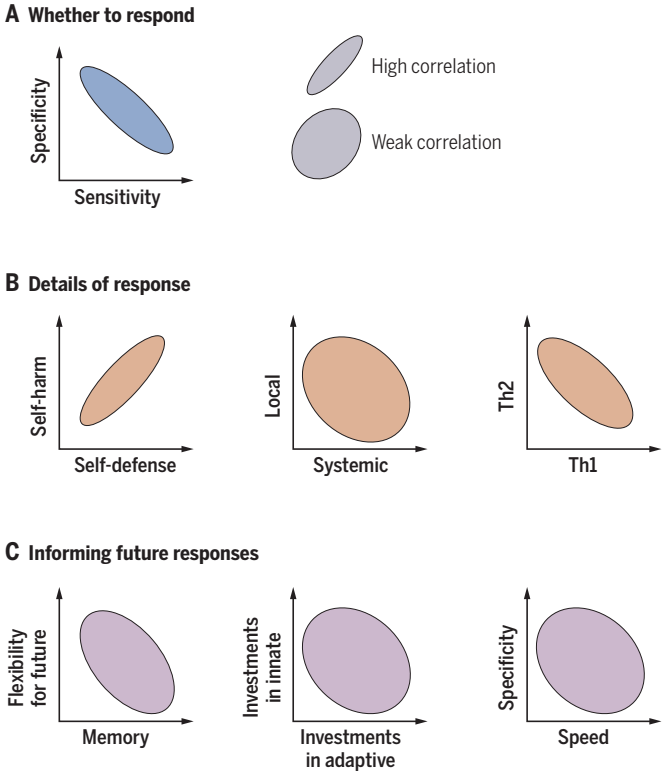


Fig. 2. Trade-offs hypothesized to have shaped immune evolution through selection as well as to govern immune function across the life course may be tightly or weakly constrained (indicated by the correlation structure, noting that representations provided are currently only conjectures). There are several factors that these trade-offs can be organized around. (**A**) What constitutes an immune trigger and thereby determines whether to respond. For example, many lines of evidence suggest greater "sensitivity" (the probability of a positive response in an individual who has the infection) rather than specificity (defined as the probability of a negative response in an individual who does not have the disease) in the female immune response, increasing protection from infectious disease but also increasing vulnerability to autoimmunity (more "false positives") (*70*). (**B**) The details of the response once triggered with many potential dimensions associated with a range of cost-benefits. For example, drug-based systemic immune suppression protects against inflammatory disease outcomes such as atherosclerosis ("self-harm") but at a risk of infectious disease ("reduced self-defense") (*109*). As a site of entry for many pathogens, potent local responses (such as in the mucosa) may reduce the presentation of antigen to other sites in the body, potentially reducing systemic responses. Interaction between local and systemic responses may also be generated by regulatory mechanisms such as those observed in oral immunotherapy, in which oral presentation of antigens associated with allergy or autoimmunity produce T_{reg} cell responses that reduce systemic responses and alleviate symptoms (*110*). Last, activating T_H1 pathways that trigger a cellular immune response tuned toward control of intracellular pathogens comes at the cost of suppressing T_H2 pathways that primarily target macroparasites. (**C**) Current responses can affect future responses. This is illustrated by herpesviruses, which can elicit "inflationary" memory responses that can affect future immune responses by dramatically skewing the memory repertoire (*3*). The immune response to measles may contribute to immune amnesia, creating holes in the memory B cell repertoire (*111*). Strong investment in innate responses could interfere with the development of adaptive responses, by removing immune triggers . Some pathogens, such as *Trypanosoma brucei* and Ebola, evade or disrupt specific immune responses, leading to reliance on fast, nonspecific defenses such as apolipoproteins, IgM, complement, or NK cells. By contrast, infections such as measles are targeted precisely enough that post-exposure vaccination can still reduce disease (*112*). Characterizing both their generality and how these trade-offs might operate at cellular to organismal scales is an open area of research.

CREDIT: ADAPTED BY K. HOLOSKI/*SCIENCE*

Bulk of life

After puberty, pathogen infection and reinfection and antigen exposures and reexposures will modulate both adaptive and innate immunity, which will in turn influence each other. For example, innate "endotypes" set the template for antibody responses (*59*), and robust adaptive responses can suppress future innate responses [for example, prior SARS-CoV-2 vaccination diminishes innate effector responses in subsequent infections (*60*)]. Both effects could be contingent on how hormonal differences shape immune responses (*61*), as well as microbiome and dietary features (*62*), and are likely to result in cumulative deviation in immune profiles among individuals (Fig. 1). Nevertheless, redundancies across immune actors may mean that overall functioning of immunity to specific pathogens remains similar, and homeostasis is broadly retained.

Selection by adaptive immunity defines the evolutionary trajectory of many pathogens—including influenza (*63*), coronaviruses (*64*), and noroviruses (*65*)—which in turn creates a complex set of trade-offs for the host to navigate when optimizing adaptive immune responses over short and long timescales (Fig. 2, A, B, and C). Small genetic changes in pathogens may be effectively bound and/or neutralized by previous adaptive responses, reducing demands on a potentially limited pool of native T or B cells. Larger genetic changes may result in an entirely new adaptive immune response being initiated, whereas rapid antigenic switching in single infections, as occurs as in trypanosomes (including the sleeping sickness pathogen), may lead to more emphasis on fast, nonspecific responses (Fig. 2C). However, intermediate genetic changes may result in interference between existing responses and the ability to develop new ones (*32*). This gap in responsiveness may determine how rapidly the host immune repertoire goes out of date as pathogens evolve in response to immune selection. The overall immune strategy might be characterized as one of "bend, not break," in which continual infection risk results in better sampling of the environment and thus updating of the repertoire.

Overall, a combination of strategies across compartments of the immune response (local and mucosal versus systemic, and memory versus new responses) may allow for titration, in which only a subset of responses are updated, whereas others remain to limit the pathogen burden. The interdependence of the different components of the immune response, or tightness of the trade-offs (Fig. 2), will define the strategy that best balances costs and benefits and might inform both vaccine design and how vaccines can be best targeted over a life course. As expected, because the flexibility of immune responses intersects with the many heterogeneities in antigen exposure among individuals and redundancy among immune actors, divergence in immune profiles is marked over the bulk of the life span, including among monozygotic twins. Divergence in twins discordant for exposure to pathogens, such as cytomegalovirus (CMV), is particularly marked (Fig. 1) (*3*).

Sex contributes to immune heterogeneity through chromosomal and hormonal differences. Incomplete silencing of genes on the X chromosome can both affect vulnerability to infection in males (*66*) and increase the risk of autoimmunity in females (*67*). After puberty, hormonal differences (*68*) add short (monthly) and potentially long (reproductive cycle) contributions to heterogeneity. Data from cohorts experiencing gender-affirming testosterone treatment (*69*) reveal modulation away from interferon responses and toward cytokines, such as IL-6, which has a pleiotropic role in inflammation and haematopoeisis. Sex differences presumably are partly defined by differing trade-offs shaped by different roles around reproduction (*70*) and the demands of pregnancy.

Pregnancy

Pregnancy is another major life event that causes at least temporary immune convergence (Fig. 1C). It was initially thought to require extensive maternal immunosuppression, which seems unlikely from an evolutionary perspective, given the resulting maternal risks. The

emerging picture is of immunomodulation enabled by local interactions (*71*). The developing fetus evades rejection through a combination of an invisibility cloak [fetal cells in contact with maternal blood do not express human lymphocyte antigen (HLA); those that do express the least variable of HLA molecules] and local expression of immunosuppressive receptors, such as HLA-G, which interact predominantly with a local tolerogenic set of immune cells known as uterine natural killer (NK) cells (*71*).

Predominantly local immune interactions allow systemic lines of maternal immune defense to remain largely in place. Nevertheless, systemic changes do occur, including increased abundance of T_{reg} cells (*72*), particularly early during pregnancy, and a bias from T helper 1 (T_H1) responses required during implantation toward T_H2 responses during the rest of pregnancy (Fig. 2B). These changes can result in remission of some autoimmune diseases, such as multiple sclerosis (*73*), but intensification of others, including systemic lupus erythematosus (*74*). Recent mouse studies indicate that B cells have reduced activity and produce fewer inflammatory cytokines during pregnancy (*75*, *76*). The outcome may be greater vulnerability to morbidity and mortality (*72*), although the effects can be complex. In mice, estriol, a hormone produced only during pregnancy, increased tolerance to influenza, with no change in viral load (*77*). However, the 2009 H1N1 influenza virus was fatal to pregnant mice even at low viral loads, an effect attributed to reduced regeneration of lung epithelial cells through altered macrophage function (*78*).

Early-life experiences during the fetal period can set the template for later-life immune heterogeneity. In the extreme, some diseases, such as toxoplasmosis and rubella, can result in potentially serious congenital outcomes (*79*). More subtly, in mice, maternal influenza infection during pregnancy can leave offspring vulnerable to other infections (*80*). Moreover, in mice antibiotic treatment of mothers has been found to drive offspring dysbiosis by suppressing IgA antibodies in milk, resulting in a greater susceptibility to late-onset *Escherichia coli* sepsis (*81*). Conversely, also in mice, infection during pregnancy increases maternal levels of IL-6, which results in epigenetic changes in fetal intestinal epithelial stem cells that can later be protective against infection (*82*).

Senescence

Evolutionary theory predicts deterioration with age. Even under constant mortality, older individuals will tend to be rare, allowing deleterious mutations to drift to fixation (mutation accumulation). Because investments that improve survival or fertility at early ages at the expense of later ages increase fitness, these will be favored by selection, proposed by the ideas of antagonistic pleiotropy and disposable soma (*83*). The processes of resource allocation embodied by the latter have recently been augmented by the idea of system regulation and deregulation (*84*). The concept of "inflammaging" (*85*, *86*) seems to align with this: Age-associated increases in chronic, low-grade inflammation might potentially be an inevitable outcome of an inability to reorient systems optimized for protection in early life.

Organismal immunosenescence may also be inevitable if immune cells themselves senesce. Many exhibit a decrease in function as they age (*87*). However, it may be important to distinguish the postmitotic age of individual cells and the age of clones made up of cell populations that self-renew and die. There is evidence that naïve T cells in humans (*88*) and both naïve and memory T cells in mice (*89*, *90*) become intrinsically longer lived over time. This could reflect an adaptation or selection process that acts to sustain T cell numbers in the face of waning production of new cells from the thymus, but it may skew and narrow T cell repertoires toward aged cells later in life. This effect may be driven by the accumulation of mutations that eventually favor cells' persistence or capacity for outgrowth (*91*). Such clonal amplification occurs across other hematopoietic stem cell lineages (*92*). It remains unclear whether progressive increases in homeostatic "fitness" of T cell clones goes hand-in-hand with a decline in their responsiveness to pathogens. In mice, there is some evidence of functional impairment in older naïve T cells, which self-renew very rarely (*93*), but it has been shown in an infection setting that memory T cell populations can retain their proliferative capacity over more than 150 doublings, with only minor accrual of exhaustion markers (*94*). Therefore, phenotypic changes may be linked to the aging of individual cells, perhaps owing to DNA damage, or to ancestral age of the whole clonal lineage, associating with replicative senescence (*95*).

Such dynamic alterations in the function of T cells (*96*), as well as other cell types with which they interact, are associated with metabolic changes. For example, as macrophages shift from anti-inflammatory to pro-inflammatory states, they shift from oxidative phosphorylation to glycolysis (*97*). The booming field of immunometabolism has turned attention to senescence and identified promising therapeutic directions, including repurposing of drugs for metabolic disorders to treat immunosenescence (*98*).

Chronic infections, especially herpesvirus infections such as CMV, are thought to play a disproportionate role in sparking immunosenescence. Chronic antigen stimulation accelerates the replicative exhaustion of memory lymphocytes, which then unleashes the inflammatory capacity of the innate immune system. This process has been implicated as a core driver of immune divergence over the life course (*3*).

Discussion

The response that follows an immune stimulus may encompass a range of complex and often redundant components. However, there is an organizing principle in that these responses are ultimately governed and constrained by trade-offs. Characterizing this scaffolding of trade-offs at multiple scales of the immune system may open the way to improving the design of interventions, from treatment to vaccines, by revealing which components are most effective or depleted at which life stages, but also by unveiling trade-offs between current benefits and benefits that could be recouped later in life. Targeted vaccine strategies individually—by age, cohort, host genetics, or microbiota characteristics—could optimally build on or target responses that those individuals can mount at their particular stage of life. For example, as aging individuals experience declining T cell responses, vaccines that stimulate other components of the immune response might be promoted to maintain similar functions. Similarly, monoclonal antibodies and vaccines with different targets may be used to preserve or optimize future function or recognize fundamental weaknesses in specific individuals' responses. The time dependencies of immune responses raise interesting questions for optimization of interventions. Deeper knowledge of how immune investment plays out across life might provide insights into ways that interventions could take advantage of middle-life immune profiles, or how to provide protection at longer time scales.

The empirical foundations of our understanding of life-course immune heterogeneity are varied. Experimental manipulation in animal models has been foundational for disentangling processes such as immune education (*39*) or how heritable and nonheritable factors interact in shaping immune responses (*99*). A comparative approach that treats different pathogens as interrogators of trade-offs may be valuable for understanding the interplay of the components of the immune response over the life course. In humans, natural experiments in which cohorts experience distinct exposures, such as vaccine delivery associated with a particular age cutoff (*100*) or the effect of nonpharmaceutical interventions (for example, deployed to reduce SARS-CoV-2 risk) on immunological outcomes such as asthma (*101*), have the power to uncover further causes of heterogeneity in human immunity. Observations of responses to emerging infections may be especially illuminating because they decouple age from the timing of first exposures; for example, first infections of SARS-CoV-2 viruses occurred across all ages. However, the sheer complexity of interactions

and the underlying diversity of human populations, as well as their experiences, make long-term cohort studies [for example, (*102*–*105*)] a vital element in revealing mechanisms and laying the foundations for optimizing interventions, as well as recognizing immune function–associated disorders over the life course.

Last, the collection of biological samples from long-term cohorts and across different pathogen exposures is important for developing the foundations for a library of biomarkers for important immune processes. For example, as human populations age, immunosenescence drives an increasing fraction of morbidity and mortality. Markers of immune function, either pathogen-specific or general functional assays, as measures of aging and fragility could be transformative for treatment while also strengthening our understanding of core mechanisms of immune functioning. The rewards of generic treatment approaches, including wide-ranging vaccines or immunometabolic treatments, are likely to be great, especially at life stages when immune responsiveness converges. By contrast, immune divergence would potentially augment the power of personalized medicine.

REFERENCES AND NOTES

1. D. Lazzeroni, P. Concari, L. Moderato, *Ann. Intern. Med.* **174**, 717–719 (2021).
2. J. D. Planer *et al.*, *Nature* **534**, 263–266 (2016).
3. P. Brodin *et al.*, *Cell* **160**, 37–47 (2015).
4. J. Bister *et al.*, *Sci. Immunol.* **9**, eadj7168 (2024).
5. F. M. Gomes, M. Silva, A. Molina-Cruz, C. Barillas-Mury, *PLOS Pathog.* **18**, e1010939 (2022).
6. T. Kawabe, A. Sher, *Int. Immunol.* **34**, 189–196 (2022).
7. Y. Li *et al.*, *Cell* **186**, 3261–3276.e20 (2023).
8. V. Müller, S. Bonhoeffer, *Trends Immunol.* **24**, 132–135 (2003).
9. A. J. Yates, *Front. Immunol.* **5**, 13 (2014).
10. M. A. ElTanbouly, R. J. Noelle, *Nat. Rev. Immunol.* **21**, 257–267 (2021).
11. J. Merkenschlager *et al.*, *Nature* **641**, 495–502 (2025).
12. T. Boehm, *Nat. Rev. Immunol.* **25**, 141–152 (2025).
13. A. Mayer, T. Mora, O. Rivoire, A. M. Walczak, *Proc. Natl. Acad. Sci. U.S.A.* **113**, 8630–8635 (2016).
14. M. McFall-Ngai *et al.*, *Proc. Natl. Acad. Sci. U.S.A.* **110**, 3229–3236 (2013).
15. D. Calderon *et al.*, *Nat. Genet.* **51**, 1494–1505 (2019).
16. S. Naik, E. Fuchs, *Nature* **607**, 249–255 (2022).
17. S. Cobey, *Nat. Immunol.* **25**, 2015–2023 (2024).
18. A. L. Graham, E. C. Schrom II, C. J. E. Metcalf, *Trends Immunol.* **43**, 117–131 (2022).
19. Y. Luo *et al.*, *Nat. Genet.* **53**, 1504–1516 (2021).
20. E. E. McClelland, D. J. Penn, W. K. Potts, *Infect. Immun.* **71**, 2079–2086 (2003).
21. J. A. M. Borghans, J. B. Beltman, R. J. De Boer, *Immunogenetics* **55**, 732–739 (2004).
22. B. Ferwerda *et al.*, *Proc. Natl. Acad. Sci. U.S.A.* **104**, 16645–16650 (2007).
23. H. Laayouni *et al.*, *Proc. Natl. Acad. Sci. U.S.A.* **111**, 2668–2673 (2014).
24. M. E. K. Niemi, M. J. Daly, A. Ganna, *Nat. Rev. Genet.* **23**, 533–546 (2022).
25. A. Harroud, D. A. Hafler, *Science* **380**, 485–490 (2023).
26. G. Kerner *et al.*, *Cell Genom.* **3**, 100248 (2023).
27. S. Fatumo *et al.*, *Nat. Med.* **28**, 243–250 (2022).
28. C. Wagner, N. Torow, M. W. Hornef, H. Lelouard, *FEBS J.* **289**, 4731–4757 (2022).
29. G. G. Steinmann, H. K. Müller-Hermelink, *Dtsch. Med. Wochenschr.* **110**, 1300–1307 (1985).
30. R. J. Oidtman *et al.*, *Trends Microbiol.* **29**, 1072–1082 (2021).
31. C. J. E. Metcalf, A. T. Tate, A. L. Graham, *Nat. Ecol. Evol.* **1**, 1766–1772 (2017).
32. A. Schiepers *et al.*, *Nature* **615**, 482–489 (2023).
33. A. Fischer, A. Rausell, *Sci. Immunol.* **1**, eaah5861 (2016).
34. S. Nish, R. Medzhitov, *Immunity* **34**, 629–636 (2011).
35. C. J. E. Metcalf *et al.*, *R. Soc. Open Sci.* **9**, 211498 (2022).
36. N. Torow, T. W. Hand, M. W. Hornef, *Immunity* **56**, 485–499 (2023).
37. M. G. Constantinides *et al.*, *Science* **366**, eaax6624 (2019).
38. B. Tepekule, A. I. Lim, C. J. E. Metcalf, bioRxiv (2024). https://doi.org/10.1101/2024.05.20.594845.
39. D. Ramanan *et al.*, *Cell* **181**, 1276–1290.e13 (2020).
40. B. Rusconi *et al.*, *Proc. Natl. Acad. Sci. U.S.A.* **121**, e2309994121 (2024).
41. S. Vergani *et al.*, *Immunity* **55**, 1829–1842.e6 (2022).
42. J. Y. Hong, R. Medzhitov, *Trends Immunol.* **44**, 877–889 (2023).
43. C. J. Stewart *et al.*, *Nature* **562**, 583–588 (2018).
44. M. Agrawal *et al.*, *EClinicalMedicine* **36**, 100884 (2021).
45. S. Yoshida, K. Ide, M. Takeuchi, K. Kawakami, *Pediatr. Allergy Immunol.* **29**, 490–495 (2018).
46. A. Olin *et al.*, *Cell* **174**, 1277–1292.e14 (2018).
47. W. Wang *et al.*, *Nat. Microbiol.* **9**, 1676–1685 (2024).
48. L. Shenhav *et al.*, *Cell* **187**, 5431–5452.e20 (2024).
49. B. Manfroi *et al.*, *Sci. Transl. Med.* **16**, eadl1997 (2024).
50. D. K. J. Pieren, M. C. Boer, J. de Wit, *Front. Immunol.* **13**, 1031924 (2022).
51. A. J. Prendergast, P. Klenerman, P. J. R. Goulder, *Nat. Rev. Immunol.* **12**, 636–648 (2012).
52. T. J. Connors *et al.*, *Immunity* **56**, 1894–1909.e5 (2023).
53. Y. Wang *et al.*, *Nat. Immunol.* **26**, 308–322 (2025).
54. J. Wang *et al.*, *Blood* **128**, 3073–3082 (2016).
55. E. L. Shrock *et al.*, *Science* **380**, eadc9498 (2023).
56. M. Ruiz Ortega, N. Spisak, T. Mora, A. M. Walczak, *PLOS Genet.* **19**, e1010652 (2023).
57. C. M. Saad-Roy, C. J. E. Metcalf, B. T. Grenfell, *Science* **376**, 1161–1162 (2022).
58. M. Ghafari, P. Simmonds, O. G. Pybus, A. Katzourakis, *Curr. Biol.* **31**, 4689–4696.e5 (2021).
59. S. Fourati *et al.*, *Nat. Immunol.* **23**, 1777–1787 (2022).
60. L. Chan *et al.*, *Sci. Transl. Med.* **17**, eadq1086 (2025).
61. J. P. Hoffmann, J. A. Liu, K. Seddu, S. L. Klein, *Immunity* **56**, 2472–2491 (2023).
62. M. M. A. R. van Dorst *et al.*, *Nat. Rev. Immunol.* **24**, 250–263 (2024).
63. V. N. Petrova, C. A. Russell, *Nat. Rev. Microbiol.* **16**, 47–60 (2018).
64. K. E. Kistler, T. Bedford, *eLife* **10**, e64509 (2021).
65. G. I. Parra *et al.*, *PLOS Pathog.* **13**, e1006136 (2017).
66. A. L. Fink, K. Engle, R. L. Ursin, W.-Y. Tang, S. L. Klein, *Proc. Natl. Acad. Sci. U.S.A.* **115**, 12477–12482 (2018).
67. M. Souyris *et al.*, *Sci. Immunol.* **3**, eaap8855 (2018).
68. S. L. Klein, K. L. Flanagan, *Nat. Rev. Immunol.* **16**, 626–638 (2016).
69. T. Lakshmikanth *et al.*, *Nature* **633**, 155–164 (2024).
70. C. J. E. Metcalf, A. L. Graham, *Nat. Commun.* **9**, 4391 (2018).
71. A. Moffett, N. Shreeve, *Nat. Rev. Immunol.* **23**, 222–235 (2023).
72. O. Cervantes *et al.*, *Immunol. Rev.* **308**, 123–148 (2022).
73. U. R. Sharma *et al.*, *Inflammopharmacology* **29**, 987–1000 (2021).
74. D. Zucchi, R. Fischer-Betz, C. Tani, *Best Pract. Res. Clin. Rheumatol.* **37**, 101860 (2023).
75. N. Valeff *et al.*, *Genomics* **113**, 2614–2622 (2021).
76. G. Rizzuto *et al.*, *Nature* **603**, 497–502 (2022).
77. M. S. Vermillion, R. L. Ursin, S. E. Attreed, S. L. Klein, *Endocrinology* **159**, 3306–3320 (2018).
78. G. Marcelin *et al.*, *J. Virol.* **85**, 11208–11219 (2011).
79. C. J. Megli, C. B. Coyne, *Nat. Rev. Microbiol.* **20**, 67–82 (2022).
80. H. Jacobsen *et al.*, *Nat. Commun.* **12**, 4957 (2021).
81. C. Pietrasanta *et al.*, *Cell Host Microbe* **32**, 2178–2194.e6 (2024).
82. A. I. Lim *et al.*, *Science* **373**, eabf3002 (2021).
83. T. B. Kirkwood, R. Holliday, *Proc. R. Soc. London Ser. B Biol. Sci.* **205**, 531–546 (1979).
84. A. A. Maklakov, T. Chapman, *Proc. Biol. Sci.* **286**, 20191604 (2019).
85. A. Ajoolabady *et al.*, *Ageing Res. Rev.* **101**, 102540 (2024).
86. A. Singh *et al.*, *Cold Spring Harb. Perspect. Med.* **14**, a041197 (2024).
87. J. Nikolich-Žugich, *Nat. Immunol.* **19**, 10–19 (2018).
88. J. E. Mold *et al.*, *PLOS Biol.* **17**, e3000383 (2019).
89. S. Rane, T. Hogan, E. Lee, B. Seddon, A. J. Yates, ïe*Life* **11**, e78168 (2022).
90. M. E. Bullock *et al.*, *PLOS Biol.* **22**, e3002380 (2024).
91. P. L. Johnson, A. J. Yates, J. J. Goronzy, R. Antia, *Proc. Natl. Acad. Sci. U.S.A.* **109**, 21432–21437 (2012).
92. S. Jaiswal, B. L. Ebert, *Science* **366**, eaan4673 (2019).
93. H. Tsukamoto *et al.*, *Proc. Natl. Acad. Sci. U.S.A.* **106**, 18333–18338 (2009).
94. A. G. Soerens *et al.*, *Nature* **614**, 762–766 (2023).
95. M. Mittelbrunn, G. Kroemer, *Nat. Immunol.* **22**, 687–698 (2021).
96. R. I. K. Geltink, R. L. Kyle, E. L. Pearce, *Annu. Rev. Immunol.* **36**, 461–488 (2018).
97. M. Faas *et al.*, *Immunity* **54**, 2531–2546.e5 (2021).
98. K.-A. Lee, P. D. Robbins, C. D. Camell, *Curr. Opin. Pharmacol.* **57**, 107–116 (2021).
99. O. Oyesola *et al.*, *Nat. Immunol.* **25**, 1270–1282 (2024).
100. M. Eyting *et al.*, *Nature* **641**, 438–446 (2025).
101. K. Caid *et al.*, *J. Allergy Clin. Immunol. Glob.* **3**, 100340 (2024).
102. A. A. Y. Ragab *et al.*, *Immun. Ageing* **21**, 37 (2024).
103. M. G. Netea *et al.*, *Nat. Med.* **22**, 831–833 (2016).
104. G. Kuan *et al.*, *Am. J. Epidemiol.* **170**, 120–129 (2009).
105. C. Q. Jiang *et al.*, *Int. J. Epidemiol.* **46**, e16 (2017).
106. A. Olin *et al.*, *Allergy* **77**, 1583–1595 (2022).
107. V. M. Link *et al.*, *Nat. Med.* **30**, 560–572 (2024).
108. K. J. Kaczorowski *et al.*, *Proc. Natl. Acad. Sci. U.S.A.* **114**, E6097–E6106 (2017).
109. P. Roy, M. Orecchioni, K. Ley, *Nat. Rev. Immunol.* **22**, 251–265 (2022).
110. T. B. Bertolini *et al.*, *Cell. Immunol.* **359**, 104251 (2021).
111. M. J. Mina *et al.*, *Science* **366**, 599–606 (2019).
112. J. Montroy *et al.*, *Vaccine* **47**, 126706 (2025).

ACKNOWLEDGMENTS

Funding: C.J.E.M. was supported by the Princeton Catalysis Institute and Princeton Precision Health. A.L.G. was supported by the National Science Foundation (DEB-2153923). A.J.Y. was supported by the National Institutes of Health (R01 AI093870 and U01 AI150680). D.A.T.C. was supported by the National Institutes of Health (R01 AI175495 and R01AI174105). **Competing interests:** None declared. **License information:** Copyright © 2025 the authors, some rights reserved; exclusive licensee American Association for the Advancement of Science. No claim to original US government works. https://www.science.org/about/science-licenses-journal-article-reuse

Submitted 13 May 2025; accepted 9 July 2025

10.1126/science.ady9543

Check for

The Columbia deal is a tragic wake-up call

H. Holden Thorp

Last month, Columbia University entered an agreement with the US government to restore federal funding for research in exchange for actions by the university to address complaints by the Trump administration about antisemitism on campus and civil rights violations in admissions and faculty hiring. In reaching the deal, the government wielded science funding—at least $1.3 billion dollars annually—as a powerful lever to influence the university, and signing it was probably unavoidable. Although there is much to criticize in the agreement, it stands as a reminder that accepting federal dollars for research has always come with the possibility that those funds could be clawed back under circumstances deemed a misuse of taxpayer money. Universities are now witnessing this power-of-the-purse at an unparalleled magnitude.

In discussing the agreement, Claire Shipman, the acting president of Columbia, made it clear that liberating research funding was the goal of the negotiation. "This is about science," she told CNN. "It's about curing cancer, the cutting-edge, boundary-breaking science that actually benefits the country and humanity." Restoring the funding is indeed a positive outcome for the university, but the trade-offs it made reach far beyond the matter of how scientific research is conducted and how research funds are spent. Columbia has agreed to answer questions about how it handles student admissions, appoints faculty, designs curricula, and deals with protests, among other concessions, and will be expected to comply with laws that the Trump administration has a particularly strong interest in. Notably, these obligations are related mainly to undergraduate education and not to the conduct of research.

To ensure that both sides keep their commitments, the agreement appoints a "resolution monitor," which is a step down from a more onerous legally enforced order that was initially contemplated. Michael Roth, the president of Wesleyan University, who has been an outspoken critic of the Trump administration and has decried the timidity of universities in standing up for higher education, declined to criticize Columbia for entering the agreement, likening it to a parent who understandably had to pay a ransom for their kidnapped child. Many in academia believe that Columbia's decision has put other universities at risk of being required to meet the same kind of demands.

The Columbia case is a jolt to American universities, which, over the past 80 years, have enjoyed steady growth in federal support for research. After World War II, the government began investing heavily in academic research and development to bolster the nation's security. In the 1980s, when the quantitative ranking of colleges and universities began, research achievement and funding became a primary measure by which institutions valued themselves and each other. Since then, campus growth has been a top goal, and funds for research have been vigorously pursued in the name of prestige, expansion, and development. The perils of such reliance are now obvious in the case of Columbia.

The suite of problems now faced by all American universities, public and private, may well be unprecedented. There is not only intense political pressure from the government and public sentiment about costs, value, and direction but also internal unhappiness regarding academic freedom, budget decisions, divestments, and other matters. Yet underlying these challenges is the insatiable desire of institutions to have more resources. University leaders often paternalistically excuse faculty from participating in decisions that attend the trade-offs between academic principles and financial support. But every funding source—private donors, federal government, and earned revenue—comes with expectations. This quid pro quo, whether explicit or implicit, puts university administrators in a bind. Columbia decided not to challenge the government but to negotiate to preserve its life blood. Last week, Brown University followed suit and struck a deal to restore its funding. But Harvard University has gone to court to fight a similar withholding of federal support for research, although there has been speculation that a deal may be near as well.

Yet underlying these challenges is the insatiable desire of institutions to have more resources.

In the aftermath of its negotiation, scientists at Columbia should have compassion for colleagues who will bear the brunt of the agreement's terms. Although science faculty can return to their labs once the money flows again, other disciplines will be subjected to increased scrutiny of their teaching and scholarship. This will weigh most heavily on undergraduate departments, not the researchers benefiting from the return of funding. The real danger in all this tumult may be the threat it poses to the core purpose of higher education—preparing future generations for the public good. □

H. Holden Thorp* is Editor-in-Chief of the *Science* journals. hthorp@aaas.org
*H.H.T.'s son is a faculty member at Columbia University.

Published online 31 July 2025; 10.1126/science.aeb0424

Check for

RESEARCH ETHICS

Study used DNA from thousands—without consent

iPsych, which investigates the genetics of psychiatric disorders, has sent 140,000 opt-out notices amid backlash

ANNIKA INAMPUDI

In June, Sara* received an email asking whether she wanted to continue to participate in a massive, multicenter research project led by scientists at Aarhus University in Denmark. The iPsych study, the message said, had sequenced her genetic data from a blood sample taken at birth to check for specific diseases. For more than a decade, researchers had used those data, alongside Denmark's famously meticulous public record system, to investigate the genetic and environmental causes of mental illnesses.

Sara, who has been diagnosed with autism and depression, was shocked. This was the first she had heard she was part of one of the largest studies of psychiatric illness in the world. She had never consented to her data being used. "It sent me spiraling, I broke completely down," she says. "It really triggered previous experiences [of] not being treated as a human being."

Sara is one of 140,000 Danes born between 1981 and 2008 who received an opt-out notice from iPsych in late June, following critical coverage of the project's approach to consent in Danish media. When the project began in 2012, an ethics committee deemed it exempt from obtaining informed consent from those whose blood was used. The leaders of iPsych say this exemption was consistent with Danish legislation and was crucial to producing a representative data set, and that the project has anonymized and protected all sensitive information in accordance with privacy laws. They say iPsych has been transparent about the project since its inception.

But many of those who have just discovered that their data have been used—as well as some data privacy scholars—say the controversy raises ethical issues. "It's not sufficient to say that [the study] is compliant in terms of the strictly legal aspects," says Mahsa Shabani, a health law researcher at the University of Amsterdam. "You need to make sure that you are respecting the [participants'] fundamental rights."

iPsych is the brainchild of two Aarhus scientists, geneticist Anders Børglum and psychiatrist Preben Bo Mortensen, who realized the country's collection of newborn blood samples could be used to make a "uniquely Danish contribution to International research," per the study's original proposal. Since 1981, every new parent in Denmark has been offered a heel prick blood test for their baby to detect disease-causing genetic mutations—on the condition that the blood samples could be used, at any time, for research.



iPsych has extracted DNA from thousands of banked blood samples originally taken during the heel prick test for newborns.

For a long time these samples lay untouched in the national biobank. But in the 2000s, geneticists gained a new tool: the genomewide association study, which allowed them to sift through the DNA of thousands of individuals to find genetic variants linked to certain traits and diseases. Mortensen and Børglum proposed using this new method to analyze the thousands of stored samples.

The team wanted to ensure that its study represented the Danish population. But asking people to give consent inevitably skews a data set toward those who are wealthier, older, and more educated, Mortensen says. This could produce spurious results, which would have an "ethical cost," he says, so the iPsych team asked to waive this requirement. Danish law allowed a waiver, he says, providing a study doesn't endanger or inconvenience participants and if requiring consent would impair the study. In January 2012, a regional science ethics committee in Denmark agreed, giving iPsych permission to extract genetic data from the country's newborn blood samples for the next decade without the consent of the study subjects, many of whom were by now adults.

The iPsych project includes the full or partially sequenced genomes of 90,000 people with psychiatric diagnoses and 50,000 controls. By exploiting Denmark's uniquely robust and sprawling collection of data about every citizen—hundreds of registries documenting diagnoses, income and employment history, electoral participation, and more—the team has tied these genetic data to various health and social outcomes. The project has generated more than 1000 papers over the past 13 years, including studies locating areas of the genome associated with autism, schizophrenia, depression, and attention-deficit/hyperactivity disorder.

In 2019, with 2 years remaining on its original permissions, the iPsych team applied for an extension to continue to extract DNA and other biological data from banked blood samples beyond 2021. But the national ethics committee had since adopted a stricter policy for waiving

*Not her real name

informed consent requirements for research, and it refused, writing, "it would not be ethically sound" to renew the project.

Despite this decision, iPsych continues to publish new papers using the genetic data it has already extracted. This research is legal, Mortensen says: Once DNA is sequenced from the blood samples and the data stored electronically, it is regulated by data protection laws and not laws regulating the use of biological tissue. But after news reports from the Danish Broadcasting Corporation criticized the project last year, patient advocates and government officials urged Mortensen and his team to inform people that their genomes and health data are being used.

In response, iPsych sent messages to all 140,000 participants—an effort that Mortensen stresses required permission from the ethics committee, because the original proposals forbade the researchers from contacting people in the study. To prevent "more damage than good," he adds, iPsych workshopped its statement with focus groups of people with psychiatric disorders. The messages ask participants to indicate by 31 August whether they want to opt out of the study. If so, their data can no longer be analyzed, but could still be included in upcoming papers based on work that has already been completed.

Many iPsych participants feel blindsided. Camilla Fosbaek says that learning her data had been used left her feeling that her privacy had been invaded. Seeking community, she started a Facebook group for other people in the study. "Many of these people are too sick to fight," says Sophie Raae, a member of the now 200-person group. "We … want to do everything that we can to make sure that these ethical violations do not continue." Fosbaek says the group is trying to take legal action against Aarhus University and the ethics committees, although they are struggling to find a lawyer to take the case.

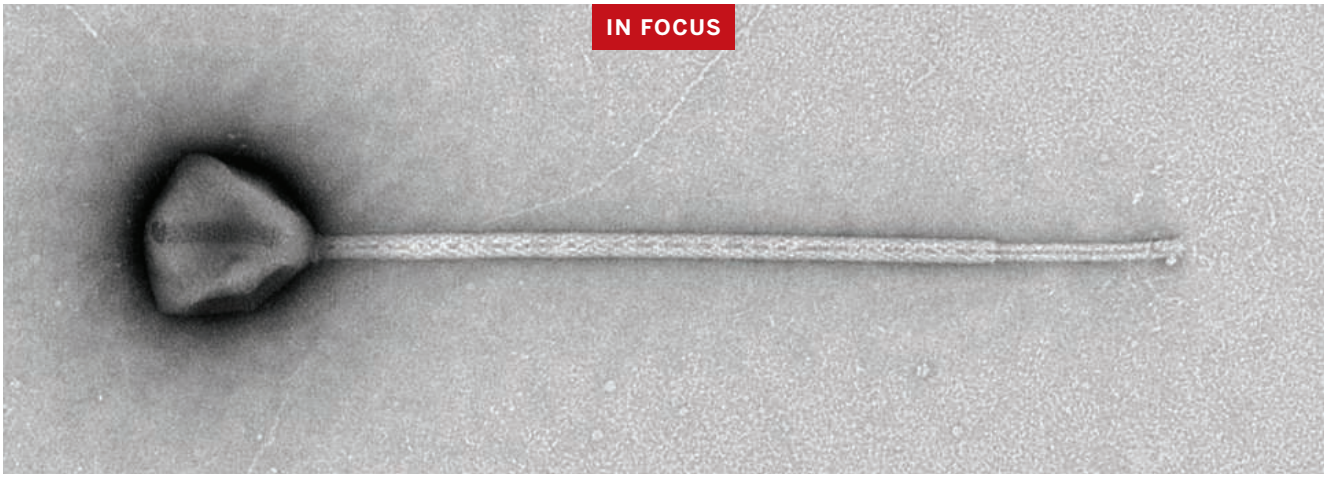
Shabani says that when people aren't aware of their participation in such projects, "it can backfire, and people may lose their trust." Allowing participants to opt out now is the bare minimum for iPsych to continue ethically, she says. But Thomas Ploug, an ethicist at Aalborg University who specializes in Danish registry data ethics, says a blanket opt-out message asks people to make an "impossible trade-off." They "have to weigh the risk of [iPsych] doing something really crazy with [their data] … or participating in valuable research." He'd rather see iPsych inform participants about the specific details of each project using their data.

Shabani and others worry the saga may undermine trust in the Danish system of record-keeping, a source of great pride for the country. It would be devastating for public health if the iPsych controversy dissuaded parents from participating in disease-detecting initiatives like heel prick tests, she adds. "You don't want people not to allow their babies to be screened because they are afraid of what will happen to their [child's] data."

Mortensen says he recognizes the responsibility that comes with working with the genetic and personal data of thousands of Danes. "I value the trust I receive by being allowed to work with this data," he says. "It is very important to me to not betray that trust in any way."

But for some of those in the study, it may be too late. Sara says iPsych has already shaken her faith in the health care system. Even though she opted out in June, she is dismayed that iPsych can continue to publish papers using her data. "I feel it in my chest," she says. "I don't know how long I will have this sort of feeling." □

IN FOCUS



Virus with record-long tail discovered

So-called giant viruses, which can contain thousands of genes and can be even larger than some bacteria, have blurred the lines between life and nonlife and sparked debate about how they evolved. Now, researchers have discovered one of these monster viruses with a record-long tail extending 2.3 micrometers behind its protein shell, or capsid. That's as long as an *Escherichia coli* bacterium and about 20 times the size of the coronavirus that causes COVID-19. The virus, called PeIV-1, was found in the Pacific Ocean, and uses its tail to enter an important photosynthetic plankton called *Pelagodinium*, the researchers reported last month in a preprint on the bioRxiv server. After the virus was engulfed by the phytoplankton, its tail disappeared. —Nazeefa Ahmed

PHOTO: GAJIGAN & STEWARD

Check for

TRUMP TRACKER

IN AT CDC, OUT AT FDA The U.S. Senate last week confirmed veteran federal scientist Susan Monarez, an immunologist and biosecurity expert, to lead the Centers for Disease Control and Prevention. Monarez, who in her confirmation hearing told senators that "vaccines save lives," is the first nonphysician in more than 70 years to head the $9.2 billion agency, whose budget the White House has proposed slashing to $4.3 billion in 2026. On the same day Monarez was confirmed, health researcher Vinay Prasad, a critic of the wide deployment of coronavirus shots, resigned as head of the center that approves vaccines and other biologics at the Food and Drug Administration. According to *Politico*, President Donald Trump personally ordered the ouster, egged on by right-wing activist Laura Loomer, who labeled Prasad as "anti-Trump" and a "progressive leftist saboteur." During his short tenure, Prasad faced blowback for his request that Sarepta Therapeutics pause shipments of Elevidys, a gene therapy for Duchenne muscular dystrophy, after two recipients died of liver failure. —Meredith Wadman

CLIMATE REPORT FACES PUSHBACK A contrarian climate assessment, released last week by the U.S. Department of Energy (DOE), has drawn outcry from researchers who say the report cherry-picks evidence to downplay the impacts of climate change. The report has been cited by the U.S. Environmental Protection Agency in its campaign to overturn its landmark 2009 endangerment finding, which established carbon dioxide as a pollutant EPA can regulate. The report argues that some of the warming attributed to fossil fuel burning is instead driven by natural cycles or variability in the Sun, and that sea level rise has not been accelerating. The authors, handpicked by DOE Secretary Christopher Wright, a fossil fuel entrepreneur, say they want to steer climate science away from alarmism and advocacy. But the report amounts to a "law brief from attorneys defending their client, carbon dioxide," said Andrew Dessler, a climate scientist at Texas A&M University, on Bluesky. —Paul Voosen

U.S. SCIENCE FUNDING

Senate panel rejects Trump's plan to slash NIH's budget

Bipartisan support for agency challenges proposed reorganization and overhead costs cap **JOCELYN KAISER**

In a stark rejection of President Donald Trump's plan to dramatically slash federally funded biomedical research in 2026, a Senate funding committee last week approved a draft bill that instead gives the National Institutes of Health (NIH) a modest raise of $400 million. It also disregards Trump's plan to gut the Centers for Disease Control and Prevention (CDC).

The bill approved by the Senate Committee on Appropriations includes $47.2 billion for NIH's base budget, or about 1% more than this year. The biomedical community would not normally celebrate such a small bump, but Trump's budget proposal would cut the agency by $18 billion, or about 40%. The Senate bill also rejects White House proposals such as a massive NIH reorganization and a plan to cap the "indirect costs" added to NIH grants, which would drastically lower overhead reimbursement universities get for conducting research. The bill joins others lawmakers have backed that challenge Trump's proposed cuts to science agencies.

At a hearing on the bill, Senate Appropriations Committee Chair Susan Collins (ME), one of several Senate Republicans who have opposed the proposed NIH cuts, emphasized that it "supports lifesaving research." Senator Patty Murray (WA), the top Democrat on the committee, pointed to spending delays and other "chaos" imposed by Trump officials on NIH and other agencies. "To the scientists wondering if there will even be an NIH by the end of this administration: This committee's resounding message is 'yes,'" she said. "Congress has your back—we're not going to give up the fight against cancer, Alzheimer's, or rare diseases. We support you and we need you to stay here and keep this research going."

The bill, which must still go to the full Senate for approval and be reconciled with a House of Representatives version, includes targeted increases for specific research areas, including $150 million for cancer research, $100 million for Alzheimer's disease, and smaller amounts for infectious disease, women's health, amyotrophic lateral sclerosis research, and several other diseases and initiatives. The Advanced Research Projects Agency for Health, an independent agency within NIH, would stay level at $1.5 billion.

The measure also maintains NIH's current 27 institutes and centers, which Trump would have folded into just eight, partly by eliminating three of them. It blocks Trump's plan to cap indirect costs at 15%, less than one-third the current rate for some schools, with an accompanying report instead endorsing a new model for calculating these rates proposed by universities. The bill and report direct NIH to restore funding for HIV vaccine research, training programs, and an infant sleep safety campaign that had been cut by Trump officials.

An amendment added to the bill also blocks another NIH move that had drawn concern: a policy begun this year that would require 50% of awards to fund all years of a research grant with a single upfront sum. The "forward funding" approach has already resulted in a sharp drop in NIH institutes' "paylines"—effectively the percentage of peer-review–approved grants it can fund—and spurred fears that over time it would force many labs to close.

Biomedical research advocates are pleased by NIH's $400 million raise. The bill "is not a subtle rebuke of the administration's budget proposal. It's a clear sign that the Senate has little interest in cutting funding for NIH in FY2026 and that the appropriators will exercise their power of the purse," says Jennifer Zeitzer, deputy executive director of the Federation of American Societies for Experimental Biology.

CDC's budget, which Trump wanted to cut by 50%, gets a

$70 million haircut but stays essentially level at $9.15 billion. And the bill rejects Trump's "haphazard plan to dismantle the CDC," according to a committee summary. The bill makes no mention of Department of Health and Human Services Secretary Robert F. Kennedy Jr.'s plan to fold several CDC disease programs into a new Administration for a Healthy America, effectively nixing that idea.

In the hearing, several lawmakers spoke out against the White House Office of Management and Budget (OMB) recently freezing $15 billion of unspent funds in NIH's 2025 budget, before backing off the action. The funding halt came as OMB Director Russell Vought appeared on a Sunday talk show disparaging NIH as needing a "dramatic overhaul" after 14 Republican Senators urged him to allow NIH to spend its full budget.

Vought ultimately released the money after frantic lobbying by patient advocacy groups and lawmakers, including some Republicans on the committee.

The House Committee on Appropriations, which is also expected to reject Trump's proposed cuts to NIH, could release its version of the spending bill covering health agencies in early September. If reconciled with the Senate bill, it would then go to the president, although many political onlookers think the 2026 fiscal year budget will become stalled and result in a continuing resolution that keeps agency budgets at their 2025 levels. □

IN FOCUS

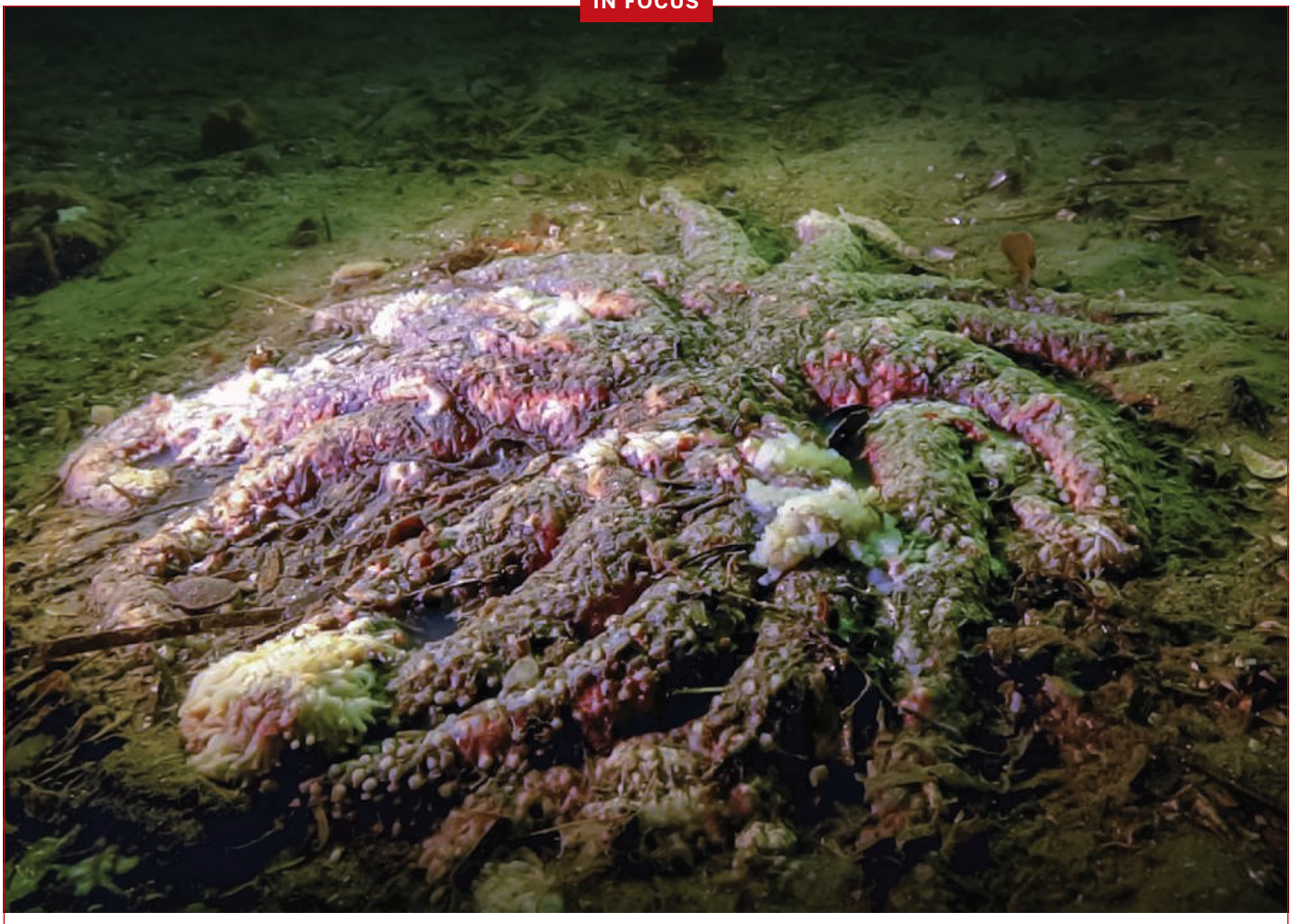
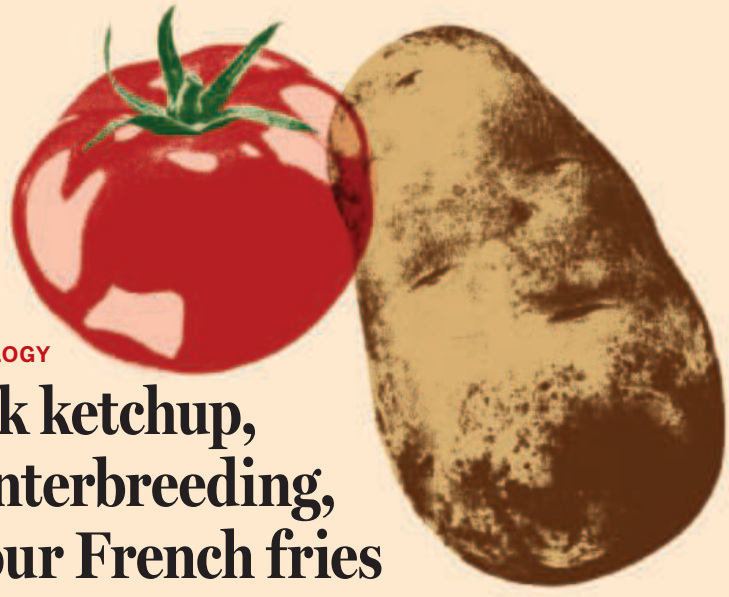


PHOTO: GRANT CALLEGARI/HAKAI INSTITUTE

Sea star killer identified

In 2013, sea stars began dying in droves in Washington state from an infectious disease that made them disintegrate within days (above). It spread quickly along the Pacific coast of North America and has since been reported globally. Yet its cause has remained a mystery. Using genetic sequencing, a team has now discovered a bacterium, distantly related to the one that causes cholera, that can kill the sunflower sea star (*Pycnopodia helianthoides*), the species most afflicted. The pathogen is *Vibrio pectenicida* strain FHCF-3, previously known to infect the larvae of two marine invertebrates. The discovery, reported this week in *Nature Ecology & Evolution*, could assist in recovery efforts. The team is developing a genetic test that could check for the presence of the bacterium in captive sea stars and aid efforts to breed more resistant ones. —Erik Stokstad



PLANT BIOLOGY

Thank ketchup, and interbreeding, for your French fries

Hybridization 9 million years ago gave potatoes the genetic knack to develop tubers, a new study finds

ERIK STOKSTAD

Tomatoes and potatoes don't only sound similar and taste good together: They're the closest of relatives, even though one has edible fruit and the other tubers. Now, researchers have determined that one may have given rise to the other. According to a study last week in *Cell*, early tomato plants hybridized with close relatives about 9 million years ago, in a tryst that yielded hybrid offspring with just the right mix of genes to make tubers.

"Tomato is the mother of potato," says genome biologist and plant breeder Sanwen Huang of the Chinese Academy of Agricultural Sciences, who led the new research.

That hybridization, the authors argue, helped early potatoes diversify into new regions and climates—from warm grasslands to cold mountain meadows—that neither of its ancestor lineages could inhabit so well. The study tells "quite a compelling story," says Jeremy Beaulieu, an evolutionary biologist at the University of Arkansas who was not involved with the research. "This is one of the most complete studies on key innovations in plants that I think I've seen."

The sacks of identical brown spuds in your local grocery store belie the incredible diversity within *Solanum tuberosum*, the single species of domesticated potato. Thousands of "landraces" of *S. tuberosum*—with tubers of many colors and shapes—are grown in the Andes mountains. Moreover, more than 100 related species of wild potato occur across the Americas, everywhere from the southern tip of Chile to the southwestern United States.

The reason for this one species' high diversity has remained unclear, as have the origins of its tubers, notes Lynn Bohs, a plant taxonomist and evolutionary biologist at the University of Utah. Previous genomic studies had revealed that tomatoes are potatoes' closest living relatives. Yet another group of three ancestral species, known as *Etuberosum*, more closely resembles potatoes, with a puzzling exception: They don't grow tubers. This discrepancy has made the emergence of these structures "a huge mystery," says Bohs, who wasn't involved with the new study.

Intrigued by this discrepancy, Huang says he and his colleagues "decided to zoom in to solve this puzzle," by sequencing the genomes of 44 wild potato species, the three *Etuberosum* species, and 15 species of wild tomato. "No one has been able to do this scale of work before," says Robin Buell, a crop genomicist at the University of Georgia.

Huang's team found that the wild potatoes have a blend of genes from tomatoes and *Etuberosum*. The pattern of these genes across the potato genome provides "a signal of ancient hybridization," Huang says. By comparing the number and types of mutations within tomato and *Etuberosum* genes, Huang and his colleagues estimated that the tomato and *Etuberosum* groups diverged from a common ancestor about 13 million years ago, presumably becoming unable to easily interbreed. Despite this barrier, the potato genomes suggest, the two lineages successfully hybridized about 9 million years ago.

This crossing is what gave proto-potatoes the knack for making tubers, Huang and his colleagues believe. For example, the new genomic analysis shows that a gene called *SP6A*, which acts as a tuber-forming switch within potatoes, came from tomatoes. Another potato gene known as *IT1*, which regulates the growth of the underground stems that swell into tubers, came from *Etuberosum*.

Tubers were a boon in two ways to the first potato plants, the team says. First, tubers store nutrients, which can help a plant endure tough conditions. Second, they let plants reproduce without pollinators or even sexual reproduction, which probably helped the new lineage overcome any lingering fertility problems.

The researchers also suspect that tubers helped early potatoes diversify into many new species. The hybridization event occurred around the time the Andes were rapidly rising, which may have created new niches the potato could fill better than its ancestors. Regardless of the Andes' influence, potatoes diversified rapidly: Since the hybridization, wild potatoes have evolved into new species about 20% faster than tomatoes and 36% faster than *Etuberosum*.

This boost makes sense to Huang. In other groups such as cichlid fish and sunflowers, hybridization creates more genetic diversity than mutations alone can provide, giving evolution more initial diversity on which to act. "Hybridization didn't just create a new species—it built an adaptive machine," Huang says.

Thomas Städler, a geneticist at ETH Zürich, isn't entirely convinced. The evidence for potatoes arising from hybridization is strong, he says, but whether this event alone led to tubers and potatoes' ability to diversify is "still a question mark" meriting follow-up study.

History aside, Huang is looking to the future. For example, plant scientists might engineer tomatoes to bear tubers by adding potato genes. Such an approach would, in some respects, riff on evolution's original handiwork in the foothills of the rising Andes. "Next time you eat potatoes," Huang says, "thank a tomato." □

SCIENTIFIC INTEGRITY

Study reveals industrial-scale publishing fraud

Sophisticated global networks are infiltrating journals to publish fake papers **CATHLEEN O'GRADY**

For years, sleuths who study scientific fraud have been sounding the alarm about the sheer size and sophistication of the industry that churns out fake publications. Now, an extensive investigation finds evidence of a range of bad actors profiting from fraud. The study, based on an analysis of thousands of publications and their authors and editors, shows paper mills—groups that sell guaranteed author slots and papers to scientists—are just part of a complex, interconnected system that includes publishers, journals, and brokers.

The paper, published on 4 August in the *Proceedings of the National Academy of Sciences*, paints a disturbing picture. Northwestern University metascientist Reese Richardson and his colleagues identify networks of editors and authors colluding to publish shoddy or fraudulent papers, report that large organizations are placing batches of fake papers in journals, and suggest brokers may serve as intermediaries between paper mills and intercepted journals. They also find that the number of fake papers—though still relatively small—seems to be increasing at a rate far greater than the scientific literature generally.

The paper shows that misconduct "has become an industry," says Anna Abalkina of the Free University of Berlin, who studies corruption in science and was not involved with the research.

Richardson and colleagues, who hope their sweeping case will attract attention and spur change, began their analysis by pinpointing corrupt editors. They focused their investigation on *PLOS ONE*, because the megajournal allows easy access to bulk metadata and publishes the names of the editors who have handled the thousands of papers it publishes each year, making it possible to detect anomalies without behind-the-scenes information. The researchers identified all the papers from the journal that had been retracted or received comments on PubPeer—a website that allows researchers to critique published work—and then identified each paper's editors.

All told, 33 editors stood out as more frequently handling work that was later retracted or criticized than would be expected by chance. "Some of these were immense outliers," Richardson says. For instance, of the 79 papers that one editor had handled at *PLOS ONE*, 49 have been retracted. Flagged editors handled 1.3% of papers published in the journal by 2024, but nearly one-third of all retracted papers.

The team also spotted that these editors worked on certain authors' papers at a suspiciously high rate. These authors were often editors at *PLOS ONE* themselves, and they often handled each other's papers. It's possible that some editors are being paid bribes, Richardson says, but "also possible that these are informal arrangements that are being made among colleagues." The researchers detected similarly questionable editor behavior in 10 journals published by Hindawi, an open-access publisher that was shuttered because of rampant paper mill activity after Wiley acquired it. A spokesperson for Wiley told *Science* the publisher has made "significant investments to address research integrity issues."

Renee Hoch, head of publication ethics at PLOS, publisher of *PLOS ONE*, said in an email to *Science* that the publisher has long been aware of networks like these, and will assess whether any of the editors implicated are still on the journal's editorial board, opening investigations if they are. She emphasizes that the study focused on PLOS because of its readily accessible data: "Paper mills are truly an industry-wide problem."

Researchers working on paper mills have long assumed that editors and authors have been colluding. The new findings are "killer evidence" for these suspicions, says Domingo Docampo, a bibliometrician at the University of Vigo. He adds that although the findings only show collusion at a limited number of journals, others are probably affected. Just last week, Retraction Watch reported that the publisher Frontiers had begun to retract 122 papers after discovering a network of editors and authors "who conducted peer review with undisclosed conflicts of interest," according to a company statement. The network of 35 individuals has also published more than 4000 papers in journals from seven other publishers, the company said. A Frontiers spokesperson said they planned to share information with the other affected publishers to enable them to investigate.

Richardson and his colleagues found that the problem goes far beyond networks of unscrupulous editors and authors scratching each other's backs. They identified what appear to be coordinated efforts to arrange the publication of batches of dubious papers in multiple journals.

The team looked at more than 2000 papers flagged on PubPeer for containing duplicated images and identified clusters of papers that all shared images. Those sets of papers were often published around the same time and in a limited selection of journals. Looking at patterns of duplicated images is an "absolutely innovative" method for investigating these networks, Abalkina says. "No one has done this before."

> "The percentage of fraudulent science is growing."
>
> **Anna Abalkina**
> Free University of Berlin

In some cases, the authors suggest, a single paper mill that infiltrated multiple journals may be responsible. But they also believe some of these clusters reflect the work of "brokers" who act as go-betweens, taking articles produced by paper mills and placing them at compromised journals.

The team dug into the workings of the Academic Research and Development Association (ARDA), based in Chennai, India, which offers services including "thesis/article writing" as well as "journal publication" in a list of dozens of journals. On a web page listing "high impact journals" on offer, ARDA says it liaises with journals



on behalf of researchers and "[ensures] they get published successfully in the High Impact Indexing Database journal of their choice."

Over several years, ARDA's list of journals has evolved, the team found, with new publications added to the list and others removed after being delisted by bibliometric databases because of fishy behavior. The journals often publish transparently "problematic" articles, Richardson says, and ARDA charges between $250 and $500 for publication, based on quotes offered to Richardson and his colleagues. The website asks authors to submit their own papers, suggesting ARDA itself is not a paper mill, but rather a go-between, Richardson says.

ARDA did not respond to a request for comment.

Organizations like these operate in broad daylight, under the guise of providing "editorial services," says Lokman Meho, an information scientist at the American University of Beirut. Although their operations may be unethical—with stark consequences for science and scientists—they don't care about trying to hide, he says, because "it is actually not illegal to run such businesses."

The problems Richardson and his colleagues documented are growing fast. The team built a list of papers identified in 55 databases of likely paper mill products, looking at the number of suspicious papers published each year between 2016 and 2020. (They excluded the past few years of data because it takes time for fraudulent papers to be discovered and retracted.) They found that the number of suspected paper mill products doubled every 1.5 years—10 times faster than the rate of growth of the scientific literature as a whole, although still a small proportion of papers overall. The number of retractions and papers flagged on PubPeer had also risen fast, doubling every 3.3 and 3.6 years, respectively, but not keeping pace with the increase in suspected fraudulent papers.

"This means that the percentage of fraudulent science is growing," Abalkina says. That poses particular risks to fields like medical science, where the fake papers sometimes make their way into systematic reviews and meta-analyses, potentially distorting our understanding of drugs and treatments, she says.

One contributor is the rapid growth of science, says Wolfgang Kaltenbrunner, a science studies scholar at Leiden University. Paper mill products are often buried in low-impact journals and are written to get little attention, he says. In small scientific communities, it is harder to hide products like these, but as some fields get larger and more anonymous, such papers can escape detection more easily. And as the scientific workforce has burgeoned, institutions have increasingly turned to evaluating scientists based on how many publications they produce, leading some researchers to bolster their records with fake papers, he says. "Perverse incentives, inflated metrics, the 'publish or perish' culture, and systemic tolerance for weak scholarship" all allow paper mills to flourish, says Li Tang, an expert on Chinese research policy at Fudan University.

Young researchers may feel forced into paying for paper mill publications to compete with peers—a ratcheting effect that is already apparent, Richardson says. The number of papers published by medical residency applicants has soared in recent years, for instance, with some students claiming authorship of dozens of papers. He says it's no coincidence that the paper mill industry targets residency applicants, especially foreign students on visas.

Docampo, Abalkina, and others say there's little in the new analysis that wasn't already strongly suspected. But the dramatic confirmation that the study offers may shift the needle, they suggest. "We're massively behind the curve on making visible and realizing the extent of the problem," Kaltenbrunner says. "The sheer scale of it is the takeaway message here." □

ARTIFICIAL INTELLIGENCE

AI-generated text surges in research papers

One-fifth of computer science papers may include AI-written sentences **PHIE JACOBS**

A massive, cross-disciplinary look at how often scientists turn to artificial intelligence (AI) to write their manuscripts has found steady increases since OpenAI's text-generating chatbot ChatGPT burst onto the scene. In some fields, the use of such generative AI has become almost routine, with up to 22% of computer science papers showing signs of input from the large language models (LLMs) that underlie the computer programs.

The study, which appears this week in *Nature Human Behaviour*, analyzed more than 1 million scientific papers and preprints published between 2020 and 2024, primarily looking at abstracts and introductions for shifts in the frequency of telltale words that appear more often in AI-generated text. "It's really impressive stuff," says Alex Glynn, a research literacy and communications instructor at the University of Louisville. The discovery that LLM-modified content is more prevalent in areas such as computer science could help guide efforts to detect and regulate the use of these tools, adds Glynn, who was not involved in the work. "Maybe this is a conversation that needs to be primarily focused on particular disciplines."

When ChatGPT was first released in November 2022, many academic journals—hoping to avoid a flood of papers written in whole or part by computer programs—scrambled to create policies limiting the use of generative AI. Soon, however, researchers and online sleuths began to identify numerous scientific manuscripts that showed blatant signs of being written with the help of LLMs, including anomalous phrases such as "regenerate response" or "my knowledge cutoff."

"On the surface, it's quite amusing," says Glynn, who compiles Academ-AI, a database that documents suspected instances of AI use in scientific papers. "But the implications of it are quite troubling." LLMs are notorious for "hallucinating" false or misleading information, Glynn explains, and when obviously AI-generated papers are published despite rounds of peer review and editing, it raises concerns about journals' quality control.

Unfortunately, it has gotten harder to spot AI's handiwork as the technology has advanced and authors who use it have become more proficient at covering their tracks. In response, scientists have looked for subtler signs of LLM use. For the new study, James Zou, a computational biologist at Stanford University, and colleagues took paragraphs from papers written before ChatGPT was developed and used an LLM to summarize them. The team then prompted the LLM to generate a full paragraph based on that outline and used both texts to train a statistical model of word frequency. It learned to pick up on likely signs of AI-written material based on a higher frequency of words such as "pivotal," "intricate," or "showcase," which are normally rare in scientific writing.

The researchers applied the model to the abstracts and introductions of 1,121,912 preprints and journal-published papers from January 2020 to September 2024 on the preprint servers arXiv and bioRxiv and in 15 *Nature* portfolio journals. The analysis revealed a sharp uptick in LLM-modified content just months after the release of ChatGPT. That this trend appeared so soon "means that people were very quickly using it right from the start," Zou says.

Certain disciplines exhibited faster growth than others, which may reflect differing levels of familiarity with AI technology (see table, below). "We see the biggest increases in the areas that are actually closest to AI," Zou explains.

By September 2024, 22.5% of computer science abstracts showed evidence of LLM modification, with electrical systems and engineering sciences coming in a close second—compared with just 7.7% of math abstracts. Percentages were also comparatively smaller for disciplines such as biomedical science and physics, but Zou notes that LLM usage is increasing across all domains: "The large language model is really becoming, for good or for bad, an integral part of the scientific process itself."

University of Tübingen data scientist Dmitry Kobak, whose recent similar study in *Science Advances* revealed that about one in seven biomedical research abstracts published in 2024 was probably written with the help of AI, is impressed by the new work. "This is very solid statistical modeling," Kobak says.

He adds that the true frequency of AI use in scientific publishing could be even higher, because authors may have started to scrub "red flag" words from manuscripts to avoid detection. The word "delve," for example, started to appear much more frequently after the launch of ChatGPT, only to dwindle once recognized as a hallmark of AI-generated text.

Although the new study primarily looked at abstracts and introductions, Kobak worries authors will increasingly rely on AI to write sections of scientific papers that reference related works. That could eventually cause these sections to become more similar to one another and create a "vicious cycle" in the future, in which new LLMs are trained on content generated by other LLMs.

Zou and his colleagues are currently planning a conference where the writers and reviewers are all AI agents, which they hope will demonstrate whether and how these technologies can independently generate new hypotheses, techniques, and insights. "I expect that there will be some quite interesting findings," he says. "I also expect that there will be a lot of interesting mistakes." □

Rise of AI The amount of artificial intelligence (AI)-generated text in scientific papers had surged by September 2024, almost 2 years after the release of ChatGPT, according to an analysis.

Field/publisher	Estimated AI usage (% papers)
Computer science	22.5
Electrical engineering and systems science (arXiv)	18
Statistics (arXiv)	12.9
bioRxiv	10.3
Physics (arXiv)	9.8
Nature portfolio (arXiv)	8.9
Mathematics (arXiv)	7.8

DATA: W. LIANG *ET AL*., *NAT HUM BEHAV* (2025) HTTPS://DOI.ORG/10.1038/S41562-025-02273-8

GLOBAL NEWS

ECUADOR AXES SCIENCE AGENCY

Ecuador's government has eliminated its independent research agency and merged its environment and energy ministries as part of a sweeping reorganization. Critics fear the moves could imperil research budgets and efforts to protect ecosystems. In a bid to cut spending and streamline bureaucracy, Ecuadorian President Daniel Noboa on 24 July got rid of six of the nation's 20 ministries and six of its nine smaller secretariats. He also fired 5000 government employees. The science secretariat will become part of a ministry for education, sport, and culture. The moves likely mean "even less funding for research," says nutrition researcher Angélica Ochoa Avilés of the University of Cuenca. She says universities could lose autonomy under the education ministry, which historically oversaw only primary and secondary education. —Kata Karáth

BUDGET CUTS COME TO CANADA

Researchers in Canada are pushing back against a 15% budget cut Prime Minister Mark Carney plans to impose on most government departments—and angling for a piece of dramatically growing military budgets. Carney began a spending review shortly after he was elected in April to deal with economic shocks from U.S. tariffs and to meet NATO military spending commitments; the multiyear budget plan is expected to be finalized later this year. Advocacy group Support Our Science wrote to Carney last week with concerns the cuts would erase promised salary increases for graduate students and postdocs and cause the country to further fall behind its peers in research funding. Meanwhile, Canada's U15 group of research-intensive universities is highlighting the role research can play in national defense, arguing in its budget submission last week that it can help the government "realize Canadian sovereignty, security and success." —Brian Owens

Check for updates

FEATURES

LOSING PROTECTION

The United States helped beat back malaria in Guinea. Now, the disease is set to soar

MARTIN ENSERINK, in Guinea
Photography by **MARTA MOREIRAS**



Germaine (left) and Salomon Tédouno sit under a mosquito net at their home in Dubréka, Guinea. The U.S. President's Malaria Initiative helped provide bed nets and many other malaria services to about half of Guinea's population.





Drugs provided to Guinea with U.S. support helped cure Mohamed Camara (left), 10, who was diagnosed with malaria at the Tamita Health Center on 17 June.

PHOTO: MARTA MOREIRAS

This story is part of a series about the impacts of U.S. funding cuts on global health, supported by the Pulitzer Center.

One morning in mid-June, a 10-year-old boy named Mohamed Camara was lying on a bed in a health center in the small Guinean town of Tamita, wearing bright blue shorts and an army-style T-shirt with Chinese characters on it. He looked listless and feverish; little pearls of sweat flowed from his forehead. He had just been diagnosed with malaria.

That morning, Mohamed's parents had taken him to the center, which sits about 20 kilometers from the Atlantic coast in Boffa prefecture. Now, they and his baby sister were sitting on the bed next to him, looking anxious. "We were very worried," said his father, Alseny Camara. They would have brought their son to the hospital earlier, he noted, but his job as a driver had taken him away from home for a few days.

Just 6 months earlier, Mohamed's parents would have been able to call a community health worker when he got sick. That person might have come to the Camaras' home on a motorcycle, taken a drop of blood, and applied it to a rapid diagnostic test, which looks a lot like a home test for COVID-19. After the thin line indicating a malaria infection had appeared, the health worker would have given the boy a first dose of drugs and explained to his parents how to continue the treatment. (If his symptoms were severe, Mohamed would have been referred to the health center instead.) A few days later, the worker would have checked in to see how Mohamed was doing.

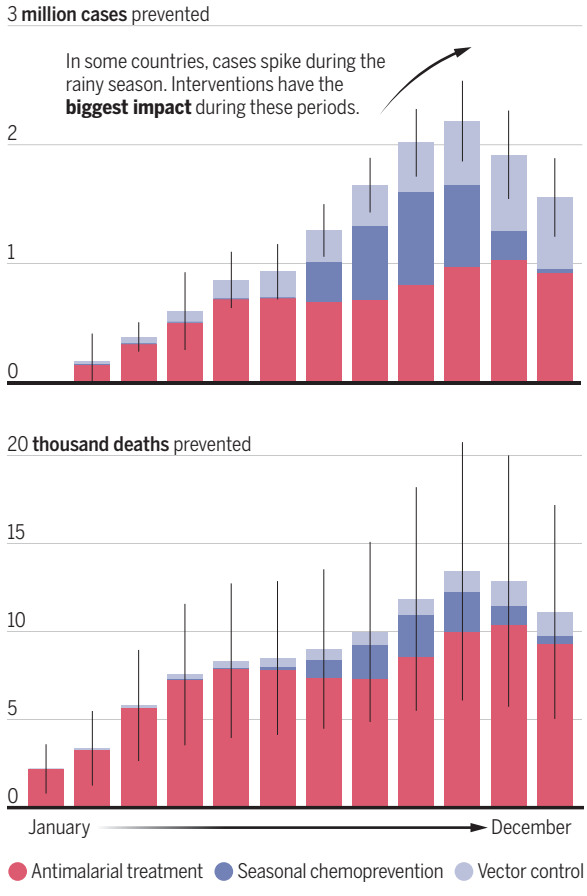
Community health workers—laypeople trained to provide a few primary health services—are an essential part of the medical system in many African countries, and they're particularly important in the fight against malaria, when a few days' delay in diagnosis and treatment can make the difference between life and death. In Guinea, where the country's entire population of more



13.6 million CASES

104 thousand DEATHS

would have been prevented across Africa this year by the malaria control measures funded by the U.S. President's Malaria Initiative (PMI) if it had continued as usual, a June paper in *The Lancet* estimated.



Lives at stake PMI supports malaria control efforts in 27 African countries. Funding freezes and cuts have put this promise in peril.

CREDITS: (GRAPHIC) M. HERSHER/*SCIENCE*; (DATA) T. L. SYMONS *ET AL*., *THE LANCET*, **405**, S0140673625008050 (2025)

than 14 million is at risk of malaria, thousands of these workers lost their jobs after the United States suddenly froze billions of dollars in foreign aid in January, just days after President Donald Trump took office.

Mohamed was lucky his parents were finally able to bring him in—and that he did not have a severe case of the disease, which is caused by a mosquito-borne parasite that can infect the brain and cause life-threatening anemia and organ failure. Once at the health center, he was put on artemether-lumefantrine, the standard drug combination for malaria. He would be fine, said his doctor, who later sent *Science* a text message confirming the boy had been discharged. But other parents may not have the means to get their child to a doctor—or not in time, said the center's director, Aïssata Camara. (She was not related to the boy; many people in this part of Guinea have the family name Camara.)

The disruption in U.S. funding for malaria control in Guinea—which amounted to some $15 million in 2024—has interrupted or put at risk many other health services in the West African nation, including the provision of diagnostic tests, drugs, and long-lasting insecticidal bed nets, as well as data collection, technical support, and training. The Trump administration has terminated much of the work of the President's Malaria Initiative (PMI), launched 2 decades ago, which funded malaria control efforts for roughly half the Guinean population, including the bustling capital, Conakry. The U.S. has also threatened to dial down its contribution to the Global Fund to Fight HIV, Tuberculosis and Malaria, which funds efforts in the remainder of the country (see map, p. 564).

There is no doubt Guinea will see malaria cases and deaths rise as a result, says Nouman Diakité, monitoring and evaluation manager at the country's National Malaria

Control Program (NMCP). "That has already started," he says. Cases in Guinea spike during the rainy season, between late May and November, when mosquito populations soar. As always, children under age 5—who account for about three-quarters of malaria deaths—and pregnant women will be hardest hit, Diakité says.

Malaria surges are also expected across the dozens of other countries where PMI has provided support, but the scale of the toll is hard to predict. In a modeling paper published in *The Lancet* in June, researchers at the Australia-based Malaria Atlas Project estimated that if PMI had continued as usual, it would have prevented 13.6 million malaria cases and 104,000 deaths across sub-Saharan Africa this year, including 250,000 cases and 450 deaths in Guinea (see graphic, p. 563).

Not all of those gains will be lost, as some U.S. funding for malaria is continuing. The U.S. Agency for International Development (USAID), where PMI was housed, has been dissolved and about 95% of its more than 10,000 employees were laid off. But in a 25 July email to *Science*, a spokesperson for the U.S. Department of State said it is "committed to ensuring a smooth integration of designated life-saving global health programs from USAID to the Department and this transition is well underway."

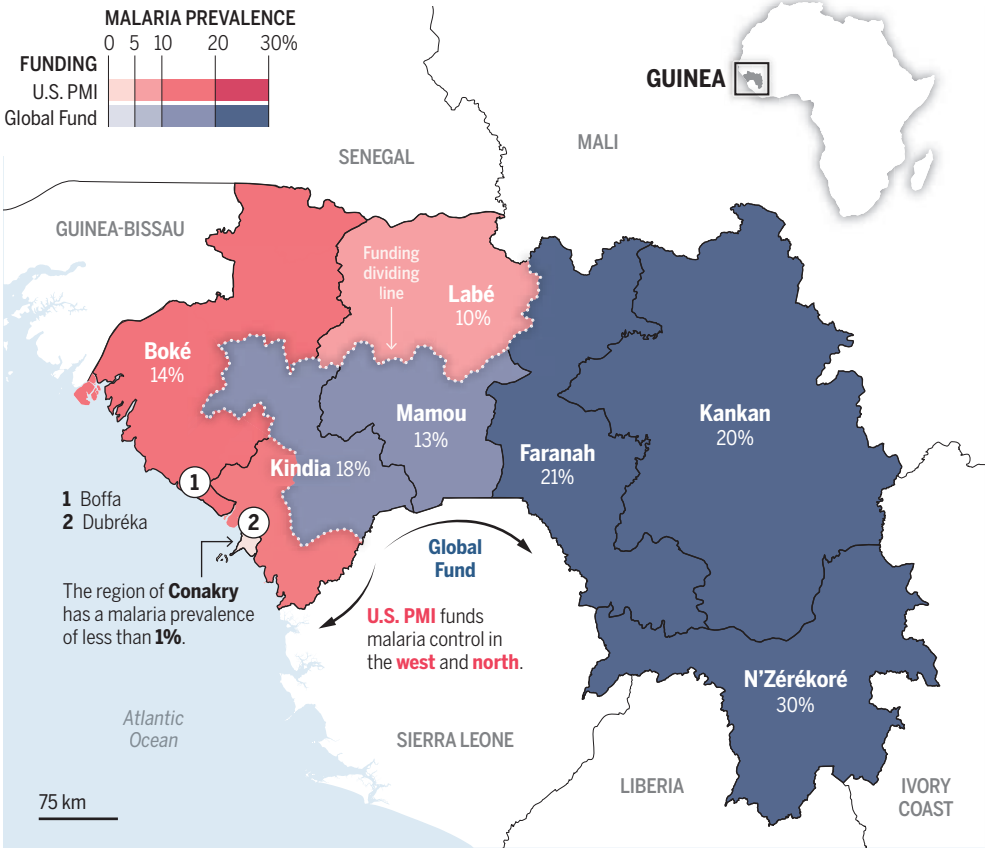
Countries are also trying to replace U.S. funding, and Guinea has bagged a few donations from nongovernmental partners. But they can make up just a tiny fraction of what's gone. And whatever the immediate impact of the cuts, public health experts expect malaria cases to soar in the coming years, as flagging mosquito control efforts allow malaria transmission to rebound. "Unfortunately, we may see some natural experiments on how rapidly things can evolve," says Regina Rabinovich, former head of the Gates Foundation's infectious diseases division and a scholar in residence at the Harvard T.H. Chan School of Public Health. "It's a tragedy."

In Guinea, health officials, scientists, and staff at health facilities told *Science* they felt abandoned by a once reliable partner. Alhassane Camara, a community health worker in a town named Keleya, was still wearing a polo shirt and a vest emblazoned with American flags and the red, white, and blue USAID logo, along with the agency's friendly tag line: "From the American people." But he had lost his income—about $50 a month—and his motorcycle, and although he was still helping families close to his home, it was no longer possible to reach those farther afield.

Tears welled up in Camara's eyes as he talked about the past 6 months, and in an emotional outburst, he suddenly switched from French, Guinea's official language, to halting English. "I beg Donald Trump! People are gonna die!" he shouted. "The small children, they die!"

Battleground

The U.S. President's Malaria Initiative (U.S. PMI) and the Global Fund to Fight HIV, Tuberculosis and Malaria each fund control efforts in different parts of Guinea, where the entire population is at risk of malaria. A 2021 survey showed the prevalence—defined as the percentage of children under age 5 who had parasites in their blood—is very low in the capital, Conakry, and higher in the eastern and southern regions.



THE U.S. HAS PLAYED an outsize role in the global fight against malaria for 2 decades. It provided more than $1 billion in bilateral funding for the disease in 2024, making it the largest government donor by far. In addition, the U.S. provides roughly one-third of the budget of the Global Fund.

That largesse began during the presidency of George W. Bush. PMI was launched with strong bipartisan support in 2006, with an initial $30 million to support malaria programs in Angola, Tanzania, and Uganda. It marked the advent of a golden era for malaria control, says Richard Steketee, who was PMI's deputy U.S. global malaria coordinator from 2018 to 2023. The Global Fund, launched in 2002, was growing rapidly, the World Bank began to make funding available for malaria in 2005, and Bill and Melinda Gates made the disease a priority for their philanthropic organization. In 2007, the couple even called for malaria to be eradicated, reviving a broken dream from the 1950s.

Major strides seemed possible. In the 1990s and early 2000s, insecticide-treated bed nets had been convincingly shown to slash cases and deaths. A new group of very effective drugs named artemisinin-based combination therapies—including the one that cured Mohamed—had

replaced older medicines to which *Plasmodium falciparum*, the most deadly malaria parasite, had become resistant. (Resistance against the combinations has emerged, primarily in Southeast Asia, but they have by and large retained their potency in Africa.) Rapid diagnostic tests made it possible to detect cases earlier and even in very remote places where the classic method—looking for parasites in the patient's blood using a laboratory microscope—isn't feasible.

PMI started procuring nets, tests, drugs, and insecticides for indoor spraying in large quantities and helping countries set up systems to distribute them and monitor whether they curbed malaria transmission. For the first time, Steketee says, "We were talking about scaling up coverage in order to achieve impact." PMI's budget grew to nearly $800 million in 2024, supporting 27 countries in sub-Saharan Africa and three more in Southeast Asia that together account for 90% of malaria cases and deaths.

One of those hot spots is Guinea, which had an estimated 4.4 million cases and more than 10,000 deaths in 2023, according to the World Health Organization's (WHO's) *World Malaria Report 2024*. More than half the population lives below the national poverty line and health services are rudimentary. Each year when the rainy season swells puddles and ponds, *Anopheles* mosquitoes swarm and bite, and feverish patients fill clinics. Most adults have had repeated bouts, gradually building up immunity against the disease. But children, whose immune systems have not learned to fight the parasites, are at much greater risk. In 2005, roughly one of every six children born in Guinea died before they turned 5 years old, many from malaria.

U.S. assistance soon began to change the picture. Thanks to the combined efforts of PMI and the Global Fund, insecticide-treated bed nets, virtually absent 20 years ago, have been introduced widely and are being replaced every 3 or 4 years in large campaigns. In regions where malaria is highly prevalent and seasonal, more than 1.1 million children under age 5 are now given anti-malarial drugs monthly during the peak transmission season, a strategy called seasonal chemoprevention that helps avert infection and disease. About half of the country's pregnant women—whose immune systems are temporarily weakened—get at least three doses of a combination antiparasitic drug named Fansidar, which protects the mother from malaria and reduces the risk of spontaneous abortion, stillbirth, premature delivery, and low birth weight.



PHOTO: MARTA MOREIRAS

In contrast to Guinea's programs for HIV and tuberculosis, its malaria effort kept running—with extra safety precautions—during West Africa's horrific 2013–16 Ebola epidemic, which killed more than 2500 Guineans. "That was a point of great pride," says Richard Reithinger, a former distinguished research fellow at RTI International, a nonprofit based in North Carolina that implemented the PMI-funded programs.

Measuring the programs' success is not straightforward. In most African countries, many malaria cases and deaths occur at home and aren't reported. One key indicator, however, is malaria prevalence, typically measured as the percentage of randomly sampled children between 6 months and 5 years of age confirmed to have malaria parasites in their blood. In Guinea, that number dropped from 44% in a 2012 nationwide survey to 17% in 2021—although there was huge variation between regions, with some reporting a prevalence of up to 30%. Child mortality dropped by one-third between 2005 and 2018. "Guinea has really made tremendous progress," Reithinger says.

THE COLLAPSE came as a complete surprise. Rumors started to circulate soon after Trump ordered a 90-day pause on foreign aid in an executive order signed on Inauguration Day, says Alioune Camara, NMCP's coordinator. Soon after, Guinea was told to stop USAID-funded activities. Camara tried to contact USAID staffers at the U.S. embassy. "I'm not allowed to tell you anything," he was told. Eventually, all the USAID employees were repatriated to the U.S.

Chaos and uncertainty have reigned since. After a review by the State Department—and a leaked USAID memo in March that warned of the devastating death toll if all foreign aid were ended—the department unfroze some "life-saving" malaria funding, including for drugs and bed nets. But an analysis by KFF, a U.S nonprofit focused on health policy, found 80% of the 157 USAID contracts that included malaria activities were terminated.

RTI International laid off almost its entire local staff in Guinea, some 60 people, Reithinger says. The organization—whose biggest client is the U.S. government—also laid off hundreds of U.S. employees, including Reithinger.

During an interview at his office 6 months later, Ibrahima Kankalabé Diallo, the top health official in Boffa prefecture, ticked off a list of 15 things the U.S. had supported that had come to a standstill or were at risk. They included paying community health workers, 378 in his district alone; the provision of essential medicines, computers, microscopes,

I beg Donald Trump! People are gonna die! The small children, they die!

Alhassane Camara
Community health worker

and motorcycles; monthly meetings with the directors of the prefecture's health centers; an ambulance; and a high-level gathering on World Malaria Day to raise awareness and keep the disease on the political agenda. "Nothing is like it was before," Diallo said.

Fakouma Camara, a biologist based in Boffa, was one of only five Guinean experts certified by WHO to do malaria diagnosis using microscopy, thanks to training provided by PMI. He had gone on to work for RTI International as a trainer, teaching community health workers across the country how to use rapid diagnostic tests and lab technicians how to do microscopy. Camara gave *Science* a copy of a poster he had presented at last year's annual meeting of the American Society of Tropical Medicine and Hygiene in New Orleans. It showed that two cycles of "supportive supervision" could help improve diagnostic practices at local labs.

Now, he was without a job and the training program had collapsed. "It's horrible," Camara said. "People talk a lot about medicines, but diagnosis is very important as well. You can't eliminate malaria if you don't do it properly."

Concerns mounted at the beginning of the rainy season. At the prefectural hospital of Dubréka, about an hour outside of Conakry, more than half of all admissions in June were for malaria. The chief pharmacist there, Alpha Baldé, showed *Science* to a storage room with dwindling stacks of boxes with the USAID logo on it. They contained antimalarial drugs—and Baldé was worried they would not be replenished.

Guinea is hardly alone. In April, a WHO rapid assessment found that more than half of the 64 malaria-endemic countries had experienced moderate or severe disruptions to malaria services. According to an online dashboard run by the Roll Back Malaria partnership, seven countries now only have a 3-month supply of rapid diagnostic tests left; five only have enough artemisinin-based combination therapy for 3 months. "There is a panic in many countries," says Maru Aregawi Weldedawit of WHO's Global Malaria Programme.

Reithinger says he expects the biggest problems in countries such as Nigeria, the Democratic Republic of the Congo (DRC), Ethiopia, and Mozambique, where the malaria burden was already high and funds for controlling the disease were insufficient even before the U.S. cuts. "Those are countries where I would expect increases in malaria incidence to be observed following this year's transmission season," he says.

The growing toll will be difficult to track because so many cases and deaths aren't counted to begin with. PMI funding helped countries collect data and ensure their quality, and its loss has added to the challenge. And in February, the Trump administration killed the USAID-supported Demographic and Health Surveys Program, which collected vast amounts of health data—including on malaria—every few years in more than 90 developing countries. "We're essentially going to be flying blind," Alioune Camara said.

THE FUTURE OF U.S. support for malaria control is unclear. In its email to *Science*, the State Department stressed, "PMI's key life-saving activities in malaria prevention and treatment are continuing." It said at least 10 contracts were still providing commodities to PMI partner countries, including more than 3 million insecticide-treated bed nets in the DRC and Ethiopia and seasonal chemoprevention for more than 7 million children in West Africa.

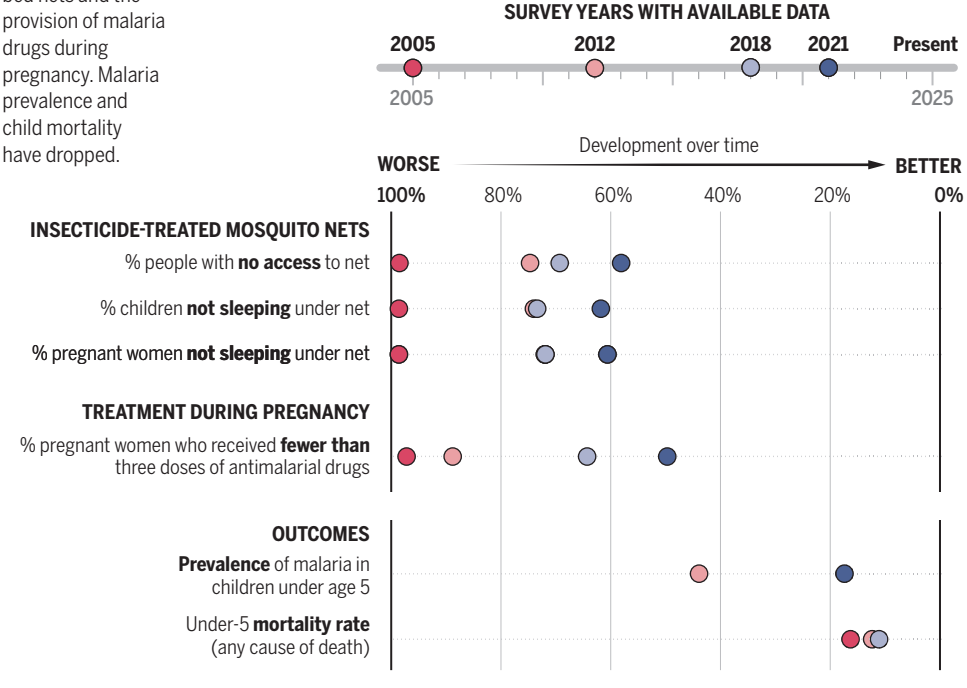
Global health leaders were somewhat heartened in late July when a key spending panel in the House of Representatives—in a rebuke to the Trump administration—voted to maintain funding for many global health programs, including for malaria, at this year's levels. But whether the bill will become law is uncertain, and even if it does, many worry that, with the existing aid structure torn to shreds and thousands laid off, the State Department will have to reinvent the wheel. "The mechanisms for that support have all been disbanded," Steketee says. "There is nobody in the countries to actually do any of the local contractual and field support work."

The fate of the Global Fund is also murky, as the U.S. and other countries reduce their commitments. Uncertainly about its financial future has recently led the fund to scale back many previously awarded grants. In late June, Alioune Camara learned the fund's $81.5 million in support for malaria control in Guinea in 2024–26 would be cut by 9.4%. The country's HIV and tuberculosis programs saw similar reductions.

But there have been glimmers of hope for Guinea. GiveWell, a U.S. charity with a strong focus on cost-effectiveness, has pledged up to $560,000

Two decades of progress

With help from the U.S. President's Malaria Initiative and other donors, Guinea has made progress in malaria control over the past 2 decades, including the introduction of long-lasting insecticide-treated bed nets and the provision of malaria drugs during pregnancy. Malaria prevalence and child mortality have dropped.



Insecticide-treated mosquito nets: Access assumes bed net is used by up to two people in each household; usage reflects behavior the night before the survey. **Treatment during pregnancy**: Reflects women ages 15–49 with a live birth in the 2 years preceding the survey who took fewer than three doses of sulfadoxine/pyrimethamine during pregnancy. **Outcomes**: Prevalence reflects percentage of children ages 6–59 months tested using microscopy who are positive for malaria. Mortality rate reflects percentage of children who die of any cause before their fifth birthday.



Aissatou Diallo (right) cries after her 12-month-old son, Mamadou Fella, was diagnosed with severe malaria at the Dubréka prefectural hospital. "He had intermittent fever for a week, and today, his fever suddenly spiked, so I rushed to the hospital," Diallo says. Some three-quarters of the world's 600,000 malaria deaths each year occur in African children under age 5.

PHOTO: MARTA MOREIRAS

to RTI International to avoid delays in this year's seasonal chemoprevention campaign, an approach GiveWell rates as highly cost-effective. The group has made donations to support the strategy in Mali, Cameroon, Ivory Coast, Togo, and Benin, reaching a total of 4.5 million children. Still, says GiveWell program officer Natalie Crispin, the group doesn't want to create the impression it can replace the vast sums the U.S. government provided: "It's a really challenging communication to get right."

In a similar vein, the Against Malaria Foundation, which has provided Guinea with bed nets since 2019, has agreed to pay $1.8 million to ensure 4.8 million nets were distributed in July in spite of the U.S. funding freeze. Two other groups together chipped in another $900,000. (In the end, the U.S. government continued to fund bed net distribution in Guinea after the USAID freeze.)

Low- and middle-income countries may also have to start spending more of their own money on malaria control. "Domestic resource mobilization," in global health parlance, has been on international agendas for many years, but the recent upheaval has given the discussion a fresh impetus. "Many countries have become heavily dependent on external funding," Weldedawit says—even those that could shoulder more of the burden themselves.

Guinea, for example, is rich in resources and one of the world's biggest bauxite producers. If only 1% of that industry's proceeds were used for health, the country could take care of malaria control itself, says Alioune Camara, who has made that case to the government. "Will they? That is the big question now."

Reithinger is "cautiously optimistic" about Guinea's future. Although the U.S. cuts will have an impact, "I think we have a tendency to underestimate country governments," he says. "I do know the Guinean health system, and I've seen how they have weathered and come out of the Ebola crisis, and how they managed the COVID crisis. … I think there is tremendous resilience in the system."

People on the ground are far less sanguine. At the Tamita health center, where new malaria patients arrived almost daily, too many things were falling by the wayside, said Aïssata Camara, the center's director. "The continuity is in danger," she said. "We want American support to come back." □

CHILDREN AT RISK

More from this series on how U.S. foreign aid cuts threaten child health around the world: https://scim.ag/USAID

Check for

COMMENTARY

PERSPECTIVES

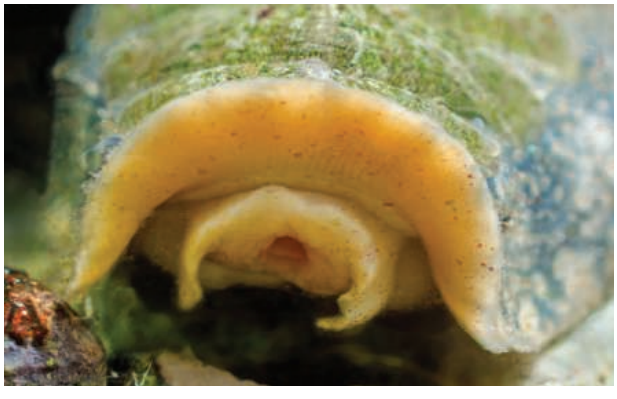
BIOMATERIALS

Hardening nature's toughest teeth

A protein that underlies the mineralization of chiton teeth is revealed

André Scheffel

Animals from diverse evolutionary lineages possess body parts composed of mineralized structures such as teeth, bones, and shells. Their hardening, referred to as biomineralization, relies on precisely orchestrated macromolecular machineries that control the type, spatial placement, nucleation, and growth of inorganic crystalline phases in an organic matrix. Identifying specific macromolecules involved in these processes helps to illuminate how nature's complex inorganic structures are formed. In particular, chitons—a class of marine mollusks (see the photo)—have exceptionally hard and abrasion-resistant teeth made of iron-based minerals. However, the underlying mechanism that governs the mineralization of iron phases in chiton teeth has been puzzling. On page 637 of this issue, Nemoto *et al.* (*1*) report that radular teeth matrix protein 1 (RTMP1) plays a central role in incorporating iron oxide mineral magnetite into chiton teeth. This points to molecular strategies that may be shared among magnetite-forming organisms that might be used in biomimetic materials chemistry.



A rasping tongue with tough, abrasion-resistant teeth that is hidden in the mouth of a chiton can scrape algae from hard rock surfaces.

Magnetite—the most prominent crystalline iron mineral produced biologically—was first identified in chitons as a key component of their tooth cusps, the pointed projections on the scraping surface (*2*). This mineral renders the teeth exceptionally hard and abrasion resistant, enabling chitons to scrape algae from rock surfaces for feeding (*3*). The biomineralization process of magnetite takes place in the radular sac, an organ that houses a tongue-like structure (the radula) that bears rows of teeth on one side (see the figure). As magnetite deposits wear and fall off at the anterior end of the radula, new teeth are continuously formed at the posterior end to compensate for the loss (*4*). Specialized cells secrete chitin fibers and proteins that form an insoluble organic matrix in the shape of the tooth. These organic blueprints undergo mineralization in several stages as they are transported toward the anterior of the radula. Mineralization begins with the precipitation of the hydrated ferric iron oxide ferrihydrite at the leading edge of the tooth cusp, then gradually progresses toward the trailing edge of the tooth cusp. This process halts partway, resulting in a layer of brownish ferrihydrite of a few tens of a nanometer thick, which subsequently transforms into magnetite, turning the color of a tooth black (see the figure). The core region of the tooth cusp is eventually filled with additional minerals such as apatite phases.

Previous investigations suggested a few cusp-specific proteins, some of which exhibit amino acid sequence features, such as a region with a high content of negatively charged residues, or predicted functions, such as ferroxidase activity that could play a role in regulating magnetite formation in chitons (*5, 6*). RTMP1 emerged as a particularly intriguing protein because it lacks sequence similarity to known proteins but contains a signal for cellular export and includes a domain that is predicted to bind chitin. In addition, RTMP1 has multiple serine residues that could promote iron oxide nucleation if they are phosphorylated. These characteristics made RTMP1 a compelling candidate for a role in the chiton tooth mineralization process.

By sequencing the expressed genes in different chiton species, Nemoto *et al.* discovered that RTMP1 is conserved across chitons, suggesting that the protein may have a chiton-specific function. Immunolabeling with an RTMP1-specific antibody demonstrated presence of the protein inside teeth and in the epithelial cells surrounding cusps that undergo iron oxide mineralization. The distribution of RTMP1 in the epithelial cells appeared to be linked to different mineralization stages. Before mineralization, the protein was diffused evenly on both sides of a tooth. After an initial deposition of iron oxide, the distribution shifted toward the nonmineralized side of a tooth. This pattern raises an intriguing question of whether the epithelial cells can sense the mineralization stage of a surrounded tooth cusp. Inside a cusp, RTMP1 appeared as narrow bands along the long axis. The protein was localized near the leading edge of the cusp before mineralization, then moved toward the trailing edge as iron oxide deposition began. This spatially restricted and changed localization of RTMP1 indicated that the protein could play a role in tooth mineralization.

Nemoto *et al.* performed various in vitro mineralization assays by using isolated, nonmineralized chiton teeth and purified RTMP1 produced in engineered yeast. In untreated isolated teeth, iron oxide formation occurred preferentially in the cusp region where RTMP1 was localized during the initial phase of maturation. By contrast, iron oxide formation was substantially reduced in control teeth that were pretreated with a protein-solubilizing detergent, which removed unbound proteins. A mineralization experiment that used engineered yeast showed that purified RTMP1 readily binds to iron ion (Fe^{3+}) and chitin fibers. Chitin fibers to which RTMP1 was already bound were subsequently decorated with iron oxide nanoparticles. These results indicate that RTMP1 could either promote iron oxide mineralization or facilitate binding of iron oxide particles to the fibers.

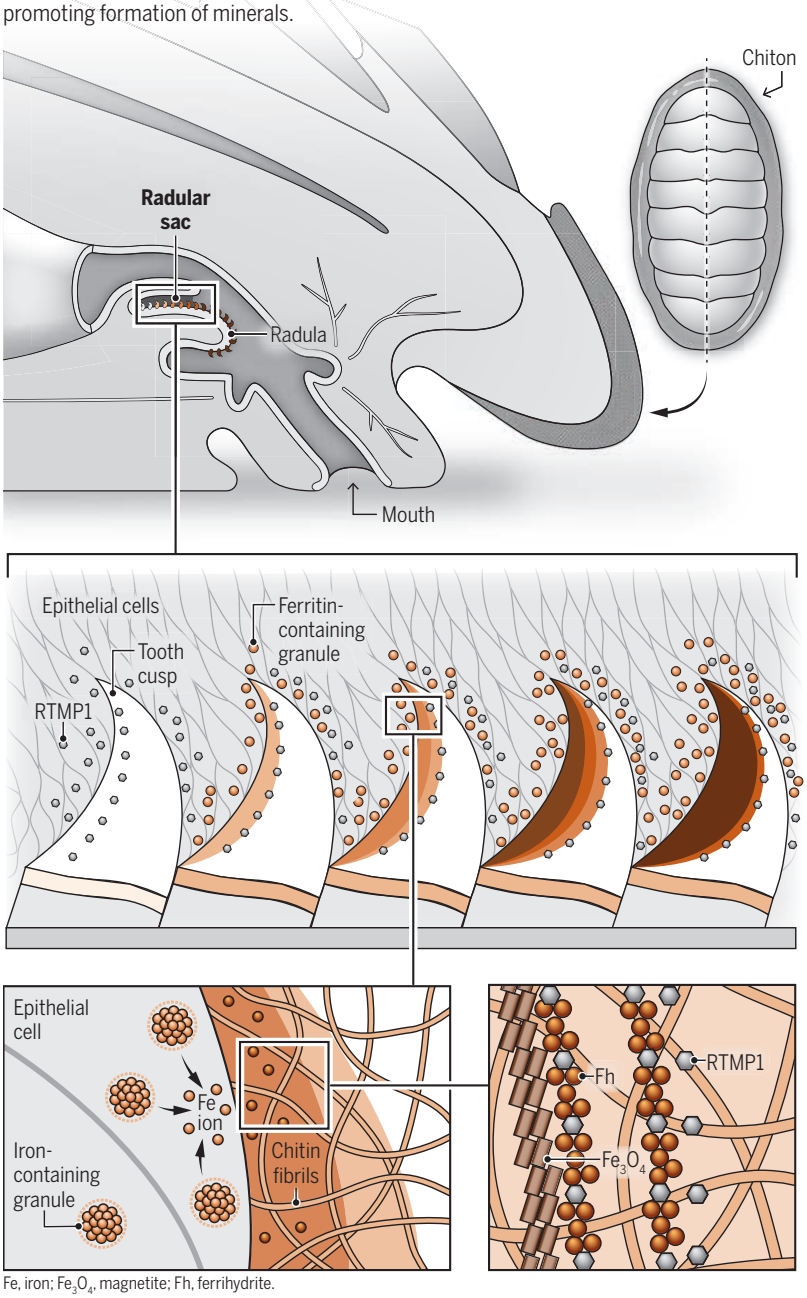
To further elucidate the direct role of RTMP1 in iron oxide mineralization, Nemoto *et al.* conducted an in vivo experiment in which RTMP1-encoding RNA was selectively degraded in cells through an approach called RNA interference. Double-stranded RNA that targets RTMP1-encoding mRNA was injected into chitons. The injected specimens showed an average 69% reduction in RTMP1 mRNA in the radular tissue, which suggests a substantial decrease in RTMP1 protein synthesis in epithelial cells surrounding the cusp. The compromised chitons exhibited an abnormal progression of iron oxide phase transformation in the three teeth that matured (mineralized) after the tooth in which iron oxide deposition was visible. The teeth cusps of the chitons with reduced RTMP1 levels remained brown instead of exhibiting the normal color progression observed during mineralization (from light brown to dark brown to black). These results support that there is a role for RTMP1 in regulating magnetite formation.

The method of Nemoto *et al.* offers a way to investigate the molecular details of magnetite biomineralization in a eukaryotic system and extracellular environment. Such molecular insights have only been available for magnetotactic bacteria, which produce magnetite crystals within their cells inside of vesicles (*7*). Although several proteins that regulate magnetite nucleation and growth have been identified in these bacteria, the underlying molecular and structural mechanisms of their activities remain largely elusive (*8*). In contrast to chitons, magnetotactic bacteria are fully amenable to genetic modification and could provide a powerful genetic tool. This, combined with their being easily handled in the laboratory, could be exploited to uncover more details about RTMP1. For example, testing whether RTMP1 and its genetically engineered variants could rescue bacterial mutants that produce poorly crystalline iron oxides could reveal which parts of the protein possess mineralization activity. Beyond this, the methodological and gene expression groundwork laid by Nemoto *et al.* could enable further gene discovery in chitons, such as structural homology–based and sequence feature–based bioinformatics approaches, as well as targeted manipulation of the expression of proteins of interest to uncover new players in magnetite biomineralization.

Molecular details of biomineralization processes could provide the ability to mimic nature's mineralization strategies for the synthesis of new materials. In this context, insights from magnetite biomineralization in chiton teeth may inspire new approaches for patterning substrates with magnetic magnetite crystals. This could lead to advanced materials with tailored magnetic properties for sensing and magnetic storage applications and new designs of abrasion-resistant and self-sharpening materials. □

Biomineralization of chiton teeth

Crystalline iron mineral is a key component that makes chiton teeth exceptionally hard and abrasion resistant. Radular teeth matrix protein 1 (RTMP1) plays a central role in teeth mineralization by either facilitating binding of iron oxide particles on chitin fibers or promoting formation of minerals.



Fe, iron; Fe_3O_4, magnetite; Fh, ferrihydrite.

GRAPHIC: N. BURGESS/*SCIENCE*

REFERENCES AND NOTES

1. M. Nemoto *et al.*, *Science* **389**, 637 (2025).
2. H. A. Lowenstam, *Geol. Soc. Am. Bull.* **73**, 435 (1962).
3. J. C. Weaver *et al.*, *Mater. Today* **13**, 42 (2010).
4. D. Joester, L. R. Brooker, *Iron Oxides* (2016), pp. 177.
5. M. Nemoto *et al.*, *Proteomics* **12**, 2890 (2012).
6. M. Nemoto *et al.*, *Sci. Rep.* **9**, 856 (2019).
7. R. Uebe, D. Schüler, *Nat. Rev. Microbiol.* **14**, 621 (2016).
8. A. Lohße *et al.*, *J. Bacteriol.* **196**, 2658 (2014).

10.1126/science.adz8241

Institute of Microbiology, University of Greifswald, Greifswald, Germany.
Email: andre.scheffel@uni-greifswald.de

Check for

OPTOELECTRONICS

Moiré eyes detect the dim

Unusual electronic behavior of a moiré superlattice helps detect a single light particle

Denis Bandurin

In near darkness, the human eyes can no longer perceive the faintest glow of light, even though light is not truly gone. Photons (particles, or quanta, of light) across a wide range of wavelengths still bounce around. Detecting this quantum trace of light is important in many technologies, including quantum communication and computing, remote sensing, and biomedical imaging. However, it is extremely challenging to sense a faint light signal, particularly a single photon, under practical conditions relevant for a system to operate. On page 644 of this issue, Nowakowski *et al.* (*1*) report moiré superlattices that display unexpected electronic properties from an engineered structure. The new material, which is formed by stacking two atomically thin crystalline layers with slightly different lattice constants at a small twist angle, could detect a single photon. This offers a new detection principle for twistronics (twist-induced quantum effects) in the field of optoelectronics.

The approach... could open new avenues in fields where single-photon sensitivity matters...

A single-photon detector is a highly sensitive device that can sense individual photons even at a very low light level. Devices such as photomultiplier tubes (*2*), avalanche photodiode detectors (*3*), and superconducting nanowire single-photon detectors (*4*) have long been used in the quantum sensing of light (*5*). These mechanisms convert individual photons to measurable electronic signals. Photomultiplier tubes offer high sensitivity but require high-voltage operation and are bulky compared with solid-state devices. An avalanche photodiode detector operates at room temperature with a decent efficiency in the visible and near-infrared wavelengths. However, its quantum efficiency (a measure of converting incident photons to a measurable signal) falls sharply and the noise signal increases at wavelengths larger than 2 μm. A superconducting nanowire single-photon detector has near-100% efficiency but requires cryogenic cooling and struggles in the mid-infrared spectrum (3 to 10 μm) and beyond, in which photon energies are too low. Some progress has been made by using advanced materials such as ultrathin tungsten silicide superconducting films (*6*), moiré superconductors (*7*), and high-temperature superconductors (*8*, *9*). Nonetheless, combining high sensitivity to mid-infrared light and elevated temperature operation above 20 K, where cryocoolers become relatively cheap, remains a challenge.

Moiré superlattices form when two atomically thin crystalline layers—such as graphene or its relatives—are stacked with a slight rotational misalignment or a small mismatch in their atomic spacing. This misalignment creates a repeating wave interference pattern, called a moiré pattern. This substantially reshapes the behavior of the electrons of the material, which affects electronic properties and results in exotic quantum phenomena (*10*, *11*). Over the past decade, these systems granted access to emergent effects in the fields of superconductivity, magnetism, and strongly interacting systems (*12*–*14*). Nowakowski *et al.* show that moiré superlattices can exhibit a rare transport phenomenon in planar two-dimensional crystals called negative differential conductance. This is a property in which the electrical current decreases as the applied voltage increases, which contrasts with the classic Ohm's law, in which current is always proportional to voltage.

The negative differential conductance in moiré superlattices discovered by Nowakowski *et al.* enabled single-photon detection. The authors placed bilayer graphene on top of a single hexagonal boron nitride layer. These atomically flat materials have atomic lattices with a slightly different repeated pattern of atoms in the crystal structure. The small lattice mismatch creates a moiré potential—a landscape of potential energy with regular peaks and valleys—that changes the electronic properties of the superlattice and slows the motion of electrons. When a strong in-plane electric field is applied, electrons are driven into regions where their velocity effectively reverses, causing the current to decrease even as the voltage increases. Under a steady operating current, this negative differential conductance enabled a bistable regime: The system can stably reside in two distinct states with different voltage drops across the device. Electrons became effectively trapped in one of the states. This bistability is so fragile that even a single mid-infrared photon could knock the system from one state into another, resulting in a macroscopic change in the output current signal. By exploiting emergent phenomena in a moiré superlattice, Nowakowski *et al.* achieved single-photon sensitivity at mid-infrared frequencies and temperatures as high as 25 K, which are operating conditions that traditional superconducting detectors struggle in. The underlying concept is simple. A current-biased moiré superlattice that is tuned to a metastable point can rapidly switch states upon absorbing a single photon.

The approach of Nowakowski *et al.* is promising for compact, low-power optoelectronics and could open new avenues in fields where single-photon sensitivity matters, such as remote sensing, free-space communication (wireless data transmission through open space), night vision, quantum key distribution (cryptography), and remote sensing. Future work will need to clarify how scalable, fast, and noise tolerant such detectors can become and whether similar bistabilities arise in other superlattices. Moiré materials, which have been long studied for their exotic correlated ground states—specific quantum mechanical states with strong interactions between particles—now reveal a functional nonlinearity usable at the level of individual quanta of light. The ability of a material to trap electrons and sense single photons without the machinery of superconductivity is noteworthy. □

REFERENCES AND NOTES

1. K. Nowakowski *et al.*, *Science* **389**, 644 (2025).
2. V. K. Zworykin, G. A. Morton, L. Malter, *Proc. Inst. Radio Eng.* **24**, 351 (1936).
3. R. J. McIntyre, *IEEE Trans. Electron Dev.* **ED13**, 164 (1966).
4. G. N. Gol'tsman *et al.*, *Appl. Phys. Lett.* **79**, 705 (2001).
5. R. H. Hadfield, *Nat. Photonics* **3**, 696 (2009).
6. G. G. Taylor *et al.*, *Optica* **10**, 1672 (2023).
7. G. Di Battista *et al.*, *Sci. Adv.* **10**, eadp3725 (2024).
8. I. Charaev *et al.*, *Nat. Nanotechnol.* **18**, 343 (2023).
9. R. L. Merino *et al.*, *2D Mater.* **10**, 021001 (2023).
10. L. A. Ponomarenko *et al.*, *Nature* **497**, 594 (2013).
11. B. Hunt *et al.*, *Science* **340**, 1427 (2013).
12. Y. Cao *et al.*, *Nature* **556**, 43 (2018).
13. Y. Cao *et al.*, *Nature* **556**, 80 (2018).
14. L. Balents, C. R. Dean, D. K. Efetov, A. F. Young, *Nat. Phys.* **16**, 725 (2020).

10.1126/science.aea5235

Department of Materials Science and Engineering, National University of Singapore, Singapore. Email: dab@nus.edu.sg

Check for

NEUROSCIENCE

Improving Alzheimer's disease immunotherapy

A modified antibody targeting amyloid-β reduces adverse events and increases efficacy in a mouse model

Mengen Xing[1] and **Weihong Song**[1,2]

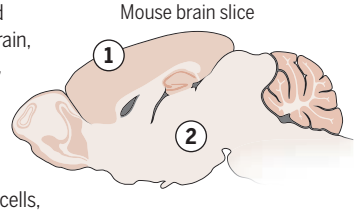
Alzheimer's disease (AD) is the most common neurodegenerative disease leading to dementia. A key pathological hallmark of AD is the formation of neuritic plaques composed of aggregated amyloid-β protein (Aβ). The US Food and Drug Administration (FDA)–approved antibody drugs aducanumab, lecanemab, and donanemab (*1*–*3*) have demonstrated modest efficacy in reducing Aβ plaque burden and slowing cognitive decline but do not halt disease progression (*4*). Their clinical impact is also limited by inefficient delivery across the blood-brain barrier (BBB) and the frequent occurrence of amyloid-related imaging abnormalities (ARIA), which are adverse effects characterized by cerebral edema (ARIA-E) or microhemorrhages (ARIA-H). On page 617 of this issue, Pizzo *et al.* (*5*) report a modified antibody against Aβ that uses the transferrin receptor to cross the BBB, substantially improving antibody delivery to the brain in a mouse model of AD. The modified antibody was also associated with markedly reduced incidence of ARIA-like pathology.

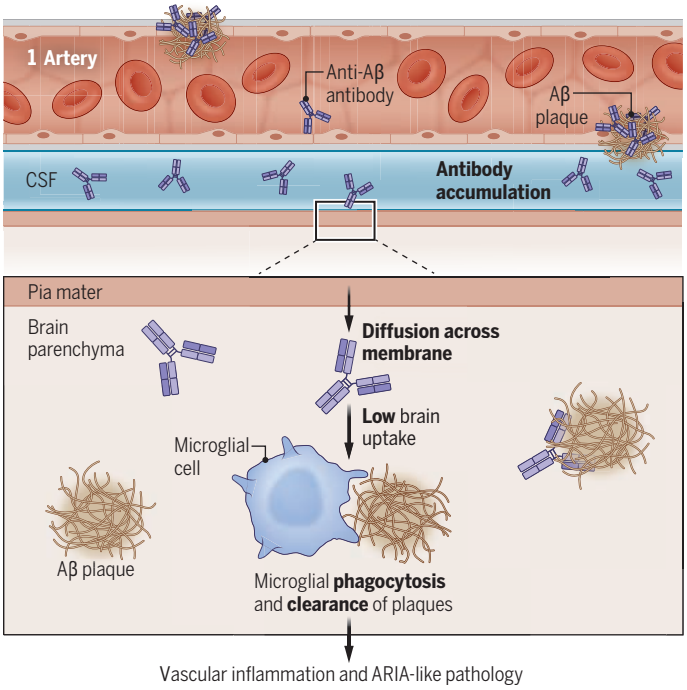
The anti-Aβ antibodies approved by the FDA for treatment of AD are administered by intravenous infusion; however, the BBB restricts the transfer of most macromolecules from the blood to the brain. Therefore, these antibody-based therapeutics are thought to cross the choroid plexus [network of capillaries that produces cerebrospinal fluid (CSF)] to the CSF, gaining entry to superficial brain tissue by diffusing across the membrane covering the surface of the brain. Once in the brain, the fragment antigen-binding domain (Fab) of these antibodies binds to soluble Aβ protofibrils or the pyroglutamate species of aggregated Aβ. The fragment crystallizable region (Fc) domain of the antibody binds to Fc-γ receptors (FcγRs) on microglia (brain-resident immune cells), thus facilitating microglial phagocytosis of the Aβ-antibody complex (*6*).

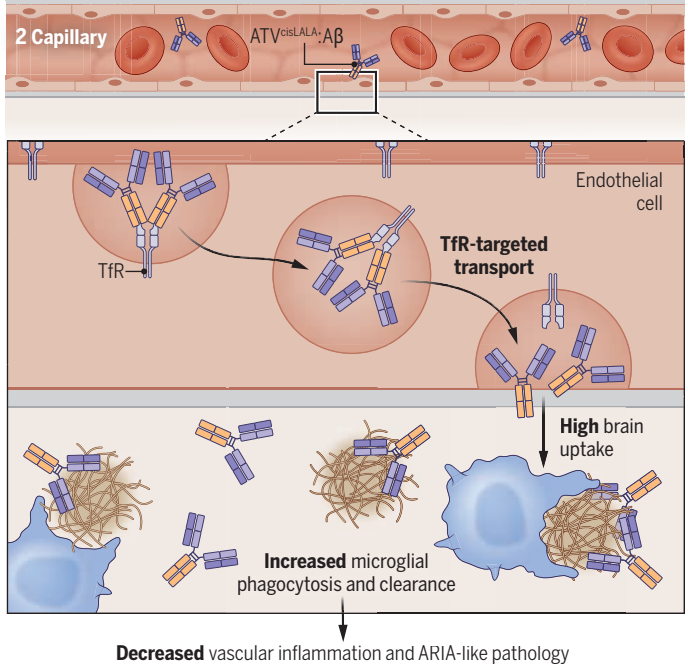
ARIA, particularly in individuals carrying the ε4 allele of the gene encoding apolipoprotein E (APOE) (*2, 3, 7*), remains a major limitation of current Aβ immunotherapies (*8*). It occurs in up to one-third of treated individuals, with severe outcomes reported in some cases (*4, 9*), including one reported death attributed directly to severe ARIA (*10*). The incidence and severity of ARIA increase with higher dosing and, although the mechanism underlying ARIA is not yet fully understood, it is thought that the blood-circulating antibody targets and accumulates at vascular Aβ deposits, triggering perivascular inflammation and vascular damage. These vascular deposits of

Helping antibodies access the brain

Conventional anti-amyloid-β (Aβ) antibodies are thought to pass from the blood to the cerebrospinal fluid (CSF) at the choroid plexus and to enter the brain by passive diffusion from CSF spaces such as those surrounding the arteries on the surface of the brain, resulting in limited penetration into the brain tissue (parenchyma). These antibodies also accumulate around cerebral vessels, increasing their engagement with vascular Aβ and elevating the risk of amyloid-related imaging abnormalities (ARIA) (**1**). By contrast, the fragment crystallizable (Fc) region (orange) of the antibody transport vehicle (ATV)^{cisLALA}:Aβ antibody has been engineered to bind to transferrin receptors (TfRs) on the endothelial cells of capillary walls, enabling active transport across the blood-brain barrier. This increases antibody access to Aβ plaques deep in the brain tissue and reduces ARIA-like pathology (**2**). The ATV^{cisLALA}:Aβ Fc region also contains mutations that reduce binding to the Fcγ receptor on immature red blood cells, a common adverse effect of TfR-targeted antibodies.







GRAPHIC: N. BURGESS/*SCIENCE*

Aβ are considered a driver of Aβ pathology in AD pathogenesis and are the hallmark of cerebral amyloid angiopathy (CAA) (*11*).

To address these issues, Pizzo *et al.* generated an antibody transport vehicle (ATV) that targets the transferrin receptor on the brain endothelial cells, the core component of the BBB. The transferrin receptor–mediated transport mechanism is a physiological process that allows specific macromolecules to cross the BBB through the endothelial cells that form the walls of capillaries in the brain, rather than entering through CSF and perivascular spaces. Therefore, this form of receptor-mediated transcytosis is a target for strategies designed to deliver large therapeutic molecules to the brain. For example, the transferrin receptor–targeted anti-Aβ antibody trontinemab is currently in clinical trials (NCT04639050) (*12*).

...receptor-mediated transcytosis is a target for strategies designed to deliver large therapeutic molecules to the brain.

The ATV platform designed by Pizzo *et al.* incorporates a transferrin receptor–binding domain into the Fc region of the antibody scaffold. However, the simultaneous binding of antibodies to both transferrin receptor and FcγRs on early precursors of red blood cells can result in the loss of reticulocytes (immature red blood cells) and cytotoxicity (*13*). To overcome this, Pizzo *et al.* introduced Leu^{234}→Ala/Leu^{235}→Ala (LALA) mutations asymmetrically into one arm of the Fc region of the antibody to generate $ATV^{cisLALA}$, which reduces FcγR binding. The authors tested $ATV^{cisLALA}$ in cell culture in vitro and in mice in vivo and found that the antibody retained transferrin receptor engagement without inducing cytotoxicity and reticulocyte loss.

Pizzo *et al.* then fused the $ATV^{cisLALA}$ Fc region (which includes the LALA mutations and the transferrin receptor-binding domain) to the Fab regions of an anti-Aβ antibody to generate $ATV^{cisLALA}$:Aβ. Given the role that microglial cells are thought to have in anti-Aβ clearance of plaques, the authors examined the effects of $ATV^{cisLALA}$ on the interaction between the antibody and microglia. $ATV^{cisLALA}$:Aβ did not impair microglial-mediated phagocytosis of Aβ in an ex vivo cell-based assay and was associated with a similar degree of in vivo microglial uptake and recruitment to plaques as conventional anti-Aβ antibodies (an acute high-dose paradigm was used to match brain exposure of the different antibodies).

Most conventional anti-Aβ antibodies accumulate predominantly in CSF compartments, such as the choroid plexus and perivascular spaces (*14*). By contrast, $ATV^{cisLALA}$:Aβ exhibited a broader parenchymal and vasculature distribution across the brain and achieved a five- to eightfold increase in brain concentration in the 5xFAD mouse model of AD. Using three-dimensional and light sheet imaging, Pizzo *et al.* found that a conventional anti-Aβ antibody largely accumulated along major surfaces of leptomeningeal arteries. These are blood vessels on the surface of brain that supply oxygen and nutrients to the inner two membranes that cover the brain (leptomeninges) and are common sites of vascular Aβ deposition. By contrast, $ATV^{cisLALA}$:Aβ showed limited association with these arteries and instead exhibited greater targeting of Aβ deposits within the brain tissue (see the figure). This redistribution is functionally relevant because it reduces exposure of the antibody to vascular Aβ deposits. Accordingly, Pizzo *et al.* found that, compared with a conventional anti-Aβ antibody, $ATV^{cisLALA}$:Aβ attenuated vascular inflammation and substantially mitigated ARIA-like pathology in a mouse model exhibiting CAA pathology.

ARIA has long been considered an unavoidable risk of anti-Aβ immunotherapy. However, Pizzo *et al.* contribute evidence that, by minimizing spatial interactions with CAA, altering the route of antibody entry into the brain can reduce vascular exposure and mitigate ARIA-like pathology. This suggests that ATV-based anti-Aβ antibodies could be used at higher doses or for longer periods than is safe for conventional anti-Aβ antibodies—this is especially important for individuals at high risk of ARIA such as APOE ε4 carriers. However, further investigation is needed to confirm these observations in additional preclinical models of AD.

Although the study by Pizzo *et al.* focused on an Aβ-targeting therapy, the transferrin receptor–targeted ATV platform that they developed has other potential applications. AD is also characterized by intracellular accumulations of hyperphosphorylated tau protein in neurons. Tau-targeting antibodies have been developed and may also benefit from improved delivery to the brain tissue. In addition, transferrin receptor–based delivery of lysosomal enzymes to the central nervous system has shown potential in preclinical models of lysosomal storage disorders, which are a group of genetic disorders caused by deficiencies of specific lysosomal enzymes (*15*). The modular design of the ATV system allows diverse Fab domains to be paired with the modified Fc region containing the transferrin receptor-binding motif, which enables the platform to be adapted for a wide range of therapeutic molecules and multiple disease contexts.

Despite the potential advantages of $ATV^{cisLALA}$:Aβ, several important questions warrant investigation before clinical translation. For example, what is the long-term fate of $ATV^{cisLALA}$:Aβ in the brain, and how does it affect Aβ proteostasis (processes that maintain protein homeostasis) in animal models of aging or late-stage AD? It is also not clear whether the distribution of $ATV^{cisLALA}$:Aβ differs between mouse and human brains. Addressing these questions will be critical for determining whether the ATV platform is suitable for clinical application. The findings of Pizzo *et al.* provide more than preclinical proof of concept; they also establish a framework for therapeutic design. By precisely controlling the route of antibody entry and modulating its function, $ATV^{cisLALA}$:Aβ overcomes long-standing limitations of AD immunotherapy. Platforms such as $ATV^{cisLALA}$:Aβ represent the next generation of promising approaches, offering the potential to achieve enhanced efficacy and reduced adverse effects in brain-targeted therapeutics. □

REFERENCES AND NOTES

1. J. Sevigny *et al.*, *Nature* **537**, 50 (2016).
2. J. R. Sims *et al.*, *JAMA* **330**, 512 (2023).
3. C. H. van Dyck *et al.*, *N. Engl. J. Med.* **388**, 9 (2023).
4. T. E. Golde, A. I. Levey, *Science* **382**, 1242 (2023).
5. M. E. Pizzo *et al.*, *Science* **389**, eads3204 (2025).
6. S. Wang *et al.*, *Cell* **185**, 4153 (2022).
7. S. Budd Haeberlein *et al.*, *J. Prev. Alzheimers Dis.* **9**, 197 (2022).
8. Y. Zhang, H. Chen, R. Li, K. Sterling, W. Song, *Signal Transduct. Target. Ther.* **8**, 248 (2023).
9. J. Travis, *Science* **380**, 571 (2023).
10. N. J. Reish *et al.*, *N. Engl. J. Med.* **388**, 478 (2023).
11. Y. Feng *et al.*, *Alzheimers Dement.* **21**, e14543 (2025).
12. H. P. Grimm *et al.*, *MAbs* **15**, 2261509 (2023).
13. A. Couch *et al.*, *Sci. Transl. Med.* **5**, 183 (2013).
14. N. Khoury *et al.*, *Nat. Commun.* **16**, 1822 (2025).
15. A. Arguello *et al.*, *J. Exp. Med.* **219**, e20211057 (2022).

ACKNOWLEDGMENTS

The authors acknowledge support from the National Natural Science Foundation of China (82230043 and 82293642 to W.S., 82301615 to M.X.) and Department of Science and Technology of Zhejiang Province (2023ZY1018 and 2024SSYS0054 to W.S.). The authors thank B. J. Song for his input and editing assistance.

10.1126/science.adz8959

[1]Center for Geriatric Medicine, International Center for Alzheimer's Research, Prevention and Treatment, The First Affiliated Hospital and Oujiang Laboratory; Key Laboratory of Alzheimer's Disease of Zhejiang Province, Institute of Aging, Wenzhou Medical University, Wenzhou, Zhejiang, China. [2]State Key Laboratory of Macromolecular Drugs and Large-scale Preparation, Wenzhou Medical University, Wenzhou, Zhejiang, China. Email: weihong@wmu.edu.cn

Check for

IMMUNOLOGY

Opening the gateway to food-induced anaphylaxis

Cysteinyl leukotrienes are important drivers of the anaphylactic response to ingested food antigens

Tamara T. Haque[1,2] and **Mark H. Kaplan**[1,2]



Allergy to peanuts is the deadliest food allergy and affects 1 to 2% of people worldwide.

Food allergy is an incurable chronic condition that affects more than half a billion people worldwide. Allergies to food arise when the immune system mounts an adaptive response to food antigens, and subsequent exposure results in the cross-linking of allergen-specific immunoglobulin E (IgE)–high-affinity IgE receptor (FcεRI) complexes on mast cells. Cross-linking triggers these immune cells to release factors that cause allergic symptoms ranging from mild local reactions to life-threatening anaphylaxis. Puzzlingly, the quantity of food-specific IgE does not accurately predict allergic symptoms upon exposure and some "sensitized-but-resistant" individuals have measurable food-specific IgE but can ingest the food without symptomatic reactions (*1*). On pages 614 and 613 of this issue, Hoyt *et al.* (*2*) and Bachtel *et al.* (*3*), respectively, report that cysteinyl leukotrienes (CysLTs) are important drivers of oral, IgE-mediated anaphylaxis, offering hope of a potential therapeutic approach for treating food allergy.

Hoyt *et al.* sought to understand why some strains of mice are susceptible to oral food-induced anaphylaxis, whereas others are resistant despite equal IgE-producing capabilities. This led to the identification of genetic variants in the gene encoding dipeptidase 1 (DPEP1), an enzyme that catabolizes cysteinyl leukotriene D4 (LTD4) into cysteinyl leukotriene E4 (LTE4). Both leukotrienes are lipids involved in inflammation. Resistant strains expressed a DPEP1 variant with higher catabolic activity in the jejunal microvillar membrane and the lamina propria of the small intestine, whereas susceptible strains had DPEP1 variants with lower catabolic activity and expression limited to the jejunal microvillar membrane. The authors further demonstrated that LTD4 promoted allergen transport across the gut epithelium into the tissue and circulation. Mouse strains with more LTD4, because of its reduced catabolism by DPEP1, had increased allergen transport and peripheral blood allergen concentrations and developed anaphylaxis.

Bachtel *et al.* examined the differences between oral (mucosal) and systemic (parenteral) exposure of allergen in murine models of anaphylaxis. This approach also led to the identification of a critical role for CysLTs in oral anaphylaxis. Notably, in both studies, the CysLT synthesis inhibitor, zileuton, attenuated orally induced anaphylaxis but had no effect on anaphylaxis when the allergen was parenterally administered through intravenous or intraperitoneal routes. In the study of Bachtel *et al.*, this result was associated with CysLTs produced by a specific subset of intestinal mast cells. Mast cells can be divided into subsets on the basis of anatomical and tissue location and by protease content. These characteristics are also tied to differences in histological staining patterns (*4*, *5*). In humans, the presently accepted subgroups are based on the type of protease that is released upon degranulation: chymase, tryptase, or both. Tryptase-producing mast cells are usually found in mucosal surfaces, although they are not yet well-defined in humans. In mice, mast cells located in connective tissues and organs such as the lungs, trachea, skin, peritoneal cavity, and submucosa of the intestines are collectively considered connective tissue mast cells. These usually express mast cell proteases 4 to 7 (MCPT4 to MCPT7). By contrast, mucosal mast cells are found in mucosal linings of the

PHOTO: CREATIVE TOUCH IMAGING LTD./NURPHOTO/GETTY IMAGES

gastrointestinal tract and lungs and express MCPT1 and MCPT2. In the lung, mucosal mast cells are generated in response to type 2 inflammation, which is characteristic of chronic inflammatory conditions such as asthma. By contrast, connective tissue mast cells are constitutively present (*6*). Mucosal mast cells can also be distinguished from their connective tissue counterparts by the expression of Mas-related G protein–coupled receptor member X2 (Mrgprx2), which triggers IgE-independent degranulation (*7*). Bachtel *et al.* determined that in response to allergens, mucosal mast cells primarily produce leukotrienes, whereas connective tissue mast cells primarily produce histamine.

Before the studies by Hoyt *et al.* and Bachtel *et al.*, evidence of a clear division of labor between mast cell subsets was lacking, beyond that dictated by their location. By defining subsets according to the mRNA molecules present in each subset (using the method single-cell RNA sequencing), Bachtel *et al.* found that mucosal mast cells expressing the protease MCPT1 in the lining of the intestine produced less histamine but more CysLTs than connective tissue mast cells. CysLTs released from the mucosal subset were critical for orally induced anaphylaxis but not anaphylaxis after peritoneal exposure, which was dependent on histamine released from connective tissue mast cells.

The identification of [leukotriene D4] as a modifier of food-induced anaphylaxis... provides a target for understanding why there are sensitized-but-resistant patients.

These observations agree with a previous report that mucosal mast cells expressing MCPT1 were specifically activated in orally challenged mice and that connective tissue mast cells expressing MCPT7 were primarily activated by parenteral exposure of allergen (*8*). Similarly, another study investigated the role of basophils, mast cells, and connective tissue mast cells in mouse models of anaphylaxis to peanut (*9*). That work used mouse strains engineered to lack all mast cells and basophils, connective tissue mast cells alone, or basophils alone and demonstrated that anaphylaxis triggered by parenteral exposure to peanut was partially reliant on mast cells and/or basophils. The anaphylaxis observed in mast cell–deficient animals appeared to be driven by platelet-activating factor, which is most likely induced by IgG-mediated activation of neutrophils as well as macrophages (*10*). This is consistent with the findings by Bachtel *et al.* and others who verified that oral exposure to an allergen is largely dependent on IgE, whereas exposure through parenteral routes is not. This is also reminiscent of the impact of interleukin 9 in orally induced anaphylaxis and airway hyperresponsiveness (such as constriction) to an allergen but not in parenteral allergen-induced anaphylaxis (*11*–*13*).

Notably, by studying mice lacking both CysLT receptors 1 and 2 (CysLTR1 and CysLTR2), Bachtel *et al.* demonstrated that the receptors nonredundantly promote mucosal mast cell expansion, with a larger contribution from CysLTR1. Acute administration of montelukast, a small-molecule inhibitor of CysLTR1, did not protect against orally induced anaphylaxis. Similarly, oral allergen exposure was not affected by inhibition of either CysLTR1 or CysLTR2 but was partially blocked by inhibition of both receptors. These observations further support a role for CysLTs in orally Induced anaphylaxis, potentially by promoting expansion and effector functions of mucosal mast cells. Taken together, these results indicate a potential redundancy in the acute function for both CysLT receptors in orally induced anaphylaxis but nonredundancy in mucosal mast cell expansion.

There are some differences in the studies of Hoyt *et al.* and Bachtel *et al.* that could be associated with the models used, such as the agents used to sensitize animals to allergens. Another important distinction is the effect of CysLTs on allergen transfer into the circulation and the extent of systemic mast cell activation. Also, the source of LTD4 was nonhematopoietic cells in Hoyt *et al.* and hematopoietic cells in Bachtel *et al.* These observations suggest that in patients, there could be multiple sources of CysLTs, depending on conditions and potentially on variations in the synthesis and responsiveness of cells. Because altered microbiome and sustained signaling by interleukin 4 (a cytokine produced by various immune cells that promotes allergic inflammation) can overcome some of the differences observed in these strains, it is possible that microbial metabolites or immune signals can modify the activity of these pathways.

Zileuton is a small-molecule inhibitor of CysLT synthesis that is being used now to treat asthma. Because Hoyt *et al.* and Bachtel *et al.* show that zileuton can inhibit orally induced anaphylaxis, future translational studies are warranted that examine the effectiveness of zileuton in preventing anaphylactic food allergic reactions in humans. The mechanism proposed by both studies seems plausible in patients, as Hoyt *et al.* provide some data to support a CysLT-dependent pathway in humans. Although little is known about the role of CysLTs in human intestinal mast cell development and anaphylaxis, their production increases in humans after anaphylaxis (*14*).

Predicting which patients will have severe allergic reactions remains a major clinical challenge. CysLTs were primarily thought to be involved in late-phase anaphylaxis symptomology. The identification of LTD4 as a modifier of food-induced anaphylaxis in mouse models where sensitization and IgE production did not differ provides a target for understanding why there are sensitized-but-resistant patients. Polymorphisms in the generation and metabolism of CysLTs could provide an approach for identifying patients most at risk. Moreover, there are likely additional mechanisms for the sensitized-resistant phenomenon because some patients can be sensitized to multiple food antigens and be symptomatic to some but resistant to others. It remains to be determined whether the mechanisms proposed by Bachtel *et al*. and Hoyt *et al*. are antigen specific. □

REFERENCES AND NOTES

1. C. A. Keet, R. A. Wood, E. C. Matsui, *J. Allergy Clin. Immunol.* **130**, 1207 (2012).
2. L. R. Hoyt *et al*., *Science* **389**, eadp0240 (2025).
3. N. D. Bachtel *et al*., *Science* **389**, eadp0246 (2025).
4. A. A. Irani, N. M. Schechter, S. S. Craig, G. DeBlois, L. B. Schwartz, *Proc. Natl. Acad. Sci. U.S.A.* **83**, 4464 (1986).
5. H. R. Katz, R. L. Stevens, K. F. Austen, *J. Allergy Clin. Immunol.* **76**, 250 (1985).
6. T. Derakhshan *et al*., *J. Exp. Med.* **218**, e20200321 (2021).
7. M. Tauber *et al*., *J. Exp. Med.* **220**, e20230570 (2023).
8. S. Benedé, M. C. Berin, *PLOS ONE* **13**, e0190453 (2018).
9. L. L. Reber *et al*., *J. Allergy Clin. Immunol.* **132**, 881, 11 (2013).
10. F. D. Finkelman, *J. Allergy Clin. Immunol.* **120**, 506, quiz 516 (2007).
11. A. Pajulas *et al*., *Mucosal Immunol.* **16**, 432 (2023).
12. E. E. Forbes *et al*., *J. Exp. Med.* **205**, 897 (2008).
13. H. Osterfeld *et al*., *J. Allergy Clin. Immunol.* **125**, 469 (2010).
14. M. Nassiri, O. Eckermann, M. Babina, G. Edenharter, M. Worm, *J. Allergy Clin. Immunol.* **137**, 312 (2016).

10.1126/science.adz6439

[1]Department of Pediatrics, Indiana University School of Medicine, Indianapolis, IN, USA. [2]Department of Microbiology and Immunology, Indiana University School of Medicine, Indianapolis, IN, USA. Email: tthaque@iu.edu; mkaplan2@iu.edu

Check for

POLICY FORUM

QUANTUM TECHNOLOGY

Quantum technology governance: A standards-first approach

Standards offer a flexible, globally harmonized path to govern early-stage quantum technologies while preserving innovation, security, and international cooperation

Mateo Aboy[1,2], Urs Gasser[3], I. Glenn Cohen[4], Mauritz Kop[5]

Quantum technologies are advancing rapidly, with considerable implications across fields, from secured communication networks to drug discovery (*1*–*4*). Studies report a 10-fold increase in quantum technology patents over the past two decades, underscoring the field's growing strategic importance (*5*). However, alongside these advancements come substantial risks, such as cybersecurity threats, dual-use potential, and global competition for quantum leadership (*6*–*8*). These developments raise foundational questions: How should these transformative technologies be governed? What frameworks will best ensure responsible development while fostering continued innovation and stakeholder trust? Should regulation be introduced now, or are there more effective approaches for this early stage of technological development? (*8*–*12*) We highlight ongoing but underrecognized standardization efforts in encouraging a standards-first approach to governance. At this nascent stage, flexible and globally harmonized consensus standards can lay a solid foundation for innovation, foster trust, and provide a basis for future regulatory frameworks as quantum technologies mature.

Governance decisions—especially in emerging fields such as quantum technologies—can shape how discoveries transition from theoretical advances to practical innovations. For the broader scientific community, the governance of quantum technologies directly influences the pace and direction of research, the development of real-world applications, and cross-border collaboration. Historically, lessons from transformative technologies such as the internet, biotechnology, and artificial intelligence (AI) illustrate that early governance frameworks are critical to maintaining stakeholder trust while ensuring sustained scientific and technical progress. For quantum technologies, where research spans across disciplines—from physics and computer science to materials engineering and cryptography—establishing a shared framework becomes essential to reduce barriers, foster interdisciplinary collaboration, and avoid fragmentation across regions.

Governance frameworks that incorporate flexible standards provide researchers and innovators with helpful guidelines for experimentation and development. This ensures that technical benchmarks and definitions are harmonized, facilitating international cooperation and accelerating scientific discovery. Additionally, well-crafted governance frameworks bolster public trust by addressing ethical concerns, ensuring safety, and mitigating risks associated with dual-use applications of quantum technologies. Trust is particularly critical in fields such as quantum communication and sensing, where public and governmental confidence will determine the scale of adoption.

THE QUANTUM GOVERNANCE CHALLENGE

Although at different stages of development, quantum technologies already promise transformative impacts across industries. Policymakers and stakeholders must carefully balance fostering innovation and economic growth with managing risks such as national security threats, economic disruption, and human rights concerns. For instance, quantum sensing may be used to improve biomedical diagnostics technologies, yet quantum encryption-breaking tools might threaten global cybersecurity. Additionally, global competition over quantum leadership raises concerns about equitable access and responsible development.

Given the magnitude of the predicted societal impact of quantum technologies, there is a natural inclination to turn to regulation as a means of governance. However, many proponents and much discussion of regulation appear to be not well informed of the many pragmatic resources already available and being pursued under standards-setting processes. Making standards the basis of a governance model is a promising approach at this early phase when most issues are technical rather than tied to specific real-world applications. International standards facilitated by organizations such as the International Organization for Standardization (ISO), the International Electrotechnical Commission (IEC), and the Institute of Electrical and Electronics Engineers (IEEE) can offer tangible advantages by creating shared definitions, performance benchmarks, and technical protocols that foster global interoperability. ISO includes more than 170 national bodies working on international consensus standards across 839 committees with a strong track record. Since 1946, ISO has created more than 25,000 standards and supporting documents covering almost all aspects of technology, management, and manufacturing. Work on international standards is one of the areas where global collaboration has been effective, resulting in agreed-upon international consensus standards that define the requirements for governance through quality management systems (QMSs), interoperability standards, and others.

Unlike regulations, which can be rigid and slow to adapt, standards can evolve more rapidly in response to technological breakthroughs, making them particularly suited to the fast-paced nature of quantum development. For example, as quantum-AI hybrid technologies emerge, updating standards on interoperability and safety metrics will be far quicker than introducing new legislation. Thus, by laying a flexible foundation, standards can help ensure responsible innovation while providing a basis for future regulatory frameworks when quantum technologies become more widely deployed.

HOW STANDARDS CAN HELP

In the context of quantum technologies, standards offer a practical solution to several key governance challenges, including interoperability, and cybersecurity risks. By defining shared technical baselines and best practices, standards can foster global collaboration, build public trust, and reduce regulatory uncertainty, enabling innovation while ensuring responsible development.

International standards organizations such as ISO and IEC (ISO/IEC) facilitate global alignment by reducing trade barriers and supporting cross-border cooperation. Because standards are typically voluntary and function as "soft law," they support flexible compliance and international cooperation without imposing binding legal constraints. This is particularly important for quantum technologies, which rely on international research and supply chains. For example, in the medical devices industry, standard ISO 13485 has been widely recognized and implemented to demonstrate compliance with regulatory frameworks like the European Union (EU) Medical Device Regulation (MDR) and the US Food and Drug Association's Quality Management System Regulation, promoting harmonized standards and consistent auditing processes across global markets. This approach not only ensures safety and quality but also simplifies market access and accelerates commercialization. Even when such QMS standards are voluntary, such as the ISO 27001 information security standard, they can serve as a bridge to regulatory compliance, with adoption incentivized by strategic de-risking and enhanced stakeholder trust rather than solely direct economic benefits. Whereas technical standards define what a product must do, the QMS ensures the product is designed, built, deployed, and maintained to those specifications, and QMS standards define how that system must be structured, audited, and documented—encompassing both technical compliance and the broader regulatory and ethical context. QMS standards help ensure adherence to governance goals, regulatory requirements, and quality standards, such as through harmonized standards for risk management, impact assessment, design controls, product development, corrective and preventive actions, and periodic auditing.

The benefits of standards are well demonstrated in other technical fields. In computing, telecommunications, and networking, standards have enabled the rapid growth of complex systems by ensuring interoperability and compatibility across regions. Similarly, in quantum technologies, standards can define protocols, common interfaces, and technical specifications, ensuring that components from different suppliers work together effectively, thereby stimulating innovation and commercialization.

Standards vary in their scope and purpose. Some, like IEEE P7130 Standard for Quantum Computing Definitions, establish common terminology to facilitate clear communication across the quantum field. Others, such as ISO 13485, focus on quality management to ensure compliance with regulatory requirements. Even with technologies at early stages of development, foundational standards for terminology and benchmarks are helpful to prevent early fragmentation. The collaborative nature of international harmonized standards development encourages broad participation, helping to align industry practices and build trust among stakeholders. For example, ISO 27001, a standard for information security, is widely adopted across industries to ensure robust cybersecurity measures.

Well-designed standards also promote innovation by establishing common platforms and interfaces, allowing companies to focus on differentiation and value creation. In the case of the internet, standards such as ISO/IEC 7498, which defines the Open Systems Interconnection model, laid the foundation for protocols that ensured interoperability, enabling the growth of global networks. The same principle applies to quantum technologies.

Beyond interoperability, standards can address critical safety and security concerns. For example, ISO/IEC 18033 and National Institute of Standards and Technology (NIST) cryptographic standards define encryption systems to protect sensitive data, whereas ISO 14117, a standard for electromagnetic compatibility, ensures that active implantable medical devices function correctly in their electromagnetic environment. Similar standards for quantum technologies could help ensure that devices meet stringent safety and security requirements.

Globally agreed-upon standards can also help create and expand markets for quantum technologies by reducing uncertainty and establishing common expectations. As these technologies continue to evolve, international standards will be essential for guiding responsible innovation, fostering stakeholder trust, and laying the groundwork for future regulatory frameworks.

TOWARD QUANTUM STANDARDS: RECENT DEVELOPMENTS AND ACTIVITIES

Responsible Research and Innovation frameworks—already embedded in the UK's Quantum Hubs and EU Flagship programs—illustrate how stakeholder engagement and ethical foresight can align with standards development. Similarly, standards could serve as a cornerstone for quantum technology governance, guiding responsible innovation, fostering trust, and promoting international cooperation in this transformative field. Many of the ethical, legal, social, policy, and interoperability (ELSPI) concerns raised by commentators as justifications for early regulation are already being addressed by various standard-centric initiatives.

For instance, a key risk often cited to justify quantum regulation is the potential for quantum computers to break existing encryption protocols, such as the widely used Rivest-Shamir-Adleman cryptosystem. Although this is a serious concern, the question remains: Is regulation the best tool to manage such risks? What form of regulation could ensure appropriate risk management without stifling innovation? Importantly, the risk associated with encryption-breaking capabilities is already being proactively addressed by post-quantum cryptography standardization initiatives (see the table). For example, NIST has been actively working on developing standards for encryption algorithms that are resistant to quantum computing attacks. The NIST Post-Quantum Cryptography Standardization efforts illustrate how well-designed standards can proactively tackle critical cybersecurity risks posed by quantum technologies.

That said, although post-quantum cryptography cannot simply be legislated into existence, targeted government-led initiatives (*1*), such as investment to accelerate the development of quantum-safe cryptographic solutions or export controls on sensitive technologies, can complement ongoing standardization efforts. Once the downside risks associated with encryption-breaking capabilities are properly managed through collaborative technical efforts to develop quantum-safe cryptosystems, further advancements in quantum technologies will offer considerable societal benefits (*6*, *7*, *9*).

A notable recent development in the field of quantum standards is the formation of the new ISO/IEC Joint Technical Committee (JTC 3) on Quantum Technologies in January 2024. The JTC 3 aims to standardize quantum technologies comprehensively, covering areas ranging from quantum computing terminology and nomenclature (ISO/IEC 4879) to quantum computing, quantum simulation, quantum metrology, quantum sources, quantum detectors, and quantum communications. The establishment of the JTC 3 committee reflects the growing importance of quantum technologies and the need for standardization in this rapidly evolving field (see the table). This is a highly international technical committee, with representation from the US, UK, Europe, Japan, South Korea, and China, among others.

Beyond cybersecurity, standardization efforts are critical for fostering technology governance and global cooperation as well as ensuring interoperability in quantum technologies. The newly established ISO/IEC JTC 3 on Quantum Technologies represents

Quantum standards activities by organization

Standards initiative	Description
ISO/IEC (international)	
JTC 3	Standardization in quantum technologies, including computing, simulation, metrology, sources, detectors, and communications
JTC 1/WG 14/CD 4879	Quantum computing — Terminology and vocabulary
JTC 1/WG 14/PWI TR 18157	Introduction to quantum computing
JTC 1/WG 14/PWI TR 18670	General requirements for quantum resource simulation platform
JTC 1/WG 14/PWI TR 18660	Quantum machine-learning datasets
IEEE (international)	
P7130	Standard for quantum computing definitions
P7131	Quantum computing performance metrics and performance benchmarking
P1943	Standard for post-quantum network security
P3172	Recommended practice for post-quantum cryptography migration
P3120	Standards for quantum computing architecture
P1947	Standard for quantum cybersecurity framework
P3155	Standard for programmable quantum simulator
P1913	Software-defined quantum communication
P3185	Standard or hybrid quantum-classical computing
P2995	Trial-use standard for quantum algorithm design and development
P3329	Standard for quantum computing and simulation energy efficiency
NIST (United States)	
FIPS 203	Module-lattice-based key-encapsulation mechanism standard
FIPS 204	Module-lattice-based digital signature standard
FIPS 205	Stateless hash-based digital signature standard
FIPS 206	FALCON post-quantum encryption algorithm (in progress)
ETSI (Europe)	
White Paper No. 8	Quantum Safe Cryptography and Security
White Paper No. 27	Implementation Security of Quantum Cryptography
CEN/CENELEC	
CEN-CLC/JTC 22	CEN-CLC/JTC 22 aligns its efforts with international standards organizations, such as ETSI and IEC/ISO JTC 3; the committee ensures that its standardization efforts support European market needs, legislative frameworks, and key European Union policies and principles
WG 1	Quantum technology strategic advisory group
WG 2	Quantum metrology, sensing, and enhanced imaging, and quantum-enabling technologies
WG 3	Quantum computing and simulation
WG 4	Quantum communication and quantum cryptography
QED-C	
	QED-C is a membership organization available to corporations, academic and research institutions, and other entities related to the quantum industry from 39 countries; goals include identifying gaps in standards, technology, and workforce and addressing those gaps through collaboration

CD, committee draft; CEN, European Committee for Standardization; CEN-CLC, joint collaboration between CEN and CENELEC; CENELEC, European Committee for Electrotechnical Standardization; ETSI, European Telecommunications Standards Institute; FALCON, Fast Fourier Lattice-based Compact Signatures over Nth-degree Truncated Polynomial Ring Units (NTRU); FIPS, Federal Information Processing Standard; IEC, International Electrotechnical Commission; IEEE, Institute of Electrical and Electronics Engineers; c; JTC, Joint Technical Committee; JTC 1, Joint Technical Committee 1 – Information Technology; JTC 3, Joint Technical Committee 3 – Quantum Technologies; NIST, National Institute of Standards and Technology; PWI, preliminary work Item; QED-C, Quantum Economic Development Consortium; TR, technical report; WG, working group.

a key step toward aligning international efforts by defining shared terminology, technical requirements, and interoperability standards. This committee, with participation from across the globe, reflects a growing international consensus on the need for standardization in this rapidly evolving field. Such collaboration helps ensure that quantum technologies can develop within a globally harmonized framework, reducing fragmentation and enabling cross-border innovation. Continued participation from China, the US, and Europe underscores the potential for standards harmonization even among geostrategic competitors.

Complementing the work of ISO/IEC JTC 3, the IEEE Quantum Initiative supports standards activities aimed at addressing industry needs. Present IEEE efforts include projects focused on software-defined quantum communication (P1913), post-quantum network security (P1943), quantum computing architecture (P3120), and quantum computing energy efficiency (P3329). These initiatives illustrate the breadth of ongoing standardization work and highlight how multiple stakeholders—governments, industries, and international bodies—are collaborating to create a robust framework for quantum technology governance (see the table). Rather than relying solely on national regulatory frameworks, standards offer a flexible, globally harmonized approach to guide quantum technologies toward responsible and beneficial development.

QMS standards often incorporate ELSPI considerations by requiring risk assessments, user safety, transparency, traceability, and accountability. For example, ISO 13485 requires risk management across a medical device's life cycle to protect patient safety, which aligns with ethical principles like nonmaleficence and beneficence. Some QMS standards consider the impact on society, such as accessibility, inclusion, and user rights. Medical device standards include usability engineering (e.g., IEC 62366) to ensure that devices are safe and effective for diverse user populations. Similarly, ISO 27001 incorporates principles such as data minimization, access control, and security by design, all of which address privacy risks and align with rights-based frameworks like the EU General Data Protection Regulation. Standards such as the ISO 27001 have several articles where ELSPI issues need to be considered and documented. For example, Clause 4 of ISO 27001 calls for organizations to understand their context and the expectations of stakeholders, explicitly including societal values, ethical norms, and legal obligations. Clause 6 emphasizes planning for information security risks—not only technical threats but also potential harms to individuals, such as surveillance and discrimination—encouraging the inclusion of human rights impact assessments. Together, such provisions ensure that

ELSPI considerations are embedded across the technical, organizational, and human dimensions of information security management.

As these technologies mature, international standards can serve as a cornerstone for future regulatory efforts, ensuring safety, security, regulatory agility, and interoperability while maintaining the pace of innovation.

A PATH FORWARD

Many of the governance-related concerns raised by scholars and policy-makers, including cybersecurity risks posed by quantum computing and global cooperation on technology governance, are already being addressed through various ISO/IEC and IEEE standardization efforts. Drawing on lessons from other fields, such as medical devices and information security, where harmonized standards have successfully guided or been incorporated within regulatory frameworks, we recommend the establishment of a consensus-driven Quantum Technology QMS (QT-QMS) under ISO/IEC. This QT-QMS should integrate quantum-specific governance principles, including ethical, legal, and societal implications, as well as established risk management standards. The QT-QMS model is best suited to quantum technologies approaching commercialization, particularly in computing, communication, and sensing, whereas other subfields may require further technical development.

As quantum technologies transition from research and development to real-world deployment, adopting a comprehensive QT-QMS framework would enable the structured management of design, development, deployment, and life cycle processes. This approach would help ensure responsible innovation, robust risk management, and the integration of ELSPI considerations throughout the development and application of quantum technologies as part of the impact assessment embedded in the QMS process. The QT-QMS could integrate and align with existing standards. For example, incorporation of well-established standards like ISO 27001 for information security would help enhance the overall security and resilience of quantum systems, whereas standards such as ISO 27005 for risk management would provide a consistent framework for addressing complex risk scenarios. Adopting AI standards like ISO 42001 could help manage the distinctive challenges and opportunities presented by quantum-AI hybrid technologies. Updating ISO 27002, which presently outlines 144 controls for managing information security risks under ISO 27001, to include technical controls for post-quantum cryptography, would help proactively mitigate emerging cybersecurity threats posed by quantum technologies. A certifiable QT-QMS standard could help simplify future regulatory efforts and help increase regulatory agility given that future regulation could incorporate these standards by reference.

Most often, the ideal way forward is to integrate regulation with standards by incorporating these standards to demonstrate regulatory compliance. As is the case now with ISO 13485 for medical devices or ISO 27001 for information security, relying on QMS standards to document regulatory compliance offers various benefits, including periodic updates without having to change the underlying legislation or regulation, periodic certification by accredited third parties or notified bodies, and globally harmonized auditing like the Medical Device Single Auditing Program (MDSAP). This approach offers various advantages: It allows different jurisdictions to maintain their distinctive legal traditions and regulatory frameworks while ensuring global compliance through a harmonized international standard. This harmonization simplifies the regulatory process for manufacturers, as compliance with a globally recognized standard like ISO 13485 can simultaneously meet the requirements of multiple regulatory authorities, thereby easing market access across different regions. Incorporating standards by reference ensures that regulatory compliance remains consistent and streamlined (e.g., enabling a medical device single-audit program such as the MDSAP where auditors and notified bodies only need to check for compliance against a single harmonized standard). This practice not only enhances global market access and legal certainty but also promotes high-quality and safe products by ensuring that manufacturers adhere to rigorous, internationally recognized standards and periodic recertifications. Finally, the incorporation of a standard by reference into the regulation or practically as an accepted means to show regulatory compliance helps effectively deal with technological change. For example, whereas a regulation such as the EU MDR stays the same, the ISO 13485 standard is periodically revised to account for technological changes and best practices.

Standards alone are not a complete solution. Although standards offer flexibility, concerns remain about some standards' legitimacy when driven by self-interested actors, and the political nature of international standards setting can introduce geopolitical friction. Although less of an issue for ISO/IEC QMS standards, the technical standard-setting processes defining architectures and interfaces require robust safeguards to ensure fairness, inclusivity, and legitimacy while preventing path dependency, lock-in effects, and anti-competitive behavior (*12*, *13*). As quantum technologies mature, an integrated approach that combines the strengths of standards with targeted regulatory interventions will likely be necessary. Regulation may need to define clear "red lines" for specific high-risk quantum applications or address sensitive public policy issues, such as export controls on critical quantum technologies. Although standards play a foundational role, they are complemented by national regulations, export controls, and multilateral agreements (e.g., the trilateral security partnership between Australia, the UK, and the US, resulting in the AUKUS Quantum Arrangement) that collectively shape quantum governance. By adopting a holistic governance approach that builds on the ongoing standardization efforts, policy-makers and stakeholders can foster a globally aligned framework that promotes innovation, ensures interoperability, and addresses societal concerns. The governance choices made today will greatly influence the trajectory of these transformative technologies, shaping their future societal impact. □

REFERENCES AND NOTES

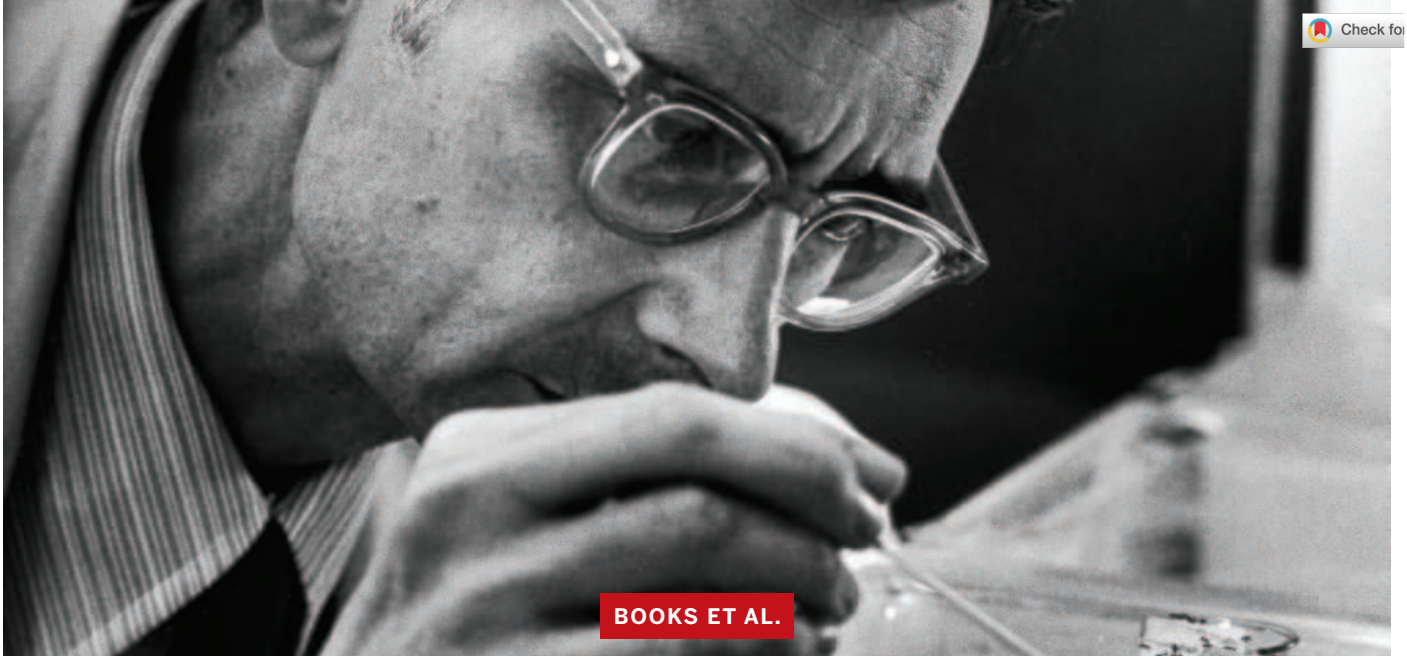
1. C. Monroe, M. G. Raymer, J. Taylor, *Science* **364**, 440 (2019).
2. J. Preskill, *Quantum* **2**, 79 (2018).
3. F. F. Flöther, P. F. Griffin, *Res. Dir. Quantum Technol.* **1**, e7 (2023).
4. D. Maheshwari, B. Garcia-Zapirain, D. Sierra-Sosa, *IEEE Access* **10**, 80463 (2022).
5. M. Aboy, T. Minssen, M. Kop, *IIC Int. Rev. Ind. Prop. Copyr. Law* **53**, 853 (2022).
6. M. Kop *et al*., *Quantum Sci. Technol.* **9**, 035013 (2024).
7. M. Kop *et al*., *UC Law Sci. Technol. J.* **15**, 63 (2024).
8. UK Regulatory Horizons Council (RHC), "Regulating quantum technology applications: government response to the RHC" (RHC, 2024); https://assets.publishing.service.gov.uk/media/65ddc83bcf7eb10015f57f9f/RHC_regulation_of_quantum_technology_applications.pdf.
9. U. Gasser, E. De Jong, M. Kop, *Nat. Phys.* **20**, 525 (2024).
10. T. Dekker, F. Martin-Bariteau, *Can. J. Law Technol.* **20**, 179 (2023).
11. C. J. Hoofnagle, S. L. Garfinkel, *Law and Policy for the Quantum Age* (Cambridge Univ. Press, 2022).
12. J. Lerner, J. Tirole, *Science* **343**, 972 (2014).
13. W. Mattli, T. Büthe, *World Polit.* **56**, 1 (2003).

ACKNOWLEDGMENTS

The authors acknowledge support from a Novo Nordisk Foundation Grant for a scientifically independent International Collaborative Bioscience Innovation & Law (Inter-CeBIL) Programme (grant no. NNF23SA0087056).

10.1126/science.adw0018

[1]Centre for Intellectual Property and Information Law, University of Cambridge, Cambridge, UK. [2]Centre for Law, Medicine, and Life Sciences, University of Cambridge, Cambridge, UK. [3]School of Social Sciences and Technology, Technical University of Munich, Munich, Germany. [4]Harvard Law School, Harvard University, Cambridge, MA, USA. [5]Stanford Center for Responsible Quantum Technologies, Stanford University, Stanford, CA, USA. Email: ma608@cam.ac.uk



CLASSICS REVISITED

Revisiting the human sociobiology debate

What have we learned 50 years on?

Gillian R. Brown[1], H. Clark Barrett[2], Kevin N. Lala[3]



Edward O. Wilson Harvard University Press, 1975. 697 pp.

SOCIOBIOLOGY: THE NEW SYNTHESIS | During the 1960s and early 1970s, several influential theories emerged in evolutionary biology, stemming from the hypothesis that natural selection is best understood as acting at the level of the gene rather than at the level of the group or species (*1*). This new theoretical framework revolutionized the study of animal behavior, leading to the rejection of naïve "group selection" arguments. Harvard University biologist Edward O. Wilson's landmark 1975 book, *Sociobiology: The New Synthesis*, the first comprehensive textbook on the topic, brought together these conceptual advances under the umbrella term of "sociobiology" and demonstrated in an engaging manner that they provided a coherent new approach to studying a range of animal social behaviors, including cooperation, communication, aggression, and parental care. Although many of Wilson's specific ideas about human behavior have subsequently been disproved or discredited, the book remains an influential contribution to the evolutionary behavioral sciences. Fifty years after its publication, we reflect here on how resolving the human sociobiology debate remains pertinent to the current times and what lessons have—or have not—been learned in the intervening period.

Human behavior is more nuanced than entomologist E. O. Wilson conveyed in his landmark book, *Sociobiology*.

THE PERILS OF EVOLUTIONARY STORYTELLING

Sociobiology's first 26 chapters were mostly uncontentious, and the contemporary field of behavioral ecology was built upon the theoretical ideas that Wilson presented. However, in the book's final chapter, he applied his ideas to humans and discussed a range of sensitive topics, including gender roles; between-population differences; and the genetics of homosexuality, intelligence, and social class. This chapter provoked a storm of controversy and led to what became known in the social sciences as the "human sociobiology" debate (*2*).

Some of Wilson's contemporaries stated their disappointment that *Sociobiology* lacked the nuance that an anthropologist or social scientist might have brought to the topic (*2*). Others were outright hostile toward Wilson's approach and accused him of using a framework that represented the latest reincarnation of eugenics and race theories. Human sociobiology was criticized for its overreliance on genetic determinism, reductionism, and storytelling (*1*), and the term "sociobiology" quickly fell out of favor among academics.

Wilson later admitted to his political naivety when approaching the topic of human behavior (*3*) while remaining adamant that his version of sociobiology did not assume the existence of human races (*4*). Having built an illustrious academic career in entomology and biodiversity, Wilson was writing on topics outside of his expertise, which may have led him to repeat some of the simplifications and biases about human behavior that were common in the academic literature at the time. However, for many, his legacy was tainted by this misstep and by his inadvisable support of race scientists who misused scientific methods to support their prejudiced agendas (*5*).

One of the core contemporaneous criticisms of human sociobiology, as propagated by various researchers, was that it relied too heavily on biological determinism (*1*). The suggestion that genes were the sole or dominant determinant of an individual's behavior, attributes, or skills and that genetic variation explained differences between genders, social classes, and racialized groups concerned critics. The assertion was that genes controlled one's capacity to develop a certain array of traits and that, for some traits, the potential outcomes were extremely limited, while for others, the outcomes were more easily influenced by experiences or environments (*4*). Crucially, in *Sociobiology*, Wilson made bold statements about which traits were inherited and constrained by genes without offering concrete evidence to support such claims.

Wilson later acknowledged that many of his ideas about human evolution were speculative and would perhaps be disproved (*3*). However, *Sociobiology* lent evolutionary storytelling about human behavior and cognition an air of scientific legitimacy. That legacy is manifest today, as speculative "gene for trait X" stories abound and the complexities of human development are often not acknowledged in the media.

BEYOND NATURE VERSUS NURTURE

One lesson that has been learned since the publication of *Sociobiology* is that a long-standing dichotomy known as "nature versus nurture" does not provide a satisfactory account of human behavior. Polarized explanations that solely emphasize either genes and physiological processes ("nature") or environmental factors, learning, and culture ("nurture") are never sufficient. Rather, a compelling explanation requires recognizing both as playing important roles in behavioral development (*6*).

In recent years, science has gone beyond the simplistic recognition that both nature and nurture influence behavior, investigating precisely how genes, learning, and culture, and a multitude of other causally relevant factors, influence behavior across individual life spans and evolutionary time frames. In doing so, we have learned that human behavior, including between-group differences, is shaped by a variety of developmental processes that integrate internal variables, external factors, and legacy effects from previous generations in a reciprocally causal manner. For instance, learning can modify gene expression, and parental experiences can be epigenetically inherited by offspring.

One research field that has continued to probe the genetic underpinnings of human behavior and cognition is behavioral genetics, which, during the late 20th century, commonly relied on twin studies to generate sizable estimates of the heritability of traits such as cognitive abilities and personality. However, recent approaches, such as genome-wide association studies, indicate that the amount of variance in behavioral or cognitive phenotypes that is accounted for by genetic differences is generally small (<5% of trait variance). Researchers in this field have defended their attempts to study links between genes and phenotypes (*7*, *8*), whereas others have argued that any genetic accounts that ignore the role of developmental processes inevitably provide an impoverished understanding of phenotypic traits (*9*). It has also become clear that there is far more to biological inheritance than genes (*10*), with diverse nongenetic (e.g., epigenetic, symbiotic, and ecological) inheritance mechanisms now well documented, including effects through which experiences of the parental generation (e.g., trauma and famine) and other aspects (e.g., wealth, toxins, and nongenetic disease) can be passed on to the next generation.

CULTURE MEETS THE GENOME

Since the publication of *Sociobiology*, the evolutionary human sciences have matured into a pluralist, interdisciplinary field in which a range of evolutionary methods, including comparative approaches, are being deployed to analyze human behavior and cognition (*1*). For example, psychologists and neuroscientists have begun to understand evolved structure in the human brain, and human behavioral ecologists are using optimization principles to explain behavioral diversity. Evolutionary models have also been applied to human cultural traits with the goal of understanding how the frequencies of social norms and institutions change over time. Through these efforts, we have learned that human cultural activities can generate niche construction, thereby influencing the form of natural selection acting back on a population and shaping developmental conditions for their offspring.

Wilson correctly argued that human culture would need to be placed at the center of any understanding of the human mind, although his assumption that "genes hold culture on a leash" (*4*) incorrectly downplayed the strength of transgenerational cultural transmission. We now know that it is no less true that by modifying selection and gene expression, culture can hold genes on a leash.

RACE, GENES, AND SCIENTIFIC RESPONSIBILITY

Like other species, humans often inadvertently construct environments that affect the lives of future generations. The topics of race and racism provide an illustrative example. That "race" is not a biologically meaningful category for humans has long been established (*11*). Genetic data support neither the notion that human populations can be divided into racially distinct groups nor that separate genetic lineages are associated with racialized groups (*12*). Human genetic and phenotypic variation is also substantially greater within than between populations, and those genetic variants that do exhibit geographic variation demonstrate gradual, clinal distributions rather than distinct boundaries.

Research suggests that differences that might be found between socially defined racialized groups (e.g., disease incidence and scholastic performance) in fact result from ongoing histories of racialization that manifest in structural inequalities and differential treatment of people on the basis of perceived race. These inequitable niches persist through the legacies of heritable, yet nongenetic, biological components and inherited environments that differ in their wealth, amenities, and opportunities (*12*, *13*).

Many political and social landscapes have witnessed the reemergence of simplistic, inaccurate views about human behavior, with individuals facing discrimination on the basis of their ethnicity, gender, and/or disability status. Pseudoscientific ideas that are often framed by "evolutionary" backstories are used to perpetuate and deepen inequalities, restrict freedoms, and support harmful ideologies (*12*, *14*). Some scientists attempt to shield potentially injurious work from criticism by appealing to the "value-free ideal" of science, which holds, incorrectly, that the ethical, political, and social implications of research can be separated from science. But academics have an obligation to report their research findings accurately and to consider how their research might be misused or misreported.

SOCIOBIOLOGY'S LEGACY

The legacy of *Sociobiology* can be viewed from two angles. Undoubtedly, many of Wilson's conclusions need to be qualified or rejected as being overly simplistic, perpetuating stereotypes, and stretching beyond the bounds of the evidence. Some of the long-standing criticisms of human sociobiology, such as its overreliance on genetic deterministic accounts of human phenotypes, remain valid and have contributed to debates about how to integrate an understanding of genetic mechanisms with a growing emphasis on developmental processes. However, the scientific concepts that Wilson championed revolutionized the behavioral sciences, directly leading to the emergence of novel, and eventually nuanced and integrative, approaches to studying the evolution of human behavior.

REFERENCES AND NOTES

1. G. R. Brown, K. N. Lala, *Sense and Nonsense: Evolutionary Perspectives on Human Behaviour* (Oxford Univ. Press, ed. 3, 2024).
2. U. Segerstråle, *Defenders of the Truth: The Sociobiology Debate* (Oxford Univ. Press, 2000).
3. E. O. Wilson, *Naturalist* (Island Press, 1994).
4 E. O. Wilson, *On Human Nature* (Harvard Univ. Press, 1978).
5. D. Sepkoski, M. Borrello, *Hist. Stud. Nat. Sci.* **55**, 44 (2025).
6. E. Fox Keller, *The Mirage of a Space between Nature and Nurture* (Duke Univ. Press, 2010).
7. K. P. Harden, *Nat. Rev. Genet.* **24**, 197 (2024).
8. R. Plomin, *Blueprint: How DNA Makes Us Who We Are* (MIT Press, 2018).
9. D. S. Moore, K. Kampourakis, N. Gericke, *Hum. Dev.* 10.1159/000543465 (2025).
10. K. N. Lala, T. Uller, N. Feiner, M. Feldman, S. F. Gilbert, *Evolution Evolving: The Developmental Origins of Adaptation and Biodiversity* (Princeton Univ. Press, 2024).
11. J. L. Graves Jr., A. H. Goodman, *Racism, Not Race: Answers to Frequently Asked Questions* (Columbia Univ. Press, 2022).
12. K. N. Lala, M. W. Feldman, *Proc. Natl. Acad. Sci. U.S.A.* **121**, e2322874121 (2024).
13. P. Ivey Henry, M. R. Spence Beaulieu, A. Bradford, J. L. Graves Jr., *Evol. Med. Public Health* **11**, 112 (2023).
14. L. Bachaud, S. E. Johns, *Evol. Hum. Sci.* **5**, e28 (2023).

ACKNOWLEDGMENTS

The authors thank Sarah B. Hrdy for valuable feedback and discussion.

10.1126/science.ady6081

[1]School of Psychology and Neuroscience, University of St Andrews, St Andrews, UK. [2]Department of Anthropology, University of California, Los Angeles, CA, USA. [3]School of Biology, University of St Andrews, St Andrews, UK. Email: grb4@st-andrews.ac.uk

SCIENCE LIVES

Roxie Laybourne, the first forensic ornithologist

A new biography probes the life of a taxidermist turned avian investigator



The Feather Detective: Mystery, Mayhem, and the Magnificent Life of Roxie Laybourne
Chris Sweeney
Avid Reader Press, 2025. 320 pp.

Vijaysree Venkatraman

On 4 October 1960, Eastern Air Lines Flight 375 took off from Logan International Airport on a clear fall evening and plunged almost immediately into the waters of Boston Harbor, killing all but 10 of the 72 people on board. It remains the deadliest plane crash in New England history.

When the head of the Federal Aviation Administration (FAA) announced the cause of the crash, the public was incredulous. A flock of European starlings, each weighing less than 3 ounces, had brought down the 98,000-pound plane. In total, the plane's engines had ingested fewer than a dozen of the medium-sized songbirds, but the freak accident highlighted the threat the creatures posed to airplanes in flight.

Knowing which species and weights of birds hit planes frequently could help manufacturers build bird-resistant aircraft and enable ecologists to guide programs to reduce bird populations near runways. In the tragedy's aftermath, the FAA instructed all airlines to mail "a feather or more" of birds sucked into aircraft engines to the Smithsonian's National Museum of Natural History. There, it fell to taxidermist Roxie Laybourne to take the mangled bits of bird—often just wisps of degraded feathers—and make an accurate species identification. Insiders now call the process, which involves examining feathers' microstructures, the "Roxie method."

In *The Feather Detective*, Chris Sweeney traces Laybourne's career as the world's first forensic ornithologist, who made aviation safer and whose work also helped build criminal cases against murderers and poachers. Laybourne died in 2003, so Sweeney's account draws on interviews with her colleagues, court transcripts, press clippings, correspondence, and archival recordings, including an eight-part oral history interview conducted by the Smithsonian.



Laybourne's careful identifications of bird species made aviation safer and helped prosecute killers and poachers.

Laybourne started her career as an unpaid apprentice at the North Carolina State Museum, where she discovered a talent for taxidermy. To become a full-fledged scientist, which she aspired to do despite having a full-time job, a troubled marriage, and a toddler, she enrolled in a graduate program in zoology at North Carolina State University.

In 1944, on a professor's recommendation, Laybourne applied for a temporary taxidermist position at the Smithsonian's National Museum of Natural History and moved to Washington, DC. As she skinned birds and prepared specimens, her superiors noticed her work and her work ethic. At the end of the year, she joined the US Fish and Wildlife Service (FWS) but also stayed on at the Museum of Natural History, where she continued working with thousands of bird specimens. "You learn a lot washing feathers [if] you can pay attention," she argued. Six years after arriving in Washington, DC, she completed her master's degree at George Washington University.

The Federal Bureau of Investigation (FBI) eventually sought Laybourne's expertise as well. Typically, her work for them involved matching a feather found at the scene of a crime with an object that belonged to the perpetrator or the victim, for example, a pillow or a down jacket. Even though her efforts helped to prosecute criminals, her FWS boss felt that this "service work" distracted from the laboratory's research mandate and abolished it in 1974. However, she continued her feather identification work as a private consultant.

By the early 1980s, Laybourne realized it was time to start handing down her hard-won knowledge to promising young researchers, but mentoring did not come easily to her. Her criticisms could sting. FBI special agent Doug Deedrick, whom Laybourne trained to become the bureau's in-house feather expert, recalls that she "wouldn't hesitate to give [him] a 'slap across the face,' so to speak," when he failed to meet her expectations, Sweeney writes.

Beth Ann Sabo, an apprentice of Laybourne's at the Smithsonian who persisted despite her mentor's tough love, left to lead feather-related work at a high-tech forensic lab in Oregon dedicated to crimes against nature, and Laybourne's quest for potential successors continued. She saw promise in technician Carla Dove. Laybourne, who had endured secondary status and snide comments because she did not have a PhD, arranged for the US Air Force, which outsourced bird strike identification to the Smithsonian, to fund her protégé's doctoral studies.

When the museum celebrated its sesquicentennial anniversary in 1996, Laybourne, who was then in the sixth decade of her career, set up a table on the National Mall to share her work with the public. Marcy Heacker, a veterinary technician looking for a career change, approached her. Through an accelerated apprenticeship, Heacker ended up training in forensic ornithology with Laybourne.

Dove and Heacker may have reported to Laybourne professionally, but each worried about her as if she were their mother, Sweeney writes. When Laybourne died at the age of 92, the two women carrying her scientific legacy forward were among the pallbearers at her funeral.

Of the 34 portraits that constitute the Smithsonian's Division of Birds "Hall of Fame," Laybourne remains the sole woman. Although the "Roxie method" creator may never become a household name, this engagingly written biography brings her remarkable story to a wider audience.

10.1126/science.adx2662

The reviewer is a science journalist in Boston, MA, USA. Email: v.vijaysree@gmail.com



If approved, a new law in Brazil will make criminal activities, such as this illegal gold mining within the borders of the Jamari National Forest, more prevalent.

PHOTO: ANDRÉ DIB

Brazil's "devastation bill" empowers criminals

Criminal activities are slowly expanding across the Amazon region, causing severe harm to local social-ecological systems (*1*). An organized crime system benefits from illegal economies and markets based on narcotraffic, land-grabbing, and laundering of money and environmental assets, as well as from corrupt politicians involved in these economies (*2*). Crime syndicates are closely associated with illegal mining, logging, wildlife trafficking, predatory fishing, forest burning, and deforestation (*1*, *3*). Regional deterioration of democracy and the rule of law, along with the spread of chaos, corruption, violence, and territorial control, have allowed the illegal and legal economies to become intertwined (*4*). Brazil's recently passed Bill 2159/2021, known as the "devastation bill," will facilitate continued expansion of criminal activity. President Lula should veto the bill, and Brazil's Congress should accept the veto. If necessary, the Federal Supreme Court should stop the bill's implementation.

Bill 2159/2021 will severely weaken environmental governance and boost illegal economies that empower organized crime (*5*, *6*). The bill exempts activities such as mining and soy and cattle production from formal licensing procedures by Brazil's environmental agencies. These activities will be allowed to proceed through self-declaration alone, despite the potential social-ecological consequences. Plans will be able to proceed even in Indigenous and Quilombola territories that are awaiting legal titling, putting almost one-third of Indigenous territories at risk (*7*). Considering the role of crime syndicates in mining, agriculture, and cattle farming, Bill 2159/2021 will enable organized crime to gain more wealth, territory, and political power while weaking the local governance through fear and corruption.

Given the recent expansion of crime syndicates in the Amazon region (*1*–*4*), the bill could empower criminals and accelerate their territorial expansion, with disastrous consequences for ecosystems, local livelihoods, and Indigenous peoples. Crime syndicates could force Indigenous peoples from their ancestral territories, thereby opening more space for crime in both urban and forest landscapes (*1*). The recent intrusion and social-ecological chaos in the Yanomami Indigenous territory demonstrates how the growth of illegal economies can enable a shift into a crime-dominated regime (*4*). Instead of weakening the environmental governance system, Brazil should halt implementation of the new law and advance policies that strengthen local environmental governance actors and institutions.

Andre Giles[1] and Bernardo M. Flores[2,3,4]

[1]Center for Agricultural Sciences (CCA), Federal University of Santa Catarina (UFSC), Florianópolis, Brazil. [2]Amazon Regional Observatory, Amazon Cooperation Treaty Organization (ORA/OTCA), Brasília, Brazil. [3]Instituto Juruá, Manaus, Brazil. [4]EqualSeaLab, University of Santiago de Compostela, Santiago de Compostela, Spain. Email: andregiles.bio@gmail.com; mflores.bernardo@gmail.com

REFERENCES AND NOTES

1. E. S. Brondizio, *Ambio* **54**, 923 (2025).
2. G. R. Canale *et al.*, *Revista Campo-Território* **19**, 1 (2024).
3. Igarapé Institute, "Follow the money: Environmental crimes and illicit economic activities in Brazilian Amazon production chains," Strategic Paper 63, 29 April 2024.
4. F. d. A. Costa *et al.*, "Land market and illegalities: The deep roots of deforestation in the Amazon" (Policy Brief, Science Panel for the Amazon, 2024).
5. F. Wenzel, "Ahead of hosting COP30, Brazil is set to weaken environmental licensing," Mongabay, 29 May 2025.
6. M. L. Canineu, "Brazil should reject bill gutting environmental licensing," Human Rights Watch, 10 June 2025.
7. Instituto Socioambiental, "Análise dos impactos do Projeto de Lei n.º 2.159/2021 (Lei Geral do Licenciamento Ambiental) sobre Terras Indígenas, Quilombolas e Unidades de Conservação" (Technical Report, Instituto Socioambiental, 2025).

10.1126/science.adz7734

Brazil's dangerous environmental licensing bill

On 17 July, Brazil's Congress approved Bill 2159/2021 (*1*), which aims to simplify the environmental licensing process in Brazil, an essential process for terrestrial and maritime economic activities. Proponents argue that the current system is excessively bureaucratic, delaying projects that are important to the country's development (*2*). However, the policies in the bill represent a setback in environmental protection and social participation in decisions that affect Brazil's rich biomes.

If enacted, the environmental licensing changes included in Bill 2159/2021 would threaten both the Brazilian Atlantic Forest and coastal ecosystems. The bill would make it easier to obtain project approvals. In some cases, corporations will be able to declare a project by simply filling out an online form and committing to uphold regulations, without meeting any requirements for an environmental impact assessment before the project begins. The bill would also limit public participation in licensing decisions, reducing the number of public hearings and making access to information difficult. States and municipalities would have more autonomy to issue licenses, even though many do not have the technical knowledge to make science-based decisions. The bill would also grant amnesty for past environmental violations by pardoning environmental liabilities of companies that undertake new commitments, undermining accountability for environmental harm.

Brazil is home to vast areas of tropical ecosystems (*3*, *4*), and the country's protected areas shelter substantial biodiversity and support traditional populations (*5*). The Atlantic Forest is a biodiversity hotspot, an ecosystem with high species diversity and many endemic species. Despite conservation and restoration efforts, the Atlantic Forest is severely threatened by deforestation and habitat loss (*4*). The provisions in Bill 2159/2021 will exacerbate environmental degradation by allowing increased human activities, including industrial and urban development, in vulnerable ecosystems and protected areas.

Instead of moving forward with the passage of Bill 2159/2021, Brazilian politicians should support conservation and restoration projects and enforce Brazil's current environmental laws. They should also support outreach efforts that encourage everyone, including citizens, scientists, and businesspeople to reconnect with nature and recognize how important Brazil's ecosystems are to the country and the world. Only a collective effort to protect Brazil's remaining tropical forests and shoreline can save them from urbanization and agricultural threats.

Emanuela W. A. Weidlich

Institute of Ecology, Leuphana University of Lüneburg, Lüneburg, Germany. Email: emanuela.ww@gmail.com

REFERENCES AND NOTES

1. Brazilian Senate, Bill 2159/2021; https://www25.senado.leg.br/web/atividade/materias/-/materia/148785.
2. Brazilian Confederation of Agriculture and Livestock (CNA), "For CNA, the Environmental Licensing Bill modernizes, reduces bureaucracy and prevents the country from losing competitiveness (Trans.)," 17 July 2025; https://www.cnabrasil.org.br/noticias/para-cna-pl-do-licenciamento-ambiental-moderniza-desburocratiza-e-evita-perda-de-competitividade-ao-pais.
3. J. Barlow *et al.*, *Nature* **559**, 517 (2018).
4. M. C. Marques, W. Trindade, A. Bohn, C. E. Grelle, in *The Atlantic Forest: History, Biodiversity, Threats and Opportunities of the Mega-diverse Forest* (Springer, 2021), pp. 3–23.
5. A. B. Rylands, K. Brandon, *Conserv. Biol.* **19**, 612 (2005).

10.1126/science.aea7981

Community support for inclusive US education

The Trump administration is working to dismantle inclusive education efforts by opposing diversity, equity, and inclusion (*1*); encouraging divisive actions in K-12 schools such as banning books (*2*) and excluding transgender children from sports (*3*); and terminating more than US$1 billion of government-funded awards granted to training programs, professional development, and research to advance inclusive STEM education (*4*, *5*). As science, technology, engineering, and mathematics (STEM) educators and researchers, we call on the administration to reverse these harmful policies. In the meantime, we urge the STEM education community and institutions to continue their efforts to make education at all levels more inclusive and equitable.

The administration's actions aim to prevent educators from addressing instructional inequities. Exclusionary and divisive educational practices create disparate outcomes and contribute to higher attrition among students from marginalized groups (*6*). By perpetuating such practices, the policies are likely to exacerbate social inequities, with negative effects on US health care, technology, and economic outcomes (*7*). These setbacks will put the country in a precarious global position.

Despite these policies, experts in education, including STEM educators, researchers, and faculty, can stay true to their values and continue to influence teaching practices (*8*) by building sustained and trusting relationships with colleagues and sharing knowledge about evidence-based teaching practices (*9*–*12*). The education community should continue to disseminate information and explain that the government's policies are not grounded in evidence. Institutions should continue to advance the mission of high-quality education by investing in ongoing efforts to improve instruction and support diverse students. University administrations can reward teaching innovation, foster instructional planning and teaching collaborations, and build networks between education experts and other faculty (*9*–*12*). Although individual and institutional efforts are most effective in conjunction with evidence-based government policies, research shows that experts in education can facilitate positive changes by leaning into community (*9*–*12*).

Emily P. Driessen and A. Kelly Lane

Department of Biological Teaching and Learning, University of Minnesota, Minneapolis, MN, USA. Email: aklane@umn.edu

REFERENCES AND NOTES

1. US Office of the President, "Ending radical and wasteful government DEI programs and preferencing" (Executive Order 14151, 20 January 2025).
2. US Office of the President, "Ending radical indoctrination in K-12 schooling" (Executive Order 14190, 29 January 2025).
3. US Office of the President, "Keeping men out of women's sports" (Executive Order 14201, 5 February 2025).
4. Grant Watch, "NIH grant terminations in 2025" (NIH, 2025); https://grant-watch.us/nih-data.html.
5. National Science Foundation, "Updates on NSF priorities" (NSF, 2025); https://www.nsf.gov/updates-on-priorities.
6. E. Seymour, A. B. Hunter, R. P. Harper, *Talking About Leaving Revisited: Persistence, Relocation, and Loss in Undergraduate STEM Education* (Springer, 2019).
7. L. E. Gomez, P. Bernet, *J. Natl. Med. Assoc.* **111**, 383 (2019).
8. E. P. Driessen, A. L. Steele, R. A. Costello, P. Brewer, C. J. Ballen, *PLOS ONE*, **19**, e0312243 (2024).
9. S. D. Bush, J. A. Rudd, M. T. Stevens, K. D. Tanner, K. S. Williams, *PLOS ONE* **11**, e0150914 (2016).
10. T. C. Andrews, E. P. Conaway, J. Zhao, E. L. Dolan, *CBE Life Sci. Educ.* **15**, ar15 (2016).
11. A. K. Lane *et al.*, *Int. J. STEM Educ.* **9**, 53 (2022).
12. A. K. Lane *et al.*, *Proc. Natl. Acad. Sci. U.S.A.* **117**, 22665 (2020).

10.1126/science.adz3963

SUBMIT NOW

NEXTGEN VOICES: NATIONAL ASSESSMENTS IN VERSE

Add your voice to *Science*! Our new NextGen Voices survey is now open: In the form of a haiku, assess the state of science in your country. What are your country's science-related strengths and weaknesses?

To submit, go to www.science.org/nextgen-voices

Deadline for submissions is 21 August. A selection of the best responses will be published in the 3 October issue of *Science*. Anonymous submissions will not be considered.

SYNTHETIC BIOLOGY

Orthogonal T7 speeds up protein evolution

Continuous evolution of proteins in the lab is often slow because normal mutation rates in bacteria are very low. Diercks *et al.* investigated whether a highly mutagenic DNA replication system could speed up evolution in *Escherichia coli* without harming the host genome. They engineered an orthogonal T7 replisome that replicates only target plasmids at mutation rates 100,000 times higher than normal while leaving the rest of the genome unchanged. Using this system, the authors rapidly evolved TEM-1 β-lactamase to gain much stronger resistance to several antibiotics in under a week. This approach could greatly accelerate protein engineering and antibiotic resistance studies. —Di Jiang *Science* p. 618, 10.1126/science.adp9583

ARCHAEOLOGY

Social inequality in ancient Central Europe

Influential models of the rise of social inequality posit that the appearance of advanced agricultural technologies such as the plow led to a rapid and sustained increase in economic inequality, the establishment of private property, and intergenerational transmission of wealth. Duffy *et al.* used mortuary evidence and house size data from more than 100 sites dating from 6000 to 1000 BCE to examine this model in the Carpathian Basin of Central Europe. They found that inequality varied remarkably little over time, and when it did increase, it was of limited duration. The authors argue that inequality was tempered by leveling mechanisms, including communal projects and community fissioning. By contrast, the rise of inequality in the Near East during the same period was more rapid and enduring. —Mark Aldenderfer

Sci. Adv. (2025) 10.1126/sciadv.adu0323

CHEMICAL PHYSICS

Fluctuations throughout the molecule

Quantum ground-state fluctuations are crucial phenomena in nature, affecting many processes, including quantum phase transitions and chemical reactions. Earlier studies on the topic only showed single fluctuating bond angles or bond distances, such as those in triatomic molecules. Richard *et al.* used the distinctive capabilities of x-ray–induced Coulomb explosion imaging to obtain accurate single-molecule data, which enabled the direct observation of collective fluctuations across all atoms in the complex polyatomic molecule 2-iodopyridine (C_5H_4NI). The presented method advances the ability to address various time-resolved chemistry experiments that present a formidable challenge for other time-resolved imaging techniques that typically rely on averaging measurements over many molecules. —Yury Suleymanov

Science p. 650, 10.1126/science.adu2637

CANCER

A sensitive accomplice in immune escape

Sensory neurons often innervate tumors. Restaino *et al.* found that these neurons cooperate with tumors to suppress antitumor immunity (see the Focus by Boyd and Borniger). Melanoma and head and neck cancer cells secreted small extracellular vesicles containing cargo that actively recruited sensory neurons, which in turn induced the differentiation and recruitment of myeloid-derived suppressor cells and enhanced tumor-induced suppression of infiltrating T cells. These findings identify an active role for sensory neurons in the tumor microenvironment in facilitating immune escape. —Leslie Ferrarelli

Sci. Signal. (2025) 10.1126/scisignal.ads7889

MAGNETIC SENSING

Flexible, strong magnetoelectric sensors

Co-crystallization between surface-functionalized ferromagnetic monolayers and a ferroelectric polymer created a mechanically strong magnetoelectric sensor for energy-efficient magnetic sensing. He *et al.* formed strong crystalline interfaces between magnetic vanadium selenide monolayers bearing carboxylate groups as a filler within poly(vinylidene fluoride). These interfaces limited polymer chain motion that would otherwise dissipate energy during use. The resulting films had a high magnetocapacitive coefficient of 23.6% and were used as a wrist-wearable sensor that had performance comparable to a standard gaussmeter. —Phil Szuromi

Science p. 623, 10.1126/science.adt2741

BIOMINERALS

The biochemistry that controls iron-hard teeth

The major lateral radula teeth of chitons are formed from magnetite and other biominerals in a way that makes them very hard and wear resistant. As the cusps wear out, they are replaced by newly formed teeth from behind. Nemoto *et al.* expanded on prior studies of these organisms by exploring the molecular mechanism of magnetite biomineralization (see the Perspective by Scheffel). The authors demonstrate that one protein, which they call radular teeth matrix protein 1 (RTMP1), controls iron oxide deposition and differs from other magnetite-precipitating proteins found in magnetotactic bacteria. —Marc S. Lavine

Science p. 637, 10.1126/science.adu0043; see also p. 568, 10.1126/science.adz8241

METALLURGY

Tracking twins in a magnesium alloy

Dark-field x-ray microscopy has revealed the three-dimensional details of deformation twinning inside an embedded grain in a bulk, polycrystalline magnesium-aluminum alloy. Lee *et al.* studied twinning in these lightweight alloys because twins can both accommodate plastic strain and serve as unwanted crack initiation sites. Under applied stress, twins appeared as irregular ellipsoid shapes. The authors studied preferential growth directions and how twinning relates to dislocation accumulation that precedes crack initiation. —Phil Szuromi

Science p. 632, 10.1126/science.adv3460

Edited by **Michael Funk**

IMMUNOLOGY

Route to averting food allergies

Cysteinyl leukotrienes (CysLTs) are inflammatory mediators implicated in allergic responses, particularly asthma. Two studies examined the role of CysLTs in the development of anaphylaxis in response to ingested food allergens in mice. Hoyt *et al*. found that CysLTs promoted the transport of intact food allergens from the gut lumen into the tissue. Mice that did not experience anaphylaxis had variants of DPEP1, an enzyme that metabolizes CysLTs, linked to augmented enzymatic activity. Batchel *et al*. found that when cells from the hematopoietic compartment could not synthesize CysLTs, mice had attenuated responses to ingested allergens. Mast cells within the intestinal epithelium could synthesize and respond to CysLTs. In both studies, blocking the synthesis of CysLTs using the drug zileuton before or concurrent with food-allergen exposure prevented the symptoms associated with anaphylaxis in mice (see the Perspective by Haque and Kaplan). —Sarah H. Ross

Science p. 614, 10.1126/science.adp0240, p. 613, 10.1126/science.adp0246; see also p. 573, 10.1126/science.adz6439

CELL BIOLOGY

Remodeling the neuronal skeleton

The cytoskeleton provides mechanical support to the cell while also enabling cells to remodel themselves in response to their environment. The membrane-associated periodic skeleton (MPS) is a component of the neuronal cytoskeleton mostly found in axons. Heller *et al*. investigated the dynamics of MPS using live-cell super-resolution imaging. The authors discovered that MPS is remarkably dynamic, undergoing repeated cycles of disassembly and reformation over much of the axon's length. Mechanistically, MPS remodeling is regulated by calcium ions and involves actin stabilization, calpain-dependent proteolysis, and protein kinase C–mediated adducin phosphorylation. These results provide valuable insights for understanding how cells carry out their most fundamental activities. —Mattia Maroso

Science p. 615, 10.1126/science.adn6712

DISEASE GENOMICS

A noncoding diagnosis

Despite recent advances in human genetics and genomics and the increasing accessibility of genome sequencing, most patients with genetic disorders still do not have a molecular diagnosis. In many cases, this is likely due to diseases being caused by noncoding genetic variants, which can alter gene expression but are not as well understood as mutations in the coding sequence itself. To detect such disease-causing variants in gene promoters, Jaganathan *et al*. developed a deep neural network called PromoterAI to specifically identify promoter variants that change gene expression and demonstrated its ability to find genetic diagnoses for patients with rare diseases. —Yevgeniya Nusinovich

Science p. 616, 10.1126/science.ads7373

NEUROSCIENCE

Targeting for safety

Immunotherapies for Alzheimer's disease (AD) hold promise for slowing or reversing the progression of the disease. However, they are associated with the development of amyloid-related imaging abnormalities (ARIAs), thus raising important safety concerns. Pizzo *et al*. developed an antibody transport vehicle targeting the transferrin receptor for brain delivery of amyloid-β antibodies that significantly reduced ARIA-like lesions and improved plaque target engagement in a mouse model of amyloid deposition. The approach works by improving biodistribution across the blood-brain barrier (see the Perspective by Xing and Song) and has the potential to improve the safety and efficacy of immunotherapies for AD. —Mattia Maroso

Science p. 617, 10.1126/science.ads3204; see also p. 571, 10.1126/science.adz8959

OPTOELECTRONICS

Single-photon detection in moiré superlattices

The ability to detect single photons is key to many areas of research, including quantum technologies, astronomy, and spectroscopy. Present state-of-the-art detectors typically operate at ultralow temperatures (below 1 kelvin) and are limited to visible wavelengths. Nowakowski *et al*. designed a single-photon detector based on moiré superlattice structures comprising graphene and hexagonal boron nitride heterostructures (see the Perspective by Bandurin). Tuning the electronic bands by twisting the layers relative to each other extends the sensitivity to longer wavelengths (above 11 micrometers), and the system is operable at relatively high temperatures (20 kelvin). Because it is compatible with complementary metal-oxide-semiconductor processing, this approach can be incorporated into integrated photonic circuits. —Ian S. Osborne

Science p. 644, 10.1126/science.adu5329; see also p. 570, 10.1126/science.aea5235

KIDNEY DISEASE

Cellular senescence and loss of Y

Hematopoietic loss of Y chromosome (LOY) is associated with diseases of aging, but the role of cellular senescence downstream of LOY is unclear, especially in kidney disease. Arai *et al*. found that LOY was increased in in patients with kidney disease and associated with cellular senescence. Renal dysfunction and cellular senescence were accelerated in older male mice that had bone marrow with Y chromosome deletions. Senolytic treatment prevented disease progression in this mouse model, and treatment with antibodies targeting programmed cell death protein 1 (PD-1) and signal regulatory protein α (SIRPα) reduced senescence and rescued injured renal pathology. These data show that hematopoietic LOY acts through immune regulators to impair clearance of senescent cells in models of kidney disease. —Brandon Berry

Sci. Transl. Med. (2025) 10.1126/scitranslmed.adv4071

DENDRITIC CELLS

GM-CSF nurtures lung dendritic cells

Conventional dendritic cells (cDCs) are composed of cDC1 and cDC2 subsets, but the specific factors controlling their differentiation and function in the lungs are not well defined. Using genetically engineered mice, Gschwend *et al.* found that the cytokine granulocyte-macrophage colony-stimulating factor (GM-CSF) is required for the development of a subset of pulmonary cDC2s expressing the C-type lectin CD301b. Despite localizing to lymphocyte-rich adventitial cuffs, CD301b$^+$ cDC2s required GM-CSF derived from alveolar epithelial type 2 cells for their development and to generate airway inflammation in response to house dust mite allergen. These findings identify GM-CSF as a key regulator of cDCs and type 2 immune responses in the lungs. —Claire Olingy

Sci. Immunol. (2025) 10.1126/scitranslmed.adt0688

Check for

IN OTHER JOURNALS

Edited by **Corinne Simonti** and **Jesse Smith**

ANIMAL BEHAVIOR

Amazonian allies



Positive or neutral interactions between individuals from different species have been identified across taxa, from dolphins and whales to coyotes and badgers. In almost all cases of animal "friendships," we don't know why the two have come together, although hypotheses include increasing foraging opportunities or protection. Adding to this list, Camerlenghi *et al*. serendipitously captured an interaction between a common opossum and an ocelot, species that are often prey and predator. Contact with other researchers revealed three other independent camera-trap events in the Peruvian Amazon. Experiments showed that opossums are attracted to ocelot scent, further suggesting intentional pairing. Increasing examples of such relationships suggest that these pairings are not as rare as we thought and may be a window into the complex lives of animals. —Sacha Vignieri *Ecosphere* (2025) 10.1002/ecs2.70322

Multiple instances of ocelots and opossums traveling together have been documented in the Amazon.

PHOTOS: CAMERLENGHI *ET AL.*

SIGNAL TRANSDUCTION

Forcing tooth development

Mechanical forces provide important information cues during development, which are sometimes interpreted directly by responsive cells. Meng *et al.* describe an alternative system in which communication between neurons and mesenchymal cells regulates the force-dependent growth of molars in postnatal mice. As tooth roots grow, they apply pressure on mechanosensory neurons expressing Piezo2 ion channels. Channel activation causes calcium-dependent secretion of platelet-derived growth factor A from the neurons, which in turn acts on the dental mesenchyme to promote further tooth root development. Such neuronal mechanotransduction circuits could be potential targets for therapeutic interventions to promote tissue regeneration. —L. Bryan Ray

Proc. Natl. Acad. Sci. U.S.A. (2025) 10.1073/pnas.2504103122

CANCER

NOD2 mutations and immunotherapy

Cancer immunotherapy can be highly successful for certain patients, but many tumors do not respond. Barnet *et al.* examined genome-sequencing data from patients with metastatic non-small-cell lung cancer who received single-agent anti–PD-1 immunotherapy. Inherited loss-of-function (LOF) mutations in the gene *NOD2*, which functions in immune and inflammatory responses, were present in 30% of patients classified as "exceptional immune responders." By contrast, inherited gain-of-function mutations in the gene *RIPK2*, which enhances NOD2 signaling, were found in 61% of nonresponding patients. Individuals who experienced immune-related adverse events had better overall survival, which was further improved if they harbored *NOD2* LOF mutations. *NOD2* genotyping may therefore help to identify patients who may respond to anti–PD-1 monotherapy. —Priscilla N. Kelly

Proc. Natl. Acad. Sci. U.S.A. (2025) 10.1073/pnas.2314258122

ENVIRONMENTAL POLICY

Overly lenient pollution policy

Most US air pollution regulations are inefficient and could be much more stringent. Shapiro and Walker analyzed thousands of transactions from 40 markets encompassing 60% of US economic activity, in which industrial plants entering a region were required under the Clean Air Act to offset their pollution by paying incumbents in that region to reduce their own pollution. Under efficient policy, the marginal benefits to society from reducing pollution should be greater than or equal to the price of pollution offsets. The authors found that for most regions and pollutants, the marginal benefits were more than 10 times the mean offset price, indicating that existing policies generally are too lenient. —Brad Wible

Am. Econ. Rev. (2025) https://www.aeaweb.org/articles?id=10.1257/aer.20230761



Scrubbed emissions from the DTE Energy coal-fired power plant in Monroe, Michigan

NEUROSCIENCE

How to suppress unwanted actions

The substantia nigra pars reticulata (SNr) is an important structure of the basal ganglia that helps to select desired actions while suppressing unwanted ones. Yoshida and Hikosaka investigated how individual SNr neurons in primates modulate activity to facilitate or inhibit actions, and whether input from glutamatergic neurons provides the causal drive for the suppressive processes. The authors recorded from macaque SNr neurons during a sequential choice task in which the monkeys either selected or rejected a presented target. Neurons decreased firing rates for desirable targets and increased those for undesirable ones. Blockade of glutamatergic projections to the SNr altered reaction times and rejection behaviors. These results indicate a contributory role for excitatory inputs in behavioral inhibition and further our understanding of SNr function. —Peter Stern

Proc. Natl. Acad. Sci. U.S.A. (2025) 10.1073/pnas.2427032122

PHOTOCATALYSTS

Harmful emissions into clean fuel

Alcohol fuels such as ethanol can potentially be produced by reducing carbon dioxide using solar energy. However, poor production efficiency and selectivity have limited the widespread adoption of this approach. Guo *et al.* developed a cost-effective heterogeneous catalyst made of well-dispersed Cu_4 clusters and Cu single atoms on a carbon nitride substrate. The relative density of Cu_4 clusters was tuned by adjusting the initial Cu precursor concentration. Through comprehensive experimental characterization and theoretical calculations, the authors showed that *CO can form on both Cu_4 clusters and Cu single-atom sites. However, the C–C coupling step, which is critical for efficient alcohol production, requires strong synergy between the two sites. —Jack Huang

Angew. Chem. Int. Ed. (2025) 10.1002/anie.202423666

ATMOSPHERIC METHANE

A growing influence

The atmospheric concentration of methane, the second most important greenhouse gas after carbon dioxide, increased markedly during the year 2020. Potential causes for this increase include greater wetland methane emissions or lower atmospheric OH abundance due to lower nitrogen oxide emissions during the COVID-related slowdown. Now, Yoon *et al.* suggest another possible reason: anomalously high atmospheric isoprene abundances. Isoprene oxidation reduces the amount of OH in the atmosphere, in turn leading to lower rates of methane destruction and thus higher methane concentrations, illustrating another way that the biosphere could have affected the methane budget that year. —Jesse Smith

Geophys. Res. Lett. (2025) 10.1029/2025GL114712

Check for

RESEARCH ARTICLE SUMMARY

CELL BIOLOGY

The membrane skeleton is constitutively remodeled in neurons by calcium signaling

Evan Heller†, Naina Kurup†‡, Xiaowei Zhuang*

Full article and list of author affiliations: https://doi.org/10.1126/science.adn6712

INTRODUCTION: Super-resolution imaging has revealed that the membrane skeleton in neurons adopts a periodic structure in which actin filaments form evenly spaced rings around the circumference of neurites, with adjacent rings connected by spectrin tetramers. Termed the membrane-associated periodic skeleton (MPS), this highly organized network is present in diverse neuronal cell types and conserved across animal species. It plays an important role in a variety of neuronal functions, from serving as a signaling platform to providing mechanical support for axons.

RATIONALE: An important question about the MPS is whether it is dynamic and if so, whether its dynamics are important for neuronal functions. Cytoskeletal structures exhibit an interesting dichotomy between stability and plasticity, balancing the demands of performing long-lasting functions such as mechanical support with the capacity to remodel to meet the changing needs of the cell. For example, actin, intermediate filaments, and microtubules form elaborate and persistent structures that are nevertheless subject to constant remodeling.

In certain circumstances involving strong external stimuli, the MPS can be actively degraded, such as in response to G-protein coupled receptor (GPCR) activation, during axon degeneration, and in response to stimulation of synaptic activity. Although these observations suggest that the MPS has a capacity to remodel in specific circumstances, it has generally been considered a stable structure.

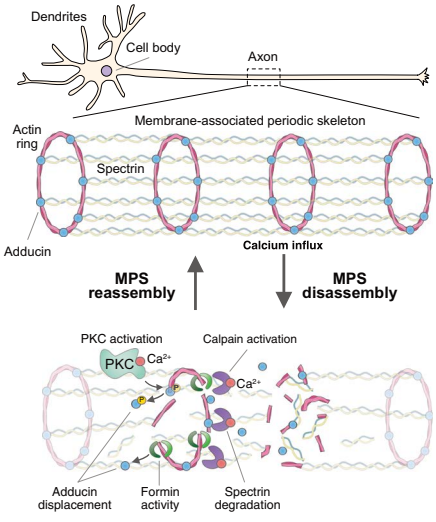
RESULTS: We used live-cell structured illumination microscopy (SIM) to explore the dynamics of the MPS and how these dynamics contribute to essential functions of the neuron. We discovered that the MPS exhibits widespread dynamics in which regions undergo cycles of disassembly and reassembly even in the absence of external stimulation. To determine what drives these dynamics, we investigated multiple intracellular pathways and found that MPS remodeling is driven by a cascade of enzymatic processes activated by calcium signaling.

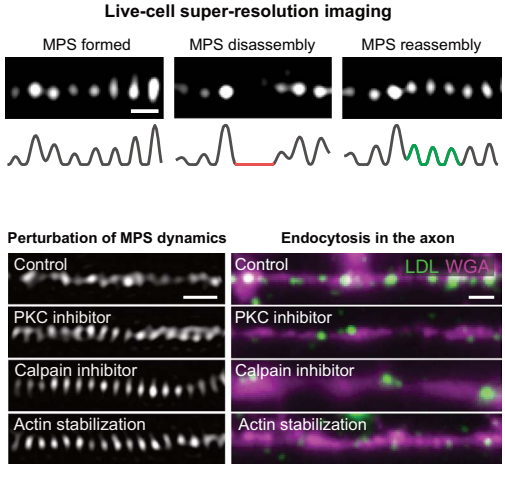
In particular, Ca^{2+} influx activates the protein kinase C (PKC), leading to phosphorylation of the actin-capping protein, adducin, which in turn destabilizes the actin rings and promotes disassembly of the MPS. In addition, Ca^{2+} activates the protease, calpain, which degrades spectrin. Formins, regulators of actin polymerization, also contribute to these dynamics, potentially by displacing adducin from actin rings, leading to MPS destabilization. These dynamics are enhanced by neuronal activity, and functionally we found that MPS dynamics promote endocytosis in the axon. These results suggest that the presence of the MPS could inhibit cellular processes that require membrane access or deformation and must be temporarily and locally removed to facilitate these processes without compromising the ability of the MPS to perform other functions.

CONCLUSION: Our results have uncovered dynamics of the MPS that involve the repeated local disassembly and rebuilding of an apparently stable scaffold. MPS dynamics are driven by Ca^{2+} signaling, triggering a cascade of events involving multiple pathways. These dynamics facilitate endocytosis and likely other functions that require membrane access or deformation. MPS dynamics could also regulate signaling at the membrane by adjusting the availability of membrane receptors. A full understanding of the interplay between MPS remodeling and neuronal activity remains an open question. □

*Corresponding author. Email: zhuang@chemistry.harvard.edu (X.Z.) †These authors contributed equally to this work. ‡Present address: Ginkgo Bioworks, Boston, MA, USA. Cite this article as E. Heller *et al.*, *Science* 389, eadn6712 (2025). DOI: 10.1126/science.adn6712

The MPS undergoes constitutive dynamics in neurons. The MPS undergoes repeated cycles of local disassembly and reassembly. These dynamics are driven by Ca^{2+} influx, activating the protein kinase C, which phosphorylates adducin and destabilizes the actin ring, and the calpain protease, which degrades spectrin. These events in turn cause the degradation of the MPS. Functionally, MPS dynamics enhance endocytosis in neurons.





CELL BIOLOGY

The membrane skeleton is constitutively remodeled in neurons by calcium signaling

Evan Heller[1,2,3]†, Naina Kurup[1,2,3]†‡, Xiaowei Zhuang[1,2,3]*

The membrane skeleton in neurons adopts a periodic lattice structure in which actin filaments, capped by adducin and tropomodulin, form ring-shaped structures connected by spectrin tetramers along neurites. This membrane-associated periodic skeleton (MPS) is important for many neuronal functions. Using live-cell super-resolution imaging, we found that the MPS is surprisingly dynamic, undergoing local disassembly and reformation constitutively in axons. MPS remodeling is driven by calcium signaling, leading to actin-ring destabilization through protein kinase C–mediated adducin phosphorylation and to spectrin degradation by calpain. Formin, an actin-nucleating and -polymerizing enzyme, plays a dual role in MPS remodeling and maintenance. MPS remodeling is enhanced by neuronal activity and functionally facilitates endocytosis. Our results highlight the importance of a dynamic membrane skeletal structure in neuronal function.

The cytoskeleton plays an important role in a variety of cellular functions, from mechanical support for cells and intracellular cargo transport to mitosis of replicating cells and synaptic plasticity in neurons. In performing these functions, the cytoskeleton exhibits an interesting dichotomy in that it forms a rich and elaborate array of persistent structures out of filaments that are dynamic (*1*, *2*). For example, actin filaments in the cell cortex form a network that confers mechanical support and maintains cell shape (*3*) while the network of intermediate filaments provides cells with additional strength and stiffness (*4*). Actin, intermediate filaments, and microtubules also help to shape and position intracellular organelles (*4*–*5*), and actin and microtubules additionally form molecular tracks for intracellular cargo transport by motor proteins (*2*). The stability of these cytoskeletal structures, however, is counterbalanced by dynamics, as even apparently long-lived networks are remodeled over time to meet the changing needs of the cell. This dichotomy between stability and plasticity is particularly important in the case of neurons, which must survive the entire lifespan of the animal and maintain long-term stability of neural networks (*6*) while simultaneously allowing local remodeling of neurites and synapses, which enables learning and adaptation (*7*, *8*).

In neurons, super-resolution imaging has revealed a quasi-one-dimensional, periodic submembrane cytoskeletal structure termed the membrane-associated periodic skeleton (MPS) (*9*). In this structure, actin filaments, capped by adducin and tropomodulin, form ring-shaped structures that are evenly spaced at ~180 to 190 nm intervals by spectrin tetramers along axons and some dendrites (*9*–*15*). The abundance of actin-capping proteins in the ring (*9*, *15*) suggests that it may consist of multiple short, capped actin filaments, analogous to the short actin filaments present in the erythrocyte membrane skeleton, whereas an electron microscopy (EM) study suggests the possibility that the actin ring is made of a pair of long, intertwined filaments (*16*).

[1]Howard Hughes Medical Institute, Harvard University, Cambridge, MA, USA. [2]Department of Chemistry and Chemical Biology, Harvard University, Cambridge, MA, USA. [3]Department of Physics, Harvard University, Cambridge, MA, USA. ***Corresponding author. Email: zhuang@chemistry.harvard.edu (X.Z.)** †These authors contributed equally to this work. ‡Present address: Ginkgo Bioworks, Boston, MA, USA.

The MPS is present in diverse neuronal cell types (*17*, *18*) and is conserved across animal species (*18*). It plays a critical role in a variety of functions in neurons, including organizing membrane proteins (*9*, *19*–*23*), signal transduction (*23*), mechanosensation (*24*), tension buffering (*25*), axon degeneration (*26*, *27*), axon-diameter control (*15*, *28*, *29*), and neurite-neurite interactions (*15*, *22*). Genetic perturbation of the MPS in mice causes a range of neurological impairments (*30*, *31*) and hereditary mutations of MPS components in humans are associated with neurological diseases (*32*, *33*).

Unlike other cytoskeletal structures, the dynamic properties of the MPS remain largely unexplored. In some specific functions, the MPS is actively degraded in response to an external stimulus. For example, when functioning as a signaling platform to enable G-protein coupled receptor (GPCR)- or cell-adhesion molecule (CAM)-mediated signal transduction in neurons, the MPS is actively degraded by calpain upon stimulation of GPCRs and CAMs, and such degradation modulates signaling strength (*23*). The MPS is also degraded upon trophic deprivation–induced axon degeneration (*26*, *27*). In addition, F-actin can be remodeled from actin rings in the MPS into longitudinal fibers in dendrites in response to synaptic activity stimulation (*34*). Neuronal activity stimulation can also cause an increase in longitudinal actin fibers in axons, with a modest reduction in actin ring periodicity, in the axon initial segment (*35*). Although these observations are limited to specific circumstances involving the application of strong external stimuli, they suggest that the MPS has a capacity to remodel.

However, the MPS is generally considered to be a stable structure. The MPS is thought to provide the mechanical support required to maintain axon integrity during animal movement (*9*, *36*). The role of the MPS as a scaffold for proper localization of functionally important membrane proteins (*9*, *19*–*23*) similarly suggests a need for stability. Experimental evidence to date also suggests MPS stability; previous fluorescence recovery after photobleaching experiments have shown slow turnover of MPS components (*10*, *37*, *38*) and the MPS exhibits a high resistance to actin depolymerizing drugs (*9*, *10*, *39*). Because of the challenges associated with visualizing the MPS in live neurons, live-cell MPS imaging studies are relatively rare (*10*, *28*, *40*) and real-time live imaging to date has only revealed radial expansion and contraction of the MPS to accommodate large cargoes passing through axons (*28*). The dynamics of MPS therefore remain largely unknown.

The MPS is dynamic and undergoes constitutive disassembly and reassembly

To study the dynamic properties of the MPS in live neurons, we generated a Cre-inducible knock-in of mNeonGreen in the C-terminus of mouse βII-spectrin (spectrin-mNeonGreen, Fig. 1A) and used it to image the MPS in cultured hippocampal neurons at 14 to 16 days in vitro (DIV) using lattice structured illumination microscopy (SIM) (*41*). We observed that the MPS was highly dynamic and exhibited repeated cycles of disassembly and reassembly even under unstimulated conditions (Fig. 1, B to E, and movie S1).

We performed SIM imaging across several different timescales with different time resolutions. Most of our experiments were carried out using a time resolution of 15 sec with a total imaging duration of 225 sec (~4 min). At this timescale, the MPS appeared dynamic along much of the length of axons, where stretches of the MPS are disassembled and reassembled, often over multiple cycles (Fig 1B). We observed similar dynamics for other structural components of the MPS by imaging neurons expressing green fluorescent protein (GFP)-tagged adducin or F-actin labeled with silicon rhodamine (a dye named SiR-actin) (*40*) (fig. S1). We confirmed that the observed cycles of disappearance and reappearance of the MPS signal were not due to local movements of the axon or bulk flow of the membrane by co-imaging with the membrane marker CellBrite, which showed that axons stayed in focus as the MPS disassembled (Fig. 1C and fig. S2).

We also performed SIM imaging of spectrin-mNeonGreen at a faster time resolution of 1 sec. However, photobleaching limited our acquisition

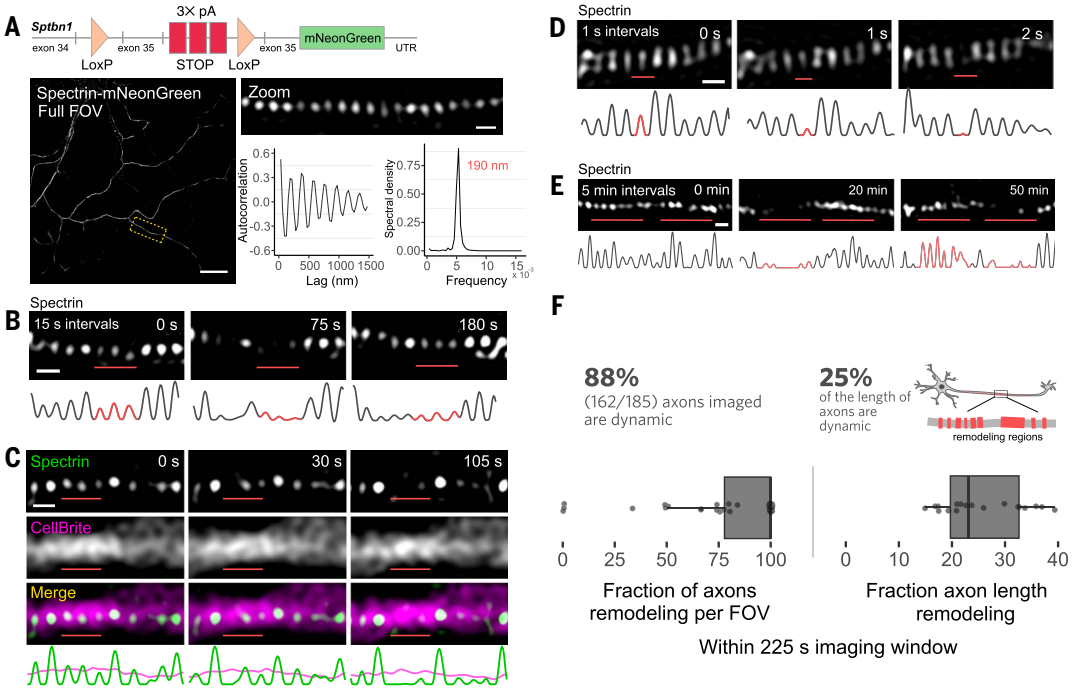


Fig. 1. The MPS undergoes constitutive remodeling. (**A**) Characterization of MPS dynamics in the βII-spectrin mNeonGreen conditional knock-in mouse by live-cell SIM imaging. (Top) Schematic of the conditional knock-in construct, which expresses a βII-spectrin-mNeonGreen fusion protein in the presence of *Cre*. (Bottom) SIM image of a DIV 15 neuron expressing specrin-mNeonGreen. (Left) Full field of view (FOV). (Top right) Zoom-in of boxed region on the left. (Bottom right) Autocorrelation function of the spectrin-mNeonGreen signal along the axons (left, averaged over 45 axonal regions) and spectral density analysis of the autocorrelation function (right) showing a periodic distribution of βII-spectrin with ~190-nm spacing along the axon. (**B**) Example MPS remodeling (disassembly and reassembly) from live-cell SIM imaging at a 15-sec time resolution over a 225-sec imaging duration, with intensity traces shown below. Remodeling regions are highlighted in red. (**C**) Live-cell two-color SIM imaging of the MPS (top) and the membrane dye CellBrite Steady (middle), with composite images and intensity traces (green, βII-spectrin; magenta, CellBrite) shown below. (**D** and **E**) Same as in (B), but for MPS remodeling events from SIM images acquired at 1-sec (D) and 5-min (E) time resolution. Full sequence of the images taken at 5-min resolution is shown in fig. S3A. (**F**) (Left) Fraction of axons per FOV exhibiting MPS remodeling during a standardized 225-sec imaging window. (Right) Fraction of axon length undergoing MPS remodeling during the 225-sec imaging window. In all figures, elements in statistical quantification plots, including boxplot elements and error bars, are defined in the statistics section of the Materials and Methods. Statistics for (F) are shown in table S2. Scale bars: 10 μm (A); 250 nm [(B) to (E), zoom-ins of (A)].

to ~20 total timepoints in SIM imaging. At this timescale, we observed disappearance (or substantial reduction in intensity) and reappearance of individual MPS rings (Fig. 1D), although such events were infrequent, with relatively few events observed as a result of the short 20-sec imaging duration. At the other end of the spectrum, to gain insight into the extent of MPS remodeling over longer timescales, we increased the imaging duration to 1 hour by reducing the time resolution to 5 min. In this regime, we observed more substantial examples of MPS remodeling, in which long stretches of MPS disappeared and reappeared (Fig. 1E and fig. S3) but individual transitions were often not well-resolved as a result of the low time resolution.

Overall, the 15-sec time resolution provided a good balance between resolving individual MPS transitions and capturing a sufficient number of transitions to quantify the prevalence of remodeling. Our quantifications showed that MPS remodeling occurred in > 80% of all axons observed and covered 20 to 30% of the length of axons during the ~4-min imaging window (Fig. 1F and fig. S1, C and F). At any given time, only a small fraction of the MPS underwent remodeling, often exhibiting repeated cycles of local disappearance and reappearance, suggesting that regions of the MPS transition from a relatively long-lived static state to a short-lived labile state in which it undergoes cycles of degradation and reformation. MPS remodeling primarily occurred in the medial and distal regions of axons and rarely in regions proximal to the cell body (fig. S4A). When we co-labeled synaptic sites during live cell imaging of the MPS, we found that most of the observed remodeling events occurred outside of synapses, but the percentage of axonal length exhibiting remodeling appeared to be comparable both within and outside of synaptic sites (fig. S4, B to D).

The fact that we observed similar remodeling not only with fluorescent fusion proteins of βII-spectrin and adducin, but also with the small-molecule F-actin-binding dye SiR-actin, suggests that such dynamics are unlikely to be caused by the fluorescent reporters. Moreover, our observations of constitutive MPS remodeling suggest that, in a snapshot, a small fraction of the MPS should exhibit imperfections arising from the dynamics, which should be visible in fixed-cell immunofluorescence images that are free from potential perturbation by fluorescent reporters in live cells. Indeed, super-resolution stochastic optical reconstruction microscopy (STORM) images of fixed neurons showed that ~30% of axonal length was covered by imperfect MPS (fig. S5), consistent with our live-cell imaging results. Because mNeonGreen labeling of endogenous spectrin allows uniform labeling and clear visualization of the MPS without being masked by other actin structures or potential artifacts caused by overexpression of MPS components and thus offering a convenient and robust way to observe MPS remodeling, we used this labeling scheme for quantitative and mechanistic characterizations of MPS dynamics below.

Calcium signaling drives MPS remodeling

Next, we investigated the mechanisms underlying MPS remodeling. Because many different processes could contribute to MPS remodeling, we first used conventional diffraction-limited imaging, which has a higher throughput than super-resolution imaging, to perform an initial

screen. Although mNeonGreen fluorescence was largely uniform in these conventional images because the periodic spacing of the MPS (~180 to 190 nm) is below the diffraction limit, we reasoned that when stretches of the MPS disassemble and reassemble, we should observe the disappearance and reappearance of the spectrin signal in segments of the axons. Using this approach, we could more rapidly screen perturbations that potentially affect MPS dynamics, which could then be validated by super-resolution imaging.

As expected, diffraction-limited imaging showed disappearance (or substantial reduction in intensity) and reappearance of the spectrin-mNeonGreen signal in stretches of axons in cultured hippocampal neurons (fig. S6A). To quantify these dynamics, we computed the autocorrelation function of the fluorescent signal over time in time-lapse diffraction-limited images of axons (Fig. 2A and fig. S6B). The amplitude of this autocorrelation function measures the extent to which the fluorescence signal changes and hence reflects the prevalence of MPS remodeling; the more prevalent the remodeling, the higher the autocorrelation amplitude. As controls, we transduced neurons with a cytoplasmic GFP or labeled the neuronal membrane with CellBrite. In both cases, the autocorrelation amplitude was substantially smaller than that observed for spectrin-mNeonGreen (fig. S6B), in which the small residual fluctuations could be due to small movements of the axon or the flow of proteins and lipids (*42*).

Using this approach, we screened several intracellular processes that are potentially linked to spectrin, actin, and membrane remodeling using pharmacological inhibitors and activators. These processes include (i) clathrin-dependent and -independent endocytosis, which may remodel or perturb membrane structures; (ii) microtubules, which could interact with the MPS (*39*), and microtubule-dependent transport—particularly the dynein–dynactin-driven microtubule transport, in which spectrin plays a pivotal role (*43*); (iii) myosin-II, which has been shown to be associated with actin filaments in the MPS (*15, 28, 29*); (iv) calcium signaling, which can regulate cytoskeletal modeling and spectrin degradation (*44*); and (v) actin polymerization and depolymerization, which can affect the integrity of the MPS (*9, 10*).

Our screen showed that inhibitors of endocytosis (PitStop and dynasore), dynein-dependent transport on microtubules (dynarrestin), the actin-dependent motor myosin-II [blebbistatin (Bleb)] and its upstream regulator, ROCK (Y-27632), as well as a microtubule depolymerizing drug [nocodazole (Noco)], did not have substantial effects on spectrin dynamics, as reflected by the autocorrelation amplitude of the spectrin signal (Fig. 2B). By contrast, perturbation of intracellular Ca^{2+} concentration and actin stability had a strong effect on spectrin dynamics. Reducing intracellular Ca^{2+} concentration with the Ca^{2+} chelator, BAPTA, substantially reduced spectrin dynamics (Fig. 2B). Concordantly, increasing intracellular Ca^{2+} concentration using the photo-uncaging of a cell-permeable caged Ca^{2+} compound, NP-EGTA (*45*), markedly increased spectrin dynamics (Fig. 2B). In addition, spectrin dynamics were substantially reduced by jasplakinolide (Jasp), a drug that stabilizes actin filaments, suggesting that actin polymerization/depolymerization also play a role in MPS dynamics.

Although diffraction-limited imaging is efficient in screening a large number of potential candidate factors, direct observation of the structure and dynamics of the MPS requires super-resolution imaging. Having uncovered intracellular Ca^{2+} as a potential regulator of MPS dynamics, we therefore returned to live-cell SIM imaging of the MPS, using spectrin-mNeonGreen as a marker, to directly probe and quantify the effects of these perturbations. Compared with control samples treated with

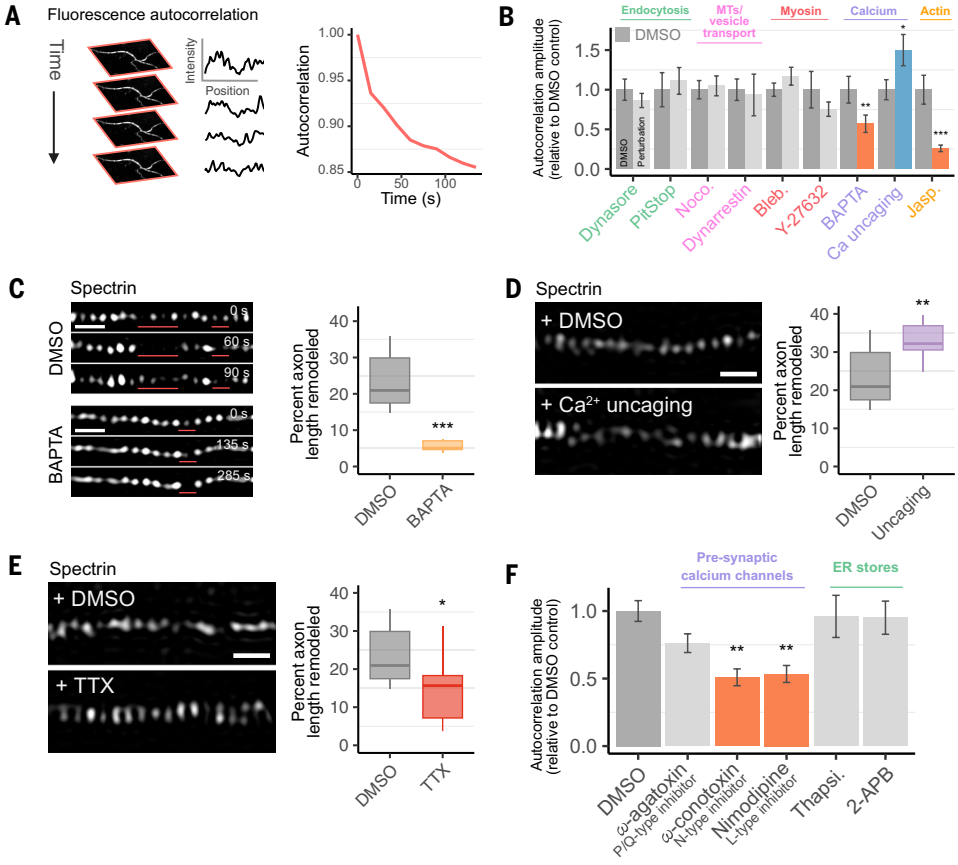


Fig. 2. Calcium signaling drives MPS remodeling. (**A**) Schematic of fluorescence autocorrelation analysis used to quantify spectrin dynamics in diffraction-limited imaging. (Left) Spectrin-GFP intensity changes along the axon in consecutive frames of imaging. (Right) For each axon, intensity changes as a function of time are quantified by an autocorrelation function, whose amplitude reflects the prevalence of remodeling. (**B**) Screen of potential regulators of MPS remodeling using diffraction-limited imaging. Average autocorrelation amplitudes normalized to the DMSO control are plotted. (**C**) (Left) Snapshots from representative live SIM imaging of spectrin-mNeonGreen in axons treated with 10 μM of the Ca^{2+} chelator, BAPTA, or DMSO control 30 min prior to imaging. Remodeling regions are indicated with red lines. (Right) Fraction of axon length exhibiting MPS remodeling over the 225-sec imaging window. Experiments in (C) to (E) were performed together with a shared DMSO control. (**D**) (Left) Representative snapshots of spectrin-mNeonGreen in axons treated with 10 μM caged Ca^{2+} (NP-EGTA, lower panel) or DMSO. Continuous low-intensity 405-nm illumination was used to induce Ca^{2+} uncaging at a relatively low degree. (Right) Fraction of axonal length exhibiting MPS remodeling. (**E**) (Left) Representative snapshots of spectrin-mNeonGreen in axons treated with 1 μM TTX to silence neuronal activity or DMSO control 30 min prior to imaging. (Right) Fraction of axonal length exhibiting MPS remodeling. (**F**) Measurement of MPS dynamics in diffraction-limited imaging of spectrin-mNeonGreen expressing neurons treated with inhibitors of P/Q-type Ca^{2+} channels (ω-agatoxin IVA), N-type Ca^{2+} channels (ω-conotoxin), and L-type Ca^{2+} channels (nimodipine), as well as inhibitors of Ca^{2+} uptake [thapsigargin (Thapsi)] or Ca^{2+} release (2-APB) from ER stores. Average autocorrelation amplitudes normalized to DMSO control are plotted. Statistics for (B) to (F) are shown in table S2. Scale bars in (C) to (E), 500 nm.

dimethyl sulfoxide (DMSO), treatment of neurons with the Ca^{2+} chelator BAPTA considerably reduced the prevalence of MPS remodeling, quantified as the fraction of axon length exhibiting MPS disassembly and reassembly over the course of our 225-sec imaging window (Fig. 2C). Concordantly, continuous low-level uncaging of Ca^{2+} increased the prevalence of MPS remodeling (Fig. 2D). Both results are in agreement with our screen using diffraction-limited imaging.

Neuronal activity promotes MPS dynamics

Because action potentials generated by neuronal activity are a primary driving force for Ca^{2+} influx in neurons, we next used tetrodotoxin (TTX) to block action potentials and tested the effect of this drug on MPS remodeling. With TTX treatment, we observed a reduction in the prevalence of MPS remodeling (Fig. 2E), but not at the magnitude of direct chelation of intracellular Ca^{2+} by BAPTA (Fig. 2C), suggesting that neuronal activity can promote MPS remodeling, but is not the sole factor driving it.

The means by which TTX influences MPS remodeling is likely through the inhibition of intracellular Ca^{2+} spiking activity associated with action potentials. However, because the magnitude of the TTX effect was substantially lower than that of Ca^{2+} chelation by BAPTA, other sources of Ca^{2+} activity must also play a role in MPS remodeling. Indeed, when we imaged Ca^{2+} spiking in neurons using the Ca^{2+} indicator dye (Cal-520), both TTX and BAPTA abolished transient Ca^{2+} spikes (fig. S7A). However, Ca^{2+} chelation with BAPTA also led to a sustained reduction in resting Ca^{2+} concentration in the neurons, whereas TTX did not affect resting Ca^{2+} concentration (fig. S7B).

To further explore the sources of the Ca^{2+} influx that contribute to MPS remodeling, we measured spectrin dynamics in the presence of various toxins that inhibit voltage-gated Ca^{2+} channels or affect the uptake and release of Ca^{2+} from local ER stores. We found that inhibition of N-type Ca^{2+} channels (by ω-conotoxin) and L-type Ca^{2+} channels (by nimodipine) both led to a reduction in spectrin dynamics (Fig. 2F and fig. S7). Perturbing ER calcium stores (inhibiting Ca^{2+} uptake into the ER with thapsigargin or Ca^{2+} release from the ER with 2-APB), by contrast, had little effect on MPS dynamics (Fig. 2F). These results suggest that Ca^{2+} influx through voltage-gated Ca^{2+} channels, encompassing both action potential–induced depolarization and subthreshold depolarization from spontaneous synaptic activity, are likely sources of Ca^{2+} driving MPS dynamics. However, other sources of local Ca^{2+} likely also contribute to MPS dynamics. We also observed that Ca^{2+} channels exhibited colocalization with the MPS (fig. S8), which could potentially facilitate the rapid effect of Ca^{2+} influx on MPS remodeling.

MPS dynamics is promoted by multiple Ca^{2+}-dependent enzymatic processes

The results described above indicate that Ca^{2+} plays a primary role in MPS dynamics. We next investigated the potential molecular mechanisms underlying Ca^{2+}-driven MPS remodeling. To this end, we first used diffraction-limited imaging to screen the effects of several calcium-dependent enzymes that can potentially act on MPS components (Fig. 3A). These include (i) calpain, a Ca^{2+}-dependent protease that can cleave spectrin and actin (*46*); (ii) protein kinase C (PKC), a Ca^{2+}-dependent kinase that can phosphorylate adducin (*47, 48*); and (iii) calmodulin (CaM), the Ca^{2+}-bound form of which interacts with Ca^{2+}/CaM-dependent protein kinase II (CaMKII) (*49*), which is associated with the MPS (*15*). Spectrin and adducin also contain CaM-binding domains that regulate the stability of actin-spectrin complexes (*50*–*52*). We found that inhibition of PKC using GF 109203X (GFX) and inhibition of calpain using MDL 28170 (MDL), calpastatin, or calpain inhibitor II strongly reduced spectrin dynamics, measured by autocorrelation analysis of time-lapsed diffraction-limited images, whereas inhibition of CaM with the inhibitor, W-7, or CamKII with the inhibitors KN93 and KN62 had no appreciable effect (Fig. 3B). Other Ca^{2+}-dependent processes may also contribute to MPS dynamics, among them the Ca^{2+}-dependent conformational change of the EF-hand motifs in spectrin, which alters the strength of its interaction with actin (*53*–*55*), although we did not test the EF-hand effect in this work.

Ca^{2+}-dependent PKC activity promotes MPS dynamics

PKC is a major Ca^{2+}-dependent effector of signaling at the membrane (*47, 56*) that is also known to phosphorylate adducin, a component of the MPS (*9, 48, 57*). To further validate that PKC inhibition affects MPS remodeling, we imaged spectrin-mNeonGreen knock-in neurons using live-cell SIM imaging to directly resolve the MPS structure and observed that PKC inhibition by GFX substantially reduced the prevalence of MPS remodeling (Fig. 3C). Concordantly, enhancement of PKC activity by phorbol 12-myristate 13-acetate [(PMA), a PKC activator] caused a substantial increase in MPS dynamics (Fig. 3C and fig. S9). Together, these results highlight PKC as a major effector of Ca^{2+} in mediating MPS remodeling.

Next, we explored the phosphorylation targets of PKC that could affect MPS dynamics. Although phosphorylation of spectrin could regulate its stability in the membrane (*58*), PKC is not known to directly phosphorylate spectrin. Among the most likely targets of PKC in the MPS is adducin, which caps actin filaments in the actin rings of the MPS and interacts with both actin and spectrin, serving as a linker that strengthens actin-spectrin interactions in many cell types (*57, 59*). Adducin phosphorylation by PKC is known to result in adducin dissociation from actin and to diminish its ability to recruit spectrin, reducing actin-spectrin complex stability (*48, 57*). We thus tested whether PKC-induced phosphorylation of adducin is involved in MPS remodeling.

First, we directly imaged PKC together with spectrin to examine whether PKC is associated with the MPS. We imaged βII-spectrin using an antibody that targets its C-terminus, which is located at the midpoint of the spectrin heterotetramer connecting actin rings of the MPS (Fig. 3D, schematic). Two-color SIM imaging revealed that PKC adopts a periodic distribution in some axonal regions, localizing to sites midway between bands of spectrin, with the two being anticorrelated with each other (Fig. 3, D and E). These results suggest that PKC is associated (likely transiently) with the actin rings and point to adducin as the potential target of PKC in the MPS. Further supporting this notion, we found that inhibition of PKC by GFX decreased phospho-adducin signal in axons, whereas activation of PKC by PMA had the opposite effect, increasing phospho-adducin signal (Fig. 3F). These results indicate that PKC indeed regulates adducin phosphorylation in neurons.

To test whether adducin plays a role in MPS remodeling, we depleted adducin from neurons using a virally delivered short hairpin RNA (shRNA) against adducin. Because the MPS is degraded in neurons from adducin-knockout animals (*15*), we transduced neurons with shRNA at concentrations that maintain a reasonable degree of MPS integrity (fig. S10). Under these conditions, we observed a substantial increase in the prevalence of MPS remodeling (Fig. 3G). Finally, we tested whether adducin knockdown could counter the reduction in MPS dynamics caused by PKC inhibition. We observed that, although PKC inhibition by GFX substantially reduced MPS dynamics, adducin knockdown largely compensated for this effect when we combined GFX treatment with adducin knockdown (Fig. 3G). Taken together, these results suggest that phosphorylation of adducin by PKC, which could reduce actin filament stability and destabilize actin-spectrin interactions, promotes MPS remodeling, although we cannot rule out the possibility that phosphorylation of other targets by PKC may also contribute to MPS remodeling.

Actin-filament stability and dynamics play a role in MPS remodeling.

The notable effect of perturbing PKC and adducin suggests that stability of the actin rings plays an important role in MPS dynamics. Indeed,

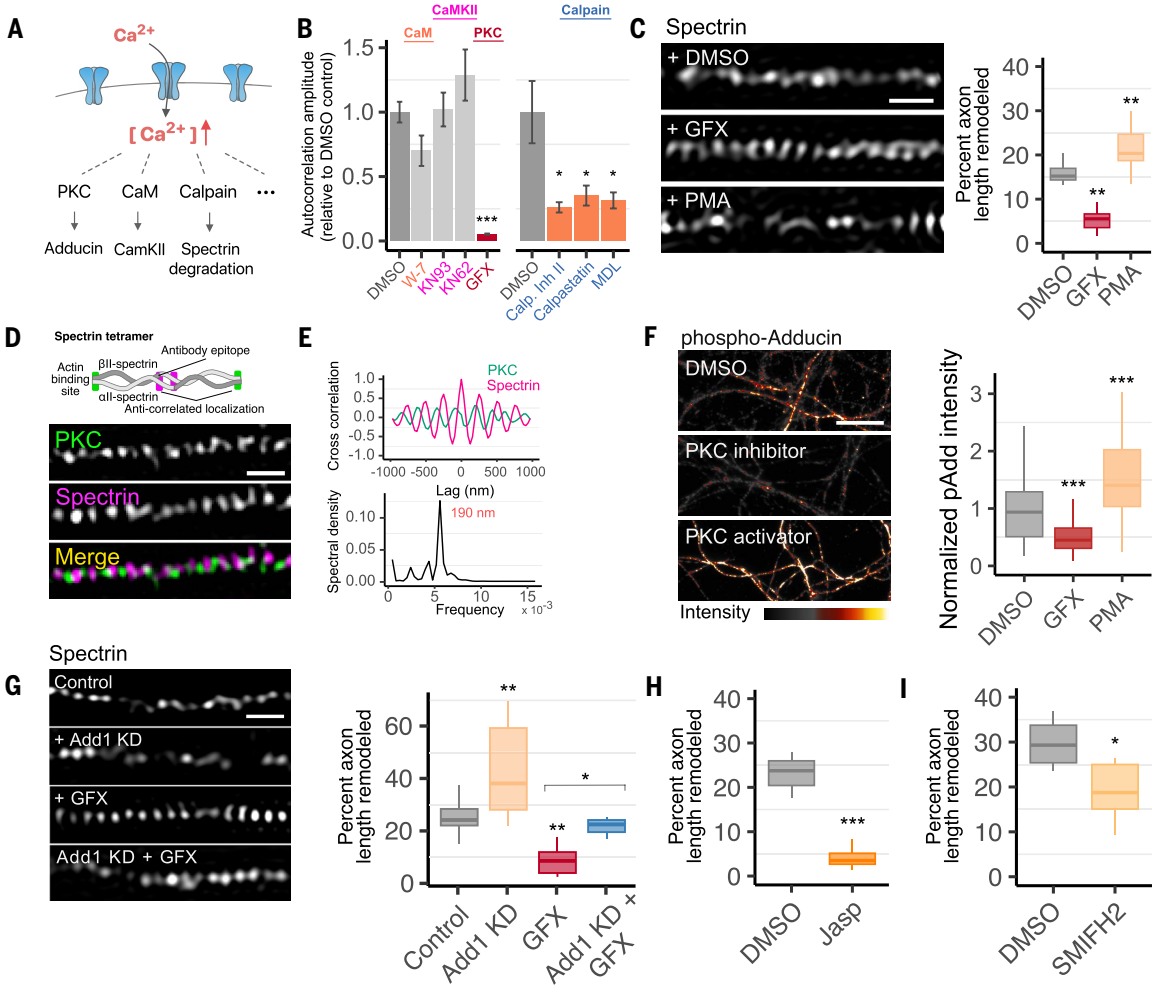


Fig. 3. PKC-mediated adducin phosphorylation promotes MPS remodeling. (**A**) Schematic of several Ca^{2+} signaling pathways that may act on the MPS. (**B**) Screen of several major effectors of calcium signaling in MPS remodeling by diffraction-limited imaging. (Left) W-7: calmodulin inhibitor; KN93 and KN62: CamKII inhibitors; GFX: PKC inhibitor. (Right) Multiple calpain inhibitors. (**C**) (Left) Representative snapshots of spectrin-mNeonGreen in axons treated with 10 μM of the PKC inhibitor, GFX, 1 μM of the PKC activator PMA, or DMSO control 30 min prior to SIM imaging. (Right) Fraction of axon length exhibiting MPS remodeling. (**D**) Two-color SIM imaging of PKC and spectrin in fixed neurons, illustrating the periodic distribution of PKC in an anticorrelated manner with that of spectrin in some regions of axons. The schematic shows the spectrin epitope and actin binding sites. (**E**) (Top) Cross-correlation analysis of PKC and spectrin in two-color SIM images (green). The average cross-correlation of seven axonal regions exhibiting high PKC periodicity is plotted. Magenta indicates autocorrelation of spectrin. (Bottom) Spectral analysis of the average autocorrelation of 27 axonal regions from 3 FOVs showing a periodic distribution of PKC with a 190-nm interval. (**F**) Measurement of adducin phosphorylation by PKC in axons. Representative images of fluorescence intensity (left) and quantification of normalized intensity (right) of phosphorylated adducin signal in axons following PKC inhibition with 10 μM GFX or activation using 1 μM PMA as compared with DMSO control. (**G**) (Left) Representative snapshots from live SIM imaging of spectrin-mNeonGreen neurons treated with control shRNA, shRNA targeting adducin 1 (Add 1 KD), GFX to inhibit PKC, or adducin shRNA together with GFX. (Right) Fraction of axon length exhibiting MPS remodeling under these conditions. (**H**) Fraction of axon length exhibiting MPS remodeling in neurons treated with 10 μM Jasp to stabilize actin filaments or DMSO control for 30 min prior to live SIM imaging. These experiments were performed together with those in Fig. 4, A and G, with a shared DMSO control. (**I**) Fraction of axon length exhibiting MPS remodeling in neurons treated with 30 μM of the formin inhibitor, SMIFH2, or DMSO control for 10 minutes prior to imaging. Statistics for (B, C, and F to I) are shown in table S2. Scale bars, 500 nm (C, D, and G); 10 μm (F).

our diffraction-limited imaging and SIM imaging of the MPS both indicated that stabilization of actin filaments with Jasp resulted in a substantial reduction in the prevalence of MPS remodeling (Figs. 2B and 3H). This stabilization by Jasp could occur after PKC-mediated adducin phosphorylation, which uncaps actin filaments and makes them prone to depolymerization. It is also possible that a certain degree of basal actin depolymerization occurs independently of PKC or Ca^{2+} signaling, which is inhibited by Jasp.

In addition to PKC-induced adducin phosphorylation, we wondered whether other factors that regulate actin filaments could also influence MPS dynamics. We therefore screened two major families of actin filament nucleation/elongation factors for a potential effect on MPS dynamics using diffraction-limited imaging. This included mediators of branched actin (*60*) and linear actin (*61*, *62*) formation. We observed that inhibition (by CK666) of Arp2/3, a nucleator of branched actin filaments (*63*), did not affect MPS dynamics appreciably (fig. S11A), consistent with previous observations that MPS is not substantially disrupted by Arp2/3 inhibition (*39*). By contrast, short-term inhibition (10 minutes, by SMIFH2) of formin, a nucleator and polymerizer of linear actin filaments (*64*), substantially reduced MPS dynamics (fig. S11A). To validate this result, we performed live-cell SIM imaging of the MPS in neurons treated with SMIFH2 and found that short-term formin inhibition indeed resulted in a moderate reduction in the prevalence of MPS remodeling (Fig. 3I).

The formin family of linear actin nucleators have previously been implicated in MPS maintenance (*39*). Consistent with this work, we found that the formins mDia2, Daam1, and Fmn2 were associated with the actin rings of the MPS (fig. S11, B to G), albeit only in isolated stretches of the axon, suggesting that their association with the MPS is transient or local. Long-term (3-hour) inhibition of formins with the inhibitor SMIFH2 as well as shRNA-mediated knockdown of mDia2 both resulted in partial, moderate loss of the MPS (figs. S12 and S13). Our results thus suggest that formins have a dual role in MPS maintenance and dynamics. Mechanistically, since both formin and adducin bind to the barbed end of actin filaments, formin binding could displace adducin from actin filaments (*65*–*67*), leading to MPS destabilization and promoting remodeling, because adducin binds to both actin and spectrin and stabilizes the actin-spectrin complex (*48*, *57*, *59*). Thus, short-term inhibition of formin could lead to increased adducin binding to actin filaments, stabilizing the actin-spectrin complex and the MPS. In the long term, however, formin inhibition could slowly deplete the axon of actin filament supplies, resulting in a reduced ability to repair the MPS after its disassembly.

Ca^{2+}-dependent spectrin proteolysis by calpain promotes MPS dynamics

Our screen results (Fig. 3B) suggest that, in addition to PKC, Ca^{2+}-dependent proteolysis by calpain also contributes to spectrin dynamics. To validate this, we performed live-cell SIM imaging of the MPS in spectrin-mNeonGreen knock-in neurons and found that inhibition of calpain by MDL indeed substantially reduced the prevalence of MPS remodeling (Fig. 4A).

Spectrin is a target of the Ca^{2+}-dependent protease calpain, and calpain-mediated proteolysis has the potential to regulate membrane skeleton stability (*44*, *68*). We thus asked whether spectrin proteolysis in response to Ca^{2+} contributes to MPS remodeling. To this end, we first examined the effects of applying brief pulses of Ca^{2+} to local regions of the axon using ultraviolet light to uncage a relatively high concentration of the caged Ca^{2+} compound, NP-EGTA. Immediately following uncaging, we observed a rapid, major reduction in spectrin fluorescence (Fig. 4B), corresponding to MPS degradation (fig. S14). Upon removal of the uncaging laser, the spectrin signal recovered within 5 minutes (Fig. 4B). This suggests that local increases in Ca^{2+} could degrade spectrin and the MPS.

We next probed the involvement of calpain-mediated spectrin degradation in MPS remodeling by directly imaging calpain-cleaved spectrin in axons. To this end, we performed SIM imaging of fixed neurons co-immunostained with an antibody targeting βII-spectrin and an antibody that specifically targets the calpain-cleaved form of αII-spectrin under unstimulated conditions. Cleaved spectrin was observable throughout the axon (Fig. 4C). The amount of cleaved spectrin was substantially reduced following either calpain inhibition by MDL or Ca^{2+} chelation with BAPTA (Fig. 4C), confirming that the measured signal is at least in part due to calpain-dependent cleavage and that this process is Ca^{2+}-dependent. We observed a strong correlation between the cleaved αII spectrin signal and the prevalence of MPS degradation (Fig. 4D). Together, our results suggest that calpain-mediated spectrin proteolysis plays a role in MPS remodeling downstream of Ca^{2+}.

PKC activity enhances spectrin degradation by calpain

Since PKC-induced phosphorylation of adducin and calpain-mediated cleavage of spectrin both contribute to MPS remodeling, we wondered whether these two activities are connected. To explore this, we first tested the effects of the PKC inhibitor (GFX) and the PKC activator (PMA) on spectrin cleavage by calpain in unstimulated cells. We found that calpain-cleaved αII-spectrin was reduced by PKC inhibition and increased by PKC activation (Fig. 4E), suggesting that PKC activity enhances spectrin cleavage by calpain. We next asked whether PKC inhibition could prevent the rapid degradation of spectrin following the influx of Ca^{2+}. We found that, after PKC inhibition, spectrin became resistant to degradation even in the presence of a strong Ca^{2+} uncaging pulse (Fig. 4F). Together, these results suggest the possibility that adducin phosphorylation by PKC, which promotes the dissociation of adducin and weakens the link between actin and spectrin, can enhance the accessibility of the spectrin cleavage site and thereby facilitate spectrin degradation by calpain. However, our results do not exclude the possibility that some spectrin cleavage by calpain could also occur in a PKC-independent manner.

The results above, as well as the fact that the effect of PKC inhibition on MPS dynamics is stronger than that of calpain inhibition by MDL, suggest that spectrin degradation might play a secondary role in MPS dynamics as compared with actin-ring destabilization. To further test this possibility, we compared the effects of stabilizing actin by an alternative means (with Jasp) to that of calpain inhibition with MDL. We found that the effect of Jasp was substantially stronger than that of MDL (Fig. 4G). In addition, the combined effect of both drugs was substantially stronger than that of MDL alone but not statistically significantly (P-value = 0.9) stronger than that of Jasp alone (Fig. 4G), supporting the notion that calpain-medicated spectrin cleavage is at least in part dependent on actin destabilization.

Taken together, our results suggest that actin ring destabilization caused by PKC activity is the primary driver of MPS dynamics, whereas spectrin degradation occurs downstream and also promotes MPS remodeling. However, our results do not exclude the possibility that some spectrin degradation may also occur independently of actin ring destabilization.

MPS remodeling promotes endocytosis

Our discovery of a highly regulated system of MPS remodeling implies that MPS dynamics are functionally important. Recent studies have shown that the MPS inhibits clathrin-mediated endocytosis of GPCRs upon ligand simulation (*23*) and restricts endocytosis in the AIS under resting conditions (*69*). Given the distinct form that MPS dynamics takes, in which an apparently persistent scaffold is repeatedly disassembled and rebuilt locally, we hypothesized that the presence of the MPS could inhibit cellular processes that require local membrane access or deformation, such as endocytosis, and that the MPS must be temporarily and locally removed to facilitate these processes while remaining largely intact to support other MPS functions.

To explore whether MPS remodeling serves to facilitate endocytosis, we measured basal endocytosis in axons and tested the effects of various perturbations that affect MPS dynamics. First, we measured the uptake of low-density lipoprotein (LDL) as a reporter of receptor-mediated endocytosis in unstimulated neurons. We confirmed that the measured fluorescence signal of LDL in axons was primarily due to clathrin-mediated endocytosis by using dynasore to inhibit endocytosis (Fig. 5, A and B). We then tested the effects of three perturbations shown to reduce MPS dynamics, including PKC inhibition by GFX, calpain inhibition by MDL, and actin stabilization with Jasp, as well as the effect of MPS removal by βII-spectrin knockdown. We found that all three perturbations that stabilize the MPS and reduce MPS remodeling resulted in a substantial decrease in endocytosis, whereas removal of the MPS increased endocytosis (Fig. 5, A and B). We further extended these results using the lipophilic dye, AM5-65, as a general reporter of endocytosis (fig. S15), indicating that these effects are not limited to the endocytosis of a particular ligand or receptor.

Although some of the individual perturbations that we employed are not specific to the MPS and could affect endocytosis by altering other cellular structures or processes, our observations that all three drugs that stabilize the MPS (GFX, MDL, and Jasp) similarly inhibited endocytosis support the notion that MPS dynamics facilitate endocytosis. Furthermore, unlike the other perturbations, βII-spectrin is predominantly localized to the MPS in axons, and the observation that endocytosis in axons was increased following knockdown of

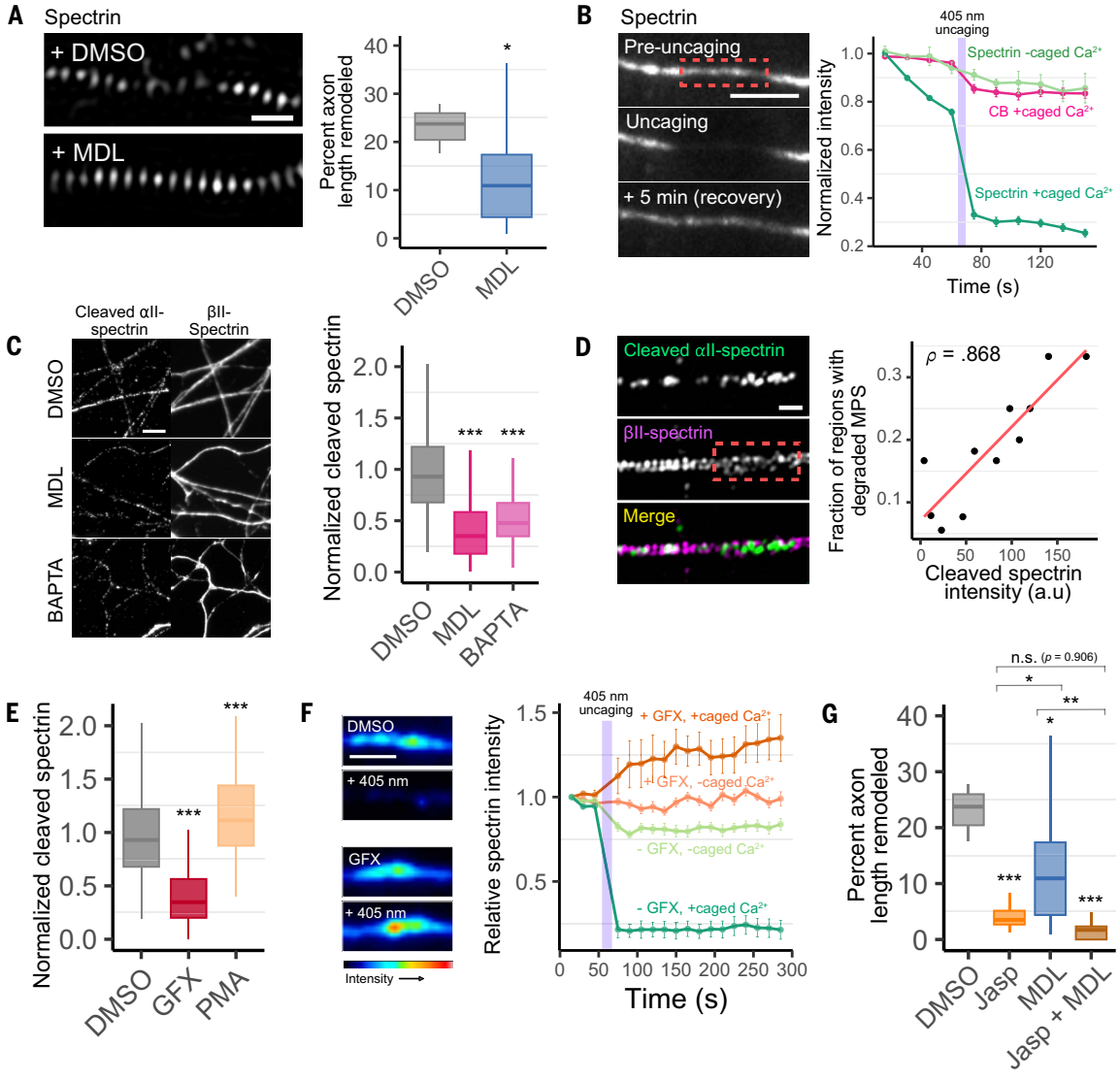


Fig. 4. Calpain-dependent spectrin proteolysis promotes MPS remodeling. (**A**) (Left) Snapshots of spectrin-mNeonGreen in axons treated with 50 μM MDL, a calpain inhibitor, or DMSO control 30 min prior to imaging. (Right) Fraction of axonal length exhibiting MPS remodeling (sharing DMSO control with experiments in Fig. 3H and 4G). (**B**) (Left) Snapshots of diffraction-limited imaging of spectrin-mNeonGreen during an intense pulse of 405-nm illumination to induce Ca^{2+} uncaging in a small region of an axon treated with 30 μM NP-EGTA. (Upper) Prior to the 405-nm illumination. (Middle) Immediately after the 405-nm pulse. (Lower) 5 minutes after the 405-nm pulse. (Right) Dark green indicates normalized spectrin-mNeonGreen intensity before and after Ca^{2+} uncaging with the time of the 405-nm uncaging pulse indicated by the purple bar. The moderate signal decrease before the 405-nm pulse is due to Ca^{2+} uncaging by the 488-nm light used to image spectrin-mNeonGreen. (Light green) Same as dark green, but without caged Ca^{2+} (NP-EGTA). (Magenta) Same as dark green, but for the intensity of CellBright (CB), a plasma membrane marker. (**C**) Co-immunofluorescence imaging of βII-spectrin and calpain-cleaved αII-spectrin in neurons treated with MDL, BAPTA, or DMSO control. Quantification of calpain-cleaved αII-spectrin is shown on the right. (**D**). (Left) Two-color SIM imaging of βII-spectrin and calpain-cleaved αII-spectrin. Dash-boxed region shows regions of high calpain activity corresponding to areas of degraded MPS. (Right) Correlation between fractions of axonal regions exhibiting degraded MPS and calpain-cleaved αII-spectrin intensity. (**E**) Cleaved αII-spectrin intensity in axons following PKC inhibition (10 μm GFX) or activation (1 μM PMA) as compared with control. (**F**) Effect of GFX on spectrin degradation in response to Ca^{2+} uncaging. (Left) Images of spectrin-mNeonGreen fluorescence axons before and after an intense pulse of 405-nm light to induce Ca^{2+} uncaging in neurons pretreated with 30 μM NP-EGTA and either 10 μM GFX (bottom panels) or DMSO control (top panels) 30 minutes prior to imaging. (Right) Spectrin intensity before and after the 405-nm uncaging pulse (purple bar) in the absence and presence of GFX. Control without caged Ca^{2+} are also shown. (**G**) Fraction of axonal length exhibiting MPS remodeling in neuron treated with Jasp, MDL, or both. Statistics for (A to G) are shown in table S2. Scale bars, 500 nm (A and D), 5 μm (B and C), and 2 μm (F).

βII-spectrin also supports the notion that disassembly of the MPS enhances endocytosis. The increase in endocytosis was only ~30% when the MPS was removed, whereas the reduction in endocytosis upon inhibition of MPS dynamics was much more substantial (70 to 80%), suggesting that the MPS imposes a strong inhibitory effect on endocytosis and that the constitutive dynamics of the MPS is sufficient to largely remove this inhibition.

Discussion

In summary, using live-cell super-resolution imaging, we made the unexpected discovery that the MPS is constitutively dynamic, exhibiting repeated cycles of local disassembly and reassembly even under unstimulated conditions. These dynamics can contribute to remodeling of large portions of the axonal membrane skeleton over the course of minutes to hours. This is particularly surprising in light of the role

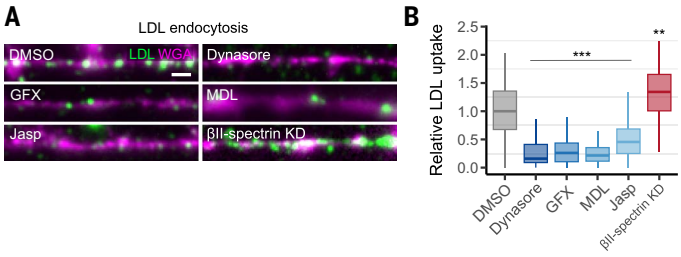


Fig. 5. MPS dynamics promote endocytosis. (**A**) Representative images of LDL (5 μg/mL) uptake in axons following a 90-min incubation in unstimulated neurons (LDL in green with the axonal membrane counterstained with WGA in magenta). (Top) Treatment of neurons with the clathrin-mediated endocytosis inhibitor (dynasore, right) and DMSO control (left) for 30 min prior to LDL uptake. (Middle and Bottom) LDL uptake following perturbations that stabilize the MPS and reduce MPS dynamics (PKC inhibition with 10 μM GFX, calpain inhibition with 50 μM MDL, and actin stabilization with 10 μM Jasp) or a perturbation that removes the MPS (βII-spectrin knockdown). (**B**) Quantification of LDL uptake in axons under the conditions shown in (A). Statistics for (B) are shown in table S2. Scale bar in (A) is 1 μm.

that the MPS is presumed to play in providing axons with mechanical support and the resistance of the MPS to degradation by pharmacological perturbations.

Our studies provide mechanistic insight into a highly regulated system of MPS remodeling (fig. S16). The primary driver of MPS remodeling is Ca^{2+} signaling, which activates multiple pathways that intersect in the process. Ca^{2+}-dependent activation of PKC leads to adducin phosphorylation, destabilizing the actin ring and weakening actin-spectrin interactions. At the same time, Ca^{2+} also activates calpain, leading to proteolysis of spectrin. Together, these activities cause the local disassembly of the MPS. The two pathways intersect in their contributions to MPS remodeling: PKC activity enhances the cleavage of spectrin by calpain and is required for the degradation of spectrin in response to a large influx of Ca^{2+} in uncaging experiments. Mechanistically, we reason that PKC-mediated phosphorylation of adducin, which promotes adducin dissociation, weakens actin-spectrin interactions and increases the accessibility of spectrin to cleavage by calpain.

Although our results have uncovered many major players regulating MPS dynamics, other Ca^{2+}-dependent mechanisms may also contribute. For example, adducin has been shown to be susceptible to calpain-dependent proteolysis in a phosphorylation-dependent manner in platelets (*70*). It is thus possible that adducin proteolysis may also contribute to MPS remodeling in axons. In addition, the EF-hand motifs of spectrin are known to undergo a Ca^{2+}-dependent conformational change that alters the strength of its interaction with actin (*53*–*55*), which may also contribute to MPS remodeling. Moreover, we have identified regulators of actin stability and filament polymerization, including members of the formin family, as contributors to MPS dynamics. It has been shown that, in addition to adducin, genetic perturbation or inhibition of other actin-binding proteins, such as tropomyosin, tropomodulin, and dematin, can also cause MPS disruption to varying degrees (*15*, *71*). It is thus possible that other actin regulators may also work together with the regulators we identified here to maintain a constitutive state of MPS turnover.

Functionally, we found that MPS remodeling facilitates endocytosis in the axon. A defining aspect of the dynamics we have uncovered here is that it involves the repeated, local destruction and rebuilding of an elaborate cytoskeletal structure at the membrane. This is perhaps because the functions of the MPS, such as its role in providing structural stability to long and delicate axons, are at odds with other important functions of the membrane, thus requiring local disruption of the MPS to facilitate these membrane functions. Indeed, we found that the presence of the MPS is inhibitory to endocytosis, and that dynamic, local disruption of the MPS promotes this membrane and cargo internalization process. Such a requirement may also hold for other cellular processes that require deformation of or access to the plasma membrane. Moreover, in the role of the MPS as an important signaling platform (*23*), the disassembly and reassembly dynamics of the MPS could regulate the availability of receptors at the cell surface as well as the proximity of co-receptors and downstream signaling molecules, thereby modulating signaling strength.

Finally, the dynamic nature of Ca^{2+} regulation in neurons suggests many ways that MPS remodeling can be fine-tuned under different conditions to adapt to the needs of the cell. Among them, our observation that inhibition of action potentials and presynaptic Ca^{2+} channels can reduce MPS dynamics suggests an interplay between the MPS and neuronal activity. Understanding the full extent of the functional consequences of MPS remodeling and its interplay with neuronal activity will be an exciting area of future study.

Materials and methods

Generation of βII-spectrin mNeonGreen conditional knock-in mice

Generation of βII-spectrin mNeonGreen conditional knock-in (cKI) mice was carried out at the Gene Targeting and Transgenic Facility at the HHMI/Janelia Research campus. The targeting construct, consisting of a LoxP-flanked alternative final exon of βII-spectrin with a C-terminal mNeonGreen fusion that is expressed upon Cre expression, was produced using recombineering techniques (*72*) and traditional molecular cloning. An 8262-base pair (bp) genomic DNA fragment containing exons 33 to 35 of *Sptbn1* was retrieved from BAC clone RP24-63C14. A LoxP site was inserted 188 bp upstream of exon 35, and a polyadenylation signal (3×SV40 PA) was inserted after the 3' untranslated region (UTR) to prevent mNeonGreen leakage before Cre excision. An FRT-NeoR-FRT-LoxP cassette was inserted after 3×PA followed by an exon 35-mNeonGreen fusion (Fig. 1A).

To facilitate embryonic stem (ES) cell targeting, CRISPR/Cas9 genome editing was used. gRNA was in vitro transcribed using the MEGA Shortscript T7 kit (ThermoFisher, AM1354), and the template was polymerase chain reaction (PCR) amplified using the following primers:

Forward, 5'- CCTTAATACGACTCACTATAGG GTCTGCGGGTGCAGAGCAGTGGGgttttagagctaGAAAtagc -3'; and

Reverse, 5'- AAAAGCACCGACTCGGTGCCACTTTTTCAAGTTGATAACGGACTAGCCTTATTTTAACTTGCTATTTCTAGCTCTAAAAC -3'.

The targeting vector, Cas9 protein (TrueCut Cas9 Protein V2, Fisher Scientific A36499) and the gRNA were co-electroporated into 1 million G1 ES cells derived from F1 hybrid blastocysts of a 129S6 (Taconic, strain 129S6/SvEvTac) × C57BL/6J (JAX, strain C57BL/6J, stock 000664) cross. G4180-resistant ES colonies were isolated and screened by nested PCR using primers outside the construct paired with primers inside the construct. The primers used for ES cell screening were as follows:

5'-arm forward primers:

Sptbn1-Scr-F1, 5'- CGCTCACTAGAGCAAAGTTG -3') and *Sptbn1-Scr-F2.* 5'- TAGGGTTCCTAGTAGGATCC -3';

5'-arm reverse primers:

Cre-Scr-R1, 5'- GAGGGACCTAATAACTTCGT -3'; and *Cre-Scr-R2.* 5'-ATGATCGGAATTGGGCTGCA -3'.

3'-arm forward primers:

mNeonGreen-Scr-F1, 5'- CCATAGGATCGAGATCCTGT -3'; and *mNeonGreen-Scr-F2,* 5'- GACTACAACAAGGTCAAGCTGT -3'

3'-arm reverse primers:

Sptbn1-Scr-R1, 5'- CAGAGCAGCAGTTCTGACTT -3'; and *Sptbn1-Scr-R2.* 5'- GACCCCAGAGATCTAATTCC -3'.

Eight ES clones with both arms positive were identified for generation of chimeric mice. Chimeric mice were generated by aggregating the ES cells with eight-cell embryos of the CD-1 strain (Charles River, strain

code 022). Chimeras were bred for 13 generations with R26FLP females (JAX stock 003946) to remove the FRT-Neo-FRT cassette. Accurate targeting was further confirmed by homozygosity tests in progenies.

Primary culture of mouse and rat hippocampal neurons

All rodent procedures were approved by the Institutional Animal Care and Use Committee (IACUC) of Harvard University. Primary mouse and rat hippocampal neurons were cultured as follows. For rat neurons, female timed-pregnant CD (Sprague Dawley) rats (Strain code 001, Charles River Laboratories, Wilmington, MA), aged 3 to 5 months, were euthanized and hippocampi were isolated from E18 embryos in Hibernate A medium without Ca^{2+} (TransnetYX, Cordova, TN). Mouse hippocampi were isolated from P0 pups (a cross between the 129S6 and C57BL/6J strains, mNeonGreen cKI). Following isolation, hippocampi were digested in 0.25% Trypsin-EDTA (1×) (Sigma, T4549) at 37°C for 15 minutes, washed in Hanks' Balanced Salt Solution (HBSS) (ThermoFisher, 14175079), and transferred to culture medium consisting of Neurobasal media (ThermoFisher, 21103049) supplemented with 2% B27 (ThermoFisher, 17504044), 2 mM GlutaMax (ThermoFisher, 35050-061), and 37.5 mM NaCl. Hippocampi were gently triturated, cells were pelleted at 300*g*, resuspended in culture medium, and plated on 18 mm poly-D-lysine-coated coverslips (NeuVitro, GG-18-1.5-pdl) at a density of 80,000 to 100,000 cells per coverslip. Cultures were maintained in a humidity-controlled incubator at 37°C with 5% CO_2, and half of the media volume was replaced every 5 to 7 days.

Adeno- and adeno-associated viral vectors and transduction of primary neurons

Adenoviral vectors expressing Adducin1 shRNA (Ad5-mCherry-U6-rm-ADD1-shRNA), scramble shRNA (Ad5-mCherry-U6-Scrmb-shRNA), mDia2 shRNA (Ad5-mCherry-U6-mDIAP3-shRNA), and Adducin1-GFP (Ad5-CMV-GFP-Adducin) were custom-ordered from Vector Biolabs (Malvern, PA). The spectrin-GFP adenoviral vector (Ad5-Spectrin-GFP) was custom-ordered from O.D. 260 (Boise, ID). Adenovirus was added to hippocampal cultures between DIV 8 to 10 to achieve a multiplicity of infection (MOI) of ~20, and transduced neurons were used for experiments 2 to 7 days later. Cultures of spectrin-mNeonGreen knock-in neurons were transduced at DIV 2 to 3 with Cre recombinase (AAV1-Cre, Vector Biolabs, 7010) at an MOI of 10,000 to induce expression of spectrin-mNeonGreen.

Antibodies

The following primary antibodies were used in this study: βII spectrin (mouse, 1:500, BD Biosciences, 612563, RRID: AB_399853), adducin (rabbit, 1:250, Abcam, ab51130, RRID: AB_867519), phospho-alpha adducin (Ser726, rabbit, 1:250, ThermoFisher, PA5-38064, RRID: AB_2554668), cleavage-specific αII-spectrin (a.a. 1171-76, rabbit, 1:250, ECM Biosciences, SP5601), VAMP2 (rabbit, 1:500, Cedarlane, 104202(SY), RRID: AB_887810), DIAPH3/mDia2 (rabbit, 1:200, ThermoFisher, PA5-85667, RRID: AB_2792806), PKC (rabbit, 1:200, Abcam, ab32376, RRID: AB_777294), Daam1 (rabbit, 1:50, ProteinTech, 14876-1-AP, RRID: AB_2089444), Fmn2 (rabbit, 1:50, ThermoFisher, PA5-65632, RRID: AB_2664990), and $Ca_v1.2$/CACNA1C (rabbit, Alomone, ACC-130). The following fluorescent dye-conjugated secondary antibodies were used at a dilution of 1:500: donkey anti-rabbit Alexa 488, donkey anti-mouse Alexa 488, donkey anti-mouse Alexa 647, and donkey anti-rabbit Rhodamine Red-X (Jackson Immunoresearch).

Immunostaining and actin labeling for fixed-cell imaging

Samples were fixed for 15 minutes with 4% paraformaldehyde in PBS with 4% sucrose at room temperature, permeabilized with 0.1% Triton-X 100 for 5 minutes, and blocked for 1 hour in buffer consisting of 5% Normal Donkey Serum and 1% bovine serum albumin (BSA) in phosphate buffered saline (PBS). Primary antibodies were incubated overnight at 4°C, and secondaries for 1 hour at room temperature. For labeling of F-actin in two-color SIM imaging, cells were incubated with 1 μM SiR-actin (Cytoskeleton, CY-SC001) or ~1.65 μM phalloidin conjugated with Alexa Fluor 647 for 1 hour at room temperature following secondary antibody staining of the other target being imaged together with actin. For labeling the membrane in fixed samples, cells were incubated with 1 μg/mL Alexa Fluor-conjungated WGA (ThermoFisher, W11261) or CellBrite Green (Biotium, 30021) at a dilution of 1:1000. For SIM imaging, coverslips were mounted in ProLong Glass antifade (ThermoFisher, P36982) and allowed to cure overnight. For STORM imaging, buffer consisted of 100 mM Tris, 10 mM NaCl, 5% glucose, 100 mM cysteamine (Sigma), and an oxygen scavenging system consisting of 0.8 mg/mL glucose oxidase (Sigma) and 40 μg/mL catalase (Roche).

Super-resolution imaging

Lattice SIM imaging was performed on a Zeiss ELYRA7 super-resolution microscope equipped with an alpha Plan-Apochromat 63×/1.46 Oil objective maintained by the Harvard Center for Biology Imaging (HCBI). Images were acquired and super-resolution images were rendered using Zeiss ZEN software with the recommended SIM processing settings. For fixed samples, 15-phase 3D SIM images were acquired. For live samples, 13 or 9-phase 2D SIM images were acquired and deconvolved using the Sparse-SIM software package (*73*). The parameters used for Sparse-SIM were: an effective NA of 2.2, 300 iterations of sparsity reconstruction with a sparsity value of 0.1, 30 iterations of Landweber deconvolution, and spatial upsampling.

STORM imaging was performed on a custom-built Olympus IX71 microscope equipped with a 100× oil-immersion objective (Olympus, UPlanSApo, N.A. 1.4) and an EM-CCD camera (Andor iXon, DV887-DCS-BV, Andor Technology). Laser lines including a 405-nm (Coherent, OBIS 405 LX 200 mW), 561 nm (Coherent, Sapphire 561-200 CW CDRH) and 640-nm (Coherent, Genesis MX 639-1000 STM) lasers were aligned to the back focal plane of the objective. A translation stage was used to shift lasers towards the edge of the objective so that the emerging light reached the sample at incidence angles slightly smaller than the critical angle of the glass-water interface, illuminating fluorophores within only a few micrometers of the coverslip surface. A ZT405/488/561/640rpc (Chroma) was used as the dichroic mirror and ZET405/488/561/640mv2 (Chroma) as the emission filter. For 3D STORM imaging, a cylindrical lens was inserted into the detection path so that images of single molecules were elongated along their x or y axes according to their position relative to the focal plane (*74*). Continuous illumination of 640-nm laser (~2 kW/cm^2) was used to excite fluorescence from Alexa 647 molecules and switch them into the dark state. Continuous 405 nm excitation (0 to 1 W/cm^2) was used to reactivate only a small, optically resolvable fraction of the fluorophores in the field of view at any given time. A typical STORM image was generated from a sequence of ~25 to 30,000 images acquired at a frame rate of 60 Hz. Super-resolution images were rendered using the fitted coordinates of single molecules by depicting them as 2D Gaussian peaks using the 3D DAOSTORM software package (*75*).

Live-cell labeling of F-actin, membranes, and synaptic sites

F-actin was labeled in live cultured neurons by adding 0.5 to 2 μM SiR-actin (Cytoskeleton, CYSC001) to the culture medium for 1 hour at 37°C, followed by three washes in live imaging buffer prior to imaging. Plasma membranes were labeled for live imaging with CellBrite Steady 650 (Biotium, 30108-T), diluted 1:1000 in culture medium with 1× enhancer, incubated for 30 minutes at 37°C, and washed for 15 minutes in live imaging buffer with three exchanges.

Actively-recycling synapses were labeled with SynaptoRed C2M (Biotium, 70019) as follows: cells were habituated for 10 min in HEPES-buffered Tyrode's solution, consisting of 128 mM NaCl, 5 mM KCl, 2 mM $CaCl_2$, 1 mM $MgCl_2$, 25 mM HEPES, and 30 mM glucose, supplemented with 5 μM DNQX and 50 μM APV (Sigma) to prevent recurrent excitation. Cells were stimulated with 45 mM KCl for 90 s in buffer

containing 10 μM SynaptoRed C2M, followed by 90 s recovery in 5 mM KCl with SynaptoRed. Cells were washed for a total of 15 minutes in live-cell imaging buffer with three exchanges prior to imaging.

Live cell imaging

For live-cell imaging, coverslips of cultured neurons were transferred to a Chamlide magnetic imaging chamber (CF-T18, Live Cell Instrument/LCI) or were plated in 35 mm MatTek glass-bottom dishes (P35G-1.5-14-C, MatTek). Culture medium was exchanged for live-cell imaging buffer consisting of Hibernate-E Low Fluorescence (TransnetYX) supplemented with 2% B27, 2 mM GlutaMax, 37.5 mM NaCl, and 0.4% w/v D-glucose. Cells were maintained at 37°C during imaging using an Chamlide CU-501 stage-top incubation system, including objective heater (Live Cell Instrument/LCI) or a full-cage environmental chamber on the Zeiss ELYRA7. Oblique-incidence imaging was performed on the custom-built Olympus IX71 microscope used for STORM imaging (see "Super-resolution imaging" section above), acquiring images at 1 s or 15 s intervals with an exposure time of 150 ms. 2D Lattice SIM imaging was performed on a Zeiss ELYRA7 super-resolution microscope, collecting 13 phase images when sampling at 15-sec intervals, and 9 phase images when sampling at 1-s intervals. Photobleaching was minimized by the use of low laser power (typically ~0.4%) and exposure times.

Quantification of MPS remodeling

Quantification of MPS remodeling from live-cell SIM movies was carried out as follows. We visually identified and marked regions of the axon in which the MPS undergoes at least one degradation and reformation cycle during the first 15 frames of imaging at 15-sec time resolution, corresponding to 225-sec total imaging time, using Fiji/ImageJ. Regions of MPS disassembly were identified by a reduction in the periodic-ring signal (typically by 80 to 100%) to near-background, while regions of MPS reformation were identified by the reappearance of distinct rings, typically with intensities that were at least 30% of the initial intensity before disassembly. Such regions appeared at different times over the length of the axon, and many such regions undergo 2 to 3 cycles of degradation and reformation. We then summed the lengths of all regions and report the prevalence of MPS remodeling as the fraction of total axon length undergoing remodeling. At least 10 axons were measured per condition from 2 to 3 independent replicates for perturbations affecting MPS remodeling.

For quantifying the prevalence of MPS remodeling within or outside synaptic sites, synapses in live, spectrin-mNeonGreen expressing neurons were labeled with SynaptoRed C2M (see "Live-cell labeling of F-actin, membranes, and synaptic sites" section above) prior to two-color SIM imaging to monitor MPS dynamics in regions inside or outside synapses. Sites of MPS remodeling that occurred within bright clusters of SynaptoRed fluorescence are considered synaptic. For comparing MPS dynamics in different regions of the axon, medial to distal regions are defined as the regions of the axon at a distance between 200 and 600 μm from the soma; proximal regions are defined as within 50 μm of the soma.

Correlation analysis of MPS dynamics and plasma membrane fluctuations

To examine whether MPS remodeling was correlated with bulk flow or other passive movements of the plasma membrane, spectrin-mNeonGreen expressing neurons were labeled with the membrane dye, CellBrite Steady 650, prior to two-color SIM imaging. Regions of the MPS undergoing remodeling were subdivided in time into disassembly events and reassembly events (transitions). For each event, the fluorescence intensities of the MPS (spectrin-mNeonGreen signal) and the membrane (CellBrite signal) in transitioning regions were measured over time. Correlation between the two signals was examined by plotting the fluorescence intensities of the MPS and membrane before and after each transition, or by generating a scatter plot of MPS intensities versus membrane intensities and determining the Pearson correlation coefficient between the two signals.

Fluorescence autocorrelation analysis of diffraction-limited movies and screening

Quantification of spectrin dynamics in diffraction-limited movies was performed using fluorescence autocorrelation analysis (*76*). Kymographs were extracted from individual axons in each movie, and the Pearson linear correlation ρ between each pair of kymograph columns separated by time interval Δt up to a maximum Δt of 150 s was computed. The autocorrelation function value at Δt is calculated as the median of ρ for all pairs of kymograph columns separated by Δt: $r(\Delta t) = median(\rho(Kymo(t), Kymo(t+\Delta t)))$. This autocorrelation function was fit with a single exponential of the form $ae^{-k\Delta t} + b$, where the amplitude, a, was used to quantify the prevalence of MPS remodeling. For screening potential regulators of MPS remodeling, neurons were treated with pharmacological inhibitors at the concentrations and durations given in table S1 or with shRNAs, and the average autocorrelation amplitudes from 20 to 30 axons pooled from 2 to 3 independent experimental replicates were compared with controls. Perturbations yielding significant fold changes over controls were selected for further analysis by live-cell SIM imaging.

Pharmacological perturbations

Neurons at DIV 14 to 16 were treated with the drugs as indicated in table S1, along with solvent control (typically DMSO), maintained at the same concentration in imaging media during imaging.

Calcium reporter dyes

To measure Ca^{2+} spiking activity in cultured neurons, cells were loaded with the Ca^{2+} indicator dye Cal-520 (AAT Bioquest, 21130) at a concentration of 2 μM in cell culture media for 45 minutes prior to live-cell TIRF imaging. Cells were imaged at a rate of 2 Hz with an exposure time of 100 ms, and spiking activity was assayed by plotting normalized changes in fluorescence intensity according to the equation $F(t) = (F(t) - F_o)/F_o$, where $F(t)$ is the fluorescence intensity at time t and F_o is the initial intensity. Resting Ca^{2+} concentrations were estimated by loading cells with the ratiometric dye, CalRed R525/650, according to the same protocol, where the ratio of emission at 525 nm to 650 nm indicates the relative Ca^{2+} concentration and allows a normalization for differences in dye loading between experimental conditions. For comparing the relative resting Ca^{2+} concentration in cells treated with BAPTA, TTX, nimodipine, ω-conotoxin, or control, 5 to 12 fields of view (FOVs) of non-spiking neurites were collected, and the average fluorescence ratio of all neurites per FOV were plotted.

Calcium uncaging

Ca^{2+} uncaging experiments were performed by loading neurons with 10 to 30 μM *o*-Nitrophenyl EGTA AM (NP-EGTA, ThermoFisher) for 45 min in cell culture media prior to transfer to live-cell imaging media. Uncaging was performed by delivering a 6-sec pulse of intense 405-nm laser illumination to small regions of axons, or by continuously delivering low-intensity illumination, while simultaneously imaging fluorescent protein constructs or dyes. The power and duration of 405 nm illumination to induce uncaging was determined empirically by imaging neurons loaded with the Ca^{2+} indicator dye Cal-520 (AAT Bioquest, 21130) as above and varying the intensity and duration of 405 nm laser pulses. Small axonal regions were targeted by inserting an iris mounted in a motorized filter wheel (FW102C, Thorlabs) into the excitation path. Ca^{2+} uncaging over large regions of coverslips was achieved by delivering pulses 405 nm illumination to the entire FOV, and automating tiled image acquisition over a 10 × 10 grid, covering an area of 400 × 400 μm in ~5 minutes. The timing of laser pulses and the iris during

image acquisition were controlled by custom microscope control software and data acquisition card (National Instruments, PCIe-6321). Ca^{2+} uncaging during live-cell SIM imaging was achieved by continuous low-power 405 nm excitation during imaging.

Characterization of MPS imperfections in fixed imaging

To examine the correspondence between the prevalence of MPS remodeling observed in live-cell imaging and the appearance of the MPS in fixed-cell imaging, we trained a fully convolutional neural network to classify regions of the MPS as being "imperfect" or "intact" in SIM images of fixed neurons using the STEDActinFCN software package (*34*). The training set supplied to the software consisted of seven 2D SIM images of βII-spectrin in axons of DIV 14 neurons, in which regions of imperfect and intact MPS were manually annotated. Following verification of the software's model to accurately classify regions of the MPS by visual inspection, 27 large FOV SIM images were supplied, yielding a set of 66 axons in which regions of the MPS were segmented by their classification. The prevalence of imperfect MPS in axons was quantified as a fraction of the total area covered by the axon.

Correlation analysis of spatial distributions in super-resolution imaging

One-dimensional (1D) autocorrelation analyses along the length of axons were used to measure the periodicity of the MPS and associated proteins in regions of axons, as previously described (*10*). For SIM images, regions were chosen at random from 10 to 60 μm stretches of axons, and a 1D pixel intensity profile along the long axis of the axons was used; for STORM images, regions were chosen from 2 to 5 μm stretches, and the localization distribution was projected along the axonal long axis to obtain a 1D distribution profile. The 1D autocorrelation function, $AC(\Delta x)$ was calculated from these profiles using the equation:

$$AC(\Delta x) = \frac{\sum_{x=1}^{N-\Delta x} \left(I(x)-\bar{I}\right)\left(I(x+\Delta x)-\bar{I}\right)}{\sum_{x=1}^{N} \left(I(x)-\bar{I}\right)^2},$$

where $\bar{I}$ is the average of $I(x)$, the 1D spatial distribution of the signal, and Δx is the lag. The average 1D autocorrelation function was determined from 50 to 100 axonal regions unless otherwise indicated. For quantifications of spatial autocorrelation amplitude, the amplitude was defined as the difference between the first peak (located at ~190 nm when considering only positive values) and the average of the first two valleys (at approximately ~95 nm and ~285 nm) of the average autocorrelation function.

To compare the spatial distributions of proteins relative to spectrin in two-color SIM images, we obtained 1D intensity profiles as above and computed the 1D cross-correlation function $CC(\Delta x)$ using the equation:

$$CC(\Delta x) = \frac{\sum_{x=1}^{N-\Delta x} \left(I_1(x)-\bar{I_1}\right)\left(I_2(x+\Delta x)-\bar{I_2}\right)}{\sum_{x=1}^{N} \left(I_1(x)-\bar{I_1}\right)\left(I_2(x)-\bar{I_2}\right)}$$

where $I_1(x)$ and $I_2(x)$ are the 1D spatial distributions of the two channels, $\bar{I_1}$ and $\bar{I_2}$ are their averages, and Δx is the lag.

Correlation of calpain activity with MPS degradation

To examine the correlation between calpain activity and MPS degradation, we used an antibody specific to αII-spectrin that has been cleaved by calpain as a reporter of calpain activity in fixed and immunostained neurons. Calpain activity was quantified by measuring the fluorescence intensity of cleaved αII-spectrin staining, and the degree of MPS degradation was quantified from super-resolution images by measuring the spatial autocorrelation amplitude of βII-spectrin in the same regions of the axon. To generate the correlation plot in Fig. 4D, regions of immunostained axons with varying cleaved spectrin intensities were grouped into 12 equally spaced bins and the fraction of regions with degraded MPS was plotted. Regions of the MPS exhibiting an autocorrelation amplitude less than 0.2 (see "Correlation analysis of spatial distributions in super-resolution imaging") were classified as having degraded MPS, confirmed by visual inspection.

Endocytosis assays

To measure endocytosis in axons, unstimulated neurons were incubated with either 5 μg/mL low-density lipoprotein (LDL) labeled with Alexa Fluor 594 (ThermoFisher, L35353) for 90 minutes or 4 μM of the lipophilic dye, AM4-65 (Biotium, 70039), for 30 minutes at 37°C. Cells were washed for 15 minutes in ice-cold Tyrode's solution containing 0.5 μM TTX with three exchanges, followed by fixation, immunostaining, and imaging by widefield or confocal microscopy. In drug perturbation experiments, cells were treated with drugs for 30 minutes prior to the endocytosis assay. LDL endocytosis was quantified as the number of fluorescent puncta, corresponding to internalized LDL, per unit area of the axon and normalized to DMSO-treated control. Fluorescent puncta in axons were counted by manually segmenting axons in Fiji/ImageJ on the basis of a membrane co-stain, followed by automated spot detection using the ComDet ImageJ plugin (https://github.com/UU-cellbiology/ComDet) with an approximate particle diameter of 300 nm and an intensity threshold of 25 standard deviations above background. AM dye endocytosis was quantified by measuring the internalized dye fluorescence following manual segmentation of axons using a membrane co-stain as above.

Statistics

All statistical analyses and plotting were performed in the R statistical environment (*77*). In boxplots, the horizontal line depicts the median and the box depicts the interquartile range (IQR) of the data. Whiskers extend to 1.5 times the IQR, with potential outliers omitted. Bar plots depict the mean ±SEM. A two-tailed, unpaired *t*-test was used to assess the level of significance between two experimental conditions. When three or more conditions were compared, we used a one-way or two-way analysis of variance (ANOVA) followed by Tukey's Honestly Significant Difference (HSD) posthoc test. An F-test was used to determine the significance of a fit when using linear regression. For assessing statistical significance when comparing time-series data, the mean of the final three timepoints was used. In figures, significance is indicated as follows: n.s., not significant; *, $P < 0.05$; **, $P < 0.01$; ***, $P < 0.001$. A complete description of *P*-values, replicate numbers, and statistical tests used for the results presented in individual figures is provided in table S2.

REFERENCES AND NOTES

1. D. A. Fletcher, R. D. Mullins, Cell mechanics and the cytoskeleton. *Nature* **463**, 485–492 (2010). doi: 10.1038/nature08908; pmid: 20110992
2. R. P. Tas, L. C. Kapitein, Exploring cytoskeletal diversity in neurons. *Science* **361**, 231–232 (2018). doi: 10.1126/science.aat5992; pmid: 30026215
3. K. J. Chalut, E. K. Paluch, The actin cortex: A bridge between cell shape and function. *Dev. Cell* **38**, 571–573 (2016). doi: 10.1016/j.devcel.2016.09.011; pmid: 27676427
4. N. Schwarz, R. E. Leube, Plasticity of cytoplasmic intermediate filament architecture determines cellular functions. *Curr. Opin. Cell Biol.* **85**, 102270 (2023). doi: 10.1016/j.ceb.2023.102270; pmid: 37918274
5. Y. Shibata, J. Hu, M. M. Kozlov, T. A. Rapoport, Mechanisms shaping the membranes of cellular organelles. *Annu. Rev. Cell Dev. Biol.* **25**, 329–354 (2009). doi: 10.1146/annurev.cellbio.042308.113324; pmid: 19575675
6. G. Smith, S. T. Sweeney, C. J. O'Kane, A. Prokop, How neurons maintain their axons long-term: An integrated view of axon biology and pathology. *Front. Neurosci.* **17**, 1236815 (2023). doi: 10.3389/fnins.2023.1236815; pmid: 37564364
7. C. Dillon, Y. Goda, The actin cytoskeleton: Integrating form and function at the synapse. *Annu. Rev. Neurosci.* **28**, 25–55 (2005). doi: 10.1146/annurev.neuro.28.061604.135757; pmid: 16029114
8. J. C. Nelson, A. K. H. Stavoe, D. A. Colón-Ramos, The actin cytoskeleton in presynaptic assembly. *Cell Adh. Migr.* **7**, 379–387 (2013). doi: 10.4161/cam.24803; pmid: 23628914

9. K. Xu, G. Zhong, X. Zhuang, Actin, spectrin, and associated proteins form a periodic cytoskeletal structure in axons. *Science* **339**, 452–456 (2013). doi: 10.1126/science.1232251; pmid: 23239625
10. G. Zhong *et al.*, Developmental mechanism of the periodic membrane skeleton in axons. *eLife* **3**, e04581 (2014). doi: 10.7554/eLife.04581; pmid: 25535840
11. E. D'Este, D. Kamin, F. Göttfert, A. El-Hady, S. W. Hell, STED nanoscopy reveals the ubiquity of subcortical cytoskeleton periodicity in living neurons. *Cell Rep.* **10**, 1246–1251 (2015). doi: 10.1016/j.celrep.2015.02.007; pmid: 25732815
12. B. Han, R. Zhou, C. Xia, X. Zhuang, Structural organization of the actin-spectrin-based membrane skeleton in dendrites and soma of neurons. *Proc. Natl. Acad. Sci. U.S.A.* **114**, E6678–E6685 (2017). doi: 10.1073/pnas.1705043114; pmid: 28739933
13. N. Unsain, F. D. Stefani, A. Cáceres, The actin/spectrin membrane-associated periodic skeleton in neurons. *Front. Synaptic Neurosci.* **10**, 10 (2018). doi: 10.3389/fnsyn.2018.00010; pmid: 29875650
14. C. Leterrier, Putting the axonal periodic scaffold in order. *Curr. Opin. Neurobiol.* **69**, 33–40 (2021). doi: 10.1016/j.conb.2020.12.015; pmid: 33450534
15. R. Zhou *et al.*, Proteomic and functional analyses of the periodic membrane skeleton in neurons. *Nat. Commun.* **13**, 3196 (2022). doi: 10.1038/s41467-022-30720-x; pmid: 35680881
16. S. Vassilopoulos, S. Gibaud, A. Jimenez, G. Caillol, C. Leterrier, Ultrastructure of the axonal periodic scaffold reveals a braid-like organization of actin rings. *Nat. Commun.* **10**, 5803 (2019). doi: 10.1038/s41467-019-13835-6; pmid: 31862971
17. E. D'Este *et al.*, Subcortical cytoskeleton periodicity throughout the nervous system. *Sci. Rep.* **6**, 22741 (2016). doi: 10.1038/srep22741; pmid: 26947559
18. J. He *et al.*, Prevalent presence of periodic actin-spectrin-based membrane skeleton in a broad range of neuronal cell types and animal species. *Proc. Natl. Acad. Sci. U.S.A.* **113**, 6029–6034 (2016). doi: 10.1073/pnas.1605707113; pmid: 27162329
19. C. Leterrier *et al.*, Nanoscale architecture of the axon initial segment reveals an organized and robust scaffold. *Cell Rep.* **13**, 2781–2793 (2015). doi: 10.1016/j.celrep.2015.11.051; pmid: 26711344
20. D. Albrecht *et al.*, Nanoscopic compartmentalization of membrane protein motion at the axon initial segment. *J. Cell Biol.* **215**, 37–46 (2016). doi: 10.1083/jcb.201603108; pmid: 27697928
21. E. D'Este, D. Kamin, F. Balzarotti, S. W. Hell, Ultrastructural anatomy of nodes of Ranvier in the peripheral nervous system as revealed by STED microscopy. *Proc. Natl. Acad. Sci. U.S.A.* **114**, E191–E199 (2017). doi: 10.1073/pnas.1619553114; pmid: 28003466
22. M. Hauser *et al.*, The spectrin-actin-based periodic cytoskeleton as a conserved nanoscale scaffold and ruler of the neural stem cell lineage. *Cell Rep.* **24**, 1512–1522 (2018). doi: 10.1016/j.celrep.2018.07.005; pmid: 30089262
23. R. Zhou, B. Han, C. Xia, X. Zhuang, Membrane-associated periodic skeleton is a signaling platform for RTK transactivation in neurons. *Science* **365**, 929–934 (2019). doi: 10.1126/science.aaw5937; pmid: 31467223
24. M. Krieg, A. R. Dunn, M. B. Goodman, Mechanical control of the sense of touch by β-spectrin. *Nat. Cell Biol.* **16**, 224–233 (2014). doi: 10.1038/ncb2915; pmid: 24561618
25. S. Dubey *et al.*, The axonal actin-spectrin lattice acts as a tension buffering shock absorber. *eLife* **9**, e51772 (2020). doi: 10.7554/eLife.51772; pmid: 32267230
26. N. Unsain *et al.*, Remodeling of the actin/spectrin membrane-associated periodic skeleton, growth cone collapse and f-actin decrease during axonal degeneration. *Sci. Rep.* **8**, 3007 (2018). doi: 10.1038/s41598-018-21232-0; pmid: 29445221
27. G. Wang *et al.*, Structural plasticity of actin-spectrin membrane skeleton and functional role of actin and spectrin in axon degeneration. *eLife* **8**, e38730 (2019). doi: 10.7554/eLife.38730; pmid: 31042147
28. T. Wang *et al.*, Radial contractility of actomyosin rings facilitates axonal trafficking and structural stability. *J. Cell Biol.* **219**, e201902001 (2020). doi: 10.1083/jcb.201902001; pmid: 32182623
29. A. R. Costa *et al.*, The membrane periodic skeleton is an actomyosin network that regulates axonal diameter and conduction. *eLife* **9**, e55471 (2020). doi: 10.7554/eLife.55471; pmid: 32195665
30. C. Y.-M. Huang *et al.*, αII spectrin forms a periodic cytoskeleton at the axon initial segment and is required for nervous system function. *J. Neurosci.* **37**, 11311–11322 (2017). doi: 10.1523/JNEUROSCI.2112-17.2017; pmid: 29038240
31. C. Y.-M. Huang, C. Zhang, D. R. Zollinger, C. Leterrier, M. N. Rasband, An αII spectrin-based cytoskeleton protects large-diameter myelinated axons from degeneration. *J. Neurosci.* **37**, 11323–11334 (2017). doi: 10.1523/JNEUROSCI.2113-17.2017; pmid: 29038243
32. J. S. Morrow, M. C. Stankewich, The spread of spectrin in ataxia and neurodegenerative disease. *J. Exp. Neurol.* **2**, 131–139 (2021). pmid: 34528024
33. S. Li *et al.*, Spectrins and human diseases. *Transl. Res.* **243**, 78–88 (2022). doi: 10.1016/j.trsl.2021.12.009; pmid: 34979321
34. F. Lavoie-Cardinal *et al.*, Neuronal activity remodels the F-actin based submembrane lattice in dendrites but not axons of hippocampal neurons. *Sci. Rep.* **10**, 11960 (2020). doi: 10.1038/s41598-020-68180-2; pmid: 32686703
35. D. Micinski, P. Hotulainen, Actin polymerization and longitudinal actin fibers in axon initial segment plasticity. *Front. Mol. Neurosci.* **17**, 1376997 (2024). doi: 10.3389/fnmol.2024.1376997; pmid: 38799616
36. M. Hammarlund, E. M. Jorgensen, M. J. Bastiani, Axons break in animals lacking beta-spectrinβ. *J. Cell Biol.* **176**, 269–275 (2007). doi: 10.1083/jcb.200611117; pmid: 17261846
37. S. Okabe, N. Hirokawa, Turnover of fluorescently labelled tubulin and actin in the axon. *Nature* **343**, 479–482 (1990). doi: 10.1038/343479a0; pmid: 1689016
38. J. Sangerman, A. L. Gard, A. Shah, S. R. Goodman, Synthesis, assembly, and turnover of alpha and beta-erythroid and nonerythroid spectrins in rat hippocampal neurons. *Brain Res.* **849**, 128–138 (1999). doi: 10.1016/S0006-8993(99)02026-0; pmid: 10592294
39. Y. Qu, I. Hahn, S. E. D. Webb, S. P. Pearce, A. Prokop, Periodic actin structures in neuronal axons are required to maintain microtubules. *Mol. Biol. Cell* **28**, 296–308 (2017). doi: 10.1091/mbc.e16-10-0727; pmid: 27881663
40. G. Lukinavičius *et al.*, Fluorogenic probes for live-cell imaging of the cytoskeleton. *Nat. Methods* **11**, 731–733 (2014). doi: 10.1038/nmeth.2972; pmid: 24859753
41. D. Li *et al.*, ADVANCED IMAGING. Extended-resolution structured illumination imaging of endocytic and cytoskeletal dynamics. *Science* **349**, aab3500 (2015). doi: 10.1126/science.aab3500; pmid: 26315442
42. J. Dai, M. P. Sheetz, Axon membrane flows from the growth cone to the cell body. *Cell* **83**, 693–701 (1995). doi: 10.1016/0092-8674(95)90182-5; pmid: 8521486
43. D. N. Lorenzo *et al.*, *Proc. Natl. Acad. Sci. U.S.A.* **116**, 15686–15695 (2019). doi: 10.1073/pnas.1820649116; pmid: 31209033
44. A. S. Harris, J. S. Morrow, Proteolytic processing of human brain alpha spectrin (fodrin): Identification of a hypersensitive site. *J. Neurosci.* **8**, 2640–2651 (1988). doi: 10.1523/JNEUROSCI.08-07-02640.1988; pmid: 3074159
45. K. R. Delaney, V. Shahrezaei, Uncaging calcium in neurons. *Cold Spring Harb. Protoc.* **2013**, 1115–1124 (2013). doi: 10.1101/pdb.top079491; pmid: 24298037
46. E. Metwally, G. Zhao, Y. Q. Zhang, The calcium-dependent protease calpain in neuronal remodeling and neurodegeneration. *Trends Neurosci.* **44**, 741–752 (2021). doi: 10.1016/j.tins.2021.07.003; pmid: 34417060
47. C. Tanaka, Y. Nishizuka, The protein kinase C family for neuronal signaling. *Annu. Rev. Neurosci.* **17**, 551–567 (1994). doi: 10.1146/annurev.ne.17.030194.003003; pmid: 8210187
48. Y. Matsuoka, X. Li, V. Bennett, Adducin is an in vivo substrate for protein kinase C: Phosphorylation in the MARCKS-related domain inhibits activity in promoting spectrin-actin complexes and occurs in many cells, including dendritic spines of neurons. *J. Cell Biol.* **142**, 485–497 (1998). doi: 10.1083/jcb.142.2.485; pmid: 9679146
49. N. Ataei, A. M. Sabzghabaee, A. Movahedian, Calcium/calmodulin-dependent protein kinase II is a ubiquitous molecule in human long-term memory synaptic plasticity: A systematic review. *Int. J. Prev. Med.* **6**, 88 (2015). doi: 10.4103/2008-7802.164831; pmid: 26445635
50. P. A. Kuhlman, C. A. Hughes, V. Bennett, V. M. Fowler, A new function for adducin. Calcium/calmodulin-regulated capping of the barbed ends of actin filaments. *J. Biol. Chem.* **271**, 7986–7991 (1996). doi: 10.1074/jbc.271.14.7986; pmid: 8626479
51. Y. Matsuoka, C. A. Hughes, V. Bennett, Adducin regulation. Definition of the calmodulin-binding domain and sites of phosphorylation by protein kinases A and C. *J. Biol. Chem.* **271**, 25157–25166 (1996). doi: 10.1074/jbc.271.41.25157; pmid: 8810272
52. S. B. Glantz *et al.*, Sequential degradation of alphaII and betaII spectrin by calpain in glutamate or maitotoxin-stimulated cells. *Biochemistry* **46**, 502–513 (2007). doi: 10.1021/bi061504y; pmid: 17209560
53. C. Korsgren, S. E. Lux, The carboxyterminal EF domain of erythroid alpha-spectrin is necessary for optimal spectrin-actin binding. *Blood* **116**, 2600–2607 (2010). doi: 10.1182/blood-2009-12-260612; pmid: 20585040
54. B. Machnicka *et al.*, Spectrins: A structural platform for stabilization and activation of membrane channels, receptors and transporters. *Biochim. Biophys. Acta* **1838**, 620–634 (2014). doi: 10.1016/j.bbamem.2013.05.002; pmid: 23673272
55. D. N. Lorenzo, R. J. Edwards, A. L. Slavutsky, Spectrins: Molecular organizers and targets of neurological disorders. *Nat. Rev. Neurosci.* **24**, 195–212 (2023). doi: 10.1038/s41583-022-00674-6; pmid: 36697767
56. C. Larsson, Protein kinase C and the regulation of the actin cytoskeleton. *Cell. Signal.* **18**, 276–284 (2006). doi: 10.1016/j.cellsig.2005.07.010; pmid: 16109477
57. K. L. Barkalow *et al.*, Alpha-adducin dissociates from F-actin and spectrin during platelet activation. *J. Cell Biol.* **161**, 557–570 (2003). doi: 10.1083/jcb.200211122; pmid: 12743105
58. B. Machnicka, R. Grochowalska, D. M. Bogusławska, A. F. Sikorski, M. C. Lecomte, Spectrin-based skeleton as an actor in cell signaling. *Cell. Mol. Life Sci.* **69**, 191–201 (2012). doi: 10.1007/s00018-011-0804-5; pmid: 21877118
59. K. M. Abdi, V. Bennett, Adducin promotes micrometer-scale organization of beta2-spectrin in lateral membranes of bronchial epithelial cells. *Mol. Biol. Cell* **19**, 536–545 (2008). doi: 10.1091/mbc.e07-08-0818; pmid: 18003973
60. P. H. Chia, B. Chen, P. Li, M. K. Rosen, K. Shen, Local F-actin network links synapse formation and axon branching. *Cell* **156**, 208–220 (2014). doi: 10.1016/j.cell.2013.12.009; pmid: 24439377
61. A. Ganguly *et al.*, A dynamic formin-dependent deep F-actin network in axons. *J. Cell Biol.* **210**, 401–417 (2015). doi: 10.1083/jcb.201506110; pmid: 26216902
62. C. Leterrier, P. Dubey, S. Roy, The nano-architecture of the axonal cytoskeleton. *Nat. Rev. Neurosci.* **18**, 713–726 (2017). doi: 10.1038/nrn.2017.129; pmid: 29097785
63. L. M. Machesky, K. L. Gould, The Arp2/3 complex: A multifunctional actin organizer. *Curr. Opin. Cell Biol.* **11**, 117–121 (1999). doi: 10.1016/S0955-0674(99)80014-3; pmid: 10047519

64. N. Courtemanche, Mechanisms of formin-mediated actin assembly and dynamics. *Biophys. Rev.* **10**, 1553–1569 (2018). doi: 10.1007/s12551-018-0468-6; pmid: 30392063
65. J. P. Bombardier *et al.*, Single-molecule visualization of a formin-capping protein 'decision complex' at the actin filament barbed end. *Nat. Commun.* **6**, 8707 (2015). doi: 10.1038/ncomms9707; pmid: 26566078
66. S. Shekhar *et al.*, Formin and capping protein together embrace the actin filament in a ménage à trois. *Nat. Commun.* **6**, 8730 (2015). doi: 10.1038/ncomms9730; pmid: 26564775
67. S. Xia *et al.*, Nanoscale architecture of the cortical actin cytoskeleton in embryonic stem cells. *Cell Rep.* **28**, 1251–1267.e7 (2019). doi: 10.1016/j.celrep.2019.06.089; pmid: 31365868
68. R. J. Hu, V. Bennett, In vitro proteolysis of brain spectrin by calpain I inhibits association of spectrin with ankyrin-independent membrane binding site(s). *J. Biol. Chem.* **266**, 18200–18205 (1991). doi: 10.1016/S0021-9258(18)55255-8; pmid: 1833394
69. F. Wernert *et al.*, The actin-spectrin submembrane scaffold restricts endocytosis along proximal axons. *Science* **385**, eado2032 (2024). doi: 10.1126/science.ado2032; pmid: 39172837
70. D. M. Gilligan, R. Sarid, J. Weese, Adducin in platelets: Activation-induced phosphorylation by PKC and proteolysis by calpain. *Blood* **99**, 2418–2426 (2002). doi: 10.1182/blood.V99.7.2418; pmid: 11895774
71. A. Abouelezz *et al.*, Tropomyosin Tpm3.1 is required to maintain the structure and function of the axon initial segment. *iScience* **23**, 101053 (2020). doi: 10.1016/j.isci.2020.101053; pmid: 32344377
72. P. Liu, N. A. Jenkins, N. G. Copeland, A highly efficient recombineering-based method for generating conditional knockout mutations. *Genome Res.* **13**, 476–484 (2003). doi: 10.1101/gr.749203; pmid: 12618378
73. W. Zhao *et al.*, Sparse deconvolution improves the resolution of live-cell super-resolution fluorescence microscopy. *Nat. Biotechnol.* **40**, 606–617 (2022). doi: 10.1038/s41587-021-01092-2; pmid: 34782739
74. B. Huang, W. Wang, M. Bates, X. Zhuang, Three-dimensional super-resolution imaging by stochastic optical reconstruction microscopy. *Science* **319**, 810–813 (2008). doi: 10.1126/science.1153529; pmid: 18174397
75. H. Babcock, Y. M. Sigal, X. Zhuang, A high-density 3D localization algorithm for stochastic optical reconstruction microscopy. *Opt. Nanoscopy* **1**, 6 (2012). doi: 10.1186/2192-2853-1-6; pmid: 25431749
76. N. Chenouard, F. Xuan, R. W. Tsien, Synaptic vesicle traffic is supported by transient actin filaments and regulated by PKA and NO. *Nat. Commun.* **11**, 5318 (2020). doi: 10.1038/s41467-020-19120-1; pmid: 33087709
77. R Core Team, A language and environment for statistical computing (R Foundation for Statistical Computing, 2024); https://www.R-project.org/.

ACKNOWLEDGMENTS

We thank C. Guo and the Gene Targeting and Transgenic Facility at the HHMI/Janelia Research campus for generating the spectrin mNeonGreen cKI mice; the Harvard Center for Biological Imaging and its staff for maintenance of and assistance with the Zeiss ELYRA 7 structured illumination microscope used in this study; L. S. Durán and A. Halpern for assistance with custom microscope hardware; and R. Zhou and J. He for design and testing of spectrin fluorescence fusion protein constructs. **Funding:** We acknowledge funding provided by a postdoctoral fellowship from the Helen Hay Whitney Foundation to E.H. and a postdoctoral fellowship from the Jane Coffin Childs Memorial Fund to N.K. X.Z. is a Howard Hughes Medical Institute Investigator. **Author contributions:** Conceptualization: E.H., N.K., and X.Z. Methodology: E.H., N.K., and X.Z. Software: E.H. and N.K. Validation: E.H. and N.K. Formal analysis: E.H. and N.K. Investigation: E.H. and N.K. Resources: E.H., N.K., and X.Z. Data curation: E.H. and N.K. Writing – original draft: E.H., N.K., and X.Z. Writing – review & editing: E.H., N.K., and X.Z. Visualization: E.H. and N.K. Supervision: X.Z. Project administration: X.Z. Funding acquisition: X.Z. **Competing interests:** The authors declare no competing financial interests. **Data and materials availability:** All data are available in the manuscript or supplementary materials. **License information:** Copyright © 2025 the authors, some rights reserved; exclusive licensee American Association for the Advancement of Science. No claim to original US government works. https://www.science.org/about/science-licenses-journal-article-reuse. This research was funded in whole or in part by Howard Hughes Medical Institute (HHMI), a cOAlition S organization. The author will make the Author Accepted Manuscript (AAM) version available under a CC BY public copyright license.

SUPPLEMENTARY MATERIALS

science.org/doi/10.1126/science.adn6712
Figs. S1 to S16; Tables S1 and S2; Movie S1

Submitted 21 December 2023; resubmitted 2 March 2025; accepted 12 May 2025
10.1126/science.adn6712

Check for

RESEARCH ARTICLE SUMMARY

IMMUNOLOGY

Cysteinyl leukotrienes stimulate gut absorption of food allergens to promote anaphylaxis in mice

Laura R. Hoyt *et al.*

Full article and list of author affiliations: https://doi.org/10.1126/science.adp0240

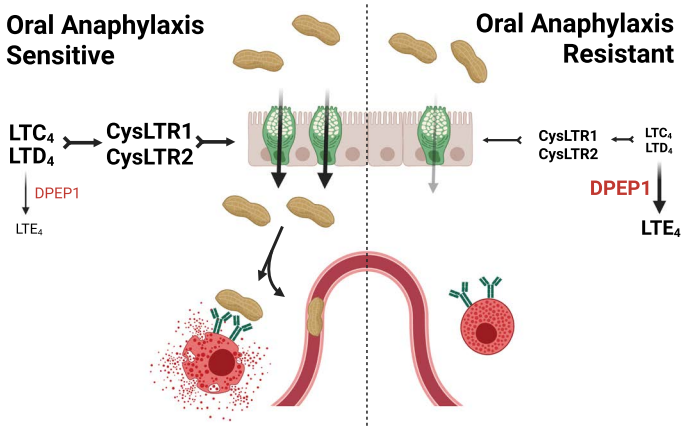
INTRODUCTION: Allergic reactions to food are mediated by cross-linking of preformed food-specific immunoglobulin E (IgE) antibodies bound to tissue mast cells upon allergen exposure. However, some people who have food-specific IgE do not have any allergic reaction to that food and are considered "sensitized tolerant." How this population remains unresponsive to allergens is unclear, but understanding the underlying mechanisms could identify approaches for treating food allergy.

RATIONALE: To identify the genetic causes of a sensitized tolerant state, we studied an unexplained aspect of food allergy in mouse models. With rare exceptions, the commonly used C57BL/6 mouse strain demonstrates anaphylaxis to food allergens when challenged systemically, but not orally, despite robust IgE production, thus potentially modeling a sensitized tolerant state. The intestinal epithelium is composed of tight junctions that allow ions and small molecules to pass through paracellular transport. Proteins are primarily absorbed as amino acids or small polypeptides that are unable to cross-link IgE, which recognize whole epitopes. Therefore, anaphylaxis can only occur when submucosal mast cells encounter minimally digested food allergens; delivery of intact allergens has been shown to occur by transcellular transport through intestinal secretory cells. We thus hypothesized that transcellular allergen transport is genetically regulated and thereby susceptibility to anaphylaxis.

RESULTS: We found that oral anaphylaxis–resistant C57BL/6 mice have gut barriers that are impermeable to intact food allergens relative to susceptible strains such as C3H/HeJ even before allergic sensitization. Resistance correlated with reduced transport of allergens through secretory cells of the small intestine. Using a forward genetic screen of oral anaphylaxis, we identified a resistance gene, *dipeptidase 1* (*Dpep1*), which encodes an enzyme expressed in the intestinal epithelium that catabolizes a cysteinyl leukotriene (CysLT) lipid inflammatory molecule. Although CysLTs are important mediators of allergic responses, a mechanistic connection between CysLTs and food allergen transport is unknown. We found that oral anaphylaxis–susceptible mice had elevated CysLTs in the gut, suggesting impaired DPEP1 enzymatic activity. Indeed, blockade of DPEP1 with cilastatin enhanced allergen absorption in anaphylaxis-resistant mice. Conversely, inhibition of leukotriene synthesis with zileuton reduced allergen absorption and prevented anaphylaxis after oral challenge in susceptible mice.

CONCLUSION: We discovered a mechanism by which CysLTs promote allergen absorption in the gut, thus increasing susceptibility to anaphylaxis after allergen ingestion. This function was distinct from their classical role in mediating anaphylaxis symptoms. Although multiple genetic and environmental factors likely modulate anaphylaxis, our data implicate DPEP1 as one modulator of intestinal allergen absorption in mice. Our work indicates that the intestinal barrier can protect sensitized individuals from experiencing allergic symptoms upon food ingestion, which could be achieved by reducing gut CysLTs with zileuton. This suggests that blocking leukotriene synthesis could be a treatment for food allergies. Moreover, our investigations have advanced the understanding of what regulates oral anaphylaxis in mouse models, paving the way for physiological allergen exposures to be modeled in C57BL/6 genetically modified mice. □

Corresponding author: Adam Williams (adam.williams@northwestern.edu); Stephanie C. Eisenbarth (stephanie.eisenbarth@northwestern.edu) Cite this article as L. R. Hoyt *et al.*, *Science* **389**, eadp0240 (2025). DOI: 10.1126/science.adp0240



Tuning food allergen transport by gut epithelial cells to trigger anaphylaxis. Reduced DPEP1 activity causes leukotriene (LTC_4 and LTD_4) accumulation in the gut, acting on the CysLT receptors 1 and 2 (CysLTR1 and CysLTR2). This promotes food allergen transport through goblet cells to the submucosa and bloodstream, where IgE-loaded mast cells are activated to trigger anaphylaxis. [Figure created with BioRender.com]

IMMUNOLOGY

Cysteinyl leukotrienes stimulate gut absorption of food allergens to promote anaphylaxis in mice

Laura R. Hoyt[1,2], Elise Liu[1,2,3], Eli C. Olson[4,5], Danielle R. Jacobsen[4,5], Emily R. Siniscalco[2,5], Rebecca A. Krier-Burris[4,5], Kara G. Greenfield[4,5], Caleb D. McBride[4,5], Mia M. Alfajaro[1,2], Julien A.R. Amat[1,2], Zhe Zhao[1,2], Lan Xu[1,2], Vivek Philip[6], Aditi Verma[4,5], Slim Fourati[4,5], Donna L. Senger[7,8], Lingdi Zhang[9], Supinda Bunyavanich[9], Sarah E. Glass[10,11,12], Robert J. Coffey[10,11,12], Craig B. Wilen[1,2], Adam Williams[4,5]*, Stephanie C. Eisenbarth[1,2,4,5]*

Food-specific immunoglobulin E (IgE) triggers life-threatening anaphylaxis; however, for unclear reasons, some people with food-specific IgE are asymptomatic upon allergen consumption. We studied strains of mice with different sensitivities to anaphylaxis when orally challenged with allergen to identify possible causes. In resistant C57BL/6 mice, intestinal goblet cells transported less food allergen than did anaphylaxis-susceptible strains, even before allergic sensitization. In a forward genetic screen, resistance was correlated with *dipeptidase 1* (*Dpep1*) variants. DPEP1 is expressed in intestinal epithelium and catabolizes leukotriene D_4 (LTD_4). Blocking DPEP1 with cilastatin, deleting *Dpep1*, or administering LTD_4 orally enhanced allergen transport in resistant mice. Conversely, pretreatment of susceptible mice with a synthesis inhibitor, zileuton, abrogated allergen absorption and oral anaphylaxis, indicating that this could be an approach to treating food allergy.

Food allergy affects millions of children and adults with increasing prevalence and with limited therapeutic options (*1*). The most severe form of food allergy results in systemic and potentially life-threatening anaphylaxis. It is difficult to predict an allergic individual's risk of anaphylaxis upon allergen exposure and to prevent anaphylaxis upon accidental exposure (*2*). Oral immunotherapy is used to treat peanut allergy, but it does not work for all patients and can itself cause anaphylaxis (*1*).

Food-specific immunoglobulin E (IgE) is the central mediator of anaphylactic reactions (*1*); however, some people with IgE to food allergens can ingest these foods without having symptoms, which is called "sensitized tolerance" or "asymptomatic sensitization" (*3*–*7*). Therefore, IgE against food allergens is necessary but not sufficient for anaphylaxis, indicating that other biological factors modify the risk of responding to an allergen. For this reason, oral food challenges remain the gold standard for diagnosing symptomatic food allergy. Understanding the genetic and environmental factors that result in sensitized tolerance could reveal approaches for mitigating anaphylaxis risk in those with symptomatic food allergies.

Because food allergy results from interactions between multiple different environmental and genetic risk factors (*8*), isolating a single factor regulating the allergic response is challenging. Inbred mouse models of food allergy can reveal mechanisms of allergic sensitization and anaphylaxis partly because they have a well-defined genetic composition. To identify the genetic causes of unresponsiveness, we studied an unexplained aspect of food allergy in mouse models. With rare exceptions [i.e., germ-free mice (*9*) and mice genetically modified to enhance interleukin-4 signaling or mast cell numbers (*10*–*13*)], the commonly used C57BL/6 mouse strain demonstrates anaphylaxis to food allergens only when challenged systemically, not orally (*14*–*17*), and despite robust IgE production. Therefore, most studies using conventional wild-type C57BL/6 mice bypass the gut to deliver antigen systemically through either an intravenous or intraperitoneal challenge (*15*, *18*–*26*). This oral anaphylaxis resistance phenotype resembles a sensitized tolerant state in humans. Although C3H/HeJ mice also readily generate IgE, they are rarely used for immunologic studies. This strain was one of the first used for food allergy research (*27*, *28*) because it is susceptible to anaphylaxis after oral challenge in many (*15*, *28*–*36*), but not all (*14*, *37*), research facilities. The cause of oral anaphylaxis susceptibility differences between these strains remains unknown. Using susceptible C3H/HeJ and resistant C57BL/6 strains, we performed a forward genetic screen to identify the potential resistance gene(s) for oral anaphylaxis. This approach revealed an unexpected leukotriene-mediated pathway in the small intestine (SI) that regulates how intact proteins are transported across the gut epithelium to trigger mast cell activation to food allergens and induce anaphylaxis.

Results

Mice resistant to oral anaphylaxis have reduced allergen absorption from the gut

To determine whether oral anaphylaxis resistance is specific to C57BL/6 mice, we cohoused multiple inbred strains of mice for 2 weeks to control for environmental differences between cages and strains and then sensitized the mice with peanut and cholera toxin (PN+CT) by oral gavage once weekly for 6 weeks (Fig. 1A) (*15*). This sensitization protocol induces robust antibody responses, including IgE, to codelivered food allergens. One week after the final sensitization, mice were fasted for 4 hours and challenged with crude peanut extract (CPE) by oral gavage to induce an anaphylactic allergic reaction, which can be measured in mice by tracking a drop in core body temperature of >3°C and symptoms indicative of anaphylaxis (fig. S1A). We confirmed our previous results (*15*) and those of others that C57BL/6 mice are resistant to anaphylaxis (*18*–*26*) after oral peanut challenge (Fig. 1B). By contrast, C3H/HeJ mice and the closely related C3H/HeOuJ strain that has intact TLR4 function were susceptible to anaphylaxis after oral challenge (Fig. 1B). Similarly, a typical strain used in multiple allergy models, BALB/c, also demonstrated susceptibility to oral anaphylaxis (Fig. 1B), consistent with previous work (*11*, *38*–*40*). Therefore, of the strains we tested, only C57BL/6 mice failed to undergo anaphylaxis after oral peanut challenge.

We found that the difference in phenotype between C57BL/6 mice and the other strains was not due to differences in sensitization because all strains had equivalent levels of serum antipeanut IgE, IgG1, and IgA (Fig. 1C and fig. S1B). This suggested that the pathways responsible for sensitization (IgE production) and allergic reaction (anaphylaxis) to allergen challenge can be dissociated. Posttranslational modifications can modulate the ability of IgE to bind to mast cells and trigger degranulation (*41*). To verify that all four mouse strains generated equivalently functional antipeanut IgE, we challenged mice systemically with peanut extract intraperitoneally. In contrast to oral peanut challenge, all strains of mice displayed signs of severe

[1]Department of Laboratory Medicine, Yale University School of Medicine, New Haven, CT, USA. [2]Department of Immunobiology, Yale University School of Medicine, New Haven, CT, USA. [3]Section of Rheumatology, Allergy & Immunology, Yale University School of Medicine, New Haven, CT, USA. [4]The Department Medicine, Division of Allergy and Immunology, Northwestern University Feinberg School of Medicine, Chicago, IL, USA. [5]Center for Human Immunobiology, Northwestern University Feinberg School of Medicine, Chicago, IL, USA. [6]The Jackson Laboratory, Bar Harbor, ME, USA. [7]Lady Davis Institute for Medical Research, Jewish General Hospital, Montreal, PQ, Canada. [8]Gerald Bronfman Department of Oncology, McGill University, Montreal, PQ, Canada. [9]Department of Genetics & Genomic Sciences, Department of Pediatrics, Icahn School of Medicine at Mount Sinai, New York, NY, USA. [10]Department of Cell and Developmental Biology, Vanderbilt University School of Medicine, Nashville, TN, USA. [11]Department of Medicine, Vanderbilt University Medical Center, Nashville, TN, USA. [12]Epithelial Biology Center, Vanderbilt University Medical Center, Nashville, TN, USA.
***Corresponding author. Email: adam.williams@northwestern.edu (A.W.); stephanie.eisenbarth@northwestern.edu (S.C.E.)**

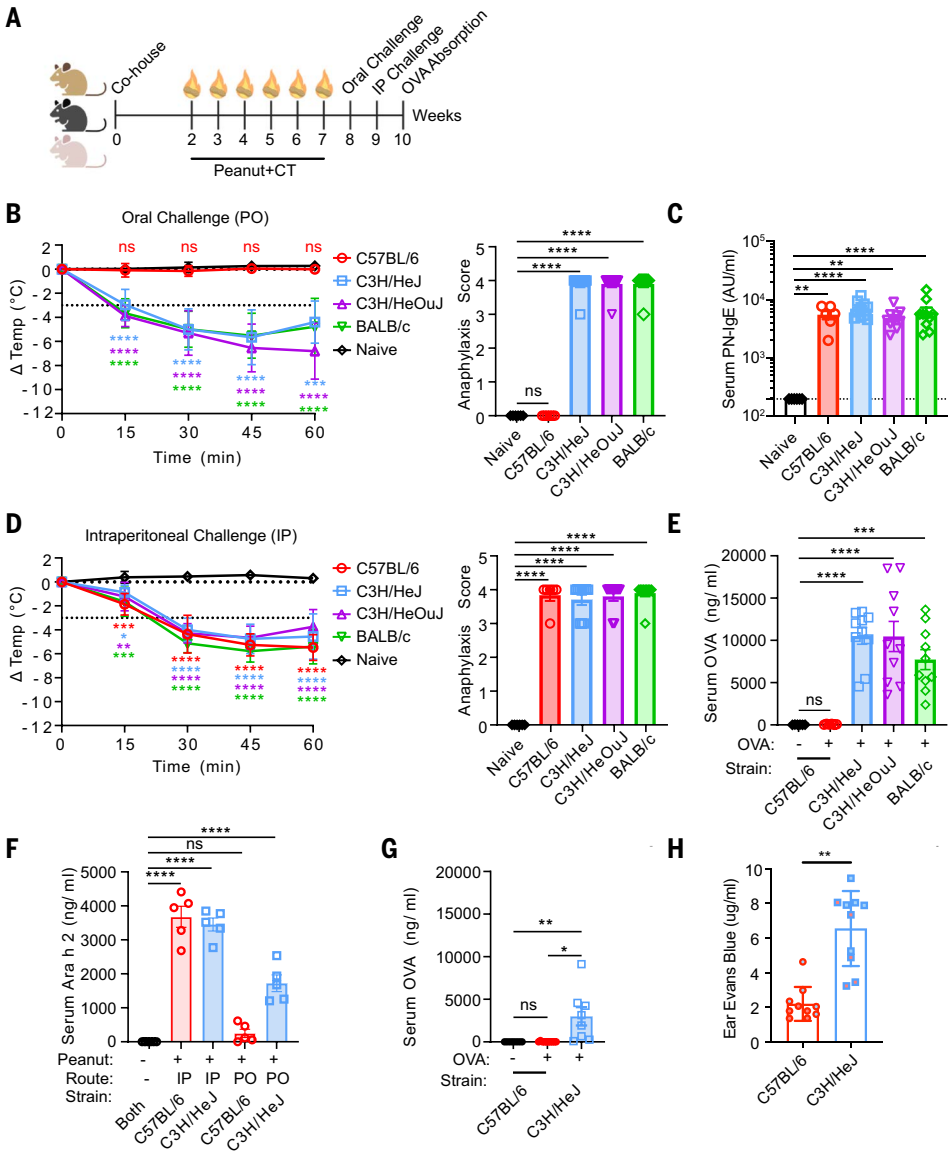


Fig. 1. C57BL/6 mice are resistant to oral peanut challenge, which correlates with decreased gastrointestinal antigen absorption. (**A**) Sensitization model for (B) to (F). C57BL/6, C3H/HeJ, C3H/HeOuJ, and BALB/c mice were cohoused for 2 weeks, and then sensitized with PN+CT orally once weekly for 6 weeks. One and 2 weeks after completion of sensitization, mice were challenged with CPE orally (PO) and intraperitoneally (IP), respectively. On the third week after peanut sensitization, gut permeability to OVA was measured. (**B**) Rectal temperature change over 60 min and anaphylaxis score at 45 min after oral challenge with CPE. Bold dashed line at 0 change and thin dashed line at −3°C indicate cutoffs for the anaphylaxis response. (**C**) Serum peanut (PN)-IgE levels measured by ELISA on the last day of PN+CT sensitization. Dashed line indicates ELISA limit of detection. (**D**) Rectal temperature change over 60 min and anaphylaxis score at 45 min after intraperitoneal challenge with peanut protein. (**E**) Serum OVA levels measured by ELISA 30 min after oral gavage with OVA at week 10. (**F**) Serum Ara h 2 levels measured by ELISA 30 min after intraperitoneal or oral challenge with peanut extract. (**G**) Serum OVA levels measured by ELISA in naïve (unsensitized) C57BL/6 and C3H/HeJ mice 30 min after oral gavage with OVA. (**H**) PCA of orally challenged mice. Naïve C57BL/6 and C3H/HeJ mice were injected with serum from peanut-sensitized C57BL/6 (light red fill) or C3H/HeJ (light blue fill) mice injected into their right or left ears before being challenged 24 hours later with an oral gavage of CPE. Extravasation of Evans blue dye in the ear tissue is shown. Thick dotted lines denote 0°C, and thin dotted line denotes −3°C rectal temperature [(B) and (D)] or the limit of detection (C). For each experiment, groups were compared with a naïve [(B) to (D)], no OVA [(E) and (G)], or no CPE (F) group by one-way ANOVA. For (H), C57BL/6 and C3H/HeJ mice were compared by a Wilcoxon paired *t* test. Points represent individual mice [(B) to (H)]. Error bars represent means ± SD [(B) and (D)] or means ± SEM [(C) and (E) to (H)] for five to 10 mice per group. **P* < 0.05, ***P* < 0.01, ****P* < 0.001, *****P* < 0.0001; ns, not significant. Combined data from three or four independent experiments [(A) to (E) and (G)] or one representative experiment of two [(F) and (H)] are shown.

anaphylaxis to intraperitoneal challenge, as measured by a drop in core body temperature and high clinical anaphylaxis scores (Fig. 1D).

Because bypassing the gut barrier with a systemic allergen challenge led to anaphylaxis in C57BL/6 mice, we tested whether undigested protein transport from the gut to the circulation was impaired (*15*, *42*–*44*). We gavaged mice with ovalbumin (OVA), the predominant allergen found in eggs, and measured serum OVA levels 30 min later. All mice were allergically sensitized to peanut, but not to OVA, and therefore did not have anti-OVA immunoglobulins, which might alter allergen-specific uptake (*45*). C57BL/6 mice displayed reduced systemic OVA absorption relative to oral anaphylaxis–susceptible strains of mice (Fig. 1E), indicating that decreased intestinal absorption of intact food allergens correlated with protection from oral anaphylaxis. For all subsequent experiments, C3H/HeJ mice were used as oral anaphylaxis–susceptible mice.

To directly test whether C57BL/6 mice failed to react to oral peanut challenge because the requisite allergens were not absorbed systemically, we compared the level of Ara h 2 (a primary IgE-targeted peanut antigen) in the blood 30 min after peanut challenge using a method similar to that used in human sera to detect Ara h 6 after peanut consumption (*42*). Mice were sensitized for 6 weeks and then challenged orally and 1 week later intraperitoneally with peanut (fig. S1C). Although C57BL/6 and C3H/HeJ mice had similarly high levels of Ara h 2 in their serum 30 min after intraperitoneal challenge, the same C57BL/6 mice had low levels of serum Ara h 2 relative to C3H/HeJ mice after oral challenge (Fig. 1F).

It has been proposed that food-specific antibodies and allergic inflammation increase allergen absorption from the gut (*45*). Therefore, we tested whether OVA absorption differed in unsensitized C3H/HeJ versus C57BL/6 mice at steady state. Naïve C57BL/6 mice had >100-fold lower intestinal absorption of OVA compared with naïve C3H/HeJ mice (Fig. 1G). To characterize the size of particles capable of traversing the intestinal barrier, we gavaged naïve C57BL/6 and C3H/HeJ mice with nondigestible 4-, 40-, and 70-kDa fluorescein isothiocyanate (FITC)–dextran and measured serum FITC fluorescence 2 hours later (*44*). Like OVA absorption and consistent with our previous findings (*15*), C3H/HeJ mice had increased intestinal uptake of both 4- and 40-kDa FITC-dextran (fig. S2, A and B). Neither strain displayed any intestinal uptake of 70-kDa FITC-dextran (fig. S2C). This suggested

that a homeostatic pathway regulates intact antigen transport of molecules <70 kDa from the gut, which differs in oral anaphylaxis–susceptible versus –resistant mice.

Prausnitz-Kustner reactions, which are induced by the transfer of sera from an allergic patient into a nonallergic recipient followed by oral allergen challenge, suggest that intact allergens are systemically absorbed after ingestion in humans (*46*). We used the same approach to test whether the increased intestinal permeability observed in C3H/HeJ was functionally relevant. We injected pooled sera from peanut-sensitized C57BL/6 or C3H/HeJ mice into either the right or left ear of naïve C57BL/6 and C3H/HeJ mice and challenged with peanut orally 24 hours later to measure passive cutaneous anaphylaxis (PCA). Using an intravenous injection of Evans blue dye to detect vascular leak into the ear as a measure of local mast cell activation, we found that naïve C3H/HeJ mice displayed more dye extravasation into their ears relative to C57BL/6 mice regardless of whether the injected sera were derived from C57BL/6 or C3H/HeJ mice (Fig. 1H). Thus, naïve C3H/HeJ mice absorbed orally delivered antigens into their systemic circulation, which could reach distant sites and induce mast cell degranulation.

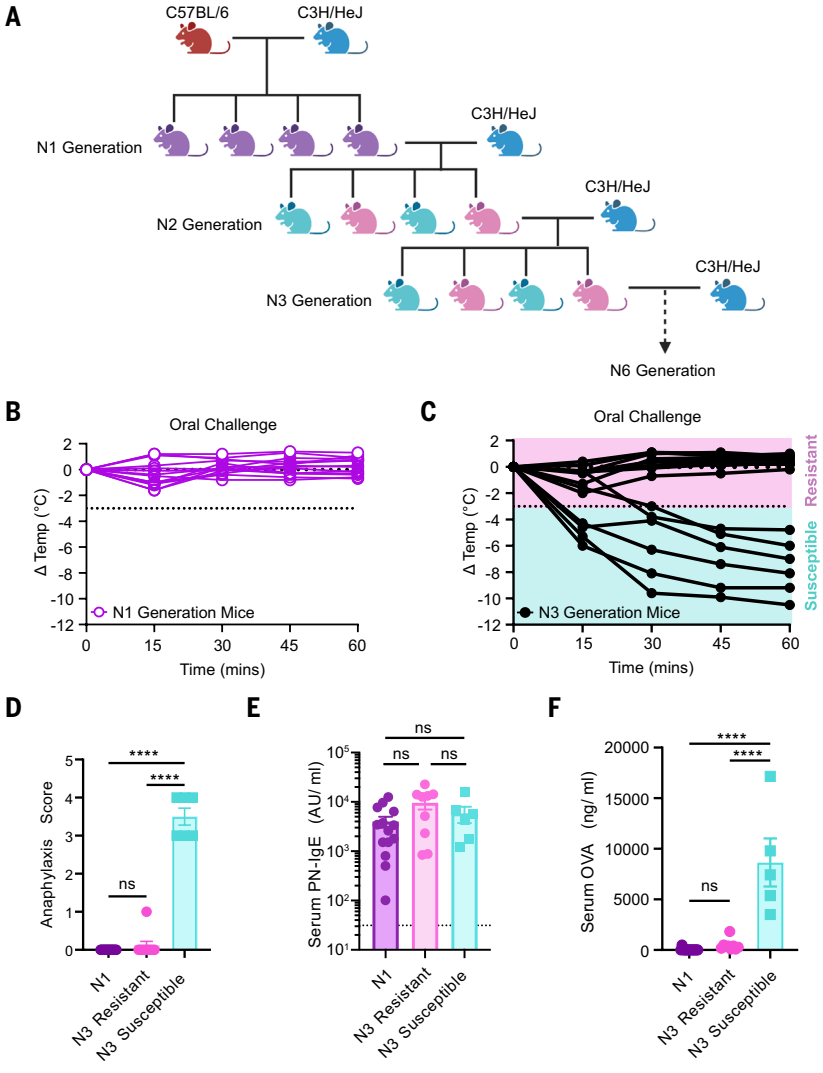


Fig. 2. Resistance to oral anaphylaxis is an autosomal-dominant trait correlated with reduced intestinal permeability to protein antigens. (**A**) Breeding scheme for the forward genetic screen. C57BL/6 (red) and C3H/HeJ (blue) mice were crossed, and oral anaphylaxis–resistant offspring (purple and pink) from each generation were crossed to C3H/HeJ mice. Oral anaphylaxis–susceptible mice are represented in teal. All offspring were allergically sensitized for 6 weeks with PN+CT before oral challenge for phenotyping. (**B**) Rectal temperature change from allergically sensitized N_1 mice after oral challenge with CPE. (**C**) Rectal temperature change from allergically sensitized N_3 generation mice after oral challenge with CPE. A change in core body temperature of <−3°C denotes resistance to oral anaphylaxis (pink), and a change in core body temperature ≥−3°C denotes susceptibility to oral anaphylaxis (teal). (**D**) Anaphylaxis score of N_1 and N_3 generation mice 45 min after oral challenge with CPE. (**E**) PN-IgE levels of N_1 and N_3 generation mice measured by ELISA on the last day of PN+CT sensitization. Dashed line indicates limit of detection of ELISA. (**F**) Serum OVA levels of N_1 and N_3 generation mice measured by ELISA 30 min after oral gavage with OVA. Dotted lines denote 0° and −3°C rectal temperature [(B) and (C)] or the limit of detection (E). Groups were compared by one-way ANOVA [(D) to (F)]. Points represent individual mice [(B) to (F)]. Error bars represent means ± SEM [(D) to (F)] for five to 14 mice per group. *P < 0.05, **P < 0.01, ***P < 0.001, ****P < 0.0001. Combined data from two independent experiments are shown.

Resistance to oral anaphylaxis is an autosomal-dominant trait in mice

Because the oral anaphylaxis–susceptible strains are more closely related to each other than they are to C57BL/6 mice, we hypothesized that a genetic component dictates resistance to oral anaphylaxis. To test this, we created N_1 (backcross one) mice by crossing resistant C57BL/6 mice with susceptible C3H/HeJ mice (Fig. 2A). We sensitized the N_1 generation with PN+CT for 6 weeks and then challenged them orally with CPE. The entire N_1 generation was resistant to anaphylaxis after oral challenge (Fig. 2B). Therefore, we crossed resistant N_1 offspring back to the susceptible C3H/HeJ parental strain and tested for oral anaphylaxis susceptibility after 6 weeks of sensitization with PN+CT (Fig. 2A). We found that ~50% of the N_2 (backcross two) generation were susceptible to oral challenge (fig. S3A). Given that gut microbial communities can influence food allergy susceptibility (*9*, *13*), we performed 16*S* rRNA sequencing of stool bacteria after sensitization to peanut. There were no differences in the stool microbial diversity between oral anaphylaxis–resistant and –susceptible N_2 littermate mice (fig. S3B).

When we crossed an oral anaphylaxis–resistant N_2 mouse with the parental C3H/HeJ oral anaphylaxis–susceptible strain, ~50% (nine of 15) of the N_3 (backcross three) offspring were oral anaphylaxis resistant as determined by hypothermia (Fig. 2C), anaphylaxis score (Fig. 2D), and serum mast cell protease (mMCP-1) levels (fig. S3C). Anaphylaxis susceptibility did not correlate with serum peanut IgE (Fig. 2E). Instead, oral anaphylaxis–susceptible N_3 mice had higher intestinal absorption of OVA than either the N_1 generation mice or the oral anaphylaxis–resistant N_3 generation mice (Fig. 2F). Maximal hypothermia experienced during oral challenge correlated with OVA permeability among individual N_3 mice (fig. S3D). These results indicated that both resistance to oral challenge and low intestinal allergen uptake are autosomal-dominant traits.

Nonhematopoietic cells dictate resistance to oral anaphylaxis

To address whether nonhematopoietic or hematopoietic (presumably immune) cells promote an allergen-impermeable intestinal barrier, we transplanted bone marrow from either resistant C57BL/6 or susceptible C3H/HeJ mice into oral anaphylaxis–resistant N_1 mice (Fig. 3A). Because N_1 mice are a cross of the two parental strains, the bone marrow from each parental strain

was accepted. Transplantation efficacy was validated by H-2K^b (C57BL/6) versus H-2K^k (C3H/HeJ) expression on blood leukocytes (fig. S4, A to C). Tissue mast cells are slowly replicating cells, so they might not be adequately cleared by irradiation. Therefore, we confirmed that lamina propria (LP) mast cells were >90% donor derived in transplanted N_1 mice (fig. S4, D to F).

We sensitized the transplanted mice, along with their nonirradiated N_1 littermates and both C57BL/6 and C3H/HeJ mice as controls, and measured their response to oral and intraperitoneal peanut challenge. Regardless of the bone marrow donor or transplantation status, all N_1 mice failed to respond to oral peanut challenge (Fig. 3B) despite producing peanut IgE (Fig. 3C). Consistent with successful allergic sensitization, all strains of mice responded to intraperitoneal peanut challenge (Fig. 3D). Transplanted N_1 recipient mice, regardless of bone marrow donor, maintained low levels of intestinal OVA absorption that were comparable to nontransplanted N_1 and C57BL/6 mice (Fig. 3E). Therefore, replacement of the hematopoietic and immune cell compartment with bone marrow from susceptible mice did not impart oral anaphylaxis susceptibility. This suggested that an autosomal-dominant gene in nonhematopoietic cells, likely the gut epithelium, prevents allergen absorption in the intestine and subsequent oral anaphylaxis.

Oral anaphylaxis and allergen absorption correlate with reduced dipeptidase 1 activity

We performed a forward genetic screen of anaphylaxis resistance to identify the causal gene(s) for this autosomal-dominant trait by further backcrossing resistant mice to the susceptible parental C3H/HeJ strain. At each generation, we determined which offspring were anaphylaxis resistant after sensitization to select them for the subsequent backcross (Fig. 2A).

We performed quantitative trait locus mapping with Mini Mouse Universal Genotyping Array (MiniMUGA) single-nucleotide polymorphisms (SNPs) to map regions of the chromosome inherited from C57BL/6 versus C3H/HeJ mice in susceptible versus resistant offspring. This approach uses 11,125 of the most informative SNPs from 120 classical inbred mouse lines (data S1). The only region within the genome that was heterozygous for C57BL/6 and C3H/HeJ alleles in most resistant mice and homozygous for C3H/HeJ alleles in all susceptible mice was the distal portion of chromosome 8 between 119 and 130 megabase pairs (Fig. 4A and data S1). Comparison of the annotated genomic sequences identified 44 genes within this region with potential coding sequence differences between C57BL/6 and C3H/HeJ mice (data S2). However, because of the lower quality of the genome-sequencing data currently available for the C3H/HeJ strain, coding differences reported for some genes may have resulted from sequencing errors, so the true number of genes with coding differences is likely lower. We therefore generated RNA-sequencing (RNA-seq) data from jejunal tissue of C57BL/6 and C3H/HeJ mice, which allowed us to rule out mutations in 10 genes based on perfect alignment of C3H/HeJ mRNA to the C57BL/6 reference genome (data S2), leaving 34 genes within this region with potential coding sequence differences between the two strains. We next analyzed publicly available single-cell RNA-seq datasets from human or mouse intestine. Aside from housekeeping genes, *dipeptidase 1* (*Dpep1*) had the highest expression in the intestinal epithelial cells of mice and humans from the candidate gene list (Fig. 4B and fig. S5A). As shown from our RNA-seq data, there were only a limited number of genes within this region that were differentially expressed between C57BL/6 and C3H/HeJ mice (fig. S5A, teal dots), and all were of low abundance relative to *Dpep1* (fig. S5A and data S3). These data suggested that *Dpep1* might be the causal gene responsible for the phenotypic difference in oral anaphylaxis between these strains.

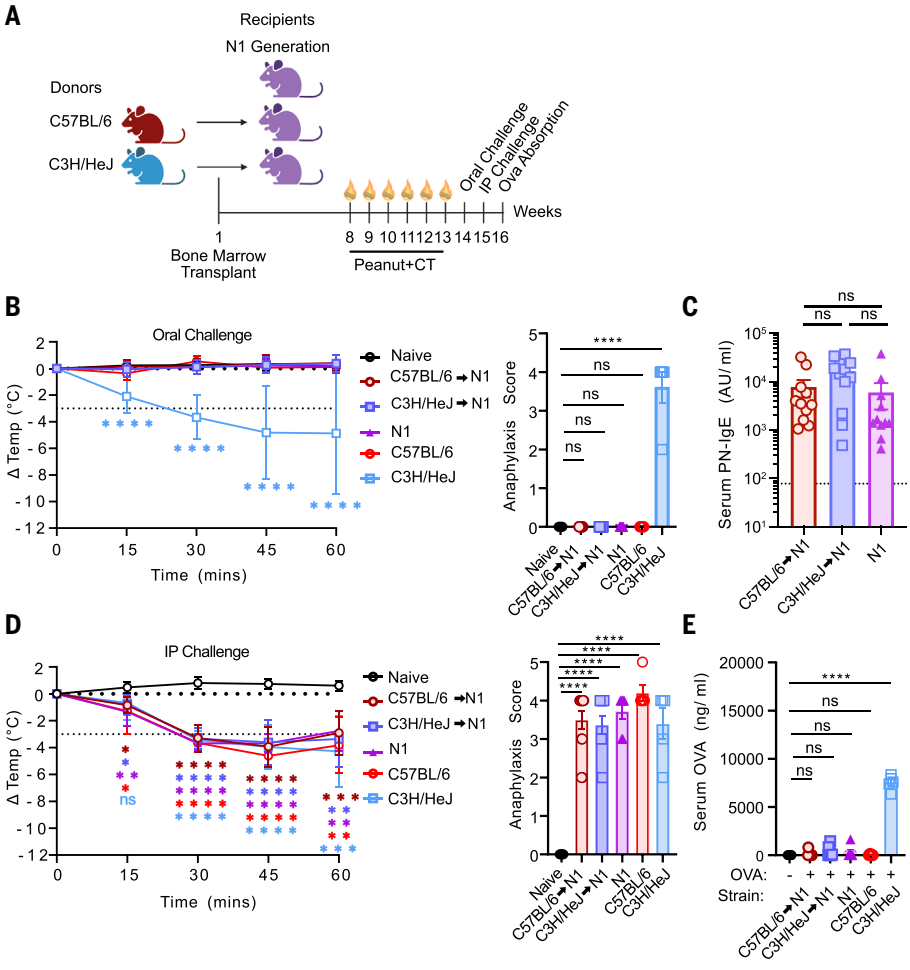


Fig. 3. Nonhematopoietic cells mediate resistance to oral anaphylaxis. (**A**) Model for bone marrow transfer, allergic sensitization, and challenge. (**B**) Rectal temperature change from allergically sensitized C57BL/6, C3H/HeJ, N_1 generation mice, and N_1 recipients of either C57BL/6 or C3H/HeJ bone marrow over 60 min and anaphylaxis scores at 45 min after oral challenge with CPE. (**C**) Serum PN-IgE levels of N_1 generation mice and C57BL/6 and C3H/HeJ bone marrow recipient mice measured by ELISA on the last day of PN+CT sensitization. Dashed line indicates limit of detection of ELISA. (**D**) Rectal temperature change and anaphylaxis scores at 45 min of mice in (B) after intraperitoneal challenge with peanut protein. (**E**) Serum OVA levels of mice in (B) measured by ELISA 30 min after oral gavage with OVA. Dotted lines denote 0° or −3°C rectal temperature [(B) and (D)] or the limit of detection (C). Groups were compared with naïve [(B) and (D)], no OVA (E), or between all groups (C) by one-way ANOVA. Points represent individual mice [(B) to (E)]. Error bars represent means ± SD [(B) and (D)] or means ± SEM [(C) and (E)] for four to 12 mice per group. *P < 0.05, **P < 0.01, ***P < 0.001, ****P < 0.0001. Combined data from two independent experiments are shown.

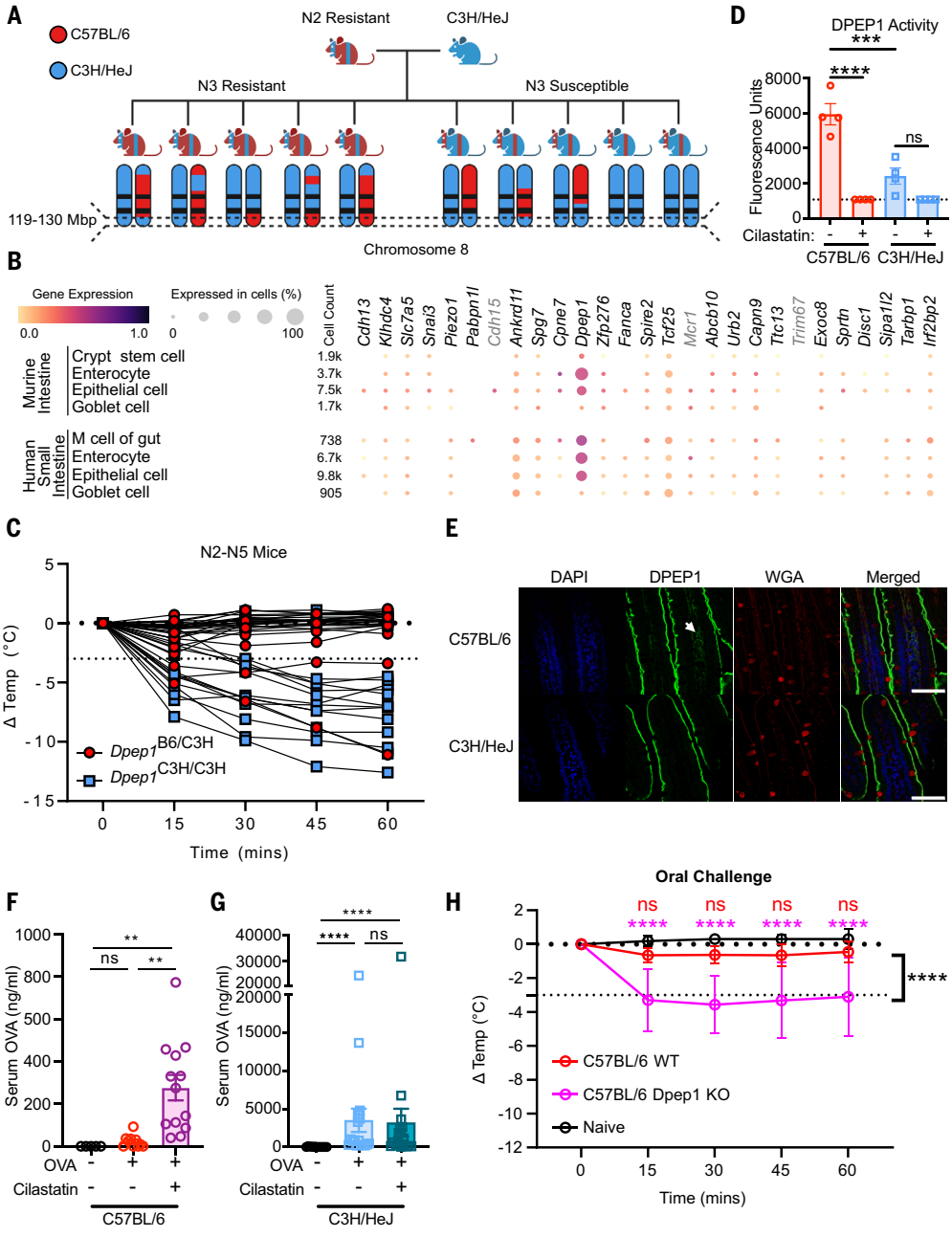


Fig. 4. Allelic variants of *Dpep1* are associated with resistance to oral anaphylaxis. (**A**) MiniMuga SNP analysis of five oral anaphylaxis–resistant and five oral anaphylaxis–susceptible N_3 generation littermates. Diagram of regions of C57BL/6 (red) and C3H/HeJ (blue) DNA within chromosome 8 of each mouse is shown. (**B**) Expression of selected genes from the CELLxGENE scRNA-seq dataset from murine or human intestinal nonhematopoietic cells. Genes with potential amino acid differences between the C57BL/6 and C3H/HeJ strains were selected based on annotated sequence differences and confirmed by RNA-seq analysis. For genes indicated in light gray, there was insufficient read depth to confirm or refute the predicted sequence differences (see the Materials and methods for additional information). (**C**) Rectal temperature change from allergically sensitized $Dpep1^{B6/C3H}$ (red) and $Dpep1^{C3H/C3H}$ (blue) N_2 to N_5 generation mice after oral challenge with CPE. A change in core body temperature of <−3°C denotes resistance to oral anaphylaxis, and a change in core body temperature >−3°C denotes susceptibility to oral anaphylaxis. (**D**) After 2 weeks of cohousing, DPEP1 activity was assessed in 250 μg of jejunal tissue from C3H/HeJ and C57BL/6 mice using a fluorescence-based Gly-D-Phe cleavage assay. To confirm specificity of the assay, samples were treated with or without the DPEP1 enzymatic inhibitor cilastatin before mixing with Gly-D-Phe. Limit of detection (dotted line) was determined with blank wells where lysis buffer was added. (**E**) Representative images of the jejunum sections from naïve cohoused C57BL/6 and C3H/HeJ mice stained with DAPI (blue), wheat germ agglutinin (WGA; red), and anti-DPEP1 (green). Scale bar, 100 μm. Arrow highlights DPEP1 staining within the LP of C57BL/6 mice. (**F** and **G**) Serum OVA levels as measured by ELISA 30 min after OVA oral administration in naïve C57BL/6 (F) or C3H/HeJ (G) mice pretreated intravenously with cilastatin or vehicle 30 min before oral gavage. (**H**) Rectal temperature change from allergically sensitized C57BL/6 $Dpep1^{+/+}$and $Dpep1^{-/-}$ and naïve mice after oral challenge with CPE. Statistics in red and pink represent allergic C57BL/6 $Dpep1^{+/+}$ (red) and $Dpep1^{-/-}$ (pink) compared with the naïve group. Black stars indicate *P* values for C57BL/6 $Dpep1^{+/+}$ compared with $Dpep1^{-/-}$ for each time point. Dotted lines denote 0° and −3°C rectal temperature [(C) and (H)]. For each experiment, groups were compared with each other by one-way ANOVA. Points represent individual mice [(C), (D), (F), and (G)]. Error bars represent means ± SEM [(D), (F), and (G)] or means ± SD (H) for five to 13 mice per group. **P* < 0.05, ***P* < 0.01, ****P* < 0.001, *****P* < 0.0001. Combined data from at least three independent experiments [(C) to (F)] and one representative of two independent experiments [(A) and (B)] are shown. Images in (E) are representative of *n* = 7 C57BL/6 mice or *n* = 7 C3H/HeJ mice.

Dpep1 encodes an enzyme that cleaves leukotriene D_4 (LTD_4) into leukotriene E_4 (LTE_4) (*47*) (fig. S5B); it also has β-lactamase activity and can act as an adhesion receptor for neutrophils (*48*). Leukotriene C_4 (LTC_4) and the downstream metabolites LTD_4 and LTE_4 comprise a group of inflammatory mediators called cysteinyl leukotrienes (CysLTs). CysLTs are produced by mast cells in the setting of allergic inflammation and act to increase vascular permeability, smooth muscle contraction, and mucus secretion (*31*); they can also act as chemoattractants for mast cells and eosinophils (*47*, *49*). Although CysLTs are primarily derived from myeloid cells during inflammation, epithelial cells from the gut and lung, such as tuft cells, can synthesize LTC_4 at steady state (*50*–*52*). LTC_4 is rapidly converted into LTD_4 by the enzyme gamma-glutamyl transpeptidase (GGT) and then to LTE_4 by DPEP1 (*47*, *49*, *53*).

Using a *Dpep1* intronic SNP that was different between C57BL/6 and C3H/HeJ strains, we genotyped all generations of N_2 to N_5 mice from our forward genetic screen, and the *Dpep1* strain of origin correlated well with oral anaphylaxis susceptibility (Fig. 4C): 82.4% of mice that were homozygous for C3H/HeJ *Dpep1* were susceptible to oral challenge, similar to the rate of anaphylaxis in wild-type C3H/HeJ mice. Conversely, 91.3% of C57BL/6:C3H/HeJ *Dpep1*-heterozygous mice were resistant to oral anaphylaxis, strongly implicating the region containing *Dpep1* in mediating anaphylaxis susceptibility to oral challenge.

To understand how DPEP1 might differ between C57BL/6 and C3H/HeJ mice, we investigated whether naïve C57BL/6 and C3H/HeJ mice expressed different amounts of *Dpep1* mRNA in the jejunal RNA-seq dataset; however, both strains expressed equivalent *Dpep1* mRNA (fig. S6A and data S3). Moreover, both strains expressed equal amounts of DPEP1 protein in jejunal homogenates as shown by Western blot (fig. S6B). In the Ensembl genome database, the annotated gene model for *Dpep1* differs between C57BL/6 and C3H/HeJ strains at exon 1 with a different ATG start site, resulting in an alternative predicted N terminal amino acid sequence. However, 5′ rapid amplification of cDNA ends (5′ RACE) using RNA isolated from jejunal tissue revealed similar 5′ start sites in both strains, indicating that the N-terminal amino acid sequence is likely identical between C57BL/6 and C3H/HeJ mice (fig. S6C). Comparing the predicted amino acid sequence revealed a single amino acid difference in the sixth coding exon at position 190 with a His in C57BL/6 (His^{190}) and a Gln in C3H/HeJ (Gln^{190}), which we confirmed by cDNA sequencing and RNA-seq (fig. S6D). BALB/c mice also have a single amino acid difference in DPEP1 from C57BL/6 at position 358, with an Asn in C57BL/6 and C3H/HeJ (Asn^{358}) and a Ser in BALB/c (Ser^{358}), which we confirmed by cDNA sequencing (fig. S6D). In humans, Asn^{358} is predicted to be glycosylated, but because of the lack of a glycosylation motif in the C57BL/6 and C3H/HeJ mouse DPEP1 sequences, this is not likely the case for mice (*54*).

Alignment of the DPEP1 amino acid sequences with 116 mammalian sequences available in the National Center for Biotechnology Information (NCBI) protein database showed that Gln is the predominant amino acid present at position 190 among mammals, including humans and C3H/HeJ mice, whereas Asp is the predominant amino acid present at position 358 among mammals, including humans and C57BL/6 and C3H/HeJ mice (fig. S7, A to C). His^{190} falls outside of the known DPEP1 active site (*55*) and is located on the protein's exterior in a region with an unknown function (fig. S6, E and F). To investigate the nature of the substitution, we analyzed the predicted amino acid sequence using the Eukaryotic Linear Motif resource (*56*), which highlighted that the 190 position lies between two Ser residues, Ser^{189} and Ser^{193}, which are potential sites for phosphorylation by various kinases (data S4). We further evaluated these sites using Phosformer (*57*). In the C3H/HeJ strain, the first of the two Ser residues is adjacent to a Gln residue forming an SQ motif, which is a preferential substrate for phosphorylation by the phosphatidylinositol 3-kinase (PI3K)–related protein kinase (PIKK) family (*58*) (data S5). In both strains, the two Ser residues are followed by a Pro residue, forming an SP motif, a common site for phosphorylation by Pro-directed kinases (*59*) (data S5). Thus, we concluded that it is possible that this region is an important site for the regulation of DPEP1 function and may operate differently between C57BL/6 and C3H/HeJ mice.

We investigated whether DPEP1 activity differed between different mouse strains, which could be attributed either to their sequence or abundance. DPEP1 has several substrates other than LTD_4, including β-lactams and certain dipeptides. Therefore, we used an assay that measures the conversion of the dipeptide Gly-D-Phe into Gly and D-Phe by DPEP1 (*48*). We found higher DPEP1 enzymatic activity in jejunal lysates from naïve C57BL/6 mice compared with C3H/HeJ mice (Fig. 4D). DPEP1 protein abundance, as measured by Western blot, was similar between the mouse strains (fig. S6B). C57BL/6 mice also had higher gut DPEP1 enzymatic activity than BALB/c mice (fig. S8A). Because we used cell lysates rather than isolated proteins, we applied two approaches to confirm that the readout of the assay could be attributed to DPEP1. First, a drug used clinically to block DPEP1 enzymatic activity, cilastatin, abolished activity from gut samples in vitro (Fig. 4D and S8, A and B). Second, gut samples from C57BL/6 mice lacking DPEP1 protein (*48*) due to a frameshift mutation in exon 3 of *Dpep1* (C57BL/6 $Dpep1^{-/-}$ mice) (fig. S6B) showed no detectable enzymatic activity, demonstrating that the assay is specific to DPEP1 (fig. S8B).

Both enzymatic activity and localization can mediate enzymatic function by altering access to relevant substrates. Although both C57BL/6 and C3H/HeJ mice displayed DPEP1 staining by immunofluorescence on the jejunal microvillar membrane, only C57BL/6 mice displayed DPEP1 protein within the LP of jejunal tissues (Fig. 4E); C57BL/6 $Dpep1^{-/-}$ mice had no staining (fig. S9A). Using the same antibody clone, human small intestinal biopsies displayed a staining pattern similar to C3H/HeJ mice, with DPEP1 expression only on the microvillar membrane (fig. S9, B and C). Therefore, both humans and C3H/HeJ mice have Gln at position 190 and both show limited DPEP1 staining in the LP. These data suggested that DPEP1 localizes to the LP only in C57BL/6 mice, possibly due to the His at position 190 in this strain, and there maintains its enzymatic activity to reduce LTC_4 and LTD_4 locally within the villus, thus reducing allergen absorption.

To test this hypothesis, we treated naïve C57BL/6 mice with the DPEP1 enzymatic inhibitor cilastatin intravenously 30 min before oral OVA administration. We indeed observed increased OVA uptake into the systemic circulation in treated C57BL/6 mice (Fig. 4F). Consistent with lower DPEP1 activity in C3H/HeJ mice, cilastatin had no impact on intestinal OVA absorption in C3H/HeJ mice (Fig. 4G). To test whether enhanced DPEP1 activity mediated resistance to oral anaphylaxis in C57BL/6 mice, we sensitized DPEP1-deficient mice (*48*) to peanut. After oral peanut challenge, the core body temperature of C57BL/6 $Dpep1^{-/-}$ mice decreased relative to cohoused C57BL/6 $Dpep1^{+/+}$ mice, which were not different from naïve mice (Fig. 4H). These data indicated that reduced DPEP1 enzymatic activity, either by genetic change or drug inhibition, results in augmented intestinal absorption of protein antigens and anaphylaxis.

CysLTs increase antigen absorption and oral anaphylaxis susceptibility

Because C57BL/6 mice displayed reduced intestinal permeability in the naïve state, we tested whether CysLT levels differed in the SI of naïve C57BL/6 and C3H/HeJ mice by liquid chromatography–tandem mass spectrometry (LC-MS/MS). There was no difference in the amount of the upstream metabolite arachidonic acid between strains; however, C57BL/6 mice had decreased LTC_4 and LTD_4 in their jejunum compared with C3H/HeJ mice (Fig. 5A), consistent with higher DPEP1 enzymatic activity in C57BL/6 mice (Fig. 4D).

To test whether CysLTs directly promote allergen absorption, we coadministered OVA with either vehicle or LTD_4 orally to naïve C57BL/6 and C3H/HeJ mice and found that LTD_4 increased luminal OVA absorption in both strains (Fig. 5B). The enzymatic product of

DPEP1, LTE_4, is more stable than either LTC_4 or LTD_4 and signals primarily through GPR99/CYSLTR3 (*Oxgr1*) in the lung, where it plays an important role in asthma pathogenesis (*47*, *60*, *61*). However, we observed little expression of *Oxgr1* in the gut (data S3). Accordingly, coadministration of LTE_4 did not increase OVA absorption in either strain (fig. S10A), indicating that LTE_4 is not the primary CysLT regulating allergen absorption in the gut. To determine whether exogenous LTD_4 could render C57BL/6 mice susceptible to oral anaphylaxis, we challenged allergically sensitized C57BL/6 mice orally with peanut mixed with either vehicle or LTD_4. To control for the effects of LTD_4 itself on anaphylaxis symptoms, an additional group of allergically sensitized C57BL/6 mice were treated orally with LTD_4 without allergen. Only sensitized C57BL/6 mice treated with both peanut and LTD_4 displayed signs of anaphylaxis, as measured by a drop in core body temperature and anaphylaxis symptoms, indicating that LTD_4 could render C57BL/6 mice acutely susceptible to oral anaphylaxis when coadministered with an allergen (Fig. 5C). These results were consistent with reduced enzymatic function of DPEP1 in C3H/HeJ mice resulting in elevated LTD_4 in the SI, which is sufficient to promote allergen absorption and oral anaphylaxis.

To determine whether CysLTs may be relevant to human food allergy, we examined the expression of genes within the CysLT synthesis pathway in peripheral whole blood cells from patients that were sensitized to peanut after oral peanut challenge to determine whether they had a high threshold (HT) or low threshold (LT) of reactivity to peanut. Although there were no differences at baseline, 4 hours after allergen challenge, whole blood cells from LT food allergic patients up-regulated the expression of arachidonate 5-lipoxygenase (*ALOX5*) and arachidonate 5-lipoxygenase activating protein (*ALOX5AP*), which together mediate the first step in CysLT production. This indicated an increase in systemic CysLT production during symptomatic response to food allergens in LT food allergy (fig. S10B).

Antigen passages in the gut are promoted by CysLTs

Luminal contents can gain access to the systemic circulation through multiple routes. Small molecules can cross through loosened or damaged tight junctions, whereas larger, intact proteins have recently been shown to be transported through goblet cell–associated antigen passages (GAPs) and secretory antigen passages (SAPs) (*62*, *63*). In addition, enterocytes can take up luminal contents, which then become digested within lysosomes, but this route is unlikely to trigger anaphylaxis because IgE recognition requires conformationally intact allergens (*64*) (*43*, *65*).

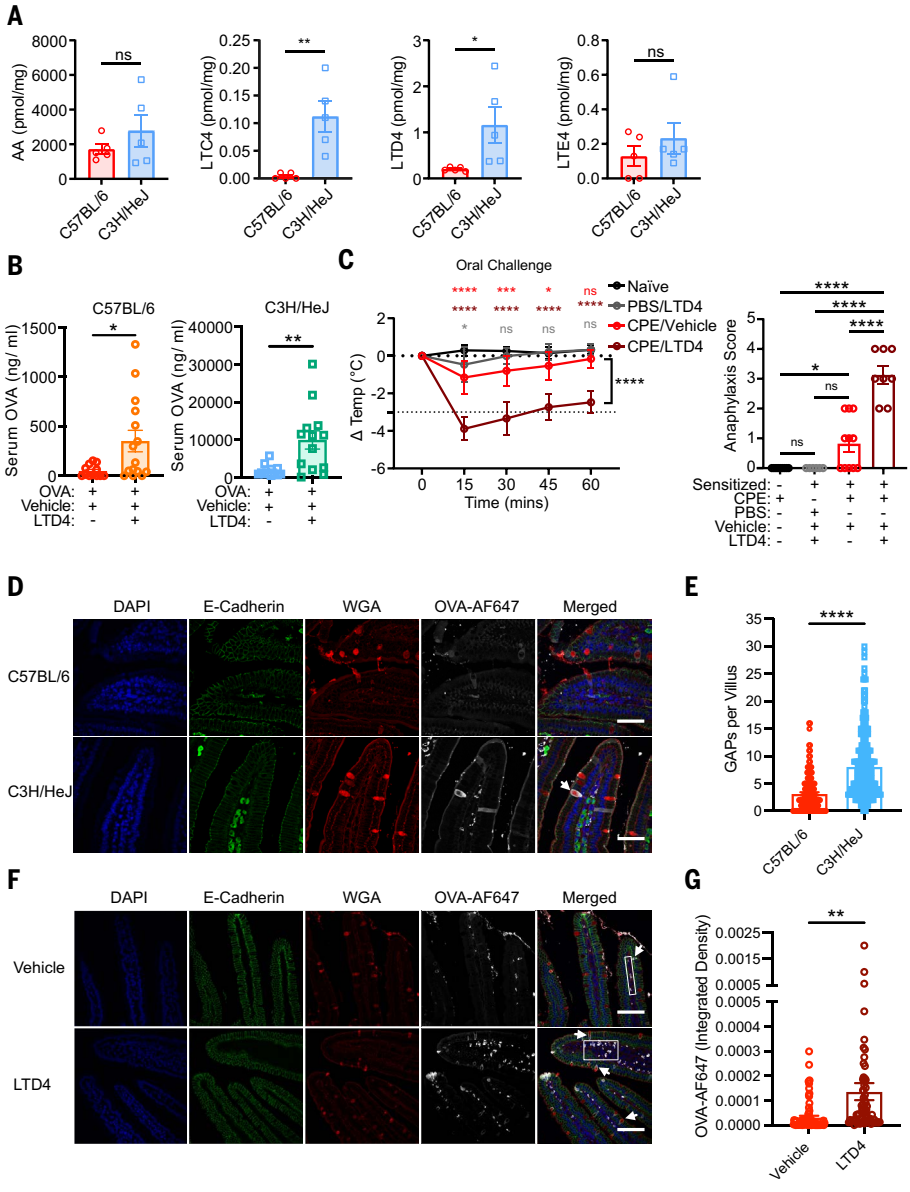


Fig. 5. LTD_4 mediates increased antigen absorption and oral anaphylaxis susceptibility. (**A**) LC-MS/MS measurement of jejunal eicosanoids from naïve C57BL/6 and C3H/HeJ mice. (**B**) Serum OVA levels measured 30 min after oral gavage of naïve C57BL/6 and C3H/HeJ mice with either LTD_4 or vehicle with OVA. (**C**) Rectal temperature change and anaphylaxis score from allergically sensitized C57BL/6 and naïve mice after oral challenge with CPE mixed with LTD_4 or vehicle or with PBS and LTD_4. Statistics in red, maroon, and gray represent allergic C57BL/6 mice treated with CPE + LTD_4, CPE + vehicle, or PBS + LTD_4, respectively, compared with the naïve group. Statistics in black represent allergic C57BL/6 mice treated with CPE + LTD_4 compared with CPE + vehicle for each time point. (**D**) Representative images from the jejuna of naïve C57BL/6 and C3H/HeJ mice gavaged with OVA-AF647 (white) and stained with DAPI (blue), anti–E-cadherin (green), and WGA (red). Scale bar, 50 um. White arrow highlights a representative OVA-AF647 containing GAP. (**E**) Quantitation of the number of OVA-AF647$^+$WGA$^+$ GAPs per villus from (D). (**F**) Representative images from the jejuna of naive C57BL/6 mice gavaged with OVA-AF647 (blue) mixed with vehicle or LTD_4 and stained with anti–E-cadherin (red) and WGA (green). White arrows highlight representative OVA-AF647 containing GAPs. White box indicates a representative area within the LP containing OVA-AF647. (**G**) Quantitation of the OVA-AF647 integrated density of the LP tissue within the villi from (F) using ImageJ software. For each experiment, groups were compared with each other by one-way ANOVA (C) or by an unpaired *t* test with Welch's correction [(A), (B), (E), and (G)]. Dotted lines denote 0° and −3°C rectal temperature (C). Points represent individual mice [(A) to (C)] or individual mouse small intestinal villi [(E) and (G)]. Error bars represent means ± SD (C) or means ± SEM [(A), (B), (E), and (G)] for five to 15 mice per group. **P* < 0.05, ***P* < 0.01, ****P* < 0.001, *****P* < 0.0001. Combined data from three or four independent experiments [(B) and (C)], one representative experiment of two [(A) and (F)], or three independent experiments (D) are shown. Images in (D) are representative of *n* = 10 C57BL/6 mice or *n* = 9 C3H/HeJ mice. Images in (F) are representative of *n* = 5 vehicle-treated and *n* = 7 LTD_4-treated C57BL/6 mice.

To assess how protein antigens are taken up by oral anaphylaxis–susceptible C3H/HeJ mice, we gavaged naïve C57BL/6 and C3H/HeJ mice with OVA-AF647 and harvested jejunal tissue 3 min later for histology. A blinded investigator quantified the number and percentage of GAPs per villus that were actively taking up OVA-AF647. We found that C3H/HeJ mice had more GAPs per villus than C57BL/6 mice, as well as some nongoblet cells transporting OVA-AF647 across the jejunal epithelium (Fig. 5, D and E, and fig. S10C). We sought to determine whether LTD_4 could promote intestinal antigen uptake by gavaging naïve C57BL/6 mice with OVA-AF647 mixed with either vehicle or LTD_4. We found that C57BL/6 mice treated with OVA-AF647 in the presence of LTD_4 displayed more OVA-AF647 fluorescence within the LP jejunal villi relative to vehicle–treated mice (Fig. 5, F and G). This indicated that CysLTs can rapidly induce the uptake of intact luminal antigens.

Inhibition of CysLTs impairs allergen absorption and oral anaphylaxis

We tested whether acutely inhibiting LTC_4 and LTD_4 could prevent anaphylaxis by blocking their receptors or their production. LTC_4 and LTD_4 signal through two G protein–coupled receptors, CYSLTR1 and CYSLTR2, to induce allergic inflammation (fig. S5B) (*47*, *49*, *53*). We treated allergically sensitized C3H/HeJ mice orally with the US Food and Drug Administration (FDA)–approved CYSLTR1 inhibitor montelukast 1 hour before oral challenge. Pretreatment with montelukast did not inhibit susceptibility to oral challenge as measured by hypothermia or clinical anaphylaxis score (Fig. 6A). Montelukast also did not alter intestinal OVA absorption in naïve C3H/HeJ mice (Fig. 6B). Pretreatment of allergically sensitized C3H/HeJ mice with the CYSLTR2 inhibitor HAMI-3379 intraperitoneally 1 hour before oral challenge also did not mitigate oral anaphylaxis relative to vehicle (fig. S11A).

These data suggested that blockade of CYSLTR1 or CYSLTR2 individually might not be sufficient to inhibit allergen absorption. To test for receptor redundancy, we pretreated allergically sensitized C3H/HeJ mice with combined oral montelukast and IP HAMI-3379 or vehicle 1 hour before oral peanut challenge. Dual CYSLTR1/2 inhibition with combined montelukast/HAMI-3379 inhibited oral anaphylaxis, albeit incompletely; these data suggested that both receptors must be inhibited simultaneously to prevent anaphylaxis to oral allergen (fig. S11B).

Given that blocking two independent receptors may be inefficient and that HAMI-3379 is not approved for use in humans, we decided to ablate all CysLT production using the FDA-approved drug zileuton, which inhibits the enzyme ALOX5 upstream of LTC_4 production (*49*, *66*). In mice, a previous study showed that zileuton did not prevent anaphylaxis to peanut; however, in that study, the allergen was administered intraperitoneally, thus bypassing the mucosal barrier (*25*). In our study, pretreatment of allergically sensitized C3H/HeJ mice with zileuton orally 1 hour before oral challenge with CPE completely and dose dependently prevented a drop in core body temperature and clinical symptoms of anaphylaxis relative to vehicle-treated mice (Fig. 6C and fig. S12A). Zileuton pretreatment of allergically sensitized BALB/c mice also

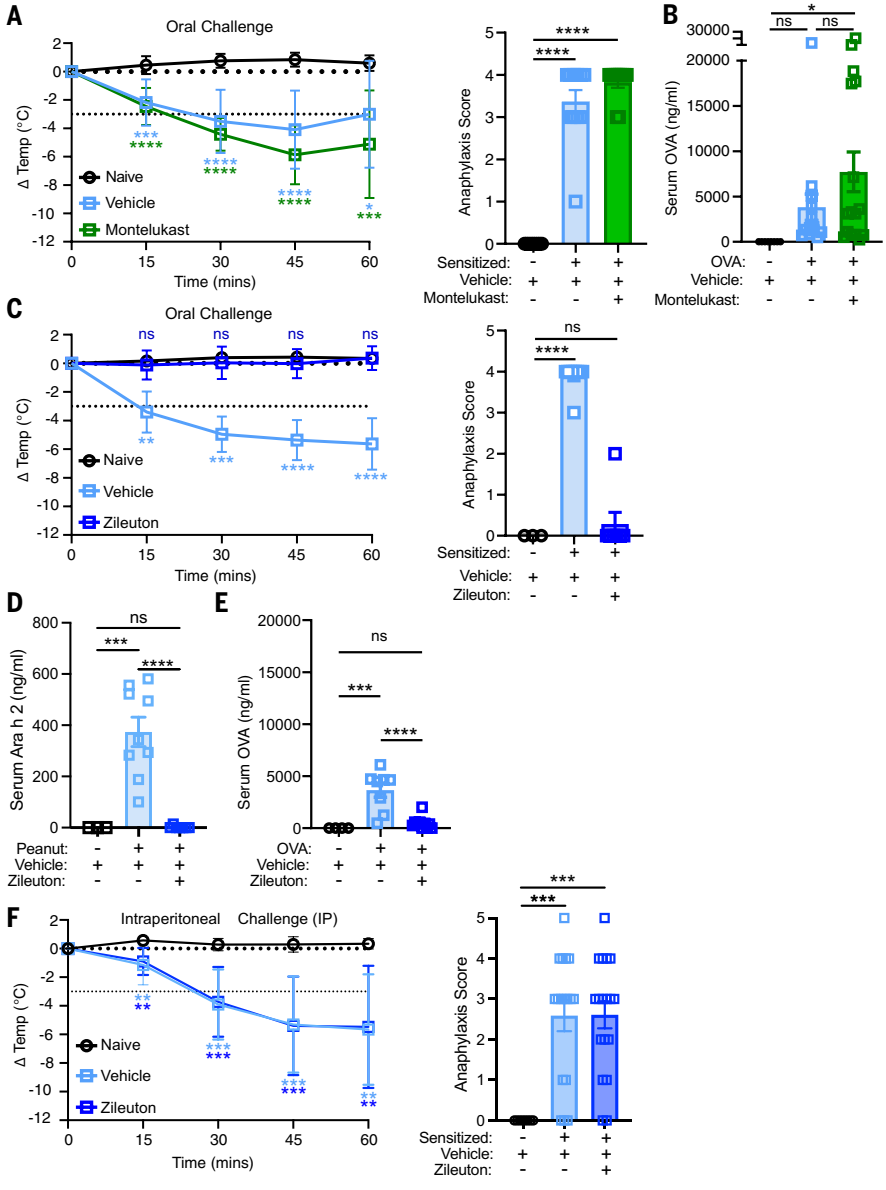


Fig. 6. Inhibition of CysLT production impairs intestinal food antigen absorption and oral anaphylaxis. (**A**) Rectal temperature change and anaphylaxis score of naïve C3H/HeJ mice and allergically sensitized C3H/HeJ mice treated with montelukast or vehicle orally 1 hour before oral challenge with CPE. (**B**) Serum OVA levels by ELISA 30 min after OVA oral gavage of naïve C3H/HeJ mice pretreated for 1 hour with montelukast or vehicle orally. (**C**) Rectal temperature change and anaphylaxis score of naïve C3H/HeJ mice and allergically sensitized C3H/HeJ mice treated orally with zileuton or vehicle 1 hour before oral challenge with CPE. (**D**) Serum Ara h 2 levels measured by ELISA 60 min after oral challenge with CPE. (**E**) Serum OVA levels of naïve C3H/HeJ mice pretreated orally with zileuton or vehicle 1 hour before oral gavage with OVA and measured in serum 30 min later. (**F**) Rectal temperature change and anaphylaxis score of naïve C3H/HeJ mice and allergically sensitized C3H/HeJ mice treated orally with zileuton or vehicle 1 hour before intraperitoneal challenge with peanut. For each experiment, groups were compared with naïve mice [(A), (C), and (F)] or with each other [(B), (D), and (E)] by one-way ANOVA. Dotted lines denote 0° and −3°C rectal temperature [(A), (C), and (F)]. Points represent individual mice [(A) to (F)]. Error bars represent means ± SD [(A), (C), and (F)] and means ± SEM [(B), (D), and (E)] for five to 10 mice per group. *$P < 0.05$, **$P < 0.01$, ***$P < 0.001$, ****$P < 0.0001$. Combined data from three or four independent experiments are shown.

inhibited anaphylaxis to oral peanut challenge (fig. S12B). Zileuton-treated C3H/HeJ mice also displayed lower levels of serum Ara h 2 after oral peanut challenge (Fig. 6D). Similarly, pretreatment of naïve C3H/HeJ mice with a single dose of zileuton 1 hour before allergen exposure reduced their intestinal absorption of OVA (Fig. 6E), indicating that CysLTs acutely augment intestinal antigen absorption both at baseline and during allergic states.

Although C57BL/6 mice were resistant to oral challenge, they were susceptible to systemic challenge (Fig. 1D), which is consistent with the hypothesis that CysLTs only regulate allergen absorption locally in the gut. We therefore predicted that acute blockade of CysLT production with zileuton should not affect the anaphylactic response to allergen administered systemically. To test this, we pretreated allergically sensitized C3H/HeJ mice with zileuton or vehicle 1 hour before intraperitoneal challenge with peanut. In contrast to oral peanut challenge, zileuton pretreatment had no protective effect on either hypothermia or the clinical anaphylaxis scores of intraperitoneally challenged mice (Fig. 6F), which is consistent with previous observations (*25*) and confirms that zileuton's effect on oral anaphylaxis is not due to suppressing symptoms. Therefore, we conclude that CysLTs selectively promote oral anaphylaxis.

Discussion

We discovered an unexpected mechanism by which CysLTs promote allergen absorption in the gut, thus regulating when food allergens can trigger anaphylaxis. We propose that both genetic and environmental factors that affect CysLT-mediated allergen transport across the gut determine whether a sensitized patient will undergo anaphylaxis upon allergen ingestion. Such a mechanism could explain how sensitized tolerant patients avoid anaphylaxis or why some sensitized patients only undergo anaphylaxis when cofactors are present, many of which affect the levels of CysLTs (*67*–*69*). Indeed, factors that increase intestinal permeability in humans have been associated with increased risk of anaphylaxis (*68*–*71*).

Leukotrienes are assumed to function as effector molecules mediating many of the signs and symptoms of an allergic response (*47*, *49*, *53*, *60*). However, the role of leukotrienes in food allergy has been largely dismissed. Indeed, montelukast has been shown to have only modest effects in patients with food allergy (*72*). We propose that leukotrienes establish a setpoint for allergen absorption under homeostatic (nonallergic) conditions, which is distinct from their classic role as the "slow-reacting substances of anaphylaxis." This is consistent with our finding that zileuton prevented anaphylaxis to oral but not systemic peanut challenge and that LTD_4 promotes anaphylaxis when given with allergen but not alone. Our findings also raise the possibility that the lack of allergen avoidance behavior recently reported in sensitized C57BL/6 mice could be due to reduced allergen absorption during feeding because of reduced gut CysLTs (*73*, *74*). The absence of oral anaphylaxis in C57BL/6 mice has hindered progress in understanding the pathophysiology of food allergy. We may now overcome this obstacle by developing food allergy models using physiologic allergen exposures in readily available C57BL/6 genetically modified mice. Future work should also test whether microbial and environmental factors modulate allergen absorption dictated by genetically encoded factors. C3H/HeJ susceptibility to oral anaphylaxis differs between research facilities, suggesting that such modulation is possible.

We postulate that this system may be important to establish oral tolerance to food antigens in the healthy state. However, in the presence of allergic sensitization, amplification of this leukotriene pathway would further enhance food allergen transport to submucosal mast cells, thereby establishing a positive feedback loop for anaphylaxis. Indeed, we observed increased allergen transport in sensitized mice compared with naïve mice, which was accompanied by increased intestinal mast cells (*11*), a major producer of CysLTs (*53*), and was previously correlated with oral anaphylaxis and intestinal permeability (*75*, *76*). Recent work demonstrated that gut-resident mast cells are skewed toward CysLT, rather than histamine, production (*77*). Therefore, mast cells during homeostasis, and perhaps in response to their environment, could dynamically regulate allergen sampling through CysLT production.

Although multiple genetic and environmental factors likely modulate the anaphylactic response (*30*, *37*), our data implicate DPEP1 as a major modulator of intestinal allergen absorption in mice, with C57BL/6 polymorphisms in *Dpep1* correlated with reduced gut LTC_4 and LTD_4, decreased intestinal allergen uptake, and resistance to oral anaphylaxis. Work studying the pharmacokinetics of imipenem and meropenem (which are metabolized by DPEP1) in humans indicated that there is a range of DPEP1 enzymatic activity in the human population, but that DPEP1 activity is relatively stable over time within individuals (*78*, *79*). *DPEP1*-coding variants are rare in the human population, yet common noncoding variants are associated with altered *DPEP1* expression levels and could potentially contribute to susceptibility to anaphylaxis in some people.

Absorption into the blood of undigested proteins, including food and even enzymatically active clotting factors, after ingestion in healthy subjects has been recognized since the early 1900s (*46*, *80*). Intact food allergens can be detected in the blood and skin within 30 min after ingestion in ~80% of healthy adults and children (*46*, *81*–*84*). The kinetics of OVA presence in the blood of C3H/HeJ mice that we observed were very similar to published human data (*15*, *42*, *81*). We showed that both C3H/HeJ mice and a reference human genome encode Gln at position 190 of DPEP1, and both have an absence of DPEP1 staining in the small intestinal LP. We also observed that allergen transport is enhanced in mice after allergic sensitization, similar to a study in peanut-allergic patients showing augmented absorption of peanut allergens into the sera relative to nonallergic controls after oral challenge (*42*). In children with a suspected milk allergy, those with symptoms after oral challenge had more milk protein in their blood than the asymptomatic subset (*85*). Future work will determine how the human gut transports allergens in response to CysLTs.

A disrupted barrier hypothesis has been proposed as a mechanism mediating food allergen sensitization (*9*, *37*, *86*), yet most investigations focus on a "leaky gut/epithelium," which typically refers to impaired tight junctions between enterocytes allowing enhanced paracellular permeability. However, previous work demonstrated that intact food allergens are transcellularly transported from the gut lumen through GAPs and related SAPs (*63*, *65*, *87*). The size limitation of 70 kDa for luminal absorption that we identified is very similar to those reported for GAPs (*62*). We now show that the ability of these secretory cells to take up intact food allergens and transport them to the submucosa is augmented by CysLTs. An unexpected aspect of allergen transport that we observed was how fast it could be modified. Either blockade of DPEP1 or preventing CysLT production with zileuton affected allergen transport and anaphylaxis within hours, suggesting a finely tuned and environmentally responsive molecular regulation of allergen sampling.

The most important implication of our work is the potential use of an FDA-approved drug to prevent allergic reactions to food by inducing a sensitized tolerant state. A single dose of zileuton, an ALOX5 inhibitor that blocks all CysLT production (*66*), but not montelukast, which only blocks one of three CysLT receptors, was sufficient to inhibit intestinal allergen transport and prevent anaphylaxis after oral food challenge. Consistent with our proposed mechanism of action, zileuton did not inhibit anaphylaxis when the allergen was administered systemically, bypassing absorption through the gut. Given that the pathway we discovered is operational at steady state, it is plausible that low levels of CysLTs control allergen absorption, and therefore small reductions in CysLTs might be sufficient to stop allergen uptake. Such a drug could provide an acute preventative therapy for sensitized patients at risk of anaphylaxis during accidental or therapeutic allergen exposure.

Materials and methods

Mice

Age- and sex-matched 6- to 12-week-old mice were kept on peanut- and egg-free Teklad Global 18% Protein Rodent Diet (2018S, Harlan laboratories). Mice we housed in cages with no more than 5 mice per cage on a 12-hour light-dark cycle and were provided with nestlets for enrichment. Mice were euthanized with 100% isoflurane followed by cervical dislocation. WT C57BL/6N mice were purchased from the National Cancer Institute (Charles River Laboratories), C3H/HeJ, C3H/HeOuJ and BALB/c mice were purchased from The Jackson Laboratory (JAX). C57Bl/6 *Dpep1*$^{-/-}$ Insert C mice were kindly donated by Dr. Donna L. Senger at McGill University (*48*). C3H/HeJ mice from JAX were crossed with C57BL/6N mice. Resulting N_1 mice and oral anaphylaxis resistant N_2-6 mice were then backcrossed for 6 generations with wildtype C3H/HeJ mice to generate C3H/HeJ mice that were a mix of both resistant and susceptible to oral anaphylaxis. Genotypes of mice were ascertained using MiniMuga SNP Analysis (Transnetyx) and primers F-5′ CAAACCTGTGCCTTTATCCATTCAGTA 3′ and R-5′ CCACGGAATGGGCAGGAT 3′ with probes differentiating between C57BL/6N (5′-CCACCCACTCTGTACCT-3) or C3H/HeJ (5′-CACCCACCCTGTACCT-3′) Dpep1 target SNP rs49721117 which is A in C57BL/6N and G in C3H/HeJ mice present in intron 2 of Dpep1. Before each experiment, mice were cohoused such that at least one mouse of each genotype was present in each mouse cage. Female mice were used for all experiments using C57BL/6, C3H/HeJ, C3H/HeOuJ and BALB/c mice. A mix of male and female littermates were used for any experiments using backcrossed mice (N_2 to N_5 generations). All protocols used in this study were approved by the Institutional Animal Care and Use Committee at the Yale University School of Medicine and Northwestern University Feinberg School of Medicine.

MiniMUGA SNP analysis

Using a custom R script, we obtained genotype calls for each of the 10 N_3 (C3H/HeJ × C57BL/6NJ) samples across each MiniMuga marker. For each of the 11,125 markers on the array, genotype calls were classified as CC (homozygous C3H/HeJ), BC (heterozygous, C57BL/6NJ, C3H/HeJ) or BB (homozygous C57BL/6NJ). Only informative (3444) and segregating (1125) markers were used in subsequent analyses. For each of these markers, we calculated the frequency of genotypes that were either susceptible or resistant.

Immunization and challenge

Six- to 8-week-old mice were immunized weekly for 6 weeks by oral gavage with 5mg ground blanched peanut (Western Mixers Produce & Nuts) with 10 μg cholera toxin (List Biologicals) in 200 μl of 0.2 M sodium bicarbonate buffer per mouse. After 6 weeks of immunization, mice were rested for at least one week, with 2 weeks being optimal, before oral or IP challenge, typically performed in the afternoon. Mice were challenged orally with 800 μl of homemade CPE (CPE at 70 to 80 mg/ml peanut protein; see method below) in 0.6 to 1 M sodium bicarbonate buffer resulting in ~60 mg of peanut protein per mouse. For intraperitoneal challenge, mice were given either 500 μg purified peanut protein (Greer) in 200 μl of phosphate-buffered saline (PBS) or homemade CPE (see method below) diluted 1:10 in PBS and injecting 200 μl (resulting in 1.4 to 1.6 mg of peanut protein per mouse). Rectal temperature was measured every 15 min for up to 60 min, clinical symptoms scores were assessed at 45 min as described previously (*15*), and sera were collected for analysis 1-hour post-challenge. Mice were excluded from analysis if they experienced visible aspiration of orally gavaged CPE, with bubbles of liquid visible from their nose, to exclude the confounding impact of material absorbed through the respiratory epithelium. In all graphs, a bold dashed lines at 0° change indicates the expected response in naive mice and the thin dashed line at −3° indicates cutoff for anaphylaxis response (some temperature variability is expected due to the procedure itself without contribution from an immune reaction).

For experiments using LTD_4 (Cayman Chemicals), LTD_4 (2000ng) or vehicle (2.5% ethanol) was mixed with 800 μl of (70-80mg/ml peanut protein) CPE or 800 μl of PBS immediately before gavage. For experiments using zileuton (Cayman Chemicals) or montelukast (Cayman Chemicals), zileuton (25-100mg/kg) or montelukast (10mg/kg) or vehicle were administered by oral gavage in 200 μl in 0.5% methylcellulose 1 hour before challenge. For experiments using HAMI-3379 (Cayman Chemicals), HAMI-3379 (0.4mg/kg) or vehicle (1% EtOH) were given by IP injection in 200 μl of PBS 1 hour before oral challenge. For optimal resuspension of zileuton in 0.5% methylcellulose, samples were sonicated using a probe sonicator.

Making of CPE

CPE was made fresh before each challenge. Twelve grams (50% protein by weight) of defatted unroasted, unsalted peanut powder (Crazy Richard's) was added to a 50 ml conical tube and mixed with 25 ml of freshly made 0.6 to 1 M sodium bicarbonate solution. This solution was allowed to sit for 45 min at room temperature (RT), with stirring every 15 min. Peanut mixture was spun at 2000*g* for 30 min. The liquid phase was removed and saved, and the remaining peanut solids were spun for an additional 15 min at 2000*g*. The second liquid phase was removed and added to the previous liquid phase. This resulted in 70 to 80 mg/ml (by BCA assay) of peanut protein.

Serum collection

Serum was collected after 6 weeks of peanut sensitization and after oral challenge. Collected blood was incubated at RT for 1 hour and the resulting clot removed. For OVA gut permeability experiments, serum was spun down immediately after collection to prevent hemolysis and OVA degradation. Samples were centrifuged for 10 min at 1500*g* at RT and sera were collected and stored at −80°C before analyses.

Gut permeability to ovalbumin analysis

A 100 mg/ml solution of OVA (Sigma A5503) was prepared in sterile PBS without filtration. Mice were fasted for 4 hours, and each mouse was then administered 800 μl of the OVA solution by oral gavage. 30 min after OVA administration, mice were bled, and blood was processed immediately and frozen to avoid OVA degradation. Mice were excluded from analysis if they experienced visible aspiration of orally gavaged OVA, with bubbles of liquid visible from their nose, to exclude the confounding impact of material absorbed through the respiratory epithelium. OVA levels in serum were detected by ELISA (see below). For experiments using LTD_4 and LTE_4 (Cayman Chemicals) with OVA administration, leukotrienes were kept on dry ice and 200ng of either LTE_4 or LTD_4 in ethanol or an equivalent volume of ethanol was spiked into 800 μl OVA/PBS immediately before gavage. For experiments using cilastatin (Cayman Chemicals), 200 μl of cilastatin (500 mg/kg) or vehicle (10% DMSO/PBS) was administered by retro-orbital injection 30 min before OVA gavage. For experiments using zileuton or montelukast, zileuton (100 mg/kg) or montelukast (10 mg/kg) or vehicle were administered by oral gavage in 200 μl in 0.5% methylcellulose 1 hour before OVA administration.

Gut permeability to FITC-dextran analysis

Naïve C3H/HeJ and C57BL/6 mice were cohoused for at least 2 weeks before experimentation. Mice were fasted for four hours, then each mouse was administered 10 mg of FITC-dextran (4-, 40-, or 70-kDa) (Sigma) in 300 μl of 0.5% methylcellulose (Sigma). Two hours after FITC-dextran administration, mice were bled, and serum was collected. Serum FITC emission was then detected in a Gemini EM Microplate Reader (Molecular Devices) with an excitation at 485nm and detection at 538 nm. Fluorescence levels of sera from 3 C57BL/6 and 3 C3H/HeJ mice that had received vehicle alone was averaged to determine the baseline level of serum autofluorescence. Samples were excluded if the serum had visible hemolysis (defined as visibly red

serum), as heme increases the background of FITC fluorescence. Calculated values were determined using a FITC-dextran standard diluted in PBS.

Enzyme-linked immunosorbent assay

Serum samples were analyzed by ELISA for measurement of peanut-specific antibodies, serum OVA, serum Ara h 2, or serum mMCP-1.

For peanut-specific antibodies, 20 μg/ml peanut protein (Greer) in carbonate buffer was coated on 96-well Maxisorp plates (Thermo Fisher Scientific) overnight at 4°C. Plates were blocked with 1% BSA in PBS at RT for 1-hour followed by the addition of serially diluted serum samples with a 2-hour incubation at 37°C. Peanut-specific antibodies were detected with horseradish peroxidase (HRP)–conjugated goat anti-mouse IgE, IgG1, or IgA (Southern Biotech) antibodies at 37°C. Anti-peanut IgE was obtained from pooled serum supernatant from hyper-immunized mice and used as standards, represented as arbitrary units assigned to ELISA standards (AU)/ml.

For detection of serum OVA, plates were coated with mouse anti-chicken ovalbumin capture antibody (TOSGAA1, BioLegend, 1:500 in carbonate buffer) at 4°C overnight. Plates were blocked in 2% BSA/0.05% Tween 20/PBS (blocking buffer) for 2 hours at RT. Serum (diluted 1:20 in blocking buffer) and OVA standard (OVA solution in PBS diluted to 100 ng/ml in blocking buffer) were serially diluted down the plate in blocking buffer and incubated for 1 hour at RT. Plates were washed and incubated with mouse anti-chicken ovalbumin detection antibody (F2-3.58, Bio X Cell, 1:770 in blocking buffer) for 1 hour at RT, washed 4x and incubated with HRP-conjugated goat anti-mouse IgG1 (Southern Biotech, 1:6000 in blocking buffer) for 30 min at RT before washing and detection with stabilized chromogen tetramethylbenzidine (Life Sciences). Reaction was rapidly stopped by addition of 3N HCl and read at OD 450 on a microplate reader (Molecular Devices).

Serum Ara h 2 and mMCP-1 were measured by a kit (InBio and Invitrogen respectively) according to the manufacturer's instructions.

Peripheral blood mononuclear cell isolation

Blood was collected by retro-orbital bleed into 200 μl of 1mM EDTA/PBS. Red blood cells were lysed by the addition of H_2O for 30 s, followed by an equal volume of 2× PBS. Cells were washed and resuspended in 2% fetal bovine serum (FBS) in PBS containing EDTA (5 mM) for staining.

Isolation of LP mast cells

All steps were performed using RPMI media supplemented with 1% penicillin and streptomycin, 1% L-Gln, 25 mM Hepes, 1× nonessential amino acids, 1× Sodium Pyruvate, and 50 μM β-mercaptoethanol ("Serum-free RPMI"). Additional reagents were added to the media at specific steps noted below. After harvest, the SI was removed by cutting 1mm from the stomach and 1 mm above the cecum. The SI was cut open longitudinally for removal of fecal matter through repeated washing in Hanks balanced salt solution. While processing subsequent samples, the cleaned intestine was stored in RPMI with 10% FBS on ice. After cleaning, each SI was cut into 1- to 2-cm pieces and placed into a conical flask containing RT serum-free RPMI with added 3% FBS, 5 mM EDTA, and 0.145 mg/ml dithiothreitol. The samples were stirred at 600 rpm at 37°C in an incubator with 5% CO_2 for 20 min. The SI pieces were then washed thrice with 30 s of vigorous shaking in Serum-free RPMI with 2 mM EDTA. Between each wash, the medium was poured through a strainer and discarded along with the epithelial and intra-epithelial lymphocyte fraction, and the remaining SI pieces were collected into fresh medium. A final wash was performed using RT serum-free RPMI with no additives and samples were washed through a clean strainer. Subsequently, the SI was cut into fine pieces before incubation with stirring, in the same conditions as previous step, in 10 ml of serum-free RPMI medium with 1 mg/ml collagenase IV (Worthington Biochemical #LS004189) and 0.05% DNase I (Sigma-Aldrich #D5025). After 30 min of digestion, the reaction was stopped with 10ml cold Serum-free RPMI with 3% FBS. The sample was then ground through a 70-μM cell strainer with the plunger of a 3-ml syringe before centrifugation at 450*g*. The pellet was then resuspended and filtered again through a 40-μM cell strainer before centrifugation at 450*g*. Enrichment of lymphocytes was performed through separation of cells using a 30% Percoll gradient. Centrifugation was performed at 730*g* (acceleration: 4, deceleration: 2 at 20°C). The resulting pellet contained LP cells.

Bone marrow transplantation

Six- to 8-week-old N_1 (C57BL/6 × C3H/HeJ) mice were irradiated with two doses of 600 rad 3 hours apart. Two hours after the second irradiation, 1×10^6 bone marrow cells from naïve C57BL/6 or C3H/HeJ donor mice were adoptively transferred by IV injection into irradiated recipient mice. All experiments with bone marrow transplanted mice were performed 8 weeks after bone marrow transplant to allow cellular reconstitution. N_1 generation littermates were left unirradiated and used as controls.

H-2K analysis by flow cytometry

PBMCs were incubated with a fluorochrome-conjugated antibody cocktail containing anti-mouse H-2K^k (AF3-12.1, BD OptiBuild), H-2K^b (AF6-88.5, BioLegend), and CD16/32 (2.4G2, BD Pharmingen) for 30 min at 4°C. All antibodies and dyes were purchased from BioLegend unless otherwise indicated. Flow cytometry was performed on a Cytoflex (Beckman Coulter) flow cytometer and analyzed by FlowJo software (Version 10.8.0, TreeStar). LP mast cells were incubated for 20 min at RT in surface-staining antibodies anti-mouse CD45, c-Kit, FcεRI, IgE, H-2K^k, H-2K^b, CD4, CD8, CD19, CD16/32, and Live/Dead (Zombie NIR) diluted in 10% FBS 1mM EDTA in PBS and were washed after staining by centrifugation at 450*g* for 5 min. Cells were fixed using the BD Cytofix/Cytoperm Fixation and Permeabilization Kit (BD Bio Cat# 554714) and washed by centrifugation at 620*g* for 5 min. Flow cytometry data was acquired on a CytoFLEX LX Flow Cytometer (Beckman Coulter) and analyzed with FlowJo v10.10.0.

Eicosanoid quantitation by mass spectrometry

Jejunal segments from naïve C57BL/6 and C3H/HeJ mice were collected immediately distal to the first Peyer's Patch and snap frozen. Targeted eicosanoid quantification was carried out at the UCSD Lipidomics Core. Briefly, eicosanoids were purified using strata-x polymeric reverse-phase columns (8B-S100-UBJ Phenomenex), reconstituted in 50 μl of buffer A (63% H20, 37% ACN, 0.02% acetic acid), and analyzed by reverse-phase ultraperformance liquid chromatography with mass spectrometry using a Sciex 6500 Qtrap mass spectrometer using previously described methods (*88*). Eicosanoid concentrations were then normalized to tissue weight.

Rapid amplification of cDNA ends

RNA was extracted from murine jejunum tissue using the RNeasy Mini kit (Qiagen). 5′ first-strand cDNA synthesis from the extracted RNA was performed using the SMARTer RACE 5′/3′ Kit (Takara Bio). RACE was performed as per. SMARTer RACE 5′/3′ Kit manufacturer instructions using a *Dpep1*-specific primer with a sequence of 5′-GATTACGC CAAGCTTCACAGCGGCTTTGGCACCTCCGTG-3′ (Takara Bio). RACE products were run on a 1.5% agarose gel and DNA from bands was extracted using the Nucleospin Gel and PCR Clean-Up Kit (Takara Bio). Gel-purified RACE products were combined with the linearized pRACE vector and the In-Fusion Snap Assembly Master Mix according to SMARTer RACE 5′/3′ Kit instructions (Takara Bio). The product of this reaction was used to transform Stellar Competent Cells using Stellar Competent Cells Protocol PT5055-2 (Takara Bio). Transformations were plated on LB Agar plates with 100 μg/ml Ampicillin, 119 μg/ml IPTG, and 80 μg/ml X-GAL (Molecular Toxicology, Inc) and incubated

at 37°C overnight. Individual colonies were picked and grown in LB with 100 μg/ml ampicillin at 37°C, 160 RPM overnight. Plasmid DNA was isolated using the ZR Plasmid Miniprep-Classic Kit (Zymo Research) and sequenced by Plasmidsaurus. The *Dpep1* sequence identified within the plasmid was aligned to the murine *Dpep1* sequence using UCSC's DNA BLAST-Like Alignment Tool (BLAT). RACE-ready cDNA synthesized from extracted C57BL/6 and C3H/HeJ RNA was also used to sequence a portion of *Dpep1* exon 6 that was reported to contain an SNP between the strains. cDNA was amplified using polymerase chain reaction (PCR) (forward primer: 5′-CTAATACGACTCA CTCGACAACTGGCTTGTGGAC-3′, reverse primer: 5'-GATTACGCCAA GCTTTCATGACACCCAAGCGGTTC-3′) and purified using the Nucleospin Gel and PCR Clean-Up Kit (Takara Bio). The purified PCR product was combined with the linearized pRACE vector and used to transform Stellar Competent Cells (Takara Bio). Plasmids were isolated from transformed clones and sequenced as described above.

RT-PCR analysis

RNA was extracted from murine jejunum tissue using the RNeasy Mini kit (Qiagen). cDNA was synthesized from 1000 ng of total RNA using the Ultrapure SMART MMLV Reverse Transcriptase (Takara Bio). Quantitative PCR was performed with the KAPA SYBR FAST qPCR Master Mix (KAPA Biosystems) and RNA expression was normalized to *Actb* expression. Primers were Dpep1 forward and reverse: PrimeTime Mm.PT.58.31167241.g primers (IDT) spanning exons 5-6, Actb forward: 5′-AGATCAAGATCATTGCTCCTCCTG-3′, and Actb reverse: 5′-CAGCTCAGTAACAGTCCGCC-3′.

DPEP1 activity assay

Fluorometric detection of dipeptidase enzyme activity was performed as originally established by Heywood and Hooper (*89*) and Rajotte and Ruoslahti (*90*) with minor modifications as described in (*48*). Jejunum sections were collected, rinsed in cold PBS, and immediately snap-frozen in liquid nitrogen. The frozen tissue segments were weighed and homogenized at 50 mg/ml RIPA lysis buffer containing 100-mM octyl-glucopyranoside in the absence of protease inhibitors. Lysates (500, 250, and 50 μg) were first incubated in triplicate with 50 μl of the dipeptidase substrate Gly-D-Phe (1 mM) either in the presence or absence of the DPEP1 inhibitor cilastatin (1 mM) at 37°C for 1 hour and 40 min in a black 96-well clear bottom plate. After incubation, reaction assay buffer (50 μl/well) was added and incubated at 37°C for 40 min in the dark. The fluorescence signal generated from the conversion of Gly-D-Phe to D-Phe by DPEP1, followed by conversion to 6, 69-dihydroxy-(1, 19-biphenyl)-3, 39-diacetic acid in the presence of D-amino acid oxidase and peroxidase was measured using a fluorescence plate reader with excitation at 317nm and emission at 414 nm.

DPEP1 protein model and motif identification

Three-dimensional protein models were generated using the complete amino acid sequences of DPEP1 by AlphaFold Multimer version 2.3.2 (*91*). The models were aligned and visualized using Pymol version 2.5.7. For protein motif identification the complete DPEP1 amino acid FASTA sequences were analyzed using The Eukaryotic Linear Motif Resource (*56*). Potential kinase candidates and differences between wild-type and mutant versions of the allele were identified using Phosformer, trained on its provided dataset (*57*). The peptide sequences used for input were DDEAESHGLSP (C57BL/6) and DDEAESQGLSP (C3H/HeJ). Both peptides were fit against the complete human kinase sequence data provided in the Phosformer github page.

CELLxGENE analysis

The online CZ CELLxGENE portal (*92*) as used to analyze expression of selected genes in human and mouse single-cell RNA-seq (scRNA-seq) datasets from large intestine (mouse) and SI (human). Data from relevant cell types was manually selected for viewing. Of the 44 genes that with potentially divergent amino acid sequences between C57BL/6 and C3H/HeJ any genes without an obvious single ortholog in humans were removed from the analysis. In addition, inspection of the reads for each gene from bulk RNA-seq analysis of jejunal tissue from C57BL/6 and C3H/HeJ mice (see below) was used to confirm or refute predicted coding sequence divergence between the two strains. Finally, the housekeeping gene RPL3 was removed from the analysis as it was highly expressed in all cell types.

Microbiome DNA extraction, ribosomal RNA gene sequencing, and data processing

Littermate N_2 generation mice were weaned and housed together. At 6 weeks of age, mice were sensitized with six weekly immunizations with PN+CT. After sensitization, at least two stool pellets were taken from each mouse, pooled together in a single tube and snap-frozen on dry ice. Samples were randomized across the entire study before DNA extraction. Total DNA from mouse stool pellets was extracted using a modified Qiagen QIAamp 96 DNA QIAcube HT protocol. For each sample, a single stool pellet (10 to 60 mg total weight) was added to a Qiagen PowerBead 0.7-mm garnet tube with 1ml of Qiagen InhibitEX buffer. Samples were incubated at 65°C for 10 min and 95°C for 10 min. The samples were then mechanically lysed for 2 cycles of 30 s at 3700 RPM on a Qiagen Powerlyzer 24 Homogenizer, with a 1-min rest period between cycles. Samples were centrifuged at 10,000*g* for 1 min, and then 200 μl of this lysate was mixed with 285 μl of AL Buffer and 5 μl of Proteinase K. The lysate was incubated for 10 min at 70°C and cooled on ice for 5 min. 485 μl of this lysate was transferred to a QIACube HT instrument, where the lysate was combined with 200 μl of 100% ethanol and bound to the QIAmp 96 plate. Each well of the QIAmp 96 plate was washed with 600 μl of AW1 Buffer, AW2 Buffer, and then 100% Ethanol. DNA was eluted with 100 μl of AE Buffer without using TopElute fluid. DNA was quantified using the Quant-iT 1X dsDNA HS Assay Kit, and 4ng of DNA per sample was used for each amplification. The 16*S* rRNA gene V1-V3 region was amplified using Accuprime Taq High Fidelity Enzyme from ThermoFisher Scientific. The primers used incorporated Illumina dual indices and sequencing adapters with the after 16*S* rRNA gene V1-V3 priming regions: 27F (5′-AGAGTTTGATCCTGGCTCAG) and 534R (5′-ATTACCGCGGCTGCTGG). The V1-V3 region was amplified with the following cycling parameters: 95°C × 2 min, 30× (95°C × 20 s, 56°C × 30 s, 72°C × 1 min), 4°C hold. DNA extractions and library preps were completed by Microbial Genomic Services at The Jackson Laboratory for Genomic Medicine. S. aureus was used as a positive extraction control and Qiagen InhibitEX buffer alone was used as a negative extraction control. For PCR, Rhodobacter sphaeroides (ATCC 17023; 24 ng/ μl concentration with a total of 2 μl in PCR well) was used as a positive PCR control whereas 4 μl of water alone was used as a negative PCR control. Amplicons were pooled for sequencing using Illumina 2x300 bp V3 reagents on a MiSeq instrument at The Jackson Laboratory for Genomic Medicine Genome Technologies Service. 16*S*-Seq sequencing reads were assembled and denoised using the DADA2 plugin (*93*) of QIIME2 (version 2023.9 (*94*)). Operational taxonomic unit counts were generated using the DADA2 plugin (*93*) of QIIME2 (version 2023.9 (*94*). Alpha diversity analysis was done using QIIME2 (version 2023.9 (*94*)).

DPEP1 amino acid alignment

Mammalian sequences of DPEP1 were retrieved using the command-line tool from NCBI accessed on 16 September 2024. Gathered sequences were manually curated to remove duplicates and limited to 400 to 420 amino acids in length to focus on complete sequences only. The final number reached 116 of individual complete sequences. Additionally, the amino acid sequence corresponding to *Mus musculus* (C3H/HeJ and BALB/c) sequenced by our group was added to reach a total sequence number of 118. All these sequences were aligned and

grouped by sequence similarity using MUSCLE (including a 16 maximum iterations) (*95*). Alignment was manually curated to correct for artefactual gaps. Sequence identity metrics was extracted from the alignment and visualized in R Studio v4.2.2 software using ggplot2 package, and 27 representative sequences were selected and visualized in more details using ggmsa package (*96*).

OVA-AF647 and DPEP1 jejunal immunofluorescence

Naïve cohoused C57BL/6 and C3H/HeJ mice were fasted for 4 hours and administered 0.6 mg of OVA-AF647 (Thermo Scientific) in 300 µl of PBS by gavage. Three minutes later, mice were euthanized, intestines were flushed with 1 ml of 10% neutral buffered formalin (NBF) and 1 cm of jejunal tissue was harvested and placed in 700 µl of 10% NBF. Mouse FFPE slides were sectioned in the Northwestern Histology Core. Formalin-fixed paraffin-embedded slides were baked at 60°C for 30 min to adhere sections. Slides were rehydrated in Coplin jars with one 15 min then one 5-min wash in CitriSolv (Decon #1601), two 5-min washes each in 100% ethanol (PolySciences #09860-1), 95% EtOH, 80% EtOH, 70% EtOH, and diH2O. Slides were dipped in 99°C diH2O for 10 s, then incubated in 99°C Antigen Retrieval Solution (eBioscience #00-4955-58) for 15 min. Slides were washed in fresh PBS (Gibco #14190144) before staining. OCT frozen tissue slides were brought to RT, then fixed in 100% acetone for 10 min. Slides were allowed to dry slightly, then washed twice in PBS for 3 min before staining. Sections were bordered with a lipid pen (Vector Labs #H-4000), and without allowing tissue to dry the sections were blocked using 2.5% BSA in PBS for 10 min as lipid pen marking dried. Anti-DPEP1 (CST #84292) antibody at 1:100 or E-cadherin (BioLegend #147301) at 1:250 diluted in 2.5% BSA were incubated in a humidity chamber at RT in the dark overnight. Slides were washed for 5 min three times with 0.1% Tween-20 (MP Biomedicals #11TWEEN201-CF) and 1% BSA in PBS. Secondary antibody anti-Rabbit-AF488 (Invitrogen #A11008) or anti-Rat-AF488 (Invitrogen #A11006) was stained at 1:1000 dilution in 2.5% BSA for 1 hour at 37°C in a humidity chamber or overnight at RT. Slides were washed as above. WGA conjugated with Rhodamine (Vector Labs #RL-1022-5) was stained at 1:300 in 2.5% BSA for 1 hour at 37°C in a humidity chamber, then washed as above. Slides were mounted with ProLong Gold Antifade mounting medium with 4′,6-diamidino-2-phenylindole (DAPI; Invitrogen #P36931). Coverslips were added and cured overnight in the dark. Slides were stored at 4°C until imaged using a Nikon A1 Confocal microscope. A blinded investigator quantitated the number and percent of OVA-AF647^{+} goblet cells (WGA^{+}) per well oriented villus from randomized images. For experiments testing the effect of LTD_4, 0.6 mg OVA-AF647 was mixed with either 750ng LTD_4 or 2.5% EtOH immediately before administration (maintained on dry ice until mixing) by oral gavage as above and intestines were harvested 3 min later. For quantitation of OVA-AF647 within the LP of jejunal villi in LTD_4 experiments, images were processed in ImageJ (Fiji) by a blinded investigator from randomized images. To do this, the LP of longitudinally cut villi were cropped out of the merged image and the image was then separated into individual color channels. The OVA-AF647 integrated density was then measured for each villi using the Measure tool in ImageJ. The groups were then unblinded and plotted in GraphPad with each point representing a single villus.

Oral PCA

Fifteen microliters of sera from pooled peanut sensitized C57BL/6 or C3H/HeJ mice were injected intradermally into the left or right ear of a naïve C57BL/6 or C3H/HeJ mouse, respectively. Sixteen hours later, the recipient mice were deprived of food for 4 hours. They were then injected intravenously with 100 µl of 2% Evans blue dye and immediately challenged with 800 µl of homemade CPE (70 to 80 mg/ml protein) through oral gavage. 45 min later, mice were euthanized, and ear pinnae were harvested and incubated in formamide before assaying for Evans Blue concentration. Ears were incubated at 56°C in 500 µl of formamide for 72 hours before being assayed for Evans blue concentration at 650 nm using a spectrophotometer.

Mouse RNA-seq analysis

Naïve 6- to 8-week-old cohoused C57BL/6 and C3H/HeJ mice were euthanized, and jejuna harvested, flushed with cold PBS, and immediately flash frozen. Frozen jejuna were ground using a mortar and pestle and then homogenized in a weight-normalized quantity of QIAzol Lysis Reagent (catalog number 79306). RNA was then extracted using the Qiagen miRNeasy Mini Kit (catalog number 217004). The stranded mRNA-seq was conducted in the Northwestern University NUSeq Core Facility. Briefly, total RNA samples were checked for quality using RNA Integrity Number equivalent (RIN) generated from Agilent TapeStation 4200 using RNA ScreenTape. RNA quantity was determined with Qubit fluorometer. The Illumina Stranded mRNA Prep Kit was used to prepare sequencing libraries from 200 ng of high-quality RNA samples (RIN>7). The Kit procedure was performed without modifications. This procedure includes mRNA purification and fragmentation, cDNA synthesis, 3′ end adenylation, Illumina adapter ligation, library PCR amplification and validation. Libraries were sequenced using an Illumina NovaSeq X Plus sequencer producing paired-end 150 base reads. Sequenced reads were aligned to the mouse genome (Ensembl GRCm39 version 110) using the STAR aligner (version 2.7.9a) and counted using HTSeq (version 2.0.2). Differential expression was performed on the raw counts using the R package edgeR (version 4.2.1) by fitting a generalized linear model for each gene (dependent variable) using the mice strain as the independent variable. A likelihood ratio test was used to test for gene differential expression between mouse strains (i.e., regression coefficient different from 0). The Benjamini-Hochberg adjustment was used to correct for multiple testing. SNPs were identified using the GATK RNA-seq germline SNPs and InDel pipeline with default options (version: 4.4.0.0) (*97*). SNPs were finally validated by manual inspection of aligned reads.

Whole blood transcriptomic analysis

Children were recruited from the Jaffe Food Allergy Institute, Mount Sinai Health System, New York. The participants were aged 4-14 years and underwent double-blind, placebo-controlled food challenge to peanut. Peripheral blood samples were collected pre-and post-challenge for both peanut and placebo (*98*). Transcriptomic profiles were generated from the blood samples and the gene expression profiles were normalized and transformed to log(CPM) using voom in the limma R package (*99*). The differences between transcript expression levels post and pre-challenge were calculated using the following equation: Delta of $\log CPM(\text{transcript}) = [\log CPM(\text{transcript}_{\text{postchallenge on peanut}} - \log CPM(\text{transcript})_{\text{prechallenge on peanut}}] - [\log CPM(\text{transcript})_{\text{postchallenge on placebo}} - \log CPM(\text{transcript})_{\text{prechallenge on placebo}}]$.The changes of transcript expression levels before and after challenge were compared between peanut allergy and nonallergic groups.

Western blots

Jejunum sections were collected, rinsed in cold PBS, and immediately snap-frozen in liquid nitrogen. The frozen tissue segments were weighed and homogenized at 50 mg tissue per ml RIPA lysis buffer containing 100 mM octyl-glucopyranoside in the presence of protease inhibitors. Lysates were cleared by spinning at 13,000 rpm for 15 min at 4°C. Lysate supernatants were boiled with loading buffer and DTT, then loaded into SDS-PAGE gels and run at 120V for 1 hour. Proteins were transferred to a methylcellulose membrane and blocked for 1 hour at RT with 5% BSA in TBST. Membranes were blotted with anti-DPEP1 at 1:1000 (CellSignaling Technology #84292) and anti-GAPDH at 1:2000 (Cell Signaling Technology #5174). Membranes were washed 3X with TBST, then blotted with IRDye 800CW donkey anti-rabbit (Li-Cor, #926-32213) secondary antibody at 1:10,000 in 5% BSA

TBST for 1 hour at RT, followed by washing and visualization using a Bio-Rad GelDoc.

Immunohistochemistry

Staining was performed as previously described with antigen retrieval performed using pH 6.0 citrate buffer (*100*) The primary antibodies used were: anti-DPEP1 (Cell Signaling Technology #84292). Tissue processing by formalin-fixed paraffin embedding (FFPE) was conducted by the Vanderbilt University Medical Center (VUMC) Translational Pathology Shared Resource (TPSR).

For immunohistochemistry, human tissue samples were procured under IRB protocols approved by the Vanderbilt University School of Medicine: umbrella IRB (list IRB #070166). Deidentified samples obtained with consent were obtained from the NIH Cooperative Human Tissue Network. Age and sex of the donors were not provided. For whole blood transcriptional analysis, the human subjects study was approved by the Mount Sinai Institutional Review Board. Written informed consent was obtained from the parent/guardian of each participant. Age and sex of the participants were as previously reported (*98*).

Statistical analysis

Except for 16*S* rRNA and bulk jejunal RNA-seq data, all statistical analyses were performed using Prism software (Graphpad Software). Exact tests used are denoted in figure legends. For the 16s rRNA-seq, a Wilcoxon rank-sum test was used to test for differences in Shannon diversity between susceptible and resistant mice. Statistical significance was defined as $^{*}P < 0.05$, $^{**}P < 0.01$, $^{***}P < 0.001$, and $^{****}P < 0.0001$.

REFERENCES AND NOTES

1. H. Renz *et al.*, Food allergy. *Nat. Rev. Dis. Primers* **4**, 17098 (2018). doi: 10.1038/nrdp.2017.98; pmid: 29300005
2. L. M. Bartnikas, S. H. Sicherer, Fatal anaphylaxis: Searching for lessons from tragedy. *J. Allergy Clin. Immunol. Pract.* **8**, 334–335 (2020). doi: 10.1016/j.jaip.2019.11.005; pmid: 31950906
3. M. Álvaro *et al.*, Tolerance to egg proteins in egg-sensitized infants without previous consumption. *Allergy* **69**, 1350–1356 (2014). doi: 10.1111/all.12483; pmid: 25040899
4. N. Nicolaou *et al.*, Allergy or tolerance in children sensitized to peanut: Prevalence and differentiation using component-resolved diagnostics. *J. Allergy Clin. Immunol.* **125**, 191–197.e13 (2010). doi: 10.1016/j.jaci.2009.10.008; pmid: 20109746
5. H. A. Sampson, D. G. Ho, Relationship between food-specific IgE concentrations and the risk of positive food challenges in children and adolescents. *J. Allergy Clin. Immunol.* **100**, 444–451 (1997). doi: 10.1016/S0091-6749(97)70133-7; pmid: 9338535
6. D. M. Fleischer *et al.*, Oral food challenges in children with a diagnosis of food allergy. *J. Pediatr.* **158**, 578–583.e1 (2011). doi: 10.1016/j.jpeds.2010.09.027; pmid: 21030035
7. N. J. Osborne *et al.*, Prevalence of challenge-proven IgE-mediated food allergy using population-based sampling and predetermined challenge criteria in infants. *J. Allergy Clin. Immunol.* **127**, 668–676.e2 (2011). doi: 10.1016/j.jaci.2011.01.039; pmid: 21377036
8. S. H. Sicherer *et al.*, The natural history of egg allergy in an observational cohort. *J. Allergy Clin. Immunol.* **133**, 492–499.e8 (2014). doi: 10.1016/j.jaci.2013.12.1041; pmid: 24636473
9. A. T. Stefka *et al.*, Commensal bacteria protect against food allergen sensitization. *Proc. Natl. Acad. Sci. U.S.A.* **111**, 13145–13150 (2014). doi: 10.1073/pnas.1412008111; pmid: 25157157
10. O. T. Burton *et al.*, Immunoglobulin E signal inhibition during allergen ingestion leads to reversal of established food allergy and induction of regulatory T cells. *Immunity* **41**, 141–151 (2014). doi: 10.1016/j.immuni.2014.05.017; pmid: 25017467
11. E. E. Forbes *et al.*, IL-9- and mast cell-mediated intestinal permeability predisposes to oral antigen hypersensitivity. *J. Exp. Med.* **205**, 897–913 (2008). doi: 10.1084/jem.20071046; pmid: 18378796
12. R. Tachdjian *et al.*, In vivo regulation of the allergic response by the IL-4 receptor alpha chain immunoreceptor tyrosine-based inhibitory motif. *J. Allergy Clin. Immunol.* **125**, 1128–1136.e8 (2010). doi: 10.1016/j.jaci.2010.01.054; pmid: 20392476
13. A. Abdel-Gadir *et al.*, Microbiota therapy acts via a regulatory T cell MyD88/RORγt pathway to suppress food allergy. *Nat. Med.* **25**, 1164–1174 (2019). doi: 10.1038/s41591-019-0461-z; pmid: 31235962
14. K. Orgel *et al.*, Genetic diversity between mouse strains allows identification of the CC027/GeniUnc strain as an orally reactive model of peanut allergy. *J. Allergy Clin. Immunol.* **143**, 1027–1037.e7 (2019). doi: 10.1016/j.jaci.2018.10.009; pmid: 30342892
15. J. A. Gertie *et al.*, Oral anaphylaxis to peanut in a mouse model is associated with gut permeability but not with Tlr4 or Dock8 mutations. *J. Allergy Clin. Immunol.* **149**, 262–274 (2022). doi: 10.1016/j.jaci.2021.05.015; pmid: 34051223
16. C. Y. Chen *et al.*, Induction of interleukin-9-producing mucosal mast cells promotes susceptibility to IgE-mediated experimental food allergy. *Immunity* **43**, 788–802 (2015). doi: 10.1016/j.immuni.2015.08.020; pmid: 26410628
17. E. B. Brandt *et al.*, Mast cells are required for experimental oral allergen-induced diarrhea. *J. Clin. Invest.* **112**, 1666–1677 (2003). doi: 10.1172/JCI19785; pmid: 14660743
18. R. Jiménez-Saiz *et al.*, Lifelong memory responses perpetuate humoral T_H2 immunity and anaphylaxis in food allergy. *J. Allergy Clin. Immunol.* **140**, 1604–1615.e5 (2017). doi: 10.1016/j.jaci.2017.01.018; pmid: 28216433
19. K. Bruton *et al.*, Interrupting reactivation of immunologic memory diverts the allergic response and prevents anaphylaxis. *J. Allergy Clin. Immunol.* **147**, 1381–1392 (2021). doi: 10.1016/j.jaci.2020.11.042; pmid: 33338539
20. D. K. Chu *et al.*, IL-33, but not thymic stromal lymphopoietin or IL-25, is central to mite and peanut allergic sensitization. *J. Allergy Clin. Immunol.* **131**, 187–200.e8 (2013). doi: 10.1016/j.jaci.2012.08.002; pmid: 23006545
21. D. K. Chu *et al.*, T helper cell IL-4 drives intestinal Th2 priming to oral peanut antigen, under the control of OX40L and independent of innate-like lymphocytes. *Mucosal Immunol.* **7**, 1395–1404 (2014). doi: 10.1038/mi.2014.29; pmid: 24781052
22. L. Knoops, J. Louahed, J. Van Snick, J. C. Renauld, IL-9 promotes but is not necessary for systemic anaphylaxis. *J. Immunol.* **175**, 335–341 (2005). doi: 10.4049/jimmunol.175.1.335; pmid: 15972666
23. J. J. Smit *et al.*, Contribution of classic and alternative effector pathways in peanut-induced anaphylactic responses. *PLOS ONE* **6**, e28917 (2011). doi: 10.1371/journal.pone.0028917; pmid: 22194949
24. J. Sun *et al.*, Impact of CD40 ligand, B cells, and mast cells in peanut-induced anaphylactic responses. *J. Immunol.* **179**, 6696–6703 (2007). doi: 10.4049/jimmunol.179.10.6696; pmid: 17982059
25. K. Arias *et al.*, Concurrent blockade of platelet-activating factor and histamine prevents life-threatening peanut-induced anaphylactic reactions. *J. Allergy Clin. Immunol.* **124**, 307–314.e2 (2009). doi: 10.1016/j.jaci.2009.03.012; pmid: 19409603
26. K. Arias *et al.*, Distinct immune effector pathways contribute to the full expression of peanut-induced anaphylactic reactions in mice. *J. Allergy Clin. Immunol.* **127**, 1552–1561.e1 (2011). doi: 10.1016/j.jaci.2011.03.044; pmid: 21624619
27. D. P. Snider, J. S. Marshall, M. H. Perdue, H. Liang, Production of IgE antibody and allergic sensitization of intestinal and peripheral tissues after oral immunization with protein Ag and cholera toxin. *J. Immunol.* **153**, 647–657 (1994). doi: 10.4049/jimmunol.153.2.647; pmid: 8021502
28. X.-M. Li, B. H. Schofield, C.-K. Huang, G. I. Kleiner, H. A. Sampson, A murine model of IgE-mediated cow's milk hypersensitivity. *J. Allergy Clin. Immunol.* **103**, 206–214 (1999). doi: 10.1016/S0091-6749(99)70492-6; pmid: 9949309
29. V. Morafo *et al.*, Genetic susceptibility to food allergy is linked to differential TH2-TH1 responses in C3H/HeJ and BALB/c mice. *J. Allergy Clin. Immunol.* **111**, 1122–1128 (2003). doi: 10.1067/mai.2003.1463; pmid: 12743580
30. M. E. H. Bashir, S. Louie, H. N. Shi, C. Nagler-Anderson, Toll-like receptor 4 signaling by intestinal microbes influences susceptibility to food allergy. *J. Immunol.* **172**, 6978–6987 (2004). doi: 10.4049/jimmunol.172.11.6978; pmid: 15153518
31. X.-M. Li *et al.*, A murine model of peanut anaphylaxis: T- and B-cell responses to a major peanut allergen mimic human responses. *J. Allergy Clin. Immunol.* **106**, 150–158 (2000). doi: 10.1067/mai.2000.107395; pmid: 10887318
32. F. Capobianco *et al.*, Oral sensitization with shrimp tropomyosin induces in mice allergen-specific IgE, T cell response and systemic anaphylactic reactions. *Int. Immunol.* **20**, 1077–1086 (2008). doi: 10.1093/intimm/dxn065; pmid: 18562336
33. B. Proust *et al.*, A single oral sensitization to peanut without adjuvant leads to anaphylaxis in mice. *Int. Arch. Allergy Immunol.* **146**, 212–218 (2008). doi: 10.1159/000115889; pmid: 18268389
34. H. Kiyono, J. L. Babb, S. M. Michalek, J. R. McGhee, Cellular basis for elevated IgA responses in C3H/HeJ mice. *J. Immunol.* **125**, 732–737 (1980). doi: 10.4049/jimmunol.125.2.732; pmid: 6967087
35. D. Dunkin, M. C. Berin, L. Mayer, Allergic sensitization can be induced via multiple physiologic routes in an adjuvant-dependent manner. *J. Allergy Clin. Immunol.* **128**, 1251–1258.e2 (2011). doi: 10.1016/j.jaci.2011.06.007; pmid: 21762973
36. M. C. Berin, Y. Zheng, M. Domaradzki, X.-M. Li, H. A. Sampson, Role of TLR4 in allergic sensitization to food proteins in mice. *Allergy* **61**, 64–71 (2006). doi: 10.1111/j.1398-9995.2006.01012.x; pmid: 16364158
37. J. M. Smeekens *et al.*, Fecal IgA, antigen absorption, and gut microbiome composition are associated with food antigen sensitization in genetically susceptible mice. *Front. Immunol.* **11**, 599637 (2021). doi: 10.3389/fimmu.2020.599637; pmid: 33542716
38. H. Gao, R. Jorgensen, R. Raghunath, P. K. W. Ng, V. Gangur, An adjuvant-free mouse model using skin sensitization without tape-stripping followed by oral elicitation of anaphylaxis: A novel pre-clinical tool for testing intrinsic wheat allergenicity. *Front. Allergy* **3**, 926576 (2022). doi: 10.3389/falgy.2022.926576; pmid: 36238931
39. J.-M. Leyva-Castillo *et al.*, Mechanical skin injury promotes food anaphylaxis by driving intestinal mast cell expansion. *Immunity* **50**, 1262–1275.e4 (2019). doi: 10.1016/j.immuni.2019.03.023; pmid: 31027995
40. A. Pablos-Tanarro, I. López-Expósito, D. Lozano-Ojalvo, R. López-Fandiño, E. Molina, Antibody production, anaphylactic signs, and T-cell responses induced by oral

sensitization with ovalbumin in BALB/c and C3H/HeOuJ mice. *Allergy Asthma Immunol. Res.* **8**, 239–245 (2016). doi: 10.4168/aair.2016.8.3.239; pmid: 26922934
41. K. -T. C. Shade *et al.*, Sialylation of immunoglobulin E is a determinant of allergic pathogenicity. *Nature* **582**, 265–270 (2020). doi: 10.1038/s41586-020-2311-z; pmid: 32499653
42. H. Bernard *et al.*, Circulating Ara h 6 as a marker of peanut protein absorption in tolerant and allergic humans following ingestion of peanut-containing foods. *Clin. Exp. Allergy* **50**, 1093–1102 (2020). doi: 10.1111/cea.13706; pmid: 32648641
43. R. T. Strait *et al.*, Ingested allergens must be absorbed systemically to induce systemic anaphylaxis. *J. Allergy Clin. Immunol.* **127**, 982–989.e1 (2011). doi: 10.1016/j.jaci.2011.01.034; pmid: 21354602
44. A. Hayashi, N. Sakamoto, K. Kobayashi, T. Murata, Enhancement of prostaglandin D_2-D prostanoid 1 signaling reduces intestinal permeability by stimulating mucus secretion. *Front. Immunol.* **14**, 1276852 (2023). doi: 10.3389/fimmu.2023.1276852; pmid: 37942331
45. H. Li *et al.*, Transcytosis of IgE-antigen complexes by CD23a in human intestinal epithelial cells and its role in food allergy. *Gastroenterology* **131**, 47–58 (2006). doi: 10.1053/j.gastro.2006.03.044; pmid: 16831589
46. M. Walzer, A direct method of demonstrating the absorption of incompletely digested proteins in normal human beings: A preliminary report. *J. Immunol.* **11**, 249–252 (1926). doi: 10.4049/jimmunol.11.4.249
47. Y. Kanaoka, K. F. Austen, Roles of cysteinyl leukotrienes and their receptors in immune cell-related functions. *Adv. Immunol.* **142**, 65–84 (2019). doi: 10.1016/bs.ai.2019.04.002; pmid: 31296303
48. S. R. Choudhury *et al.*, Dipeptidase-1 is an adhesion receptor for neutrophil recruitment in lungs and liver. *Cell* **178**, 1205–1221.e17 (2019). doi: 10.1016/j.cell.2019.07.017; pmid: 31442408
49. S. K. Samuchiwal, J. A. Boyce, Role of lipid mediators and control of lymphocyte responses in type 2 immunopathology. *J. Allergy Clin. Immunol.* **141**, 1182–1190 (2018). doi: 10.1016/j.jaci.2018.02.006; pmid: 29477727
50. J. W. McGinty *et al.*, Tuft-cell-derived leukotrienes drive rapid anti-helminth immunity in the small intestine but are dispensable for anti-protist immunity. *Immunity* **52**, 528–541.e7 (2020). doi: 10.1016/j.immuni.2020.02.005; pmid: 32160525
51. S. Ualiyeva *et al.*, Tuft cell-produced cysteinyl leukotrienes and IL-25 synergistically initiate lung type 2 inflammation. *Sci. Immunol.* **6**, eabj0474 (2021). doi: 10.1126/sciimmunol.abj0474; pmid: 34932383
52. A. J. Jame *et al.*, Human bronchial epithelial cells express an active and inducible biosynthetic pathway for leukotrienes B4 and C4. *Clin. Exp. Allergy* **37**, 880–892 (2007). doi: 10.1111/j.1365-2222.2007.02733.x; pmid: 17517102
53. F. D. R. Henkel, J. Esser-von Bieren, Not just "leuko" after all: Epithelial leukotriene production in type 2 immunity. *Sci. Immunol.* **7**, eabn4876 (2022). doi: 10.1126/sciimmunol.abn4876; pmid: 34995094
54. C. UniProt, UniProt: The universal protein knowledgebase in 2025. *Nucleic Acids Res.* (2024).
55. S. Keynan, N. M. Hooper, A. J. Turner, Identification by site-directed mutagenesis of three essential histidine residues in membrane dipeptidase, a novel mammalian zinc peptidase. *Biochem. J.* **326**, 47–51 (1997). doi: 10.1042/bj3260047; pmid: 9337849
56. M. Kumar *et al.*, ELM-the eukaryotic linear motif resource-2024 update. *Nucleic Acids Res.* **52** (D1), D442–D455 (2024). doi: 10.1093/nar/gkad1058; pmid: 37962385
57. Z. Zhou *et al.*, Phosformer: An explainable transformer model for protein kinase-specific phosphorylation predictions. *Bioinformatics* **39**, btad046 (2023). doi: 10.1093/bioinformatics/btad046; pmid: 36692152
58. D. A. Mordes, D. Cortez, Activation of ATR and related PIKKs. *Cell Cycle* **7**, 2809–2812 (2008). doi: 10.4161/cc.7.18.6689; pmid: 18769153
59. D. A. Fantz, D. Jacobs, D. Glossip, K. Kornfeld, Docking sites on substrate proteins direct extracellular signal-regulated kinase to phosphorylate specific residues. *J. Biol. Chem.* **276**, 27256–27265 (2001). doi: 10.1074/jbc.M102512200; pmid: 11371562
60. M. Lee, J. A. Boyce, N. A. Barrett, Cysteinyl leukotrienes in allergic inflammation. *Annu. Rev. Pathol.* **20**, 115–141 (2024). doi: 10.1146/annurev-pathmechdis-111523-023509; pmid: 39374430
61. L. G. Bankova *et al.*, Leukotriene E4 elicits respiratory epithelial cell mucin release through the G-protein-coupled receptor, GPR99. *Proc. Natl. Acad. Sci. U.S.A.* **113**, 6242–6247 (2016). doi: 10.1073/pnas.1605957113; pmid: 27185938
62. J. R. McDole *et al.*, Goblet cells deliver luminal antigen to CD103+ dendritic cells in the small intestine. *Nature* **483**, 345–349 (2012). doi: 10.1038/nature10863; pmid: 22422267
63. T. K. Noah *et al.*, IL-13-induced intestinal secretory epithelial cell antigen passages are required for IgE-mediated food-induced anaphylaxis. *J. Allergy Clin. Immunol.* **144**, 1058–1073.e3 (2019). doi: 10.1016/j.jaci.2019.04.030; pmid: 31175877
64. J. K. Gustafsson *et al.*, Intestinal goblet cells sample and deliver lumenal antigens by regulated endocytic uptake and transcytosis. *eLife* **10**, e67292 (2021). doi: 10.7554/eLife.67292; pmid: 34677124
65. S. Ménard, N. Cerf-Bensussan, M. Heyman, Multiple facets of intestinal permeability and epithelial handling of dietary antigens. *Mucosal Immunol.* **3**, 247–259 (2010). doi: 10.1038/mi.2010.5; pmid: 20404811
66. J. Drazen, Clinical pharmacology of leukotriene receptor antagonists and 5-lipoxygenase inhibitors. *Am. J. Respir. Crit. Care Med.* **157**, S233–S237 (1998). doi: 10.1164/ajrccm.157.6.mar-5; pmid: 9647605
67. T. M. Laidlaw, J. A. Boyce, Updates on immune mechanisms in aspirin-exacerbated respiratory disease. *J. Allergy Clin. Immunol.* **151**, 301–309 (2023). doi: 10.1016/j.jaci.2022.08.021; pmid: 36184313
68. H. Matsuo *et al.*, Exercise and aspirin increase levels of circulating gliadin peptides in patients with wheat-dependent exercise-induced anaphylaxis. *Clin. Exp. Allergy* **35**, 461–466 (2005). doi: 10.1111/j.1365-2222.2005.02213.x; pmid: 15836754
69. M. P. Giannetti, Exercise-induced anaphylaxis: Literature review and recent updates. *Curr. Allergy Asthma Rep.* **18**, 72 (2018). doi: 10.1007/s11882-018-0830-6; pmid: 30367321
70. J. Bartra, G. Araujo, R. Muñoz-Cano, Interaction between foods and nonsteroidal anti-inflammatory drugs and exercise in the induction of anaphylaxis. *Curr. Opin. Allergy Clin. Immunol.* **18**, 310–316 (2018). doi: 10.1097/ACI.0000000000000461; pmid: 29889141
71. N. Brandt, E. Eller, A. Pahlow Mose, C. Bindslev-Jensen, C. G. Mortz, The influence of acetylsalicylic acid and alcohol on absorption kinetics of hen´s egg white in a human passive cutaneous anaphylaxis model. *Food Nutr. Res.* 65 (2021). doi: 10.29219/fnr.v65.7618; pmid: 35903146
72. M. Takahashi *et al.*, New efficacy of LTRAs (montelukast sodium): It possibly prevents food-induced abdominal symptoms during oral immunotherapy. *Allergy Asthma Clin. Immunol.* **10**, 3 (2014). doi: 10.1186/1710-1492-10-3; pmid: 24438769
73. E. B. Florsheim *et al.*, Immune sensing of food allergens promotes avoidance behaviour. *Nature* **620**, 643–650 (2023). doi: 10.1038/s41586-023-06362-4; pmid: 37437602
74. T. Plum *et al.*, Mast cells link immune sensing to antigen-avoidance behaviour. *Nature* **620**, 634–642 (2023). doi: 10.1038/s41586-023-06188-0; pmid: 37438525
75. R. Ahrens *et al.*, Intestinal mast cell levels control severity of oral antigen-induced anaphylaxis in mice. *Am. J. Pathol.* **180**, 1535–1546 (2012). doi: 10.1016/j.ajpath.2011.12.036; pmid: 22322300
76. K. R. Groschwitz, S. P. Hogan, Intestinal barrier function: Molecular regulation and disease pathogenesis. *J. Allergy Clin. Immunol.* **124**, 3–20, quiz 21–22 (2009). doi: 10.1016/j.jaci.2009.05.038; pmid: 19560575
77. N. D. Bachtel *et al.*, Intestinal mast cell-derived leukotrienes mediate the anaphylactic response to ingested antigens. *Science* **389**, eadp0246 (2025).
78. S. R. Norrby, B. Björnegård, F. Ferbert, K. H. Jones, Pharmacokinetics of imipenem in healthy volunteers. *J. Antimicrob. Chemother.* **12**, 109–124 (1983). doi: 10.1093/jac/12.suppl_D.109; pmid: 6583194
79. I. Nilsson-Ehle, M. Hutchison, S. J. Haworth, S. R. Norrby, Pharmacokinetics of meropenem compared to imipenem-cilastatin in young, healthy males. *Eur. J. Clin. Microbiol. Infect. Dis.* **10**, 85–88 (1991). doi: 10.1007/BF01964413; pmid: 1864280
80. C. Mills, S. E. Dorst, G. Mynchenberg, J. Nakayama, Absorption from the intestine and excretion through the kidney of an unaltered complex protein substance, tissue fibrinogen. *Am. J. Physiol.* **63**, 484–498 (1923). doi: 10.1152/ajplegacy.1923.63.3.484
81. S. Husby, J. C. Jensenius, S.-E. Svehag, Passage of undegraded dietary antigen into the blood of healthy adults. Further characterization of the kinetics of uptake and the size distribution of the antigen. *Scand. J. Immunol.* **24**, 447–455 (1986). doi: 10.1111/j.1365-3083.1986.tb02133.x; pmid: 3764346
82. B. Ratner, H. L. Gruehl, Passage of native proteins through the normal gastro-intestinal wall. *J. Clin. Invest.* **13**, 517–532 (1934). doi: 10.1172/JCI100602; pmid: 16694226
83. C. G. Dirks *et al.*, Does absorption across the buccal mucosa explain early onset of food-induced allergic systemic reactions? *J. Allergy Clin. Immunol.* **115**, 1321–1323 (2005). doi: 10.1016/j.jaci.2005.03.027; pmid: 15940158
84. A. Pahlow Mose *et al.*, The quest for ingested peanut protein in human serum. *Allergy* **75**, 1721–1729 (2020). doi: 10.1111/all.14109; pmid: 31715004
85. P. Juvonen, I. Jakobsson, T. Lindberg, Macromolecular absorption and cows' milk allergy. *Arch. Dis. Child.* **66**, 300–303 (1991). doi: 10.1136/adc.66.3.300; pmid: 2025004
86. K. L. Pothoven, R. P. Schleimer, The barrier hypothesis and Oncostatin M: Restoration of epithelial barrier function as a novel therapeutic strategy for the treatment of type 2 inflammatory disease. *Tissue Barriers* **5**, e1341367 (2017). doi: 10.1080/21688370.2017.1341367; pmid: 28665760
87. D. H. Kulkarni *et al.*, Goblet cell associated antigen passages support the induction and maintenance of oral tolerance. *Mucosal Immunol.* **13**, 271–282 (2020). doi: 10.1038/s41385-019-0240-7; pmid: 31819172
88. O. Quehenberger *et al.*, Lipidomics reveals a remarkable diversity of lipids in human plasma. *J. Lipid Res.* **51**, 3299–3305 (2010). doi: 10.1194/jlr.M009449; pmid: 20671299
89. S. P. Heywood, N. M. Hooper, Development and application of a fluorometric assay for mammalian membrane dipeptidase. *Anal. Biochem.* **226**, 10–14 (1995). doi: 10.1006/abio.1995.1184; pmid: 7785760
90. D. Rajotte, E. Ruoslahti, Membrane dipeptidase is the receptor for a lung-targeting peptide identified by in vivo phage display. *J. Biol. Chem.* **274**, 11593–11598 (1999). doi: 10.1074/jbc.274.17.11593; pmid: 10206967
91. J. Jumper *et al.*, Highly accurate protein structure prediction with AlphaFold. *Nature* **596**, 583–589 (2021). doi: 10.1038/s41586-021-03819-2; pmid: 34265844
92. C. Z. I. C. S. Program *et al.*, CZ CELLxGENE Discover: A single-cell data platform for scalable exploration, analysis and modeling of aggregated data. *Nucleic Acids Res.* (2024).
93. B. J. Callahan *et al.*, DADA2: High-resolution sample inference from Illumina amplicon data. *Nat. Methods* **13**, 581–583 (2016). doi: 10.1038/nmeth.3869; pmid: 27214047

94. E. Bolyen *et al.*, Reproducible, interactive, scalable and extensible microbiome data science using QIIME 2. *Nat. Biotechnol.* **37**, 852–857 (2019). doi: 10.1038/s41587-019-0209-9; pmid: 31341288
95. R. C. Edgar, MUSCLE: A multiple sequence alignment method with reduced time and space complexity. *BMC Bioinformatics* **5**, 113 (2004). doi: 10.1186/1471-2105-5-113; pmid: 15318951
96. L. Zhou *et al.*, ggmsa: A visual exploration tool for multiple sequence alignment and associated data. *Brief. Bioinform.* **23**, bbac222 (2022). doi: 10.1093/bib/bbac222; pmid: 35671504
97. A. McKenna *et al.*, The Genome Analysis Toolkit: A MapReduce framework for analyzing next-generation DNA sequencing data. *Genome Res.* **20**, 1297–1303 (2010). doi: 10.1101/gr.107524.110; pmid: 20644199
98. L. Zhang *et al.*, Joint transcriptomic and cytometric study of children with peanut allergy reveals molecular and cellular cross talk in reaction thresholds. *J. Allergy Clin. Immunol.* **153**, 1721–1728 (2024). doi: 10.1016/j.jaci.2023.12.028; pmid: 38272374
99. C. W. Law, Y. Chen, W. Shi, G. K. Smyth, voom: Precision weights unlock linear model analysis tools for RNA-seq read counts. *Genome Biol.* **15**, R29 (2014). doi: 10.1186/gb-2014-15-2-r29; pmid: 24485249
100. Q. Zhang *et al.*, Supermeres are functional extracellular nanoparticles replete with disease biomarkers and therapeutic targets. *Nat. Cell Biol.* **23**, 1240–1254 (2021). doi: 10.1038/s41556-021-00805-8; pmid: 34887515
101. 16*S*-sequencing data for: R. Hoyt, E. Liu, E. C. Olson, D. R. Jacobsen, E. R. Siniscalco, R. A. Krier-Burris, K. G. Greenfield, C. D. McBride, M. M. Alfajaro, J. A. R. Amat, Z. Zhao, L. Xu, V. Philip, A. Verma, S. Fourati, D. L. Senger, L. Zhang, S. Bunyavanich, S. E. Glass, R. J. Coffey, C. B. Wilen, A. Williams, S. C. Eisenbarth, Cysteinyl leukotrienes stimulate gut absorption of food allergens to promote anaphylaxis in mice, Zenodo (2025); doi: 10.5281/zenodo.15149326
102. Bulk RNA-seq data for: R. Hoyt, E. Liu, E. C. Olson, D. R. Jacobsen, E. R. Siniscalco, R. A. Krier-Burris, K. G. Greenfield, C. D. McBride, M. M. Alfajaro, J. A. R. Amat, Z. Zhao, L. Xu, V. Philip, A. Verma, S. Fourati, D. L. Senger, L. Zhang, S. Bunyavanich, S. E. Glass, R. J. Coffey, C. B. Wilen, A. Williams, S. C. Eisenbarth, Cysteinyl leukotrienes stimulate gut absorption of food allergens to promote anaphylaxis in mice, Zenodo (2025); doi: 10.5281/zenodo.15149011

ACKNOWLEDGMENTS

We thank C. Berin, B. Bochner, and N. Hooper for wonderful discussions and critical review of this manuscript. This research was supported in part through the computational resources and staff contributions provided by the Genomics Compute Cluster which is jointly supported by the Feinberg School of Medicine, the Center for Genetic Medicine, and Feinberg's Department of Biochemistry and Molecular Genetics, the Office of the Provost, the Office for Research, and Northwestern Information Technology. The Genomics Compute Cluster is part of Quest, Northwestern University's high-performance computing facility, with the purpose to advance research in genomics. We thank Yale Flow Cytometry cores for their assistance with flow cytometry services. The Core is supported in part by National Cancer Institute Cancer Center Support grant NIH P30 CA016359. We would also like to acknowledge the JAX Scientific Services for 16*S* rRNA sequencing. This work was supported by the Northwestern University Interdepartmental ImmunoBiology Flow Cytometry Core Facility and the RHLCCC Flow Cytometry Facility supported by Cancer Center Grant (NCI CA060553). For imaging studies, tissue preparation and sectioning services were provided by the Northwestern University Mouse Histology and Phenotyping Laboratory (MHPL), which is supported by NCI P30-CA060553 awarded to the Robert H. Lurie Comprehensive Cancer Center. Imaging work was performed at the Northwestern University Center for Advanced Microscopy (RRID: SCR_020996) generously supported by CCSG grant P30 CA060553 awarded to the Robert H. Lurie Comprehensive Cancer Center. The CysLT pathway and graphical abstract were created with BioRender.com (licenses ZT27RH6FLS and ND27MBZOY7, respectively).
Funding: This work was supported by an Ira & Diana Riklis Family Research Award in Food Allergy; the Food Allergy Science Initiative (FASI), Inc.; the Food Allergy Fund (FAF); the National Institutes of health (grants R01 AI136942 and R01 AI168016 to S.C.E. and A.W.); grant R56 AI155497 to S.C.E.; grant U19AI136053 to S.B.; and grant P50 CA236733 to R.J.C.); and the Nicholas Tierney Memorial GI Cancer Fund (R.J.C. and S.E.G.) **Author contributions:** Computational analysis: S.F., V.P., A.V., C.D.M., J.A.R.A.; Conceptualization: L.R.H., S.C.E., A.W., C.B.W.; Experimental: L.R.H., E.L., D.R.J., E.C.O., E.R.S., M.M.A., Z.Z., L.X., R.A.K., K.G.G., S.B., L.Z., D.L.S., S.E.G.; Funding acquisition: S.C.E., A.W., R.J.C.; Supervision: S.C.E., A.W., C.B.W., R.J.C.; Visualization: L.R.H., S.C.E., A.W., S.F., C.D.M., J.A.R.A., S.E.G.; Writing – original draft: L.R.H., S.C.E., A.W.; Writing – review & editing: L.R.H., S.C.E., A.W., C.B.W., E.C.O., D.R.J., R.A.K., E.L., J.A.R.A., E.R.S., S.F., A.V., S.E.G. **Competing interests:** The authors declare no competing interests. **Data and materials availability:** The 16*S* sequencing data have been deposited in the Gene Expression Omnibus (GEO) under number GSE261022. RNA-seq data have been deposited in GEO under number GSE285568. The code used to analyze the 16*S* rRNA-seq (*101*) and the code used to analyze RNA-seq of jejunal tissue (*102*) are available on Zenodo. All other data needed to evaluate the conclusions of the study are available in the main text or the supplementary materials. DPEP1 knockout mice can be obtained from D.L.S. under a material transfer agreement with the Lady Davis Institute for Medical Research. **License information:** Copyright © 2025 the authors, some rights reserved; exclusive licensee American Association for the Advancement of Science. No claim to original US government works. https://www.science.org/about/science-licenses-journal-article-reuse

SUPPLEMENTARY MATERIALS

science.org/doi/10.1126/science.adp0240
Figs. S1 to S12; Data S1 to S5; MDAR Reproducibility Checklist
Submitted 3 March 2024; resubmitted 9 January 2025; accepted 30 May 2025
10.1126/science.adp0240

Check for

RESEARCH ARTICLE SUMMARY

IMMUNOLOGY

Intestinal mast cell–derived leukotrienes mediate the anaphylactic response to ingested antigens

Nathaniel D. Bachtel, Jaime L. Cullen, Min Liu, Steven A. Erickson, Vassily I. Kutyavin, Darine W. El-Naccache, Esther B. Florsheim, Jaechul Lim, Zuri A. Sullivan, Raiden Imaeda, Andrew Hudak, Cuiling Zhang, Ruslan Medzhitov*

Full article and list of author affiliations: https://doi.org/10.1126/science.adp0246

INTRODUCTION: Food allergies are a growing medical problem in the industrialized world. In the most extreme cases, allergic reactions manifest as anaphylaxis, a life-threatening state of bronchoconstriction and hemodynamic collapse, which occurs when food antigens enter the bloodstream and activate immunoglobulin E (IgE)–primed mast cells throughout the body. This view has led to diverse models studying anaphylaxis through intravenous administration of food antigens; however, this perspective minimizes the importance of local exposure to food antigens in mucosal tissues in the gut.

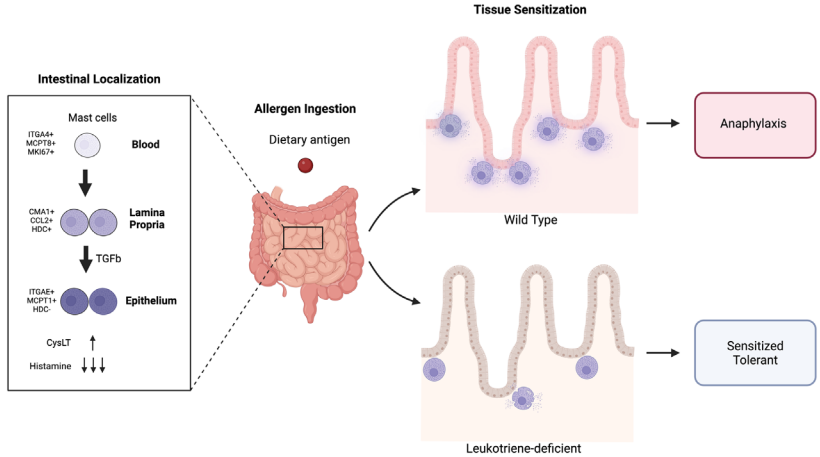
RATIONALE: Mouse models of food allergy utilize repeated gastrointestinal administration of allergen, which increases anaphylactic responses to ingestion over time. This hypersensitive state is associated with an increase in the number of mucosal mast cells in the small intestine, and studies utilizing mice deficient in intestinal mast cell expansion suggest that this population is critical for food-induced anaphylaxis to occur. We used bulk and single-cell RNA sequencing, in vitro culture models, and flow cytometry to analyze intestinal mast cell biology and to identify factors governing oral anaphylaxis susceptibility and severity.

RESULTS: Intestinal mast cells expanded during experimental food allergy in a manner that required IgE-mediated stimulation of Fcε receptor 1 (FcεR1). These mast cells were largely found within the epithelium of the intestine. Intestinal mast cells localized to the epithelium were distinct from the connective tissue mast cells found throughout the body, as well as those found within the lamina propria of the intestine, because they expressed different integrins, had a reduced histamine synthetic capacity, and enhanced cysteinyl leukotriene production. Treatment of bone marrow–derived mast cells with transforming growth factor–β (TGFβ) in vitro induced changes to cell-surface markers and inflammatory mediators that were similar to those observed in mast cells isolated from the intestinal epithelium. Blocking αvβ6 integrin, which can liberate TGFβ, changed the expression of the integrins expressed by the epithelial mast cells in vivo.

We interrogated the role for cysteinyl leukotrienes in our food allergy model using mice that lacked expression of enzymes involved in leukotriene synthesis or where leukotriene receptors had been knocked out. The knockout mice were compared with wild-type controls after both groups had been administered allergen intragastrically or through intravenous injection. Mice deficient in arachidonate 5-lipoxygenase (aLOX5) or leukotriene C4 synthase (LTC4S) were protected from anaphylaxis resulting from intragastric challenge, whereas that induced by intravenous injection was unaltered. Genetic deficiency of cysteinyl leukotriene receptor 1 (CysLTR1) or CysLTR2 individually reduced intestinal mast cell expansion and mirrored this protection. However, only acute blockade of aLOX5, but not of CysLTR1 or CysLTR2, ameliorated responses to intragastric challenge without affecting local mast cell expansion.

CONCLUSION: Cysteinyl leukotrienes were required for anaphylaxis after gastrointestinal exposure to allergens, but not to systemic allergens. We propose that cysteinyl leukotrienes have dual functions in food allergy in mice by promoting mucosal mast cell expansion and by stimulating acute sensitization to oral anaphylaxis through signaling to epithelial cells, neurons, and group 2 innate lymphoid cells (ILC2s). Other conditions capable of driving leukotriene excess in the intestines or ILC2 activation may act as cofactors toward the development of severe anaphylactic responses to foods. Thus, local intestinal responses may be acutely targetable as a therapeutic strategy to prevent anaphylaxis in severely food-allergic individuals. □

*Corresponding author. Email: ruslan.medzhitov@yale.edu Cite this article as N. D. Bachtel *et al.*, *Science* **389**, eadp0246 (2025). DOI: 10.1126/science.adp0246



Intestinal mast cell differentiation highlights mediator requirements for oral anaphylaxis. Profiling of intestinal mast cells revealed a dominant epithelial population with functions influenced by epithelial cues. TGFβ secreted through epithelium-specific αvβ6 integrin regulated the phenotype of mast cells within the epithelium and enhanced leukotriene synthesis. Leukotrienes were selectively required for anaphylaxis originating from ingestion, but not from intravenous injection. This effect was associated with decreased mucosal mast cell expansion and acutely altered mast cell responsiveness. [Figure created with BioRender.com]

IMMUNOLOGY

Intestinal mast cell–derived leukotrienes mediate the anaphylactic response to ingested antigens

Nathaniel D. Bachtel[1], Jaime L. Cullen[1], Min Liu[1], Steven A. Erickson[1], Vassily I. Kutyavin[1]†, Darine W. El-Naccache[1], Esther B. Florsheim[2], Jaechul Lim[3], Zuri A. Sullivan[4], Raiden Imaeda[1], Andrew Hudak[1], Cuiling Zhang[1], Ruslan Medzhitov[1,5,6]*

Anaphylaxis is a life-threatening complication of food allergen exposure. Although mechanisms governing anaphylaxis after intravenous injection are defined in mice, these models neglect mucosal exposure that accompanies ingestion. We investigated the role of mast cells within the intestine of mice and found that oral anaphylaxis required immunoglobulin E–Fcε receptor 1 (IgE-FcεR1) signaling. Intestinal mast cells were a heterogeneous population, shaped by epithelial cues. Compared with connective tissue mast cells found throughout the body, intestinal mast cells largely resided in the epithelium, displayed divergent transcriptomes and effector functions, and had a diminished ability to generate histamine, but they enhanced leukotriene synthesis. Mice genetically deficient in cysteinyl leukotriene synthesis, or those treated with the arachidonate 5-lipoxygenase (aLOX5) antagonist zileuton, were protected from oral antigen–induced responses, whereas those elicited by intravenous injection were unaltered.

Food allergies are exaggerated immune responses against protein antigens found in food (*1*–*5*). These immune responses are thought to be predominantly driven by immunoglobulin E (IgE)–mediated recognition of dietary antigens, leading to cross-linking and degranulation of mast cells throughout tissues. In the most severe cases, food allergen exposure leads to anaphylaxis, a life-threatening condition characterized by bronchoconstriction, vascular leak, and hemodynamic collapse (*6*). Although mast cell mediators that can drive anaphylaxis induced by intravenous allergen administration have been identified in mice, those capable of doing so secondary to ingestion remain unclear (*7*, *8*). This suggests that mucosal exposure alters the requirements needed to produce anaphylactic responses and that identifying such pathways could offer treatment options for food allergies and related conditions.

Ingestion preferentially drives food antigens to the gastrointestinal lumen, where they must traverse the epithelial layer before being exposed to the mucosal immune system. This transport occurs predominantly in the proximal small intestine and is mediated by an active process involving interleukin-13 (IL-13)–mediated secretory cell antigen passages and increases in paracellular permeability (*9*). Studies utilizing IgE and Fcε receptor 1α (FcεR1α)–deficient strains and those lacking the mast cell growth factor IL-9 suggest that local intestinal mast cells play crucial roles in driving this response (*10*–*13*). Mice overexpressing IL-9 display enhanced intestinal mast cell expansion, epithelial barrier permeability, and susceptibility to oral anaphylaxis, whereas IL-9/IL-9R knockout (KO) mice are resistant to oral but not intravenous allergen challenge (*14*, *15*). We reasoned that enhancing understanding about the development and function of intestinal mast cells could define mediators contributing to food-induced anaphylaxis.

We focused on cysteinyl leukotrienes (CysLTs) as potential candidates secreted by intestinal mast cells to augment oral anaphylaxis severity. CysLTs are eicosanoid lipid mediators that are produced by multiple cell types of hematopoietic and nonhematopoietic origin in response to diverse environmental signals (*16*). They are formed by the oxidation of arachidonic acid by 5-lipoxygenase [arachidonate 5-lipoxygenase (aLOX5)] and accessory protein 5-lipoxogenase-activating protein (FLAP) to become leukotriene A4 (LTA4) (*17*–*19*). LTA4 is then conjugated to glutathione by the enzyme LTC4 synthase (LTC4S) to form LTC4 and exported from the cell (*20*, *21*). Extracellular LTC4 is rapidly converted to LTD4 by γ-glutamyl transferase (GGT) and γ-glutamyl leukotrienase (GGL) and terminally to LTE4 by dipeptidase (DPEP) enzymes, which are abundant in the intestinal epithelium (*22*, *23*). Thus, there are multiple steps by which CysLTs may be elevated in the intestine through changes to their synthesis and degradation. CysLTs mediate their effects through three receptors that differ in their relative affinities for each species: CysLTR1 binds predominantly to LTD4 with lesser affinity for LTC4 and LTE4, CysLTR2 binds with equal affinities for LTC4 and LTD4, and CysLTR3 (OXGR1) binds selectively to LTE4 (*24*–*26*). These receptors differ in their cellular expression, but the outcome of stimulating these receptors largely converges on indirect or direct activation of group 2 innate lymphoid cells (ILC2s) (*27*–*29*). Given that ILC2s are potent sources of IL-9 and IL-13, which both sensitize to oral anaphylaxis, CysLT engagement could thus serve as a link between local intestinal responses and severe anaphylactic reactions (*30*–*33*).

Results

Ingested allergen–induced anaphylaxis relies on IgE-FcεR1 signaling

Prior studies report IgE-dependent requirements for oral anaphylaxis but differ in the susceptibility of mouse background strains and experimental food allergy paradigms used (*34*–*36*). We began by testing the ovalbumin (OVA)–alum model, whereby BALB/cJ mice are sensitized subcutaneously two times with phosphate-buffered saline (PBS) or OVA adsorbed in aluminum hydrogel and subsequently boosted by multiple intragastric challenges delivered by oral gavage. Sensitization elicits IgE-class switching and production of antigen-specific IgE by B cells, whereas boosting activates and recruits intestinal immune cells, drives IL-9–mediated intestinal mast cell expansion, and ultimately results in oral anaphylaxis susceptibility. Allergen-inducible gastrointestinal transit time (GITT) was measured at challenge 5 by administering a mixture of food allergen and carmine red dye and quantifying the time until red stool was observed in the cage; oral anaphylaxis was assessed at challenge 6 by rectal thermometry (Fig. 1A and fig S1A). Given that IL-4 is necessary for B cells to class switch to IgE antibodies and that FcεR1α binds to IgE on the surface of mast cells and basophils, IL-4Rα KO, IgE KO, and FcεR1α KO mice were utilized to determine whether the responses observed were attributable to IgE-FcεR1α signaling (*37*, *38*). Lastly, FcεR1α-DTR mice, which express diphtheria toxin receptor under the FcεR1α locus, were utilized to conditionally ablate mast cells and basophils upon administration of diphtheria toxin (*39*).

Quantification of total and OVA-specific IgE and IgG1 antibodies confirmed that IgE production was absent from IL-4Rα KO and IgE KO mice, whereas it remained unaltered in FcεR1α KO or DT-treated FcεR1α-DTR mice (Fig. 1B). OVA-specific IgG1 antibodies were present in all strains. Serial blood draws taken 1 hour after every other challenge revealed escalating mast cell protease 1 (MCPT1) serum levels

[1]Department of Immunobiology, Yale University School of Medicine, New Haven, CT, USA. [2]School of Life Sciences, Arizona State University, Tempe, AZ, USA. [3]College of Veterinary Medicine and Research Institute for Veterinary Science, Seoul National University, Seoul, Republic of Korea. [4]Department of Molecular and Cellular Biology, Harvard University, Cambridge, MA, USA. [5]Howard Hughes Medical Institute, Chevy Chase, MD, USA. [6]Tananbaum Center for Theoretical and Analytical Human Biology, Yale University School of Medicine, New Haven, CT, USA. ***Corresponding author. Email: ruslan.medzhitov@yale.edu** †Present address: ICC, Early Oncology R&D, AstraZeneca, Gaithersburg, MD, USA.

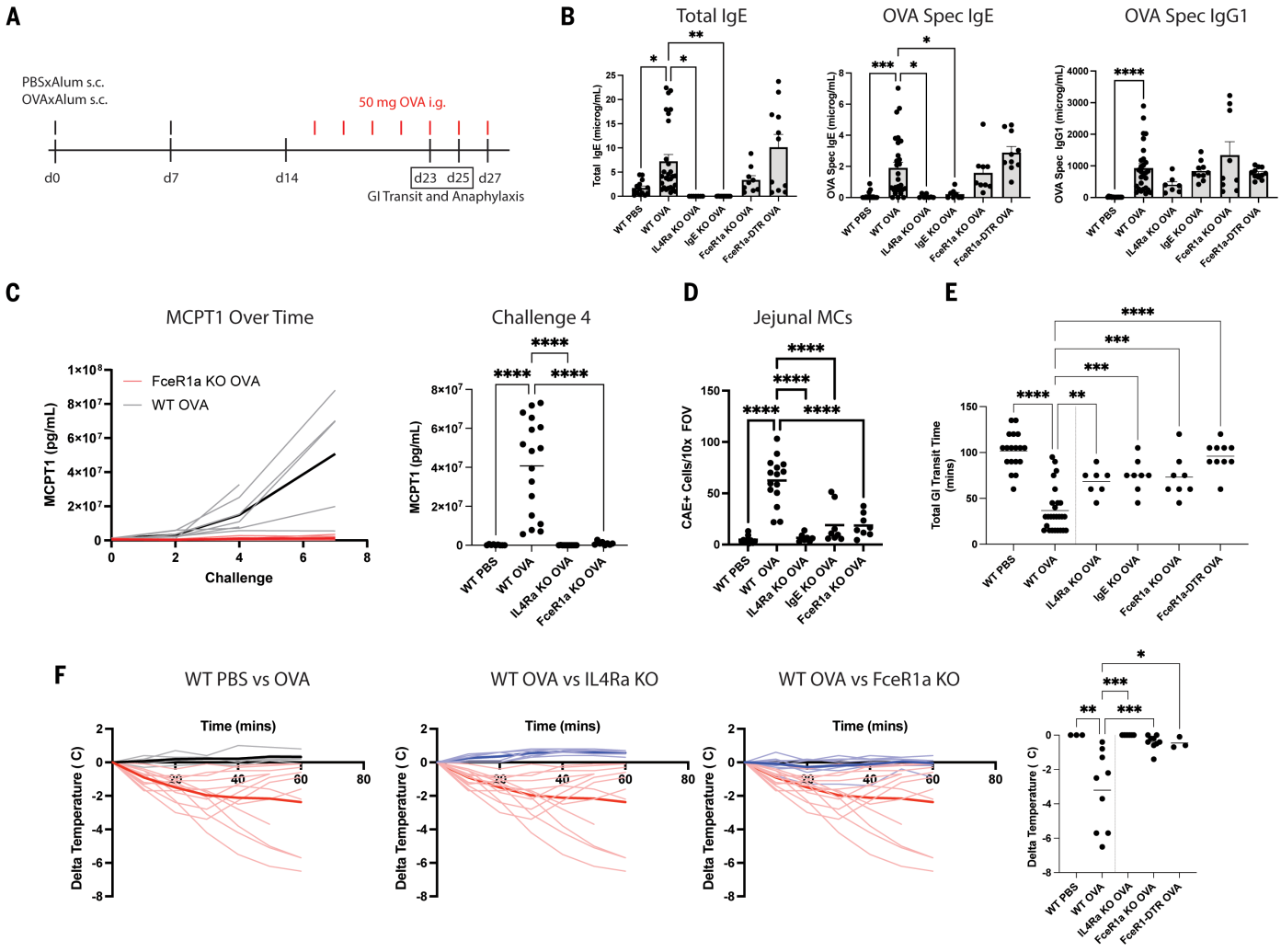


Fig. 1. The IgE-FcεR1α axis is required for ingested food–induced anaphylaxis. (**A**) Experimental scheme: WT BALB/cJ, IL-4Rα KO, IgE KO, FcεR1 KO, or FcεR1-DTR mice were sensitized and challenged with intragastric (i.g.) OVA. s.c., subcutaneous. (**B**) Serum levels of total IgE, OVA-specific (Spec) IgE, and OVA-specific IgG1 antibodies at day 27. (**C**) MCPT1 levels over time between sensitized WT (black) and FcεR1 KO mice (red) and at challenge 4 across strains. (**D**) Quantification of CAE^{+} mast cells/10× jejunal field of view (FOV). (**E**) Total GITT of allergic or control mice at the fifth OVA challenge by carmine red total gastrointestinal transit assay. (**F**) Temperature drop over time to sixth i.g. OVA challenge between control (black) and sensitized (red) WT mice, sensitized WT (red), and IL-4Rα KO mice (blue), and sensitized WT (red) and FcεR1 KO (blue) mice. Greatest temperature drop in 1 hour is also plotted. $n = 4$ to 28 mice per group, pooled from at least 2 independent experiments. Statistics were performed by one-way analysis of variance (ANOVA) with multiple comparisons test. Each dot represents an individual mouse. Horizontal lines represent mean. Error bars represent SEM. In temperature curves in (C) and (F), each dark line represents mean of a group and each light line represents values of an individual mouse. $^{*}P < 0.05$, $^{**}P < 0.01$, $^{***}P < 0.001$, and $^{****}P < 0.0001$.

in sensitized mice, which were absent in FcεR1α KO and IL-4Rα KO mice, highlighting increased levels of IgE-mediated mast cell degranulation (Fig. 1C). Indeed, expansion of mucosal mast cells, as determined by chloroacetate esterase (CAE) staining of jejunal segments, was notable in wild-type (WT) mice but reduced in those deficient in IgE-FcεR1α signaling (Fig. 1D). This suggested that mast cell degranulation initiated local expansion in this experimental paradigm. Although none of the strains tested displayed altered baseline GITT (fig. S1B), each displayed a ~25% reduction in GITT upon oral allergen administration as compared with ~75% in WT mice (Fig. 1E and fig. S1C), and all displayed ~85 to 100% less severe hypothermic responses elicited by oral challenge (Fig. 1F). Thus, cardinal features of anaphylaxis induced by oral antigens, including diarrhea and allergen-induced drop in body temperature in this model, were strongly reliant on IgE-FcεR1α signaling.

We next investigated whether anaphylaxis induced by intravenous injection was also dependent on IgE-FcεR1α signaling (fig. S1D). BALB/cJ mice were sensitized with PBSxAlum or OVAxAlum but then challenged with OVA intravenously rather than intragastrically on day 14. We observed no requirement for either FcεR1α-expressing cells (fig. S1E) or IgE (fig. S1F) upon intravenous allergen challenge, suggesting major contributions of IgG1-induced anaphylaxis at the doses utilized (*40*–*42*).

Given that oral challenge elicited anaphylactic symptoms, we sought to examine the degree of mast cell activation across tissues. We utilized staining for toluidine blue (TB), which labels mast cell metachromatic granules and enables identification of degranulated mast cells by poor intracytoplasmic staining or elevated extracellular granule release (*43*).

We compared degranulated mast cells in the ear pinna, stomach, and bronchus induced after the sixth oral challenge (fig. S1G) with

mice that had passive IgE-dependent anaphylaxis induced by being primed systemically with antigen-specific IgE and challenged intravenously with antigen (fig. S1H). We observed mast cell degranulation in all tissues examined after oral challenge, although the percentage of degranulated cells was at most half of that observed upon intravenous injection (fig. S1, I and J). Thus, oral anaphylaxis represented a state of mild, but not absent, systemic engagement of mast cells.

We utilized the peanut and cholera toxin model (*35*) in BALB/cJ mice to determine whether the same requirements for oral anaphylaxis could be generalized to other allergens and adjuvants (fig. S1K). Oral peanut challenge induced no change to body temperature (fig. S1L); however, a response to intravenous challenge with crude peanut extract was detectable (fig. S1, M and N), suggesting that differences between mouse colonies, background strains, or pathogen burden may influence the effectiveness of the peanut and cholera toxin model in driving oral allergen–induced anaphylaxis.

From our data, we concluded that oral anaphylaxis represents a state of mild systemic and strong local mast cell activation that is reliant on IgE-FcεR1α signaling.

Intestinal mast cells are a heterogeneous population shaped by TGFβ

Mast cells comprise two distinct lineages, connective tissue mast cells (CTMCs) and mucosal mast cells (MMCs), which display different developmental trajectories, tissue localizations, and functions (*44*). CTMCs express high levels of negatively charged proteoglycans that can be stained with conjugated avidin and are located near the muscularis layer of the intestine. By contrast, MMCs stain poorly with avidin, but positively for MCPT1, and are found in the lamina propria (LP) and epithelial layers (*45*). MMCs can be distinguished from CTMCs because they lack expression of the Mrgprb2 receptor and because they express mucosal- and epithelium-homing integrins (*46*, *47*). Given that CTMCs are seeded during embryonic development, they are negative for integrin β7, whereas mast cell progenitors require expression of the integrin α4β7 and extravasate into the intestine by interacting with MADCAM-1 (*48*, *49*). MMC progenitors proliferate in the LP and gradually decrease α4 and increase CD103 (ITGAE) as they home to the epithelium (*50*).

We performed flow cytometry on cells isolated from the small intestine of naïve BALB/cJ mice to determine the composition of intestinal mast cell populations under homeostatic conditions. We hypothesized that intestinal mast cells may express molecules involved in oral anaphylactic responses (fig. S2). We observed that LP mast cells constitute approximately 0.01 to 0.02% of lineage-negative CD45$^+$ cells, whereas they comprise 0.025 to 0.05% of the epithelial [intraepithelial lymphocyte (IEL)] fraction (Fig. 2A). Within the LP, we observed three distinct mast cell populations on the basis of integrin staining. Approximately 50 to 60% of mast cells were negative for β7 integrin, suggestive of a sizable population of connective tissue mast cells, with 20 to 40% positive for α4 and β7 and 10 to 20% positive for CD103 and β7 but lacking α4 expression. The epithelial population was almost entirely composed of CD103/β7$^+$ mast cells (85 to 95%), suggestive of terminally differentiated mast cells attached to the epithelial layer (Fig. 2B). Besides integrin expression, these mast cells differed in the expression of canonical mast cell surface markers, with α4β7$^+$ and CD103β7$^+$ mast cells expressing a lower mean fluorescence intensity (MFI) of suppression of tumorigenicity 2 (ST2) protein relative to β7$^-$ mast cells (Fig. 2C).

To understand the functions and development of these populations of mast cells, we sorted IEL and LP mast cells from WT BALB/cJ mice that had been sensitized and challenged once orally and performed RNA sequencing (RNA-seq). The primary differences observed were between mast cells sorted from different compartments of the small intestine (fig. S3, A and B, and data S1). Sorted epithelial mast cells were enriched in transcripts for *Mcpt1* and *Itgae*, whereas they were relatively deficient for *Mrgprb2* and *Cma1* expression, which is in line with our prior observations regarding localization of connective tissue and MMCs between these sites (Fig. 2D and fig. S3, C to E).

B cell and epithelial cell transcripts were also observed as being differentially expressed between sorted IEL and LP mast cell populations, suggestive of minor cellular contamination introduced during sorting. Therefore, we performed single-cell RNA-seq (scRNA-seq) of mast cells sorted from mice sensitized and challenged five times with oral allergen (fig. S3F and data S2). With nonmast cells removed from the dataset, we found transcriptional differences between mast cells found in LP and IEL sorted samples (fig. S3G). Unbiased harmony clustering revealed nine independent clusters, all of which expressed *Kit* and *FcεR1a* (Fig. 2E; fig. S3, H and I; and data S3) (*51*). Pseudotime analysis, beginning from the *Itga4*$^+$ *Mcpt8*$^+$ mast cell progenitor cluster 8, revealed a developmental spectrum from cluster 2 LP cells—which closely resembled connective tissue mast cells but largely did not express *Mrgprb2*—and ending with clusters 0, 1, which were the most prevalent cell types found in the epithelial layer (Fig. 2, F and G, and fig. S3, J to M) (*52*). Given the substantial transcriptional overlap between *Mrgpr2b*$^+$ mast cells and cluster 2, we performed differentially expressed gene (DEG) analysis to identify genes most associated with the acquisition of the epithelial mast cell phenotype by comparing this cluster with clusters 0,1 (Fig. 2H, fig. S3N, and data S4). The top DEGs increased in expression in IEL mast cells were molecules involved in cell adhesion (*Cdh1*), integrins (*Itgax*, *Itgae*), incretin metabolism (*Dpp4*), synapse formation (*Nlgn2*), cytokine signaling (IL-25 and IL-17β receptor, *Il17rb*), and notch signaling (*Hey1*), whereas expression of *Tpsb2*, *Ndrg1*, and *Plaur* was strongly suppressed (Fig. 2H, fig. S3O, and data S5). Many of these genes overlapped with those defined in a recent study in helminth infection, suggesting a conserved terminal phenotype expanded in states of type 2 inflammation (*53*).

We used ingenuity pathway analysis (IPA) to predict upstream regulators of the epithelial mast cell phenotype, of which transforming growth factor–β (TGFβ) was the strongest predicted extracellular signal regulating epithelial mast cell development (Fig. 2I, fig. S3P, and data S6). To determine whether TGFβ was capable of mimicking the transcriptional and functional changes that we observed between mast cell subsets, we cultured BALB/cJ female bone marrow–derived mast cells with the mast cell survival factor, stem cell factor (SCF), in the presence or absence of TGFβ for 7 days (fig. S4A) (*52*). TGFβ treatment markedly enhanced the cell-surface expression of CD103 and MCPT1, as measured by flow cytometry, while down-regulating ST2 (Fig. 2J, fig. S4, B and C).

Prior studies have suggested that epithelial TGFβ, which is liberated by the αvβ6 integrin, drives MMC protease expression (*54*, *55*). To determine whether αvβ6 may similarly underly the acquisition of the epithelial mast cell phenotype in the intestines of food-allergic mice, we sensitized BALB/cJ mice with PBSxAlum or OVAxAlum subcutaneously and subsequently treated them with isotype or αvβ6-neutralizing antibody (3G9) throughout the oral challenge phase (Fig. 2K and fig. S4F) (*56*). Although 3G9 treatment did not alter mast cell expansion and localization to the epithelial layer (fig. S4G), it reduced mast cell expression of ITGβ7 and CD103, while increasing ST2 (fig. S4, H and I). Furthermore, MCPT1 levels were suppressed in sensitized 3G9-treated mice despite an increased frequency of IEL mast cells relative to isotype-treated mice (Fig. 2L and fig. S4J). Effects on oral antigen–induced anaphylactic responses were less clear, with one experiment suggesting suppression and another displaying modest or no effect between groups (fig. S4K). We concluded that intestinal mast cells were a heterogeneous mucosal population that differentiates in response to αvβ6-mediated epithelial TGFβ release.

Intestinal mast cell differentiation skews mediator production

Intravenous injection of allergens in mice drives anaphylaxis through *Mrgprb2*$^+$ CTMCs and the release of histamine (*57*, *58*). These *Mrgprb2*$^+$ mast cells are located throughout the body but are the considerable

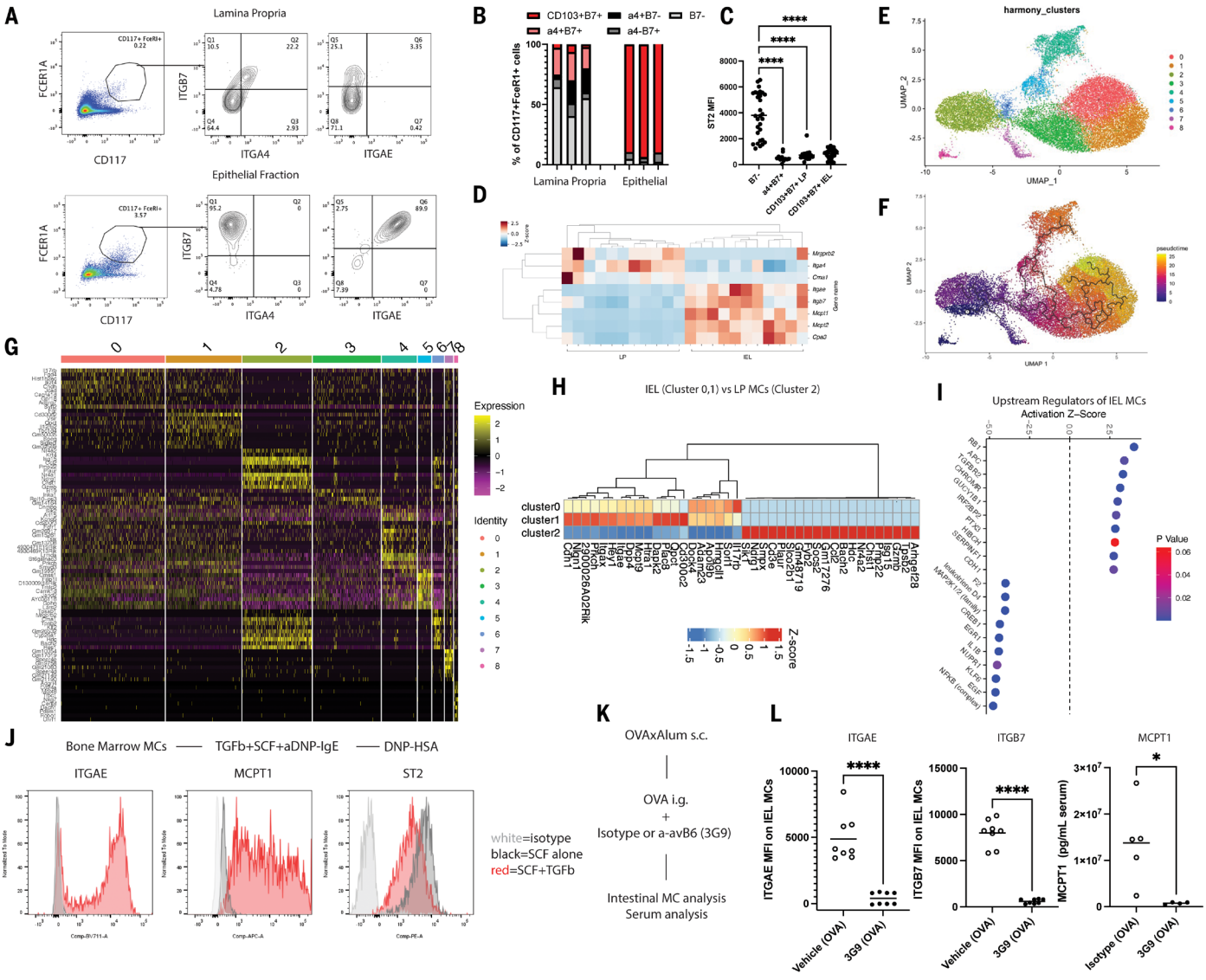


Fig. 2. Intestinal mast cells are shaped by epithelial cues. (**A**) Staining of CD117 and FcεR1 in LP and intraepithelial immune cells from naïve BALB/cJ mouse small intestine with ITGB7, ITGA4, and ITGAE staining (gated as in fig. S2). (**B**) Percentage of $\beta7^-$, $\alpha4\beta7^+$, and $CD103\beta7^+$ mast cells in intraepithelial and LP fractions (each bar represents a single naïve mouse) and (**C**) ST2 MFI of mast cell subsets with different integrin staining. RNA-seq was performed on sorted intraepithelial or LP mast cells from BALB/cJ mice sensitized and challenged once with 20 mg of i.g. OVA (**D**) Heatmap of mast cell proteases and integrins between sorted populations. (**E**) scRNA-seq clusters of intestinal mast cells sorted from sensitized BALB/cJ mice challenged five times with 50 mg i.g. OVA (22,171 cells were analyzed). (**F**) Pseudotime analysis of intestinal mast cell development starting from *Mcpt8*$^+$*Itga4*$^+$ mast cell precursors. (**G**) Heatmap of top 10 DEGs between each mast cell cluster. (**H**) Heatmap of top DEGs between IEL mast cells (clusters 0,1) and LP mast cells (cluster 2). (**I**) IPA analysis of these DEGs reveals predicted upstream regulators. (**J**) Bone-marrow mast cells (MCs) were treated with TGFβ+SCF for 7 days, and effects on epithelial mast cell shaping were quantified by flow cytometry. (**K**) BALB/cJ female mice were sensitized as previously described and challenged with OVA in conjunction with isotype or αvβ6-neutralizing antibody (3G9) treatment, and (**L**) expression of ITGAE and ITGB7 on intestinal mast cells and of serum MCPT1 levels after challenge were quantified. $n = 3$ to 30 mice per group. All data were pooled from at least two independent experiments except for scRNA-seq data, which were obtained in one. Each box in heatmap in (D) represents mast cells sorted from a single mouse. scRNA-seq plots in (E) to (I) represent data from IEL and LP mast cells sorted from two mice, sequenced separately, and concatenated for final analysis. Statistics were performed by one-way ANOVA with multiple comparisons test for (C), or unpaired *t* test for (L). Each dot represents an individual mouse. Horizontal lines represent mean. $^*P < 0.05$, $^{**}P < 0.01$, $^{***}P < 0.001$, and $^{****}P < 0.0001$.

minority at mucosal sites such as the lung and intestine. Given that oral challenge reflected a state of high-local and low-systemic mast cell activation, we hypothesized that shaping of mast cells in the intestines may lead to altered histaminergic requirements for responses originating from ingestion.

Utilizing a recently published multitissue mast cell scRNA-seq atlas, we compared marker genes of key clusters identified in the intestine with other tissues throughout the body (Fig. 3A) (*59*). *Mcpt1* and *Itgae* were only observed in mast cells originating from the gastrointestinal tract, whereas *Mrgprb2* and a CTMC-associated protease, *Cma1*, were dominant in nearly all other tissues tested. Expression of histidine decarboxylase (*Hdc*), the enzyme required for mast cell histamine synthesis, was associated with the connective tissue phenotype and minimally expressed in the intestine, whereas 5-LOX activating protein (*Alox5ap*), an enzyme necessary for leukotriene production, was more prevalent in intestinal mast cells.

Examination of our intestine-intrinsic sequencing datasets revealed that not all intestinal mast cells were deficient in *Hdc*. Those isolated

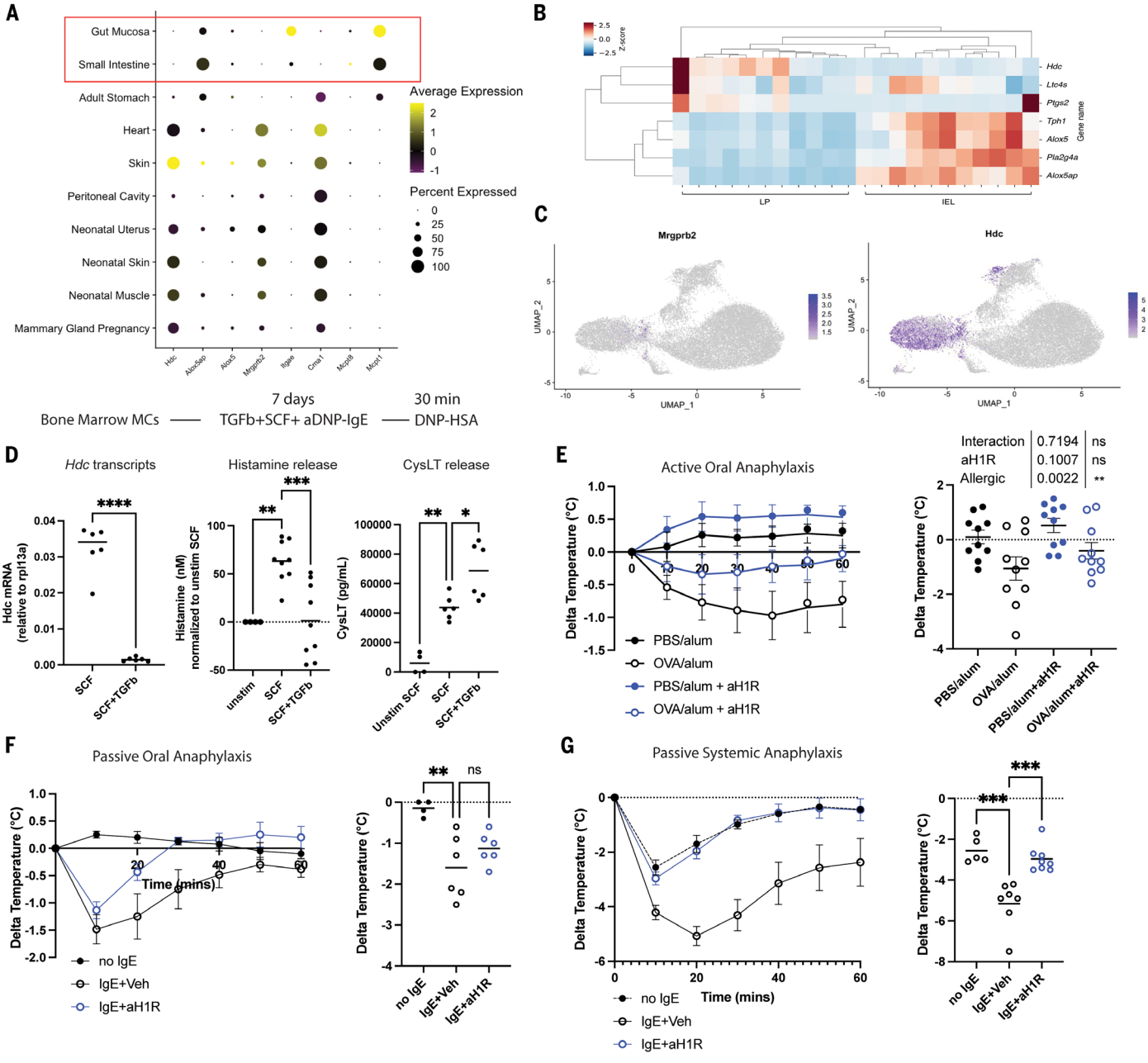


Fig. 3. Intestinal mast cell differentiation skews mediator production. (**A**) Dot plot of key mast cell marker and effector genes across tissues (*59*). (**B**) Heatmap of mast cell mediators differentially expressed by IEL and LP mast cells by bulk RNA-seq. (**C**) Uniform manifold approximation and projection (UMAP) plot demonstrating minimal *Mrgprb2*$^{+}$ mast cells and loss of *Hdc* with intestinal mast cell development (22,171 cells were analyzed). (**D**) *Hdc* transcripts and histamine and CysLT release by enzyme-linked immunosorbent assay (ELISA) of bone-marrow MCs treated with SCF+TGFβ for 7 days. (**E**) Effects of H1R antagonism on severity of active oral anaphylaxis in BALB/cJ mice was assessed by means of triprolidine pretreatment. (**F**) Effects of H1R antagonism on passive oral anaphylaxis and (**G**) passive systemic anaphylaxis were similarly examined. $n = 4$ to 10 mice per group, pooled from at least two independent experiments. $n = 4$ to 9 technical replicates from three independent experiments for (D). Each box in heatmap in (B) represents mast cells sorted from a single mouse. scRNA-seq plot in (C) represents data from IEL and LP mast cells sorted from two mice, sequenced separately, and concatenated for final analysis. Statistics were performed with unpaired *t* test in (D), left panel; one-way ANOVA with multiple comparisons in (D), middle and right panels, (F), and (G); and two-way ANOVA in (E) . For temperature curves in (E) to (G), each dot represents mean ± SEM for each group. For greatest delta temperature graphs in (E) to (G), each point represents a single mouse. Horizonal bars represent mean ± SEM when shown. *$P < 0.05$, **$P < 0.01$, ***$P < 0.001$, and ****$P < 0.0001$. ns, not significant.

from the LP were histamine rich relative to the dominant population found in the intraepithelial layer (Fig. 3B and fig. S3E), and this was not due to the presence of *Mrgprb2*$^{+}$ connective tissue mast cells at this site (Fig. 3C). Rather, we hypothesized that intestinal mast cells transitioned through a transient transcriptional state similar to that of CTMCs (including expression of *Hdc* and *Cma1*) after entering the intestine, which was altered as they localized to the epithelium and terminally differentiated.

As TGFβ was sufficient to drive gene expression of bone marrow mast cells toward an epithelial mast cell phenotype, we isolated bone marrow mast cells and tested the effect of TGFβ treatment in vitro on transcription and the release of select mediators. TGFβ treatment

decreased *Hdc* mRNA by ~20 fold. Genes involved in leukotriene generation were also changed in expression, with *Alox5ap* being upregulated ~twofold by TGFβ and *Ltc4s* being down-regulated (Fig. 3D and fig. S4D). Histamine (Fig. 3D) and prostaglandin D2 (PGD2) (fig. S4E) release were suppressed after degranulation induced by aDNP-IgE and DNP-HSA treatment (DNP, dinitrophenyl; HSA, human serum albumin), whereas MCPT1 (fig S4E) and CysLT synthesis (Fig. 3D) were enhanced.

Histamine mediates its effect on IgE-dependent anaphylaxis to intravenous allergens dominantly through histamine receptor 1 (H1R), which can be blocked by acute pharmacological antagonism with triprolidine (*60*, *61*). Administration of triprolidine 30 min before oral challenge did not block a drop in body temperature (Fig. 3E); however, the percentage of mice that dropped greater than 2° in body temperature was reduced. Similarly, triprolidine pretreatment had a nonsignificant effect on anaphylaxis elicited by passively priming mice with TNP-IgE (TNP, trinitrophenyl) and subsequently challenging intragastrically with TNP-OVA (Fig. 3F).

These observations did not seem to be due to ineffectiveness in dosing, timing, or pharmacological properties of triprolidine itself, because mice passively sensitized with IgE and challenged intravenously were nearly completely protected (Fig. 3G). We therefore concluded that a local nonhistaminergic response mediated by intestinal mast cells precedes and, in some cases, sensitizes to more severe reactions that follow.

Hematopoietic CysLTs are required for the acute oral anaphylaxis response

We focused on leukotrienes as nonhistamine molecules that could be important in gastrointestinal allergic reactions because enzymes required for leukotriene biosynthesis and its release were enhanced by intestinal mast cell differentiation. To examine this possibility, we sensitized BALB/cJ mice with PBSxAlum or OVAxAlum and treated them with the aLOX5 antagonist zileuton throughout the oral challenge phase (Fig. 4A and fig. S5A). Zileuton-treated mice displayed no alterations in levels of allergen-specific IgE or IgG1 antibodies (fig. S5B) but exhibited reduced mast cell expansion and degranulation (fig. S5, C and D) relative to vehicle-treated controls. Zileuton-treated mice did not show a decrease in body temperature (Fig. 4A) nor a decrease in GITT (fig. S5E) in response to oral challenge with OVA. We repeated the experiment but treated with zileuton only 1 hour before GITT evaluation instead of throughout the boosting phase (Fig. 4B and fig. S5F). Intestinal mast cell expansion was not different between vehicle or zileuton-treated mice, but MCPT1 levels were reduced by half (fig. S5, G and H). After oral antigen exposure, acute zileuton treatment prevented a decrease in body temperature (Fig. 4B) and ameliorated allergen-induced reductions in GITT to approximately one-third of sensitized vehicle-treated levels (fig. S5I).

We considered that zileuton may be able to inhibit allergen-inducible changes in intestinal permeability—which could explain such an acute effect—but did not find evidence of changes in uptake of 4-kDa or 70-kDa dextrans when co-gavaged with allergen in food-allergic mice (fig. S5J). Systemic mast cell degranulation, as measured by TB staining of ear pinna, stomach, and bronchus 1 hour after oral challenge, was also not reduced upon acute zileuton pretreatment (fig. S5K). Furthermore, treatment of bone marrow mast cells in vitro with zileuton led only to minor reductions in degranulation, as measured by beta-hexosaminidase release (fig. S5, L and M).

To investigate whether activity of aLOX5 in the gut mucosa was required for anaphylaxis, we sensitized BALB/cJ mice with PBSxAlum or OVAxAlum as previously described and pretreated them with Zileuton 1 hour before intravenous allergen administration (Fig. 4C). We also compared C57BL/6J aLOX5 KO mice with C57BL/6J littermate controls after sensitization and intravenous challenge (fig. S5N). Blocking or deficiency in aLOX5 did not impact the decrease in body temperature after systemic antigen challenge nor impact symptoms of anaphylaxis (Fig. 4C and fig. S5, O and P); however, an effect on hemoconcentration was observed by measurement of blood hematocrit levels (fig. S5Q). We concluded that leukotrienes mediated anaphylactic response to oral antigens but that this was not dependent on altered intestinal permeability or systemic mast cell activation.

To determine whether the effects of zileuton were attributable to the actions of CysLTs, we sensitized and challenged LTC4S KO mice or WT littermates with oral allergen (Fig. 4D and fig. S5R). No differences were observed in antigen-specific IgE or IgG1 levels, although LTC4S KO mice displayed a mildly elevated level of total IgE relative to WT controls (fig. S5S). MMCs were unchanged in number; however, serum levels of MCPT1 induced by oral challenge were reduced approximately by half (fig. S5, T and U). LTC4S KOs were partially protected from oral allergen–inducible reductions in GITT and were completely protected from a decrease in body temperature (Fig. 4D and fig. S5V).

CysLTs can be produced by hematopoietic and nonhematopoietic sources, including tuft cells (*62*, *63*). We sought to examine whether deficiency in the hematopoietic compartment would protect from oral anaphylaxis. We utilized a mixed bone marrow chimera model whereby WT, LTC4S KO, or a 1:1 mixture of WT and LTC4S KO bone marrow was transplanted into sublethally irradiated FcεR1-DTR [red mast cell and basophil reporter (RMB)] mice (Fig. 4E). After waiting 8 weeks for bone marrow reconstitution, these mice were sensitized and orally challenged as described in Fig. 4D. The body temperature of nonirradiated control mice dropped less than a degree at the fourth oral challenge, whereas mice that had WT bone marrow transplanted into RMB recipients (WT->RMB) dropped an average of 5° in body temperature (Fig. 4F). This increased hypothermic response was associated with an early rapid rise in MCPT1 serum levels at challenge 2 in all irradiated chimeric mice compared with nonirradiated controls (fig. S5W). This suggests that some aspect of irradiation and bone marrow reconstitution may have sensitized to oral challenge and increased intestinal mast cell activity. The magnitude in which body temperature decreased in mice that were transplanted with LTC4S KO bone marrow (LTC4S->RMB) was reduced, whereas irradiated mice transplanted with a 1:1 mixture of WT and LTC4S KO bone marrow (WT/LTC4S->RMB) displayed no difference relative to the WT->RMB group. MCPT1 serum levels were generally associated with the protection observed. We thus concluded that CysLTs originating from the hematopoietic compartment were required for ingested allergen–induced anaphylaxis.

The severity of the hypothermic response upon oral challenge in the OVA-alum model could be influenced by the effects of leukotrienes on both mast cell expansion (secondary to repeated intragastric challenges) and roles in the anaphylactic event itself. We therefore used passive models during which mice are administered antigen-specific IgE and subsequently challenged with antigen to elucidate how leukotrienes could influence events not attributable to mast cell expansion (fig. S6A). We utilized a model whereby mice were passively sensitized with aDNP-IgE and challenged intravenously with DNP-HSA. One week later, the same mice were passively sensitized with aTNP-IgE and challenged with TNP-OVA intragastrically (*64*–*66*). Intestinal mast cells were quantified 1 week after intragastric challenge, and blood was collected 1 hour after each challenge to measure mast cell degranulation. Both antigen-IgE clone combinations (aDNP-IgE + DNP-HSA and aTNP-IgE + TNP-OVA) elicited comparable hypothermic responses when antigen was administered intravenously, and the use of two clones of differing specificities prevented cross-reactivity between challenges (fig S6B). These features enabled comparison of hypothermic responses elicited by IgE-mediated intravenous challenge to intragastric challenge in the same mice.

IgE-dependent anaphylaxis induced by intravenous antigen administration was largely unaltered by deficiency in CysLT function, either

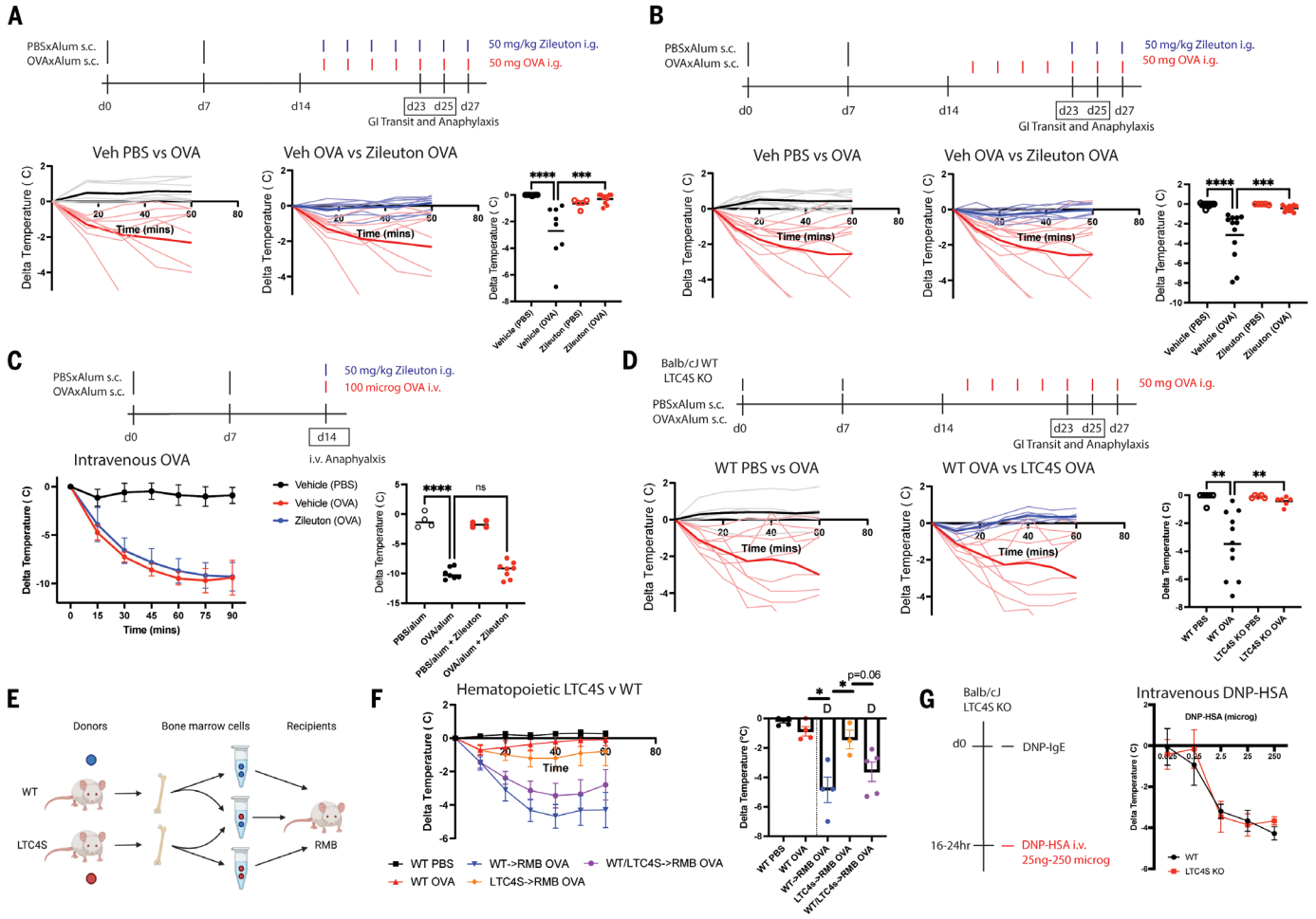


Fig. 4. Hematopoietic CysLT production constitutes an acutely inhibitable pathway required for oral anaphylaxis. (**A**) Effect of chronic zileuton administration on severity of active oral anaphylaxis in BALB/cJ. WT control (black) and sensitized (red) mice treated with vehicle were compared with WT sensitized mice treated with vehicle (red) or zileuton (blue). (**B**) Effects of acute zileuton administration from fifth challenge on severity of oral anaphylaxis in BALB/cJ. WT control (black) and sensitized (red) mice treated with vehicle were compared with WT sensitized mice treated with vehicle (red) or zileuton (blue). (**C**) Effects of acute zileuton administration on severity of intravenous anaphylaxis. (**D**) Effect of LTC4S KO or WT BALB/cJ status on severity of active oral anaphylaxis. WT control (black) and sensitized (red) mice were compared with sensitized WT (red) and LTC4S KO mice (blue). (**E**) FcεR1-DTR (RMB) mice were sublethally irradiated and transplanted with bone marrow cells derived from WT or LTC4S KO mice, or a mix of 1:1 WT and LTC4S KO mice. The mice were then rested for 8 weeks before being sensitized and orally challenged as previously described. (**F**) Temperature drop over time after fourth oral OVA challenge and greatest temperature drop. "D" denoted death within a mouse group. Dashed line separates nonirradiated mice (left) from irradiated chimeras (right). (**G**) LTC4S KO mice were passively sensitized with aDNP-IgE and challenged 16 to 24 hours later with 25 ng to 250 μg of DNP-HSA intravenously and anaphylaxis severity assessed by greatest rectal temperature over the ensuing hour. $n = 3$ to 11 mice per group for mouse experiments across two to three independent experiments except for panels (E) and (F), which are from one experiment. Statistics were performed by one-way ANOVA with multiple comparisons in (A) to (D) and (G) and by unpaired t test in (F). Each dot in greatest temperature drop plots represents an individual mouse. In temperature drop plots in (C), (F), and (G), each point represents mean ± SEM. In temperature curves in (A), (B), and (D), each dark line represents mean of a group and each light line represents values of an individual mouse. *$P < 0.05$, **$P < 0.01$, ***$P < 0.001$, and ****$P < 0.0001$.

by genetic knockout of LTC4S or loss of either of the receptors CysLTR1 or CysLTR2 (fig. S6C), with potential effects of LTC4S KO on hematocrit elevations seen at the dose administered (fig S6D). Intragastric challenge led to a much milder hypothermic response that was completely dependent on LTC4S and CysLTR1 for its induction (fig. S6E), with a role for LTC4S on hematocrit elevations also observed (fig S6F). MCPT1 quantified 1 hour after each challenge was increased in LTC4S KO and CysLTR2 KO strains, and intestinal mast cells detectible in the IEL and LP were unaltered in frequency as compared with WT controls (fig. S6, G and H). Thus, CysLTs and CysLTR1 display elevated importance during IgE-dependent reactions occurring from gastrointestinal exposure, and these effects did not appear attributable to decreased intestinal mast cell frequencies nor degranulation.

The selective role for leukotrienes in gastrointestinal challenge could reflect differences in the importance of these mediators at different concentrations of allergen that reach the bloodstream. To examine this possibility, we passively sensitized LTC4S KO or WT mice with aDNP-IgE and subsequently challenged them with DNP-HSA at doses ranging from 25 ng to 250 μg, encompassing systemic doses of allergen described after oral challenge (Fig. 4G and fig. S6I). At each allergen concentration administered intravenously, there was no effect of LTC4S deficiency on body temperature responses (fig. S6, J and K), and we therefore concluded that the requirement of CysLTs in oral anaphylaxis was tissue-intrinsic.

CysLT receptor 1 and 2 are individually required for MMC expansion but do not acutely influence oral anaphylaxis

To determine which CysLT receptors were required for the effects on food allergen–induced diarrhea and oral anaphylactic temperature decreases, we sensitized and challenged WT, CysLTR1 KO, and CysLTR2

KO mice (fig. S7A). We observed no effect on OVA-specific or total IgE antibodies or OVA-specific IgG1 antibodies between these mice (fig. S7B). However, we observed a substantial decrease in MCPT1 in the blood that was similar to that observed in LTC4S KO mice (fig. S7C). Both CysLTR1 KO mice and CysLTR2 KO mice displayed a pronounced reduction in CAE^+ jejunal mast cells (fig. S7D) and were protected from allergen-induced reductions in GITT (fig. S7E). In the absence of allergen challenge, CysLTR1 KOs had decreased GITTs relative to WT controls.

Although both strains displayed attenuated decreases in body temperature after oral allergen exposure relative to WT mice, CysLTR1 KOs had half the temperature drop of CysLTR2 KOs, suggesting a contribution of both receptors with a predominant effect of CysLTR1 (fig. S7F). Treatment with the CysLTR1 antagonist montelukast before each oral challenge also prevented body temperature changes in response to antigen and reduced intestinal mast cell expansion, whereas treatment with the CysLTR2 antagonist HAMI3379 led to variable effects relative to CysLTR2 KOs (fig. S8, A to G). Acute administration of montelukast 1 hour before oral challenges 5 and 6 in PBSxAlum- or OVAxAlum-sensitized BALB/cJ mice afforded no protection from oral anaphylaxis, unlike zileuton administration (fig. S8, H to N). These data would suggest an acute multireceptor requirement in mediating anaphylaxis after active sensitization and challenge, whereas CysLTR1 and CysLTR2 function nonredundantly to drive MMC expansion.

Discussion

Whereas some individuals sensitized to food antigens develop anaphylaxis upon ingestion, others do not. Although intestinal mast cell expansion and epithelial permeability are associated with reactivity to food proteins clinically, understanding the molecules that contribute toward developing anaphylaxis in sensitized individuals could guide the development of therapeutic interventions. By taking advantage of mouse models susceptible to oral challenge, we characterized the developmental trajectory of intestinal mast cells and linked their tissue-intrinsic gene expression profiles with altered anaphylaxis requirements based on the route of exposure.

A speculative model to explain the requirements of MMC-derived CysLTs in oral anaphylaxis could relate to rapid local activation of tissue ILC2s. In experimental food allergy, the function of ILC2s is IgE-dependent, and all three CysLTRs converge on ILC2 activation either through direct means or through the production of epithelial cues such as IL-33 and IL-25 and neuropeptides such as neuromedin U (*27*–*29*, *33*, *67*, *68*). This may explain why we observed that antagonizing aLOX5 acutely prevented oral anaphylaxis, but blocking CysLTR1 or CysLTR2 individually did not. ILC2 activation triggers production of IL-9 and IL-13, augmenting intestinal mastocytosis and intestinal permeability, respectively, through secretory cell–associated antigen passages and paracellular pathways (*9*, *12*, *14*, *30*). Histaminergic requirements for oral anaphylaxis were only observed in the most severely affected allergic mice, and this would be consistent with leukotrienes representing a response capable of bridging ingestion to systemic exposure. Acute aLOX5 inhibition did not inhibit the passage of fluorescently labeled dextrans from intestine to blood nor inhibit systemic mast cell activation. This suggests that leukotrienes may affect readouts of anaphylaxis that are due to intestine-intrinsic actions such as activation of thermoregulatory neurons in the hindbrain (*69*).

The role of CysLTs in human food allergy is poorly understood. Although leukotrienes are detectible in the serum of patients undergoing anaphylaxis, it is not certain whether their inhibition can reduce reactions to oral allergen challenge (*70*, *71*). In a retrospective analysis of children with food allergies, treatment with the CysLTR1 antagonist, pranlukast, reduced blood eosinophil counts, serum IgE, and serum IL-4 and IL-5 but was not associated with reduced severity of clinical reactions (*72*). By contrast, a small retrospective study using montelukast sodium pretreatment acutely during oral immunotherapy, whereby individuals are given small doses of food antigens as a means of desensitization, reduced symptoms and helped patients achieve their target dose (*73*). Oral immunotherapy for food allergies appears to decrease the synthesis of eicosanoids, including leukotrienes, over the treatment course and reduces clinical reactivity (*74*). Whether mechanisms known to induce leukotriene production and reduce reactivity thresholds to food allergen ingestion—such as alcohol consumption, NSAID ingestion, or exercise (*75*–*80*)—do so in leukotriene-dependent manners is another open question.

Although the role of IgE in food-allergic responses in humans is well accepted, the role of MMCs remains controversial (*81*). Local mast cell expansion has been observed histologically and functional differences described historically, but transcriptional profiling of mast cells from the intestinal mucosa of food-allergic individuals remains elusive (*82*–*84*). Most isolation protocols solely examine the LP, which our data suggest may preclude analysis of mast cells within the epithelial layer. The developmental trajectory of intestinal mast cells we observed in food-allergic mice was similar to that identified in nasal polyps of patients with aspirin-exacerbated respiratory disease (AERD), a population associated with leukotriene excess and atopy in humans (*85*). TGFβ was associated with the transcriptional shaping of these intraepithelial mast cells, resulting in increased CysLT secretion in humans. We propose that there may be common differentiation trajectories for mast cells at different mucosal barrier sites that are conserved across species. The scRNA-seq data presented here may help to develop genetic tools enabling specific manipulation of MMCs to determine their roles in the body.

The study of food allergies is hindered by differences in susceptibility of mouse background strains, with the widely used C57BL/6J being resistant to oral anaphylaxis. Hoyt *et al*. reported that a mutation affecting dipeptidase 1 (DPEP1), an epithelial brush-border enzyme that converts LTD4 to LTE4, underlies the susceptibility of the food allergy–prone C3H/HeJ mouse strain (*86*). Combined with the results presented here, these findings suggest that DPEP1 dysfunction may act to enhance the effects of intestinal mast cell degranulation at the epithelial interface. Together, these findings reveal a critical role of leukotrienes in anaphylactic reaction to ingested allergens.

Materials and methods

Animals

All animal care and experimentation were approved by the Institutional Animal Care and Use Committee of Yale University School of Medicine and are consistent with the NIH, USA, guidelines. Mouse lines were interbred in our facilities to obtain the final strains described in the text. Genotyping was performed according to the protocols established for the respective strains by The Jackson Laboratories or published by the donating investigators. Mice were maintained at the Yale University animal facilities in temperature-(22°C) and humidity-controlled rooms, in a 12 hours light/dark cycle with free access to standard chow diet (Teklad 2018S, Envigo) and water. Mice were euthanized by CO_2 asphyxiation.

Female mice at 6 to 10 weeks of age were used for all experiments. BALB/cJ (000651), C57BL/6J(000664), C57BL/6 FcεRI KO (B6.129S2(Cg)-Fcer1atm1Knt/J, 010512), BALB/c Il4ra KO (BALB/c-Il4ratm1Sz/J, 003514) (*87*), aLOX5 KO (B6.129S2-Alox5^{tm1Fun}/J) (*88*), LTC4sKO (C.129S7(B6)-Ltc4stm1Blam/J, 0309539) (*21*), CysLTR1 KO (C.B6-Cysltr1tm1Ykn/J, 030960) (*26*), CysLTR2 KO (C.B6-Cysltr2tm1Ykn/J,031718) (*25*) mice were purchased from The Jackson Laboratories and maintained in our facilities. BALB/cJ IgE KO mice were generously provided by H. C. Oettgen (Harvard University), and RMB mice (B6. Ms4a2tm1Mal310) (*39*) were generously provided by P. Launay (Université Paris Diderot). RMB mice, FcεRI KO, and IgE KO mice were backcrossed more than eight times onto BALB/cJ for this study. We used littermate controls in all experiments.

Chimeric mice were generated as previously described (*1*). BALB/cJ WT or LTC4S-KO mice were used as donors in bone marrow transplant experiments. FceR1-DTR-TdTom RMB mice underwent a lethal total-body

irradiation with two doses of 500 rad (Gammacell 40 ^{137}Cs γ-irradiation source), with an interval of 3 hours between the first and the second irradiation. Fresh, unseparated bone marrow cells (10×10^6 per mouse) were injected into the tail vein of the irradiated recipient mice 4 hours after lethal irradiation. Chimerism efficiency was checked by flow cytometry 8 weeks post-irradiation and transplant using peripheral blood, and reconstituted mice were used 2 months after bone marrow transplantation.

Drug treatments

Zileuton 50 mg/kg (Tocris), montelukast sodium 10 mg/kg (Cayman Chemical Co.) and HAMI3379 0.4mg/kg (Cayman Chemical Co.), were administered 1 hour prior to each oral challenge, or starting 1 hour before the fifth oral challenge as described in the text. Zileuton was administered via oral gavage in 0.5% methylcellulose, while montelukast and HAMI3379 were delivered by intraperitoneal challenge in sterile PBS. All control groups received appropriate vehicle solutions (*1*). H1R inhibition in active and passive anaphylaxis experiments was achieved by treatment with 200 μg of triprolidine 30 min prior to oral or systemic allergen challenge (*61*). The αvβ6 neutralizing monoclonal antibody 3G9 was generated as previously described (*56*). Mice were treated twice per week with 10 mg/kg of 3G9 or IgG1 isotype control (InVivoMAb) in InVivoPure pH 7.0 Dilution Buffer as previously described (*89*) with the first dose being given the morning prior to first oral challenge and last given within 4 days of the experimental endpoint.

Mast cell depletion

For mast cell depletion, sensitized RMB mice were injected i.p. with 0.05 mg/kg of diphtheria toxin (Sigma Aldrich D0564) three times every other day as previously described starting on day 14 (1 week after the second s.c. sensitization) (*1*). Because this protocol was efficient at depleting mast cells even in heterozygous RMB mice, we used both mutants and heterozygotes as mast cell-depleted models.

Experimental food allergy model

The active food-allergy model using ovalbumin (OVA) and the adjuvant, aluminum hydrogel (Alum), has been previously described (*1*). Briefly, mice were sensitized on day 0 and day 7 by subcutaneous injection of 0.25 mg/kg endotoxin-free ovalbumin (BIOVendor 321001) adsorbed in 50 mg/kg aluminum hydroxide gel (alum, Invivogen vac-alu-250) and diluted to a final volume of 0.2 ml in sterile phosphate buffered saline (PBS) pH=7.4. Controls received an antigen-free sensitization (referred to as PBS/alum or PBS). Mice were bled on day 14 for antibody titer measurements and subsequently challenged 7 times by oral gavages with 50 mg grade III OVA (Sigma-Aldrich A5378) in 0.2 ml of PBS on days 14, 16, 18, 20, 22, 24, and 26. In most experiments, mice were bled 1 hour after every other challenge for MCPT1 quantification as described below. Allergen-induced GITT measurements were performed on challenge 5, oral anaphylactic temperature drop on challenge 6, and the mice were humanely euthanized by CO_2 asphyxiation for terminal analysis 1 hour after challenge 7.

The oral anaphylaxis paradigm using peanut and cholera toxin model was performed as previously described (*35*) except that the systemic peanut challenge was administered the week after oral challenge to confirm successful sensitization.

Total GITT

Mice were sensitized and challenged as described in the "Experimental Food Allergy Model" section. On the fifth oral challenge, mice were singly housed in cages with free access to food and water and were subsequently gavaged with 50 mg of OVA mixed with 6% carmine red (C1022, Sigma-Aldrich) in 0.5% methylcellulose (M0512, Sigma-Aldrich). Mice were monitored every 15 min for the occurrence of diarrhea and/or red in the stool. GITT was measured as the time from oral gavage until carmine red dye was seen in the stool. Mice were co-housed after the assay was complete for each mouse. In cases where zileuton, montelukast, HAMI3379, or drug cocktails were administered, mice were administered these reagents via the denoted routes and concentrations 1 hour prior to the fifth oral challenge. Allergen-inducible GITT was represented as a fraction of each sensitized mouse's GITT divided by the average of the GITT of un-sensitized mice within each group.

Active oral anaphylaxis

Mice were sensitized and challenged as described in the "Experimental Food Allergy Model" section. After the sixth oral gavage, the rectal temperature of each mouse was measured every 10 min for 1 hour via rectal thermometry (Thermalert TH5). In cases where mice were administered zileuton, montelukast, or HAMI3379, mice were administered these reagents via the denoted routes 1 hour prior to the 6th oral challenge (as described above).

Active systemic anaphylaxis model

Mice were sensitized on day 0 and 7 with OVA adsorbed in Alum hydrogel as described above. On day 14, mice were bled for antibody levels to ensure proper sensitization. On day 16, these mice were challenged with 100 μg of grade V OVA intravenously. Temperature was measured every 15 min thereafter by rectal thermometry (Thermalert TH5). The greatest temperature drop was calculated by subtracting the baseline temperature of each mouse from the lowest temperature they reached during the recording time, with hematocrit being collected at 1 hour after challenge. Symptom scoring was performed as previously described (*8*) where 0 denoted no symptoms, 1 = mouth/ear scratching with hind leg, 2 = decreased activity, isolation, and puffiness around eyes/mouth, 3 = motionless for >1 min, lying prone on stomach, 4 = no response to prodding or whisker stimuli, and 5 = tremor, convulsion, and death.

Generation of TNP-OVA

TNP-conjugated ovalbumin was generated as previously described with minor modifications (*66*). Briefly, 500 mg of grade III OVA (Sigma) was resuspended in 10 ml of 0.1 M NaHCO3 buffer pH9.6 and mixed with 4 ml of 25mg/ml TNP-e-Aminocaprolyl-OSU (ChemCruz, resuspended in DMSO). The resulting solution was wrapped in foil and mixed overnight on a rotating mixer. The following day, the TNP-OVA was purified using Amicon Ultra 4 3K Filter Devices (Sigma) and subsequently washed in-column four times with 4 ml of sterile PBS. The TNP-OVA was then isolated from the column filter and resuspended in 2.5 ml to yield a concentration of approximately 200mg/ml TNP-OVA. Efficiency of isolation of this approach was confirmed using Bradford assay and via a protein gel followed by Coomassie stain with an OVA standard.

Passive IgE-dependent anaphylaxis models

6- to 10-week-old mice were primed on day 0 with 10 μg of aDNP-IgE (Sigma, SPE7) intraperitoneally in 200 μl of PBS and challenged intravenously 16 to 24 hours later with 250 μg of DNP-HSA (LGC Bio Tech) in 100 μl of PBS. Temperature was measured prior to i.v. challenge and every 10 min afterwards for 1 hour. At 1 hour, mice were bled using hematocrit (Hct) tubes (BD Clay Adams Sure Prep Tubes) to measure vascular leak, and at 2 hours for MCPT1 measurements by ELISA. One week later, the same mice were administered 10 μg of aTNP-IgE (BD557080) in 200 μl of PBS intraperitoneally. 16 to 24 hours later, they were challenged with 50 mg of TNP-OVA (homemade, as described above) intragastrically in 250 μl of PBS. Body temperature was measured prior to gavage, and every 10 min after for 1 hour. Mice were bled at 1 hour for Hct determination and 2 hours for MCPT1, as described above. In experiments pertaining to leukotriene deficiency's effect on passive anaphylaxis, 1 week following passive oral anaphylaxis challenge, the small intestine was harvested to measure epithelial and lamina propria mast cells as described below, and serum was taken for MCPT1 measurements in the absence of allergen challenge.

TB mast cell degranulation assay

Mast cell degranulation assessment was based on 1-μm TB-stained sections of ear pinna, bronchi, or stomach using a modified version of the protocol used in prior studies (*43*, *90*). One hour after intragastric challenge with 50 mg of OVA in sensitized or control mice treated with vehicle or 50 mg/kg of zileuton, or 1 hour after intravenous challenge with or without 250 μg of DNP-HSA in aDNP-IgE primed mice, mice were humanely euthanized with a lethal dose of ketamine/xylazine and fixed with a 10-ml perfusion of ice cold PBS followed by 10 ml of 10% NBF. Tissues were then harvested and further fixed overnight in 10% NBF at room temperature. Single sections from each tissue were obtained, stained, and then submitted for slide-scanning at 40X resolution. Tissues were then annotated, mast cells counted in QuPath and classified as normal or degranulated based on (i) extent of granules exhibiting fusion with the cell membrane (ii) granules identified immediately proximally to the cell of interest, and/or (iii) alterations in staining/extrusion of the cell.

Gastrointestinal permeability determination

Gastrointestinal permeability was measured via multiplexed intragastric gavage of 4-kDa FITC-Dextran (20 mg, Sigma Aldrich), and 70-kDa TMR-Dextran (10 mg, Sigma Aldrich) in 250 μl of water per mouse as previously described (*91*). Briefly, mice 6 to 10 weeks old were fasted for 4 hours, treated with 50 mg/kg of zileuton or vehicle for 1 hour, gavaged with the above dextran mixture and serum was isolated 3 hours later for determination of 4-/70-kDa dextran by fluorescence using a SpectraMax M5 (Molecular Devices). Each mouse's intestinal permeability was measured on day 28 after five intragastric challenges with 50-mg grade III OVA/mouse. For the last measurement (sixth oral challenge), 50 mg OVA was mixed with the above tracers and gavaged together with serum harvested 3 hours later.

Epithelial cell and LP isolation

Single-cell suspensions of small intestinal epithelium and LP were prepared as described (*92*). Briefly, the small intestine was isolated and opened longitudinally. Its contents were then rinsed in PBS following the removal of Peyer's patches. The tissue was then cut into 2- to 3-cm segments and incubated in RPMI media (ThermoFisher) containing 5 mM EDTA, 0.145 mg/ml DTT, and 3% FBS at 37°C with 5% CO_2 for 20 min with agitation. Pieces of intestine were washed in RPMI containing 2 mM EDTA to separate the epithelial fraction. LP digestion was performed using 0.1 mg/ml Liberase TL (Roche #540102001) and 0.5 mg/ml DNAse (DN25, Sigma-Aldrich) in RPMI for 30 min at 37°C with 5% CO_2. Digested tissue was sequentially strained through 70-μm micron and 40-μm strainers and washed in RPMI containing 3% FBS. The epithelial fraction was also subjected to a 30% Percoll (GE17-0891-01, Sigma Aldrich) density gradient by centrifugation in preparation for sorting. Cells were then stained for flow cytometric analysis.

Small intestinal mast cell flow cytometry and FACS

Single-cell suspensions were treated with anti-CD16/32 (Fc block) (14-9161-73, ThermoFisher) and stained with either ethidium monoazide bromide (ThermoFisher #E1374) in 2% FBS in PBS or Zombie Yellow (Biolegend #423103) in PBS to identify live and dead cells. Cells were then stained with a selection of the following antibodies at a concentration of 1 mg/ml except where otherwise indicated: FITC-IgE (clone R35-72; BD Biosciences #553415), PE-FceRI (clone MAR-1; eBioscience 12-5898-82), PE-integrin beta7 (clone FIB504; eBioscience 12-5867-42, 1.25 mg/ml), APC-CD11b (clone M1/70; ThermoFisher #17-0112-82), APC-CD8a (clone 53-6.7; BD Biosciences #553035), PE/Cy7-CD117 (clone 2B8; eBioscience #25-1171-82), APC/eFluor780-CD19 (clone eBio1D3; eBioscience #47-0193-82), Alexa700-CD3 (clone 17A2; Biolegend #100216 , 2.5 mg/ml), Alexa700-CD4 (clone RM4-5; Invitrogen #56-0042-82), BUV395-CD45 (clone 30-F11; BD Biosciences #564279), eFluor450-FceRI (clone MAR-1; eBioscience 48-5898-82), PerCP-eFluor710-CD49d (Integrin alpha 4) (clone R1-2; eBioscience 46-0492-82), BUV737-CD103 (Integrin alpha E) (clone 2E7; eBioscience #367-1031-82), biotin-ST2 (clone DJ8; MDBioproducts #101001B, 5 mg/ml), and SuperBright600-Streptavidin (Invitrogen #63-4317-82) . Cells were fixed with 1.6% paraformaldehyde (Electron Microscopy Sciences, #15710). Flow cytometry was performed using either a BD LSRII analyzer equipped with the following lasers: 355 nm (UV), 405 nm (violet), 488 nm (blue), and 633 nm (red) or a BD Symphony analyzer equipped with the following lasers: 355 nm (UV), 405 nm (violet), 488 nm (blue), 561 nm (yellow green), 637 nm (red), and 780 nm (NIR). Data was analyzed using FlowJo software. Gates were drawn according to fluorescence minus one (FMO) controls.

Histological quantification of intestinal mast cell

The middle 10cm of small intestine was harvested 1 hour after the seventh OVA gavage, flushed once intraluminally with 1xPBS, followed by once with 10% NBF. Intestines were then opened longitudinally and fixed overnight on Whatman paper in 10% NBF at room temperature and subsequently rolled into Swiss rolls as previously described. The intestines were then dehydrated, embedded in paraffin, cut, and stained via naphthol chloroacetate-esterase stain by the Yale Pathology Tissue Service. Mast cells were quantified by counting five independent 10x FOV for CAE+ cells and averaging them to obtain an average per independent sample.

Total and OVA-specific antibody quantification

Serum levels of total IgE and OVA-specific IgE and IgG1 antibodies were determined by ELISA, as previously described (*1*), with slight modifications for OVA-specific IgE. For total IgE, ELISA-grade plates (490012-252, VWR) were coated overnight at 4°C with 2 mg/ml of anti-mouse IgE (553413, clone R35-72, BD Pharmingen) in 0.1 M sodium carbonate buffer pH 9.5. Plates were blocked with 1% BSA (Fisher BP1600-1) for 2 hours at room temperature. Serum from sensitized and control mice was diluted up to 1:50 and incubated for 2 hours at room temperature. Purified mouse IgE (BD Biosciences 557079) was used as the standard with the highest concentration of 100 ng/ml followed by twofold dilutions to create a standard curve. Afterwards, 500 ng/ml of biotin-conjugated anti-IgE detection antibodies (553419, clone R35-118, BD Biosciences) were incubated for 1 hour at room temperature followed with another incubation of diluted HRP-conjugated streptavidin (554066, BD Biosciences) for 30 min at room temperature. Plates were then incubated in the dark at room temperature with TMB substrate reagent (555214, BD Biosciences) until developed. Plates were read at 450 nm immediately after adding stop solution (3M H_2SO_4). Between each step, plates were washed five times with 0.05% Tween-20 in PBS. OVA-specific IgG1 antibodies in the serum were assayed by direct ELISA. Plates were coated overnight at 4°C with 20 mg/ml of grade V OVA (A5503, Sigma-Aldrich) in coating buffer (0.1 M sodium carbonate pH 9.5). After the blocking step, serum samples were diluted up to 1:10,000 and incubated for 1 hour at room temperature. Purified mouse BALB/c IgG1 (557273, clone MOPC-31C, BD Biosciences) was used as the standard with the highest concentration at 100 ng/ml. Biotin-conjugated mouse IgG1 (553441, clone A85-1, BD Biosciences) was used for detection at 100 ng/ml. The HRP-conjugated streptavidin, substrate reagents, blocking and washing solutions used for the IgG1 ELISA were the same as described above for IgE ELISAs. Serum concentrations of OVA-specific IgE were also assayed by direct ELISA method. Plates were coated overnight at 4°C with 100 μg/ml of grade V OVA (A5503, Sigma-Aldrich) in coating buffer (0.1 M sodium carbonate pH 9.5). After the blocking step, serum samples were diluted up to 1:50 and incubated for 1 hour at room temperature. Purified mouse anti-OVA IgE (7091, clone E-C1, Chondrex) was used as the standard with the highest concentration at 3 μg/ml Bound OVA-specific IgE was detected by incubation with a mouse IgE-HRP (Southern Biotech, 1110-05) for 1 hour at RT. Development using TMB, quenching with H2SO4, and detection was performed as above.

MCPT1 quantification

Serum was collected at either day 14 (after sensitization but prior to oral challenge) or 1 hour after 50 mg OVA (III) i.g. administration on challenges 2, 4, and 7. MCPT1 was quantified by ELISA (Invitrogen, Cat#88-7503-88). For passive anaphylaxis experiments, serum MCPT1 measurements were made at 2 hours post-challenge instead.

In vitro MMC treatment with TGFβ and mediator quantification

Bone marrow was isolated from the femurs and tibia of adult female BALB/cJ mice and passed through a 70-μm strainer to produce a single cell suspension. Isolated bone marrow cells were cultured in DMEM supplemented with 25 mM HEPES, 1% pen/strep, 1% non-essential amino acids, 2 mM L-glutamine, 1% sodium pyruvate, 10% fetal bovine serum, 50 uM β-mercaptoethanol, and 30 ng/ml recombinant mouse IL-3 (Peprotech, 213-13) for at least 6 weeks to generate bone marrow-derived mast cells. Mast cell purity was observed to be at least 95% based on expression of Fcer1a and c-Kit. These bone marrow mast cells were then cultured with 5 ng/ml IL-3 (Peprotech, 213-13) and 100 ng/ml SCF (Peprotech, 250-03), with or without 25 ng/ml TGF-B1(R&D, 240-B-003) for 7 days as previously described (*52*). On the seventh day, the mast cells were collected for RNA isolation or flow cytometric analysis, described below. In experiments involving antigen stimulation, mast cells were sensitized with 2 ug/ml anti-DNP IgE (Sigma, SPE7) on the sixth day. On the seventh day, they were washed three times with serum-free media and then challenged with 10 ng/ml DNP-HSA (LGC Bio Tech) in serum-free media for 30 min. Afterwards, the media was collected for ELISA for MCPT1 (as previously described), PGD2 (Cayman Chemical, 512031), CysLTs (Cayman Chemical, 500390), and Histamine (Cayman Chemical, 589651) quantification.

Flow cytometric evaluation of in vitro bone marrow mast cell cultures

Bone marrow mast cells were first incubated with Zombie Yellow (1:500 in PBS) for 15 min at room temperature. Then they were washed and incubated with anti-CD16/32 (Fc block, 1:400), anti-CD117-PE-Cy7 (1:400), anti-Fcer1a-FITC (1:200), anti-LPAM1-BV421 (1:100), anti-CD103-BV711 (1:100), and anti-ST2-PE (1:80), or the corresponding isotype controls in PBS + 0.5% BSA for 20 min on ice. For detection of MCPT1, mMCPT1 antibody (TG6.1, Invitrogen), was conjugated to Alexa Flour 647 using AF647 Labeling Kit (Invitrogen) according to the manufacturer's instructions. For MCPT-1 staining, the cells were then fixed and permeabilized with the BD Cytofix/Cytoperm kit according to the manufacturer's instructions, followed by incubation with anti-MCPT1-AF647 (1:200) in permeabilization buffer for 20 min on ice. 123count eBeads (Thermo Fisher) were added to the samples for cell number quantitation. Flow cytometry was conducted with a BD FACSymphony Cell Analyzer and the data were analyzed with FlowJo.

RNA isolation, cDNA synthesis, and qRT-PCR

RNA was isolated from samples using an RNeasy Micro Kit (Qiagen) and cDNA was synthesized using MMLV reverse transcriptase (Clontech) with oligo(dT) primers. qRT PCR was performed on CFX384 Real-Time System (Bio-Rad) using PerfeCTa SYBR Green Supermix (Quanta Biosciences) and gene-specific primers, and transcripts were normalized to Rpl13a. A list of the primers utilized in this study can be found in data S7.

Bulk RNA-seq

RNA was extracted from sorted mast cells using an RNeasy Plus Micro Kit (Qiagen), and library construction was performed using a SMART-seq2 protocol (*93*). Sequencing libraries were sequenced on an Illumina NextSeq 500 (38 × 38 bp paired-end run). Sequencing reads were aligned to the mouse transcriptome (GRCm38 ensembl v101; cDNA and ncRNA) and quantified by Kallisto (v0.45.0) (*94*) with a k-mer index 25 and 60 bootstrapping. The expression of transcript was calculated in TPM (transcripts per million). The expression of the gene was calculated by aggregating the TPM of all matched transcripts. Statistical analyses for differentially expressed genes were performed by tximport and DESeq2 (*95*).

Intestinal mast cell single-cell analysis

Mice were sensitized against OVA and challenged intragastrically five times with OVA as described above. Small intestinal LP and epithelial fractions of immune cells were subsequently isolated and mast cells from each fraction sorted using a FACS Aria cell sorter into ice cold 10% FBS in dPBS w/o Ca, Mg, or EDTA. Sorted cells from two sensitized mice (two LP and two IEL samples) were then spun down, counted, and prepared separately using the Chromium GEM-X Single Cell 3′ v4 assay (10X Genomics) according to the manufacturer's protocol at the Keck Microarray Shared Resource at Yale School of Medicine. Libraries were sequenced on a NovaSeq 6000 by the Yale Center for Genome Analysis.

Quality control and scRNA-seq analysis

The data quality control and processing were performed with Seurat (*96*) and R packages (R version 4.3.3). 31,934 cells from all samples were merged initially. For quality control, we used quality metrics for the initial filtering. Cell complexity score was calculated by using the formula $\mathrm{Log}_{10}\left(\frac{\text{Number of genes}}{\text{Number of UMI}}\right)$ (UMI = Unique Molecular Identifier) as an index to measure the potential artifact or contamination in the samples. Cells with > 500 UMI count, > 500 genes, and > 0.8 complexity score were retained. After exclusion of poor-quality cells, we were left with 23,333 cells. We processed the data by running Seurat v5 pipeline. The raw count of the retained data was normalized, and variable features were identified with NormalizeData and FindVariableFeatures functions, respectively. We next linearly transformed the normalized data using the ScaleData function. RunPCA and RunUMAP were performed for dimension reduction. All data samples were integrated using the Harmony package (*51*). After integration, 14 clusters were identified using FindNeighbors and FindClusters on integrated data with a resolution of 0.6. Of these, we noted that clusters 8, 9, 11, 12, and 13 expressed markers prototypical for B cells, smooth muscle cells, and epithelial cell types (differentially expressed marker genes such as *Ighm*, *Myocd*, *Vwf*, *Cnn1*, etc.). Thus, for analysis of mast cell intrinsic transcripts, we excluded cells on the basis of B cells, smooth muscle cells, and epithelial cells, which left us with 22,171 intestinal mast cells expressing *FcεRI* and c-*Kit* markers. The intestinal mast cells were then re-clustered into nine identified clusters. We next assessed the DEGs using the FindMarkers function with a) an adjusted *P* value <0.05; b) an average Log_2 fold change > 1 or < −1; c) a percentage of cells (pct) where the feature was detected > 0.1 in either group. The potential differentiation trajectory was inferred and plotted using Monocle3 toolkits (*97*). Differentially expressed genes between clusters 0,1 versus cluster 2 with the absolute $\log_2$ fold change >= 1 and the adjusted *P* value < 0.05 were subset for the downstream IPA and Gene Ontology (GO) enrichment analysis. For IPA analysis upstream regulators of the differentially expressed genes between cluster 0,1 versus cluster 2 were predicted and interpreted using the Core Analysis function in the IPA software (QIAGEN; version 01-23-01). GO enrichment of the differentially expressed genes between cluster 0,1 versus cluster 2 (with average Log_2 fold change >1 or <−1 and adjusted *P* value <0.05) was performed using the clusterProfiler R package (*98*) based on the hallmark gene set from the Molecular Signatures Database (MSigDB) (*99*), with pathway *P* value cutoff of 0.5 and *Q* value cutoff of 1 after *P* value adjustment using Benjamini–Hochberg (BH) multiple testing. An additional dataset of mast cells from the gut, peritoneal cavity, and skin was downloaded from Tauber *et al.* (*59*) and processed as their descriptions All plots in this analysis were generated by the Seurat visualization methods, the ggplot2, and the EnhancedVolcano packages.

Statistical analysis

All statistical analyses except for bulk and single-cell RNA-seq data were performed using Graphpad Prism Software. Exact tests utilized are

denoted in figure legend or in supplemental text. Statistical significance is defined as $*P < 0.05$, $**P < 0.01$, $***P < 0.001$, and $****P < 0.0001$.

REFERENCES AND NOTES

1. E. B. Florsheim *et al.*, Immune sensing of food allergens promotes avoidance behaviour. *Nature* **620**, 643–650 (2023). doi: 10.1038/s41586-023-06362-4; pmid: 37437602
2. E. B. Florsheim, Z. A. Sullivan, W. Khoury-Hanold, R. Medzhitov, Food allergy as a biological food quality control system. *Cell* **184**, 1440–1454 (2021). doi: 10.1016/j.cell.2020.12.007; pmid: 33450204
3. M. Profet, The function of allergy: Immunological defense against toxins. *Q. Rev. Biol.* **66**, 23–62 (1991). doi: 10.1086/417049; pmid: 2052671
4. T. Plum *et al.*, Mast cells link immune sensing to antigen-avoidance behaviour. *Nature* **620**, 634–642 (2023). doi: 10.1038/s41586-023-06188-0; pmid: 37438525
5. N. W. Palm, R. K. Rosenstein, R. Medzhitov, Allergic host defences. *Nature* **484**, 465–472 (2012). doi: 10.1038/nature11047; pmid: 22538607
6. S. Anvari, J. Miller, C. Y. Yeh, C. M. Davis, IgE-Mediated Food Allergy. *Clin. Rev. Allergy Immunol.* **57**, 244–260 (2019). doi: 10.1007/s12016-018-8710-3; pmid: 30370459
7. F. D. Finkelman, Anaphylaxis: Lessons from mouse models. *J. Allergy Clin. Immunol.* **120**, 506–515 (2007). doi: 10.1016/j.jaci.2007.07.033; pmid: 17765751
8. K. Arias *et al.*, Concurrent blockade of platelet-activating factor and histamine prevents life-threatening peanut-induced anaphylactic reactions. *J. Allergy Clin. Immunol.* **124**, 307–314, 314.e1–314.e2 (2009). doi: 10.1016/j.jaci.2009.03.012; pmid: 19409603
9. T. K. Noah *et al.*, IL-13-induced intestinal secretory epithelial cell antigen passages are required for IgE-mediated food-induced anaphylaxis. *J. Allergy Clin. Immunol.* **144**, 1058–1073.e3 (2019). doi: 10.1016/j.jaci.2019.04.030; pmid: 31175877
10. R. Ahrens *et al.*, Intestinal mast cell levels control severity of oral antigen-induced anaphylaxis in mice. *Am. J. Pathol.* **180**, 1535–1546 (2012). doi: 10.1016/j.ajpath.2011.12.036; pmid: 22322300
11. E. B. Brandt *et al.*, Mast cells are required for experimental oral allergen-induced diarrhea. *J. Clin. Invest.* **112**, 1666–1677 (2003). doi: 10.1172/JCI19785; pmid: 14660743
12. C. Y. Chen *et al.*, Induction of Interleukin-9-Producing Mucosal Mast Cells Promotes Susceptibility to IgE-Mediated Experimental Food Allergy. *Immunity* **43**, 788–802 (2015). doi: 10.1016/j.immuni.2015.08.020; pmid: 26410628
13. J. M. Leyva-Castillo *et al.*, Mechanical Skin Injury Promotes Food Anaphylaxis by Driving Intestinal Mast Cell Expansion. *Immunity* **50**, 1262–1275.e4 (2019). doi: 10.1016/j.immuni.2019.03.023; pmid: 31027995
14. E. E. Forbes *et al.*, IL-9- and mast cell-mediated intestinal permeability predisposes to oral antigen hypersensitivity. *J. Exp. Med.* **205**, 897–913 (2008). doi: 10.1084/jem.20071046; pmid: 18378796
15. H. Osterfeld *et al.*, Differential roles for the IL-9/IL-9 receptor α-chain pathway in systemic and oral antigen-induced anaphylaxis. *J. Allergy Clin. Immunol.* **125**, 469–476.e2 (2010). doi: 10.1016/j.jaci.2009.09.054; pmid: 20159257
16. J. Z. Haeggström, C. D. Funk, Lipoxygenase and leukotriene pathways: Biochemistry, biology, and roles in disease. *Chem. Rev.* **111**, 5866–5898 (2011). doi: 10.1021/cr200246d; pmid: 21936577
17. J. D. Clark, N. Milona, J. L. Knopf, Purification of a 110-kilodalton cytosolic phospholipase A2 from the human monocytic cell line U937. *Proc. Natl. Acad. Sci. U.S.A.* **87**, 7708–7712 (1990). doi: 10.1073/pnas.87.19.7708; pmid: 2217203
18. G. K. Reid *et al.*, Correlation between expression of 5-lipoxygenase-activating protein, 5-lipoxygenase, and cellular leukotriene synthesis. *J. Biol. Chem.* **265**, 19818–19823 (1990). doi: 10.1016/S0021-9258(17)45446-9; pmid: 2174053
19. B. Samuelsson, S. E. Dahlén, J. A. Lindgren, C. A. Rouzer, C. N. Serhan, Leukotrienes and lipoxins: Structures, biosynthesis, and biological effects. *Science* **237**, 1171–1176 (1987). doi: 10.1126/science.2820055; pmid: 2820055
20. B. K. Lam, J. F. Penrose, G. J. Freeman, K. F. Austen, Expression cloning of a cDNA for human leukotriene C4 synthase, an integral membrane protein conjugating reduced glutathione to leukotriene A4. *Proc. Natl. Acad. Sci. U.S.A.* **91**, 7663–7667 (1994). doi: 10.1073/pnas.91.16.7663; pmid: 8052639
21. Y. Kanaoka, A. Maekawa, J. F. Penrose, K. F. Austen, B. K. Lam, Attenuated zymosan-induced peritoneal vascular permeability and IgE-dependent passive cutaneous anaphylaxis in mice lacking leukotriene C4 synthase. *J. Biol. Chem.* **276**, 22608–22613 (2001). doi: 10.1074/jbc.M103562200; pmid: 11319240
22. M. E. Anderson, R. D. Allison, A. Meister, Interconversion of leukotrienes catalyzed by purified gamma-glutamyl transpeptidase: Concomitant formation of leukotriene D4 and gamma-glutamyl amino acids. *Proc. Natl. Acad. Sci. U.S.A.* **79**, 1088–1091 (1982). doi: 10.1073/pnas.79.4.1088; pmid: 6122208
23. E. M. Kozak, S. S. Tate, Glutathione-degrading enzymes of microvillus membranes. *J. Biol. Chem.* **257**, 6322–6327 (1982). doi: 10.1016/S0021-9258(20)65143-2; pmid: 6122685
24. Y. Kanaoka, A. Maekawa, K. F. Austen, Identification of GPR99 protein as a potential third cysteinyl leukotriene receptor with a preference for leukotriene E4 ligand. *J. Biol. Chem.* **288**, 10967–10972 (2013). doi: 10.1074/jbc.C113.453704; pmid: 23504326
25. T. C. Beller, A. Maekawa, D. S. Friend, K. F. Austen, Y. Kanaoka, Targeted gene disruption reveals the role of the cysteinyl leukotriene 2 receptor in increased vascular permeability and in bleomycin-induced pulmonary fibrosis in mice. *J. Biol. Chem.* **279**, 46129–46134 (2004). doi: 10.1074/jbc.M407057200; pmid: 15328359
26. A. Maekawa, K. F. Austen, Y. Kanaoka, Targeted gene disruption reveals the role of cysteinyl leukotriene 1 receptor in the enhanced vascular permeability of mice undergoing acute inflammatory responses. *J. Biol. Chem.* **277**, 20820–20824 (2002). doi: 10.1074/jbc.M203163200; pmid: 11932261
27. T. Liu *et al.*, Type 2 Cysteinyl Leukotriene Receptors Drive IL-33-Dependent Type 2 Immunopathology and Aspirin Sensitivity. *J. Immunol.* **200**, 915–927 (2018). doi: 10.4049/jimmunol.1700603; pmid: 29282304
28. J. von Moltke *et al.*, Leukotrienes provide an NFAT-dependent signal that synergizes with IL-33 to activate ILC2s. *J. Exp. Med.* **214**, 27–37 (2017). doi: 10.1084/jem.20161274; pmid: 28011865
29. L. G. Bankova *et al.*, The cysteinyl leukotriene 3 receptor regulates expansion of IL-25-producing airway brush cells leading to type 2 inflammation. *Sci. Immunol.* **3**, eaat9453 (2018). doi: 10.1126/sciimmunol.aat9453; pmid: 30291131
30. J. B. Lee *et al.*, IL-25 and CD4(+) TH2 cells enhance type 2 innate lymphoid cell-derived IL-13 production, which promotes IgE-mediated experimental food allergy. *J. Allergy Clin. Immunol.* **137**, 1216–1225.e5 (2016). doi: 10.1016/j.jaci.2015.09.019; pmid: 26560039
31. H. Xu *et al.*, Transcriptional Atlas of Intestinal Immune Cells Reveals that Neuropeptide α-CGRP Modulates Group 2 Innate Lymphoid Cell Responses. *Immunity* **51**, 696–708.e9 (2019). doi: 10.1016/j.immuni.2019.09.004; pmid: 31618654
32. P. Licona-Limón, L. K. Kim, N. W. Palm, R. A. Flavell, TH2, allergy and group 2 innate lymphoid cells. *Nat. Immunol.* **14**, 536–542 (2013). doi: 10.1038/ni.2617; pmid: 23685824
33. J. von Moltke, M. Ji, H. E. Liang, R. M. Locksley, Tuft-cell-derived IL-25 regulates an intestinal ILC2-epithelial response circuit. *Nature* **529**, 221–225 (2016). doi: 10.1038/nature16161; pmid: 26675736
34. L. M. Bartnikas *et al.*, Epicutaneous sensitization results in IgE-dependent intestinal mast cell expansion and food-induced anaphylaxis. *J. Allergy Clin. Immunol.* **131**, 451–60.e1, 6 (2013). doi: 10.1016/j.jaci.2012.11.032; pmid: 23374269
35. J. A. Gertie *et al.*, Oral anaphylaxis to peanut in a mouse model is associated with gut permeability but not with Tlr4 or Dock8 mutations. *J. Allergy Clin. Immunol.* **149**, 262–274 (2022). doi: 10.1016/j.jaci.2021.05.015; pmid: 34051223
36. K. Orgel *et al.*, Genetic diversity between mouse strains allows identification of the CC027/GeniUnc strain as an orally reactive model of peanut allergy. *J. Allergy Clin. Immunol.* **143**, 1027–1037.e7 (2019). doi: 10.1016/j.jaci.2018.10.009; pmid: 30342892
37. F. D. Finkelman *et al.*, IL-4 is required to generate and sustain in vivo IgE responses. *J. Immunol.* **141**, 2335–2341 (1988). doi: 10.4049/jimmunol.141.7.2335; pmid: 2459206
38. U. Blank *et al.*, Complete structure and expression in transfected cells of high affinity IgE receptor. *Nature* **337**, 187–189 (1989). doi: 10.1038/337187a0; pmid: 2521376
39. A. Dahdah *et al.*, Mast cells aggravate sepsis by inhibiting peritoneal macrophage phagocytosis. *J. Clin. Invest.* **124**, 4577–4589 (2014). doi: 10.1172/JCI75212; pmid: 25180604
40. K. Arias *et al.*, Distinct immune effector pathways contribute to the full expression of peanut-induced anaphylactic reactions in mice. *J. Allergy Clin. Immunol.* **127**, 1552–61.e1 (2011). doi: 10.1016/j.jaci.2011.03.044; pmid: 21624619
41. F. Jönsson *et al.*, Mouse and human neutrophils induce anaphylaxis. *J. Clin. Invest.* **121**, 1484–1496 (2011). doi: 10.1172/JCI45232; pmid: 21436586
42. I. Miyajima *et al.*, Systemic anaphylaxis in the mouse can be mediated largely through IgG1 and Fc gammaRIII. Assessment of the cardiopulmonary changes, mast cell degranulation, and death associated with active or IgE- or IgG1-dependent passive anaphylaxis. *J. Clin. Invest.* **99**, 901–914 (1997). doi: 10.1172/JCI119255; pmid: 9062348
43. Y. Taketomi *et al.*, Lipid-orchestrated paracrine circuit coordinates mast cell maturation and anaphylaxis through functional interaction with fibroblasts. *Immunity* **57**, 1828–1847.e11 (2024). doi: 10.1016/j.immuni.2024.06.012; pmid: 39002541
44. N. Nakano, J. Kitaura, Mucosal Mast Cells as Key Effector Cells in Food Allergies. *Cells* **11**, 329 (2022). doi: 10.3390/cells11030329; pmid: 35159139
45. J. Bienenstock, A. D. Befus, F. Pearce, J. Denburg, R. Goodacre, Mast cell heterogeneity: Derivation and function, with emphasis on the intestine. *J. Allergy Clin. Immunol.* **70**, 407–412 (1982). doi: 10.1016/0091-6749(82)90001-X; pmid: 6183305
46. D. F. Dwyer *et al.*, Human airway mast cells proliferate and acquire distinct inflammation-driven phenotypes during type 2 inflammation. *Sci. Immunol.* **6**, eabb7221 (2021). doi: 10.1126/sciimmunol.abb7221; pmid: 33637594
47. B. D. McNeil *et al.*, Identification of a mast-cell-specific receptor crucial for pseudo-allergic drug reactions. *Nature* **519**, 237–241 (2015). doi: 10.1038/nature14022; pmid: 25517090
48. M. F. Gurish *et al.*, Intestinal mast cell progenitors require CD49dbeta7 (alpha4beta7 integrin) for tissue-specific homing. *J. Exp. Med.* **194**, 1243–1252 (2001). doi: 10.1084/jem.194.9.1243; pmid: 11696590
49. R. Gentek *et al.*, Hemogenic Endothelial Fate Mapping Reveals Dual Developmental Origin of Mast Cells. *Immunity* **48**, 1160–1171.e5 (2018). doi: 10.1016/j.immuni.2018.04.025; pmid: 29858009

50. L. G. Bankova, D. F. Dwyer, A. Y. Liu, K. F. Austen, M. F. Gurish, Maturation of mast cell progenitors to mucosal mast cells during allergic pulmonary inflammation in mice. *Mucosal Immunol.* **8**, 596–606 (2015). doi: 10.1038/mi.2014.91; pmid: 25291985
51. I. Korsunsky *et al.*, Fast, sensitive and accurate integration of single-cell data with Harmony. *Nat. Methods* **16**, 1289–1296 (2019). doi: 10.1038/s41592-019-0619-0; pmid: 31740819
52. T. Derakhshan *et al.*, Lineage-specific regulation of inducible and constitutive mast cells in allergic airway inflammation. *J. Exp. Med.* **218**, e20200321 (2021). doi: 10.1084/jem.20200321; pmid: 32946563
53. L. Yang *et al.*, Intraepithelial mast cells drive gasdermin C-mediated type 2 immunity. *Immunity* **57**, 1056–1070.e5 (2024). doi: 10.1016/j.immuni.2024.03.017; pmid: 38614091
54. P. A. Knight *et al.*, Enteric expression of the integrin α(v)β(6) is essential for nematode-induced mucosal mast cell hyperplasia and expression of the granule chymase, mouse mast cell protease-1. *Am. J. Pathol.* **161**, 771–779 (2002). doi: 10.1016/S0002-9440(10)64236-8; pmid: 12213704
55. K. Sugimoto *et al.*, The αvβ6 integrin modulates airway hyperresponsiveness in mice by regulating intraepithelial mast cells. *J. Clin. Invest.* **122**, 748–758 (2012). doi: 10.1172/JCI58815; pmid: 22232213
56. P. H. Weinreb *et al.*, Function-blocking integrin $\alpha_v\beta_6$ monoclonal antibodies: Distinct ligand-mimetic and nonligand-mimetic classes. *J. Biol. Chem.* **279**, 17875–17887 (2004). doi: 10.1074/jbc.M312103200; pmid: 14960589
57. Y. Makabe-Kobayashi *et al.*, The control effect of histamine on body temperature and respiratory function in IgE-dependent systemic anaphylaxis. *J. Allergy Clin. Immunol.* **110**, 298–303 (2002). doi: 10.1067/mai.2002.125977; pmid: 12170272
58. M. Tauber *et al.*, Landscape of mast cell populations across organs in mice and humans. *J. Exp. Med.* **220**, e20230570 (2023). doi: 10.1084/jem.20230570; pmid: 37462672
59. N. Gaudenzio *et al.*, Landscape of Mast cell populations across organs in mice and humans, *Dryad* (2023); https://www.doi.org/10.5061/dryad.np5hqbzzz.doi: 10.5061/dryad.np5hqbzzz
60. J. B. Wechsler, H. A. Schroeder, A. J. Byrne, K. B. Chien, P. J. Bryce, Anaphylactic responses to histamine in mice utilize both histamine receptors 1 and 2. *Allergy* **68**, 1338–1340 (2013). doi: 10.1111/all.12227; pmid: 24112077
61. R. T. Strait, S. C. Morris, M. Yang, X. W. Qu, F. D. Finkelman, Pathways of anaphylaxis in the mouse. *J. Allergy Clin. Immunol.* **109**, 658–668 (2002). doi: 10.1067/mai.2002.123302; pmid: 11941316
62. S. Ualiyeva *et al.*, Tuft cell-produced cysteinyl leukotrienes and IL-25 synergistically initiate lung type 2 inflammation. *Sci. Immunol.* **6**, eabj0474 (2021). doi: 10.1126/sciimmunol.abj0474; pmid: 34932383
63. J. W. McGinty *et al.*, Tuft-Cell-Derived Leukotrienes Drive Rapid Anti-helminth Immunity in the Small Intestine but Are Dispensable for Anti-protist Immunity. *Immunity* **52**, 528–541.e7 (2020). doi: 10.1016/j.immuni.2020.02.005; pmid: 32160525
64. R. T. Strait *et al.*, Ingested allergens must be absorbed systemically to induce systemic anaphylaxis. *J. Allergy Clin. Immunol.* **127**, 982–989.e1 (2011). doi: 10.1016/j.jaci.2011.01.034; pmid: 21354602
65. Z. Y. Kucuk *et al.*, Induction and suppression of allergic diarrhea and systemic anaphylaxis in a murine model of food allergy. *J. Allergy Clin. Immunol.* **129**, 1343–1348 (2012). doi: 10.1016/j.jaci.2012.03.004; pmid: 22465213
66. R. T. Strait, S. C. Morris, F. D. Finkelman, IgG-blocking antibodies inhibit IgE-mediated anaphylaxis in vivo through both antigen interception and FcγRIIb cross-linking. *J. Clin. Invest.* **116**, 833–841 (2006). doi: 10.1172/JCI25575; pmid: 16498503
67. O. T. Burton *et al.*, IgE promotes type 2 innate lymphoid cells in murine food allergy. *Clin. Exp. Allergy* **48**, 288–296 (2018). doi: 10.1111/cea.13075; pmid: 29247574
68. C. S. N. Klose *et al.*, The neuropeptide neuromedin U stimulates innate lymphoid cells and type 2 inflammation. *Nature* **549**, 282–286 (2017). doi: 10.1038/nature23676; pmid: 28869965
69. C. Bao *et al.*, A mast cell-thermoregulatory neuron circuit axis regulates hypothermia in anaphylaxis. *Sci. Immunol.* **8**, eadc9417 (2023). doi: 10.1126/sciimmunol.adc9417; pmid: 36930731
70. C. Denzlinger, C. Haberl, W. Wilmanns, Cysteinyl leukotriene production in anaphylactic reactions. *Int. Arch. Allergy Immunol.* **108**, 158–164 (1995). doi: 10.1159/000237133; pmid: 7549503
71. E. Ono *et al.*, Increased production of cysteinyl leukotrienes and prostaglandin D2 during human anaphylaxis. *Clin. Exp. Allergy* **39**, 72–80 (2009). doi: 10.1111/j.1365-2222.2008.03104.x; pmid: 19128354
72. Y. Yamakawa *et al.*, Effects of leukotriene receptor antagonists on peripheral eosinophil counts and serum IgE levels in children with food allergy. *Drugs R D.* **10**, 147–154 (2010). doi: 10.2165/11586150-000000000-00000; pmid: 20945945
73. M. Takahashi *et al.*, New efficacy of LTRAs (montelukast sodium): It possibly prevents food-induced abdominal symptoms during oral immunotherapy. *Allergy Asthma Clin. Immunol.* **10**, 3 (2014). doi: 10.1186/1710-1492-10-3; pmid: 24438769
74. Y. V. Virkud *et al.*, Immunomodulatory metabolites in IgE-mediated food allergy and oral immunotherapy outcomes based on metabolomic profiling. *Pediatr. Allergy Immunol.* **35**, e14267 (2024). doi: 10.1111/pai.14267; pmid: 39530396
75. F. Wölbing, J. Fischer, M. Köberle, S. Kaesler, T. Biedermann, About the role and underlying mechanisms of cofactors in anaphylaxis. *Allergy* **68**, 1085–1092 (2013). doi: 10.1111/all.12193; pmid: 23909934
76. I. Bjarnason *et al.*, Mechanisms of Damage to the Gastrointestinal Tract From Nonsteroidal Anti-Inflammatory Drugs. *Gastroenterology* **154**, 500–514 (2018). doi: 10.1053/j.gastro.2017.10.049; pmid: 29221664
77. J. Sánchez-López *et al.*, Food-dependent NSAID-induced hypersensitivity (FDNIH) reactions: Unraveling the clinical features and risk factors. *Allergy* **76**, 1480–1492 (2021). doi: 10.1111/all.14689; pmid: 33289951
78. S. Dua *et al.*, Effect of sleep deprivation and exercise on reaction threshold in adults with peanut allergy: A randomized controlled study. *J. Allergy Clin. Immunol.* **144**, 1584–1594.e2 (2019). doi: 10.1016/j.jaci.2019.06.038; pmid: 31319102
79. P. J. Manning *et al.*, Inhibition of exercise-induced bronchoconstriction by MK-571, a potent leukotriene D4-receptor antagonist. *N. Engl. J. Med.* **323**, 1736–1739 (1990). doi: 10.1056/NEJM199012203232504; pmid: 2174121
80. F. Bishehsari *et al.*, Alcohol and Gut-Derived Inflammation. *Alcohol Res.* **38**, 163–171 (2017). pmid: 28988571
81. R. A. Wood *et al.*, Omalizumab for the Treatment of Multiple Food Allergies. *N. Engl. J. Med.* **390**, 889–899 (2024). doi: 10.1056/NEJMoa2312382; pmid: 38407394
82. L. Enerbäck, Mucosal mast cells in the rat and in man. *Int. Arch. Allergy Appl. Immunol.* **82**, 249–255 (1987). doi: 10.1159/000234199; pmid: 2437041
83. C. C. Fox, A. M. Dvorak, S. P. Peters, A. Kagey-Sobotka, L. M. Lichtenstein, Isolation and characterization of human intestinal mucosal mast cells. *J. Immunol.* **135**, 483–491 (1985). doi: 10.4049/jimmunol.135.1.483; pmid: 2582045
84. F. L. Pearce *et al.*, Functional characteristics of mucosal and connective tissue mast cells of man, the rat and other animals. *Int. Arch. Allergy Appl. Immunol.* **77**, 274–276 (1985). doi: 10.1159/000233808; pmid: 2409025
85. T. Derakhshan *et al.*, Human intraepithelial mast cell differentiation and effector function are directed by TGF-β signaling. *J. Clin. Invest.* **135**, e174981 (2025). doi: 10.1172/JCI174981; pmid: 39744949
86. L. R. Hoyt *et al.*, Cysteinyl leukotrienes stimulate gut absorption of food allergens and promote anaphylaxis in mice. *Science* **389**, eadp0240 (2025).
87. N. Noben-Trauth *et al.*, An interleukin 4 (IL-4)-independent pathway for CD4+ T cell IL-4 production is revealed in IL-4 receptor-deficient mice. *Proc. Natl. Acad. Sci. U.S.A.* **94**, 10838–10843 (1997). doi: 10.1073/pnas.94.20.10838; pmid: 9380721
88. X. S. Chen, J. R. Shelter, E. N. Johnson, C. D. Funk, Role of leukotrienes revealed by targeted disruption of the 5-lipoxygenase gene. *Nature* **372**, 179–182 (1994). doi: 10.1038/372179a0; pmid: 7969451
89. Z. W. Peng *et al.*, Integrin αvβ6 critically regulates hepatic progenitor cell function and promotes ductular reaction, fibrosis, and tumorigenesis. *Hepatology* **63**, 217–232 (2016). doi: 10.1002/hep.28274; pmid: 26448099
90. T. Takeishi, T. R. Martin, I. M. Katona, F. D. Finkelman, S. J. Galli, Differences in the expression of the cardiopulmonary alterations associated with anti-immunoglobulin E-induced or active anaphylaxis in mast cell-deficient and normal mice. Mast cells are not required for the cardiopulmonary changes associated with certain fatal anaphylactic responses. *J. Clin. Invest.* **88**, 598–608 (1991). doi: 10.1172/JCI115344; pmid: 1864969
91. S. D. Chanez-Paredes, S. Abtahi, W. T. Kuo, J. R. Turner, Differentiating Between Tight Junction-Dependent and Tight Junction-Independent Intestinal Barrier Loss In Vivo. *Methods Mol. Biol.* **2367**, 249–271 (2021). doi: 10.1007/7651_2021_389; pmid: 33830456
92. Z. A. Sullivan *et al.*, γδ T cells regulate the intestinal response to nutrient sensing. *Science* **371**, eaba8310 (2021). doi: 10.1126/science.aba8310; pmid: 33737460
93. S. Picelli *et al.*, Full-length RNA-seq from single cells using Smart-seq2. *Nat. Protoc.* **9**, 171–181 (2014). doi: 10.1038/nprot.2014.006; pmid: 24385147
94. N. L. Bray, H. Pimentel, P. Melsted, L. Pachter, Near-optimal probabilistic RNA-seq quantification. *Nat. Biotechnol.* **34**, 525–527 (2016). doi: 10.1038/nbt.3519; pmid: 27043002
95. M. I. Love, W. Huber, S. Anders, Moderated estimation of fold change and dispersion for RNA-seq data with DESeq2. *Genome Biol.* **15**, 550 (2014). doi: 10.1186/s13059-014-0550-8; pmid: 25516281
96. Y. Hao *et al.*, Dictionary learning for integrative, multimodal and scalable single-cell analysis. *Nat. Biotechnol.* **42**, 293–304 (2024). doi: 10.1038/s41587-023-01767-y; pmid: 37231261
97. J. Cao *et al.*, The single-cell transcriptional landscape of mammalian organogenesis. *Nature* **566**, 496–502 (2019). doi: 10.1038/s41586-019-0969-x; pmid: 30787437
98. T. Wu *et al.*, clusterProfiler 4.0: A universal enrichment tool for interpreting omics data. *Innovation* **2**, 100141 (2021). doi: 10.1016/j.xinn.2021.100141; pmid: 34557778
99. A. Liberzon *et al.*, The Molecular Signatures Database (MSigDB) hallmark gene set collection. *Cell Syst.* **1**, 417–425 (2015). doi: 10.1016/j.cels.2015.12.004; pmid: 26771021
100. N. D. Bachtel *et al.*, Intestinal mast cell-derived leukotrienes mediate the anaphylactic response to ingested antigens, Zenodo (2025); https://www.doi.org/10.5281/zenodo.15420173.

ACKNOWLEDGMENTS

We are grateful to the members of the Medzhitov lab and Food Allergy Science Initiative (FASI) members for insightful discussions and help, especially C. Zhang, S. Yu, and C. and S. Annicelli for mouse colonies and in vivo experiments. We thank D. Dwyer (Brigham and Women's Hospital) for suggestions regarding scRNA-seq analysis of intestinal mast cells; H. C. Oettgen (Boston Children's Hospital) for the IgE KO BALB/cJ mice; P. Launay (INSERM, France) for the RMB (FcεR1-DTR mice); and D. Sheppard (University of California San Francisco) for providing the αvβ6-neutralizing antibody (3G9) and suggesting methods of its use. We also thank Yale Flow Cytometry for its assistance with FACS service, Yale Pathology Tissue Services for its assistance with histological analysis, and the Keck Microarray Shared Resource (KMSR) at Yale University and the Yale Center for Genome Analysis (YCGA) for their assistance with scRNA-seq services. Images were created with BioRender.com. **Funding:** This work was supported by a Ruth L. Kirschstein Predoctoral Individual National Research Service Award from the National Institutes of Allergy and Infectious Diseases (NIAID) of the NIH, F30AI174787 (N.D.B); NIH grant 1R01AI144152 and NIAID grant P01AI179273-P1 (R.M.); the Food Allergy Science Initiative (R.M.); the Blavatnik Family Foundation (R.M.); and the Howard Hughes Medical Institute (R.M.). **Author contributions:** Conceptualization: N.D.B., R.M.; Funding acquisition: N.D.B., J.L.C., R.M.; Investigation: N.D.B., J.L.C., V.I.K., D.W.E.-N., R.I., A.H., E.B.F., J.L., Z.A.S., M.L.; Methodology: N.D.B., J.L.C., V.I.K., D.W.E.-N., S.A.E., C.Z., E.B.F., J.L., Z.A.S., M.L.; Supervision: R.M.; Visualization: N.D.B., J.L.C., V.I.K., J.L., M.L.; Writing – original draft: N.D.B., J.L.C., R.M.; Writing – review & editing: N.D.B., J.L.C., V.I.K., D.W.E.-N., S.A.E., R.I., A.H., J.L., Z.A.S., M.L., R.M. **Competing interests:** N.D.B. and R.M. are coinventors on the patent application (International Patent Application No. PCT/US23/84085, US Provisional Patent Application No. 63/387,297f) submitted by Yale University that covers suppression of food allergic reactions by leukotriene modifiers. The other authors declare that they have no competing interests. **Data and materials availability:** All data needed to evaluate the conclusions in the paper are present in the paper or the supplementary materials. Bulk sequencing and scRNA-seq of intestinal mast cells generated for this paper can be accessed through the Gene Expression Omnibus under accession no. GSE293906. Code utilized in the analysis of this data to produce each figure can be found at Zenodo (*100*). Single-cell RNA-seq of mast cells in different tissues used to generate Fig. 3A can be found at the nonprofit data repository Dryad (*59*). **License information:** Copyright © 2025 the authors, some rights reserved; exclusive licensee American Association for the Advancement of Science. No claim to original US government works. https://www.science.org/about/science-licenses-journal-article-reuse. This article is subject to HHMI's Open Access to Publications policy. HHMI lab heads have previously granted a nonexclusive CC BY 4.0 license to the public and a sublicensable license to HHMI in their research articles. Pursuant to those licenses, the Author Accepted Manuscript (AAM) of this article can be made freely available under a CC BY 4.0 license immediately upon publication.

SUPPLEMENTARY MATERIALS

science.org/doi/10.1126/science.adp0246
Figs. S1 to S9; Data S1 to S7; MDAR Reproducibility Checklist

Submitted 3 March 2024; resubmitted 14 January 2025; accepted 30 May 2025

10.1126/science.adp0246

Check for

RESEARCH ARTICLE SUMMARY

NEUROSCIENCE

Transferrin receptor–targeted anti-amyloid antibody enhances brain delivery and mitigates ARIA

Michelle E. Pizzo *et al.*

Full article and list of author affiliations:
https://doi.org/10.1126/science.ads3204

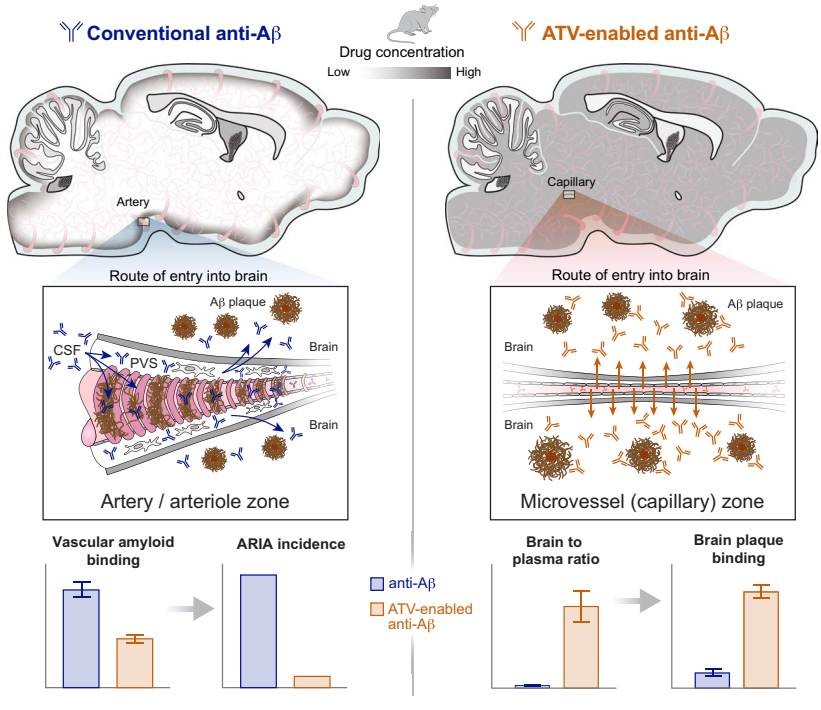
INTRODUCTION: Poor penetration of biotherapeutics across the blood-brain barrier (BBB) limits their utility for the treatment of neurological diseases. One strategy to enhance brain exposure is through receptor-mediated transport, which uses proteins expressed on endothelial cells that line the brain vasculature. The most well-studied of these is the transferrin receptor (TfR), which has the highest expression in capillaries and much lower expression in arteries and arterioles. We previously described a transport vehicle (TV) with TfR binding engineered into the human immunoglobulin G1 (huIgG1) Fc domain that increases brain exposure and parenchymal biodistribution of protein therapeutics.

RATIONALE: The first generation of amyloid-β protein (Aβ) immunotherapy for Alzheimer's disease (AD) is clinically approved. However, amyloid-related imaging abnormalities (ARIA), caused by vascular inflammation, remain a key safety concern for this class of therapeutics. Additionally, limited central nervous system (CNS) transport of anti-Aβ suggests that there is an opportunity to further enhance target engagement and efficacy. Although TfR-based brain-delivery platforms have shown promise, these often contain symmetrical Fc mutations to prevent immune cell engagement to mitigate TfR-related hematology liabilities. The resulting effectorless molecules may be suitable for some therapeutics, but efficacy for Aβ immunotherapy requires FcγR engagement.

RESULTS: We engineered an antibody transport vehicle (ATV) with asymmetrical Fc mutations ($ATV^{cisLALA}$) that mitigated TfR-related hematology liabilities while preserving the ability to induce microglia phagocytosis of Aβ ex vivo and plaque reduction in vivo. $ATV^{cisLALA}$:Aβ showed broad brain parenchymal distribution, with reduced localization to arteries owing to its predominant capillary-enabled BBB crossing. By contrast, anti-Aβ was highly enriched at arterial perivascular spaces where vascular amyloid localizes and likely plays a role in the induction of an inflammatory response and ultimately ARIA. Notably, this differentiated route of entry into the CNS with $ATV^{cisLALA}$:Aβ resulted in near-complete elimination of ARIA-like lesions and vascular inflammation normally associated with anti-Aβ treatment in 5xFAD mice, an AD mouse model exhibiting robust vascular amyloid.

CONCLUSION: The $ATV^{cisLALA}$-mediated CNS delivery of anti-Aβ enhances brain exposure, biodistribution, and Aβ plaque target engagement throughout the parenchyma. Additionally, this distribution pattern may also protect against vascular damage observed with anti-Aβ. Taken together, $ATV^{cisLALA}$:Aβ has the potential to substantially improve the next generation of Aβ immunotherapy. □

Corresponding author: Y. Joy Yu Zuchero (zuchero@dnli.com) Cite this article as M. E. Pizzo *et al.*, *Science* **389**, eads3204 (2025). DOI: 10.1126/science.ads3204



Transferrin receptor–mediated brain delivery of anti-amyloid mitigates ARIA. Conventional anti-Aβ therapeutics for AD enter the brain through CSF and perivascular spaces (PVS) where vascular amyloid resides, causing inflammation and ARIA-like lesions in mice. ATV-enabled anti-Aβ crosses the BBB through capillaries, using transferrin receptor–mediated transport to enhance distribution throughout the brain parenchyma. This differentiated route of entry into the CNS increases brain plaque binding and reduces ARIA in a mouse model of AD.

NEUROSCIENCE

Transferrin receptor–targeted anti-amyloid antibody enhances brain delivery and mitigates ARIA

Michelle E. Pizzo[1], Edward D. Plowey[2], Nathalie Khoury[1], Wanda Kwan[1], Jordan Abettan[2], Sarah L. DeVos[1]†, Claire B. Discenza[1], Timothy Earr[1]‡, David Joy[1], Ming Lye-Barthel[2], Elysia Roche[1], Darren Chan[1], Jason C. Dugas[1], Kapil Gadkar[1], Stefan Hamann[2], René Meisner[1], Jennifer Sebalusky[2], Ana Claudia Silva Amaral[2], Isabel Becerra[1], Roni Chau[1], Johann Chow[1], Allisa J. Clemens[1]§, Mark S. Dennis[1], Joseph Duque[1], Laura Fusaro[1], Jennifer A. Getz[1], Mihalis S. Kariolis[1], Do Jin Kim[1], Kendra J. Lechtenberg[1]¶, Amy Wing-Sze Leung[1], Arash Moshkforoush[1], Hoang N. Nguyen[1], Emmanuel S. Ojo[1], Elliot R. Thomsen[1], Vanessa O. Torres[1], Pascal E. Sanchez[1], Lu Shan[1], Adam P. Silverman[1], Zachary K. Sweeney[1]; Hilda Solanoy[1], Raymond Tong[1], Meredith E. Calvert[1], Ryan J. Watts[1], Robert G. Thorne[1,3], Paul H. Weinreb[2], Dominic M. Walsh[2], Joseph W. Lewcock[1], Thierry Bussiere[2], Y. Joy Yu Zuchero[1]*

Amyloid-related imaging abnormalities (ARIA), side effects of anti-amyloid drugs seen in magnetic resonance imaging of the brain, are a major safety concern in patients with Alzheimer's disease. We developed an antibody transport vehicle (ATV) targeting transferrin receptor (TfR) for brain delivery of anti-amyloid-β protein (anti-Aβ) using asymmetrical Fc mutations ($ATV^{cisLALA}$) that mitigates TfR-related liabilities and retains effector function when bound to Aβ. Administration of $ATV^{cisLALA}$:Aβ in mice exhibited broad brain distribution and enhanced parenchymal plaque target engagement. This biodistribution reduced ARIA-like lesions and vascular inflammation. Taken together, $ATV^{cisLALA}$ has the potential to improve the next generation of Aβ immunotherapy through enhanced biodistribution mediated by transport across the blood-brain barrier.

Monoclonal antibodies (mAbs) and other biotherapeutics poorly penetrate the blood-brain barrier (BBB) after systemic administration, limiting their utility in the treatment of neurological diseases. This challenge has led to strategies for active BBB transport in which binding to specific proteins expressed on brain endothelial cells can enable receptor-mediated transport, with transferrin receptor (TfR) being the most well validated (*1*–*8*). We previously described a transport vehicle (TV) with TfR binding engineered into the human immunoglobulin G1 (huIgG1) crystallizable fragment (Fc) domain yielding a modular platform that does not require appended sequences and can be paired with antibodies (ATV) (*7*–*9*), enzymes (ETV) (*10*, *11*), proteins (PTV) (*12*), or oligonucleotides (OTV) (*13*).

TfR-binding antibodies are often unable to fully preserve effector function owing to depletion of TfR-expressing erythrocyte precursor cells in the blood and bone marrow (*14*–*16*). It is unclear whether this issue is dependent on molecular architecture, and limited data exist on whether architecture alone can prevent reticulocyte loss and anemia (*1*, *6*). Consequently, TfR-based delivery platforms often introduce symmetrical Fc mutations to prevent immune cell engagement, creating effectorless molecules (*6*–*8*, *11*, *12*, *15*). Although this may be suitable for some central nervous system (CNS) therapeutics, others may require FcγR engagement.

Amyloid beta-protein (Aβ) accumulation in plaques within the brain is a key driver of Alzheimer's disease (AD) (*17*–*19*), and plaque removal (*20*)—likely through microglia-mediated phagocytosis—depends on effector function (*21*–*23*). Recent clinical successes of some Aβ antibodies support the amyloid hypothesis as a promising disease-modifying therapeutic approach (*24*, *25*). However, limited BBB (*26*) and cerebrospinal fluid (CSF) transport (*27*–*30*) suggests that there is an opportunity to further enhance target engagement and efficacy. Additionally, amyloid-related imaging abnormalities (ARIA) remain a key safety concern for this class of therapeutics. Although the mechanisms that cause ARIA are incompletely understood, the occurrence of these adverse events appears to be linked to vascular amyloid deposition, presence of the *APOE ε4* allele, and dose (*31*–*34*). These dose-limiting adverse events hinder efficacy in certain patient populations; therefore, improving safety and efficacy will be critical to their broader adoption.

We report the development of $ATV^{cisLALA}$:Aβ, a TfR-based antibody transport vehicle platform engineered with asymmetric effector-reducing mutations in the huIgG1 Fc, paired with anti-Aβ. This platform (i) safely preserves antibody-mediated effector function, (ii) improves brain exposure and target engagement, and (iii) reduces ARIA-like lesions in a mouse model with amyloid pathology. We propose that the improved ARIA profile with $ATV^{cisLALA}$:Aβ results from a distinct brain entry route and biodistribution compared to standard anti-Aβ antibody.

Effector function status of ATV variants affects in vitro activity

TfR-mediated reticulocyte loss occurs when antibodies simultaneously bind both TfR and FcγR on TfR-expressing early erythroid progenitors (*15*). We previously introduced L234A/L235A ("LALA") mutations in the huIgG1 Fc of ATV to reduce FcγR binding (*7*). Because ATV molecules are generated using knob-in-hole technology (*35*), we tested whether FcγR binding could be limited to one side of the Fc while preserving TfR binding. Thus, we engineered LALA mutations into either the knob ($ATV^{cisLALA}$) or hole side ($ATV^{transLALA}$) of the Fc and compared the properties of these variants to a molecule that has symmetrical LALA (ATV^{LALA}) and an ATV with a wild-type Fc (ATV^{WT}) (Fig. 1A and fig. S1).

Antibody-dependent cell cytotoxicity (ADCC) and complement-dependent cytotoxicity (CDC) contribute to TfR-mediated hematology liabilities observed in vivo (*15*). We assessed in vitro cell-killing with ATV variants containing the previously described BACE1 Fabs (fig. S1A) (*7*), which have limited binding to the cells, hence isolating the impact of TfR binding on ADCC and CDC activity. We showed that $ATV^{cisLALA}$:BACE1 exhibited an attenuation of TfR-mediated ADCC similar to that observed with ATV^{LALA}:BACE1, whereas $ATV^{transLALA}$:BACE1 retained ADCC magnitude similar to that observed with ATV^{WT}:BACE1 (Fig. 1B). These results suggest that the location of the "LALA" mutations relative to TfR binding affects TfR-mediated ADCC: $ATV^{transLALA}$ preserves TfR-mediated effector function, likely by maintaining FcγR access, whereas $ATV^{cisLALA}$ blocks FcγR engagement and thus TfR-mediated ADCC.

To assess whether ATV variants trigger CDC-mediated killing, we used Chinese hamster ovary (CHO) cells overexpressing huTfR and measured lactate dehydrogenase (LDH) release. Unlike the anti-TfR mAb with WT huIgG Fc, none of the ATV molecules induced CDC on TfR-expressing target cells (Fig. 1C and fig. S1A). This suggests that the Fc-binding orientation to TfR likely prevents hexameric C1 interactions required for TfR-mediated CDC (*36*).

We next evaluated whether $ATV^{cisLALA}$ retains Fab target–mediated effector function. We used murine CD20-binding Fabs (fig. S1B),

[1]Denali Therapeutics, Inc., South San Francisco, CA, USA. [2]Biogen, Cambridge, MA, USA. [3]Department of Pharmaceutics, University of Minnesota, 9-177, Weaver-Densford Hall, Minneapolis, MN, USA. ***Corresponding author. Email: zuchero@dnli.com** †Present address: Curie.Bio, Cambridge, MA, USA. ‡Present address: Altos Labs, Inc., Redwood City, CA, USA. §Present address: Vaxcyte, San Carlos, CA, USA. ¶Present address: Michael J. Fox Foundation, New York, NY, USA.

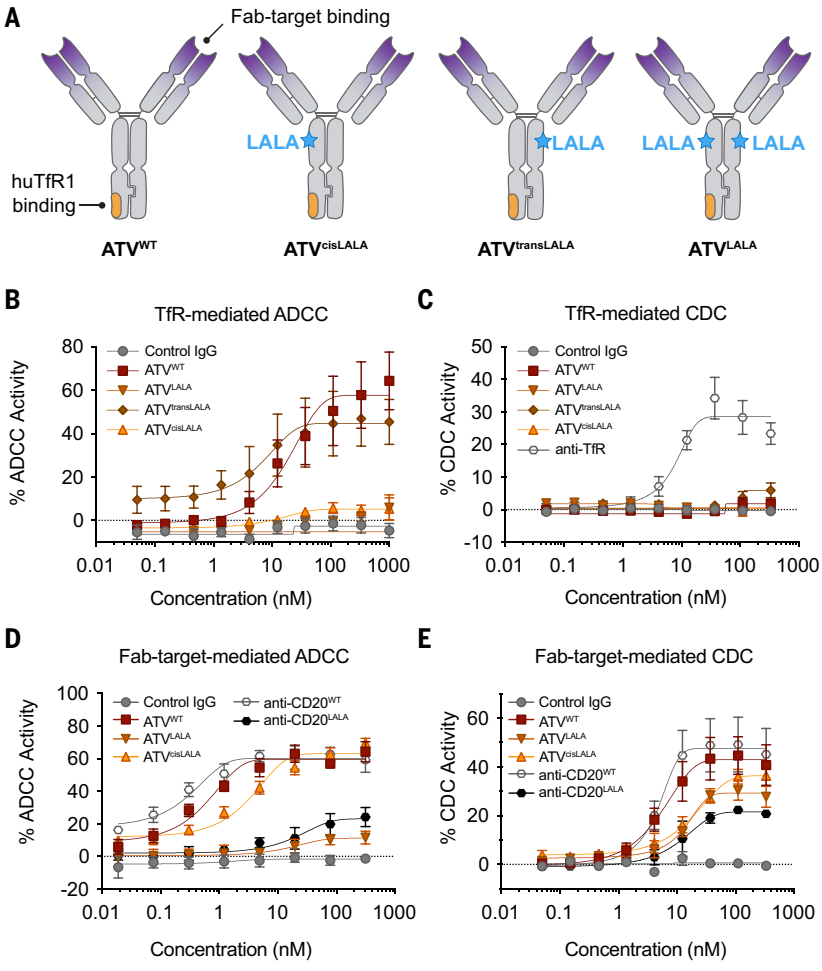


Fig. 1. Asymmetrical cisLALA Fc mutations mitigate TfR-mediated but maintain Fab-target–mediated ADCC and CDC in vitro. (**A**) Schematics of ATV molecular architectures indicating L234A/L235A (LALA) mutations, if present. (**B** and **C**) In human TfR-expressing cells, ATVs with control BACE1 Fabs were used to evaluate ADCC-induced killing of Ramos cells by isolated human NK cells (B) or CDC-induced killing of huTfR-overexpressing CHO cells (C). (**D**) Murine CD20-expressing A20 lymphoma cells were treated with ATV formats targeting murine CD20 to evaluate Fab target–mediated ADCC by isolated human NK cells. (**E**) Human CD20–expressing Raji cells were treated with ATV formats targeting human CD20 to evaluate Fab target–mediated CDC. All graphs represent $n = 3$ to 4 replicate experiments except anti-CD20^{LALA} in (E), which had $n = 2$ replicate experiments. See fig. S1 for additional details on molecules. ATV huTfR apical domain affinity is ~100 nM.

known to mediate ADCC and CDC on lymphoma cells (*37*), and showed that ATV^{cisLALA}:CD20 targeting elicited strong ADCC on A20 murine lymphoma cells with a maximum effect (E_{max}) similar to that of ATV^{WT}:CD20 and anti-CD20 mAb with WT huIgG Fc, albeit with a slight shift in half-maximal effective concentration (EC_{50}) (Fig. 1D). As expected, ATV^{LALA}:CD20 and anti-CD20^{LALA} reduced ADCC. All molecules elicited CDC activity with human CD20 Fabs (fig. S1C), although ATV^{cisLALA}:CD20, ATV^{LALA}:CD20, and anti-CD20^{LALA} had slightly reduced activity (Fig. 1E). Together, these assays suggested that ATV^{cisLALA} eliminates TfR-mediated cytotoxicity while preserving Fab-target-mediated effector function.

ATV^{cisLALA} architecture mitigates in vivo hematology liability in mice

To determine whether mitigation of in vitro TfR-mediated ADCC with ATV^{cisLALA} translates in vivo, we formatted ATV effector variants onto anti-Aβ Fabs and evaluated the hematology impacts after systemic dosing in the previously described TfR$^{mu/hu}$ knock-in (KI) mice (*7*). A single 10 mg/kg intravenous dose of ATV^{WT}:Aβ caused near-complete depletion of circulating reticulocytes, whereas ATV^{cisLALA}:Aβ and ATV^{LALA}:Aβ showed no effects (Fig. 2A). Similar patterns were observed in bone marrow, where ATV^{cisLALA} and ATV^{LALA} had no impact on reticulocytes compared with the anti-Aβ control, whereas ATV^{WT}:Aβ reduced reticulocytes (Fig. 2B). Furthermore, 13 weekly administrations of ATV^{cisLALA}:Aβ at therapeutically relevant doses had no effect on blood reticulocytes, red blood cell count, or hemoglobin (fig. S2, A to C), suggesting that ATV^{cisLALA} preserved hematology safety under chronic administration. Additionally, ATV^{cisLALA}:Aβ also had no effect on brain and vascular TfR expression after single or repeated doses compared with anti-Aβ (fig. S2, D to G), suggesting that acute and chronic dosing did not induce TfR protein degradation.

Other TfR-based CNS delivery platforms have used alternative architectures to increase brain exposure while maintaining FcγR binding (*1*, *2*). One approach adds a C-terminal TfR binding domain to a WT huIgG Fc, potentially reducing FcγR access and minimizing immune activation while bound to TfR but retaining Fab target–mediated effector function (*1*). To compare this architecture to ATV^{cisLALA}, we generated an anti-Aβ antibody with WT huIgG Fc with a C-terminal TfR-binding Fab (TfR$^{C\text{-term Fab}}$:Aβ, Fig. 2C) and compared it to ATV^{cisLALA} with similar huTfR binding affinity. Both showed reductions in plasma exposure compared with anti-Aβ (Fig. 2D) and enhanced brain exposure 24 hours post-dose (Fig. 2E), suggesting similar TfR-driven pharmacokinetics despite architectural differences. However, only TfR$^{C\text{-term Fab}}$:Aβ reduced circulating reticulocytes (Fig. 2F), consistent with other prior reports using a similar TfR-binding architecture (*6*). These findings suggest that steric hindrance alone was insufficient to protect against effector-function driven depletion of TfR-expressing reticulocytes, and ATV^{cisLALA} specifically mitigates this risk while retaining TfR engagement.

ATV^{cisLALA}:Aβ retains ability to induce microglial phagocytosis ex vivo and reduce plaques in vivo

We investigated whether the cisLALA mutations retain the ability to induce anti-Aβ–mediated phagocytosis, a critical component of amyloid plaque removal (*23*, *38*). Fc modifications did not alter Aβ binding (fig. S3A). Using flow cytometry, we incubated dissociated TfR$^{mu/hu}$ KI mouse brain cells with fluorescein (FAM)–labeled Aβ aggregates (fig. S4A) and one of the following: control IgG, anti-Aβ (WT Fc), ATV^{WT}:Aβ, ATV^{cisLALA}:Aβ, or ATV^{LALA}:Aβ. Cells were then assessed by flow cytometry to detect the number of FAM-Aβ–positive and FAM-Aβ–negative microglia (fig. S4D). This ex vivo paradigm was designed to specifically measure microglial phagocytosis of these molecules and avoids confounding effects of differential brain exposure and biodistribution between non-ATV and ATV molecules. Microglial uptake of FAM-Aβ was similar for anti-Aβ, ATV^{cisLALA}:Aβ, and ATV^{WT}:Aβ but reduced for ATV^{LALA}, consistent with a reduction in functional FcγR engagement (Fig. 3, A and B). Lack of FAM-Aβ signal at 4°C (fig. S4, B and C) confirmed that the observed increase in fluorescence intensity was due to phagocytic uptake, rather than binding to the cell surface.

To test in vivo activity, we crossed 5xFAD transgenic mice, a mouse model of AD (*39*), with TfR$^{mu/hu}$ KI mice (*7*) and used an acute multi-dose paradigm at high doses to match brain exposures for ATV^{LALA}:Aβ, ATV^{cisLALA}:Aβ, and anti-Aβ groups to isolate the role of the Fc mutations on microglial recruitment. Although bulk brain lysate concentrations

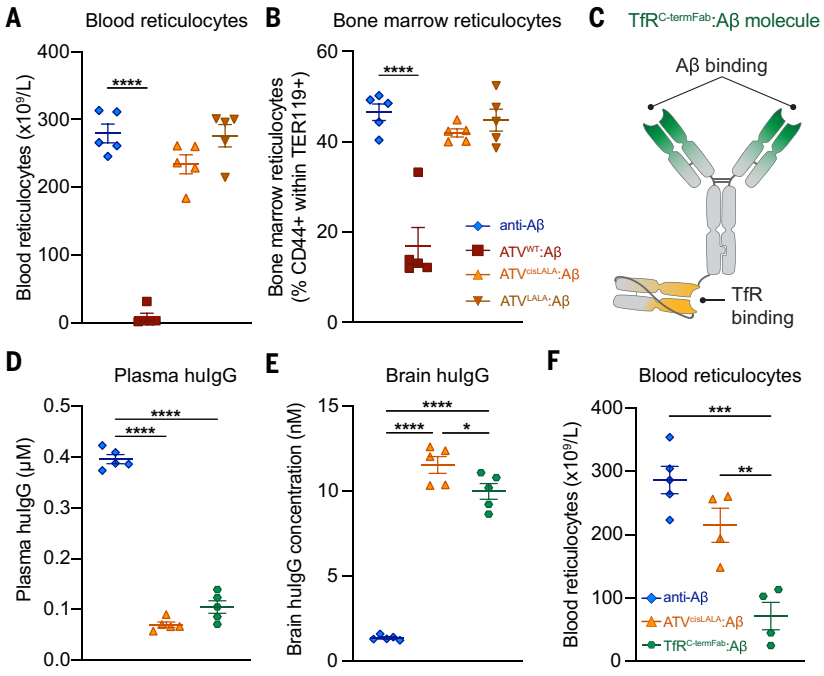


Fig. 2. ATV^{cisLALA}:Aβ, but not TfR$^{C\text{-}term\ Fab}$:Aβ, mitigates in vivo reticulocyte loss in mice. (**A** and **B**) Circulating blood (A) or bone marrow (B) reticulocytes in TfR$^{mu/hu}$ KI mice 24 hours after a single intravenous dose (10 mg/kg) of anti-Aβ or ATV:Aβ variants. (**C**) An alternative architecture of TfR$^{C\text{-}term\ Fab}$:Aβ generated for comparison of effector function–mediated reticulocyte response. (**D** to **F**) Plasma (D) and brain (E) concentrations as measured by ELISA, and blood reticulocytes (F) 24 hours after a single intravenous dose (10 mg/kg) of anti-Aβ, ATV^{cisLALA}:Aβ, or TfR$^{C\text{-}term\ Fab}$:Aβ in TfR$^{mu/hu}$ KI mice. Graphs display mean ± SEM. Only significant differences are indicated on graphs; [(A), (B), (D) to (F)] one-way analysis of variance (ANOVA) with multiple comparisons; [(A) and (B)] Dunnett's post hoc versus anti-Aβ control, ***$P < 0.001$; [(D) to (F)] Tukey's post hoc comparing all groups, *$P < 0.05$, **$P < 0.01$, ***$P < 0.001$, ****$P < 0.0001$. ATV and TfR$^{C\text{-}term\ Fab}$ affinities: ~500 nM [(A) and (B) huTfR apical domain] or ~40 to 50 nM [(D) to (F) full-length huTfR].

were similar across all groups owing to the high dose and frequency (50 mg/kg Q3Dx4, fig. S4E), the two ATV molecules showed stronger plaque immunodecoration, indicating better target engagement, possibly due to improved parenchymal biodistribution (fig. S4, F and I). Colocalization of the activated microglial-macrophage marker CD68 with Aβ plaques revealed similar microglial recruitment between ATV^{cisLALA}:Aβ and anti-Aβ treatment, with a reduced ability for the effectorless ATV^{LALA}:Aβ (Fig. 3C and fig. S4, G and J). Despite the relatively short treatment duration, both ATV^{cisLALA}:Aβ and anti-Aβ reduced the burden of small plaques (30 to 125 μm^2), whereas ATV^{LALA}:Aβ did not, consistent with the reduced ability to recruit microglia for this effectorless variant (Fig. 3D). The reduction in the small plaques during this short treatment period may reflect that (i) these plaques are more readily cleared and/or (ii) new plaque formation was prevented (fig. S4, H and J). These findings suggest that ATV^{cisLALA}:Aβ retains sufficient effector function to activate microglia in vivo, enabling plaque clearance and/or prevention of new plaque formation.

ATV^{cisLALA}:Aβ shows broad brain distribution and greater target engagement

We hypothesized that TfR-mediated entry across the BBB would lead to broader and differentiated brain distribution compared with anti-Aβ. Spatial analysis of anti-Aβ and ATV^{cisLALA}:Aβ in TfR$^{mu/hu}$ KI mice 1 day post-dose showed anti-Aβ localized mainly with CSF-associated cells and compartments, including the choroid plexus, periventricular regions, pial surfaces, leptomeningeal cells, and perivascular spaces, particularly along the ventral brain and CSF cisterns (Fig. 4, A to C), consistent with non-ATV antibodies entering the brain via the CSF compartment (*9*). Confocal imaging showed high anti-Aβ signal around choroid plexus vessels (fig. S5A), likely from high plasma concentrations (fig. S6A) and extravasation across fenestrated choroid plexus vasculature (*40*). By contrast, ATV^{cisLALA}:Aβ showed widespread signal across the brain, including in both the vasculature and parenchyma (Fig. 4, D to F, and fig. S5C), with minimal choroid plexus signal (Fig. 4E and fig. S5B), likely owing to lower plasma concentration relative to anti-Aβ (fig. S6A) and a lack of TfR expression on choroid plexus endothelial cells to mediate transport (*41*). Thus, ATV^{cisLALA}:Aβ not only increased overall brain concentrations but also resulted in a broader, whole-brain distribution, consistent with our findings for non-targeted antibodies compared with ATVs (*9*).

To determine whether plaque burden has an impact on brain uptake, we dosed 4-month-old 5xFAD;TfR$^{mu/hu}$ KI mice at therapeutically relevant doses. ATV^{cisLALA}:Aβ achieved five to eight times higher brain concentrations compared with anti-Aβ at all doses 24 hours post-dose (Fig. 4G) despite lower plasma concentrations from expected target-mediated peripheral clearance where TfR is also widely expressed (fig. S6B). Percent brain:plasma concentrations were higher for ATV^{cisLALA}:Aβ, indicating a more efficient transport into the brain compared with anti-Aβ (Fig. 4H). ATV^{cisLALA}:Aβ also revealed greater plaque target engagement by immunodetection (Fig. 4, I to K), and the distribution patterns reflected differentiated CNS entry (fig. S7, A to H), similar to what was observed in non–plaque-bearing mice. CSF drug exposure was similar between the molecules tested (fig. S6C) despite the differences reported in brain concentrations (Fig. 4G), consistent with previous reports indicating that CSF drug exposure does not correlate with brain exposure for ATVs (*7*) and is consistent with predominant transport of ATVs across the BBB (*9*).

We next used tissue clearing and three-dimensional (3D) imaging to further visualize ATV^{cisLALA}:Aβ and anti-Aβ distribution associated with brain surface structures (leptomeningeal arteries and perivascular spaces) that are prone to cerebral amyloid angiopathy (CAA), a common vascular pathology in AD (*42*). Engagement of CAA by anti-Aβ antibodies is hypothesized to be a trigger for the perivascular inflammatory response that likely underlies ARIA, adverse events observed in patients treated with amyloid immunotherapy (*43*–*47*). Light sheet imaging of immunolabeling-enabled three-dimensional imaging of solvent-cleared organs (iDISCO)-cleared hemibrains from 5xFAD;TfR$^{mu/hu}$ KI mice dosed at 10 mg/kg revealed anti-Aβ mainly localized to larger, connected volumes on the brain surface in a pattern consistent with major surface arteries, presumably associated with arterial perivascular spaces and leptomeningeal cells (particularly around CSF cisterns), and limited parenchymal signal (Fig. 4, L and N, and figs. S7, I and K, and S8, A, C, and D). By contrast, ATV^{cisLALA}:Aβ was predominantly associated with putative parenchymal plaques (Fig. 4M) and to a limited extent with leptomeningeal arteries (figs. S7, J and K, and S8, B, E, and F). Additional immunostaining for Aβ and alpha–smooth muscle actin (αSMA) confirmed the presence of CAA in the 5xFAD;TfR$^{mu/hu}$ KI mice, even at a relatively young age (fig. S8). ATV^{cisLALA}:Aβ-treated mice showed a greater correlation of huIgG and Aβ within plaques (Fig. 4N), whereas anti-Aβ–treated mice showed a higher correlation between huIgG and αSMA-positive, vascular Aβ (Fig. 4O and fig. S7, C to F).

ATV^{cisLALA}:Aβ reduces ARIA-like lesions in mice

We hypothesized that anti-Aβ's higher vascular and perivascular localization with CAA could increase the inflammatory responses and ARIA

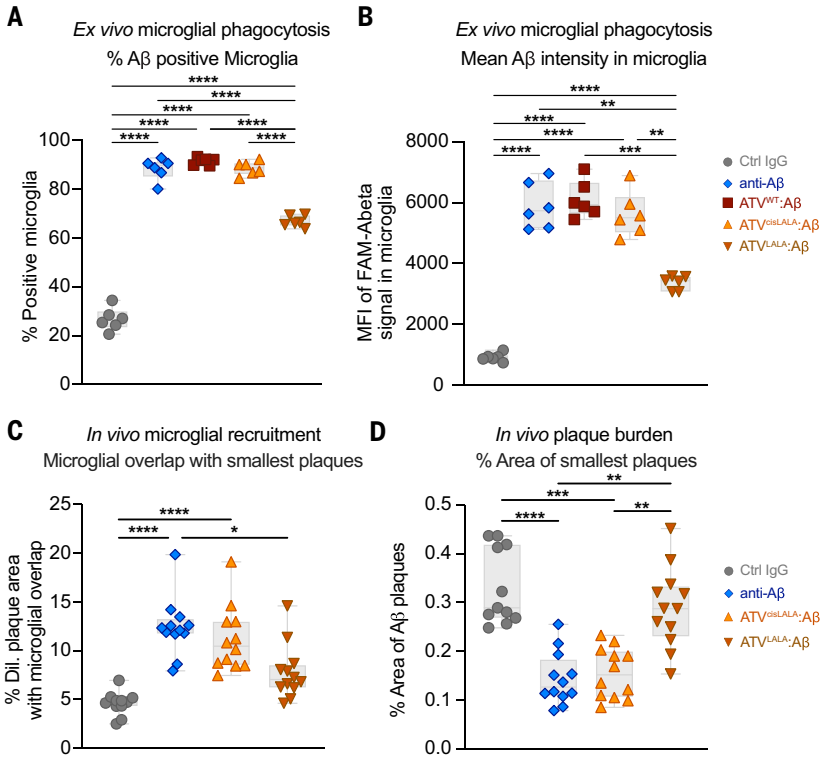


Fig. 3. ATV^{cisLALA}:Aβ retains the ability to induce microglia phagocytosis ex vivo and recruits microglia to clear plaques in vivo. (**A** and **B**) Freshly perfused brains from TfR$^{mu/hu}$ KI mice were dissociated, and brain cells were incubated with FAM-labeled Aβ and either control IgG, anti-Aβ, or ATV:Aβ variants at 37°C to assess ex vivo phagocytosis. (A) Percentage of Aβ^{+} live microglia, as measured by flow cytometry. (B) Mean fluorescence intensity (MFI) of Aβ signal in microglia. (**C** and **D**), In vivo phagocytosis was assessed using an acute multidose paradigm (50 mg/kg Q3Dx4, intraperitoneal) in mixed sex 5xFAD;TfR$^{mu/hu}$ KI mice (~3.5 months of age) to achieve similar brain exposure for all groups by the terminal time point of 12 days. (C) IHC quantification of CD68^{+} microglial overlap with plaques and a small, dilated region immediately surrounding plaques. (D) Percentage tissue area of the smallest (30 to 125 μm^2) Aβ plaques (D). Only significant differences indicated on graphs; [(A) and (B)] one-way ANOVA with multiple comparisons; Tukey's post hoc comparing all groups. [(C) and (D)] Kruskal-Wallis test with Dunn's multiple comparisons of all groups. *$P < 0.05$, **$P < 0.01$, ***$P < 0.001$, ****$P <$ 0.0001. ATV huTfR apical domain affinities: ~1200 nM [(A) and (B)] or ~500 nM [(C) and (D)].

risk compared to ATV^{cisLALA}:Aβ. We used the chimeric (ch) 3D6 anti-Aβ antibody known to induce CAA-associated microhemorrhages in AD mouse models (*48*–*53*), and a robust mouse ARIA model was recently described using this molecule (*54*). Addition of the ATV to ^{ch}3D6 did not affect Aβ binding (fig. S3B). We confirmed widespread presence of CAA in untreated 5xFAD;TfR$^{mu/hu}$ KI mice (fig. S10), further validating the model's utility for evaluating treatment-related ARIA.

5xFAD;TfR$^{mu/hu}$ KI mice received weekly doses of 5 mg/kg ^{ch}3D6^{WT} or ATV^{cisLALA}:3D6 (Fig. 5A). A lower ATV^{cisLALA}:3D6 dose group (1.75 mg/kg) was included to match the expected brain area under the curve of ^{ch}3D6^{WT} (fig. S11, A to F, and tables S1 and S2). As no ARIA-like magnetic resonance imaging (MRI) events were detected by week 4 for any of the groups, we increased the dose at week 5 for all groups (to 10 and 3 mg/kg, respectively). By week 8, nearly all mice (10 of 11) treated with ^{ch}3D6^{WT} had ARIA-like MRI lesions (Fig. 5B), whereas only one mouse in the dose-matched ATV^{cisLALA}:3D6 had evidence of ARIA-like lesions, despite its higher predicted brain exposure compared with ^{ch}3D6^{WT}. Pharmacokinetic (PK) modeling and the plasma huIgG concentrations confirmed that the predicted brain exposures for the ^{ch}3D6^{WT} (10 mg/kg) and ATV^{cisLALA}:3D6 (3 mg/kg) groups were well-matched (fig. S11, D to F).

To better separate the contribution of ATV-mediated distribution versus effector function in the mitigation of ARIA events, we generated two additional molecules: ^{ch}3D6^{kLALA} (with asymmetric LALA mutations on huIgG Fc) and ATV^{WT}:3D6 (with wild-type huIgG Fc) (Fig. 5A). We selected the doses to achieve similar brain exposures for all groups using the same modeling approach as in the previous study (fig. S11, G to I) to avoid the interpretations from being confounded by differences in brain exposure. Mice treated with ^{ch}3D6^{WT} (10 mg/kg) developed ARIA-like lesions starting at week 3, with 8 of 10 mice displaying at least one lesion by week 10 (Fig. 5C). The MRI score, accounting for size and severity of lesions, for ^{ch}3D6^{WT}-treated animals was also the highest among all groups (table S3). ^{ch}3D6^{kLALA} treatment resulted in 2 of 10 mice developing ARIA-like lesions in the last week of the study. Neither ATV^{WT}:3D6 nor ATV^{cisLALA}:3D6 groups had any ARIA-like events throughout the study (Fig. 5C and table S3).

MRI scans revealed lesions of varying severity and location. ARIA-like lesions were associated with both hyperintensities and hypointensities in scans collected using a T2w MRI sequence (Fig. 5D and figs. S12 and S13). T2-hyperintense convexity lesions or T2-hyperintense cortical lesions were located within the meningeal space or in the depth of the cortex, respectively. T2-hyperintense focal cortical lesions were visualized as bright and well-circumscribed signals, whereas T2-hyperintense diffuse lesions were visualized as attenuated signals occupying a large volume. T2-hypointense lesions were usually small in size and well-circumscribed within the brain parenchyma. They were less frequent than T2-hypertense lesions and occurred as individual lesions or as an evolution of T2-hyperintense lesions. Taken together, these MRI findings demonstrate that ATV^{WT} and ATV^{cisLALA} architectures effectively mitigated ARIA-like events.

ATV^{cisLALA}:Aβ reduces vascular inflammation and disruption

Blinded histopathologic examination of coronal brain sections in ARIA study 2 (Fig. 5C) revealed that ^{ch}3D6^{WT}-treated mice exhibited frequent Grade 3 to 4 leptomeningeal vascular inflammation, perivascular and diffuse-parenchymal albumin immunoreactivity, and perivascular hemosiderin deposits (Fig. 6, A to D, and fig. S14). Mice treated with ^{ch}3D6^{kLALA} or ATV^{WT}:3D6 showed reduced meningovascular inflammation, mainly mild to moderate, with only sparse Grade 4 vascular inflammation and mural compromise. ATV^{cisLALA}:3D6-treated mice showed only rare Grade 1 foci of meningovascular inflammation, without abnormal vascular permeation and perivascular hemosiderin (Fig. 6, A to D). Though far less prevalent than foci of meningovascular inflammation, cortical microinfarcts were present in most ^{ch}3D6^{WT}-treated mice (Fig. 6E and fig. S15); ATV^{WT}:3D6-treated mice showed no microinfarcts. One microinfarct was observed in one of the ATV^{cisLALA}:3D6-treated mice, and its histologic features (astrogliosis with lack of macrophage activity) suggested that it may have preceded ATV^{cisLALA}:3D6 treatment (Fig. 6E and fig. S15C). A heatmap of these pathologic changes revealed concordance of vascular pathologies with MRI lesions (Fig. 6F and figs. S12 to S15). Similar reductions in meningovascular inflammation, vascular mural leakage, and microinfarct pathologies were observed in mice treated with equal or exposure-matched doses of ATVcisLALA:3D6 compared to ch3D6 in study 1 (Fig. 5B and fig. S16).

Inflammatory responses also differed among the treatment groups in these long-term studies. In ARIA study 1, no changes in glial

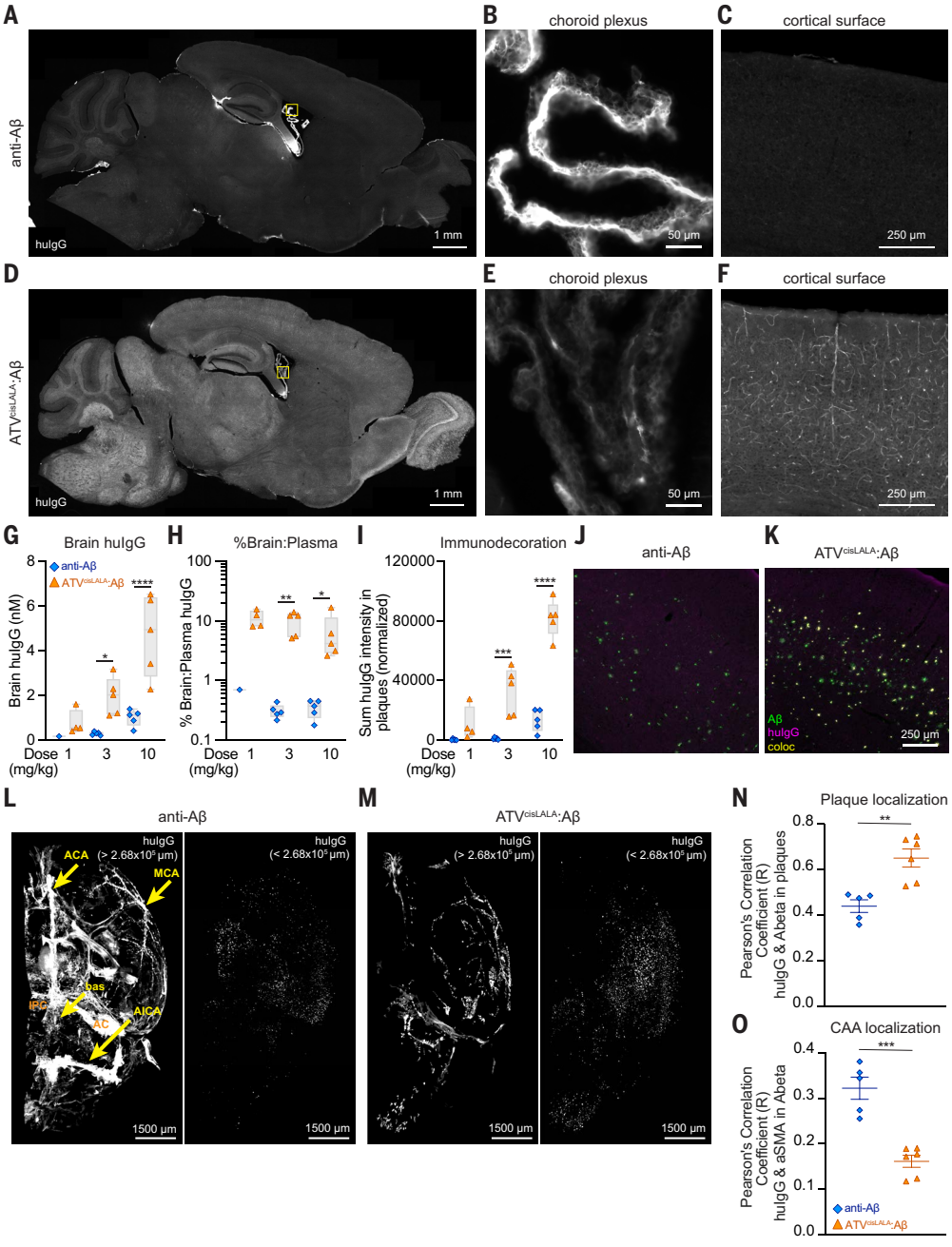


Fig. 4. ATV^{cisLALA}:Aβ has superior brain biodistribution, target engagement, and reduced association with arteries. (**A** to **F**) huIgG distribution in brain 24 hours after an intravenous dose (25 mg/kg) in TfR$^{mu/hu}$ KI mice. (**G** to **K**) huIgG concentrations measured by ELISA in brain or plasma of 5xFAD;TfR$^{mu/hu}$ KI mice 24 hours post-dose [(G) and (H); $n = 4$ of 5 samples below the limit of quantification for anti-Aβ], and quantification of huIgG signal in Aβ plaques by IHC (I); representative cortex images [(J) and (K), 10 mg/kg dose]. (**L** to **O**) 5xFAD;TfR$^{mu/hu}$ KI mice were intravenously dosed with AF750 (10 mg/kg)–conjugated ATV^{cisLALA}:Aβ or anti-Aβ and assessed 24 hours post-dose. [(L) and (M)] huIgG staining, $n = 2$ mice per group; signal segmented on the basis of size as indicated (merged channels in fig. S7, I and J). [(N) and (O)] Pearson's correlation based on quantification of Aβ, αSMA, and huIgG staining, $n = 5$ to 6 mice per group (fig. S7). Yellow arrows in (L) indicate arterial labeling from fig. S7K; anterior cerebral artery (ACA), middle cerebral artery (MCA), basilar artery (bas), anterior inferior cerebellar artery (AICA), interpeduncular cistern (IPC), ambient cistern (AC). Only significant differences are indicated on graphs; [(G) and (H)] one-way ANOVA; Sidak's multiple comparisons test paired by dose, $^*P < 0.05$, $^{**}P < 0.01$, $^{***}P < 0.001$, $^{****}P < 0.0001$; [(N) and (O)] two-tailed t test on Fisher-transformed correlation coefficients, $^{**}P < 0.01$, $^{***}p < 0.001$. ATV huTfR apical domain affinities: ~500 nM [(G) to (O) or ~1200 nM [(A) to (F)].

fibrillary acidic protein (GFAP)–defined astrogliosis were observed in ^{ch}3D6^{WT} or ATV^{cisLALA}:3D6 groups (fig. S17, A and C). However, complement 3d, linked to reactive astrocytes (*55*), was increased only in ^{ch}3D6^{WT}-treated mice (fig. S17, B and C) and is consistent with the correlation between glial reactivity and anti-Aβ–induced microhemorrhages (*56*). In ARIA study 2, activated parenchymal border macrophages were observed in the leptomeninges of ^{ch}3D6^{WT}- and ^{ch}3D6^{kLALA}- treated mice, consistent with the increased incidences of meningovascular inflammation in these regions, but not in either of the ATV groups (fig. S18, A and C). No widespread increase in microglial or macrophage reactivity was observed in the whole cortex for any group (fig. S18B). Together, these MRI, histopathology, and immunohistochemistry (IHC) results show that ATV reduced the incidence of ARIA-like lesions and underlying vascular inflammation observed with anti-Aβ in an amyloid deposition mouse model.

Discussion

We demonstrate that the TfR-targeted ATV^{cisLALA} platform improves brain exposure, target engagement, and parenchymal biodistribution compared with an unmodified anti-Aβ antibody in a mouse model of AD. Its asymmetrical Fc engineering mitigates TfR-related hematologic liabilities while maintaining microglial engagement critical to Aβ phagocytosis. An additional benefit of TfR-enabled delivery is the shifted biodistribution away from large arteries and arterioles—key CAA sites—contributing to the almost complete elimination of vascular inflammation, microhemorrhages, and microinfarcts in an ARIA mouse model. Thus, ATV-mediated delivery not only improves drug biodistribution and target engagement but may also protect against vascular damage observed with amyloid immunotherapies.

Despite recent approvals of several anti-Aβ mAbs for AD, ARIA remains a common safety concern (*32*, *33*, *57*, *58*). The causes of ARIA with amyloid therapies are not fully understood but likely involve antibody binding to CAA and activation of perivascular macrophages that lead to vascular leakage and microhemorrhages (*52*, *59*). ARIA tends to be transient but can cause serious side effects and complicate treatment. Our results show that ATV^{cisLALA}:Aβ markedly reduces the incidence of ARIA-like adverse events in 5xFAD mice, largely owing to its distinct biodistribution compared to anti-Aβ. Although both effector function and TfR-mediated delivery play key roles in the mitigation of ARIA-like events, the asymmetric anti-Aβ^{kLALA} was able to reduce, but not eliminate, the incidence of ARIA

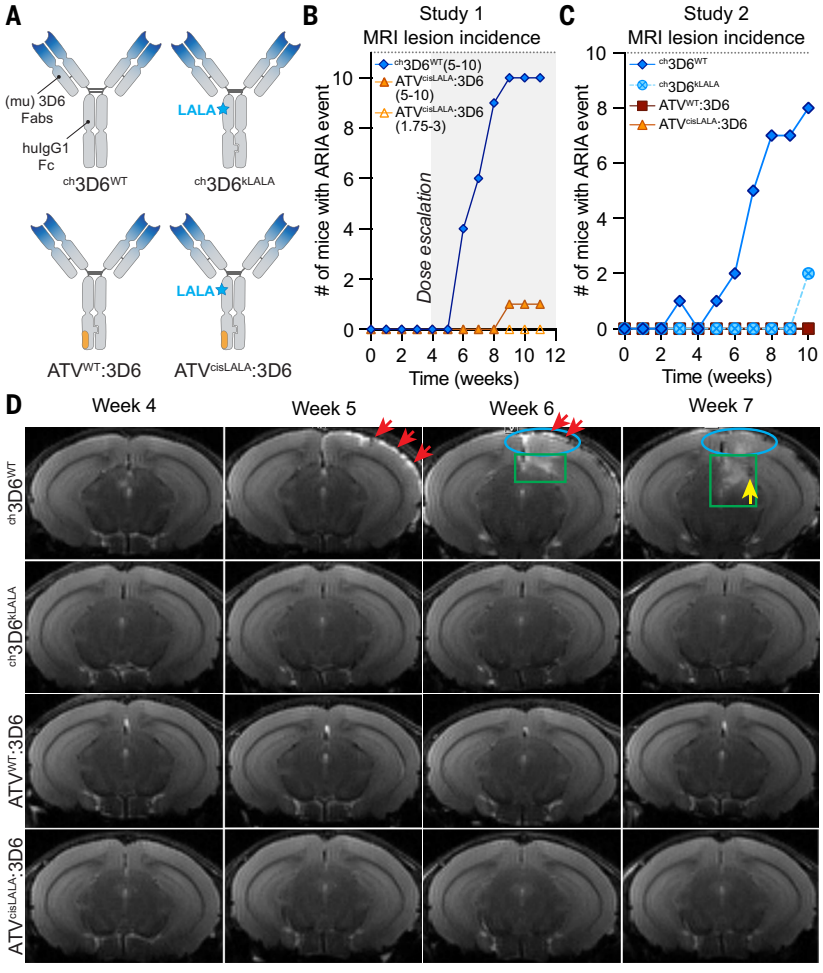


Fig. 5. TfR-mediated brain delivery reduces incidence of ARIA-like lesions in 5xFAD;TfR$^{mu/hu}$ KI mice. (**A**) Schematics of the molecules designed to assess roles of effector function and TfR-mediated brain uptake in occurrence of ARIA. (**B**) Incidence of ARIA-like lesions determined by weekly T2w MRI scans in 13-month-old male 5xFAD;TfR$^{mu/hu}$ KI mice treated with ^{ch}3D6^{WT}, ATV^{cisLALA}:3D6 dose-matched (closed triangle), or ATV^{cisLALA}:3D6 brain-exposure–matched (open triangle) starting at 5 or 1.75 mg/kg and increasing to 10 or 3 mg/kg, respectively, at the fifth dose ($n = 11$ mice per group). (**C**) Incidence of ARIA-like lesion determined by weekly T2w MRI scans in mixed sex 11- to 13-month-old 5xFAD;TfR$^{mu/hu}$ KI mice treated with ^{ch}3D6 (10 mg/kg) or brain-exposure–matched ATV variants (3 mg/kg) ($n = 10$ mice per group). (**D**) Representative scans from study in (C) were collected using a T2w MRI sequence. Several types of ARIA-like lesions were detected in mice treated with ^{ch}3D6^{WT}: hyperintense convexity lesion (red arrow, weeks 5 and 6), hyperintense diffuse cortical (blue oval, weeks 6 and 7), subcortical lesion (green rectangle, weeks 6 and 7), and hypointense focal subcortical lesion (yellow arrow, week 7). See additional examples in figs. S12 and 13.

compared to anti-Aβ with WT huIgG. Only ATV architectures (both cisLALA and WT) were able to eliminate MRI and histopathology findings, supporting the predominant role of TfR-mediated biodistribution in reducing ARIA. Even higher doses of ATV^{cisLALA}:Aβ resulted in only a marginal increase in ARIA incidence. Further studies are needed to refine the dosing window and assess benefits in high-risk populations like *APOE ε4* carriers.

The path by which the molecule enters the CNS may play a major role in ARIA incidence. Unmodified antibodies have greatly restricted transport across the BBB (*9*, *26*, *60*) and likely enter the CNS via the choroid plexus and/or other extracellular pathways to reach the CSF (*9*, *61*–*63*), where they rely on diffusion across leptomeningeal fibroblasts (*30*, *64*, *65*) to reach superficial parenchymal brain (*9*, *61*–*63*); further diffusion through the tortuous extracellular spaces to reach deeper sites is greatly restricted (*27*, *66*). By contrast, increased TfR expression on capillaries and postcapillary venules (*67*), coupled with the high density of the neurovascular network (*68*), allows for short diffusion distances after BBB transcytosis. Indeed, our 3D imaging showed widespread parenchymal distribution of ATV^{cisLALA}:Aβ, greater plaque target engagement, and far less accumulation around large surface arteries, consistent with reduced expression of TfR on arterial endothelial cells (*67*). Because the accumulation of Aβ around arteries may be up to fivefold higher than around veins in brains of AD patients (*45*), and the high capillary and low arterial expression of TfR is also observed in human brain vasculature (*69*, *70*), our data support a model whereby capillary-driven delivery likely avoids arterial CAA, reducing ARIA risk. Indeed, recent interim clinical data with TfR-enabled anti-Aβ trontinemab demonstrated rapid amyloid plaque clearance and reduced ARIA incidence (NCT04639050). These findings support the clinical utility of a TfR-targeted anti-amyloid approach for AD.

The 5xFAD model consists of multiple mutations in AD risk genes specific to familial AD. Whether ARIA mitigation with ATV^{cisLALA} persists at higher doses and/or longer duration of treatment in both familial and sporadic AD will be most appropriately addressed in the clinical setting. Recent cryo–electron microscopy (cryo-EM) data revealed Aβ filaments extracted from brains of APP^{Swe} and PSEN1^{M146V} mice (both mutations present in the 5xFAD) to be almost identical to those found in sporadic AD patients (*71*), thus supporting the utility of the current model for Aβ-related endpoints. Additionally, although the 5xFAD is not widely established as an AD mouse model for CAA, we observe prominent vascular amyloid by 3 to 3.5 months (fig. S8). This is consistent with previous reports of 5xFAD mice displaying CAA in leptomeningeal and penetrating cortical vessels, as well as recent reports of its utility as a mouse model of ARIA after anti-Aβ treatment (*54*, *72*). Although the mouse ARIA studies are substantially shorter than treatments in the clinical setting, the duration is line with general preclinical mouse safety studies.

In summary, ATV^{cisLALA} offers a promising platform for safer and more effective amyloid immunotherapy. It enables widespread brain distribution and target engagement, while reducing ARIA risk via capillary TfR-mediated transport. This approach may enhance the therapeutic index of anti-amyloid antibodies, supporting its further development for AD treatment.

Materials and methods

Reagents and characterization assays

Expression and purification of recombinant antibodies and ATVs: ATVs were generated as previously described (*7*). Briefly, three expression plasmids consisting of the heavy-chain ATV-knob, heavy chain hole, and light chain were cotransfected in Expi293 or ExpiCHO cells at a ratio of 1:1:2 according to manufacturer's instructions. Recombinant ATV variants were subsequently purified from conditioned media by loading supernatant over a protein A column (GE Mab Select SuRe). The column was washed with 10 column volumes of phosphate-buffered saline (PBS), pH 7.4. ATVs were eluted with 50 mM sodium citrate, pH 3.0 containing 150 mM NaCl, and immediately neutralized with 200 mM arginine, 137 mM succinic acid, pH 5.0. The ATVs were

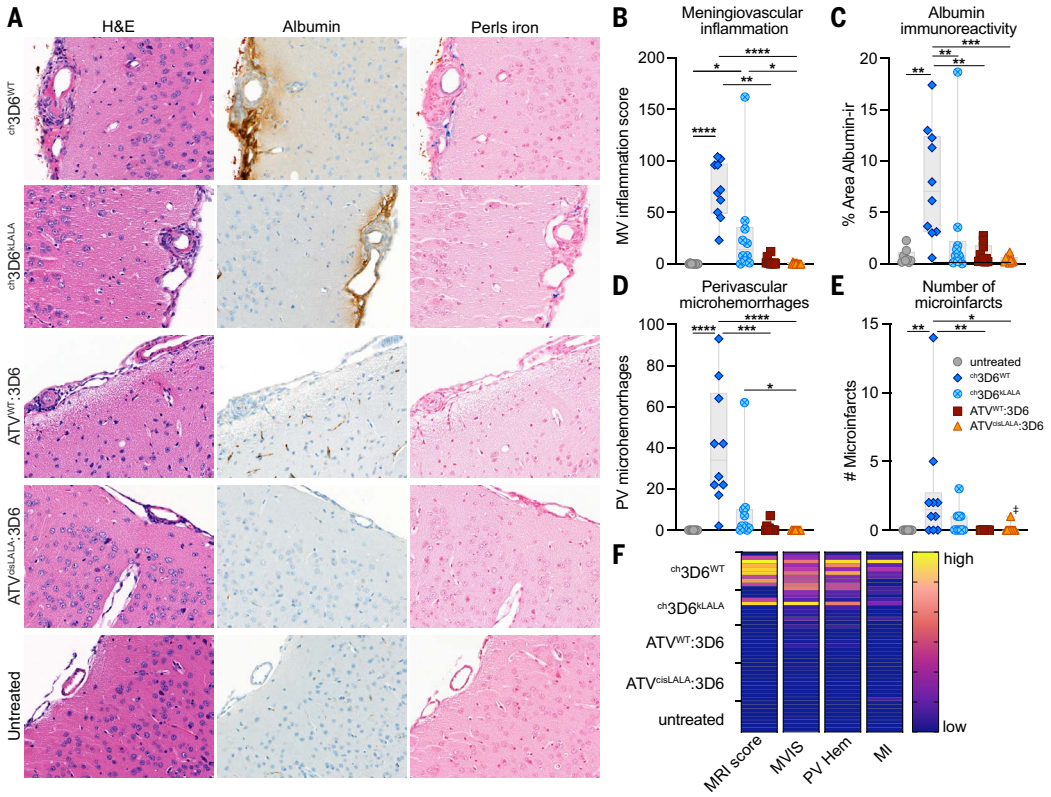


Fig. 6. ^{ch}3D6-induced meningovascular pathology is mitigated by both TfR-mediated brain uptake and asymmetrical FcγR binding. (**A** to **F**) Blinded histopathological assessment of brains from mixed sex 5xFAD;TfR$^{mu/hu}$ KI mice treated with ^{ch}3D6 (10 mg/kg) or exposure-matched ATV variants (3 mg/kg). (A) Representative images of hematoxylin and eosin (H&E) albumin immunoreactivity, and Perls iron from ARIA study 2. Animal IDs are indicated in table S3. [(B) to (E)] Summated meningovascular (MV) inflammation scores (MVIS) (B), cortical albumin immunoreactivity (ir) (C), Perls-reactive perivascular (PV) hemosiderin (D), and microinfarcts (MI) (E). ‡The single microinfarct in the ATV^{cisLALA}:3D6 group demonstrated histologic features of remote occurrence (astrogliosis without macrophage activity) and lacked associated meningovascular inflammation, suggesting that it was not induced by the treatment. (F) Heatmap demonstrating the animal-by-animal correlations of ARIA-like MRI lesions and histopathologic changes; heatmap scales in order from left to right: 0 to 10, 0 to 170, 0to 100, 0 to 15. Only significant differences are indicated on graphs; (C) one-way ANOVA with multiple comparisons and Tukey's post hoc comparing all groups, $^{**}P < 0.01$, $^{***}P < 0.001$. [(B), (D), and (E)] Kruskal-Wallis test with Dunn's post hoc comparing all groups $^{*}P < 0.05$, $^{**}P < 0.01$, $^{***}P < 0.001$, $^{****}P < 0.0001$. ATV huTfR apical domain affinity: ~1200 nM.

further purified by size-exclusion chromatography (SEC) (GE Superdex200) using 200 mM arginine, 137 mM succinic acid, pH 5.0 as running buffer. The purified ATV molecules were confirmed by intact mass liquid chromatography–mass spectrometry (LC-MS), and purity of >95% was confirmed by SDS–polyacrylamide gel electrophoresis (PAGE) and analytical high-performance liquid chromatography (HPLC)–SEC.

Anti-Aβ antibodies used in the current studies were recombinantly generated on the basis of publicly available sequence information, and their characteristics were previously reported: 3D6 is the murine parent of bapineuzumab (*23*). ^{ch}3D6 used in the mouse ARIA studies is the chimeric version of murine 3D6 that incorporates a humanized Fc portion. "Anti-Aβ" antibody shares similar characteristics with aducanumab (*58*).

TfR affinity measurements by surface plasmon resonance (SPR): The affinities of TfR-binding molecules for recombinant human human TfR^{apical} were determined by SPR using a Biacore 8K instrument in 1X HBS-EP+ running buffer (GE Healthcare Life Sciences, BR100826). Molecules were immobilized on a Series S CM5 chip (Cytiva, 29149603) using a Human Fab Capture Kit (Cytiva, 29234601) at 10 μg/ml at a flow rate of 10 μl/min for 30 s. Serial threefold dilutions of recombinant human TfR^{apical} at concentrations of 24.5, 74.0, 222, 667, and 2000 nM were injected at a flow rate of 30 μl/min for 60 s followed by a 60 s dissociation using a single cycle kinetics method.

For affinity evaluation of binding to full-length human TfR ECDs, a Biacore series S sensor chip SA (Cytiva, 29104992) was immobilized with recombinant human TfR ECD at 1 μg/ml at a flow rate of 10 μl/min for 30 s. Serial threefold dilutions of the molecules at concentrations of 24.5, 74.0, 222, 667, and 2000 nM were injected at a flow rate of 30 μl/min for 60 s followed by a 120 s dissociation.

Data analysis was conducted using Biacore Insight Evaluation software (version 2.0.15.12933). 1:1 Languir model of simultaneous fitting of K_{on} and K_{off} was used for human TfR binding kinetics and affinity analysis.

The approximate binding affinity of TfR-binding molecules to human TfR is listed in the figure legends for each experiment.

Monomer, oligomer, and fibril generation and Aβ ELISA: For preparation of monomeric Aβ peptides, $Aβ_{1-40}$ powder (Anaspec, AS-24235) was reconstituted in hexafluoroisopropanol (HFIP) at a concentration of 1 mg/ml. The $Aβ_{1-40}$ solution was aliquoted 50 μl/vial and dried under N_2 gas and stored as $Aβ_{1-40}$ film in HFIP at −80°C. To form the monomers, the $Aβ_{1-40}$ film HFIP was dissolved in dimethyl sulfoxide (DMSO) and then diluted to the target concentration in assay buffer before using.

For preparation of oligomeric $Aβ_{1-42}$ and fibrillar $Aβ_{1-42}$, $Aβ_{1-42}$ Film in HFIP (Anaspec, AS-64129) was resuspended in DMSO at concentration of 5 mg/ml and then diluted into PBS at a concentration of 1 mg/ml. To form the oligomeric $Aβ_{1-42}$, diluted $Aβ_{1-42}$ in PBS was

incubated for 3 days at 37°C. To form the fibrillar $A\beta_{1\text{-}42}$, diluted $A\beta_{1\text{-}42}$ in PBS was incubated for 7 days at 37°C and then was centrifuged at 14,000*g* for 15 min at 4°C. Fibrillar $A\beta_{1\text{-}42}$ was dissolved in PBS. Dynamic light scattering (DLS) was used to validate the quality of Aβ preparations.

The binding specificity of anti-Aβ to the different amyloid beta species was measured by enzyme-linked immunosorbent assay (ELISA) (IBL America, 27725). 100 μl of 0.4 nM antibodies and 100 μl of monomeric, oligomeric or fibrillar Aβ were mixed in the kit's "U-plate for primary incubation" and incubated for 90 min at room temperature with shaking at 300 rpm. 150 μl of the mixture was added into the precoated plate and incubated for 60 min at room temperature. After three washes with PBS containing 0.05% Tween-20 (PBST), 100 μl mouse-anti-human HRP (Thermo Fisher Scientific, 05-4220) in blocking buffer [2% bovine serum albumin (BSA) in PBS] was added and incubated for 1 hour at room temperature with shaking at 300 rpm. After four washes with PBST, 100 μl of TMB chromogen was added, incubated 30 min in the dark, and followed by addition of 100 μl of stop solution. Absorbance at 450 nm with a reference of 570 nm was measured with a microplate luminometer (BioTek Neo2).

FAM (fluorescein)–labeled $A\beta_{1\text{-}42}$ fibrils: FAM-labeled $A\beta_{1\text{-}42}$ (0.5 mg) (Anaspec, AS-23525-05) was resuspended with 100 μl DMSO followed by 1 ml PBS dilution to 100 μM. The solution is incubated at 37°C with shaking for 24 hours. The FAM-amyloid beta fibrils were then transferred to a 1.5 ml ultracentrifuge tube and spun at 100,000*g* for 30 min at 4°C in an ultracentrifuge. The supernatant was then discarded, and the pellet was resuspended in 1 ml PBS followed by extensive pipetting. The ultracentrifugation was then repeated followed by two additional rounds of washing. The pellet was resuspended in a final volume of 111 μl PBS and stored at −80°C. Dynamic light scattering (DLS) was used to characterized Aβ preparations.

Dynamic light scattering: 30 μl of Aβ solution (1 mg/ml) was loaded into a 384-well plate black with clear bottom (Costar). The plate was sealed with a film and centrifuged at 1000 rpm for 5 min and loaded onto DynaPro Plate Reader III (Wyatt Technology). Readings were performed using the Dynamics v7 software at 25°C with a 5 s reading per well and an average of 10 measurements.

In vitro assays

ADCC and CDC assays: For ADCC assays, target cells (Ramos (ATCC, CRL-1596, RRID: CVCL_0597) or A20 (ATCC, TIB-208)) were plated at 10,000 cells/well and opsonized with antibodies or ATVs of interest for 30 min at 37°C. Effector natural killer (NK) cells were isolated from human peripheral blood (AllCells) using Rosette Sep NK isolation kit (Stem Cell Technologies, 15025). NK cells were stimulated overnight with IL-21 (20 ng/ml, R&D Systems). Effector cells were added to target cells at 25:1 effector:target cells ratio (250,000 cells/well) for 4 hours. Cytotoxicity was evaluated by LDH expression using CytoTox 96 Non-radioactive cytotoxicity assay kit (Promega, G7890). Results were normalized to the control without any polypeptides and calculated as the percentage of maximum lysis (1% Triton X-100) in target cells.

For CDC assays, target cells (CHO-huTfR (generated by ChemPartner, full-length human TfR in CHO-K1 cells) or Raji (ATCC, CCL-86) were plated at 200,000 cells/well in serum-free media. CHO cells were engineered to stably overexpress TfR. As above, cells were opsonized with antibodies or ATV variants for 30 min at 37°C. 50 μl of diluted baby rabbit complement proteins (Bio-rad Laboratories, C12CA) was added to each well, and cells were incubated for 4 hours. Cytotoxicity was evaluated by LDH expression using the CytoTox-ONE homogeneous membrane integrity assay kit (Promega, G7890). Results were normalized to the control without antibody or ATV and calculated as the percentage of maximum lysis in target cells. Anti-murine CD20 (18B12) and anti-human CD20 (rituxumab) were recombinantly generated based on publicly available sequence information.

Animals and in vivo studies

Mouse care, use, and study design: All animal procedures were performed in adherence to ethical regulations and protocols approved by Denali Therapeutics or Biogen Institutional Animal Care and Use Committee. Mice were group-housed when possible, provided enrichment, and had access to water and standard rodent diet ad libitum on a 12-hour light/dark cycle. Age and sex of animals were evenly distributed across treatment groups and time points where possible. Before and during studies, mice were monitored for health issues and excluded from study inclusion or downstream analyses if serious concerns were observed. Animals were pseudo-randomized into experimental groups with cage-mates distributed into unique experimental groups when possible. Number of animals per group was determined based on historical experience and/or power analyses for specific study endpoints. Animals and samples were assigned a unique ID to pseudo-blind and randomize samples during analysis. Unless otherwise specified, at terminal time points mice were deeply anesthetized with 2.5% avertin (intraperitoneal) prior to transcardial perfusion with ice-cold PBS at a rate of 5 ml/min using a peristaltic pump (Gilson, Minipuls 3). Exclusion criteria for sample analysis included signal below the established analytical levels of detection or technical errors.

5xFAD;$TfR^{mu/hu}$ KI mouse model generation: $TfR^{mu/hu}$ KI mice (7) were crossed with hemizygous B6.Cg-Tg(APPSwFlLon,PSEN1*M146L*L286V)6799Vas mice (background strain C57BL/6JRccHsd) at QPS Austria GmbH to generate the 5xFAD;$TfR^{mu/hu}$ KI model used in the acute multidose phagocytosis study. For other studies, the colony was rederived at the The Jackson Laboratory using sperm from males of the QPS-developed colony and female $TfR^{mu/hu}$ KI mice; a genome scan of $n = 3$ mice from the JAX colony revealed that the mice had a 99.62% C57Bl/6J background.

Ex vivo phagocytosis: Naïve $TfR^{mu/hu}$ KI mice (3 months old, males, $n = 6$) were perfused with 1x PBS and the brains (including cerebellum excluding the olfactory bulb) were used for single-cell dissociation. Cells were dissociated according to kit instructions using the Adult Brain Dissociation Kit (Miltenyi Biotec, 130-107-677) and gentleMACS Octo Dissociator. To eliminate excessive debris and myelin, the kit's Debris Removal Solution was applied, and the final cell pellet was resuspended in 200 μl 0.5% BSA in dPBS (with calcium and magnesium). To quantify the number of live microglia per sample, a small fraction of the cells was taken and stained with Cd11b-BV421 (BioLegend 101251, RRID:AB_2562904, 1:100), CD45-APC (BD Biosciences Cat 559864, RRID:AB_398672, 1:100), and Fc block (BioLegend 101320, RRID:AB_1574975, 1:100) for 15 min at 4°C followed by washes and resuspension in FACS buffer (1% BSA + 1 mM EDTA in PBS) containing propidium iodide (PI; Miltenyi Biotec, 130-093-233). This cell fraction was then mixed with CountBright Plus Absolute Counting Beads (Thermo Fisher Scientific, C36995) and loaded on an FACSAria III Cell sorter (BD Biosciences). By using the number of live microglial cells calculated from this fraction, cells from each sample were then split into the respective treated samples such that each contained 50,000 live microglia combined with 10 nM of the respective antibody and 100 nM FAM-$A\beta_{1\text{-}42}$ fibrils. The treated samples were then incubated at 37°C for 30 min with gentle agitation every 15 min. Control samples were treated with 10 nM of the respective antibody and 100 nM FAM-$A\beta_{1\text{-}42}$ fibrils but incubated at 4°C instead for 30 min. After these incubations, the treated samples were washed and stained with Cd11b-BV421 (BioLegend 101251, RRID:AB_2562904, 1:100), CD45-APC (BD Biosciences Cat

559864, RRID:AB_398672, 1:100), and Fc block (BioLegend 101320, RRID:AB_1574975, 1:100) for 15 min at 4°C followed by washes and resuspension in FACS buffer containing PI. On the sorter, 10,000 live microglia were recorded per treated sample along with the intensity of the FAM signal. To quantify the intensity of FAM signal per live microglial cells, analysis was performed on FlowJo 10.8.1.

Hematology and TfR expression after chronic dosing in 5xFAD;TfR$^{mu/hu}$ KI mice: 5xFAD;TfR$^{mu/hu}$ KI mice (male, 16-17 weeks of age, $n = 20$/group) received weekly intraperitoneal injections of anti-Aβ or ATV^{cisLALA}:Aβ at 1, 3, or 10 mg/kg for 12 weeks. Anti-CD4 antibody (Ref BP0003-R050, BioXCell) was administered intraperitoneally (ip) every 2 weeks, starting 1 day before the first dosing of compounds (0.5 mg/animal). Ten mice per group received no in-life blood collections during the study and had blood sampled at termination (24 hours after the 13th dose) for complete blood count and reticulocyte analysis by a veterinary lab (Quality Vet Lab, Davis, CA, USA). An additional untreated group (male, 16-17 weeks of age at termination, $n = 23$) was also included for comparison.

Mouse blood and bone marrow reticulocyte studies in TfR$^{mu/hu}$ KI mice: TfR$^{mu/hu}$ KI mice (*7*) (female, 11-13 weeks of age, $n = 5$/group) were restrained and received a single intravenous tail vein injection of anti-Aβ, ATV:Aβ variants, or TfR$^{C\text{-}termFab}$:Aβ molecules. At terminal time points, mice were deeply anesthetized with 2.5% avertin (intraperitoneal). Terminal whole blood was collected by intracardiac puncture and portioned into EDTA coated tubes. Mice were then perfused transcardially with ice-cold PBS for approximately 4-6 min at 5 ml/min using a peristaltic pump (Gilson, Minipuls 3). Whole blood was kept at 4°C for quantification of reticulocytes by a veterinary lab (Quality Vet Lab, Davis, CA, USA). Plasma samples were generated after centrifugation of blood at 18,213*g* for 7 min at 4°C. Freshly perfused and extracted brains were dissected on a cold block on wet ice and a portion immediately snap-frozen in tubes on dry ice; plasma and brain were stored at −80°C for further huIgG quantification.

After perfusion of the mice, femurs and/or tibias were collected and all muscle removed, the epiphysis cut from the shaft of the bones and placed into a 0.5 ml tube with a small hole at the bottom inside a 1.5 ml tube, and the marrow centrifuged out at 18,213*g* speed for 3 min at 4°C.

Bone marrow samples from each animal were dissociated into single cells in 200 µl of FACS buffer (2% FBS and 1mM EDTA in PBS). After being spun down at 300*g* for 5 min in FACS tubes, the supernatant was discarded, and the cells were resuspended in 200 µl of FACS buffer. 40 µl of sample and 10 µl of control were added to a 96-well, round-bottom plate. The plate was washed with 100 µl of FACS buffer per well and spun down at 300*g* for 5 min. After emptying the plate, the cells were resuspended and blocked with 100 µl per well of 1:50 Mouse-Fc block (BioLegend 101320, RRID:AB_1574975) in FACS buffer for 5 min. The plate was spun down at 300*g* for 5 min before staining with 100 µl per well of Fixable Viability Dye (BD Biosciences #564406, 1:200), rat anti-CD44/APC (eBioscience, 17-0441-82, 1:100), rat anti-TER119/PE (eBioscience, 12-5921-831:100), and isotype control antibodies for 30 min. The plate was washed, spun down, and emptied two more times before the cells were resuspended in 75 µl FACS buffer per well.

Samples were analyzed on a FACS Canto II (BD Biosciences). To isolate the population of CD44+ reticulocytes, gates were applied in the order of cells (SSC-A/FSC-A), single cells (FSC-H/FSC-A), live cells (SSC-A/Am-Cyan-A), TER119+ (SSC-A/PE-A), and erythroids (APC-A/FSC-A). The populations of reticulocytes lie in APC-A+ and 0~50K of FSC-A. CD44+ reticulocytes were analyzed and quantified in FlowJo. Percentages of CD44+ in TER119+ were exported and plotted in GraphPad Prism.

Acute multidose phagocytosis study in 5xFAD;TfR$^{mu/hu}$ KI mice: The in vivo portion of the study was conducted at QPS Austria GmbH, an Association for Assessment and Accreditation of Laboratory Animal Care (AAALAC) accredited facility, following standard operating procedures in compliance with the Animal Care and Welfare Committee and conducted in accordance with regulations of the Ministry of Science of the Austrian government (TVG 2012). 5xFAD;TfR$^{mu/hu}$ KI mice (mixed sex, 16-17 weeks of age, $n = 11$-12 per group) received intraperitoneal injections of anti-Aβ, ATV^{LALA}:Aβ, or ATV^{cisLALA}:Aβ (approximate affinity for huTfR apical domain of 500 nM) on days 0, 3, 6, and 9. Animals were euthanized by pentobarbitol injection (600 mg/kg) prior to cardiac blood collection into K2-EDTA–coated tubes and PBS perfusion. Hemibrains were collected for immersion-fixation (2 hours in 4% paraformaldehyde at room temperature) or flash-freezing on day 12. Hemibrains were stored at 4°C in 15% sucrose during shipment then transferred to 30% sucrose in PBS until the brains sunk fully. Cryoprotected brains were sectioned on a freezing microtome (40 µm, sagittal) and sections stored in PBS with 0.01% sodium azide prior to immunohistochemistry.

Four brain sections per animal were selected for microglia and plaque immunohistochemistry; two sections were approximately 3 mm lateral to the midline and two sections were approximately at the midline (0 mm lateral). Free-floating sections were incubated for 2 hours in blocking solution (5% donkey serum in PBS with 0.3% triton X-100) at room temperature (RT), incubated overnight in blocking solution containing primary antibodies at 4°C, washed 3x for 15 min each in PBS with 0.3% triton X-100, incubated 2 hours at RT in blocking solution containing secondary antibodies, incubated 20 min in DAPI (Thermo Fisher Scientific, D1306) solution in PBS with 0.3% triton X-100, and washed 3x for 15 min each in PBS with 0.3% triton X-100. Sections were mounted onto slides and coverslipped using Prolong Glass Antifade mounting medium (Thermo Fisher Scientific, P36984). Primary antibodies included: rabbit-anti-human amyloid β (IBL America, 18584; RRID:AB_10705431, 1:500), rat-anti-CD68 (BioRad, MCA1957, RRID:AB_322219); 1:500 and secondary antibodies included: donkey-anti-rabbit IgG AF488 (Thermo Fisher Scientific, A21206, RRID:AB_2535792; 1:500), cross-adsorbed donkey-anti-rat IgG Dy555 (Thermo Fisher Scientific, SA5-10027, RRID:AB_2556607; 1:500).

Three brain sections per animal were selected for plaque and human IgG immunohistochemistry; sections were approximately 3 mm lateral to the midline. Free-floating sections were incubated for 1 hour in blocking solution (5% donkey serum in PBS with 0.3% triton X-100), incubated 2 hours in blocking solution containing rabbit-anti-human amyloid-β (IBL America, 18584; 1:500) and donkey-anti-human AF647 (Jackson ImmunoResearch, 709-606-149, RRID:AB_2340581; 1:250), washed 3x for 15 min each in PBS with 0.3% triton X-100, incubated 1 hour in blocking solution containing donkey-anti-rabbit AF488 (Thermo Fisher Scientific, A21206; 1:500) and incubated 20 min in DAPI solution in PBS with 0.3% triton X-100, and washed 3x for 15 min each in PBS with 0.3% triton X-100. All steps were performed at room temperature. Sections were mounted onto slides and coverslipped using Prolong Glass Antifade mounting medium.

Slides were imaged using a Zeiss Axioscan.Z1 slide scanner at 20X magnification and images were processed using custom macros in Zeiss ZEN software. Image processing macros automated the following steps for all images: median smoothing, extracting objects and channels of interest, channel processing (rolling-ball background subtraction, threshold equally across all animals to identify signal eliminate background, set minimum and maximum size cutoff to eliminate noise/debris). This created additional binary image channels for each processing step. The ZEN software was then used to analyze the processed images by first auto-segmenting tissue from background using DAPI channel image (smoothing and filling holes) to determine tissue section area. Binary image channels were then analyzed to measure the plaque area (by size), area of CD68^{+} microglia and overlap with

plaques and their immediate surroundings ("dilated" plaques). Plaque size bins (30-125 , 125-250, 250-500, 500-3300 μm^2) were selected based on a previously published study (*58*). The distance of dilation around each plaque was 1.4, 2.1, 2.8, or 3.5 μm for the plaque size bins of 30-125 , 125-250, 250-500, or 500-3300 μm^2, respectively.

PK and biodistribution in normal TfR$^{mu/hu}$ KI mice: TfR$^{mu/hu}$ KI mice (*7*) (male, 5-6 months of age, $n = 5$/group) were restrained and received a single intravenous tail vein injection of anti-Aβ or ATV:Aβ molecules at 25 mg/kg. In-life blood was collected by submandibular or submental puncture with a lancet into EDTA coated tubes (Sarstedt Microvette 500 K3E, 201341102). At terminal time points, mice were deeply anesthetized with 2.5% avertin (intraperitoneal); terminal blood was collected by intracardiac puncture and collection into EDTA coated tubes. Plasma samples were generated after centrifugation of blood at 18,213*g* for 7 min at 4°C. Mice were then perfused transcardially with ice cold PBS for approximately 4-6 min at 5 ml/min using a peristaltic pump (Gilson, Minipuls 3). Freshly perfused and extracted brains were dissected on a cold block on wet ice and divided for various endpoints, either immediately snap-freezing in tubes on dry ice or being immediately immersed in 4% paraformaldehyde (Electron Microscopy Sciences, 15714-S) diluted in PBS for fixation overnight at 4°C. Plasma and brain were stored at −80°C for further huIgG quantification.

Brains were transferred to PBS + 0.01% sodium azide after immersion fixation and shipped to Neuroscience Associates for sectioning using MultiBrain Technology; up to 20 hemibrains were embedded into a single gelatin block and sectioned in the sagittal plane (35 μm). Sections were collected in a series of 12 and stored in antigen preservation solution (50% PBS:50% ethylene glycol + 1% PVP) at −20°C until staining. Three to four sections per animal were allowed to come to room temperature and then washed in PBS before incubation in blocking buffer (PBS/TBS + 1% BSA + 1x fish gelatin (BioWorld 21761058) + 0.5% triton X-100 + 0.1% sodium azide) for 3 hours at room temperature on a rocker. Sections were then incubated overnight in antibodies (NeuN, Abcam, ab177487, RRID:AB_2532109, 1:1000; CD31, R&D Systems, Af3628, RRID:AB_2161028, 1:500; and donkey F(ab')2-anti-huIgG, Jackson, 709-606-149, 1:250) at 4°C, followed by 3x 15 min washes and incubation with secondary antibodies (1:500; donkey-anti-rabbit, Thermo Fisher Scientific, A11042, RRID:AB_2534099; donkey-anti-goat, Thermo Fisher Scientific, A11055, RRID:AB_2534102) and DAPI (5 μg/ml, Thermo Fisher Scientific, D1306) for 3 hours at room temperature, before 3x 15 min washes, mounting, and coverslipping with Prolong Glass (Thermo Fisher Scientific, P36984). Slides were imaged using a Zeiss Axioscan.Z1 slide scanner at 20X magnification and images were processed using custom macros in Zeiss ZEN software to segment markers of interest.

For three-dimensional image stacks, slides were also imaged using a scanning confocal microscope (Leica SP8; Leica Microsystems) operated in superresolution Lightning mode. Images were acquired for each channel using sequential scan settings, with either a 20×/0.75-NA oil objective at 80 nm pixel size (XY), 1.5 μm (Z), for a total of 19 μm depth, or with a 40×/1.30-NA oil objective at a 50 nm pixel size (XY), 500 nm (Z), for a total of 27 μm depth. All raw images were processed using the Adaptive processing algorithm from the LAS X software.

Dose-ranging brain uptake and target engagement in 5xFAD;TfR$^{mu/hu}$ KI mice: 5xFAD;TfR$^{mu/hu}$ KI mice (mixed sex, 4 months of age, n=5/group) received a single intravenous dose of anti-Aβ or ATV^{cisLALA}:Aβ at 1, 3, or 10 mg/kg and were perfused with blood and brain tissue collected as described above. Plasma and brain were stored at -80°C for further huIgG quantification. Fixed brains were transferred to PBS + 0.01% sodium azide following immersion fixation and shipped to Neuroscience Associates for sectioning using MultiBrain Technology; up to 20 hemibrains were embedded into a single gelatin block and sectioned in the sagittal plane (40 μm). Every tenth section (at an interval of 400 μm) was stained free-floating at Neuroscience Associates. All incubation solutions in following steps used Tris buffered saline (TBS) with Triton X-100 as the vehicle; all rinses were with TBS.

After rinses, the sections were treated in formic acid, rinsed, and stained with rabbit-anti-human amyloid beta (IBL America, #18584; 1:500) and donkey F(ab')$_2$-anti-huIgG (Jackson, 709-606-149, 1:500), overnight at room temperature. Following rinses, secondary antibody (donkey-anti-rabbit AF647, Jackson ImmunoResearch 711-605-152, RRID:AB_2492288, 1:500) was applied. The sections were again rinsed, then treated with a Hoechst counterstain. Following further rinses, the section was mounted on gelatin coated glass slide, then air dried. The stained slide was dehydrated in alcohols, cleared in xylene and coverslipped. Slides were imaged and analyzed as described above using a Zeiss Axioscan.Z1 slide scanner at 20X magnification and custom macros to identify plaques and huIgG overlap with plaques.

3D whole-brain imaging in 5xFAD;TfR$^{mu/hu}$ KI mice: 5xFAD;TfR$^{mu/hu}$ KI mice (female, 3-3.5 months, n=7 per group) received a single intravenous injection (10 mg/kg) of AF750-conjugated-anti-Aβ or AF750-conjugated-ATV^{cisLALA}:Aβ (approximate affinity for huTfR apical domain of 500 nM). 24 hours after dosing, mice were deeply anesthetized and transcardially perfused with ice-cold heparinized PBS (15 U/ml) for approximately 5-6 min followed by approximately 5-6 min of RT 10% neutral buffered formalin (NBF), both at 5 ml/min using a peristaltic pump (Gilson, Minipuls 3). Brains were post-fixed in NBF at RT for 24 hours, rinsed in PBS, then transferred to PBS + 0.02% sodium azide and stored at 4°C until iDISCO clearing and staining.

iDISCO brain clearing and staining

iDISCO brain clearing: For one hemisphere, $n = 2$ animals per group were stained with a secondary for the huIgG backbone of the dosed molecules (Fig. 4, L and M, and fig. S7). For the other hemisphere, $n = 1$ animal per group was used for pilot staining and the remaining $n = 6$ animals per group were stained with αSMA, Aβ, and huIgG (Fig. 4, N and O, and figs. S8 and S9).

For staining, hemi-brains were dehydrated in a methanol/water gradient on a gentle rocker, during which they were incubated for an hour each in 20, 40, 60 80, and 100% methanol (1-2x), followed by an overnight incubation in 66%dichloromethane (DCM)/33% methanol at RT. Samples were then washed twice in 100% methanol, chilled in fresh 100% methanol and bleached in fresh-chilled 5% H_2O_2 in methanol overnight at 4°C. After bleaching, samples were rehydrated in a methanol/PBS + 0.2%Triton-X100 series of 80, 60, 40, and 20% methanol at RT, after which they were washed in PBS+ 0.2%Triton-X100 and permeabilized for 3 days at 37°C in a PBS+ 0.2%Triton-X100 buffer made with 20% DMSO, 0.02% glycine and 0.02% sodium azide. Blocking and staining steps were then carried out according to the details below for either the huIgG only or huIgG, αSMA, and Aβ staining sets, or for the parallel experiment elucidating vascular anatomy, SM22. Samples were then cleared in a methanol/water gradient at RT on a gentle rocker (20, 40, 60 80, and 100% methanol), incubated in 100% methanol overnight at RT, washed in 100% methanol once more and then incubated in 66% dichloromethane (DCM)/33% methanol for 3 hours at RT. Samples were then washed in 100% DCM twice for 15 min before index-matching in dibenzyl ether (DBE). HuIgG only stained samples were imaged in DBE, while huIgG, αSMA, Aβ stained samples were switched to ethyl cinnamate (ECi) at least 24 hours before imaging in ECi.

huIgG staining (n = 2/group) or SM22 (n = 6/group): After permeabilization, samples were blocked for two days (37°C) in PBS with 0.2%Triton-X100, 10% DMSO, 6% normal donkey serum, and 0.02% sodium azide. Samples were incubated with donkey-anti-huIgG-Cy5

(1:250, Jackson ImmunoResearch, 709-175-149, RRID:AB_2340539) in PTwH (PBS with 0.2% Tween-20 and 5mg/L heparin, H3149-50KU, EMD Millipore))/3% donkey serum at 37°C for 7 days and then washed in PTwH. For the parallel experiment elucidating arterial anatomy, blocked brains were incubated in anti-SM22 primary antibody (1:1000, Abcam, ab14106, RRID:AB_443021) diluted in PBSG-T and 0.1% saponin (10 μg/ml) for 14 days with agitation at room temperature. Following primary antibody incubation, the samples are washed 3 × 2 hours in PBST, left over two days in PBST. The secondary antibody incubation was carried out for 7 days in donkey anti-rabbit AlexaFluor488 (1:500, Jackson ImmunoResearch, 711-545-152, RRID:AB_2313584) diluted in PBSG-T and 0.1% saponin (10 μg/ml), with agitation at room temperature. After secondary antibody incubation, the samples are washed 3 × 2 hours in PBST and incubated in PBST over 3 days.

huIgG, αSMA, Aβ staining (n = 6/group): After permeabilization, samples were blocked for three days (37°C) in PBS with 0.2%Triton-X100, 10% DMSO, 6% normal donkey serum, and 0.02% sodium azide. Blocked brains were incubated in anti-huIgG-DL800 (1:500, Thermo Fisher Scientific, SA510132, RRID:AB_2556712), anti-Aβ (1:400, IBL America, 18584), and anti-αSMA-DL550 (1:500, Novus, NBP2-34522R, RRID:AB_3287574) at RT for 2 weeks on gentle rocking speed. All antibodies were diluted in a PBS-based antibody incubation buffer containing 0.2% gelatin, 0.5% tritonX100, and 0.1% saponin. After incubation, tissue was washed with PTwH for 1x10 min, 1x20 min, 1x30 min, 1x 1 hour, 1x 2 hours at RT and 1x3 days at 4°C before incubation in secondary antibody. The secondary antibody incubation was carried out in antibody incubation buffer (with an additional 5 mg/liter heparin) for 7 days at RT, with donkey anti-rabbit Cy5 (1:500, Jackson ImmunoResearch, 711-175-152) and then washed in PTwH.

Whole hemibrain imaging and quantification: iDISCO cleared brains were imaged on a Lavision UltraMicroscope (Lavision Biotec GmbH) with an MVPLAPO 2X objective/0.5 NA with a 0.63x zoom. Hemibrains were imaged to collect autofluorescence and relevant channels. Additional imaging was performed using a Miltenyi Blaze (Miltenyi Biotec) light sheet microscope using a 1.1x/0.1 NA MI PLAN objective with a 1.0x zoom (fig. S8-S9). Fully cleared samples were imaged in the Miltenyi Blaze with both the 1x objective (1.1x zoom, 0.09 numerical aperture, fixed focus and blending) and the 12x objective (1x zoom, 0.19 numerical aperture, adaptive focus and adaptive blending). All images per magnification were taken with the same optimized settings with bidirectional illumination. 1x images were taken at 60% sheetwidth, at 2.4 μm steps. Excitation (Emission) as follows: 785 (805): 15%, 640 (680) 10%, and 561 (620) 10%. 12x images were taken at 10% sheetwidth, at 0.54 μm stepsize. Excitation (Emission) as follows: 785 (805): 25%, 640 (680) 9%, and 561 (620) 8%. Brain volumes were visualized in Imaris v9.9. Plaques and vasculature were segmented using custom code developed in python v3.9 using the following pipeline. First, a tissue mask was extracted from the volume by thresholding the αSMA image at a level that also segmented the autofluorescence followed by Boolean operations to fill holes and remove small objects using the morphology module of scikit-image v0.18 (*74*). Inhomogeneity in the Aβ and huIgG illumination fields was estimated by smoothing each channel with a Gaussian filter, subtracting the smoothed image from the original image, and then clamping all negative intensity values to zero. Next, plaques were segmented by thresholding the illumination corrected Aβ image followed by separation of individual plaques using the label function in scipy v1.7 (*75*). Major arteries and arterioles were segmented by thresholding the αSMA at a higher level that excluded the autofluorescence followed by Boolean operations to remove small segments and holes. Imaris was used to apply the plaque and artery masks to the huIgG channel to visualize the colocalization. Intensity of huIgG and Aβ staining were found to vary with depth from tissue surface, likely a technical artifact of the clearing and staining process in this experiment, but colocalization of huIgG signal with both Aβ and αSMA via a Pearson's correlation coefficient (PCC) was less impacted by this gradient effect. Mean intensity of huIgG, Aβ, and αSMA as well as the Pearson's correlation coefficient between Aβ and huIgG and between αSMA and huIgG were calculated per plaque and then a volume-weighted average was calculated per animal. Two tailed *t* tests were performed using the *t* test_ind function from scipy's stats module. To preserve normality assumptions, correlation coefficients were first transformed to z-scores using Fisher's z-transformation before averaging or calculating *t* tests.

Ex vivo assays

Brain homogenization and huIgG ELISA: Fresh-frozen brain samples were homogenized in 10x volume/weight of lysis buffer (1% NP40 (Thermo Fisher Scientific, 85124) in ice cold PBS with protease and phosphatase inhibitors (Roche, 04693132001 and 04906837001)) using a 3 mm bead (Qiagen, 69997) and agitation with the Tissue Lyser II (Qiagen, 85300). Samples were homogenized by two 3 min sessions at 27 Hz at 4°C. Following incubation on ice for 20 min samples were centrifuged for 20 min at 14,000*g* at 4°C. The supernatant was removed and stored at -80°C until analysis. As this method does not completely solubilize Aβ, it is expected that much of the huIgG is not recovered in the supernatant and represents a free or soluble fraction of the total huIgG.

Concentration of huIgG in plasma and brain lysates were quantified using a generic anti-human IgG sandwich-format ELISA as previously described (*76*). Plates were coated overnight with donkey anti-human IgG (Jackson Immunoresearch, 709-006-098, RRID:AB_2340485) at 1 μg/ml in sodium bicarbonate solution (Sigma, C3041-50CAP) with gentle agitation at 4°C. Plates were then washed with wash buffer (PBS + 0.05% Tween 20) three times. Assay standards and samples were diluted in PBS + 0.05% Tween 20 and 1% BSA. Standard curve was prepared at a range from 0.41 to 1500 ng/ml or 0.003 to 10 nM (BLQ <0.03 nM). Standards and diluted samples were incubated for 2 hours with agitation at RT. After incubation, plates were washed with wash buffer three times. The detection antibody, Goat anti-human IgG (Jackson ImmunoResearch, 109-036-098, RRID:AB_2337596) was used as the detection antibody and was diluted in blocking buffer (PBS + 0.05% Tween- 20 + 5% BSA) to a final concentration of 0.02 μg/ml. Plates were incubated for 1 hour with agitation at RT, washed 3x, and then developed by adding TMB substrate and incubated for 5–10 min followed by quenching with 4N H_2SO_4; plates were read using 450 nm absorbance.

Capillary depletion method for brain vasculature isolation: Brain microvessels were isolated as previously described (*7*); all steps performed at 4°C. The meninges and choroid plexuses were dissected and discarded from freshly perfused pieces of brain. The brain was then homogenized in 3.5 ml HBSS by 10 strokes with a Dounce homogenizer using the smaller diameter pestle. Samples were centrifuged for 10 min at 1000*g* to pellet cells which were then resuspended in 2 ml of 17% dextran (MW 60,000; Sigma, 31397) in HBSS. Centrifugation for 15 min at 4,122 *g* pelleted the vasculature which was then lysed in 1% NP40 in PBS with protease and phosphatase inhibitors (Roche, 04693159001 and 04906837001); samples were agitated using the Tissue Lyser II (Qiagen, 85300) for 30 s at 27 Hz and incubated for 20 min on ice. The supernatant was collected and snap frozen for Western blot after centrifugation at 12,700*g* for 10 min.

Transferrin receptor Western blot: Brain vascular lysates were prepared in 4X LDS sample buffer (Thermo Fisher Scientific, NP0007) and 10X reducing agent (Thermo Fisher Scientific, NP0009) then boiled at 95°C for 10 min. Samples (10 μg of total protein) and ladder (Precision Plus Protein Dual Color Ladder; Biorad 161-0374) were

loaded into NuPAGE 4-12% Bis-Tris Midi Protein Gels (Thermo Fisher Scientific WG1403). Samples were separated using the XCell4 SureLock system (Thermo Fisher Scientific, WR0100) followed by transfer onto nitrocellulose blots (Biorad, 1704159) using a BioRad Transblot Turbo system. Blots were blocked at room temperature in 5% nonfat milk powder for 1 hour then incubated with primary antibodies (TfR, Thermo Fisher Scientific 13-6800, RRID:AB_2533029, 1:2000; GAPDH, Abcam ab181603, RRID:AB_2687666, 1:5000) diluted in blocking buffer (Rockland, MB-070-010 TF) at 4°C overnight. Blots were washed in 3x 15 min each in TBST, incubated in secondary antibodies (goat-anti-mouse IgG1 800CW, Licor 926-32350, RRID:AB_2782997, 1:10k; goat-anti-rabbit 680RT, Licor 926-68023, RRID:AB_10706167, 1:10k) in blocking buffer (Rockland) for 2 hours, then washed in TBST three times for 15 min each. Blots were imaged and quantified using the LI-COR Odyssey CLx and Image Studio Lite Software.

Transferrin receptor Mesoscale Discovery (MSD) assay: As previously described (*8*, *69*), TfR capture and detection antibodies were conjugated to biotin and MSD Sulfo-tag NHS-Ester, respectively, according to the manufacturer's protocol. Automated robotics systems and continuous plate agitation were used to block an MSD Gold Streptavidin 384-well plate at room temperature (RT) for 1 hour in 5% MSD blocker, wash with PBST, incubate at RT for 1 hour with 0.125 µg/ml TfR-biotin capture antibody, wash again with PBST, and incubate with brain lysate at 4°C overnight. Following the overnight incubation, the 384-well plate was then washed with PBST, incubated at RT for 1 hour with 0.25 µg/ml Sulfo-tag-detection antibody, washed again with PBST, incubated at RT with 2x MSD read buffer for 10-15 min, and then read on an MSD plate reader (Meso Sector S 600). The concentrations of TfR determined by GraphPad Prism's Sigmoidal, 4PL standard curve interpolation were subsequently normalized to total lysate protein concentration. Some samples with insufficient volume available for a reliable reading were excluded from analysis.

Exposure-matched dose modeling

Mathematical modeling: The PK model outlined in fig. S11 was developed to fit $^{ch}3D6^{WT}$ and $ATV^{cisLALA}$:3D6 data in $TfR^{mu/hu}$ KI mice (males, single intravenous dose of 1 or 5 mg/kg, with plasma and brain collection as previously described; fig. S11B-C) and was subsequently utilized to estimate the doses required to match brain exposures of $^{ch}3D6^{WT}$ and $ATV^{cisLALA}$:3D6 antibodies in ARIA studies 1 and 2. The systemic PK was modeled using a two-compartment PK model (fig. S11A) with the inclusion of linear (nonspecific) and nonlinear (TfR-mediated) clearance pathways of the drug molecules from systemic circulation. Brain uptake mechanisms of nonATV ($^{ch}3D6^{WT}$) and ATV ($ATV^{cisLALA}$:3D6) molecules, primarily via low-efficiency nonspecific transport and high-efficiency TfR-mediated transcytosis across brain endothelial cells, respectively, are also incorporated in the model. TfR-mediated processes are modeled using Michaelis-Menten kinetics with the Michaelis constant dependent on the binding affinity of the molecule to the TfR. The Michaelis-Menten kinetics is used only for the ATV molecule; for the nonTV molecules that do not bind to TfR these terms were switched off. The loss of antibodies from the brain is modeled as a first-order linear elimination process.

The PK model was developed using the Simbiology Toolbox (MATLAB, MathWorks). A pooled analysis was performed to estimate one set of reference parameter values capturing systemic and brain PK of both $^{ch}3D6^{WT}$ and $ATV^{cisLALA}$:3D6 molecules in $TfR^{mu/hu}$ KI mice (fig. S11B-C). Parameter estimates are provided in Table S1, and model fits to the experimental data are demonstrated in fig. S11B-C. Fits indicate a reasonable agreement between model simulations and the PK data of both $^{ch}3D6^{WT}$ and $ATV^{cisLALA}$:3D6 molecules. Since a single parameter set is used to capture the PK data of both molecules, model fits are expected to follow the collective trend in the observed data, and as a result, mismatches with individual data points are expected.

We subsequently assessed the performance of the PK model against experimental data obtained from the ARIA studies (not included for model calibration). Model simulations show reasonable accuracy in capturing observed drug concentrations in plasma from both studies (fig. S11 D-E, G-H). The area under the curve ($AUC_{0\text{-}78\ d}$) of the simulated brain PK profiles predicts similar exposures of $^{ch}3D6^{WT}$ dosed at 5/10 mg/kg and $ATV^{cisLALA}$:3D6 at 1.75/3 mg/kg (104.73 nM.day and 100.19 nM.day, respectively), and ~3-fold higher exposures in the $ATV^{cisLALA}$:3D6 group dosed at 5/10 mg/kg (312.75 nM.day) in ARIA study 1 (fig. S11F). Similarly, brain PK simulations for ARIA study 2 (fig. S11I) predict similar brain exposures ($AUC_{0\text{-}72d}$) for the $^{ch}3D6^{WT}$ (10 mg/kg) and ATV:3D6 (3 mg/kg) groups: 119.45 and 107.64 nM.day, respectively.

PK model equations

$$dA_c / dt = IV\ dose^{*} - CL.C_c - CL_D(C_c - C_p) - (V_{m,TfR}C_c) / (K_m + C_c)$$

$$dA_p / dt = CL_D(C_c - C_p)$$

$$dC_b / dt = k_{up,ns}C_c + (k_{up,TfR}C_c) / (K_m + C_c) - k_{loss}C_b$$

$$C_c = (A_c / V_c), C_p = A_p / V_p$$

$$K_m = \alpha K_D$$

Where A_c, A_p, C_c, C_p, and C_b are model state variables and are defined in table S2. *Intravenous (IV) dose is converted from mg/kg to nmol/kg using the following formula:IV dose (nmol/kg) = IV dose (mg/kg)*1000/MW (kDa).

ARIA studies

ARIA animal model: All experimental procedures were performed in accordance with the standards of Biogen IACUC and the Cambridge Laboratory Animals Ordinance, Cambridge MA (Ordinance 1086).

ARIA experimental study design: Two ARIA studies were conducted to assess the potential for reduced ARIA incidence upon treatment with ATV:Aβ (Study 1) and to assess the role of effector function and ATV-mediated brain delivery in the potential reduction of ARIA incidence (Study 2). Following the collection of a baseline MRI scan, dosing was initiated and 5xFAD;$TfR^{mu/hu}$KI mice were administered weekly intraperitoneal injections of the treatments, with weekly MRI imaging performed within 1-3 days after weekly dosing. Study 1 was 11 weeks (12 doses) and study 2 was 10 weeks (11 doses) in length. Untreated animals were used as control and were scanned at baseline and at end of study. Males were used for study 1 (13 months of age at study start, n=11-12 per treatment group or $n = 3$ untreated) and mixed sex were used for the study 2 (11-13 months of age at study start, $n = 6$ males and $n = 4$ females per group). Anti-CD4 antibody (BioXCell, BP0003-R050) was administered ip every 2 weeks, starting 1 day before the first dosing of compounds (0.5 mg/animal). In the study 2, blood was collected from all animals prior to the first dose, and in both studies blood was collected prior to the last dose and at termination. Blood was processed to plasma and stored at −80°C for analysis.

Preparation of brain tissue for ARIA studies: Animals were euthanized with CO_2 asphyxiation 24 hours after the last dose, and blood was collected by cardiac puncture. Cardiac perfusion was initiated with

cold PBS, pH 7.2 (Gibco, 2645342), followed by 20 ml of cold 10% NBF for fixation of the meninges. The whole brain with the meninges attached was dissected out of the skull and drop fixed in 10% NBF STS containers for 1-2 days (Epredia, 53601).

ARIA MRI protocol: Mice were anesthetized with isoflurane in medical oxygen (2% induction, 1-2% maintenance). Images were acquired on a 9.4T preclinical MRI (Bruker BioSpec 94/20,) using Paravision (6.0.1) with a mouse head RF coil. Mice were secured into the head coil using a bite bar, and respiration was kept between 70-160 beats per minute. Body temperature was maintained at 37 ± 0.3°C using an MR compatible warm air heater system (Small Animal Instruments, Inc.), and temperature recorded using a rectal probe. Baseline scans were first acquired to document the absence of pre-treatment abnormalities. Weekly scans were acquired as follows: we first acquired T2 scan (slice thickness = 0.5 mm, repetition time [TR] = 4100 ms, echo time [TE] = 60 ms, averages = 10, repetitions = 1, echo spacing = 7.5 ms, rare factor = 16, flip angle = 90°FOV = 16x16 mm, matrix = 128x128, slices = 30), followed by T2* MGE (slice thickness = 0.5 mm, TR = 1800 ms, TE = 3 ms, averages = 2, repetitions = 1, echo images = 12, echo spacing = 4.5 ms, minimum echo spacing = 1.58 ms, flip angle = 30°, FOV = 16x16 mm, matrix = 160x160, slices = 30), and DWI (slice thickness = 0.5 mm, TR = 3200m, TE = 21.5 ms, averages = 1, repetitions = 1, segments = 2, flip angle = 90°, FOV = 16x16 mm, matrix = 128x60, slices = 30).

ARIA-related pathology assays and analysis: Whole brains were processed following post-fixation in 10% neutral-buffered formalin for 48-72 hours. The right hemisphere was gently marked with red ink. Brains were then sectioned in the coronal plane using a mouse brain block to produce a 6-piece coronal trim. The first cut was localized at the caudal-most visible plane of the optic tracts. One cut was placed rostral to the optic tract section and three cuts were placed caudal to the optic tract section, all at 2-mm intervals. Six coronal slabs were processed and embedded in paraffin blocks for sectioning in the rostral-to-caudal direction. Blocks were gently faced and sectioned at 5-µm thickness to produce 10 consecutive unstained slides.

One slide was stained with hematoxylin and eosin (H&E), coverslipped on a Tissue-Tak Glas automated glass coverslipper (Sakura Finetek) and imaged on a Pannoramic P250 slide scanner with a 20x objective. H&E slides were examined by EDP who was blinded to the treatment group assignments and to the MRI image data of all animals. The following grading system was applied to leptomeningeal arterioles in the 6 brain sections: Grade 0 (none) – no obvious meningovascular inflammation; Grade 1 (minimal) - perivascular mononuclear cells without obvious phagocytic morphology – when present, a focal finding; Grade 2 (mild) – subtle vascular macrophage infiltrates requiring high power examination to visualize; Grade 3 (moderate) - multiple layers of vascular macrophages that were evident at low-to-medium power; Grade 4 (severe) – any vascular inflammatory infiltrate with clear fibrinoid change. Meningovascular inflammation grade scores were 1) summarized on a per animal basis as the predominant meningovascular inflammation grade (both studies) and 2) summated for all foci of meningovascular inflammation throughout 6 brain sections for a summated meningovascular inflammation score (ARIA study 2 only). H&E slides were also examined for microinfarcts and hemorrhages.

One slide was stained with the Perls iron method (Prussian Blue Iron Kit; Polysciences Inc., 24199), coverslipped, and imaged on a Pannoramic P250 slide scanner with a 20x objective. Perls iron slides were examined for microhemorrhages. Leptomeningeal vascular profiles demonstrating 3 or more Perls-reactive hemosiderin foci and that were confirmed on H&E to contain hemosiderin pigment were counted (leptomeningeal hemosiderin foci). Perivascular hemosiderin foci around penetrating cortical arterioles (penetrating perivascular hemosiderin) were added to the total hemosiderin foci. Finally, microinfarcts that showed any hemosiderin staining were counted (hemosiderin-positive microinfarcts).

Immunohistochemistry assays for albumin and CD68 were performed on a Ventana Discovery Ultra autostainer. Heat-induced epitope retrieval was first performed at 95°C for 64 min in CC1 buffer. Slides were then incubated for 1 hour with the following primary antibodies: rabbit recombinant monoclonal anti-albumin IgG (Abcam, ab192603) at 0.5 µg/ml in Discovery antibody diluent (Roche, 760-108); or rabbit monoclonal anti-CD68 IgG (Abcam, ab283654, RRID:AB_2922954) at 0.125 µg/ml in Discovery antibody diluent. Secondary detection was performed with Discovery OmniMap anti-Rb HRP and DAB (Multimer HRP). Slides were counterstained with hematoxylin and coverslipped. All immunohistochemistry assay samples were randomized among batched runs and control slides were incorporated into all runs to prevent systematic batch effects in any treatment group. Slides were imaged on a Panoramic P250 slide scanner with a 20x objective. Cortical regions were annotated with AI-based algorithms and manually adjusted as necessary. For CD68, a leptomeningeal and subpial ROI was isolated from the remainer of the cortex by dilating a 125-µm-thick region of interest from the leptomeningeal surface into the superficial cortical parenchyma. Leptomeningeal vessels were segmented within the leptomeningeal and subpial ROI with an AI-based protocol and manually checked for accuracy. Antigen immunoreactivity (DAB signal) was analyzed with custom-designed, threshold-based segmentation protocols using median filters and respective color deconvolution filters in Visiopharm Image Analysis Software (version 2019.12.0.6842 and subsequent updates). Albumin and CD68 immunoreactivity were calculated as the summed areas of cortex immunoreactive for the antigens divided by the composite cortical area, expressed as % Area immunoreactivity.

Additional staining of astrocytes (GFAP), Aβ, brain endothelial cells (CD31), and complement 3d was conducted using FFPE slides from ARIA study 1. Slides were incubated at 60°C for 5-10 min followed by 3x 10 min washes in xylene substitute and rehydrated for 1 min each in 100, 100, 100, 95, 85, and 75% ethanol in water. Slides were washed 3x in water then immersed in photobleaching solution (4.5% H2O2 + 25 mM NaOH in PBS) for 2 hours in between two broad spectrum LED light pads (HSK Artist tracing light box, B07HYMYBNF) before rinsing in PBS and incubating in 1x antigen retrieval buffer (Vector Laboratories, H3300) in an electric pressure cooker for 20 min. Slides were cooled to room temperature and loaded into Sequenza Manual Staining slide rack (Thermo Fisher Scientific, 73310017) for subsequent steps. Slides were rinsed with PBS containing 0.3% triton X-100 (PBS-X) and blocked 1 hour in 1% BSA + 1x fish gelatin (BioWorld, 21761058) + 0.5% triton X-100 + 0.1% sodium azide at room temperature before incubating overnight in blocking solution containing primary antibodies at 4°C, washed 3x for 15 min each in PBS with 0.3% triton X-100, incubated 4 hours at RT in blocking solution containing secondary antibodies and DAPI (1:10k dilution, Thermo Fisher Scientific, D1306), and washed 3x for 15 min each in PBS with 0.3% triton X-100. Primary antibodies included GFAP (Novus, NBP1-05198, RRID:AB_1556315, 1:500) and complement 3d (R&D Systems, AF2655, RRID:AB_2066622, 1:100) and secondary antibodies included anti-chicken IgY-AF488 (Jackson, 703-545-155, RRID:AB_2340375, 1:500) and donkey-ranti-goat-AF647 (Thermo Fisher Scientific, A-21447, RRID:AB_2535864 1:1000). Sections were mounted onto slides and coverslipped using Prolong Glass Antifade mounting medium. After processing, some sections had substantial tissue damage and were excluded from analyses resulting in fewer animals in the final analysis relative to the full number of animals in each group. Slides were imaged using a Zeiss Axioscan.Z1 slide scanner at 20X magnification and images were processed using custom macros in Zeiss ZEN software to segment markers of interest.

REFERENCES AND NOTES

1. F. Weber *et al.*, Brain Shuttle Antibody for Alzheimer's Disease with Attenuated Peripheral Effector Function due to an Inverted Binding Mode. *Cell Rep.* **22**, 149–162 (2018). doi: 10.1016/j.celrep.2017.12.019; pmid: 29298417
2. J. Niewoehner *et al.*, Increased brain penetration and potency of a therapeutic antibody using a monovalent molecular shuttle. *Neuron* **81**, 49–60 (2014). doi: 10.1016/j.neuron.2013.10.061; pmid: 24411731
3. Y. J. Yu *et al.*, Boosting brain uptake of a therapeutic antibody by reducing its affinity for a transcytosis target. *Sci. Transl. Med.* **3**, 84ra44 (2011). doi: 10.1126/scitranslmed.3002230; pmid: 21613623
4. Y. J. Yu *et al.*, Therapeutic bispecific antibodies cross the blood-brain barrier in nonhuman primates. *Sci. Transl. Med.* **6**, 261ra154 (2014). doi: 10.1126/scitranslmed.3009835; pmid: 25378646
5. N. Bien-Ly *et al.*, Transferrin receptor (TfR) trafficking determines brain uptake of TfR antibody affinity variants. *J. Exp. Med.* **211**, 233–244 (2014). doi: 10.1084/jem.20131660; pmid: 24470444
6. S. Edavettal *et al.*, Enhanced delivery of antibodies across the blood-brain barrier via TEMs with inherent receptor-mediated phagocytosis. *Med* **3**, 860–882.e15 (2022). doi: 10.1016/j.medj.2022.09.007; pmid: 36257298
7. M. S. Kariolis *et al.*, Brain delivery of therapeutic proteins using an Fc fragment blood-brain barrier transport vehicle in mice and monkeys. *Sci. Transl. Med.* **12**, eaay1359 (2020). doi: 10.1126/scitranslmed.aay1359
8. B. van Lengerich *et al.*, A TREM2-activating antibody with a blood-brain barrier transport vehicle enhances microglial metabolism in Alzheimer's disease models. *Nat. Neurosci.* **26**, 416–429 (2023). doi: 10.1038/s41593-022-01240-0; pmid: 36635496
9. N. Khoury *et al.*, Fc-engineered large molecules targeting blood-brain barrier transferrin receptor and CD98hc have distinct central nervous system and peripheral biodistribution. *Nat. Commun.* **16**, 1822 (2025). doi: 10.1038/s41467-025-57108-x; pmid: 39979268
10. A. Arguello *et al.*, Molecular architecture determines brain delivery of a transferrin receptor-targeted lysosomal enzyme. *J. Exp. Med.* **219**, e20211057 (2022). doi: 10.1084/jem.20211057; pmid: 35226042
11. J. C. Ullman *et al.*, Brain delivery and activity of a lysosomal enzyme using a blood-brain barrier transport vehicle in mice. *Sci. Transl. Med.* **12**, eaay1163 (2020). doi: 10.1126/scitranslmed.aay1163; pmid: 32461331
12. T. Logan *et al.*, Rescue of a lysosomal storage disorder caused by Grn loss of function with a brain penetrant progranulin biologic. *Cell* **184**, 4651–4668.e25 (2021). doi: 10.1016/j.cell.2021.08.002; pmid: 34450028
13. S. J. Barker *et al.*, Targeting the transferrin receptor to transport antisense oligonucleotides across the mammalian blood-brain barrier. *Sci. Transl. Med.* **16**, eadi2245 (2024). doi: 10.1126/scitranslmed.adi2245
14. D. M. Castellanos *et al.*, Acute and chronic dosing of a high-affinity rat/mouse chimeric transferrin receptor antibody in mice. *Pharmaceutics* **12**, 852 (2020). doi: 10.3390/pharmaceutics12090852; pmid: 32911688
15. J. A. Couch *et al.*, Addressing safety liabilities of TfR bispecific antibodies that cross the blood-brain barrier. *Sci. Transl. Med.* **5**, 183ra57, 1–12 (2013). doi: 10.1126/scitranslmed.3005338; pmid: 23636093
16. W. M. Pardridge, R. J. Boado, D. J. Patrick, E. Ka-Wai Hui, J. Z. Lu, Blood-Brain Barrier Transport, Plasma Pharmacokinetics, and Neuropathology Following Chronic Treatment of the Rhesus Monkey with a Brain Penetrating Humanized Monoclonal Antibody Against the Human Transferrin Receptor. *Mol. Pharm.* **15**, 5207–5216 (2018). doi: 10.1021/acs.molpharmaceut.8b00730; pmid: 30226787
17. C. Haass, D. J. Selkoe, Soluble protein oligomers in neurodegeneration: Lessons from the Alzheimer's amyloid beta-peptide. *Nat. Rev. Mol. Cell Biol.* **8**, 101–112 (2007). doi: 10.1038/nrm2101; pmid: 17245412
18. R. C. Petersen *et al.*, NIA-AA Alzheimer's Disease Framework: Clinical Characterization of Stages. *Ann. Neurol.* **89**, 1145–1156 (2021). doi: 10.1002/ana.26071; pmid: 33772866
19. *Early Alzheimer's Disease: Developing Drugs for Treatment; FDA-2013-D-0077* (US Food and Drug Administration Center for Biologics, Evaluation and Research Center for Drug Evaluation and Research, 2024).
20. E. Karran, B. De Strooper, The amyloid hypothesis in Alzheimer disease: New insights from new therapeutics. *Nat. Rev. Drug Discov.* **21**, 306–318 (2022). doi: 10.1038/s41573-022-00391-w; pmid: 35177833
21. M. Citron, Alzheimer's disease: Strategies for disease modification. *Nat. Rev. Drug Discov.* **9**, 387–398 (2010). doi: 10.1038/nrd2896; pmid: 20431570
22. J. Koenigsknecht-Talboo *et al.*, Rapid microglial response around amyloid pathology after systemic anti-Abeta antibody administration in PDAPP mice. *J. Neurosci.* **28**, 14156–14164 (2008). doi: 10.1523/JNEUROSCI.4147-08.2008; pmid: 19109498
23. F. Bard *et al.*, Peripherally administered antibodies against amyloid beta-peptide enter the central nervous system and reduce pathology in a mouse model of Alzheimer disease. *Nat. Med.* **6**, 916–919 (2000). doi: 10.1038/78682; pmid: 10932230
24. G. G. Glenner, C. W. Wong, Alzheimer's disease: Initial report of the purification and characterization of a novel cerebrovascular amyloid protein. *Biochem. Biophys. Res. Commun.* **120**, 885–890 (1984). doi: 10.1016/S0006-291X(84)80190-4; pmid: 6375662
25. D. J. Selkoe, J. Hardy, The amyloid hypothesis of Alzheimer's disease at 25 years. *EMBO Mol. Med.* **8**, 595–608 (2016). doi: 10.15252/emmm.201606210; pmid: 27025652
26. I. St-Amour *et al.*, Brain bioavailability of human intravenous immunoglobulin and its transport through the murine blood-brain barrier. *J. Cereb. Blood Flow Metab.* **33**, 1983–1992 (2013). doi: 10.1038/jcbfm.2013.160; pmid: 24045402
27. D. J. Wolak, M. E. Pizzo, R. G. Thorne, Probing the extracellular diffusion of antibodies in brain using in vivo integrative optical imaging and ex vivo fluorescence imaging. *J. Control. Release* **197**, 78–86 (2015). doi: 10.1016/j.jconrel.2014.10.034; pmid: 25449807
28. S. B. Hladky, M. A. Barrand, The glymphatic hypothesis: The theory and the evidence. *Fluids Barriers CNS* **19**, 9 (2022). doi: 10.1186/s12987-021-00282-z; pmid: 35115036
29. N. J. Abbott, M. E. Pizzo, J. E. Preston, D. Janigro, R. G. Thorne, The role of brain barriers in fluid movement in the CNS: Is there a 'glymphatic' system? *Acta Neuropathol.* **135**, 387–407 (2018). doi: 10.1007/s00401-018-1812-4; pmid: 29428972
30. M. E. Pizzo *et al.*, Intrathecal antibody distribution in the rat brain: Surface diffusion, perivascular transport and osmotic enhancement of delivery. *J. Physiol.* **596**, 445–475 (2018). doi: 10.1113/JP275105; pmid: 29023798
31. R. Sperling *et al.*, Amyloid-related imaging abnormalities in patients with Alzheimer's disease treated with bapineuzumab: A retrospective analysis. *Lancet Neurol.* **11**, 241–249 (2012). doi: 10.1016/S1474-4422(12)70015-7; pmid: 22305802
32. R. A. Sperling *et al.*, Amyloid-related imaging abnormalities in amyloid-modifying therapeutic trials: Recommendations from the Alzheimer's Association Research Roundtable Workgroup. *Alzheimers Dement.* **7**, 367–385 (2011). doi: 10.1016/j.jalz.2011.05.2351; pmid: 21784348
33. S. Salloway *et al.*, Two phase 3 trials of bapineuzumab in mild-to-moderate Alzheimer's disease. *N. Engl. J. Med.* **370**, 322–333 (2014). doi: 10.1056/NEJMoa1304839; pmid: 24450891
34. H. Hampel *et al.*, Amyloid-related imaging abnormalities (ARIA): Radiological, biological and clinical characteristics. *Brain* **146**, 4414–4424 (2023). doi: 10.1093/brain/awad188; pmid: 37280110
35. A. M. Merchant *et al.*, An efficient route to human bispecific IgG. *Nat. Biotechnol.* **16**, 677–681 (1998). doi: 10.1038/nbt0798-677; pmid: 9661204
36. C. A. Diebolder *et al.*, Complement is activated by IgG hexamers assembled at the cell surface. *Science* **343**, 1260–1263 (2014). doi: 10.1126/science.1248943; pmid: 24626930
37. M. E. Reff *et al.*, Depletion of B cells in vivo by a chimeric mouse human monoclonal antibody to CD20. *Blood* **83**, 435–445 (1994). doi: 10.1182/blood.V83.2.435.435; pmid: 7506951
38. M. E. Bamberger, M. E. Harris, D. R. McDonald, J. Husemann, G. E. Landreth, A cell surface receptor complex for fibrillar beta-amyloid mediates microglial activation. *J. Neurosci.* **23**, 2665–2674 (2003). doi: 10.1523/JNEUROSCI.23-07-02665.2003; pmid: 12684452
39. H. Oakley *et al.*, Intraneuronal β-amyloid aggregates, neurodegeneration, and neuron loss in transgenic mice with five familial Alzheimer's disease mutations: Potential factors in amyloid plaque formation. *J. Neurosci.* **26**, 10129–10140 (2006). doi: 10.1523/JNEUROSCI.1202-06.2006; pmid: 17021169
40. H. Wolburg, W. Paulus, Choroid plexus: Biology and pathology. *Acta Neuropathol.* **119**, 75–88 (2010). doi: 10.1007/s00401-009-0627-8; pmid: 20033190
41. B. Giometto *et al.*, Transferrin receptors in rat central nervous system: An immunocytochemical study. *J. Neurol. Sci.* **98**, 81–90 (1990). doi: 10.1016/0022-510X(90)90183-N; pmid: 2230832
42. D. R. Thal, W. S. T. Griffin, R. A. I. de Vos, E. Ghebremedhin, Cerebral amyloid angiopathy and its relationship to Alzheimer's disease. *Acta Neuropathol.* **115**, 599–609 (2008). doi: 10.1007/s00401-008-0366-2; pmid: 18369648
43. S. M. Greenberg *et al.*, Cerebral amyloid angiopathy and Alzheimer disease - one peptide, two pathways. *Nat. Rev. Neurol.* **16**, 30–42 (2020). doi: 10.1038/s41582-019-0281-2; pmid: 31827267
44. A. Keable *et al.*, Deposition of amyloid β in the walls of human leptomeningeal arteries in relation to perivascular drainage pathways in cerebral amyloid angiopathy. *Biochim. Biophys. Acta* **1862**, 1037–1046 (2016). doi: 10.1016/j.bbadis.2015.08.024; pmid: 26327684
45. R. O. Weller *et al.*, Cerebral amyloid angiopathy: Amyloid beta accumulates in putative interstitial fluid drainage pathways in Alzheimer's disease. *Am. J. Pathol.* **153**, 725–733 (1998). doi: 10.1016/S0002-9440(10)65616-7; pmid: 9736023
46. S. J. Doran, R. P. Sawyer, Risk factors in developing amyloid related imaging abnormalities (ARIA) and clinical implications. *Front. Neurosci.* **18**, 1326784 (2024). doi: 10.3389/fnins.2024.1326784; pmid: 38312931
47. L. Sveikata, A. Charidimou, A. Viswanathan, Vessels Sing Their ARIAs: The Role of Vascular Amyloid in the Age of Aducanumab. *Stroke* **53**, 298–302 (2022). doi: 10.1161/STROKEAHA.121.036873; pmid: 34905943
48. W. Zago *et al.*, Vascular alterations in PDAPP mice after anti-Aβ immunotherapy: Implications for amyloid-related imaging abnormalities. *Alzheimers Dement.* **9** (Suppl), S105–S115 (2013). doi: 10.1016/j.jalz.2012.11.010; pmid: 23583235
49. R. B. DeMattos *et al.*, A plaque-specific antibody clears existing β-amyloid plaques in Alzheimer's disease mice. *Neuron* **76**, 908–920 (2012). doi: 10.1016/j.neuron.2012.10.029; pmid: 23217740

50. S. Schroeter *et al.*, Immunotherapy reduces vascular amyloid-beta in PDAPP mice. *J. Neurosci.* **28**, 6787–6793 (2008). doi: 10.1523/JNEUROSCI.2377-07.2008; pmid: 18596154
51. M. M. Racke *et al.*, Exacerbation of cerebral amyloid angiopathy-associated microhemorrhage in amyloid precursor protein transgenic mice by immunotherapy is dependent on antibody recognition of deposited forms of amyloid beta. *J. Neurosci.* **25**, 629–636 (2005). doi: 10.1523/JNEUROSCI.4337-04.2005; pmid: 15659599
52. X. Taylor *et al.*, Amyloid-β (Aβ) immunotherapy induced microhemorrhages are associated with activated perivascular macrophages and peripheral monocyte recruitment in Alzheimer's disease mice. *Mol. Neurodegener.* **18**, 59 (2023). doi: 10.1186/s13024-023-00649-w; pmid: 37649100
53. M. Pfeifer *et al.*, Cerebral hemorrhage after passive anti-Abeta immunotherapy. *Science* **298**, 1379 (2002). doi: 10.1126/science.1078259; pmid: 12434053
54. T. Bussiere, J. Abettan, J. Sebalusky, S. Hamann, A. Silva Amaral, D. Walsh, D. Bradley, E. Plowey, "Modeling mechanisms of amyloid-related imaging abnormalities (aria) in transgenic mice treated with anti-aβ immunotherapy and imaged with MRI." abstract #425, oral presentation at AD/PD, 5-9 March 2024, Lisbon, Portugal [Preprint] (2024); https://cslide.ctimeetingtech.com/adpd24/attendee/confcal/show/session/14#presentation-abstract-42585247580.
55. S. A. Liddelow *et al.*, Neurotoxic reactive astrocytes are induced by activated microglia. *Nature* **541**, 481–487 (2017). doi: 10.1038/nature21029; pmid: 28099414
56. M. Xiong *et al.*, APOE immunotherapy reduces cerebral amyloid angiopathy and amyloid plaques while improving cerebrovascular function. *Sci. Transl. Med.* **13**, eabd7522 (2021). doi: 10.1126/scitranslmed.abd7522; pmid: 33597265
57. S. Ostrowitzki *et al.*, A phase III randomized trial of gantenerumab in prodromal Alzheimer's disease. *Alzheimers Res. Ther.* **9**, 95 (2017). doi: 10.1186/s13195-017-0318-y; pmid: 29221491
58. J. Sevigny *et al.*, The antibody aducanumab reduces Aβ plaques in Alzheimer's disease. *Nature* **537**, 50–56 (2016). doi: 10.1038/nature19323; pmid: 27582220
59. M. G. Kozberg *et al.*, Blood-brain barrier leakage and perivascular inflammation in cerebral amyloid angiopathy. *Brain Commun.* **4**, fcac245 (2022). doi: 10.1093/braincomms/fcac245; pmid: 36267331
60. N. J. Abbott, L. Rönnbäck, E. Hansson, Astrocyte-endothelial interactions at the blood-brain barrier. *Nat. Rev. Neurosci.* **7**, 41–53 (2006). doi: 10.1038/nrn1824; pmid: 16371949
61. R. D. Broadwell, M. V. Sofroniew, Serum proteins bypass the blood-brain fluid barriers for extracellular entry to the central nervous system. *Exp. Neurol.* **120**, 245–263 (1993). doi: 10.1006/exnr.1993.1059; pmid: 8491281
62. S. I. Rapoport, "Passage of Proteins from Blood to Cerebrospinal Fluid" in *Neurobiology of Cerebrospinal Fluid 2*, J. H. Wood, Ed. (Springer US, 1983), pp. 233–245.doi: 10.1007/978-1-4615-9269-3_16
63. S. I. Rapoport, K. D. Pettigrew, A heterogenous, pore-vesicle membrane model for protein transfer from blood to cerebrospinal fluid at the choroid plexus. *Microvasc. Res.* **18**, 105–119 (1979). doi: 10.1016/0026-2862(79)90020-7; pmid: 481240
64. R. Pietilä *et al.*, Molecular anatomy of adult mouse leptomeninges. *Neuron* **111**, 3745–3764.e7 (2023). doi: 10.1016/j.neuron.2023.09.002; pmid: 37776854
65. M. J. Hannocks *et al.*, Molecular characterization of perivascular drainage pathways in the murine brain. *J. Cereb. Blood Flow Metab.* **38**, 669–686 (2018). doi: 10.1177/0271678X17749689; pmid: 29283289
66. R. G. Thorne, C. Nicholson, In vivo diffusion analysis with quantum dots and dextrans predicts the width of brain extracellular space. *Proc. Natl. Acad. Sci. USA* **103**, 5567–5572 (2006). doi: 10.1073/pnas.0509425103
67. M. Vanlandewijck *et al.*, A molecular atlas of cell types and zonation in the brain vasculature. *Nature* **554**, 475–480 (2018). doi: 10.1038/nature25739; pmid: 29443965
68. R. G. Thorne, "Appendix: Central Nervous System Anatomy and Physiology: Structure-Function Relationships, Blood Supply, Ventricles, and Brain Fluids" in *Drug Delivery to the Brain Physiological Concepts, Methodologies and Approaches*, vol. 33, E. C. M. de Lange, M. Hammarlund-Udenaes, R. G. Thorne, Eds. (Springer International, ed. 2, 2022), pp. 763–790.
69. V. O. Torres *et al.*, Transferrin receptor-mediated transport at the blood-brain barrier is elevated during early development but maintained across adult aging. BioRxiv 10.1101/2024.11.12.623253 [Preprint] (2024); https://doi.org/10.1101/2024.11.12.623253.
70. A. C. Yang *et al.*, A human brain vascular atlas reveals diverse mediators of Alzheimer's risk. *Nature* **603**, 885–892 (2022). doi: 10.1038/s41586-021-04369-3; pmid: 35165441
71. M. Zielinski *et al.*, Cryo-EM of Aβ fibrils from mouse models find tg-APP$_{ArcSwe}$ fibrils resemble those found in patients with sporadic Alzheimer's disease. *Nat. Neurosci.* **26**, 2073–2080 (2023). doi: 10.1038/s41593-023-01484-4; pmid: 37973869
72. P. Giannoni *et al.*, Cerebrovascular pathology during the progression of experimental Alzheimer's disease. *Neurobiol. Dis.* **88**, 107–117 (2016). doi: 10.1016/j.nbd.2016.01.001; pmid: 26774030
73. D. Joy, Supplementary code for 'Transferrin receptor–targeted anti- amyloid antibody enhances brain delivery and mitigates ARIA,' (2025); https://doi.org/10.5281/zenodo.15420410.
74. S. van der Walt *et al.*, scikit-image: Image processing in Python. *PeerJ* **2**, e453 (2014). doi: 10.7717/peerj.453; pmid: 25024921
75. P. Virtanen *et al.*, SciPy 1.0: Fundamental algorithms for scientific computing in Python. *Nat. Methods* **17**, 261–272 (2020). doi: 10.1038/s41592-019-0686-2; pmid: 32015543
76. K. S. Chew *et al.*, CD98hc is a target for brain delivery of biotherapeutics. *Nat. Commun.* **14**, 5053 (2023). doi: 10.1038/s41467-023-40681-4; pmid: 37598178

ACKNOWLEDGMENTS

The authors thank B. Benitez, K. Rebadulla, and D. Sobrepena for providing animal care and support at Denali Therapeutics; J. McInnes and A. Sani for helpful discussions; D. Xia for support and coordination of 5xFAD;TfR$^{mu/hu}$ KI mouse model colony generation; and G. Skovbjerg, U. Roostalunand, and J. Hecksher-Sørensen from Gubra for technical services, support, and advice. **Funding:** Funding for this work was provided by Denali Therapeutics, Inc. and Biogen. **Author contributions:** Conceptualization – M.E.P., E.D.P., N.K., W.K., J.A., S.L.D., P.E.S., M.L.B., A.P.S., M.E.C., R.J.W., R.G.T., P.H.W., D.M.W., J.L., T.B., Y.Z.; Formal analysis – M.E.P., E.D.P., N.K., W.K., J.A., S.L.D., D.J., R.M., A.M., M.E.C.; Investigation – M.E.P., E.D.P., N.K., W.K., J.A., S.L.D., C.B.D., T.E., D.J., M.L.B., E.R., D.C., J.C.D., K.G., S.H., R.M., J.S., A.C.S.A., I.B., R.C., J.C., A.J.C., J.D., L.F., J.A.G., D.J.K., K.J.L., A.W.L., A.M., H.N.N., E.S.O., E.R.T., V.O.T., L.S., H.S., R.T., A.P.S., M.E.C., M.S.K.; Writing, original draft – M.E.P., E.D.P., N.K., W.K., M.E.C., R.G.T., T.B., Y.Z.; Writing, reviewing & editing – M.E.P., E.D.P., N.K., C.B.D., D.J., A.M., M.E.C., R.J.W., R.G.T., P.H.W., D.M.W., J.L., T.B., Y.Z.; Supervision – E.D.P., K.G., R.M., M.S.D., P.E.S., A.P.S., Z.K.S., H.S., M.E.C., R.J.W., P.H.W., D.M.W., J.L., T.B., Y.Z. **Competing interests:** M.E.P., N.K., W.K., S.L.D., C.B.D., T.E., D.J., E.R., D.C., J.C.D., K.G., R.M., I.B., R.C., J.C., A.J.C., M.S.D., J.D., L.F., J.A.G., M.S.K., D.J.K., K.J.L., A.W.L., A.M., H.N.N., E.S.O., E.R.T., V.O.T., P.E.S., L.S., A.P.S., Z.K.S., H.S., R.T., M.E.C., R.J.W., R.G.T., J.L., and Y.Z. are currently or were previously paid employees and/or shareholders of Denali Therapeutics, Inc. E.D.P., S.H., J.A., M.L., S.H., J.S., A.C.S.A., P.H.W., D.M.W., and T.B. are currently or were previously paid employees and/or shareholders of Biogen. Work was conducted while authors were employed at Denali or Biogen. Denali has filed patent application no. PCT/US2019/012990 "Transferrin receptor-binding polypeptides and uses thereof" and PCT/US2024/021179 "Abeta-targeting proteins and methods of use," each of which is related to the subject matter of this paper. M.S.D., M.S.K., W.K., A.P.S., and Y.Z. are inventors of PCT/US2019/012990. K.G., N.K., M.E.P., and Y.Z. are inventors of PCT/US2024/021179. **Data and materials availability:** All data associated with this study are available in the main text or the supplementary materials. Code used for lightsheet image analysis can be found on Zenodo (*73*). Specific reagents generated in this study are available from Denali Therapeutics through a completed materials transfer agreement. Requests should be sent to contracts@dnli.com. **License information:** Copyright © 2025 the authors, some rights reserved; exclusive licensee American Association for the Advancement of Science. No claim to original US government works. https://www.science.org/about/science-licenses-journal-article-reuse

SUPPLEMENTARY MATERIALS

science.org/doi/10.1126/science.ads3204
Figs. S1 to S18; Tables S1 to S3; MDAR Reproducibility Checklist; Data File S1
Submitted 8 August 2024; resubmitted 29 March 2025; accepted 12 June 2025
10.1126/science.ads3204

Check for

RESEARCH ARTICLE SUMMARY

DISEASE GENOMICS

Predicting expression-altering promoter mutations with deep learning

Kishore Jaganathan†, Nicole Ersaro†, Gherman Novakovsky†, *et al.*

Full article and list of author affiliations: https://doi.org/10.1126/science.ads7373

INTRODUCTION: Within the human genome, gene transcription begins at promoters—core sequence elements that integrate inputs from proximal and distal genomic regions to precisely regulate gene expression. Disruptive mutations in promoters can lead to severe alterations in gene expression, but their impact on human health and disease remains poorly understood owing to the difficulty of distinguishing damaging mutations from benign ones.

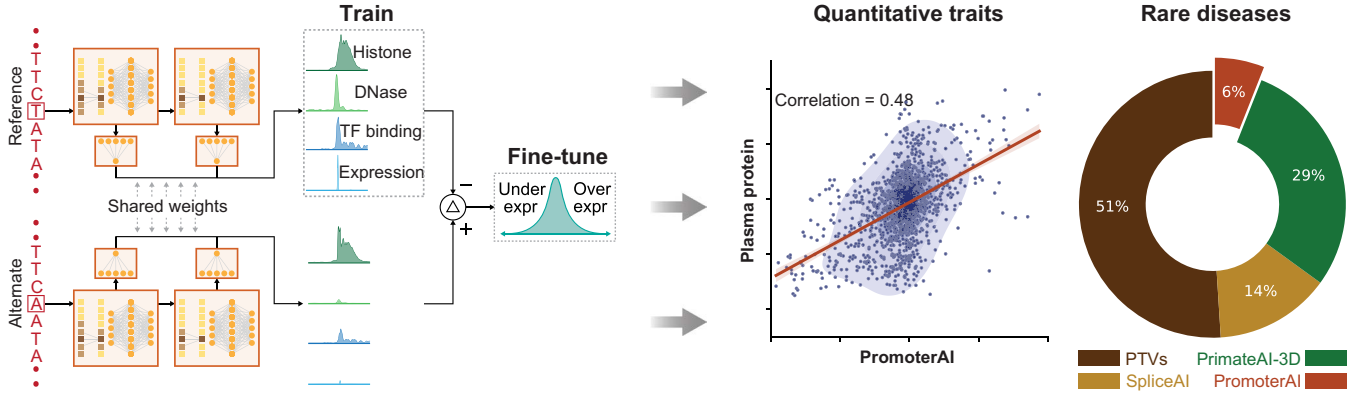
RATIONALE: Deep-learning models trained on large-scale functional genomics datasets have the potential to learn the regulatory syntax underlying transcriptional and epigenetic programs. Appropriate training datasets linking genetic variants to functional consequences are key to achieving accurate variant effect prediction.

RESULTS: PromoterAI is a deep neural network that evaluates genomic sequence at promoters to predict the effects of variants on gene expression. Initially, we trained PromoterAI to predict histone modifications, DNA accessibility, transcription factor binding, and strand-specific gene expression around transcription start sites with single-nucleotide resolution. Subsequently, we curated a training dataset consisting of thousands of rare promoter variants associated with outlier gene expression across multiple tissues, using a cohort of individuals with paired genome and RNA sequencing, while controlling for the effects of several cis- and trans-confounding variables. We used these outlier variants to fine-tune PromoterAI through a framework designed to generalize across unseen genes and datasets.

We extensively validated PromoterAI's predictions using diverse benchmarks spanning gene expression, protein abundance, quantitative trait loci, and reporter assays. Analysis of allele frequency spectra in a population cohort revealed that predicted expression-altering promoter variants were severely depleted at high allele frequencies, reflecting the removal of deleterious variants by natural selection. Across tens of thousands of individuals in the UK Biobank cohort, we observed that predicted variant effects correlated strongly with measurements of protein abundance and quantitative traits. Finally, we applied PromoterAI to undiagnosed rare-disease patients from the Genomics England cohort and found that variants predicted to cause underexpression were specifically enriched in the promoters of Mendelian disease genes associated with the patients' phenotypes, especially genes with dominant loss-of-function effects consistent with haploinsufficiency.

CONCLUSION: PromoterAI fills a critical gap in genome interpretation by enabling accurate detection of promoter variants that affect gene expression. A crucial factor in PromoterAI's effectiveness is a fine-tuning process that uses genetic variants with known expression consequences. Incorporating promoter variants into genomic analyses, where present workflows predominantly focus on coding variants, can further expand the clinical utility of personalized genome sequencing. □

Corresponding author: Kyle Kai-How Farh (kfarh@illumina.com) †These authors contributed equally to this work. **Cite this article as K. Jaganathan *et al.*, *Science* 389, eads7373 (2025). DOI: 10.1126/science.ads7373**



PromoterAI captures the functional impact of promoter variants. (Left) PromoterAI was initially trained to predict histone modifications, chromatin accessibility, transcription factor (TF) binding, and gene expression around transcription start sites, and subsequently fine-tuned using rare promoter variants associated with outlier gene expression. (Right) Predicted variant effects correlated strongly with quantitative traits across population cohorts and contributed to 6% of the diagnostic yield in a cohort of patients with rare genetic diseases. SpliceAI and PrimateAI-3D are other deep-learning models that predict variant effects. DNase, deoxyribonuclease; PTVs, protein-truncating variants.

DISEASE GENOMICS

Predicting expression-altering promoter mutations with deep learning

Kishore Jaganathan[1]†, Nicole Ersaro[1]†, Gherman Novakovsky[1]†, Yuchuan Wang[1], Terena James[1], Jeremy Schwartzentruber[1], Petko Fiziev[1], Irfahan Kassam[1], Fan Cao[1], Johann Hawe[1], Henry Cavanagh[1], Ashley Lim[1], Grace Png[1], Jeremy McRae[1], Abhimanyu Banerjee[1], Arvind Kumar[1], Jacob Ulirsch[1], Yan Zhang[1], Francois Aguet[1], Pierrick Wainschtein[1], Laksshman Sundaram[1], Adriana Salcedo[1], Sofia Kyriazopoulou Panagiotopoulou[1]‡, Delasa Aghamirzaie[1]§, Evin Padhi[2], Ziming Weng[2], Shan Dong[3,4], Damian Smedley[5], Mark Caulfield[5], Anne O'Donnell-Luria[6,7,8], Heidi L. Rehm[6,7], Stephan J. Sanders[3,4,9], Anshul Kundaje[10,11], Stephen B. Montgomery[2,10,12], Mark T. Ross[1], Kyle Kai-How Farh[1]*

Only a minority of patients with rare genetic diseases are presently diagnosed by exome sequencing, suggesting that additional unrecognized pathogenic variants may reside in noncoding sequence. In this work, we describe PromoterAI, a deep neural network that accurately identifies noncoding promoter variants that dysregulate gene expression. We show that promoter variants with predicted expression-altering consequences produce outlier expression at both the RNA and protein levels in thousands of individuals and that these variants experience strong negative selection in human populations. We observed that clinically relevant genes in patients with rare diseases are enriched for such variants and validated their functional impact through reporter assays. Our estimates suggest that promoter variation accounts for 6% of the genetic burden associated with rare diseases.

The precise control of gene expression is broadly important across human health and development, but the mechanisms by which genomic sequence encodes these intricate programs remain incompletely understood. Central to gene regulation is the promoter, the site of transcriptional initiation, which integrates signals across multiple noncoding sequence elements to determine the proper cellular and temporal context for turning genes on and off. Experimental studies of promoters have shown that they can substantially increase or decrease gene expression (*1*), suggesting that noncoding variants that fall within the promoters of clinically relevant genes may play key roles in rare genetic disorders and cancer (*2*, *3*). However, clinical interest in promoter variants has been limited, owing to the difficulty of distinguishing between functional noncoding variants that affect gene expression and those that are neutral, with only a handful of pathogenic noncoding variants in promoters having been identified to date (*4*–*12*). These challenges in finding pathogenic variants that lie outside protein-coding sequence continue to be a major hindrance to realizing the potential of personalized genome sequencing.

Deep-learning models, known for their efficacy at recognizing patterns from large volumes of unstructured data, offer a promising path forward for distilling data collected from genome-wide sequencing and functional genomics experiments into models that can accurately predict the clinical impact of human genetic variation (*13*, *14*). Recent examples that have been adopted in clinical contexts include SpliceAI (*15*), which has been cited in expert guidelines for splice variant effect prediction in rare genetic disorders and oncology (*16*), and PrimateAI-3D, which predicts missense variant effects based on protein language models and three-dimensional (3D) crystal structures (*17*). Although deep-learning models such as Evo2 (*18*), DeepSEA (*19*), Basenji (*20*), ExPecto (*21*), Enformer (*22*), PuffinD (*23*), ChromBPNet (*24*), and Borzoi (*25*) have been developed to infer the regulatory code directly from genomic sequence, predicting the effects of noncoding genetic variants remains an unmet challenge (*26*, *27*).

Results

PromoterAI predicts the effects of promoter variants on gene expression

We introduce PromoterAI, a convolutional deep neural network model that uses ~20 kb of sequence context around a promoter variant to predict its expression consequence. We first trained the model to predict histone modifications, DNA accessibility, transcription factor (TF) occupancy, and strand-specific CAGE (cap analysis of gene expression) values around transcription start sites (TSSs) at base-pair resolution (*28*, *29*). We subsequently fine-tuned the model using a curated set of rare noncoding promoter variants associated with unusually high or low gene expression to further improve its accuracy across extensive validation benchmarks, which we publish as a resource (Fig. 1A, fig. S1A, and table S1, A to G).

To create this curated list of variants for fine-tuning, we analyzed the Genotype-Tissue Expression v8 (GTEx) cohort, which consists of paired whole-genome sequencing (WGS) and RNA sequencing (RNA-seq) data across 49 tissues in 838 individuals (*30*). Specifically, we cataloged a set of rare (allele frequency <0.5%) variants in the promoters of genes [TSS ± 500 base pairs (bp)] with outlier expression across multiple tissues. These multitissue outliers were identified with a *t* test between expression *z*-scores from all measured tissues in the carriers versus the same tissues in noncarriers. To maximize confidence in the resulting outliers, when generating the expression *z*-scores, we subtracted out the contribution of other factors that also affect gene expression: principal components from the expression and genotype matrices, cis effects of common expression quantitative trait loci (eQTLs) on gene expression, and trans effects of correlated patterns of gene expression (Fig. 1B). To perform the trans-expression correction, we predicted each gene's expression using the expression of all genes residing on other chromosomes and then subtracted the predicted expression values from the observed values, because these generally reflect global patterns unrelated to the effects of promoter sequence. To assess the gain in specificity after each correction step, we compared the number of observed expression outliers to background expectation, which we estimated by shuffling the cohort, with variants being randomly reassigned between individuals. After initially correcting for genotype and expression principal components, we found 2540 multitissue outliers at a *p*-value threshold that produced 1000 outliers in the shuffled controls; this increased to 3116 after correcting for cis-eQTLs and finally to 4030 after the trans-expression correction (Fig. 1B and

[1]Illumina Artificial Intelligence Laboratory, Illumina, Inc., San Diego, CA, USA. [2]Department of Pathology, Stanford University, Stanford, CA, USA. [3]Department of Psychiatry and Behavioral Sciences, UCSF Weill Institute for Neurosciences, University of California, San Francisco, San Francisco, CA, USA. [4]Institute of Developmental and Regenerative Medicine, Department of Paediatrics, University of Oxford, Oxford, UK. [5]William Harvey Research Institute, Queen Mary University of London, London, UK. [6]Program in Medical and Population Genetics, Broad Institute of MIT and Harvard, Cambridge, MA, USA. [7]Center for Genomic Medicine and Analytic and Translational Genetics Unit, Massachusetts General Hospital, Boston, MA, USA. [8]Division of Genetics and Genomics, Boston Children's Hospital, Harvard Medical School, Boston, MA, USA. [9]New York Genome Center, New York, NY, USA. [10]Department of Genetics, Stanford University, Stanford, CA, USA. [11]Department of Computer Science, Stanford University, Stanford, CA, USA. [12]Department of Biomedical Data Science, Stanford University, Stanford, CA, USA. ***Corresponding author. Email: kfarh@illumina.com** †These authors contributed equally to this work. ‡Present address: Arsenal Biosciences, Inc., South San Francisco, CA, USA. §Present address: DELFI Diagnostics, Inc., Palo Alto, CA, USA.

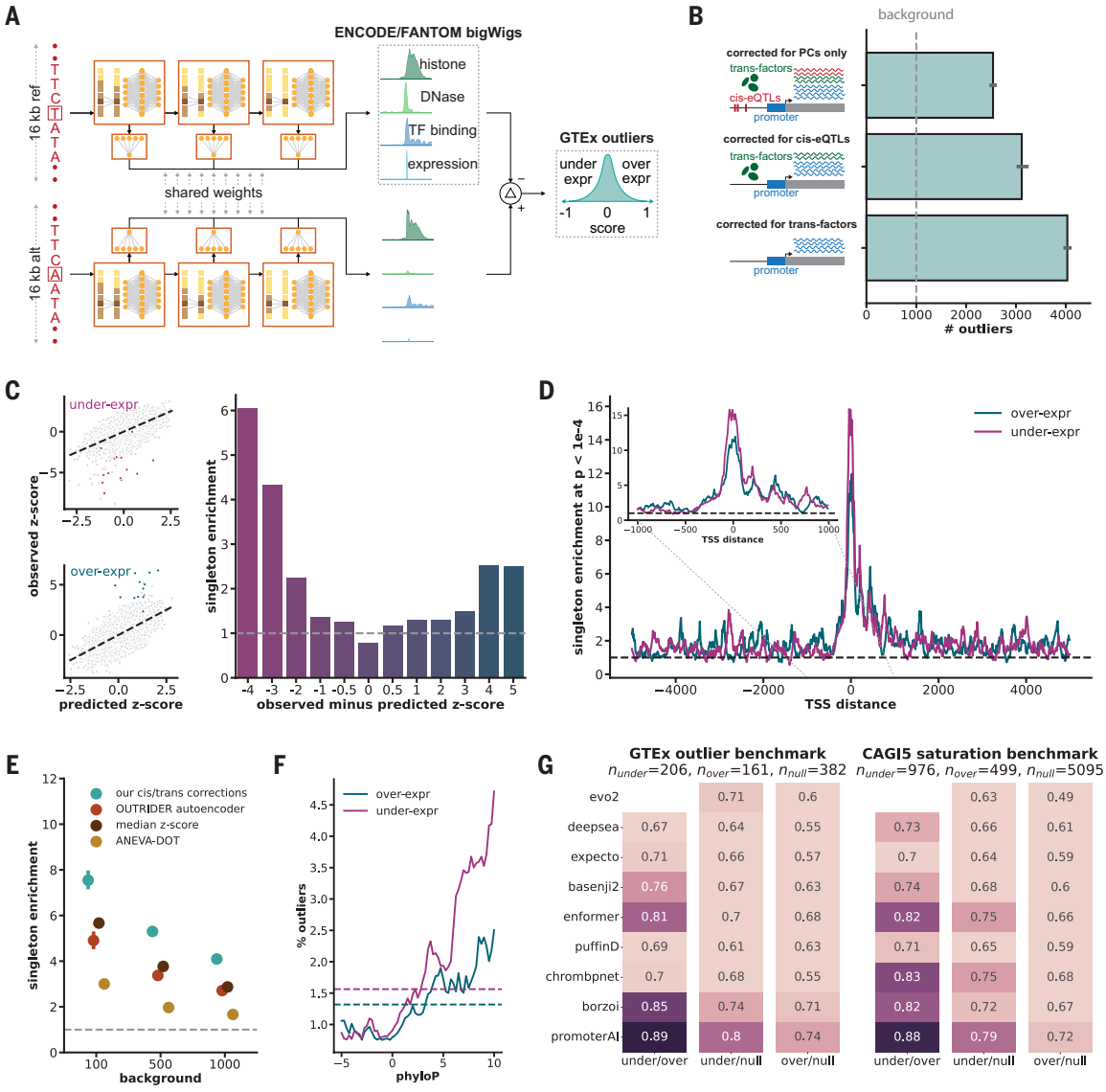


Fig. 1. Fine-tuning PromoterAI with GTEx multitissue gene expression outliers. (**A**) Schematic representation of PromoterAI. (**B**) Number of expression outliers observed in promoters (TSS ± 500 bp) at the same *p* value threshold that yields 1000 outliers in a shuffled background (gray line), after correcting expression levels for principal components (PC) (top), common cis-eQTLs (middle), and trans-patterns of gene expression (bottom). (**C**) Examples of variants with underexpression (purple) and overexpression (blue) consequences are shown, with the variant carrier's expression represented by the colored dots and the rest of the cohort shown in gray (left). Enrichment of expression outliers over shuffled background is shown for varying differences between observed *z*-scores and predicted *z*-scores, averaged across tissues (right). (**D**) Enrichment of outliers over shuffled background in overlapping 100-bp windows from 5 kb upstream to 5 kb downstream of the TSS, with 10-bp steps. (**E**) Comparing the number of outlier promoter variants detected using various methods, using three different *p* value (teal, red, and gold points) or *z*-score cutoffs (brown points) that admit 100, 500, or 1000 outliers from the shuffled background. The mean and 95% confidence interval are calculated across 10 shuffled instances. (**F**) Percentage of promoter variants that are overexpression (blue) or underexpression (purple) outliers, binned by conservation, as measured by phyloP-470 way. The dotted lines show the overall percentage of promoter variants that are expression outliers as a baseline. (**G**) Performance of PromoterAI and other models on held-out GTEx outliers (left) and CAGI5 saturation mutagenesis promoter variants (right), as measured by auROC.

table S2). Individuals whose observed gene expression deviated from their predicted gene expression were enriched up to sixfold for carrying a rare promoter variant in that gene for underexpression and 2.5-fold for overexpression (Fig. 1C). To identify the extent of the region surrounding the TSS where we can robustly identify multitissue expression outliers, we calculated enrichments of variants with significant effects on gene expression (*t* test, $p < 1 \times 10^{-4}$) within 100-bp sliding windows at distances up to 5 kb from the TSS (Fig. 1D). This analysis revealed that expression outliers were predominantly located within 500 bp upstream and downstream of the TSS. Although these enrichments improved when the analysis was restricted to conserved promoters (fig. S1B), selecting the most frequently used TSSs across tissues was critical for maximizing enrichments (fig. S1C and table S3).

We benchmarked our approach against other existing methods to quantify aberrant expression, including an unsupervised autoencoder model from OUTRIDER (*31*) and two summary statistics available from GTEx (*32*): median *z*-scores across tissues and median *p* values from an allelic imbalance test (ANEVA-DOT) (*33*). Compared with the other methods, when choosing thresholds that result in the same false

discovery rate in shuffled controls, our approach detected greater enrichment of multitissue outliers (Fig. 1E).

Using allele-specific expression to assess variants that have available phasing data, we found that alleles carrying overexpression outliers had significantly higher allelic expression compared with alleles carrying underexpression outliers ($p = 7.4 \times 10^{-29}$; fig. S1D). As a further orthogonal validation, we observed that the proportion of promoter variants with either over- or underexpression effects was highest for positions with high constraint across 470 mammals (phyloP-470 way; Fig. 1F), indicating that both types of outliers disproportionately fall within conserved sequence elements.

Next, we used multitissue outliers, as well as matched control variants that came from the promoters of the same genes but showed no effects on expression, and trained PromoterAI on the variants from the odd chromosomes (see Materials and methods for details), whereas variants from the even chromosomes were set aside for testing and evaluating the model. We benchmarked PromoterAI, Evo2, DeepSEA, Basenji, ExPecto, Enformer, PuffinD, ChromBPNet, and Borzoi on three variant classification tasks, namely, under- versus overexpression, underexpression versus control variants that did not affect gene expression (null), and overexpression versus null (Fig. 1G, left). PromoterAI performed the best out of these models across all three metrics by achieving an auROC (area under the receiver operating characteristic curve) of 0.89, 0.80, and 0.74, respectively. We also benchmarked the performance of each classifier on multiple massively parallel reporter assay (MPRA) saturation mutagenesis datasets, including the Critical Assessment of Genome Interpretation (CAGI5) dataset, where we focused on promoters of disease-associated genes (*3*), and another dataset comprising promoters with known eQTLs and hits from genome-wide association studies (GWASs) (*34*). PromoterAI achieved the best performance (Fig. 1G, right, and fig. S1E) and also demonstrated strong per-gene predictive capability, as evidenced by correlations between model scores and MPRA effect sizes calculated separately for each gene (fig. S1F).

Under- and overexpression variants primarily act by disrupting motifs

To understand the basis of PromoterAI's predictions, we systematically performed in silico mutagenesis in the vicinity of GTEx outliers, using only the variants from the even chromosomes that were set aside for testing and evaluating the model. Consistent with the model learning the underlying biological mechanisms, PromoterAI assigned high scores to variants that disrupted the motifs of TFs with widely known effects on gene expression, with several representative examples shown in Fig. 2A and fig. S2A. Underexpression variants were particularly enriched for disrupting ETS motifs (Fig. 2B), which are recognized to be involved in a wide range of regulatory processes (*35*), along with YY1, ATF1, and NRF1 motifs, which are known to have broad regulatory functions at promoters (*36*–*39*). By contrast, overexpression outliers were enriched for disrupting E2F motifs (Fig. 2B), which have roles in cell cycle control and tumor suppression (*40*), alongside other transcriptional families such as NFKB, INSM1, ERRα, and TFAP2 (*41*–*44*). We inserted these motifs along the lengths of promoters to assess their effects using PromoterAI and found that the predictions were consistent with the evidence from expression outliers (fig. S2B) while also localizing the optimal region for maximal effect to 100 bp immediately upstream and downstream of the TSS (*45*). These in silico experiments reinforce that PromoterAI successfully learns sequence determinants of promoter regulation.

We further examined the relative contributions of variants that affect gene expression by strengthening or weakening motifs using a curated list of motifs (table S4) exclusively associated with activating or repressive Gene Ontology (GO) terms (*46*). We found that underexpression outliers were enriched for weakening of motifs associated with only activating GO terms (Fig. 2C, left). By contrast, overexpression outliers were enriched for both weakening of motifs associated with only repressive GO terms and, to a lesser extent, strengthening of motifs associated with only activating GO terms (Fig. 2C, right). Similar trends were observed for motifs associated with both activating and repressive GO terms, subcategorized based on their relative proportions, although the effects were less pronounced owing to the complexity of these motifs (fig. S2C). Our results show that it is generally easier for newly occurring variants to cause outlier gene expression by disrupting existing regulatory components rather than creating new ones, as well as highlighting the important role of transcriptional repressors in promoter regulation.

Next, we investigated the contribution of fine-tuning to PromoterAI's performance, aiming to discern the specific variant types that saw the largest gains. We first stratified expression outliers by the motifs they overlapped and calculated the correlation between the actual and predicted effects of variants before and after fine-tuning. We saw substantial improvement in performance across nearly all motifs (Fig. 2D) as well as across TSS distance (fig. S2D). We also repeated the earlier analysis of inserting motifs along the lengths of promoters, using the models before and after fine-tuning. We observed that the predicted direction of effect aligned more consistently with the evidence from expression outliers after fine-tuning (fig. S2E), suggesting that fine-tuning may overcome limitations in predicting the directionality of motifs, which has been highlighted in recent papers (*26*, *27*). Moreover, we found that the nucleotide positions that experienced the largest differences in PromoterAI scores before and after fine-tuning tended to be highly conserved (Fig. 2E). Given that conservation information was not used during training or fine-tuning, these results provide independent evidence suggesting that fine-tuning with expression outliers enables the model to more effectively learn the underlying causal biological mechanisms. We show representative examples where fine-tuning led to substantial changes in PromoterAI predictions, noting that the model before fine-tuning frequently recognized the underlying motif but predicted the direction of effect incorrectly (Fig. 2F and fig. S2F).

To investigate PromoterAI's internal representations of promoter biology, we extracted feature embeddings of all canonical promoters of protein-coding genes and found that they clustered into three distinct classes (fig. S3A and table S5): a first class of 9234 genes abundantly expressed across most tissues and enriched for activating histone marks and ubiquitously expressed TFs, a second class of 3430 genes characterized by bivalent chromatin, and a third class of 6632 genes with mainly tissue-specific expression and enriched for repressive histone marks (fig. S3, B to F) (*47*). The three classes also differed in expression variability, with the first class resembling low-variability promoters and the second and third classes resembling highly variable promoters (*48*). Observing that the third promoter class bears many enhancer-like characteristics (*49*), we used PromoterAI to extract feature embeddings from distal enhancers and compared them with those from promoters. Indeed, the feature embeddings of distal enhancers closely resembled those of the third promoter class (fig. S3G). This enhancer-like promoter class was notably depleted for conserved elements, further emphasizing its distinct regulatory properties (fig. S3H).

Promoter variants that affect gene expression are under strong negative selection

To measure the extent of negative selection acting on promoter variants in human populations, we turned to the Genome Aggregation Database v3 (gnomAD) cohort (*50*, *51*), which includes WGS data from 71,702 individuals. We used PromoterAI to score each promoter variant, excluding those with protein-coding or splicing effects, and compared the number of predicted expression-altering variants at common allele frequencies (>0.1%) with the number of rare singletons. We based our analysis on the observation that natural selection purges deleterious variants over time, preventing them from becoming widespread in the population (*50*, *52*).

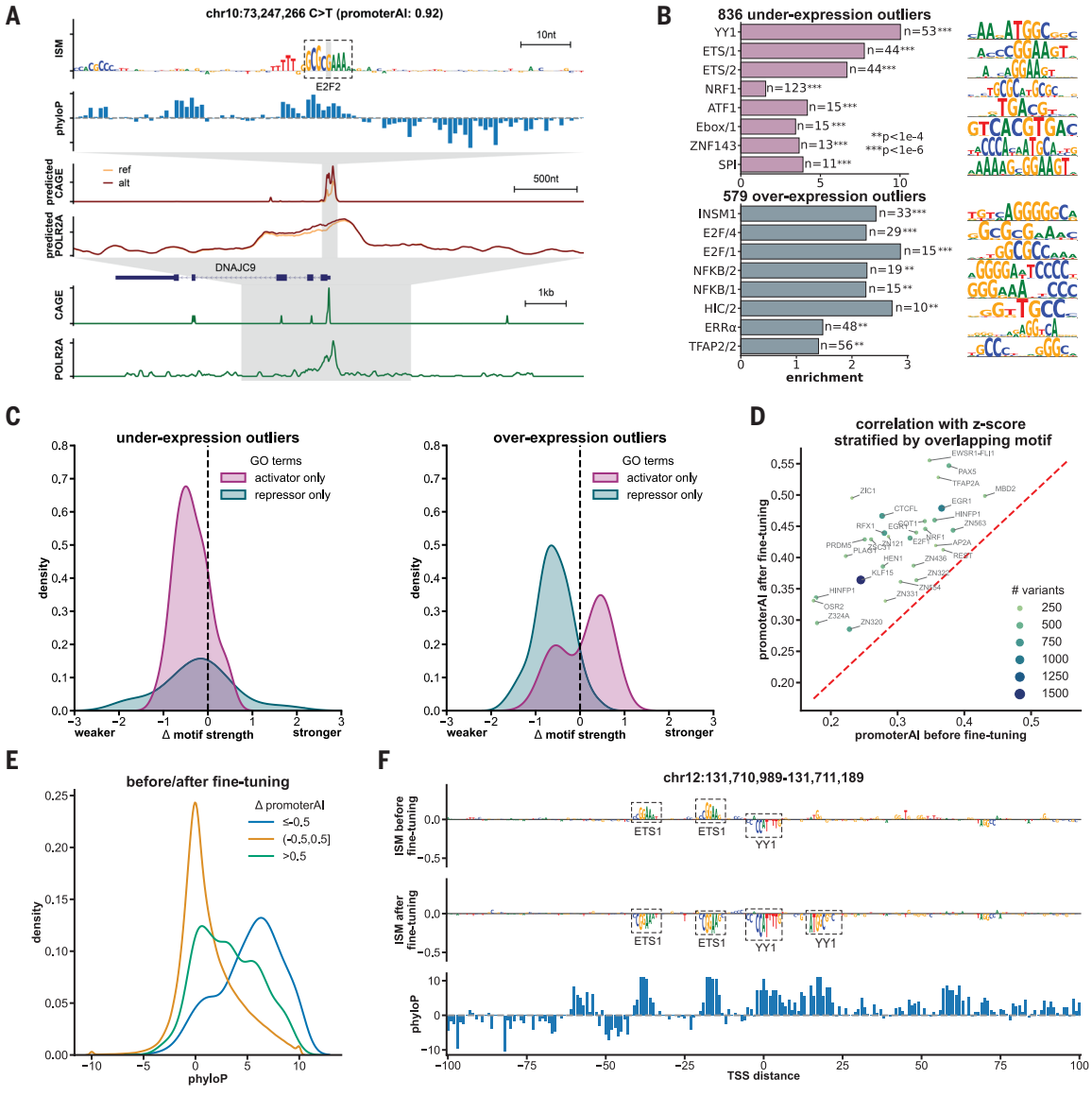


Fig. 2. PromoterAI offers insights into regulatory sequence mechanisms. (**A**) Example of an overexpression outlier (chr10:73,247,266 C>T) in the promoter of the *DNAJC9* gene that disrupts a conserved E2F2 motif. Shown from top to bottom are PromoterAI in silico mutagenesis (ISM) with positive deflection indicating predicted overexpression and negative indicating underexpression, phyloP-470 way, PromoterAI CAGE-seq predictions for the reference and alternate alleles, PromoterAI POLR2A predictions for the reference and alternate alleles, actual FANTOM5 CAGE-seq signal, and actual ENCODE POLR2A chromatin immunoprecipitation sequencing (ChIP-seq) signal. (**B**) Shown are the top eight motifs that are significantly enriched for under- or overexpression outliers relative to null variants, along with the number of outlier variants and *p* values. (**C**) For underexpression (left) and overexpression (right) outliers, the effects on motifs with only activating or only repressive GO terms are shown. Negative *x*-axis values represent motif weakening, whereas positive values represent motif strengthening. Underexpression outliers predominantly act through weakening motifs with only activating GO terms, whereas overexpression outliers more often act through weakening motifs with only repressive GO terms but can also strengthen those with only activating GO terms. (**D**) Correlation between PromoterAI scores and variant *z*-scores is shown before and after fine-tuning, with variants categorized by the motifs they overlap. Fine-tuning increases performance across a wide range of motifs. (**E**) Variants are categorized by change in PromoterAI scores before and after fine-tuning and plotted on a histogram with phyloP on the *x* axis. Variants with large score changes are more likely to be conserved, indicating that the fine-tuning step improves recognition of biologically relevant features. (**F**) ISM scores of PromoterAI before and after fine-tuning in the promoter of the *SFSWAP* gene. Fine-tuning corrects the direction of effect in two ETS1 motifs and recognizes an additional YY1 motif.

Variants predicted by PromoterAI to alter gene expression were strongly depleted of common variants relative to rare variants, indicating that expression-altering variants are being actively removed by natural selection (Fig. 3A). This depletion applied to both predicted under- and overexpression variants and became more pronounced with increasing magnitude of PromoterAI scores. At PromoterAI scores near +0.5 or −0.5, the observed depletion approached that of missense variants, whereas scores closer to +1 or −1 resulted in a depletion percentage comparable to that of nonsense variants. We further stratified genes by evolutionary constraint, as measured by probability of loss-of-function intolerance (pLI) (*52*). We observed a greater depletion for expression-altering variants in the promoters of high-pLI genes, consistent with these genes being dosage sensitive and associated with haploinsufficient disease mechanisms (Fig. 3B). We also stratified variants by TSS distance, dividing the promoter region into 10-bp nonoverlapping windows and estimating the number of

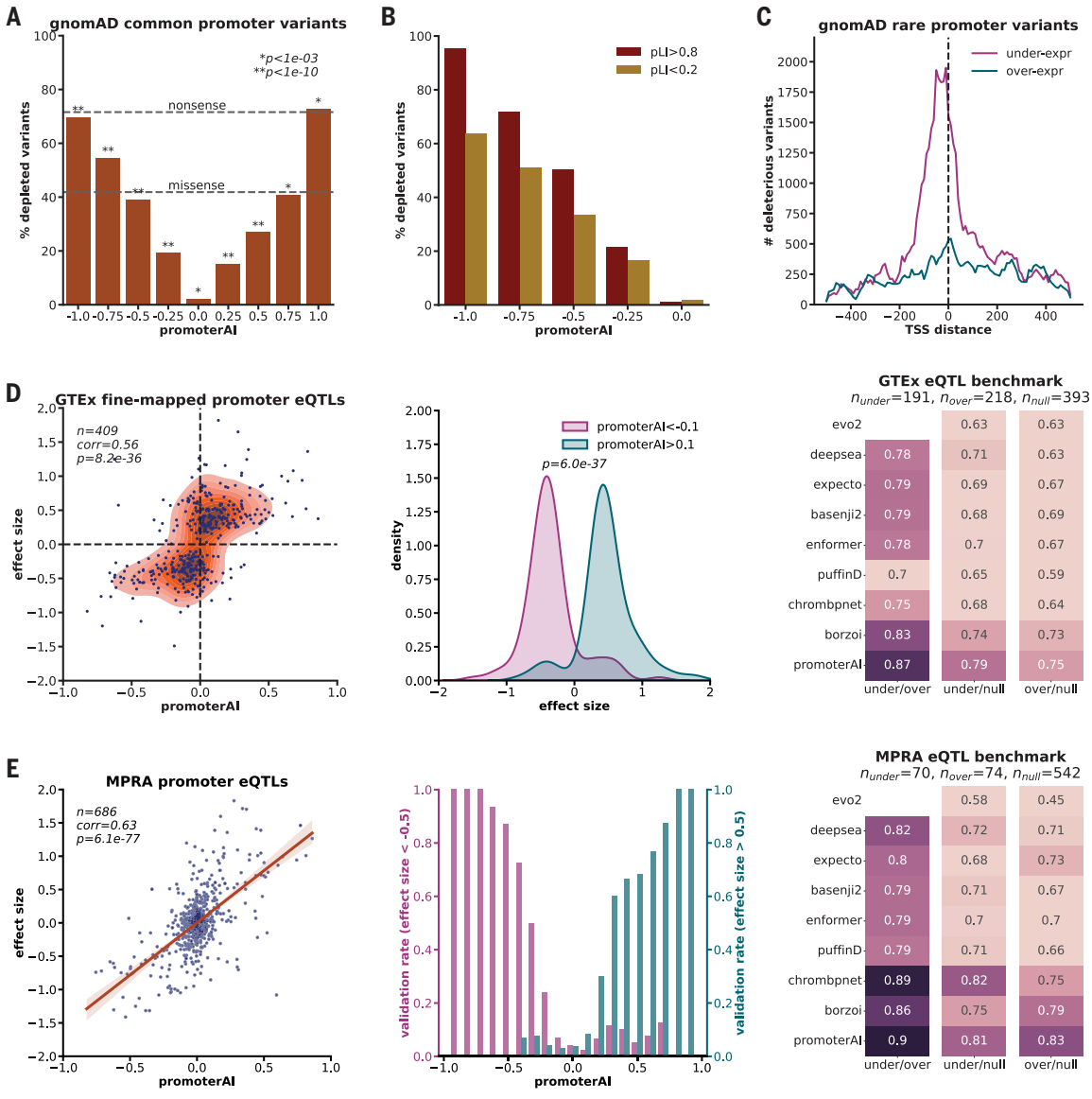


Fig. 3. Validation of PromoterAI predictions using gnomAD depletion and GTEx eQTLs. (**A**) Percentage of depleted common variants in gnomAD for different PromoterAI scores, with zero indicating no predicted effect and large negative or positive values indicating predicted under- or overexpression consequences. Depletion becomes more pronounced as PromoterAI scores approach −1 or 1, indicating that both under- and overexpression variants are subject to natural selection. (**B**) Depletion plotted separately for genes with high or low pLI, indicating that predicted underexpression variants in high-pLI genes undergo stronger purifying selection. (**C**) Under- and overexpression singleton variants in gnomAD expected to be depleted by natural selection, calculated within 10-bp nonoverlapping windows around the TSS. (**D**) Validation of PromoterAI using GTEx fine-mapped promoter eQTLs. Shown are the Pearson correlation between PromoterAI scores and effect sizes of fine-mapped promoter eQTLs (left), the observed effect size distributions of eQTLs predicted by PromoterAI to cause under- or overexpression (middle), and a comparison of the performance of PromoterAI and other models on the GTEx eQTL benchmark, with auROC shown (right). (**E**) Validation of PromoterAI using MPRA experiments consisting of promoter eQTLs. Shown are the Pearson correlation between PromoterAI scores and MPRA effect sizes of promoter eQTLs (left), MPRA validation rates across the range of PromoterAI scores (middle), and a comparison of the performance of PromoterAI and other models on the MPRA eQTL benchmark, with auROC shown (right). The shaded region indicates the 95% confidence interval.

singleton variants expected to be depleted by natural selection in each window (Fig. 3C). Similar to expression outliers being enriched near the TSS, the depletion signal also peaked in a region within 100 bp of the TSS, with a notably stronger signal for underexpression than overexpression variants, suggesting that underexpression variants tend to be more deleterious on average.

PromoterAI accurately predicts the effects of fine-mapped promoter eQTLs

We assessed PromoterAI's ability to predict the effects of fine-mapped GTEx eQTLs. For this, we identified 409 eQTLs that mapped to a single variant with posterior probability >0.9 in multiple tissues using CAVIAR (*53*), after excluding splice variants, protein-coding variants, and GTEx rare variants that were used for fine-tuning, which we followed in all subsequent benchmarking analyses. PromoterAI scores were significantly correlated with the observed eQTL effect sizes [Pearson correlation coefficient (r) = 0.56, $p = 8.2 \times 10^{-36}$; Fig. 3D, left], and variants that were predicted to cause under- or overexpression showed nearly nonoverlapping effect size distributions ($p = 6.0 \times 10^{-37}$; Fig. 3D, middle). Next, we compared PromoterAI's performance at classifying eQTLs with that of other classifiers. For this, we included 393 control promoter eQTLs from the same genes as the fine-mapped

eQTLs, focusing on those that were not prioritized by fine-mapping (posterior probability <0.1 in all tissues). For each of the three classification tasks, namely distinguishing underexpression eQTLs versus overexpression eQTLs, underexpression eQTLs versus control variants, and overexpression eQTLs versus control variants, PromoterAI's auROC was 0.87, 0.79, and 0.75, respectively, exceeding the performance of other classifiers (Fig. 3D, right). We note that the lower auROC values in this task reflect that the statistical fine-mapping procedure includes a degree of uncertainty in the assignment of the fine-mapped causal variant owing to linkage disequilibrium.

We leveraged recently generated MPRA data for these eQTLs (*34*), which directly assays the effects of fine-mapped variants in cell culture and avoids the limitations posed by linkage disequilibrium (*54*). We found a robust correlation of 0.63 ($p = 6.1 \times 10^{-77}$) between PromoterAI scores and measured effect sizes across 686 promoter eQTLs (Fig. 3E, left). We calculated the validation rates across the range of PromoterAI scores, defined as the proportion of variants with effect size in the assay exceeding the recommended cutoffs of −0.5 or +0.5. Validation rates increased monotonically with PromoterAI scores along both directions, with nearly all variants predicted to have large effects validating successfully in the assay (Fig. 3E, middle). We used the MPRA dataset as an additional benchmark to test each classifier's performance at distinguishing between overexpression, underexpression, and null variants, with PromoterAI showing the best results (Fig. 3E, right; 0.90, 0.81, and 0.83, respectively, as measured by auROC).

PromoterAI predicts protein levels and phenotypic traits in 500,000 UK Biobank individuals

The UK Biobank (UKBB) (*55*) contains both WGS and health records for 500,000 participants, making it ideal for validating PromoterAI's predictions on protein expression and quantitative clinical phenotypes in a large human cohort. We first applied PromoterAI to predict the effects of noncoding variants on blood plasma protein levels, using measurements of 2923 proteins in 54,219 UKBB participants from the Pharma Proteomics Project (*56*). We identified 104 cis-pQTLs (protein quantitative trait loci) within the promoters of these genes that were not in linkage disequilibrium with other promoter, missense, or protein-truncating variants (PTVs) and observed that their effect sizes were significantly correlated with PromoterAI scores ($r = 0.56$, $p = 7.9 \times 10^{-10}$; Fig. 4A, left), with the distribution of scores showing clear separation between under- and overexpression pQTLs (fig. S4A). The correlation decreased when linkage disequilibrium was not accounted for (fig. S4B) but improved when mRNA stability was incorporated, reaching 0.6 for pQTLs in genes with high stability (fig. S4C). Predicted under- and overexpression variants displayed wide differences in their protein expression ($p = 3.6 \times 10^{-16}$; Fig. 4A, middle) and were enriched in close proximity to the TSS (Fig. 4A, right).

We extended our analysis to 1715 rare noncoding promoter variants (allele frequency <0.1%), excluding variants with splicing or protein-coding consequences and requiring that the variants be present in at least two persons to mitigate the noise in individual protein-level measurements. Across these 54,219 individuals, PromoterAI scores were robustly correlated with measured plasma protein levels ($r = 0.48$, $p = 2.8 \times 10^{-101}$; Fig. 4B, left), with most of the rare variants with PromoterAI scores >0.5 or <−0.5 causing changes in plasma protein levels by two standard deviations or more (Fig. 4B, middle). Using this dataset as a benchmark, we assessed the ability of each classifier to distinguish between over- and underexpression, underexpression and null, and overexpression and null variants and observed that PromoterAI had the overall best performance (Fig. 4B, right; 0.91, 0.77, and 0.78, respectively, as measured by auROC).

We explored the impact of rare noncoding variants on quantitative clinical phenotypes in 500,000 UKBB participants, using a list of 100 previously published gene-phenotype pairs where rare PTVs have been reported to significantly increase or decrease the phenotype ($p < 1 \times 10^{-8}$ on rare variant burden test) (*57*). For each gene-phenotype pair, we calculated effect size using linear regression between PromoterAI scores and phenotype values and found that the effect sizes of promoter variants and PTVs were significantly correlated ($r = 0.37$, $p = 1.8 \times 10^{-4}$; Fig. 4C). Whereas promoter variants and PTVs had largely consistent effects on phenotype and direction, promoter variants generally had smaller effect sizes. Among specific gene-phenotype pairs, blood alanine aminotransferase levels were highly correlated with PromoterAI scores in the *GPT* gene ($r = 0.64$, $p = 7.6 \times 10^{-9}$; Fig. 4D, left), whereas for high-density lipoprotein (HDL) cholesterol levels, the aggregate PromoterAI scores of promoter variants in the *LCAT* and *CETP* genes exhibited a correlation of 0.55 ($p = 4.0 \times 10^{-9}$) with lab values (Fig. 4D, right). These results highlight PromoterAI's ability to identify noncoding variants that affect quantitative clinical phenotypes and biomarkers, furthering our understanding of the genetic basis of complex human traits and common diseases.

Expression-altering promoter variants are enriched in patients with rare genetic disorders

Large-scale sequencing studies of patients with rare genetic diseases have found that pathogenic protein-coding variants can be identified in fewer than half of these patients, leaving the rest without a definitive genetic diagnosis (*58*, *59*). To investigate the extent to which noncoding variants are potentially contributing to rare diseases, we applied PromoterAI to score singleton variants in the promoters of known rare-disease genes for patients in the Genomics England (GEL) cohort (*60*). We counted the number of times PromoterAI predicted an expression-altering variant in a gene that was specific to the patient's disease, based on gene panels annotated by the Genomics England PanelApp database for each rare disease (Fig. 5A) (*61*, *62*). To estimate background expectation for such matches to occur by chance, we shuffled the cohort 100 times, each time randomly reassigning variants to each individual. We focused on a set of 7948 probands with no already-prioritized variant (TIER1) and with fewer than 100 causative genes in their disease gene panels to limit noise and the likelihood of spurious matches (fig. S4, D and E). Rare heterozygous variants predicted to cause underexpression by PromoterAI (score <−0.05) were significantly enriched in genes specific to patients' disease compared with shuffled controls (1.3×, $p = 3 \times 10^{-4}$, $n = 188$). This enrichment increased when restricting the analysis to genes with an autosomal dominant inheritance pattern (1.5×, $p = 1 \times 10^{-5}$, $n = 138$) and genes with a loss-of-function mechanism (1.6×, $p = 2 \times 10^{-4}$, $n = 84$; Fig. 5, A and B) (*63*), consistent with these variants causing disease through a haploinsufficiency mechanism. To ensure that these variants reflected noncoding regulatory effects, we excluded missense, protein-truncating, and splice variants while calculating enrichments (fig. S4F).

We estimated diagnostic yield using the number of observed variants minus the expected number seen in shuffled controls across different variant categories (Fig. 5C). Overall, within this rare genetic disease cohort, we estimated that promoter variants account for 6% of the total diagnostic yield, which, when combined with the 14% attributable to cryptic splice variants (SpliceAI >0.2), implies that noncoding variants account for roughly one in five cases (Fig. 5D). As an additional control, we included synonymous variants and missense variants that were classified as benign (PrimateAI-3D <0.2) and found that neither of these variant types showed significant enrichment compared with the randomly shuffled background. We did not observe a significant enrichment for predicted overexpression variants in the annotated genes from PanelApp (fig. S4G). Given the evidence for their deleteriousness in human populations as indicated by their depletion in the gnomAD cohort, overexpression promoter variants may account for additional rare genetic disease cases, but with different genes and phenotypes than protein-coding variants.

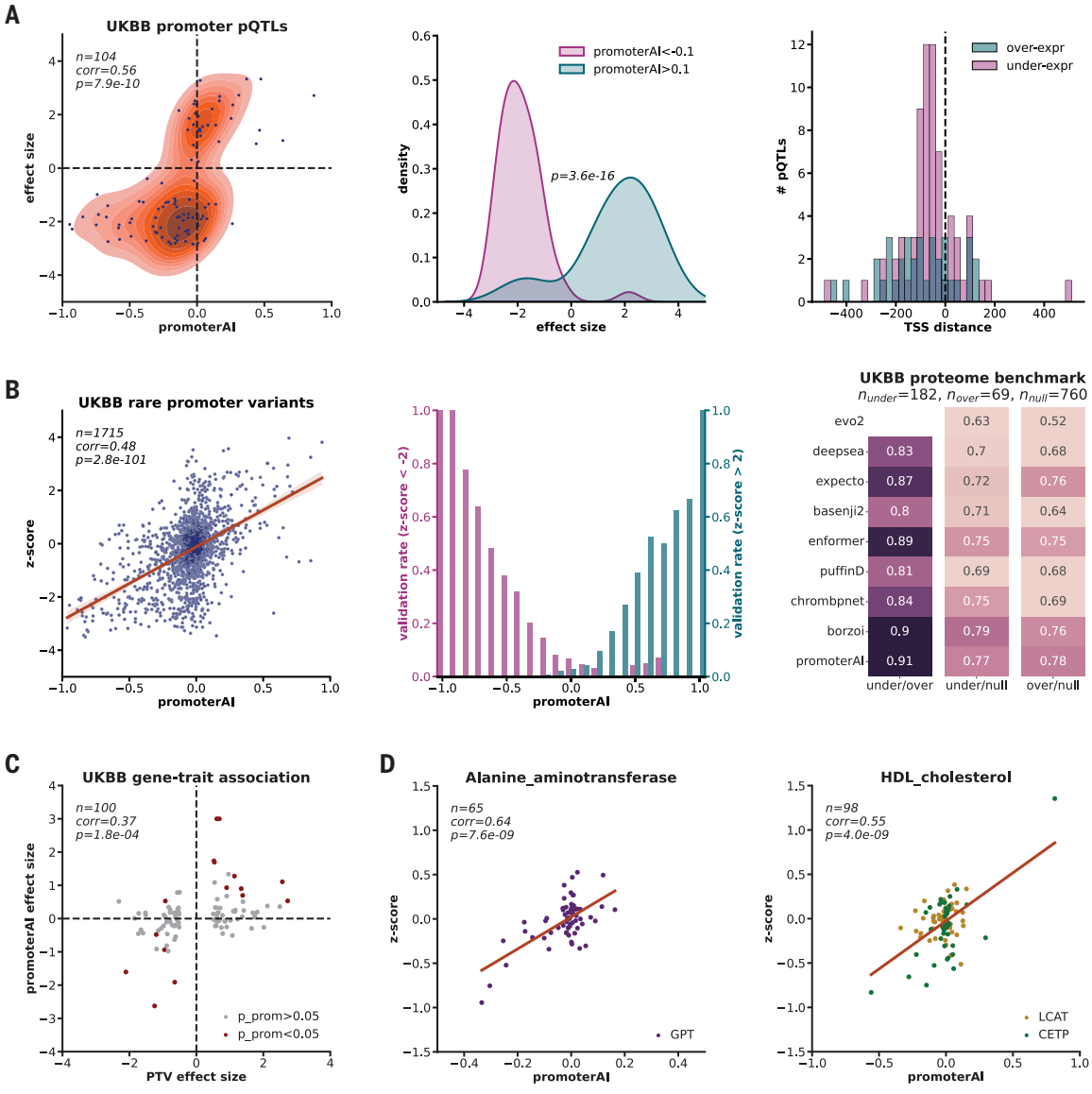


Fig. 4. PromoterAI predicts effects of noncoding variants on UKBB protein levels and quantitative phenotypic traits. (**A**) Validation of PromoterAI using UKBB promoter pQTLs. Shown are the Pearson correlation between PromoterAI scores and effect sizes of UKBB promoter pQTLs (left), observed effect size distributions of pQTLs predicted by PromoterAI to cause under- or overexpression (middle), and the distribution of UKBB promoter pQTLs around the TSS (right). (**B**) Validation of PromoterAI using proteomics measurements of UKBB rare promoter variants. Variants were required to have at least two carriers to mitigate noise in individual measurements. Shown are the Pearson correlation between PromoterAI scores and effect sizes of rare promoter variants (left), proteomics validation rates across the range of PromoterAI scores (middle), and a comparison of the performance of PromoterAI and other models on the UKBB proteomics benchmark, with auROC shown (right). (**C**) UKBB gene-trait association effect sizes predicted using PromoterAI scores correlate with those estimated from PTVs. (**D**) Shown are the Pearson correlations between alanine aminotransferase levels and PromoterAI scores of *GPT* promoter variants (left) and HDL cholesterol levels and PromoterAI scores of *LCAT* and *CETP* promoter variants (right).

We assessed PromoterAI's predictions using whole-blood RNA-seq data from 4949 predominantly undiagnosed rare-disease patients in the GEL cohort. PromoterAI scores in these probands were robustly correlated with changes in gene expression observed in blood RNA-seq data ($r = 0.61$, $p = 6.6 \times 10^{-171}$; Fig. 5E, left), and most of the variants with PromoterAI scores >0.5 or <−0.5 tended to alter gene expression by at least two standard deviations in the predicted direction (Fig. 5E, middle). We used this dataset as an additional benchmark to compare the performance of PromoterAI with that of other classifiers and found that PromoterAI outperforms other methods at separating variants that cause overexpression, underexpression, or no significant changes (null) (Fig. 5E, right; 0.90, 0.78, and 0.78, respectively, as measured by auROC). The strong correlations between RNA-seq *z*-scores and model predictions were limited to promoter-proximal variants, with little to no signal observed at more distal positions (fig. S4H). Correlations were also substantially higher for variants present in multiple individuals compared with singletons, likely reflecting reduced expression noise from aggregating across carriers. These results help reconcile our observations with those of a previous study (*26*).

We illustrate two *TERT* promoter variants that increase expression and cause interstitial pulmonary fibrosis (*6*). PromoterAI correctly identified these as overexpression variants by detecting the creation of GA-binding protein alpha chain (GABPA) binding sites (Fig. 5F, top),

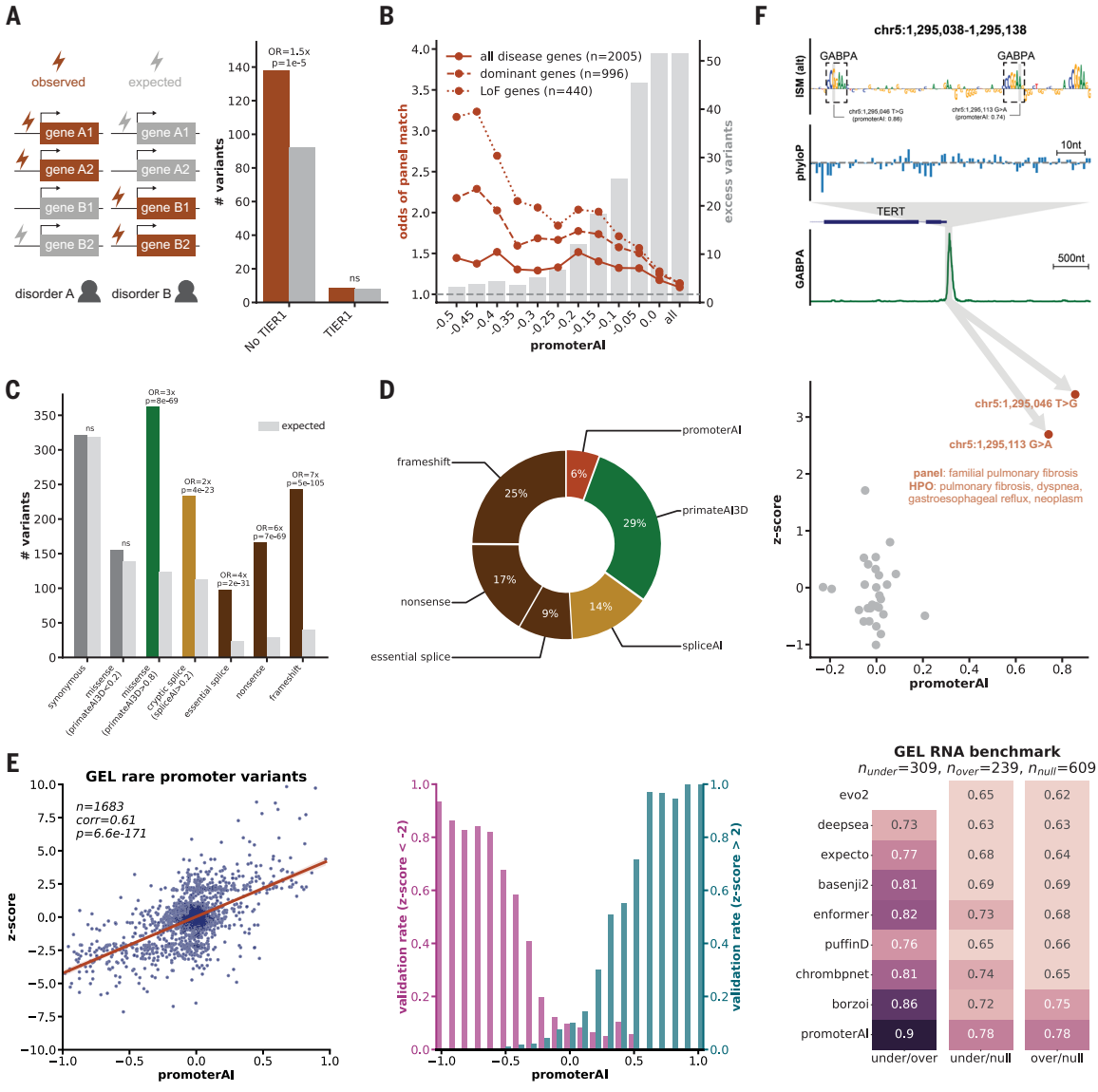


Fig. 5. PromoterAI identifies functional promoter variants in GEL rare-disease cohort. (**A**) Counts of PromoterAI-predicted underexpression variants in genes specifically matching the patients' disease (orange) versus the expected number obtained by shuffling variants across individuals (gray). Odds ratio (OR) and *p* value are shown for singleton variants with a PromoterAI score <−0.05 in dominant panel genes and were calculated using a Fisher's exact test. Individuals were split into two groups based on TIER1 variant status: those with at least one TIER1 variant, defined as high-impact or de novo moderate-impact variants in a curated list of PanelApp genes (serving as the control group), and those without any TIER1 variants. (**B**) Odds ratio for the enrichment of PromoterAI-predicted variants in matching disease genes across various PromoterAI score cutoffs (left *y* axis) and the number of excess variants over expected at each score cutoff (right *y* axis) in probands with no TIER1 variant already prioritized. The solid line included all disease genes, the dashed line was restricted to those with the dominant mode of inheritance, and the dotted line was further restricted to those with known loss-of-function (LoF) variants. Singleton variants within 500 bp of any protein-coding transcript were included, restricted to TSS with support from CAGE-seq (average read count ≥2). Counts in the legend represent the number of PanelApp genes included in each category. (**C**) Observed (colored bar) versus expected (gray) number of variants in matching dominant disease genes, shown for different categories of variant annotations. Deleterious missense was defined as PrimateAI-3D >0.8 and cryptic splice as SpliceAI >0.2; synonymous, essential splice, nonsense, and frameshift annotations were obtained with Variant Effect Predictor (VEP). ns, not significant. (**D**) Same as (C) but expressed as relative proportions. (**E**) Validation of PromoterAI using peripheral blood RNA-seq data from 4949 GEL probands. Variants were required to have at least two carriers to mitigate noise in individual measurements. Shown are the Pearson correlation of PromoterAI scores and RNA-seq *z*-scores of rare promoter variants (left), RNA-seq validation rates across the range of PromoterAI scores (middle), and PromoterAI performance compared with that of other models in predicting overexpression, underexpression, or null expression in the GEL probands, with auROC shown (right). (**F**) Example of pathogenic promoter variants in the *TERT* gene that create GABPA motifs and lead to increased expression, correctly predicted by PromoterAI (top). These variants are carried by probands in the GEL RNA-seq dataset with familial pulmonary fibrosis and show strongly increased expression relative to other promoter rare-variant carriers in this cohort (bottom).

with predictions validated by strong overexpression observed in blood RNA-seq data (Fig. 5F, bottom). Although our results show that RNA-seq can serve as additional validation, we note that when using RNA-seq–identified underexpression outliers alone (*z*-score <−2) to interpret promoter variants across the set of 4949 patients, we did not observe significant enrichment in disease genes specific to the patients' phenotype (1.01×, $p = 0.8$, $n = 188$). A plausible explanation may be tissue-specific differences in gene expression observed in blood RNA-seq data versus disease-relevant cell types, which PromoterAI circumvents by fine-tuning on multitissue expression outliers.

To experimentally validate PromoterAI's predictions, we measured the effects of 13,798 promoter variants from GEL probands with MPRA conducted in lymphoblastoid cells (table S6). We constructed 200-bp oligo libraries containing the reference and alternate alleles for each variant, cloning them into a reporter backbone with a minimal promoter and green fluorescent protein (GFP) reporter. We performed three independent transfections in GM12878 cells and sequenced plasmid DNA and RNA 24 hours after transfection. Variant effect sizes were calculated based on the change in the RNA/DNA ratio between the reference and alternate alleles. We observed a strong correlation between PromoterAI scores and MPRA effect sizes ($r = 0.64$, $p = 2.9 \times 10^{-17}$; Fig. 6A, left), reaffirming PromoterAI's ability to predict functional variants. We also found that blood RNA-seq z-scores correlated more strongly with PromoterAI scores ($r = 0.55$, $p = 4.5 \times 10^{-12}$) than MPRA effect sizes ($r = 0.45$, $p = 3.4 \times 10^{-8}$; Fig. 6A, middle and right) and that genes associated with the carriers' disease phenotype were not significantly enriched for MPRA-prioritized variants (Fig. 6B). To investigate why MPRA was less effective than PromoterAI in prioritizing variants, we examined differentially enriched motifs among predicted under- and overexpression variants for each method (Fig. 6C). Underexpression variants predicted by MPRA were enriched for factors such as TFAP2/2 and E2F/2, whereas multitissue RNA-seq (Fig. 2B) and PromoterAI found them enriched in overexpression variants, indicating a directional discrepancy in predicting motif effects between methods. Further analysis of directionally discordant predictions revealed that underexpression variants predicted only by PromoterAI were more conserved than those predicted only by MPRA (Fig. 6D). These findings highlight potential limitations of MPRA experimental data from individual cell lines for variant interpretation.

To further understand the utility of PromoterAI for rare diseases, we applied PromoterAI to known pathogenic and benign promoter variants from the ClinVar database (*64*). In classifying pathogenic versus benign promoter variants, PromoterAI achieved an auROC of 0.76, outperforming other methods (fig. S5A), although we note that the lower auROC may reflect the difficulty of correctly assigning pathogenicity to noncoding mutations. Several representative pathogenic ClinVar variants are highlighted, including four underexpression promoter variants in the *APC* tumor suppressor gene (fig. S5B) that reduce expression by disrupting YY1 binding, leading to gastric adenocarcinoma and proximal polyposis of the stomach (GAPPS) (*65*). Other examples include two underexpression promoter variants in the *LDLR* gene (fig. S5C) that disrupt SP1 binding, resulting in hypercholesterolemia (*66*–*69*); an underexpression promoter variant in the *HNF1A*

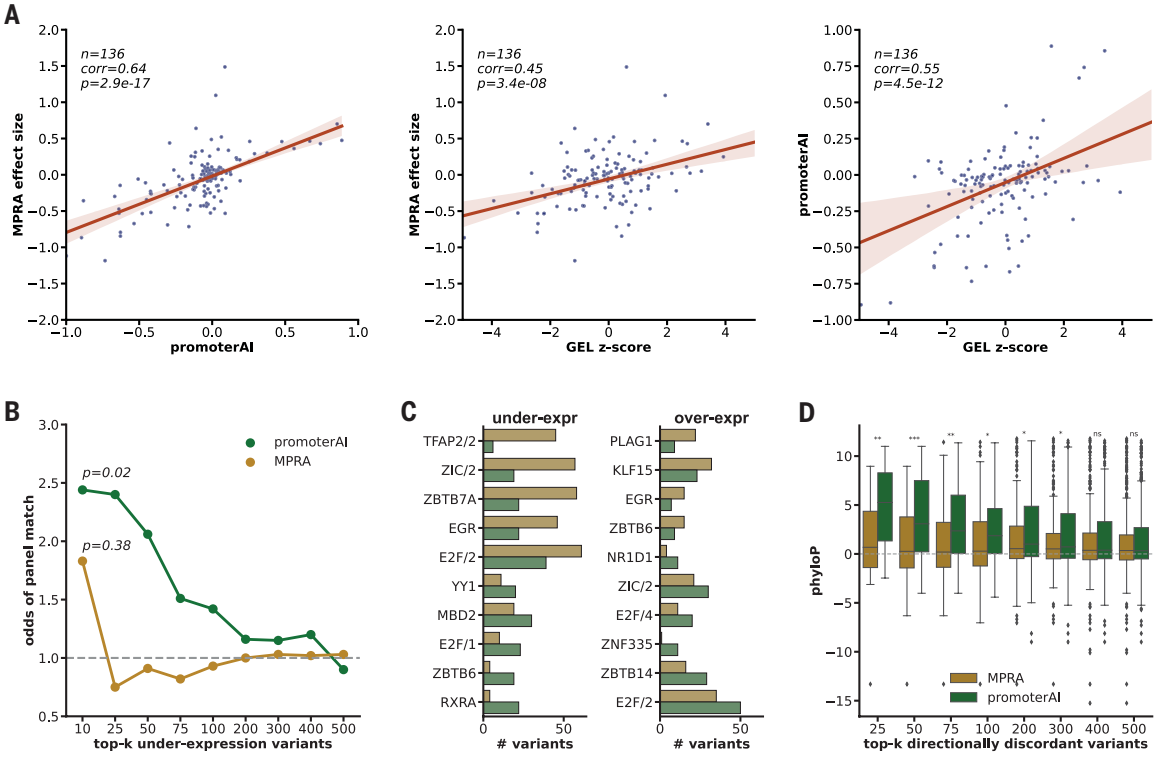


Fig. 6. Comparison of PromoterAI and MPRA as tools for prioritizing variants in the GEL rare-disease cohort. (**A**) Pearson correlations between PromoterAI scores, MPRA effect sizes, and GEL RNA-seq z-scores for variants within 100 bp of the TSS of panel genes in GEL probands. The analysis includes 66 variants with significant MPRA allelic effects ($p < 1 \times 10^{-4}$) and 70 null variants ($p > 0.05$) from the same genes. The shaded region indicates the 95% confidence interval. (**B**) Promoter variants carried by GEL probands and also assayed with MPRA were analyzed for the odds of affecting a panel gene at different score thresholds, using PromoterAI and MPRA scores. The thresholds are matched to ensure that each method predicts exactly k underexpression variants, with k varying from 10 to 500. PromoterAI shows a clear increase in odds as stricter thresholds are applied, a pattern not observed with MPRA. (**C**) Differentially enriched motifs between expression outliers predicted by PromoterAI (green) and MPRA (beige). Underexpression variants predicted by MPRA are enriched for motifs such as TFAP2/2 and E2F/2, whereas RNA-seq (Fig. 2B) and PromoterAI identify these as enriched in overexpression variants. (**D**) Shown is the distribution of phyloP-470 way values for the top-k directionally discordant variants, defined as the k most confident underexpression predictions by one method that are predicted as overexpression by the other, with k varying from 25 to 500. Green boxes represent variants classified as underexpression by PromoterAI but as overexpression by MPRA, whereas beige boxes represent variants classified as underexpression by MPRA but as overexpression by PromoterAI. Underexpression variants identified by PromoterAI show significantly higher conservation than those identified by MPRA, providing further credence to its predictions. Significant differences were assessed using a t test. ns, not significant; *$p < 0.05$; **$p < 0.01$; ***$p < 0.001$.

transcription factor gene (fig. S5D) that disrupts HNF4A binding, affecting downstream target gene expression and contributing to maturity-onset diabetes of the young (*70*); and two underexpression promoter variants in the *TH* gene (fig. S5E) that disrupt CREB binding, causing tyrosine hydroxylase deficiency and dystonia (*71*–*74*). These examples demonstrate PromoterAI's ability to identify pathogenic promoter variants that act through diverse mechanisms (fig. S5F).

As a final component of our evaluation, we summarized all benchmark comparisons using area under precision-recall curve (auPRC) to better capture performance on imbalanced datasets (fig. S6A). We also systematically evaluated the effects of core modeling choices on performance, including network architectures, target profiles, and fine-tuning strategies (figs. S6, B and C, S7, and S8). These findings reinforce the robustness of PromoterAI's performance across diverse benchmarks and evaluation metrics.

Discussion

Noncoding genetic variants account for the vast majority of genome-wide associations for common diseases (*75*, *76*), but their role in rare genetic diseases is only beginning to be defined. In a diverse rare-disease cohort, we demonstrate that promoters of disease-relevant genes are enriched for PromoterAI-predicted expression-altering variants and provide further evidence of their functional impact through MPRA experiments, suggesting that promoter variation may account for a meaningful fraction of cases not previously attributed to coding variation. A crucial factor driving PromoterAI's effectiveness compared with previous methods is fine-tuning on a large-scale dataset of gene expression outliers created using a custom outlier detection pipeline. This fine-tuning process, designed to achieve robust performance on both unseen genes and unseen datasets, improves alignment of predictions with independent evidence from sequence conservation and mitigates challenges in predicting the direction of effect for regulatory motifs.

Given that the present PromoterAI model is constrained by the relatively modest number of gene expression measurements available for training, our findings likely capture only a fraction of the potential impact of promoter variants. Future work leveraging expanded datasets may help identify additional variants, including those with tissue-specific effects or those located further away from the TSS that present models cannot predict accurately. Identifying disease genes that are sensitive to overexpression outliers could further increase the number of rare-disease cases that can be solved by promoter variants. Additionally, characterizing each gene's range of tolerance for expression variability is a key step toward bridging the gap between expression change and pathogenicity, enabling a more comprehensive identification of pathogenic promoter variation (*77*).

Moreover, conservation of sequence elements in the human genome and that of closely related species suggests that other types of noncoding elements may also contribute to rare genetic diseases (*78*), including distal enhancers, 3′ and 5′ untranslated regions, and noncoding RNAs, all of which are critical in regulating gene expression (*79*–*81*). Mounting evidence indicates that the role of variation undetected by short-read sequencing in rare genetic diseases warrants closer investigation (*82*–*84*). These findings underscore substantial gaps in our understanding of how expression changes mediated by noncoding elements contribute to disease. Resolving these complexities will help unlock the full potential of the noncoding genome for diagnostic and therapeutic applications (*85*–*87*).

Materials and methods

PromoterAI training and fine-tuning

Training dataset: We retrieved 502 bigWigs, covering Histone ChIP-seq, DNase-seq, ATAC-seq, and TF ChIP-seq assays from the Encyclopedia of DNA Elements (ENCODE) portal (*88*–*90*) (https://www.encodeproject.org/). These bigWigs were selected to ensure high data quality and diversity across key experimental targets. Specifically, we excluded experiments flagged with audit issues, considered only one biological or technical replicate per experiment, and limited our selection to at most five experiments per target. For certain important targets with known relevance to promoter biology (TBP, NFYA, NFYB, NFYC, SP1, YY1, CTCF, CTCFL, POLR2A, POLR2AphosphoS2, POLR2AphosphoS5, POLR2G, POLR2H, POLR2B, POLR3A, POLR3G, EP300, NELFE, BRD4, PAF1, EZH2, H3K36me3, H3K79me2, H3K79me1, H2AFZ, H3K27me3, H3K27ac, H4K5ac, and H4K20me1) (*37*, *47*), no experiments met our strict filtering criteria. We permitted audit exceptions for these targets to guarantee their inclusion, resulting in a final list comprising 310 human and 192 mouse experiments. We downloaded 'fold change over control' bigWigs for experiments measuring histone modification or transcription factor binding, and 'read-depth normalized signal' bigWigs for those measuring accessibility. We sourced an additional 936 CAGE-seq bigWigs (468 per strand) from the Functional Annotation of the Mammalian Genome v5 (FANTOM5) portal (*29*) (https://fantom.gsc.riken.jp/5/datahub/). In particular, we downloaded strand-specific 'CAGE tag starting site' bigWigs for 188 human and 280 mouse experiments performed on tissues. To manage dynamic range and align scales, ENCODE bigWigs were transformed using $f(x) = \text{arcsinh}(x)$, while FANTOM5 bigWigs were transformed using $f(x) = \text{arcsinh}(1000x)$.

Model architecture: The input to the model is a nucleotide sequence of length 20,480, encoded as a matrix of size $20{,}480 \times 4$, with each nucleotide represented by a one-hot vector: A as [1, 0, 0, 0], C as [0, 1, 0, 0], G as [0, 0, 1, 0], and T as [0, 0, 0, 1]. The model outputs a matrix of size 4096×970, representing predictions for 970 epigenetic and transcriptomic profiles (498 human and 472 mouse) across the central 4096 input positions (fig. S1A).

The input first passes through a fully connected layer to increase the channel dimension from 4 to 1024, followed by 24 MetaFormer blocks. Each MetaFormer block consists of two parts: the first part includes batch normalization and a depthwise convolution layer with residual connection, and the second part includes batch normalization and a feed-forward network that increases the dimension by a factor of 4 and uses ReLU activation, also with residual connection. Each block has three hyper-parameters (C, W, D) corresponding to the number of input/output channels, convolution kernel size, and convolution dilation rate, respectively, effectively capturing features spanning $(W - 1) \times D$ nucleotides. The output of every fourth MetaFormer block passes through a fully connected shortcut layer with ReLU activation to adjust the channel dimension from 1024 to 970, and the average of these outputs, followed by appropriate cropping, forms the final output. We set the kernel size to 5 throughout, which resulted in the model having ~208 million trainable parameters, and chose dilation rates such that the total feature coverage is 16,384 nucleotides. All model weights were initialized with a truncated normal distribution (mean 0 and standard deviation 0.02), while biases were initialized to 0. The model was compiled with mean-squared error (MSE) loss and AdamW optimizer (learning rate 10^{-3}, weight decay 0.01, and clip norm 0.1) (*91*).

Model training: PromoterAI was trained to predict 970 epigenetic and strand-specific transcriptomic profiles at base-pair resolution. We focused exclusively on promoter regions, using a 4096 bp window around each of the 244,939 GENCODE v39 and 81,540 GENCODE vM25 annotated TSS (*92*). Human chromosomes 1-20 and mouse chromosomes 1-19 were used for training the model, while human chromosomes 21-22 were reserved for determining early stopping.

We trained the model for 100 epochs on 8 H100 GPUs, with the learning rate and weight decay following a schedule that included a 10-epoch linear warmup and a 10-epoch linear cool-down. Each epoch used a randomly chosen 10% subset of the training data. The batch size was set to 32 (4 per GPU), with each batch randomly selected from

either human or mouse data and loss calculated only from the profiles of the chosen species. To increase data diversity, we randomly shifted TSS positions during sampling based on a truncated normal distribution (mean 0 and standard deviation 3072). Additionally, we randomly chose the prediction strand for each gene, favoring the sense strand with a 3:1 ratio over the antisense strand. The best model was determined based on the lowest validation loss achieved during training.

Model fine-tuning: PromoterAI was subsequently fine-tuned on promoter variants with known expression consequences. To this end, we started with a comprehensive list of 218,832 GTEx rare promoter variants, each with expression effects calculated from RNA-seq data across multiple tissues (table S2; details provided in the section below). To concentrate on variants that modulate expression mainly via promoter mechanisms, we excluded those located within coding sequence (cdsStart – cdsEnd) of any GENCODE v39 transcript or with SpliceAI score greater than 0.05, as coding and splice variants can often have expression consequences due to mechanisms like nonsense-mediated decay (NMD) and mRNA/protein stability alteration. Finally, we only selected variants that belonged to genes with at least one significant expression-altering variant (under- or overexpression $p < 0.01$, described in the section below). These filtering steps narrowed the list down to 57,795 variants.

For each variant, we obtained two input nucleotide sequences from the sense strand, one for reference and another for alternate allele, each of length 20,480 centered around the variant. Both sequences were processed by identical copies of the model, and the average difference between the profile predictions of the two copies across all positions and channels was calculated. The fully connected layers connecting the various MetaFormer blocks to the output were fine-tuned (~3 million parameters) to minimize MSE between this average and the known expression consequence (z-score).

We used variants from odd chromosomes between 1-20 to fine-tune the model, while variants from chromosomes 21-22 were used for determining early stopping. The other settings for fine-tuning were identical to those of the initial training phase, except that no data augmentation or learning rate schedule was used.

Model ensemble: We trained and fine-tuned two PromoterAI models, one using only human data and the other using both human and mouse data.

Variant score: For each variant, we extracted two nucleotide sequences of length 20,480 centered around the variant on the sense strand, one for reference and another for alternate allele. The difference in their predictions (alt – ref), averaged across output positions (4096 nucleotides) and channels, was used as the variant score. For each variant, the average of the scores from the two models that formed the ensemble was reported as the PromoterAI score.

GTEx multi-tissue expression outliers

Promoter variants: We used RNA-seq and WGS data from the GTEx v8 release, with the generation of these data described in (*30*) and accessed via the Database of Genotypes and Phenotypes (dbGaP) portal (*93*) (study accession phs000424.v9.p2; https://www.ncbi.nlm.nih.gov/projects/gap/cgi-bin/study.cgi?study_id=phs000424.v9.p2). In order to identify promoter variants for inclusion in expression outlier testing, we intersected PASS variants from the GTEx v8 VCF with all protein-coding TSS ± 500 bp positions, as defined by the GENCODE v39 GTF (https://www.gencodegenes.org/human/release_39.html), and then filtered to variants with allele frequency (AF) < 0.5% (restricted to singletons for analyses in Fig. 1, B to F) and located in the promoter region of the protein-coding transcript per gene with the most support from CAGE-seq across tissues. To select this transcript, we took the average read count across all tissues and cell types with CAGE-seq data available from FANTOM5 and selected the annotated transcript start site with the highest read count and used that transcript start site plus a 500 bp window both up and downstream as the promoter region for this gene. If no transcript had read count support from CAGE-seq, we used the default canonical transcript start site from GENCODE v39 to define the promoter (table S3). This definition will be consistently applied throughout this work when referring to canonical protein-coding TSS.

Generation of corrected expression z-scores across tissues: We restricted our analyses to the 49 tissues with at least 70 samples available with RNA-seq data. Within each tissue, we began with the gene-level transcripts per million (TPM) quantification from RNASeQC v1.1.9 (https://github.com/francois-a/rnaseqc) and log-transformed the expression values before scaling those values by gene and individual, after filtering for genes with a minimum TPM > 0.1 and read count > 6 in at least 20% of samples, per (*30*). We filtered to autosomal protein-coding genes only. To account for unmeasured technical or other factors influencing gene expression measurements, we corrected the resulting expression z-scores within each tissue for five genotype principal components (PCs), sex, and 30 expression PCs (available from the GTEx portal: https://gtexportal.org/home/downloads/adult-gtex/qtl) by fitting a linear model predicting scaled expression values from these factors and subtracting the predicted component.

The resulting corrected values were re-scaled within tissue by both gene and individual (the enrichment of singleton promoter variants at this step shown in the top bar of Fig. 1B). Next, we applied further correction by subtracting the gene expression values predicted by up to 5 cis-eQTLs within 1 Mb of the TSS, starting from the eQTL significant variant-gene pair summary statistics produced by (*30*), as these were largely common variants with weaker effects on gene expression than expected by rare variants. For all significant cis-eQTLs identified by (*30*) within range, we assessed the Pearson correlation of genotypes with our corrected expression values and starting from the most significant variant, if the correlation was nominally significant at $p < 0.01$, we fit a linear model predicting expression from the cis-eQTL genotype and subtracted the predicted expression values from the observed value. We repeated this process until no significantly correlated cis-eQTLs remained, or until a maximum of 5 variants were included in the correction. The corrected values were then re-scaled across genes and individuals within tissue (the enrichment of singleton promoter variants at this step shown in the middle bar of Fig. 1B).

Finally, to account for the influence of trans-factors and gene regulatory programs on gene expression, we trained a neural network to predict the expression of genes on one chromosome from the expression of genes on all other chromosomes as input, restricting to autosomes. All samples across all tissues were included in the model. To avoid overfitting, we randomly split these 15,201 samples (tissue by individual) in half and trained two models, using each to predict the expression values in the other sample set. We then subtracted those predicted expression values from the observed expression values and re-scaled within each tissue to generate our final expression z-scores per individual, gene, and tissue instance (table S2; the enrichment of singleton promoter variants at this step shown in the bottom bar of Fig. 1B). The model consisted of one fully connected hidden layer of size 1024 and was trained using an MSE loss with batch size of 32, patience of 20, dropout rate of 0.1, and normal initialization of model weights. The model was trained for a maximum of 100 epochs and was implemented in TensorFlow v2.3.0. To assess the impact of instances where predicted gene expression from this model (including the cis-eQTL and trans-expression corrections) greatly deviated from the observed z-score (averaged across measured tissues per individual), we calculated the odds that an individual with an observed – predicted mean z-score (Δz-score) within a given range carried a promoter

singleton as compared to individuals with Δz-scores not in that range. We constructed a 2×2 contingency table with rows corresponding to carrying a promoter singleton or not and columns indicating whether the individual's Δz-score for the gene falls between [start, end). We reported the resulting odds ratios across Δz-score bins ranging from [-inf, -4) and [5, inf), with intermediate bins each comprising one Δz-score unit (Fig. 1C).

Expression outlier calling and enrichments: To identify expression outliers, for each promoter variant and gene combination, we took the vector of corrected z-scores across tissues from the carrier individual and a vector of control expression values from all non-carrier individuals from the same set of tissues as measured in the carrier. For non-singleton cases, we concatenated the expression vectors across all carriers. We then performed a t-test between the two expression vectors to obtain a p-value for that variant's effect and considered the average z-score across tissues in the carrier as an estimate of the effect size as well as direction. To determine the enrichment of true positive effect variants in a given outlier set obtained using a given p-value threshold, we defined a background expectation of the number of significant variants at that threshold by shuffling the variants across individuals and repeating the test. We then took the number of real observed significant variants at that threshold divided by the number of shuffled variants observed at the same significance level in the background. When shuffling, we randomly reassigned variant sets by sampling a background individual for each original individual. We calculated these enrichments for variants with $p <$ 1e-4 (t-test) for either over- or underexpression at varying distance bins from each protein-coding gene's TSS, considering variants in sliding windows of 100 bp in length every 10 bp from 5,000 bp upstream of the TSS to 5000 bp downstream, averaging between two shuffled instances per window (Fig. 1D).

For each gene, we defined the top TSS as the GENCODE-annotated start site most frequently used across tissues based on CAGE-seq data and stratified it as conserved or not conserved based on average phyloP-470 way values around the start site, using a cutoff of two. The second most frequently used start site was defined as the secondary TSS, while all remaining start sites were categorized as other TSS. We calculated the enrichments for variants with $p < 1 \times 10^{-4}$ within 500 bp of the TSS, stratified by conservation (fig. S1B) and category (fig. S1C).

To compare other approaches measuring expression outlier effects, we downloaded the previously generated ANEVA-DOT (*33*) scores and median expression z-scores (*32*) from the GTEx portal (https://gtexportal.org/home/downloads/adult-gtex/additional_gtex_datasets) and the OUTRIDER R package (https://bioconductor.org/packages/release/bioc/html/OUTRIDER.html) (*31*). We intersected the promoter singleton gene pairs from our outlier tests with the downloaded summary statistics from GTEx and used the median ANEVA-DOT p-value and median z-score for those available. For OUTRIDER, we used the read counts from GTEx tissue samples as inputs for OUTRIDER v1.99.0. The OUTRIDER function 'filterExpression' was used to remove genes with 0 counts in all samples, followed by the 'OUTRIDER' function which performs the full OUTRIDER pipeline including an autoencoder-based correction for confounders. The z-scores from OUTRIDER output were used as input to the same t-test described above. We confirmed that using this gene filtering approach vs the filtering approach described above did not impact the results and restricted to the same set of gene-variant pairs for the t-test comparison (though not for ANEVA-DOT, as it had many missing values). To calculate enrichments across each method, we set a threshold either on the median p-value for ANEVA-DOT, the median expression z-score, the t-test p-value when applied on our corrected z-scores, or the t-test p-value when applied on the OUTRIDER autoencoder-corrected z-scores that resulted in 1000, 500, and 100 significant hits within each method after shuffling variants across individuals. We then compared the number of real significant variants at those thresholds for each method and threshold (Fig. 1E). While OUTRIDER was not designed for this multi-tissue use case, we did want to confirm that our iterative correction steps outperformed an existing autoencoder model to account for non-promoter sequence factors, but different corrections and tests may be optimal for a single tissue analysis or for other variant categories or regions. We also confirmed our expression outliers by assessing the proportion of tested promoter variants that occur at positions with 470-way phyloP (downloaded from https://hgdownload.soe.ucsc.edu/goldenPath/hg38/phyloP470way/) greater than a given threshold and confirmed that this proportion increased at higher phyloP thresholds for both significant ($p < 1 \times 10^{-4}$, t-test) over- and underexpression outliers (Fig. 1F).

To assess the average allelic effect per variant, within each tissue, we used the closest measured allelic expression single nucleotide polymorphism (aeSNP) to the gene's TSS to calculate a reference ratio for each gene-individual that carries a rare promoter variant included in the outlier test, and then inverted the reference ratio if the aeSNP was carried on a different allele than the rare promoter variant, using the SHAPEIT2 phased genotypes from GTEx (*30*). We then took an average corrected reference ratio across tissues, per variant-gene, for all variants with values in at least 5 tissues (fig. S1D). Counts per aeSNP were obtained from dbGaP (accession phs000424) (*94*).

To create the GTEx outlier benchmark, we focused on even chromosomes between 1-20, ensuring that they were not used during fine-tuning. To maximize data quality, we focused on singleton variants within 100 bp of canonical protein-coding TSS, excluding coding and splice variants, following the approach used during fine-tuning. Variants that meet these criteria were classified as underexpression outliers if they had an underexpression $p < 1 \times 10^{-4}$ (206 variants), and overexpression outliers if overexpression $p < 1 \times 10^{-4}$ (161 variants). Null variants were chosen from genes which had at least one under- or overexpression outlier, with both under- and overexpression $p > 1 \times 10^{-2}$ (382 variants; Fig. 1G, left, and table S1A).

CAGI5 saturation mutagenesis dataset

We obtained the saturation mutagenesis data of disease-associated regulatory elements through personal communication with the authors (*3*). We restricted our analysis to 9 of the 10 promoters in the dataset, excluding *FOXE1* promoter variants due to poor reproducibility, as noted by the authors, and the data being mostly nulls. Variants with underexpression $p < 1 \times 10^{-4}$ were categorized as underexpression outliers, overexpression $p < 1 \times 10^{-4}$ as overexpression outliers, and those with $p > 1 \times 10^{-2}$ as null variants. These variants, after removing splice variants (SpliceAI > 0.05), GTEx rare variants potentially seen during fine-tuning, and duplicates (we selected the first one when assayed in multiple conditions), formed our CAGI5 saturation benchmark (Fig. 1G, right, and table S1B). We also plotted the correlation between PromoterAI scores and MPRA effect sizes separately for each gene ('value' column in the dataset; fig. S1F).

MPRA saturation mutagenesis dataset

Promoter variants (canonical protein-coding TSS $\pm$ 500 bp) were selected from 128 elements containing fine-mapped GWAS loci or eQTLs that underwent saturation mutagenesis on the reference allele background(s) in K562 and HepG2 cells (*34*). Elements were further filtered such that they were active in at least one cell type (log2FC > 1). Null variants were defined as variants that did not overlap activity blocks and had limited observable effects on activity in either cell type both before and after empirical Bayes adjustment (log2FC < 0.1 and adjusted log2FC < 0.1). Over- and underexpression variants were defined as variants within activity blocks that increased or decreased activity on average across cell types (adjusted mean log2FC > 0.5 or < −0.5, respectively). Finally, splice variants, coding variants, and GTEx rare variants used during fine-tuning were excluded, as done in other

benchmarks, resulting in 773 underexpression, 275 overexpression, and 3981 null variants, which formed our MPRA saturation benchmark (fig. S1E and table S1C).

PromoterAI feature analysis

In silico mutagenesis: We scored every variant within TSS ± 100 bp of canonical protein-coding genes using PromoterAI models before and after fine-tuning. For each position, we averaged the scores across all three variants and plotted the reference base with a height reflecting the average score in sequence logo format using the *logomaker* Python package (https://logomaker.readthedocs.io/en/latest/) (*95*) (Figs. 2, A and F, and 5F; and fig. S2, A and F). The axis labels in Fig. 2F and fig. S2F indicate whether the scores were calculated using the model before or after fine-tuning, while the rest use only the model after fine-tuning. The displayed 470-way phyloP was downloaded from https://hgdownload.soe.ucsc.edu/goldenPath/hg38/phyloP470way/.

Motif enrichments: We used the FIMO tool from the MEME Suite (https://meme-suite.org/meme/index.html) (*96*) to identify sequence motifs overlapping GTEx singleton promoter variants. Our analysis focused on variants within TSS ± 100 bp, excluding those located within coding sequence of any GENCODE v39 transcript or with a SpliceAI score greater than 0.05. We scanned within 15 bp of each variant on both strands using reference and alternate alleles, retaining matches with FIMO $p < 1 \times 10^{-4}$. To reduce redundancy, we employed a curated list of 186 clustered motifs from (https://www.vierstra.org/resources/motif_clustering) (*46*) and only retained variants where the motif match was stronger on the reference allele. For each motif, we counted the number of variants with matches in over- and underexpression outliers as well as in controls. We then performed a Fisher's exact test to determine motif enrichments for over- and underexpression outliers compared to controls, ranking motifs by significance (Fig. 2B). Only motifs with at least ten variant matches were considered.

In silico motif insertion: We randomly sampled 50 loci within TSS ± 500 bp for each of the 19,296 canonical protein-coding genes. At these loci, we inserted motifs that were enriched among under- and overexpression outliers (Fig. 2B) and 5 controls (random sequences), and calculated the predicted change in PromoterAI scores. For each motif, we aggregated the effects across genes and compared them with controls at various TSS distances (fig. S2B).

We repeated this analysis using PromoterAI models before and after fine-tuning. Direction prediction accuracy was defined as the percentage of genes showing a positive score change for motifs enriched among underexpression outliers and a negative score change for motifs enriched among overexpression outliers (fig. S2E). To avoid saturation effects, for this analysis, we split the genes into two halves based on their average expression across GTEx tissues, inserting motifs enriched among underexpression outliers into the lower-expressed group and motifs enriched among overexpression outliers into the higher-expressed group.

Motif strengthening versus weakening: Motifs were classified into four categories based on gene annotations and Gene Ontology (GO) terms (*97*) using the *mygene* v3.2.2 Python package. Specifically, we searched for keywords 'activator', 'activation', 'repressor', and 'repression', and categorized motifs as either associated with only activating terms, only repressive terms, mainly activating with some repressive terms, or mainly repressive with some activating terms. For each variant, we calculated the difference in motif strength, measured as the difference in FIMO negative log p-value for the overlapping motif between the reference and alternate sequences. We plotted the distributions of these differences for variants overlapping motifs with only activating or only repressive terms (Fig. 2C and table S4), and for variants overlapping motifs with both activating and repressive terms, sub-categorized based on their relative proportions (fig. S2C).

Correlation with *z*-scores: We stratified the GTEx singleton promoter variants based on overlapping sequence motifs (identified by FIMO using the same steps applied in the motif enrichment analysis) and TSS distance (6 bins: 0-10 bp, 10-25 bp, 25-50 bp, 50-100 bp, 100-200 bp, and 200-500 bp absolute distance from the closest TSS), and calculated the Pearson correlation between z-scores and PromoterAI scores before and after fine-tuning. We plotted the correlation between z-scores and PromoterAI scores before fine-tuning on the x-axis, and the correlation between z-scores and PromoterAI scores after fine-tuning on the y-axis (Fig. 2D and fig. S2D).

Fine-tuning effects on conservation: For each variant within TSS ± 100 bp of canonical protein-coding genes, we calculated the difference in PromoterAI scores before and after fine-tuning and segregated into three categories (less than −0.5, greater than 0.5, and between −0.5 and 0.5). For each category, we plotted the 470-way phyloP distribution of the variants (Fig. 2E).

Internal representations of sequences: For the 19,296 canonical protein-coding genes, we obtained a nucleotide sequence of length 20,480 around the TSS from the sense strand and passed it through PromoterAI. We extracted the outputs of every fourth MetaFormer block, which yielded six tensors of size 19,296 × 4096 × 1024 each. These six tensors were first concatenated across the channel axis and then averaged across the length axis, resulting in a matrix of size 19,296 × 6144. We extracted the first 100 PCs of this matrix, dropped the first two as they captured simple sequence composition features like GC-content, and obtained a final embedding matrix of size 19,296 × 98. We clustered the rows of this matrix using k-means clustering to determine the cluster assignment for each gene and visualized the embeddings using universal manifold approximation and projection (UMAP) (*98*) (fig. S3A and table S5). We also visualized the embeddings exclusively for 2376 genes with at least one under- or overexpression singleton outlier (fig. S3B), as well as for 3234 genes whose promoters overlapped with annotated bivalent chromatin regions collected from (*99*) (fig. S3C). Additionally, we downloaded human candidate cis-regulatory elements with distal enhancer-like signatures from (https://screen.encodeproject.org) (*28*). For a random sample of 50,000 elements, we extracted their embeddings following the same steps as in the promoter analysis, with one key difference: instead of recalculating the principal vectors and UMAP latent spaces, we re-used the same ones from the promoter analysis to allow for direct comparison of their mappings (fig. S3G). Finally, we visualized the embeddings exclusively for 8397 genes with conserved promoters identified by average phyloP-470 way values greater than two (fig. S3H).

We obtained the JASPAR 2018 (*100*) curated set of 841 motifs from https://jaspar2018.genereg.net and 152 archetype clusters from https://www.vierstra.org/resources/motif_clustering. Using the script https://github.com/wassermanlab/JASPAR-UCSC-tracks/blob/master/scan-sequence.py, we scanned the promoter regions (TSS ± 100 bp) and identified positions with scores exceeding 850 for each motif. For each archetype, we calculated the percentage of genes in each class whose promoter contained motifs from that archetype and plotted the difference in percentages between classes (fig. S3D).

We calculated the average fold change of H3K27ac, H3K4me3, and H3K27me3 histone modifications within a 200 bp window around the TSS of 19,296 canonical protein-coding genes, and plotted the fold change distribution for the three major promoter classes (fig. S3E). We used the median TPM file from GTEx v8 to calculate the number of tissues in which each gene was expressed along with the mean expression across these tissues and repeated the analysis for these metrics (fig. S3F, left and middle). We also obtained adjusted log10_CV2

information for each gene from (*48*) and displayed the distribution for each promoter class (fig. S3F, right).

gnomAD variants

We downloaded the r3.0 VCF file from the gnomAD website (https://gnomad.broadinstitute.org/downloads) and focused only on variants marked with PASS in the FILTER column. We then filtered for variants labeled as nonsense, missense, or synonymous in the INFO column. For each variant type, we counted the number of singletons and those with AF > 0.1%. We constructed a 2 × 2 contingency table, with rows corresponding to nonsense or synonymous variants and columns corresponding to singleton or common variants. The odds ratio (OR) was calculated, and the depletion percentage was determined using the formula (1 − 1 / OR) × 100. We repeated this analysis using missense variants to obtain their depletion percentage.

We obtained PromoterAI scores for all variants within TSS ± 500 bp of canonical protein-coding genes. To calculate the depletion for a given PromoterAI score, we constructed a 2 × 2 contingency table, with the first row corresponding to variants with PromoterAI scores within 0.125 of the given score, second row corresponding to variants with PromoterAI scores between −0.05 and 0.05, and columns corresponding to singleton or common variants. The odds ratio of this contingency table was used to determine the depletion percentage at the given score (Fig. 3A). The displayed *p*-values were calculated using a chi-squared test on the contingency table. We repeated this analysis, focusing only on the subset of genes that met the required probability of loss-of-function intolerance (pLI) criteria (Fig. 3B).

To estimate the number of deleterious variants at a given TSS distance, we first calculated the odds ratio using the same procedure, with the first row corresponding to variants with PromoterAI score > 0.1 for overexpression and < −0.1 for underexpression, only counting variants that were within 5 bp of the given TSS distance. We then calculated the number of deleterious variants for each TSS distance as the number of singletons with PromoterAI score > 0.1 for overexpression and < −0.1 for underexpression, multiplied by the depletion factor (1 − 1 / OR) (Fig. 3C).

GTEx eQTLs

We downloaded the GTEx v8 CAVIAR fine-mapped eQTL analysis files from the GTEx portal (https://gtexportal.org/home/downloads/). We focused our analysis on variants within 500 bp of canonical protein-coding TSS, excluding splice variants, coding variants, and GTEx rare variants as done in other benchmarks.

Variants with CAVIAR posterior probability > 0.9 in at least 2 tissues were identified as fine-mapped eQTLs, with the average slope across tissues used as the effect size. We classified variants with negative effect size as underexpression eQTLs (191 variants) and positive effect size as overexpression eQTLs (218 variants). For these 409 variants, we plotted the correlation between PromoterAI scores and effect sizes (Fig. 3D, left). We also showed the effect size distributions of variants with PromoterAI score > 0.1 or < −0.1 (Fig. 3D, middle).

For genes with at least one under- or overexpression eQTL, variants with posterior probability < 0.1 in all tissues were categorized as null variants (393 variants). The underexpression eQTLs, overexpression eQTLs, and null variants collectively formed our GTEx eQTL benchmark (Fig. 3D, right, and table S1D).

MPRA eQTLs

We obtained the log2FC_meta, log2Skew_meta, and PIP information for the variants assayed by MPRA from (*34*). We restricted our analysis to variants within 500 bp of canonical protein-coding TSS, excluding splice variants, coding variants, and GTEx rare variants, following the same criteria used in other benchmarks.

Following guidelines from the authors, we filtered out variants with log2FC_meta < 1. For the remaining variants, we categorized them as underexpression if PIP > 0.9 and log2Skew_meta < −0.5 (70 variants), overexpression if PIP > 0.9 and log2Skew_meta > 0.5 (74 variants), and null if PIP < 0.1 with log2Skew_meta between −0.5 and 0.5 (542 variants). For these 686 variants, we plotted the correlation between PromoterAI scores and log2Skew_meta values (Fig. 3E, left). Additionally, we also calculated the validation rates for under- and overexpression predictions for various PromoterAI scores (Fig. 3E, middle). For a given PromoterAI score, the validation rate was defined as the mean proportion of variants with log2Skew_meta < −0.5 for underexpression, and log2Skew_meta > 0.5 for overexpression, among those with PromoterAI scores within 0.125 of the given score. These underexpression, overexpression, and null variants also formed our MPRA eQTL benchmark (Fig. 3E, right, and table S1E).

UKBB proteomics and phenotypic traits

We selected 454,483 individuals of European ancestry from the UKBB cohort with quantitative phenotype and genetic data, of which 48,536 had matching proteomics data spanning 2923 unique proteins obtained using the antibody-based Olink Explore 3072 PEA.

For the proteomics data, we first applied an inverse rank normal transformation (IRNT) to the raw values across individuals, then regressed out the top 90 PCs and relevant covariates, including age, sex, diet, ancestry, and medication usage (*57*). This was followed by a second IRNT on the residuals across individuals. For the quantitative phenotype data, we followed the same steps, except we did not include PC correction.

Proteomics: For the pQTL analyses (Fig. 4A), we focused on 36,976 unrelated Europeans and filtered for variants within TSS ± 500 bp of canonical protein-coding genes with allele count (AC) ≥ 3 and AF < 1% (36,748 variants). We then tested for association between 2923 protein levels and variants belonging to the same gene. Variants were encoded as 1 or 0 based on whether an individual was a carrier (heterozygous or homozygous) or not, and we performed linear regression with variant status as the input and protein level as the output to obtain association effect sizes and *p*-values. This analysis identified 742 significant pQTLs across 479 genes (multiple hypothesis corrected $p < 0.05$). We excluded splice variants, coding variants, and GTEx rare variants that might have been seen during fine-tuning, using identical criteria to those applied in the eQTL analyses, bringing the total down to 248 variants. We removed all variants that were in linkage disequilibrium with other promoter, missense, or PTVs, reducing the total to 104 variants. For these variants, we plotted the correlation between PromoterAI scores and association effect sizes (Fig. 4A, left), association effect size distribution stratified by PromoterAI score (Fig. 4A, middle), PromoterAI score distribution stratified by association effect size including insignificant promoter variants (null) (fig. S4A), and TSS distance distribution stratified by association effect size (Fig. 4A, right). We also plotted the correlation between PromoterAI scores and association effect sizes for all 248 variants, stratified by linkage disequilibrium status (fig. S4B), and further stratified by mRNA stability of the associated gene [downloaded from (*101*)] for the 104 variants not in linkage disequilibrium (fig. S4C).

For the rare variant analyses (Fig. 4B), we performed additional quality control to address the effects of increased noise. We restricted our analysis to 1656 proteins that were significant based on the rare coding variant burden test described in (*57*). Briefly, individuals were assigned a 1 or 0 to indicate if they were a carrier of at least one rare variant (AF < 0.1%) in the gene of interest. Association between the corresponding protein level and carrier status was tested using linear regression. The output *p*-values were recalibrated via permutations followed by multiple hypothesis correction. Protein-gene associations with corrected $p < 0.05$ were considered significant. To account for the effect of coding variants, for each of the 1656 proteins, we identified common coding variants (AF > 0.1%) within the gene and assigned

a 1 or 0 to indicate whether an individual was a carrier for that gene (heterozygous or homozygous) or not. We then performed linear regression, using variant status as input and the corresponding protein level as output. The predictable component of the protein level was regressed out and the residuals were standardized using an IRNT across individuals, which were then used as the z-scores for subsequent analyses. Additionally, for each protein, we excluded all samples that contained a rare coding variant (AF < 0.1%) in that gene. For each individual-protein pair, the protein's z-score was assigned to all rare promoter (AF < 0.1% and TSS ± 100 bp) variants in that individual's gene. For each variant, the final z-score was calculated as the average of all z-scores assigned to it across individuals.

As before, we excluded splice variants, coding variants, and GTEx rare variants that were seen during fine-tuning. Additionally, we only included variants with AC ≥ 2 and restricted to genes that had at least one outlier (variant with a z-score > 2 or < −2), resulting in 1715 variants. For these variants, we plotted the correlation between PromoterAI scores and z-scores (Fig. 4B, left). Additionally, we also used this dataset to calculate validation rates for under- and overexpression predictions for various PromoterAI scores following the same steps described in the MPRA eQTL section (Fig. 4B, middle). For a given PromoterAI score, the validation rate was defined as the fraction of variants with z-score < −2 for underexpression and z-score > 2 for overexpression, among those with PromoterAI scores within 0.125 of the given score. Finally, we classified variants as underexpression (z-score < −2, 182 variants), overexpression (z-score > 2, 69 variants), and null (|z-score| < 0.5, 760 variants), and used these to establish the UKBB proteome benchmark (Fig. 4B, right, and table S1F).

Phenotypic traits: Quantitative phenotypes were grouped such that the maximum absolute pairwise Pearson correlation between phenotypes from different groups was at most 0.95. Within each group, the phenotype with the most individuals was selected, resulting in a final set of 142 non-redundant phenotypes (*57*). To obtain a list of genes affecting these phenotypic traits, we conducted a rare coding variant burden test. The steps were similar to what was done for proteomics data, with one key difference: while in proteomics, we tested coding variants and protein levels from the same gene, here we tested each gene against all traits and used only PTVs. We identified 100 gene-trait pairs (45 unique traits) with an association effect size of at least 0.5, all of which remained significant after correcting for multiple hypothesis (p < 0.05). We accounted for the effects of common and rare coding variants in the same way as we did for proteomics data, by regressing out the predictable components for common coding variants and excluding samples with rare coding variants. For each individual-trait pair, the trait's residual z-score was assigned to all rare promoter (AF < 0.1% and TSS ± 500 bp) variants in the associated gene for that individual. For each variant, we calculated the final z-score as the aggregate of all z-scores assigned to it across individuals, similar to the approach used for proteomics data.

For each of these 100 genes, we performed linear regression, using PromoterAI scores of all rare variants within the promoter of that gene as input and their corresponding z-scores as output. This analysis yielded PromoterAI-calculated association effect sizes and p-values for each gene-trait pair, which we plotted against those calculated using PTVs (Fig. 4C). To maintain directional consistency, we multiplied the PTV association effect sizes by −1. We plotted the correlation between alanine aminotransferase levels and the associated *GPT* gene (Fig. 4D, left). To reduce the effects of noise through averaging, we focused on variants with AC ≥ 10. We repeated this analysis for HDL cholesterol levels and the associated *LCAT* and *CETP* genes (Fig. 4D, right). Since *CETP* had an opposite PTV direction of effect compared to *LCAT*, we multiplied their z-scores by −1 to align the effect directions before jointly plotting the correlation.

GEL rare disorder whole genomes and RNA-seq

GEL aggV2 promoter variants: To assess the enrichment of predicted underexpression variants in disorder genes, we scored promoter variants found in rare disorder probands with whole genome sequencing data from Genomics England's 100,000 Genomes Project (The National Genomic Research Library v5.1, Genomics England [https://figshare.com/articles/dataset/GenomicEnglandProtocol_pdf/4530893]; Project ID: 754). We started with the aggregated v2 (aggV2) variant call set provided by GEL and extracted variants from the 24,517 probands in the v17 sample release included in aggV2, after excluding individuals with intellectual disability. We filtered to PASS variants with read depth ≥ 10. To define promoter variants, we considered all singletons within 500 bp of any protein-coding transcript TSS as defined by the GENCODE v39 GTF. Singletons were defined as variants with AC = 1 across probands, and gnomAD AF < 0.1% within the AFR, EUR, EAS, and SAS sub-populations (obtained from GEL). We removed the top 10% of individuals by number of singletons carried genome-wide so that the number of singletons per individual followed a normal distribution.

Enrichment of variants in panel genes: To calculate the enrichment of PromoterAI predicted underexpression variants near panel genes, we filtered to 7948 probands with fewer than 100 associated panel genes, as defined by the panel to gene mappings from Genomics England's PanelApp resource (https://panelapp.genomicsengland.co.uk/panels/entities/; accessed 25 April 2023), considering genes with either 'confirmed' or 'probable' confidence, and those with no TIER1 variant reported in GEL v16, where TIER1 variants include high impact variants and de novo moderate impact variants affecting panel genes. From there, we scored all promoter singletons in the promoter region of panel genes, considering protein-coding transcripts with a minimum expression level, defined as average read count ≥ 2 as assessed by CAGE-seq data from FANTOM5 tissues and cell types. Due to the focus on pathogenicity in this assessment, driven by underexpression effects, we included only singleton variants and applied this baseline expression filter for which TSS to include.

To generate a background expectation, we shuffled variants across individuals and then assessed the number of predicted underexpression variants by PromoterAI that fall in the promoter region of panel genes for the shuffled individual. To stabilize the estimation of panel hits in the background, we repeated this shuffling process 100 times. We then calculated a 2 × 2 contingency table per PromoterAI score threshold (X) containing counts of promoter singletons with score < X, with rows corresponding to genes mapped to real or shuffled variant sets and columns corresponding to whether the disorder gene was mapped to the carrier or not. The shuffled background was summed over 100 shuffles, and we considered unique gene-individual pairs for each count. From this table, we calculated an odds ratio and p-value at each threshold via a Fisher's exact test. We first did this across all panel genes mapped to any included proband, regardless of mode of inheritance, and then further filtered to those with dominant mode of inheritance (including 'Monoallelic', 'X-linked dominant', 'Imprinted', 'Both', and 'Hemizygous' for chrX genes in males), and finally, additionally filtered dominant genes to those with known loss-of-function variants, as defined by the list generated in (*63*) (Fig. 5, A and B). We repeated this analysis for loss-of-function genes using different panel size filters (fig. S4D).

For coding variant enrichments in the same filtered set of rare disorder probands, we extracted annotations via Variant Effect Predictor (VEP) v109 (*102*) as provided by GEL to define frameshift, stop-gain, essential splice, and synonymous variants in panel genes. For missense variants, we stratified by PrimateAI-3D, using scores published in (*17*), and for cryptic splice, we filtered by SpliceAI score, using scores published in (*15*). For each AI method (PrimateAI-3D, SpliceAI, and PromoterAI), as well as synonymous variants, we removed any variants that overlapped PTVs before assessing enrichment, defined by the frameshift,

nonsense, and essential splice annotations. For synonymous, we further removed missense variants or splice variants with SpliceAI > 0.05. We then calculated odds ratios and *p*-values for the enrichment of each category near matched panel genes as described above, considering all confirmed or probable panel genes with dominant inheritance patterns (Fig. 5C). A maximum of one variant per gene-individual was counted per category. For pathogenic missense variants (PrimateAI-3D > 0.8), we repeated the analysis using different panel size filters (fig. S4E). To calculate the relative proportion of potential diagnoses in each category, we adjusted the number of observed variants in disorder genes for the background expectation for that variant class and normalized each count by the total across variant categories (Fig. 5D). We confirmed that additionally removing all missense or SpliceAI > 0.2 variants that overlapped the promoter variant set minimally impacted enrichment estimates (fig. S4, F and G).

GEL RNA-seq processing: RNA-seq data from whole blood was generated for a subset of GEL rare disorder probands, as described here: https://re-docs.genomicsengland.co.uk/rna_seq/. The RNA-seq data from 4949 individuals (4632 undiagnosed) from the Genomics England 100,000 Genomes dataset (accessed 8 January 2024) was processed largely using the same pipeline applied to GTEx samples, with the additional inclusion of age as a covariate and increasing the number of expression PCs to 200 due to the increased sample size.

As not all of the probands with RNA-seq were included in the aggV2 callset from GEL, we generated a combined VCF specifically for these samples. We used variants called from whole genome sequencing data for 4949 individuals from the Genomics England 100,000 Genomes dataset v17. For 1733 samples aligned against GRCh37, per-sample gVCFs were first jointly genotyped using Illumina's gvcfgenotyper v2019.02.26, then lifted to GRCh38 coordinates using Picard's LiftoverVcf v3.0.0 (*103*). The remaining 3216 gVCFs aligned against GRCh38 were also jointly genotyped, and the two resulting VCFs were then merged using BCFtools v1.16 (*104*). Variant sites were normalized and multiallelic sites were decomposed using vt v0.57721 (*105*), following the aggV2 variant normalization process (https://re-docs.genomicsengland.co.uk/variant_normalisation/). Based on comparisons with GATK's HaplotypeCaller (*106*, *107*), we excluded all low-quality variants with DP < 10 and GQX < 10 in our final analyses.

For the necessary expression correction steps, using the multi-sample VCF, we generated PCs by first extracting 78,656 high confidence single nucleotide polymorphisms (SNPs) meeting the following criteria: autosomal, biallelic, minor allele frequency (MAF) > 0.05, missingness < 0.01, median genotype quality > 30, median depth ≥ 30, and > 90% of heterozygous genotypes passing the ABRatio binomial test with $p > 1 \times 10^{-2}$, excluding variants in complex regions or with C/G or A/T ref/alt combinations. The high confidence SNPs were used to infer relatedness using KING v2.2.4 (*108*), and PCs were calculated based on unrelated individuals using principal component analysis (PCA) implemented by GCTA v1.94.0 (*109*). The top 5 genotype PCs were included as covariates.

Expression cis-QTLs were called according to the GTEx eQTL discovery pipeline (*30*) (https://github.com/broadinstitute/gtex-pipeline). Briefly, read counts were first normalized using the Trimmed Mean of M-values (TMM) method, excluding genes with TPM < 0.1 and read count < 6 in more than 20% of samples. The cis-QTLs (MAF > 0.01) were then mapped using tensorQTL v1.0.7 (*110*), including sex, age, top 5 genotype PCs, and top 200 expression PCs as covariates.

After generating corrected expression *z*-scores across all protein-coding genes, we assessed the correlation of PromoterAI scores for rare promoter variants carried by these probands with the associated expression *z*-score. As we did in earlier analyses, we excluded splice variants, coding variants, and rare GTEx variants used during fine-tuning. Additionally, as we consistently saw the strongest effects for variants within 100 bp of the TSS, we filtered to variants that fall within that window for the set of CAGE-selected canonical protein-coding TSS. We considered all variants with AC > 1 and < 50, as single tissue expression measurements can be quite noisy (*32*, *111*) and in the absence of multiple tissue measurements, averaging across multiple carriers can stabilize those estimates. Finally, we excluded all genes which had no variants with *z*-score > 2 or < −2, as the variant *z*-scores in these genes likely reflected measurement noise.

We used this variant set to calculate the overall correlation between PromoterAI scores and expression *z*-scores (Fig. 5E, left) as well as the proportion of variants that led to expression changes (defined as |*z*-score| > 2) at different PromoterAI score thresholds (Fig. 5E, middle). The validation rates were calculated using the same steps as in the UKBB proteomics validation to ensure consistency. We also used this variant set to create the GEL RNA benchmark, categorizing variants as underexpression (*z*-score < −2, 309 variants), overexpression (*z*-score > 2, 239 variants), and null variants (|*z*-score| < 0.5, 609 variants; Fig. 5E, right, and table S1G).

To test PromoterAI's performance further away from TSS, we calculated the correlation between RNA-seq *z*-scores and model predictions for GEL probands with RNA-seq data available, including variants up to 5 kb from the TSS, stratified by distance (fig. S4H). For comparison, we performed the same analysis with Enformer.

GEL MPRA validation

Variant selection: We included all singleton variants from the aggV2 v16 callset within 500 bp of the canonical TSS of monoallelic panel genes for probands without RNA-seq and all genes for those with RNA-seq. After filtering out variants with gnomAD AF > 0.1% and coding variants, we retained all variants that matched to the panels of their respective carriers along with a random sub-sample of an equal number of unmatched variants from the same set of genes. Additionally, we included all de novo variants within 500 bp of the canonical TSS of panel genes for probands with intellectual disability (ID), as well as randomly sampled gnomAD control variants from the same set of genes. The final dataset contained 13,798 variants after filtering for expression in the experimental cell line.

Oligonucleotide library construction: To construct MPRA libraries, we ordered three pools of 200 bp oligos from Twist Bioscience, grouped by GC content ranges (30-63%, 63-73%, and > 73%), ensuring that all reference and alternate alleles were retained within the same pool. In addition to the reference and alternate sequences, we added 5′ (ACTGGCCGCTTGACG–) and 3′ (–CGCAGGAGCCGCAGTG) adapters to each fragment. Upon receipt, the oligos were resuspended at 2 ng/μl in 10 mM Tris buffer pH 8.0, aliquoted and stored at −20°C.

Next, we implemented a random barcoding procedure as described in (*112*). For each oligo pool, 20 bp barcodes were attached to each fragment using emulsion PCR in 96 parallel reactions. The amplified emulsion mixture was broken with 2-butanol (VWR, AA43315-AK), purified using AMPure XP Beads (Beckman Coulter, A63881), and eluted in EB buffer (Qiagen, 19086). After cloning into pMPRA1 (Addgene, no. 49349) via Gibson assembly (NEB E2621L), the library was electroporated into 10-beta electrocompetent *Escherichia coli* (NEB, C3020K) in six parallel transformations using a BioRad Gene Pulser. Cultures were independently recovered in 1 ml of SOC media, followed by independent outgrowth in 20 ml of LB media containing 100 μg/ml carbenicillin (RPI, C46000-5.0) for 8 hours. After growth, cultures were pooled and purified by Qiagen Midiprep according to standard protocols.

To prepare our final library, a minimal promoter attached to GFP (minP-GFP) amplicon was ordered as a gBlock from Integrated DNA Technologies (IDT), amplified, and inserted into the plasmid library via Gibson assembly. The final plasmid pool was electroporated as before, except using twelve parallel transformations and independent outgrowth of two combined recoveries in 100 ml LB with carbenicillin. After outgrowth for 11 hours, all cultures were pooled, purified by Qiagen Maxiprep, resuspended in water, and quantified by NanoDrop and Qubit.

Mammalian cell culture and transfection: GM12878 cells were cultured in RPMI supplemented with 15% FBS and 1% penicillin/streptomycin maintaining a density of 0.2-1.0 million cells/ml at 37°C with 5% CO2. For each replicate, 1×10^8 cells were collected by centrifugation, washed with PBS, and resuspended in 1 ml RPMI containing 100 μg of plasmid library. Each replicate was transfected by electroporation with the Neon system with the following settings: 1200 V, 20 ms, 3 pulses. Electroporations were performed in 100 μl volumes, and each tip was used five times while each electroporation buffer tube was used ten times. After electroporation, cells were immediately recovered in 50 ml of RPMI with 15% FBS and no antibiotics, and incubated for 24 hours at 37°C. Three biological replicates were performed on separate GM12878 cultures.

RNA isolation and cDNA synthesis: After 24 hours of incubation, total RNA was isolated using 4 ml Trizol per replicate and Qiagen RNeasy Midi kit (Qiagen, no. 75144), following the manufacturer's protocol, including on-column DNaseI digestion. All RNA was used as input for Turbo DNase digestion according to the manufacturer's protocol. Reporter cDNA was then synthesized by reverse transcription using SuperScript III with a gene-specific primer, following the manufacturer's protocol.

Oligo-barcode mapping and barcode sequencing: For sequencing barcodes from plasmid or cDNA, PCR was performed using the following composition: 25 μl NEBNext Ultra II Q5 Master Mix (NEB, M0544L), 2.5 μl MPRA_Illumina_GFP_Forward, 2.5 μl Illumina_Universal_Adapter, 10 μl water, 10 μl sample. The reaction was cycled as follows: 95°C for 2 min, 11 cycles of (95°C for 20 s, 65°C for 15 s, 72°C for 30 s), 72°C for 2 min (*112*). Before amplification, all samples were normalized by qPCR in 10 μl with the addition of Sybr Green I. All samples were 1.8x SPRI purified into 30 μl water for indexing. All primers can be found in (*112*).

For sequencing oligo-barcode pairs, four parallel PCRs were performed with the following composition: 100 μl Q5 NEBNext MasterMix, 10 μl MPRA_Amp2Sa_Illumina_Forward, 10 μl Illumina_Universal_Adapter, 78 μl water, 2 μl plasmid library (100 ng/μl). The reaction was cycled as follows: 95°C for 2 min, 6 cycles of (95°C for 20 s, 62°C for 15 s, 72°C for 30 s), 72°C for 2 min. Reactions were pooled and 1.8x SPRI purified into 30 μl of water for indexing.

For indexing and sequencing all libraries, multiplex adapters were added in a PCR setup with the following composition: 50 μl Q5 NEBNext Master Mix, 5 μl Illumina_Multiplex [1-10], 5 μl Illumina_Universal_Adapter, 10 μl water, 30 μl sample. The reaction was cycled as follows: 95°C for 2 min, 6 cycles of (95°C for 20 s, 65°C for 30 s, 72°C for 30 s), 72°C for 2 min.

Sequencing data analysis: To map barcodes to their parent oligo sequences, we used FLASH (*113*) to merge paired-end reads. Random barcodes were extracted from each merged fragment and appended to the read name. We used STAR (*114*) to align merged reads against a reference index created from the designed library sequences. After filtering reads that did not map uniquely to a designed sequence or which had low-quality alignment scores (< 100), we extracted the resulting barcode-oligo pairs and removed sequences detected on multiple oligos.

To quantify oligo-level counts from barcodes, we used Bartender v1.1 (*115*) on each sample individually to obtain barcode clusters and correct for sequencing errors relative to our known barcode list. After clustering, we computed oligo counts by mapping each barcode to its parent oligo requiring an exact match, and summed all barcode counts within each oligo.

Statistical modeling and inference of MPRA regulatory effects: To account for variation due both sequencing depth and allelic ratios, we applied a nested fixed model using DESeq2 (*116*), described for high-depth allele-specific expression analysis that accounts for the intrinsically paired allelic design. We required a raw count mean ≥ 500 across all samples to remove very low count oligos, and then applied the nested model $count_{ijk} \sim \mu + \alpha_i + \beta_{ij} + \gamma_{ik} + \varepsilon_{ijk}$. Here, α describes the aggregate allele-independent effect observed in RNA compared to DNA, while β and γ describe sample-specific and allele-specific effects respectively. Using a linear contrast, we extracted the global RNA vs DNA average effects as expression effects, and significantly nonzero nested allelic terms indicate allelic effects.

After fitting, we tested for expression effects using a Wald test on α and tested for allele effects using a linear contrast between DNA and RNA levels of γ to test the null hypothesis that the nested allelic coefficients were equal. For both sets of summary statistics, *p*-values were adjusted for multiple testing using the Benjamini-Hochberg procedure. Given our design, inference of expression effects is better powered than allelic effects because inference of expression activity involves comparing one fragment against the distribution of all fragments, while allelic effects compare one oligo against only its allelic partner. For this reason, we required our final MPRA positive variant set to have both significant expression and allelic adjusted *p*-values (table S6).

MPRA effect size analyses: Starting with 12,069 variants that passed quality checks, we filtered down to 2392 variants from carriers with RNA-seq data. Further restricting to variants within 100 bp of the TSS reduced the size of this set to 681. Finally, focusing on genes with at least one functional MPRA hit as the rest likely reflected measurement noise, we identified 136 variants, for which we plotted the correlations between MPRA effect sizes, RNA-seq *z*-scores, and PromoterAI scores (Fig. 6A). We evaluated the enrichment of PromoterAI- and MPRA-predicted underexpression variants in panel genes (Fig. 6B), using a procedure similar to the earlier variant enrichment analyses (Fig. 5, A and B). This analysis included 346 variants across 212 genes that matched to the panels of their respective carriers, and 356 unmatched controls from the same set of genes. The odds ratios and *p*-values were calculated via a Fisher's exact test, where the contingency table contained as rows variant-gene instances with scores < X or > X at a given threshold, and the columns indicated whether the gene was matched to a panel associated with the carrier or unmatched. The thresholds were chosen to generate the same number of underexpression variants in PromoterAI and MPRA.

Out of the 12,069 variants, 416 had MPRA adjusted $p < 1 \times 10^{-4}$ for underexpression and 258 for overexpression. For comparison, the same number of predicted underexpression and overexpression variants were chosen based on PromoterAI scores. Motif enrichments were calculated for under- and overexpression variants predicted by PromoterAI and MPRA using the same procedure as in the GTEx outlier motif enrichment analysis (Fig. 2B). We displayed the counts for motifs with discrepancies between PromoterAI and MPRA, focusing on those with counts of 15 or more (Fig. 6C). We plotted the phyloP-470 way distribution for top directionally discordant variants, defined as variants for which PromoterAI scores were most negative while MPRA predicted a positive effect, and vice versa (Fig. 6D).

ClinVar analysis

We downloaded the clinvar_20240819 VCF file from https://ftp.ncbi.nlm.nih.gov/pub/clinvar/vcf_GRCh38/. We focused on single nucleotide variations (SNVs) with at least 2-star review status ('criteria_provided,_multiple_submitters,_no_conflicts', 'reviewed_by_expert_panel', or 'practice_guideline') within TSS ± 500 bp of canonical protein-coding genes, excluding splice variants, coding variants, and GTEx rare variants, as we did in all other analyses. Variants with clinical significance of either pathogenic or likely pathogenic were considered pathogenic (49 variants). For genes with at least one pathogenic variant, variants with clinical significance of either benign or likely benign were considered benign (28 variants). We increased the number of benign variants to 134 by including benign variants with 1-star review status, and variants of uncertain significance with AF > 0.1% in gnomAD. The auROC values of various models on the classification task of distinguishing

between pathogenic and benign variants were calculated (fig. S5A). We also displayed in silico mutagenesis (ISM) plots for specific pathogenic examples (fig. S5, B to E) using the same steps described in the ISM section. For several PromoterAI score thresholds, we calculated the percentage of predicted expression-altering variants that were known to be pathogenic (fig. S5F).

Comparison with other models

Evo2: We accessed the Evo2-40B model (preprint stage) through the API provided by NVIDIA (authenticated POST requests to https://build.nvidia.com/arc/evo2-40b) and followed the variant scoring instructions in https://github.com/ArcInstitute/evo2. Because language models do not inherently distinguish between under- and overexpression variants, we used the absolute difference in likelihood between the reference and alternate sequences as the variant score, and limited classification tasks to underexpression vs null and overexpression vs null. We also tested signed difference in likelihood and observed similar results across tasks.

DeepSEA: We extracted the model with pretrained weights from http://deepsea.princeton.edu/media/code/expecto/resources_20190807.tar.gz and set up a computational environment using Conda and PyTorch v1.13.1. For variant annotation, we created two 2000 bp nucleotide sequences centered on the variant on the positive strand, one with the reference and another with the alternate allele. The variant effect was computed by scoring both the sequences with the model, subtracting the reference output from the alternate output, and averaging the results across all output channels.

ExPecto: We obtained the source code from the official repository (https://github.com/FunctionLab/ExPecto). The computational environment was set up using Conda and PyTorch v1.13.1, based on the recommended guidelines. We used the same TSS annotations applied throughout this work to specify the gene association file. All other parameters were kept at their default settings, and the final variant score was calculated by averaging the predicted effects across all output channels.

Basenji2: We extracted the pretrained human model from https://github.com/calico/basenji. We created two nucleotide sequences of length 131,072 bp centered on the variant on the positive strand, one with the reference and another with the alternate allele. For each strand, we obtained outputs for 1024 bins (of size 128 bp each) and 5313 channels. Variant score was calculated by subtracting the reference output from the alternate output and averaging the results across all output bins and channels. We also tried scoring variants by centering around the TSS instead of the variant, but this approach did not improve the results.

Enformer: We downloaded the pretrained Enformer model from TensorFlow model hub (https://tfhub.dev/deepmind/enformer/1) and set up the computational environment using Conda and TensorFlow v2.4.1 following the official documentation. To score variants, we explored several approaches: (i) SNP Activity Difference (SAD) vs SNP Activity Ratio (SAR), (ii) varying the number of output bins from 1 to 896 in multiples of 2, (iii) selecting output channels (CAGE-seq, histone modifications, accessibility, transcription factor binding, CAGE-seq and histone modifications, CAGE-seq and accessibility, CAGE-seq and transcription factor binding, and all) and species (human, mouse, and all). We chose to use SAD, utilizing all 896 output bins across all human channels, as this configuration achieved the best performance on our benchmarks.

PuffinD: We obtained the source code from https://github.com/jzhoulab/puffin. For variant annotation, we created two sequences of length 100,000 bp around the variant on the positive strand. To account for strand specificity of PuffinD's predictions, we used the first five or last five output channels depending on whether the gene resided in the positive or negative strand. We also tried averaging across all ten output channels, but it did not lead to better performance. For these output channels, we used predictions within a 1 kb window around the variant for the reference and alternate alleles, specifically calculating their difference and averaging across positions and channels. We also experimented with other window sizes (200 bp, 2 kb, 20 kb, and 100 kb), but did not notice any improvements in performance.

ChromBPNet: We obtained 50 pretrained, bias-corrected ChromBPNet models (preprint stage) for DNase-seq and ATAC-seq data across five cell types (GM12878, H1ESC, HEPG2, IMR90, and K562; five cross-validation folds each) from the Kundaje lab. A Conda environment was set up following instructions from https://github.com/kundajelab/chrombpnet. Variants were scored using all models, per the guidelines in https://github.com/kundajelab/variant-scorer. We multiplied the log fold-change (logFC) and Jensen-Shannon distance (JSD) outputs from each model and averaged the resulting values across models to generate the final variant score, as this approach consistently produced the best results on our benchmarks.

Borzoi: We downloaded four pretrained Borzoi models (preprint stage) from https://github.com/calico/borzoi. A computational environment was set up using Conda and TensorFlow v2.12.0 following recommendations. We scored variants by averaging predictions across both strands and all models using several strategies: (i) SAD vs SAR, (ii) bins overlapping exons of the nearest gene vs 320 bins around the variant, (iii) selecting output channels (CAGE-seq, RNA-seq, ChIP-seq, and all). We ultimately chose SAR, bins overlapping exons of the nearest gene, and all tracks, as this configuration produced the best benchmark results.

REFERENCES AND NOTES

1. I. Mogno, J. C. Kwasnieski, B. A. Cohen, Massively parallel synthetic promoter assays reveal the in vivo effects of binding site variants. *Genome Res.* **23**, 1908–1915 (2013). doi: 10.1101/gr.157891.113; pmid: 23921661
2. A. Wakabayashi *et al.*, Insight into GATA1 transcriptional activity through interrogation of *cis* elements disrupted in human erythroid disorders. *Proc. Natl. Acad. Sci. U.S.A.* **113**, 4434–4439 (2016). doi: 10.1073/pnas.1521754113; pmid: 27044088
3. M. Kircher *et al.*, Saturation mutagenesis of twenty disease-associated regulatory elements at single base-pair resolution. *Nat. Commun.* **10**, 3583 (2019). doi: 10.1038/s41467-019-11526-w; pmid: 31395865
4. D. N. Cooper *et al.*, Genes, mutations, and human inherited disease at the dawn of the age of personalized genomics. *Hum. Mutat.* **31**, 631–655 (2010). doi: 10.1002/humu.21260; pmid: 20506564
5. E. Turro *et al.*, Whole-genome sequencing of patients with rare diseases in a national health system. *Nature* **583**, 96–102 (2020). doi: 10.1038/s41586-020-2434-2; pmid: 32581362
6. F. Gutierrez-Rodrigues *et al.*, Pathogenic TERT promoter variants in telomere diseases. *Genet. Med.* **21**, 1594–1602 (2019). doi: 10.1038/s41436-018-0385-x; pmid: 30523342
7. A. P. W. Funnell, M. Crossley, Hemophilia B Leyden and once mysterious cis-regulatory mutations. *Trends Genet.* **30**, 18–23 (2014). doi: 10.1016/j.tig.2013.09.007; pmid: 24138812
8. C. F. Wright *et al.*, Non-coding region variants upstream of *MEF2C* cause severe developmental disorder through three distinct loss-of-function mechanisms. *Am. J. Hum. Genet.* **108**, 1083–1094 (2021). doi: 10.1016/j.ajhg.2021.04.025; pmid: 34022131
9. S. Marie, V. Race, M.-C. Nassogne, M.-F. Vincent, G. Van den Berghe, Mutation of a nuclear respiratory factor 2 binding site in the 5′ untranslated region of the *ADSL* gene in three patients with adenylosuccinate lyase deficiency. *Am. J. Hum. Genet.* **71**, 14–21 (2002). doi: 10.1086/341036; pmid: 12016589
10. H. Vyas *et al.*, Prevalence and natural history of variants in the *ANKRD26* gene: A short review and update of reported cases. *Platelets* **33**, 1107–1112 (2022). doi: 10.1080/09537104.2022.2071853; pmid: 35587581
11. R. Kosem *et al.*, Cathepsin C gene 5′-untranslated region mutation in Papillon-Lefèvre syndrome. *Dermatology* **225**, 193–203 (2012). doi: 10.1159/000342509; pmid: 23108224
12. Y. J. Jang *et al.*, Disease-causing mutations in the promoter and enhancer of the ornithine transcarbamylase gene. *Hum. Mutat.* **39**, 527–536 (2018). doi: 10.1002/humu.23394; pmid: 29282796
13. G. Eraslan, Ž. Avsec, J. Gagneur, F. J. Theis, Deep learning: New computational modelling techniques for genomics. *Nat. Rev. Genet.* **20**, 389–403 (2019). doi: 10.1038/s41576-019-0122-6; pmid: 30971806

14. G. Novakovsky, N. Dexter, M. W. Libbrecht, W. W. Wasserman, S. Mostafavi, Obtaining genetics insights from deep learning via explainable artificial intelligence. *Nat. Rev. Genet.* **24**, 125–137 (2023). doi: 10.1038/s41576-022-00532-2; pmid: 36192604
15. K. Jaganathan *et al.*, Predicting splicing from primary sequence with deep learning. *Cell* **176**, 535–548.e24 (2019). doi: 10.1016/j.cell.2018.12.015; pmid: 30661751
16. L. C. Walker *et al.*, Using the ACMG/AMP framework to capture evidence related to predicted and observed impact on splicing: Recommendations from the ClinGen SVI Splicing Subgroup. *Am. J. Hum. Genet.* **110**, 1046–1067 (2023). doi: 10.1016/j.ajhg.2023.06.002; pmid: 37352859
17. H. Gao *et al.*, The landscape of tolerated genetic variation in humans and primates. *Science* **380**, eabn8197 (2023). doi: 10.1126/science.abn8197; pmid: 37262156
18. G. Brixi *et al.*, Genome modeling and design across all domains of life with Evo 2. bioRxiv 2025.02.18.638918 [Preprint] (2025); https://doi.org/10.1101/2025.02.18.638918.
19. J. Zhou, O. G. Troyanskaya, Predicting effects of noncoding variants with deep learning-based sequence model. *Nat. Methods* **12**, 931–934 (2015). doi: 10.1038/nmeth.3547; pmid: 26301843
20. D. R. Kelley *et al.*, Sequential regulatory activity prediction across chromosomes with convolutional neural networks. *Genome Res.* **28**, 739–750 (2018). doi: 10.1101/gr.227819.117; pmid: 29588361
21. J. Zhou *et al.*, Deep learning sequence-based ab initio prediction of variant effects on expression and disease risk. *Nat. Genet.* **50**, 1171–1179 (2018). doi: 10.1038/s41588-018-0160-6; pmid: 30013180
22. Ž. Avsec *et al.*, Effective gene expression prediction from sequence by integrating long-range interactions. *Nat. Methods* **18**, 1196–1203 (2021). doi: 10.1038/s41592-021-01252-x; pmid: 34608324
23. K. Dudnyk, D. Cai, C. Shi, J. Xu, J. Zhou, Sequence basis of transcription initiation in the human genome. *Science* **384**, eadj0116 (2024). doi: 10.1126/science.adj0116; pmid: 38662817
24. A. Pampari *et al.*, ChromBPNet: bias factorized, base-resolution deep learning models of chromatin accessibility reveal cis-regulatory sequence syntax, transcription factor footprints and regulatory variants. bioRxiv 2024.12.25.630221 [Preprint] (2024); https://doi.org/10.1101/2024.12.25.630221.
25. J. Linder, D. Srivastava, H. Yuan, V. Agarwal, D. R. Kelley, Predicting RNA-seq coverage from DNA sequence as a unifying model of gene regulation. *Nat. Genet.* **57**, 949–961 (2025). doi: 10.1038/s41588-024-02053-6; pmid: 39779956
26. A. Sasse *et al.*, Benchmarking of deep neural networks for predicting personal gene expression from DNA sequence highlights shortcomings. *Nat. Genet.* **55**, 2060–2064 (2023). doi: 10.1038/s41588-023-01524-6; pmid: 38036778
27. C. Huang *et al.*, Personal transcriptome variation is poorly explained by current genomic deep learning models. *Nat. Genet.* **55**, 2056–2059 (2023). doi: 10.1038/s41588-023-01574-w; pmid: 38036790
28. J. E. Moore *et al.*, Expanded encyclopaedias of DNA elements in the human and mouse genomes. *Nature* **583**, 699–710 (2020). doi: 10.1038/s41586-020-2493-4; pmid: 32728249
29. S. Noguchi *et al.*, FANTOM5 CAGE profiles of human and mouse samples. *Sci. Data* **4**, 170112 (2017). doi: 10.1038/sdata.2017.112; pmid: 28850106
30. F. Aguet *et al.*, The GTEx Consortium atlas of genetic regulatory effects across human tissues. *Science* **369**, 1318–1330 (2020). doi: 10.1126/science.aaz1776; pmid: 32913098
31. F. Brechtmann *et al.*, OUTRIDER: A statistical method for detecting aberrantly expressed genes in RNA sequencing data. *Am. J. Hum. Genet.* **103**, 907–917 (2018). doi: 10.1016/j.ajhg.2018.10.025; pmid: 30503520
32. N. M. Ferraro *et al.*, Transcriptomic signatures across human tissues identify functional rare genetic variation. *Science* **369**, eaaz5900 (2020). doi: 10.1126/science.aaz5900; pmid: 32913073
33. P. Mohammadi *et al.*, Genetic regulatory variation in populations informs transcriptome analysis in rare disease. *Science* **366**, 351–356 (2019). doi: 10.1126/science.aay0256; pmid: 31601707
34. L. Siraj *et al.*, Functional dissection of complex and molecular trait variants at single nucleotide resolution. bioRxiv 2024.05.05.592437 [Preprint] (2024); https://doi.org/10.1101/2024.05.05.592437.
35. T. Oikawa, T. Yamada, Molecular biology of the Ets family of transcription factors. *Gene* **303**, 11–34 (2003). doi: 10.1016/S0378-1119(02)01156-3; pmid: 12559563
36. P. García *et al.*, Binding of the transcription factor Atf1 to promoters serves as a barrier to phase nucleosome arrays and avoid cryptic transcription. *Nucleic Acids Res.* **42**, 10351–10359 (2014). doi: 10.1093/nar/gku704; pmid: 25122751
37. S. H. Duttke *et al.*, Position-dependent function of human sequence-specific transcription factors. *Nature* **631**, 891–898 (2024). doi: 10.1038/s41586-024-07662-z; pmid: 39020164
38. C. A. Virbasius, J. V. Virbasius, R. C. Scarpulla, NRF-1, an activator involved in nuclear-mitochondrial interactions, utilizes a new DNA-binding domain conserved in a family of developmental regulators. *Genes Dev.* **7**, 2431–2445 (1993). doi: 10.1101/gad.7.12a.2431; pmid: 8253388
39. T. C. J. Verheul, L. van Hijfte, E. Perenthaler, T. S. Barakat, The Why of YY1: Mechanisms of transcriptional regulation by Yin Yang 1. *Front. Cell Dev. Biol.* **8**, 592164 (2020). doi: 10.3389/fcell.2020.592164; pmid: 33102493
40. C. Attwooll, E. Lazzerini Denchi, K. Helin, The E2F family: Specific functions and overlapping interests. *EMBO J.* **23**, 4709–4716 (2004). doi: 10.1038/sj.emboj.7600481; pmid: 15538380
41. M. S. Lan, M. B. Breslin, Structure, expression, and biological function of INSM1 transcription factor in neuroendocrine differentiation. *FASEB J.* **23**, 2024–2033 (2009). doi: 10.1096/fj.08-125971; pmid: 19246490
42. C. Jin *et al.*, Crucial role of the transcription factors family activator protein 2 in cancer: Current clue and views. *J. Transl. Med.* **21**, 371 (2023). doi: 10.1186/s12967-023-04189-1; pmid: 37291585
43. B. Herzog *et al.*, Estrogen-related receptor α is a repressor of phosphoenolpyruvate carboxykinase gene transcription. *J. Biol. Chem.* **281**, 99–106 (2006). doi: 10.1074/jbc.M509276200; pmid: 16267049
44. Y. Lin, L. Bai, W. Chen, S. Xu, The NF-κB activation pathways, emerging molecular targets for cancer prevention and therapy. *Expert Opin. Ther. Targets* **14**, 45–55 (2010). doi: 10.1517/14728220903431069; pmid: 20001209
45. V. Agarwal *et al.*, Massively parallel characterization of transcriptional regulatory elements in three diverse human cell types. *Nature* **639**, 411–420 (2025). doi: 10.1038/s41586-024-08430-9; pmid: 39814889
46. J. Vierstra *et al.*, Global reference mapping of human transcription factor footprints. *Nature* **583**, 729–736 (2020). doi: 10.1038/s41586-020-2528-x; pmid: 32728250
47. V. Haberle, A. Stark, Eukaryotic core promoters and the functional basis of transcription initiation. *Nat. Rev. Mol. Cell Biol.* **19**, 621–637 (2018). doi: 10.1038/s41580-018-0028-8; pmid: 29946135
48. H. Einarsson *et al.*, Promoter sequence and architecture determine expression variability and confer robustness to genetic variants. *eLife* **11**, e80943 (2022). doi: 10.7554/eLife.80943; pmid: 36377861
49. T. A. Nguyen *et al.*, High-throughput functional comparison of promoter and enhancer activities. *Genome Res.* **26**, 1023–1033 (2016). doi: 10.1101/gr.204834.116; pmid: 27311442
50. K. J. Karczewski *et al.*, The mutational constraint spectrum quantified from variation in 141,456 humans. *Nature* **581**, 434–443 (2020). doi: 10.1038/s41586-020-2308-7; pmid: 32461654
51. S. Chen *et al.*, A genomic mutational constraint map using variation in 76,156 human genomes. *Nature* **625**, 92–100 (2024). doi: 10.1038/s41586-023-06045-0; pmid: 38057664
52. M. Lek *et al.*, Analysis of protein-coding genetic variation in 60,706 humans. *Nature* **536**, 285–291 (2016). doi: 10.1038/nature19057; pmid: 27535533
53. F. Hormozdiari, E. Kostem, E. Y. Kang, B. Pasaniuc, E. Eskin, Identifying Causal Variants at Loci with Multiple Signals of Association, Identifying causal variants at loci with multiple signals of association. *Genetics* **198**, 497–508 (2014). doi: 10.1534/genetics.114.167908; pmid: 25104515
54. M. Slatkin, Linkage disequilibrium—Understanding the evolutionary past and mapping the medical future. *Nat. Rev. Genet.* **9**, 477–485 (2008). doi: 10.1038/nrg2361; pmid: 18427557
55. C. Sudlow *et al.*, UK biobank: An open access resource for identifying the causes of a wide range of complex diseases of middle and old age. *PLOS Med.* **12**, e1001779 (2015). doi: 10.1371/journal.pmed.1001779; pmid: 25826379
56. B. B. Sun *et al.*, Plasma proteomic associations with genetics and health in the UK Biobank. *Nature* **622**, 329–338 (2023). doi: 10.1038/s41586-023-06592-6; pmid: 37794186
57. P. P. Fiziev *et al.*, Rare penetrant mutations confer severe risk of common diseases. *Science* **380**, eabo1131 (2023). doi: 10.1126/science.abo1131; pmid: 37262146
58. 100,000 Genomes Project Pilot Investigators, 100,000 Genomes Pilot on Rare-Disease Diagnosis in Health Care - Preliminary Report. *N. Engl. J. Med.* **385**, 1868–1880 (2021). doi: 10.1056/NEJMoa2035790; pmid: 34758253
59. Deciphering Developmental Disorders Study, Prevalence and architecture of de novo mutations in developmental disorders. *Nature* **542**, 433–438 (2017). doi: 10.1038/nature21062; pmid: 28135719
60. Genomics England, The National Genomic Research Library v5.1 (2020); www.genomicsengland.co.uk.
61. A. R. Martin *et al.*, PanelApp crowdsources expert knowledge to establish consensus diagnostic gene panels. *Nat. Genet.* **51**, 1560–1565 (2019). doi: 10.1038/s41588-019-0528-2; pmid: 31676867
62. Genomics England, PanelApp; https://panelapp.genomicsengland.co.uk/.
63. C. Sevim Bayrak *et al.*, Identification of discriminative gene-level and protein-level features associated with pathogenic gain-of-function and loss-of-function variants. *Am. J. Hum. Genet.* **108**, 2301–2318 (2021). doi: 10.1016/j.ajhg.2021.10.007; pmid: 34762822
64. M. J. Landrum *et al.*, ClinVar: Public archive of relationships among sequence variation and human phenotype. *Nucleic Acids Res.* **42**, D980–D985 (2014). doi: 10.1093/nar/gkt1113; pmid: 24234437

65. J. Li *et al.*, Point mutations in exon 1B of *APC* reveal gastric adenocarcinoma and proximal polyposis of the stomach as a familial adenomatous polyposis variant. *Am. J. Hum. Genet.* **98**, 830–842 (2016). doi: 10.1016/j.ajhg.2016.03.001; pmid: 27087319
66. J.-H. Kim *et al.*, Novel and recurrent mutations of the LDL receptor gene in Korean patients with familial hypercholesterolemia. *Mol. Cells* **18**, 63–70 (2004). doi: 10.1016/S1016-8478(23)13082-2; pmid: 15359125
67. U. M. Koivisto, J. J. Palvimo, O. A. Jänne, K. Kontula, A single-base substitution in the proximal Sp1 site of the human low density lipoprotein receptor promoter as a cause of heterozygous familial hypercholesterolemia. *Proc. Natl. Acad. Sci. U.S.A.* **91**, 10526–10530 (1994). doi: 10.1073/pnas.91.22.10526; pmid: 7937987
68. I. De Castro-Orós *et al.*, Functional analysis of LDLR promoter and 5′ UTR mutations in subjects with clinical diagnosis of familial hypercholesterolemia. *Hum. Mutat.* **32**, 868–872 (2011). doi: 10.1002/humu.21520; pmid: 21538688
69. F. Civeira *et al.*, Frequency of low-density lipoprotein receptor gene mutations in patients with a clinical diagnosis of familial combined hyperlipidemia in a clinical setting. *J. Am. Coll. Cardiol.* **52**, 1546–1553 (2008). doi: 10.1016/j.jacc.2008.06.050; pmid: 19007590
70. C. Gragnoli *et al.*, Maturity-onset diabetes of the young due to a mutation in the hepatocyte nuclear factor-4 α binding site in the promoter of the hepatocyte nuclear factor-1 α gene. *Diabetes* **46**, 1648–1651 (1997). doi: 10.2337/diacare.46.10.1648; pmid: 9313764
71. M. M. Verbeek *et al.*, Mutations in the cyclic adenosine monophosphate response element of the tyrosine hydroxylase gene. *Ann. Neurol.* **62**, 422–426 (2007). doi: 10.1002/ana.21199; pmid: 17696123
72. H.-Y. Dong, J.-Y. Feng, X.-J. Yue, L. Shan, F.-Y. Jia, Dopa-responsive dystonia caused by tyrosine hydroxylase deficiency: Three cases report and literature review. *Medicine* **99**, e21753 (2020). doi: 10.1097/MD.0000000000021753; pmid: 32872068
73. M. Ribasés *et al.*, A homozygous tyrosine hydroxylase gene promoter mutation in a patient with dopa-responsive encephalopathy: Clinical, biochemical and genetic analysis. *Mol. Genet. Metab.* **92**, 274–277 (2007). doi: 10.1016/j.ymgme.2007.07.004; pmid: 17698383
74. M. Stamelou *et al.*, Myoclonus-dystonia syndrome due to tyrosine hydroxylase deficiency. *Neurology* **79**, 435–441 (2012). doi: 10.1212/WNL.0b013e318261714a; pmid: 22815559
75. K. Watanabe *et al.*, A global overview of pleiotropy and genetic architecture in complex traits. *Nat. Genet.* **51**, 1339–1348 (2019). doi: 10.1038/s41588-019-0481-0; pmid: 31427789
76. D. Welter *et al.*, The NHGRI GWAS Catalog, a curated resource of SNP-trait associations. *Nucleic Acids Res.* **42**, D1001–D1006 (2014). doi: 10.1093/nar/gkt1229; pmid: 24316577
77. F. R. Hölzlwimmer *et al.*, Aberrant expression prediction across human tissues. *Nat. Commun.* **16**, 3061 (2025). doi: 10.1038/s41467-025-58210-w; pmid: 40157914
78. L. F. K. Kuderna *et al.*, Identification of constrained sequence elements across 239 primate genomes. *Nature* **625**, 735–742 (2024). doi: 10.1038/s41586-023-06798-8; pmid: 38030727
79. L. W. Barrett, S. Fletcher, S. D. Wilton, Regulation of eukaryotic gene expression by the untranslated gene regions and other non-coding elements. *Cell. Mol. Life Sci.* **69**, 3613–3634 (2012). doi: 10.1007/s00018-012-0990-9; pmid: 22538991
80. O. M. de Goede *et al.*, Population-scale tissue transcriptomics maps long non-coding RNAs to complex disease. *Cell* **184**, 2633–2648.e19 (2021). doi: 10.1016/j.cell.2021.03.050; pmid: 33864768
81. N. J. Sakabe, D. Savic, M. A. Nobrega, Transcriptional enhancers in development and disease. *Genome Biol.* **13**, 238 (2012). doi: 10.1186/gb-2012-13-1-238; pmid: 22269347
82. G. A. Logsdon, M. R. Vollger, E. E. Eichler, Long-read human genome sequencing and its applications. *Nat. Rev. Genet.* **21**, 597–614 (2020). doi: 10.1038/s41576-020-0236-x; pmid: 32504078
83. S. M. Hiatt *et al.*, Long-read genome sequencing for the molecular diagnosis of neurodevelopmental disorders. *HGG Adv.* **2**, 100023 (2021). doi: 10.1016/j.xhgg.2021.100023; pmid: 33937879
84. S. Negi *et al.*, Advancing long-read nanopore genome assembly and accurate variant calling for rare disease detection. *Am. J. Hum. Genet.* **112**, 428–449 (2025). doi: 10.1016/j.ajhg.2025.01.002; pmid: 39862869
85. J. M. Ellingford *et al.*, Recommendations for clinical interpretation of variants found in non-coding regions of the genome. *Genome Med.* **14**, 73 (2022). doi: 10.1186/s13073-022-01073-3; pmid: 35850704
86. W. Poller, S. Sahoo, R. Hajjar, U. Landmesser, A. M. Krichevsky, Exploration of the noncoding genome for human-specific therapeutic targets-recent insights at molecular and cellular level. *Cells* **12**, 2660 (2023). doi: 10.3390/cells12222660; pmid: 37998395
87. B. S. Gloss, M. E. Dinger, Realizing the significance of noncoding functionality in clinical genomics. *Exp. Mol. Med.* **50**, 1–8 (2018). doi: 10.1038/s12276-018-0087-0; pmid: 30089779
88. B. C. Hitz *et al.*, The ENCODE Uniform Analysis Pipelines. bioRxiv 2023.04.04.535623 [Preprint] (2023); https://doi.org/10.1101/2023.04.04.535623.
89. Y. Luo *et al.*, New developments on the Encyclopedia of DNA Elements (ENCODE) data portal. *Nucleic Acids Res.* **48**, D882–D889 (2020). doi: 10.1093/nar/gkz1062; pmid: 31713622
90. ENCODE Project Consortium, An integrated encyclopedia of DNA elements in the human genome. *Nature* **489**, 57–74 (2012). doi: 10.1038/nature11247; pmid: 22955616
91. I. Loshchilov, F. Hutter, Decoupled weight decay regularization. arXiv:1711.05101 [cs.LG] (2017).
92. A. Frankish *et al.*, GENCODE: Reference annotation for the human and mouse genomes in 2023. *Nucleic Acids Res.* **51**, D942–D949 (2023). doi: 10.1093/nar/gkac1071; pmid: 36420896
93. K. A. Tryka *et al.*, NCBI's Database of Genotypes and Phenotypes: dbGaP. *Nucleic Acids Res.* **42**, D975–D979 (2014). doi: 10.1093/nar/gkt1211; pmid: 24297256
94. S. E. Castel, F. Aguet, P. Mohammadi, K. G. Ardlie, T. Lappalainen; GTEx Consortium, A vast resource of allelic expression data spanning human tissues. *Genome Biol.* **21**, 234 (2020). doi: 10.1186/s13059-020-02122-z; pmid: 32912332
95. A. Tareen, J. B. Kinney, Logomaker: Beautiful sequence logos in Python. *Bioinformatics* **36**, 2272–2274 (2020). doi: 10.1093/bioinformatics/btz921; pmid: 31821414
96. C. E. Grant, T. L. Bailey, W. S. Noble, FIMO: Scanning for occurrences of a given motif. *Bioinformatics* **27**, 1017–1018 (2011). doi: 10.1093/bioinformatics/btr064; pmid: 21330290
97. M. Ashburner *et al.*, Gene ontology: Tool for the unification of biology. *Nat. Genet.* **25**, 25–29 (2000). doi: 10.1038/75556; pmid: 10802651
98. L. McInnes, J. Healy, N. Saul, L. Großberger, UMAP: Uniform manifold approximation and projection. *J. Open Source Softw.* **3**, 861 (2018). doi: 10.21105/joss.00861
99. F. Court, P. Arnaud, An annotated list of bivalent chromatin regions in human ES cells: A new tool for cancer epigenetic research. *Oncotarget* **8**, 4110–4124 (2017). doi: 10.18632/oncotarget.13746; pmid: 27926531
100. A. Khan *et al.*, JASPAR 2018: Update of the open-access database of transcription factor binding profiles and its web framework. *Nucleic Acids Res.* **46**, D260–D266 (2018). doi: 10.1093/nar/gkx1126; pmid: 29140473
101. V. Agarwal, D. R. Kelley, The genetic and biochemical determinants of mRNA degradation rates in mammals. *Genome Biol.* **23**, 245 (2022). doi: 10.1186/s13059-022-02811-x; pmid: 36419176
102. W. McLaren *et al.*, The Ensembl Variant Effect Predictor. *Genome Biol.* **17**, 122 (2016). doi: 10.1186/s13059-016-0974-4; pmid: 27268795
103. Broad Institute, Picard toolkit (2019); https://broadinstitute.github.io/picard/.
104. P. Danecek *et al.*, Twelve years of SAMtools and BCFtools. *Gigascience* **10**, giab008 (2021). doi: 10.1093/gigascience/giab008; pmid: 33590861
105. A. Tan, G. R. Abecasis, H. M. Kang, Unified representation of genetic variants. *Bioinformatics* **31**, 2202–2204 (2015). doi: 10.1093/bioinformatics/btv112; pmid: 25701572
106. A. McKenna *et al.*, The Genome Analysis Toolkit: A MapReduce framework for analyzing next-generation DNA sequencing data. *Genome Res.* **20**, 1297–1303 (2010). doi: 10.1101/gr.107524.110; pmid: 20644199
107. R. Poplin *et al.*, Scaling accurate genetic variant discovery to tens of thousands of samples. bioRxiv 201178 [Preprint] (2018); https://doi.org/10.1101/201178.
108. A. Manichaikul *et al.*, Robust relationship inference in genome-wide association studies. *Bioinformatics* **26**, 2867–2873 (2010). doi: 10.1093/bioinformatics/btq559; pmid: 20926424
109. J. Yang, S. H. Lee, M. E. Goddard, P. M. Visscher, GCTA: A tool for genome-wide complex trait analysis. *Am. J. Hum. Genet.* **88**, 76–82 (2011). doi: 10.1016/j.ajhg.2010.11.011; pmid: 21167468
110. A. Taylor-Weiner *et al.*, Scaling computational genomics to millions of individuals with GPUs. *Genome Biol.* **20**, 228 (2019). doi: 10.1186/s13059-019-1836-7; pmid: 31675989
111. X. Li *et al.*, The impact of rare variation on gene expression across tissues. *Nature* **550**, 239–243 (2017). doi: 10.1038/nature24267; pmid: 29022581
112. N. S. Abell *et al.*, Multiple causal variants underlie genetic associations in humans. *Science* **375**, 1247–1254 (2022). doi: 10.1126/science.abj5117; pmid: 35298243
113. T. Magoč, S. L. Salzberg, FLASH: Fast length adjustment of short reads to improve genome assemblies. *Bioinformatics* **27**, 2957–2963 (2011). doi: 10.1093/bioinformatics/btr507; pmid: 21903629
114. A. Dobin *et al.*, STAR: Ultrafast universal RNA-seq aligner. *Bioinformatics* **29**, 15–21 (2013). doi: 10.1093/bioinformatics/bts635; pmid: 23104886
115. L. Zhao, Z. Liu, S. F. Levy, S. Wu, Bartender: A fast and accurate clustering algorithm to count barcode reads. *Bioinformatics* **34**, 739–747 (2018). doi: 10.1093/bioinformatics/btx655; pmid: 29069318
116. M. I. Love, W. Huber, S. Anders, Moderated estimation of fold change and dispersion for RNA-seq data with DESeq2. *Genome Biol.* **15**, 550 (2014). doi: 10.1186/s13059-014-0550-8; pmid: 25516281

ACKNOWLEDGMENTS

Funding: This work was funded by the GREGoR (Genomics Research to Elucidate the Genetics of Rare Disease) Consortium funded by the National Human Genome Research Institute within the National Institutes of Health (E.P., Z.W.); National Human Genome Research Institute grant U01HG011755 (A.O.-L., H.L.R.); Medical Research Council Centre of Research Excellence in Therapeutic Genomics grant MR/Z504725/1 (S.J.S.); National Institute of Mental Health grant R01MH129751 (S.J.S.); Health Data Research UK QQ2 Molecules to Health Records Driver Programme (S.J.S.); and National Institutes of Health grants U01HG011762, R01AG066490, and R01MH125244 (S.B.M.). The Genotype-Tissue

Expression (GTEx) Project was supported by the Common Fund of the Office of the Director of the National Institutes of Health (commonfund.nih.gov/GTEx). Additional funds were provided by the NCI, NHGRI, NHLBI, NIDA, NIMH, and NINDS. Donors were enrolled at Biospecimen Source Sites funded by NCI/Leidos Biomedical Research, Inc., subcontracts to the National Disease Research Interchange (10XS170), Roswell Park Cancer Institute (10XS171), and Science Care, Inc. (X10S172). The Laboratory, Data Analysis, and Coordinating Center (LDACC) was funded through a contract (HHSN268201000029C) to The Broad Institute, Inc. Biorepository operations were funded through a Leidos Biomedical Research, Inc., subcontract to Van Andel Research Institute (10ST1035). Additional data repository and project management were provided by Leidos Biomedical Research, Inc. (HHSN261200800001E). The Brain Bank was supported by supplements to the University of Miami grant DA006227. Statistical Methods development grants were made to the University of Geneva (MH090941 and MH101814), the University of Chicago (MH090951, MH090937, MH101825, and MH101820), the University of North Carolina–Chapel Hill (MH090936), North Carolina State University (MH101819), Harvard University (MH090948), Stanford University (MH101782), Washington University (MH101810), and the University of Pennsylvania (MH101822). The National Genomic Research Library is managed by Genomics England Limited (a wholly owned company of the Department of Health and Social Care) and holds data provided by patients and collected by the NHS as part of their care and data collected as part of their participation in research. The National Genomic Research Library is funded by the National Institute for Health Research and NHS England. The Wellcome Trust, Cancer Research UK, and the Medical Research Council have also funded research infrastructure.
Author contributions: Conceptualization: K.J., N.E., S.B.M., K.K.-H.F.; Methodology: K.J., N.E., G.N., E.P., Z.W., S.B.M., K.K.-H.F.; Investigation: K.J., N.E., G.N., Y.W., T.J., J.S., I.K., F.C., J.H., H.C., A.L., G.P., J.M., A.B., Ar.K., J.U., Y.Z., F.A., P.W., L.S., A.S., S.K.P., D.A., E.P., Z.W., S.D.; Project administration: K.K.-H.F.; Supervision: K.J., N.E., P.F., D.S., M.C., A.O.-L., H.L.R., S.J.S., An.K., S.B.M., M.T.R., K.K.-H.F.; Writing – original draft: K.J., N.E., G.N., Y.W., A.O.-L., H.L.R., K.K.-H.F.; Writing – review & editing: K.J., N.E., G.N., E.P., Z.W., S.B.M., K.K.-H.F. **Competing interests:** Employees of Illumina are indicated in the list of author affiliations. Patent applications related to this work are US11861491B2: Deep learning-based pathogenicity classifier for promoter single nucleotide variants (S.K.P., K.K.-H.F.); WO2021055857A1: Artificial intelligence-based epigenetics (S.K.P., K.K.-H.F.); WO2024030278A1: Computer-implemented methods of identifying rare variants that cause extreme levels of gene expression (K.J., D.A., S.K.P., K.K.-H.F.); and WO2024030606A1: Artificial intelligence-based detection of gene conservation and expression preservation at base resolution (K.J.). H.L.R. has received funding for rare-disease research from Illumina and Microsoft. A.O.-L. was a consultant for Addition Therapeutics and received funding for rare-disease research from Pacific Biosciences. S.J.S. receives research funding from BioMarin Pharmaceutical. An.K. is on the scientific advisory board of SerImmune, TensorBio, and AINovo; is a consultant with Arcadia Science, Inari, and Precede Biosciences; was a consultant with Illumina and PatchBio; and has a financial stake in DeepGenomics, Immunai, and Freenome. S.B.M. is an advisory board member for MyOme, Phitech, and Valinor Discovery. **Data and materials availability:** The PromoterAI source code is available at https://github.com/Illumina/PromoterAI. Precomputed PromoterAI scores for all possible single-nucleotide variants in promoters of human protein-coding genes are available under a noncommercial license upon request. All sequencing data generated in this study have been deposited in the National Center for Biotechnology Information (NCBI) Sequence Read Archive (SRA) under BioProject accession no. PRJNA1257958. The datasets used for the analyses described in this manuscript were obtained from dbGaP (accession no. phs000424.v9.p2), UK Biobank (resource application no. 33751), and the National Genomic Research Library. **License information:** Copyright © 2025 the authors, some rights reserved; exclusive licensee American Association for the Advancement of Science. No claim to original US government works. https://www.science.org/about/science-licenses-journal-article-reuse

SUPPLEMENTARY MATERIALS

science.org/doi/10.1126/science.ads7373
Figs. S1 to S8; Tables S1 to S6; MDAR Reproducibility Checklist

Submitted 26 August 2024; resubmitted 10 January 2025; accepted 20 May 2025; published online 29 May 2025

10.1126/science.ads7373

SYNTHETIC BIOLOGY

An orthogonal T7 replisome for continuous hypermutation and accelerated evolution in *E. coli*

Christian S. Diercks[1]*, Philipp Sondermann[1], Cynthia Rong[1], Thomas G. Gillis[1], Yahui Ban[1], Celine Wang[1], David A. Dik[1,2], Peter G. Schultz[1,2]*

Systems that perform continuous hypermutation of designated genes without compromising the integrity of the host genome can substantially accelerate the evolution of new or enhanced protein functions. We describe an orthogonal DNA replication system in *Escherichia coli* based on the controlled expression of the replisome of bacteriophage T7 (T7-ORACLE). The system replicates circular plasmids that enable high transformation efficiencies and seamless integration into standard molecular biology workflows. Engineering of T7 DNA polymerase yielded variant proteins with mutation rates of 1.7×10^{-5} substitutions per base in vivo—100,000-fold above the genomic mutation rate. We demonstrated continuous evolution using the T7 replisome by expanding the substrate scope of TEM-1 β-lactamase and increasing activity 5000-fold against clinically relevant monobactam and cephalosporin antibiotics in less than 1 week.

Low organismal mutation rates [~10^{-10} substitutions per base pair (spb)] render mere passaging of cells under selective pressure an inefficient strategy for the diversification of genes on laboratory timescales (*1*, *2*). Historically, directed evolution addressed this limitation by mutagenesis in vitro [e.g., error-prone polymerase chain reaction (PCR)] followed by transformation of a microbial host with such diversified libraries for selection of phenotypic fitness (*3*–*5*). However, in vitro mutagenesis is time consuming and laborious and limits both the depth (rounds of mutagenesis) and scale (number of parallel experiments) of these experiments. Although alternative randomization strategies (e.g., DNA shuffling) have improved the efficiency of this process, the removal of ex vivo diversification by increasing in vivo mutagenicity enables continuous evolution at an accelerated pace (*6*).

Early efforts to increase in vivo mutation rates relied on chemical mutagens, engineered host DNA polymerases, and interference with host DNA repair machinery. The mutation rates that can be achieved according to these strategies are fundamentally limited by the large number of essential host genes that must be maintained faithfully to ensure survival (*7*–*10*). These limitations can be mitigated by using an orthogonal replication system where an error-prone DNA polymerase exclusively maintains a dedicated episome (*11*, *12*).

The first orthogonal replication system, OrthoRep, was developed by minimizing extranuclear plasmids of yeast that are replicated by an orthogonal cytosolic protein-primed DNA polymerase (*11*, *12*). Engineering of this DNA polymerase yielded clones with mutation rates of 10^{-5} spb that enable accelerated continuous evolution in vivo (*13*–*16*). Developing a mutagenic replication system in *Escherichia coli* will benefit from faster generation times and higher cell densities compared with yeast and enable markedly accelerated evolution experiments at the same mutation rate. Recently, a bacterial replication system, EcORep, based on the protein-primed DNA polymerase of the lytic bacteriophage PDR1, was developed for *E. coli* (*17*). However, the mutation rates that can stably be maintained in the disclosed system (~2.0×10^{-7} spb) are only modestly enhanced over genomic levels (*18*). As such, the development of a highly mutagenic orthogonal replication system in *E. coli* remains an important challenge. In this work, we describe the development of T7-ORACLE (T7 orthogonal replisome-assisted continuous laboratory evolution), a new orthogonal replication system for continuous hypermutation and accelerated evolution in *E. coli*.

Establishing an orthogonal replication system based on the bacteriophage T7 replisome

The replication of the linear double-stranded genome of T7 phage is initiated by the priming of its replisome by T7 RNA polymerase (gp1) at a T7 origin of replication (Fig. 1A) (*19*–*23*). T7 origins of replication rely on the orthogonality of the T7 RNA polymerase–promoter pair to *E. coli* RNA polymerase–promoter pairs for specificity in recruiting the replisome (Fig. 1B) (*24*). The orthogonal T7 transcript primes the T7 DNA polymerase (gp5), which further recruits the T7 helicase (gp4B) and helicase-primase (gp4A) fusion protein to the transcription bubble. The host factor thioredoxin (*trxA*) binds to the T7 DNA polymerase and serves as a β-sliding clamp. Replisome assembly initiates concerted leading and lagging strand synthesis, which further requires the presence of the T7 single-stranded DNA binding protein (gp2.5) for stabilizing the lagging strand replication loop (Fig. 1C) (*23*).

To create an orthogonal T7 replication system in *E. coli*, we generated a strain based on *E. coli* BW25113 in which all four essential T7 replisome genes (gp1, gp2.5, gp4, and gp5) are supplied in trans using plasmid-based expression systems (table S1) (*25*). We only expressed one of the two reading frames of gp4 (gp4A, helicase-primase fusion), given the reported toxicity and nonessentiality of gp4B (helicase) (*26*, *27*). Initial attempts at transforming this replisome strain with a circular plasmid carrying only a T7 origin of replication proved unsuccessful, in agreement with literature precedent (*28*).

We reasoned that additional T7 genes are required to establish an orthogonal replication system. Although not strictly essential to T7 phage replication, T7 lysozyme (gp3.5) knockout phages, in which the gene is deleted, are severely replication deficient (*29*). T7 lysozyme has two functions: cysteine hydrolase activity and inhibition of transcription by binding to T7 RNA polymerase (*30*, *31*). The concerted expression of T7 lysozyme with the other replication proteins (gp1, gp2.5, gp4, gp5; fig. S1) suggests a regulatory mechanism in which lysozyme accumulation leads to a switch from transcription to replication in the phage life cycle (*32*). Inhibition by T7 lysozyme causes abortive cycling instead of the transcription of full genes. This produces short RNA "primers" for the T7 DNA polymerase to stimulate the assembly of the T7 replisome at the T7 origin (*33*–*36*).

To stimulate replication, we fused hydrolase-deficient T7 lysozyme [C131S (Cys^{131}→Ser)] to T7 RNA polymerase (*37*). To maximize this effect, we used the T7 origin of replication φOR (Fig. 1A), for which replication stimulation by T7 lysozyme was reported to be the highest (*32*). Finally, we chose a reported exonuclease-deficient clone of T7 DNA polymerase (Δ28, T7 Sequenase 2) that had previously been used for T7 replisome-based in vitro replication assays (*38*–*41*). These changes enabled transformation of a plasmid carrying a T7 origin of replication (pOR-1; table S1), as well as stable replication for more than 2 weeks (Fig. 1, D and E). The strain showed robust growth [doubling time (T_{double}) of 29 min] and reached high cell densities [optical density at 600 nm (OD_{600}) of 7.2] in liquid culture (Fig. 1F). Mutation rates determined by fluctuation analysis showed increased mutagenesis of the T7 origin plasmid (2.81×10^{-7} spb per generation) without affecting the host genomic mutation rate (3.66×10^{-10} spb; table S4). The copy number of the T7 origin

[1]Department of Chemistry and Skaggs Institute for Chemical Biology, The Scripps Research Institute, La Jolla, CA, USA. [2]Department of Biology, California Institute for Biomedical Research (Calibr), La Jolla, CA, USA. *Corresponding author. Email: cdiercks@scripps.edu (C.S.D.); schultz@scripps.edu (P.G.S.)

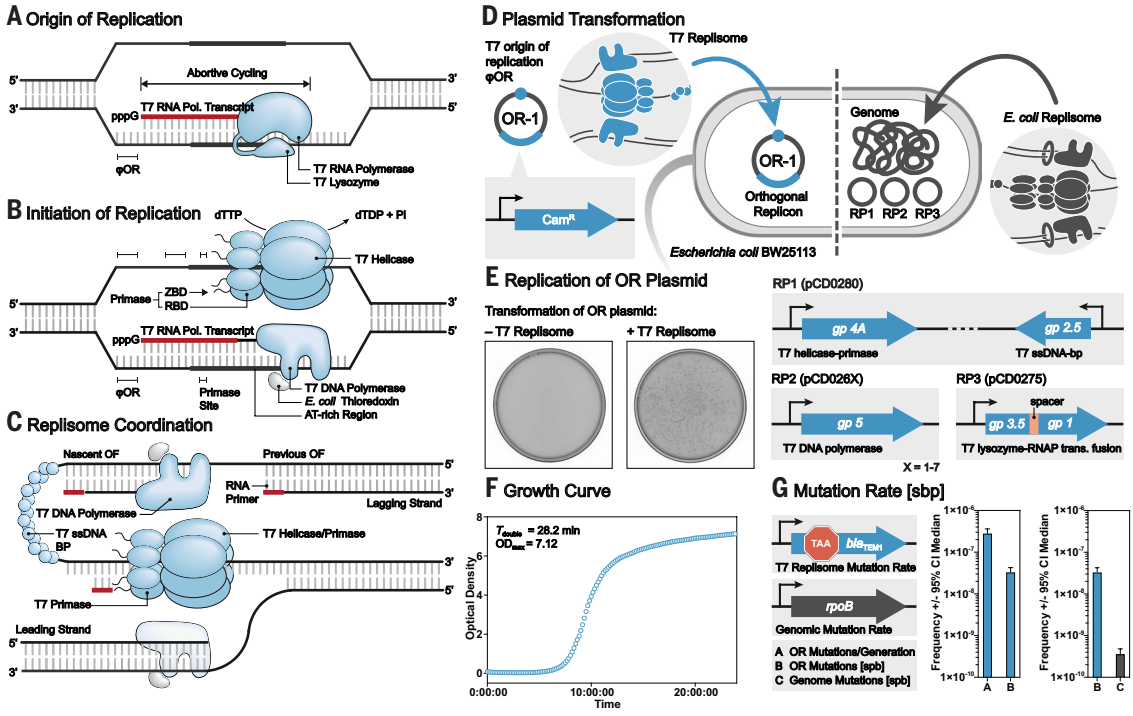


Fig. 1. Establishing an orthogonal replication system in *E. coli* based on the bacteriophage T7 replisome. (**A**) T7 RNA polymerase initiates replication by priming the replisome at the T7 origin of replication. T7 lysozyme stimulates initiation of replication. (**B**) T7 DNA polymerase is primed by the orthogonal transcript and T7 helicase and primase are recruited to the origin, leading to (**C**) concerted leading- and lagging-strand synthesis. T7 single-stranded DNA (ssDNA)–binding protein (BP) stabilizes the replication loop, and *E. coli* thioredoxin serves as a sliding clamp to increase T7 DNA polymerase processivity. AT, adenine and thymine base pair; dTDP, thymidine diphosphate; dTTP, thymidine triphosphate; Pi, inorganic phosphate. (**D**) Transformation of a plasmid with a selection marker and a T7 origin of replication is only replicated by *E. coli* strains that (**E**) provide the T7 replisome proteins in trans. Cam^R, chloramphenicol acetyltransferase gene; OR, plasmid featuring T7 origin of replication; RP, replisome expression plasmid. (**F**) T7 origin plasmids are stably maintained, and transformed strains show robust growth with a doubling time of 28 min and a final OD_{600} of 7.2. (**G**) The Δ28 mutant of T7 DNA polymerase displays an elevated mutation rate of 3.31×10^{-8} spb on the origin replicon (pOR-1), without increasing the genomic mutation rate (3.6×10^{-10} spb). CI, confidence interval.

plasmid of 8.5 was determined by quantitative PCR, yielding an adjusted mutation rate of 3.31×10^{-8} spb (Fig. 2G, fig. S13, and table S3). Notably, the transformation efficiency of the circular plasmid was determined to be 2.4×10^{10} colony-forming units per μg (cfu μg^{-1}), which is orders of magnitude higher than the transformation efficiency for the linear plasmids of OrthoRep or EcORep (*13*, *17*).

Engineering T7 DNA polymerase mutants with increased mutation rate

Three distinct mechanisms account for the high fidelity (10^{-9} to 10^{-10} spb) of DNA replication. Base selection in the T7 DNA polymerase active site accounts for a fidelity of ~10^{-5} spb, 3′-5′ exonucleolytic proofreading further increases fidelity by ~10^{-2} spb, and host mismatch repair is responsible for the remaining ~10^{-3} spb. Initially, we had used a 3′-5′ proofreading exonuclease-deficient version of T7 DNA polymerase (Δ28; Fig. 2A) (*40*–*42*). Comparison of this Δ28 mutant (3.31×10^{-8} spb) to wild-type (WT) T7 DNA polymerase (1.4×10^{-9} spb) showed a 25-fold difference in mutation rate (Fig. 2C).

Because DNA mismatch repair cannot be altered without compromising host fitness, we next targeted the fidelity of base selection in the polymerase active site to further increase mutagenicity. We selected 11 sites of T7 DNA polymerase based on studies of homologous polymerases (*10*, *43*) and generated single-site–saturation libraries at each position (i.e., R429X, V443X, R444X, L479X, E480X, N520X, A521X, K522X, T523X, F524X, Y530X, P560X, and N611X; R, Arg; V, Val; L, Leu; E, Glu; N, Asn; A, Ala; K, Lys; T, Thr; F, Phe; Y, Tyr; P, Pro; X, any residue). A replisome strain deficient in T7 DNA polymerase ($T7_{Rep\text{-}\Delta gp5}$; table S2) was transformed with these site-saturation libraries and then challenged to revert a premature ochre stop codon in the TEM-1 β-lactamase gene ($E26^*_{ochre}$) on the T7 origin plasmid (pOR-3; table S1) to restore resistance to the antibiotic carbenicillin. We sequenced surviving clones using Illumina amplicon sequencing and subjected enriched DNA polymerase mutants to fluctuation analysis. This identified three mutations (N520M, P560V, and V443K; M, Met; Fig. 2B) that were mapped onto the Δ28 mutant. N520M likely decreases geometric constraints that contribute to base-pairing selectivity given its position in the O-helix, which is in contact with incoming nucleotides in the active site. P560V is located in a flexible loop of the fingers domain that contacts this O-helix. This loop serves as a "hinge" that opens and closes the active site for incoming nucleotides. Mutations in this domain likely affect base pairing by altering the kinetics of binding of the correct or incorrect nucleotides. V443K interacts with the DNA double helix at the replication fork and might decrease base-pairing constraints by increasing the flexibility at the replication fork. The identified mutations increased the mutation rate of exonuclease-deficient T7 DNA polymerase to 6.75×10^{-7} spb for the best single mutant, 4.26×10^{-6} spb for the best double mutant, and 1.04×10^{-5} spb for the best triple mutant (Fig. 2C).

Next, we constructed a random mutagenesis library on top of the triple mutant and subjected it to the same reversion assay. This identified an additional seven sites for which single-site–saturation libraries were constructed and screened (Y24X, P84X, M146X, N171X, A433X, L437X, Q585X, and R678X; Q, Gln; figs. S2 to S4). The most beneficial mutations identified were Y24F and Q585R (Fig. 2B). Notably, the Y24F mutation is in the exonuclease domain and was found to reverse growth deficiencies observed for the single, double, and triple mutants (figs. S5 to S10 and table S5) but did not show a change in mutation rate (1.1×10^{-5} spb). The last mutation was found in the Palm domain

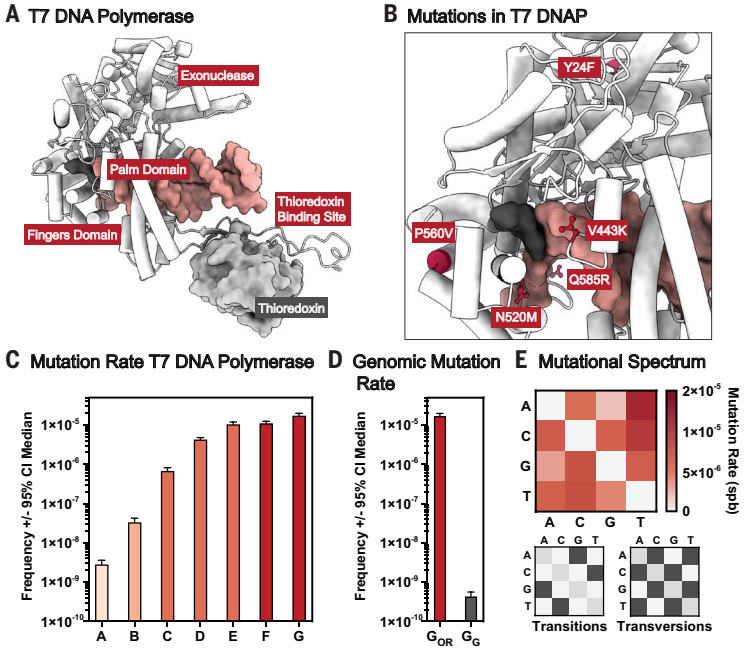


Fig. 2. Directed evolution of a mutagenic T7 DNA polymerase. (**A**) Structure of T7 DNA polymerase (white piped helices) bound to DNA (orange) and its thioredoxin cofactor (light gray). (**B**) Mutations in T7 DNA polymerase (DNAP) that decrease base-pairing fidelity (Y24F, V443K, N520M, P560V, Q585R) are highlighted in red (ball and stick representation). (**C**) Mutation rates of T7 DNA polymerase mutants as determined by fluctuation analysis. Reversion rates are converted to mutation rates by fitting the data to the Luria-Delbruck function using the Ma-Sandri-Sarkar maximum likelihood estimator. Variants are as follows: A (WT), B (Δ28), C (Δ28, N520M), D (Δ28, N520M, P560V), E (Δ28, N520M, P560V, V443K), F (Δ28, N520M, P560V, V443K, Y24F), and G (Δ28, N520M, P560V, V443K, Y24F , Q585R). (**D**) Comparison of the mutagenesis by T7 DNA polymerase mutant G on the orthogonal replicon (pOR-3; G_{OR}) to the genomic mutation rate (G_G) shows a five-order-of-magnitude increase in targeted mutagenesis and no off-target activity. (**E**) Mutational spectrum of T7 DNA polymerase mutant G in the absence of selection pressure on the orthogonal replicon (pOR-3), expressed as the substitution type–specific substitution rate (spb) for all possible base transitions and transversions.

of the polymerase and yielded a mutation rate of 1.73×10^{-5} spb for the quintuple mutant (Fig. 2C and table S3).

We investigated the mutational spectrum of the quintuple mutant by Illumina sequencing using the NovaseqX platform (two replicates of 600 million paired-end reads each) and analyzed the data using a custom analysis pipeline (*44*). The observed mutation rate across the two replicates was calculated as 1.93×10^{-5} spb, in good agreement with the results from fluctuation analysis. Heatmaps of the mutational spectrum were generated by calculating the mutational frequency of each nucleotide substitution across the two replicate datasets. We observed a fairly unbiased mutational spectrum for both transition mutations and transversion mutations (Fig. 2E).

Orthogonality to the genome was confirmed by fluctuation analysis using rifampicin resistance, which displayed a genomic mutation rate of 4.4×10^{-10} spb (Fig. 2D and table S4). Stability of the quintuple mutant was further confirmed by passaging the strain for 2 weeks, after which sequencing of the quintuple mutant of the replisome strain showed no changes in sequence and mutation rate (fig. S19). We further determined that plasmid sizes of up to 13 kb in size can be maintained (pOR-6; fig. S11 and tables S1 and S5) with comparable mutation rates (1.53×10^{-5} spb; table S3).

Continuous evolution of TEM-1 β-lactamase

Next, to demonstrate the utility of the mutagenic T7 system, which we have termed T7-ORACLE, for evolving protein function, we applied it to the continuous evolution of TEM-1 β-lactamase for an expanded substrate scope and improved activity against monobactam (aztreonam) and cephalosporin antibiotics (cefotaxime, ceftazidime, and cefepime; Fig. 3, A to C). An understanding of the mutational landscape of TEM-1 β-lactamase provides insight into the molecular basis for resistance in clinical isolates and is essential for designing next-generation β-lactam antibiotics. To this end, $T7_{rep\text{-}7}$ was transformed with a pOR-4 encoding the $bla_{TEM\text{-}1}$ β-lactamase gene (Fig. 3A and tables S1 and S2). Initial plating of the strain on antibiotic concentrations that approximate the minimum inhibitory concentration of TEM-1 against the respective antibiotics (0.1 μg ml^{-1} for aztreonam, cefotaxime, and cefepime; 0.4 μg ml^{-1} for ceftazidime) served as the starting point for evolution. For each experiment, 96 colonies were picked and passaged under increasing concentrations of antibiotic to more than 1000-fold within 6 days (100 μg ml^{-1} for aztreonam, cefotaxime, cefepime; 500 μg ml^{-1} for ceftazidime; Fig. 3B). At the end of the experiment, the coding sequences of the β-lactamase genes, as well as the p_{AmpR} promoter region, were determined (Fig. 3D and figs. S14 to S16).

Convergence of mutations across replicates was observed for all antibiotics (Fig. 3, D and E), with all enriched mutations having previously been described in clinical isolates of extended spectrum β-lactamases or laboratory evolution experiments (*45*, *46*). Both the nature and the combination of mutations differed for the four antibiotics. In addition, the entire 96-well plate for each evolution experiment was pooled after every passage and subjected to nanopore amplicon sequencing to establish a time course of when mutations occurred (Fig. 4 and figs. S17 and S18). For instance, the evolution of cefotaxime resistance (Fig. 4A) began to enrich for the G238S (G, Gly) substitution from the beginning, in agreement with the substitution being associated with increased hydrolysis of cefotaxime. After passage 3, only clones that acquired a secondary mutation, E104K, survived. E104K is generally associated with mutations G238S, R164H, or R164S (H, His) where it increases resistance to cefotaxime, ceftazidime, or aztreonam, respectively (*45*, *47*). Starting at passage 4, mutations that increased the strength of the promoter p_{AmpR} were observed. Finally, over passages 4 to 6, one of four accessory mutations was enriched in most cultures (M182T, L49M, T264M, or G92D; D, Asp), all of which have been found as secondary mutations in clinical isolates or evolution experiments (*45*). M182T increases thermodynamic stability and helps prevent aggregation. Similarly, G92D and T264M were identified in evolution campaigns that select for stabilizing and compensatory mutations (*45*). The role of L49M is unknown, but the fact that it is observed frequently in the context of cefotaxime resistance supports an adaptive effect (*45*).

In the ceftazidime resistance time-course experiment, mutations in the promoter region were observed from the outset (Fig. 4B). Additionally, mutations R164H and R164S (improved active-site access for β-lactams with large side chains) were enriched from the beginning, along with the aforementioned E104K secondary mutation. After passage 3, additional mutations (i.e., M182T, E240K, and D179G) were observed. E240K commonly occurred in combination with R164S and R164H, where it increases activity against ceftazidime and aztreonam (*45*, *47*). D179G has been observed in evolution campaigns using ceftazidime as a selective agent (*45*). Over the last three passages, the percentage of D179G mutations steadily decreased, indicating that the mutation was being outcompeted at higher antibiotic concentrations. This 1-week experiment perfectly recapitulated the vast body of work on extended-spectrum β-lactamases collected over decades, highlighting the power of the T7 evolution system in interrogating complex evolutionary fitness landscapes.

A major advantage of T7-ORACLE compared with other continuous evolution systems is that maintenance of a circular replicon enables high transformation efficiencies and integration of continuous hypermutation

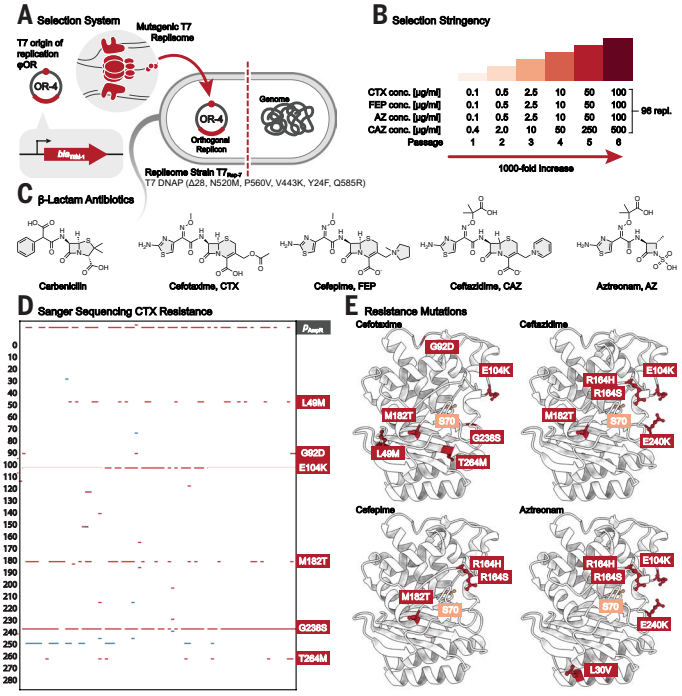


Fig. 3. Continuous evolution of TEM-1 β-lactamase. (**A**) TEM-1 β-lactamase is continuously mutagenized by the mutagenic T7 replisome ($T7_{rep\text{-}7}$, quintuple mutant). (**B**) Selection for expanded substrate scopes is achieved by passaging cells (96 replicates) in the presence of increasing amounts of cephalosporin and monobactam antibiotics. AZ, aztreonam; CAZ, ceftazidime; CTX, cefotaxime; FEP, cefepime. (**C**) Chemical structures of carbenicillin, cephalosporin β-lactams (cefotaxime, cefepime, ceftazidime), and the monobactam aztreonam. (**D**) Sanger sequencing for 96 cefotaxime-resistance evolution experiments after a 1000-fold increase in antibiotic concentration (missense mutations are marked in red and silent mutations in blue). (**E**) Structure of TEM-1 β-lactamase, with mutations that multiple replicates converge upon highlighted in red and the catalytic S70 residue highlighted in orange.

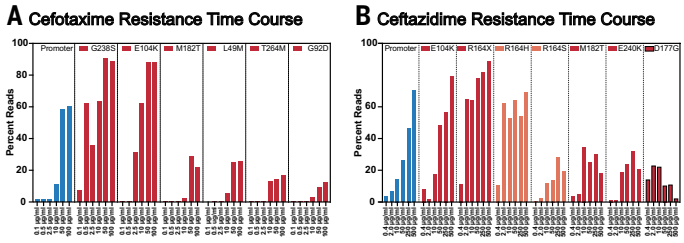


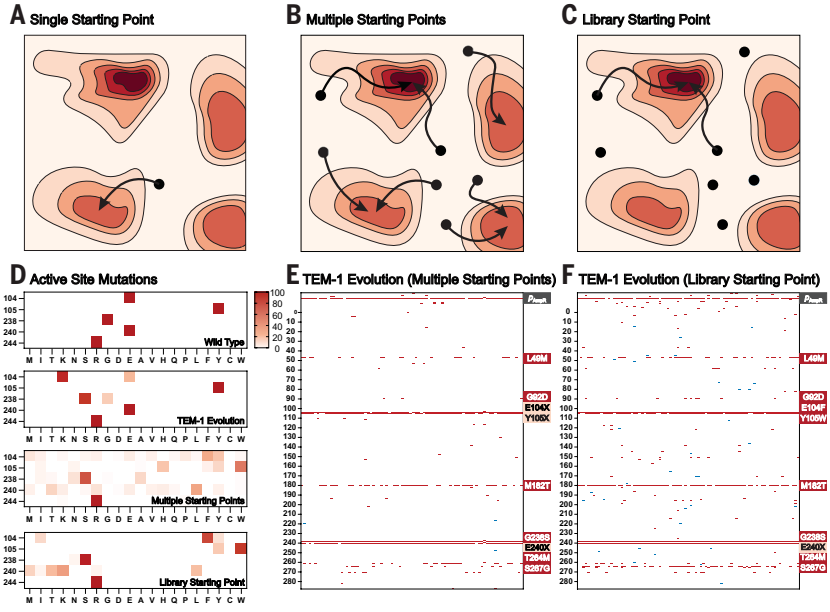
Fig. 4. Time course of β-lactamase evolution experiments. The time course for evolution of (**A**) cefotaxime and (**B**) ceftazidime resistance was interrogated by deep-sequencing of all 96 replicates after each passage (once per day). Mutations in the promoter are depicted in blue, and mutations in the TEM-1 reading frame are depicted in red and orange.

with prediversified libraries (e.g., site-saturation mutagenesis and gene shuffling). Under constant selective pressure, laboratory evolution tends to follow a path of least resistance across a hypothetical fitness landscape. This can be illustrated for the evolution of TEM-1 for activity against cefotaxime, where replicate evolution experiments broadly converge to the same solution (Fig. 3, D and E). Conceptually, this can be described as evolution trajectories on a hypothetical fitness landscape being trapped in local fitness maxima as opposed to sampling the entire landscape (Fig. 5, A to C). To overcome this limitation, we generated a site-saturation library of TEM-1 (E104X, Y105X, G238X, E240X, and R244X) covering the five residues that line the enzyme's active site. Transformation of the library plasmid pOR-5 (table S1) into the T7-ORACLE strain yielded full library coverage (3.4×10^7–member library). Ninety-six clonal starting points were picked after initial selection (0.1 μg ml^{-1} cefotaxime) and passaged under increasing selection stringency. After 5 days, the replicate evolution experiments displayed vast diversity in their active-site residues and differed from the solution for evolution of WT TEM-1 (Fig. 5, D and E). Notably, although E104K was one of the most important mutations for cefotaxime resistance in WT TEM-1, 16 distinct solutions were observed at this site in the evolution of the site-saturation library (Fig. 5D). Similarly, 14 distinct solutions were observed at site 238, seven at site 105, and seven at site 240. No substitutions for R244 were identified, indicating that this residue is essential for activity. Secondary mutations related to stability and expression levels followed similar trends as for the WT enzyme evolution (e.g., p_{AmpR}, M182T, L49M, T264M, and G92D). A second evolution experiment was carried out where, instead of 96 individual clones, the entire library was used as a starting point in each of the replicates. In this case, the active-site mutations converged again, with >80% sequence identity at four of the five sites (E104F, Y105W, G238S, and R244R; W, Trp) and divergence only being observed at site 240 (Fig. 5, D and F). In addition, starting from the entire library allowed for increasing the cefotaxime concentration even further (500 μg ml^{-1}) without any loss in viability, supporting the fact that evolution under these conditions can identify global maxima on the protein's fitness landscape. This was further corroborated by the fact that the active-site residues that converged in the experiment starting from the site-saturation library, when tested clonally, were found to be more active than the clones that converged from the evolution starting from WT TEM-1 (fig. S20).

Discussion

We have established an orthogonal replication system in *E. coli* based on the replisome of bacteriophage T7. Directed evolution of the T7 DNA polymerase for increased mutation rates yielded a replisome strain that can be continuously passaged at a mutation rate of 1.7×10^{-5} spb. The combination of the high mutagenesis rate, the fast growth rate of *E. coli*, the high transformation efficiency, and the ease with which both the *E. coli* and the circular replicon plasmid can be integrated into standard molecular biology workflows differentiates T7-ORACLE from OrthoRep and EcORep. In comparison to PACE, another highly mutagenic continuous evolution system in *E. coli*, our system benefits from simplicity and the lack of specialized equipment that is required to run evolution campaigns, as well as from the ability to autonomously run continuous evolution campaigns in a large number of replicates (*48*, *49*). One present limitation of T7-ORACLE is the lack of inducible control of the replisome proteins, which would enable control over both the copy number of the replicon as well as modulation of the mutation rate during evolution campaigns. To facilitate adaptation of the system, we constructed a strain in which all replisome genes are encoded on the genome (fig. S12 and tables S2, S3, and S5). Maintaining a circular replicon enables high transformation efficiencies of circular plasmids (2.4×10^{10} cfu μg^{-1}) and thus the integration of prediversified libraries and continuous mutagenesis into a single workflow. This was illustrated by continuous evolution campaigns in which we started with large active-site libraries to explore broader fitness landscapes. Following this approach, we identified clones with improved activity relative to those found starting from the native enzyme. This will be particularly beneficial for evolving fundamentally new, as opposed to improved, activities, as well as for investigating vast fitness landscapes through divergent, as opposed to convergent, evolution campaigns.

Fig. 5. Continuous evolution of TEM-1 β-lactamase saturation libraries. Evolutionary trajectories on a hypothetical fitness landscape for (**A**) evolution of a hypothetical gene from a single starting point and evolution of members of a site-saturation library from multiple starting points (**B**) in isolation and (**C**) in competition. (**D**) Comparison of the active-site mutations in the WT enzyme, the TEM-1 evolution campaign starting from the WT enzyme, the evolution campaign starting from isolated members of the site-saturation library, and the evolution campaign starting from the entire site-saturation library. (**E**) Sanger sequencing for 96 cefotaxime-resistance evolution experiments after starting from 96 individual colonies of a five-site saturation library of TEM-1 (E104X, Y105X, G238X, E240X, and R244X) and after a 1000-fold increase in antibiotic concentration. (**F**) Sanger sequencing for 96 cefotaxime-resistance evolution experiments after starting from 96 cultures comprising the entire TEM-1 library (E104X, Y105X, G238X, E240X, and R244X) and after a 1000-fold increase in antibiotic concentration. Missense mutations are marked in red and silent mutations in blue.



REFERENCES AND NOTES

1. J. W. Drake, *Proc. Natl. Acad. Sci. U.S.A.* **88**, 7160–7164 (1991).
2. C. K. Biebricher, M. Eigen, *Curr. Top. Microbiol. Immunol.* **299**, 1–31 (2006).
3. M. S. Packer, D. R. Liu, *Nat. Rev. Genet.* **16**, 379–394 (2015).
4. F. H. Arnold, *Acc. Chem. Res.* **31**, 125–131 (1998).
5. A. J. Simon, S. d'Oelsnitz, A. D. Ellington, *Nat. Biotechnol.* **37**, 730–743 (2019).
6. W. P. C. Stemmer, *Nature* **370**, 389–391 (1994).
7. D. M. Hillis, J. J. Bull, M. E. White, M. R. Badgett, I. J. Molineux, *Science* **255**, 589–592 (1992).
8. J. J. Bull, R. Sanjuán, C. O. Wilke, *J. Virol.* **81**, 2930–2939 (2007).
9. A. J. Herr *et al.*, *PLOS Genet.* **7**, e1002282 (2011).
10. M. Camps, J. Naukkarinen, B. P. Johnson, L. A. Loeb, *Proc. Natl. Acad. Sci. U.S.A.* **100**, 9727–9732 (2003).
11. A. Ravikumar, A. Arrieta, C. C. Liu, *Nat. Chem. Biol.* **10**, 175–177 (2014).
12. R. Tian *et al.*, *Nat. Chem. Biol.* **19**, 1504–1512 (2023).
13. A. Ravikumar, G. A. Arzumanyan, M. K. A. Obadi, A. A. Javanpour, C. C. Liu, *Cell* **175**, 1946–1957.e13 (2018).
14. G. Rix *et al.*, *Nat. Commun.* **11**, 5644 (2020).
15. A. Wellner *et al.*, *Nat. Chem. Biol.* **17**, 1057–1064 (2021).
16. E. D. Jensen *et al.*, *Microb. Biotechnol.* **14**, 2617–2626 (2021).
17. R. Tian *et al.*, *Science* **383**, 421–426 (2024).
18. R. L. Williams, C. C. Liu, *Science* **383**, 372–373 (2024).
19. C. Weigel, H. Seitz, *FEMS Microbiol. Rev.* **30**, 321–381 (2006).
20. C. C. Richardson, *Cell* **33**, 315–317 (1983).
21. A. W. Kulczyk, C. C. Richardson, *Enzymes* **39**, 89–136 (2016).
22. Y. Gao *et al.*, *Science* **363**, eaav7003 (2019).
23. S. J. Lee, C. C. Richardson, *Curr. Opin. Chem. Biol.* **15**, 580–586 (2011).
24. S. Tabor, C. C. Richardson, *Proc. Natl. Acad. Sci. U.S.A.* **82**, 1074–1078 (1985).
25. T. Baba *et al.*, *Mol. Syst. Biol.* **2**, 2006.0008 (2006).
26. H. Zhang, S.-J. Lee, A. W. Kulczyk, B. Zhu, C. C. Richardson, *J. Biol. Chem.* **287**, 34273–34287 (2012).
27. A. H. Rosenberg, S. S. Patel, K. A. Johnson, F. W. Studier, *J. Biol. Chem.* **267**, 15005–15012 (1992).
28. K. Becker, A. Meyer, T. M. Roberts, S. Panke, *Nucleic Acids Res.* **49**, 8189–8198 (2021).
29. W. T. McAllister, H.-L. Wu, *Proc. Natl. Acad. Sci. U.S.A.* **75**, 804–808 (1978).
30. B. A. Moffatt, F. W. Studier, *Cell* **49**, 221–227 (1987).
31. X. Cheng, X. Zhang, J. W. Pflugrath, F. W. Studier, *Proc. Natl. Acad. Sci. U.S.A.* **91**, 4034–4038 (1994).
32. X. Zhang, F. W. Studier, *J. Mol. Biol.* **340**, 707–730 (2004).
33. X. Zhang, F. W. Studier, *J. Mol. Biol.* **269**, 10–27 (1997).
34. D. Jeruzalmi, T. A. Steitz, *EMBO J.* **17**, 4101–4113 (1998).
35. A. Kumar, S. S. Patel, *Biochemistry* **36**, 13954–13962 (1997).
36. N. M. Stano, S. S. Patel, *J. Biol. Chem.* **279**, 16136–16143 (2004).
37. B. C. Dickinson, M. S. Packer, A. H. Badran, D. R. Liu, *Nat. Commun.* **5**, 5352 (2014).
38. S. Tabor, C. C. Richardson, *Proc. Natl. Acad. Sci. U.S.A.* **84**, 4767–4771 (1987).
39. S. Doublié, T. Ellenberger, *Curr. Opin. Struct. Biol.* **8**, 704–712 (1998).
40. B. Zhu, *Front. Microbiol.* **5**, 181 (2014).
41. T. A. Kunkel, S. S. Patel, K. A. Johnson, *Proc. Natl. Acad. Sci. U.S.A.* **91**, 6830–6834 (1994).
42. S. Doublié, S. Tabor, A. M. Long, C. C. Richardson, T. Ellenberger, *Nature* **391**, 251–258 (1998).
43. D. T. Minnick *et al.*, *J. Biol. Chem.* **274**, 3067–3075 (1999).
44. C. S. Diercks *et al.*, An orthogonal T7 replisome for continuous hypermutation and accelerated evolution in *E. coli*. Zenodo (2025); https://doi.org/10.5281/zenodo.14990911.
45. M. L. M. Salverda, J. A. G. M. De Visser, M. Barlow, *FEMS Microbiol. Rev.* **34**, 1015–1036 (2010).
46. R. Fernandes, P. Amador, C. Oliveira, C. Prudêncio, *Scientific World Journal* **2014**, 782897 (2014).
47. T. Palzkill, *Front. Mol. Biosci.* **5**, 16 (2018).
48. S. M. Miller, T. Wang, D. R. Liu, *Nat. Protoc.* **15**, 4101–4127 (2020).
49. K. M. Esvelt, J. C. Carlson, D. R. Liu, *Nature* **472**, 499–503 (2011).

ACKNOWLEDGMENTS

The authors thank K. Williams for assistance with manuscript preparation and submission. This manuscript is dedicated to the memory of Tsotne Javahishvili. **Funding:** This work was funded by National Institutes of Health grant RGM145323A. **Author contributions:** Conceptualization: C.S.D., P.G.S.; Methodology: C.S.D., P.G.S.; Investigation: C.S.D., P.S., C.R., T.G.G., Y.B., C.W., D.A.D.; Funding acquisition: P.G.S.; Supervision: C.S.D., P.G.S.; Writing – original draft: C.S.D., P.G.S.; Writing – review & editing: C.S.D., P.S., C.R., D.A.D., P.G.S. **Competing interests:** The authors declare that they have no competing interests. **Data and materials availability:** C.S.D. and P.G.S. are listed as inventors on US provisional patent application 63/670,151 submitted by Scripps Research Institute, which covers "Orthogonal DNA replication systems based on T7 replisome." Plasmids and strains listed in tables S1 and S2 are available from the authors upon reasonable request. Custom scripts can be found at Zenodo (*44*). **License information:** Copyright © 2025 the authors, some rights reserved; exclusive licensee American Association for the Advancement of Science. No claim to original US government works. https://www.science.org/about/science-licenses-journal-article-reuse

SUPPLEMENTARY MATERIALS

science.org/doi/10.1126/science.adp9583
Materials and Methods; Figs. S1 to S21; Tables S1 to S6; References (*50*–*57*);
MDAR Reproducibility Checklist

Submitted 19 April 2024; resubmitted 24 December 2024; accepted 15 May 2025
10.1126/science.adp9583

MAGNETIC SENSING

Strain-coupled, crystalline polymer-inorganic interfaces for efficient magnetoelectric sensing

Binbin He[1,2], Yuanyuan He[3], Wenhui Wang[2], Yingzhi Sun[2], Shengwen Kong[2], Jin Huang[2], Yunfei Ru[2], Bingchao Qin[1,4], Huili Ren[2], Jing He[2], Tianyi Zhao[1,2], Jing Li[1,2]*, Jiong Lu[3], Li-Dong Zhao[1,4]*, Mingjie Liu[1,2]*

Magnetoelectric sensing holds promise for flexible sensors, offering precise detection of both electric and magnetic fields with minimal power consumption. However, its practical use has been constrained by weak magnetoelectric effects and limited overall performance, particularly under mechanical strain. Herein, we fabricated robust magnetoelectric polymer-inorganic nanocomposites through an interfacial cocrystallization strategy. By leveraging diazonium chemistry on vanadium diselenide (VSe_2) monolayers, we created a submolecular-flat interface between ferromagnetic VSe_2 and ferroelectric poly(vinylidene fluoride) (PVDF) nanocrystals. This highly crystalline interface has few mobile polymer chains and thus limits energy dissipation and enhances interfacial energy transfer. The scalable composite films show exceptional magnetoelectric performance, with a magnetocapacitive coefficient of 23.6%. These films enable ultrafast magnetoelectric detection, approaching a 10-fold increase in speed compared with conventional sensors, and offer opportunities for integrating multifunctional materials such as thermoelectric coolers into wearable devices.

Magnetoelectric (ME) sensing, which couples ferroelectric polarization with magnetization (*1*–*3*), can offer low power consumption and cost-effectiveness compared with traditional Hall effect (*4*) and magnetoresistance (*5*) sensors. The ME coefficient, a key figure of merit for sensing performance, is often limited in single-phase materials because of the inherent trade-off between ferroelectricity (favored by empty *d* orbitals) and magnetism (favored by partially filled *d* orbitals). To address this competition, composite structures combining various ferroic components have been developed, achieving ME coefficients orders of magnitude larger than those of single-phase materials (*6*–*8*). Early examples include vertically aligned nanocomposites, such as $CoFe_2O_4$ nanopillars in a $BaTiO_3$ matrix, which form self-assembled hexagonal arrays (*9*). These composites enhance the ME coefficients by independently modulating ferroic orders for synergistic coupling. Among various ME responses, the magnetocapacitive (MC) effect, characterized by a magnetic field–dependent change in capacitance, has attracted interest for device integration owing to its low power consumption and potential for miniaturization. However, typical MC coefficients in reported ME composites remain low (typically <1%), which is attributed to weak strain coupling and low efficiency of interfacial energy transfer (*10*), hindering their practical application in scenarios requiring high sensitivity, rapid response, and operational stability (*11*).

[1]State Key Laboratory of Bioinspired Interfacial Materials Science, Bioinspired Science Innovation Center, Hangzhou International Innovation Institute, Beihang University, Hangzhou, China. [2]School of Chemistry, Beihang University, Beijing, China. [3]Department of Chemistry, National University of Singapore, Singapore. [4]School of Materials Science and Engineering, Beihang University, Beijing, China. ***Corresponding author. Email: chmlij@buaa.edu.cn (J.L.), zhaolidong@buaa.edu.cn (L.-D.Z.), liumj@buaa.edu.cn (M.L.)**

Recent advances, including atomic-scale layer-by-layer growth (*12*), superlattice fabrication (*13*), and interface-induced room temperature magnetoelectrics in $BaTiO_3$ (*14*), underscore the potential for enhancing ferroelectric and ferromagnetic coupling through material design and interface engineering. However, current ferromagnetic components are typically rigid inorganic materials, limiting crystallization-enhanced composition strategies to rigid superlattices. Incorporating flexible polymers into composite offers versatility but presents a challenge. Under dynamic mechanical actions, polymer chains undergo segmental motions, causing substantial energy dissipation through internal friction (*15*). This high-energy dissipation at polymer-inorganic interfaces drastically compromises ME effects (*16*, *17*). Thus, fabricating a flexible composite with strong ME coupling is still challenging.

We developed robust ME nanocomposites through interfacial cocrystallization between ferromagnetic inorganic monolayers and ferroelectric polymers. The surface functional groups facilitate lattice relaxation of VSe_2 monolayers within the polymer matrix that forms an interface that is flat at the submolecular level, which promotes poly(vinylidene fluoride) (PVDF) crystallization into its polar β phase. This highly efficient energy transfer interface enhanced both mechanical and ME properties, yielding a piezoelectric coefficient of 101.4 pm V^{-1} and a piezoelectric voltage coefficient of 1180.6×10^{-3} V m N^{-1} (Fig. 1A). The resulting films demonstrate a giant ME coupling effect, achieving a record-high MC coefficient of 23.6%. We demonstrate their potential in wearable ME sensors, featuring an ultrafast response speed (1 ms^{-1}) that represents an ~10-fold improvement over conventional sensors. Additionally, we introduce a MC sensor that can detect magnetic fields from multiple sources through ME coupling.

Fabrication of the magnetoelectric superlattices

Traditional particulate-based ME composites tend to form disordered crystals, resulting in high-energy dissipation interfaces and weak ME coupling. We designed a laminated ME film with submolecular-flat interfaces that incorporated surface-functionalized VSe_2 as ferromagnetic nanofillers that were aligned to the monolayer level within a polymer matrix. These films achieve strong ferroelectricity and ME coupling owing to the high content of ordered β-phase PVDF nanocrystals and energy-efficient interfaces (Fig. 1B). To achieve this, versatile diazonium chemistry was used to functionalize the VSe_2 monolayer with compact surface functional groups, leveraging the metallic nature of VSe_2, which is highly favorable for electrophilic coupling reactions. Specifically, electrochemically exfoliated VSe_2 monolayers, characterized by room temperature ferromagnetism, were densely functionalized with *para*-carboxybenzene functional groups (denoted as VSe_2-COOH to highlight the surface carboxyl groups). This modification addresses surface energy–induced wrinkling and aggregation, resulting in submolecular-flat nanosheets within organic matrices. These ferromagnetic nanosheets, free from surface dangling bonds, revealed excellent miscibility (up to 25 wt %) in the PVDF matrix, ensuring excellent interfacial matching within the nanocomposite. The abundant carboxyl groups on the VSe_2-COOH also provided nucleation sites for β-phase PVDF through hydrogen bonding (Fig. 1C). Their uniform dispersion created a large specific interfacial area, favoring solution-processible orientation through shear flow. Using a nanoconfined-dewetting method (Fig. 1D), amorphous PVDF nucleated onto the VSe_2-COOH nanosheets, and the polymer chains were co-oriented with the nanosheets on a superwetting substrate. This process enabled the nanocrystallization of PVDF within the submolecular-flat interface, yielding a large-scale laminated superlattice film. The coherent interface, combined with high crystallinity and efficient energy transfer in both the ferroelectric PVDF and ferromagnetic VSe_2-COOH monolayers, collectively enhanced the solution-processed superlattice, resulting in a giant ME effect and superior overall sensing performance.

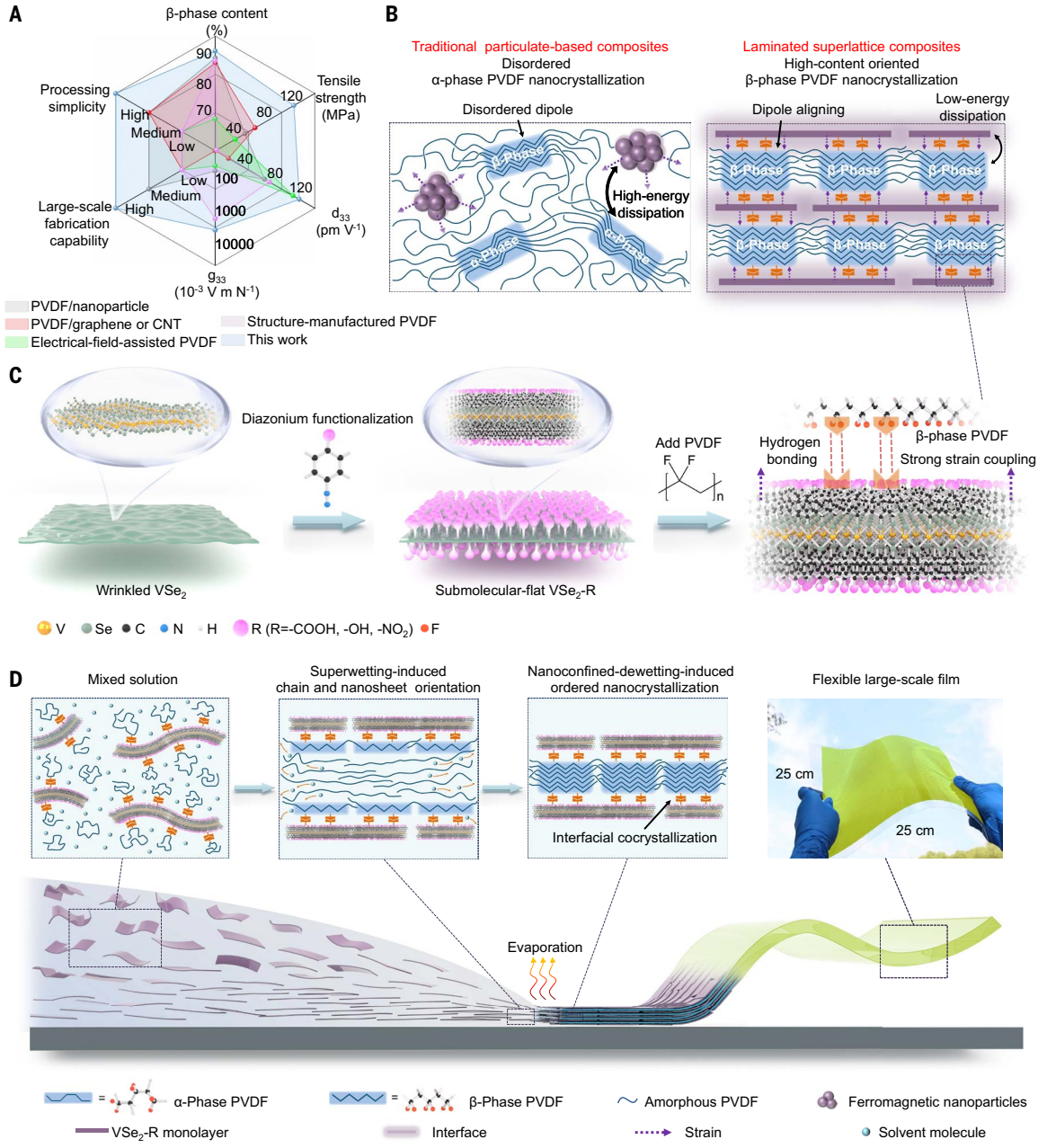


Fig. 1. Fabrication of the robust magnetoelectric films. (**A**) Radar charts comparing the performance of typical polymer-based ferroic materials. (**B**) Schematic illustration of the structure of traditional particulate-based magnetoelectric composites versus laminated magnetoelectric composites. (**C**) Schematic representation of the VSe_2 monolayer, diazonium-functionalized VSe_2 monolayer, and β-phase PVDF nucleation on the functionalized VSe_2 surface. (**D**) Schematic illustration of the fabrication process and mechanism of the magnetoelectric superlattices.

Surface functionalization of ferromagnetic VSe_2 monolayers

Compared with other nanofillers, two-dimensional (2D) nanosheets have the advantages of atomically sharp interfaces free of dangling bonds (*18*), high specific surface area that facilitates interfacial interactions with the matrix materials (*19*), and an anisotropic nature that enables properties manipulation in specific directions (*20*). These attributes allow 2D nanofillers to enhance the properties of nanocomposites (*21*), including electrical conductivity (*22*), optoelectronic response (*23*), thermal conductivity (*24*), and mechanical strength and stiffness (*25*).

Despite the importance of magnetism in composites, which enables breakthrough applications in biomedical, coating, and microelectronics fields, the exploration of intrinsic ferromagnetic monolayer-based nanocomposites is largely unexplored. Several fundamental issues, such as controllable synthesis, solution processability, and interfacial miscibility, have not been well addressed in emergent 2D magnetic materials. Intrinsic ferromagnetism in these materials was discovered in $Cr_2Gr_2Te_6$ and CrI_3 down to the bilayer and monolayer thickness limit in 2017 (*26*, *27*).

In this context, we investigated the modulation of ferroic properties in a polymer-based ferroelectric matrix using VSe_2 magnets down to monolayer thickness. Unlike most 2D ferromagnets that derive magnetism from bulk crystals, ferromagnetism in the 1T-phase VSe_2 monolayer is robust at room temperature but gradually vanishes to

paramagnetism as the thickness increases (*28*). The $3d^1$ electronic configuration in VSe_2 also imparts metallic properties and intriguing electronic interaction to this material (*29*).

To obtain crystalline VSe_2 in a high yield of ferromagnetic monolayers, we adopted the electrochemical exfoliation method to generate 1T-phased VSe_2 monolayers in large quantities (details provided in supplementary materials, materials and methods). Raman spectra show that exfoliated VSe_2 displayed characteristic peaks of the out-of-plane A_{1g} mode (*29*) with uniform Raman mapping intensity across each flake (fig. S1A). Additionally, the overall crystallinity of exfoliated VSe_2 flakes was further investigated by x-ray diffraction (XRD) (fig. S1B). The main diffraction peaks located at $2\theta = 14.5°$, 29.2°, 44.5°, and 60.6° correspond to the (001), (002), (003), and (004) lattice planes of VSe_2, respectively, reflecting the periodicity of the lattice along the *c*-direction and the typical spectral characteristics of ultrathin nanosheets (*30*). The chemical states and elemental composition were characterized by x-ray photoelectron spectroscopy (XPS) (fig. S2). The chemical states of Se *3d* and V *2p* in exfoliated VSe_2 were identical to those in bulk VSe_2 (table S1), indicating that the exfoliated sample was crystalline and free of oxidation during the exfoliation procedure.

Based on the statistical measurement shown in fig. S3, 200 exfoliated VSe_2 flakes reveal an average lateral size of 4.5 μm. Atomic force microscopy (AFM) characterization of the VSe_2 flakes indicates a representative thickness of 1.0 nm (fig. S4), which is consistent with the monolayer nature of exfoliated transition metal dichalcogenides obtained through solution exfoliation methods (*31*). To gain further atomic insight into exfoliated VSe_2, high-resolution transmission electron microscopy (TEM) and atomic resolution scanning TEM (STEM) were performed (Fig. 2, A to C, and figs. S5 to S7). The in-plane lattice constant was 3.35 Å, which agrees well with the reported value for octahedral 1T-VSe_2 (*32*). In brief, the systematic microscope characterizations confirm that the synthesized VSe_2 nanosheets exhibited large lateral size, atomic-scale thickness, and pristine 1T-phase crystal structure achieved through a simple electrochemical exfoliation method.

Another common challenge regarding 2D material–based polymer composites is stable dispersion of the 2D nanosheets, which requires matching the surface tension component of 2D flakes with those of the dispersion matrix (*33*). Generally, pristine 2D flakes tend to aggregate or precipitate in the polymer matrix or precursor solution at relatively low dispersion concentrations of <1 mg ml^{-1} (*34*). To address this issue, we used diazonium chemistry to functionalize VSe_2 monolayers and tuned their miscibility in a PVDF precursor solution.

As a demonstration, we used 4-carboxybenzenediazonium tetrafluoroborate (CBD) to clarify the versatility of surface functionalization on VSe_2. The metallic nature of VSe_2 enabled electrophilic coupling, resulting in uniform coverage of compact *para*-carboxybenzene functional groups (Fig. 2D). Fourier transform infrared spectroscopy (FTIR) was performed to verify the presence of these functional groups. The absence of characteristic N_2^+ vibration (expected at 2300 cm^{-1}) of the diazonium salt precursor indicated that diazonium precursors were thoroughly washed away, leaving no physically absorbed residues on VSe_2 (Fig. 2E). Additionally, the presence of vibrations corresponding to carboxyl groups (3438 and 1740 cm^{-1}) and the aromatic ring (1548 cm^{-1}) confirmed the covalent functionalization of *para*-carboxybenzene functional groups on VSe_2.

Thermal analysis and XPS were performed to quantify the surface coverage of *para*-carboxybenzene functional groups on VSe_2. CBD salt exhibited two weight loss stages at 119° and 187°C, corresponding to the decomposition and sublimation of the carboxyl group and aromatic ring, respectively (fig. S8A). Consistently, a synchronous thermal analyzer indicated that VSe_2-COOH displayed a similar two-stage thermal decomposition process, but at slightly higher temperatures of 164° and 332°C (fig. S8, B and C). We tentatively attributed this shift to the combined effect of strong covalent bonding between the *para*-carboxybenzene functional group and VSe_2 nanosheets (*35*), as well as the confinement caused by interlayer stacking (*36*). On the basis of the weight loss of 28% in fig. S8C, we calculated the surface coverage of the *para*-carboxybenzene to be as high as 33.6% per Se atom.

Additionally, the XPS of VSe_2-COOH revealed C=O and C=C peaks associated with the *para*-carboxybenzene functional group (fig. S9A). More importantly, in addition to the two characteristic Se peaks (Se $3d_{5/2}$ and Se $3d_{3/2}$) assigned to VSe_2 (Fig. 2F, fig. S2D, and table S1), a new peak associated with the Se–C bond appears, unambiguously indicating the successful formation of the covalent bond between the *para*-carboxybenzene group and Se atoms on the surface of VSe_2. According to the integrated area of fitting in XPS, the coverage of covalent *para*-carboxybenzene on VSe_2 was determined to be 30.5% per Se atom. This result aligned with the coverage calculated from the thermal analysis.

The magnetic property of the prepared pristine VSe_2 and modified VSe_2-COOH nanosheets was subsequently evaluated by collecting the magnetization–magnetic field (M-H) curves. In contrast with the paramagnetism and diamagnetism observed in bulk VSe_2 and the blank SiO_2/Si substrate, respectively (fig. S10, A and B), the drop-casted VSe_2 and VSe_2-COOH nanosheets on the SiO_2/Si substrate exhibited characteristic hysteresis loops at room temperature with nearly identical saturated magnetization (fig. S10C), providing direct evidence for the ferromagnetism of both the exfoliated and surface-functionalized VSe_2 samples. This result was consistent with the XPS result showing that the peak position and bonding energy of V *2p* in both VSe_2 and VSe_2-COOH were nearly the same (figs. S2C and S9B and table S1), indicating that the surface modification has a negligible influence on the electron occupation state and associated magnetic properties in the VSe_2 lattice (*29*).

PVDF-VSe_2-COOH superlattice film

Diazonium chemistry allowed us to customize VSe_2 monolayer surface with various surface functional groups to tune its miscibility in the PVDF matrix. Efficient hydrogen bonding between surface carboxyl functional groups and PVDF chains (*37*) allowed the VSe_2-COOH nanosheets to be stably dispersed in the PVDF matrix at a filling fraction up to 25 wt %, a value comparable to that of many highly dispersible 2D materials in nanocomposites, such as graphene oxide and MXene (*38*, *39*). The high miscibility of VSe_2-COOH facilitated its solution processability. For instance, conventional drop casting of the precursor solution onto a plasma-pretreated substrate with high hydrophilicity can readily form composite films up to tens of centimeters in scale (Fig. 1D).

The shear-flow force during casting caused the VSe_2-COOH nanosheets to orient uniformly in the thin film, which we could directly observe using polarizing optical microscopy. As depicted in fig. S11, the cross section of pure PVDF remained unchanged when the polarizer angle was rotated 90°, whereas the PVDF-VSe_2-COOH film transitioned from light to dark, indicating the anisotropic structure of the nanocomposite film.

Further analysis with small-angle x-ray scattering (SAXS) was conducted to study the orientation degree of VSe_2-COOH nanosheets. The 2D SAXS pattern featured a strong diffuse spot in the vertical direction (fig. S12A), and plots of the corresponding azimuthal angle (φ) revealed a sharp peak at 90° (Fig. 2G) in PVDF-VSe_2-COOH film with a filling fraction below 25 wt %, indicating that the nanosheets were horizontally oriented along the film. This orientation was beneficial for the nanoconfined dewetting–induced ordered nanocrystallization of the composite.

As quantitatively evaluated with the Maier-Saupe distribution function (Fig. 2H and table S2), the orientation order parameter reached as high as 0.71 for the PVDF-VSe_2-COOH film, confirming that the incorporation of VSe_2-COOH induces nanoscale alignment in the nanocomposite film (*40*). This result is further evidenced by the observation

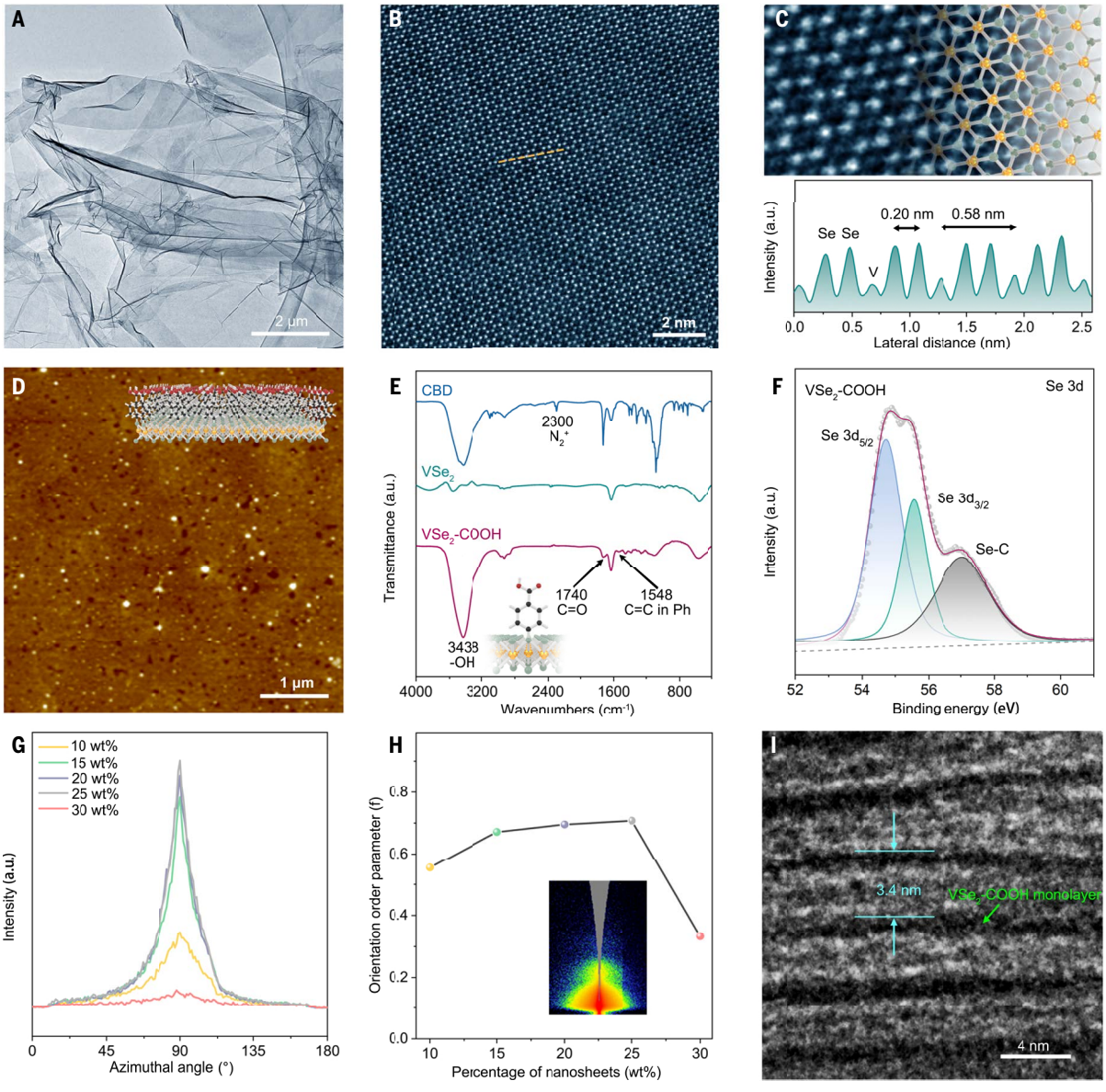


Fig. 2. Structural characterizations of the VSe_2 monolayer, VSe_2-COOH monolayer, and PVDF-VSe_2-COOH superlattices. (**A**) TEM image and (**B**) atomic-resolution STEM image of the VSe_2 monolayer. (**C**) Schematic representation of the atomic structure of the VSe_2 monolayer, with golden and green balls representing V and Se atoms, respectively. The intensity line profile along the yellow line in (B) shows the in-plane lattice constant *a*. (**D**) AFM morphological image of VSe_2-COOH surface. The inset shows the ball-and-stick representation, where gold, green, black, red, and white spheres denote V, Se, C, O, and H atoms, respectively. (**E**) FTIR spectra of CBD, VSe_2, and VSe_2-COOH. The characteristic vibrational modes of the anchored *para*-carboxybenzene functional groups on the VSe_2 surface (inset figure) are highlighted for visual reference. (**F**) High-resolution XPS spectrum of Se *3d* for VSe_2-COOH. (**G**) Azimuthal angle and (**H**) orientation order parameter of films with varying percentages of VSe_2-COOH nanosheets. The inset shows the 2D SAXS image of the PVDF-VSe_2-COOH (25 wt %) film. (**I**) The high-resolution cross-sectional TEM image of PVDF-VSe_2-COOH (25 wt %) film.

that when the content of VSe_2-COOH nanosheets exceeded 30%, the orientation order parameter dropped back to approximately 0.33 as a result of aggregation of VSe_2-COOH nanosheets.

Additionally, SAXS measurements were used to determine the average interlayer distance in the laminated film (*41*, *42*) (fig. S12B and table S2). The critical vector corresponding to the peak intensity, q_{max}, was used to calculate the interlayer distance (d) with the Bragg equation (*43*): $d = 2\pi/q_{max}$. As the VSe_2-COOH content increased, the interlayer distance gradually decreased to 3.47 nm at a filling fraction of 25%. This uniform laminated structure was further confirmed by scanning electron microscopy (SEM) (fig. S13) and TEM images (Fig. 2I). Energy-dispersive x-ray spectroscopy mapping in the SEM test demonstrated the even distribution of F, V, and Se elements throughout the nanocomposite film. The high-resolution cross-sectional TEM image of the nanocomposite film revealed the successful construction of well-oriented superlattice structures and intuitively verified the interlayer distance calculated from SAXS results. The flatter VSe_2-COOH monolayers within the superlattice also indicated the promotion of interfacial cocrystallization with diazonium functionalization (Fig. 2, A and I).

In situ XRD provided dynamic insight into the formation process of the PVDF-VSe_2-COOH film (Fig. 3, A and B, and fig. S14). As the interlayer solvent evaporates, the VSe_2-COOH nanosheets and interlayer-confined PVDF crystallize into a superlattice film (*44*), as

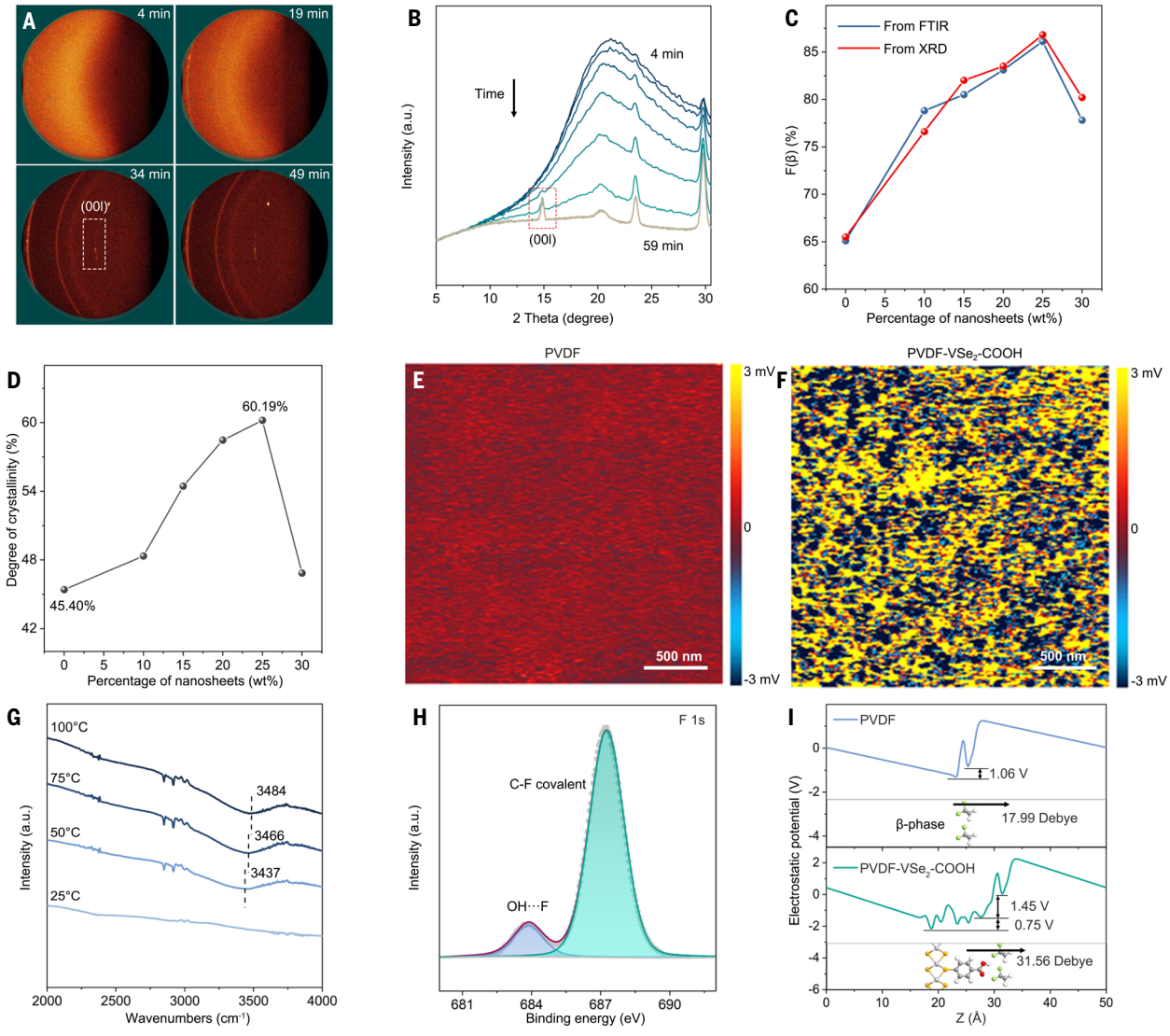


Fig. 3. Characterizations of crystallization and interfacial interaction of the PVDF-VSe_2-COOH superlattices. (**A**) Debye ring of the PVDF-VSe_2-COOH (25 wt %) film at different time points monitored by in situ XRD, illustrating the time-resolved evolution of the crystallization process. The white rectangle highlights the orientation of the (001) lattice plane of the nanosheets. (**B**) Representative XRD patterns corresponding to the specified time points. (**C**) Variation of the β-phase contents of PVDF as a function of VSe_2-COOH nanosheet percentages, calculated from XRD and FTIR spectra. (**D**) Crystallization degree of PVDF-VSe_2-COOH nanocomposite films with different filler contents. AFM-IR chemical map under irradiation with 1273 cm^{-1} (fingerprint peak of β-phase) laser of (**E**) PVDF and (**F**) PVDF-VSe_2-COOH (25 wt %) films. (**G**) Temperature-dependent FTIR spectra of the PVDF-VSe_2-COOH (25 wt %) film. (**H**) High-resolution XPS spectrum of F *1s* for PVDF-VSe_2-COOH (25 wt %) film. (**I**) Electrostatic potentials along *z* direction of β-phase PVDF monolayer before and after stacking on VSe_2-COOH surface. The inset dipole values are obtained in the corresponding 1 by 2 supercells.

revealed by the Debye ring in the 2D XRD images. After 24 min, circular arcs corresponding to the characteristic set of (001) diffraction peaks along the *c*-axis of VSe_2-COOH emerge, indicative of the enhanced alignment of VSe_2-COOH nanosheets in the drying process.

Along with the evaporation of interlayer solvents and correspondingly reduced interlayer distance, the confined PVDF within the VSe_2-COOH nanosheets transitioned into the polarized β phase, as marked by an emerging XRD peak at 20.6° (fig. S15A). This synchronous crystallization process continued until 34 min after drop casting, ultimately resulting in a cocrystalline PVDF-VSe_2-COOH superlattice film with narrow full width at half maximum XRD peaks for both VSe_2-COOH and β-phase PVDF. Curve deconvolution of the XRD pattern (fig. S16) revealed that increased content of VSe_2-COOH nanosheets led to a β-phase conversion of PVDF up to 86.8% at 25% filler content (Fig. 3C).

The crystallinity of PVDF in the composite film was assessed by several techniques. FTIR showed distinctly enhanced absorption at 840, 1168, and 1403 cm^{-1}, as evidence of the β-phase PVDF in the composite film, with a quantified ratio of 86.1% at a VSe_2-COOH filler content of 25% (Fig. 3C and figs. S15B and S17). Notably, this ratio of β phase aligned with the result obtained from XRD, representing record-high crystallinity compared with other studies (fig. S18 and table S3).

Differential scanning calorimetry and AFM analyses also indicated that the filling of VSe_2-COOH efficiently enhanced crystallinity conversion (*40*, *45*) (figs. S19 and S20). The addition of 25% VSe_2-COOH nanosheets resulted in the highest degree of crystallinity (X_c) of 60.19% compared with 45.40% for the pure PVDF. AFM infrared spectroscopy (AFM-IR) was further used to map the conformational distribution directly (Fig. 3, E and F, and fig. S21). We selected 976, 1273, and 1232 cm^{-1} to probe the samples, corresponding to the characteristic IR features of

the α, β, and γ phases of PVDF, respectively. The results indicate that the incorporation of VSe_2-COOH nanosheets into the PVDF matrix led to its conversion into the polarized β phase across the entire film.

In addition to evaluating the crystallization of each component in the composite film, we analyzed the interfacial interaction between the VSe_2-COOH nanofillers and the laminated PVDF nanocrystals. Time-dependent FTIR spectra of PVDF-VSe_2-COOH films with varying filler contents revealed interfacial hydrogen bonding (Fig. 3G and fig. S22), identified by the –OH stretching vibration of the hydrogen-bonded carboxyl group, as indicated by an absorption peak between 3300 and 3500 cm^{-1}. Given the inverse relationship between hydrogen bonding strength and temperature (*46*), the blue shift of this characteristic peak in each composite film was evidence of interfacial hydrogen bonding. Additionally, the positive correlation between IR absorption shifts and the filling content of nanosheets further supported hydrogen bonding associated with the incorporated VSe_2-COOH.

To corroborate these findings, XPS analysis was conducted to evaluate the direct hydrogen bonding between the carboxyl group and PVDF (Fig. 3H and fig. S23). The appearance of a peak at 683.9 eV (O-H…F) in the PVDF-VSe_2-COOH film indicated that the CF_2 groups interact with carboxyl groups through hydrogen bonding (*47*). Consistent with the two-stage weight loss of VSe_2-COOH observed in the thermogravimetric analysis curves (fig. S24), two additional weight losses at 255° and 397°C were observed in the PVDF-VSe_2-COOH films, which we attributed to the decomposition of *para*-carboxybenzene group on VSe_2 nanosheets. The drastically different bonding strength of the *para*-carboxybenzene group on the VSe_2 and at the interface in the composite also suggested its bonding interaction with PVDF.

Density functional theory calculations were systematically conducted (Fig. 3I and fig. S25), and the results demonstrate the stability of β-phase PVDF on the VSe_2-COOH surface through hydrogen bonding interaction through binding energy and electrostatic potential calculations. This highly stable PVDF nucleation further suggests the interfacial cocrystallization behavior within the nanocomposites.

Mechanical and ferroic properties of the superlattice films.

We investigated the mechanical properties of the PVDF-VSe_2-COOH film (fig. S26 and table S4). The synergistic effect of highly oriented VSe_2-COOH nanosheets and strong interfacial interactions between VSe_2-COOH nanofillers and the PVDF matrix at a 25% filler content enhanced tensile strength and toughness, increasing them from 8.4 to 47.8 MPa and from 1.0 to 8.0 MJ m^{-3} compared with pristine PVDF, respectively, as evidenced by the compact morphology observed in SEM (fig. S27). As an origami demonstration shown in fig. S28 reveals, the PVDF-VSe_2-COOH film could be bent and folded into various representative structures with excellent mechanical robustness and flexibility. Notably, the mechanical properties of PVDF-VSe_2-COOH film could be further enhanced through a conventional heat drawing strategy (fig. S26 and table S5) to a tensile strength of 94.8 MPa and a toughness of 19.0 MJ m^{-3}.

We used piezoresponse force microscopy (PFM) to investigate the local ferroelectric and piezoelectric properties. The electrostatic force was first evaluated using scanning Kelvin probe force microscopy (fig. S29). Then, PFM amplitude and phase images of films were acquired in the dual AC resonance tracking (DART) mode, and an equal value of surface potential was applied to the tip voltage as compensation for the electrostatic force. The PFM images display the nanodomain structure that is independent of its morphological influence (fig. S29, C and D).

The nanodomain switching behavior of the PVDF-VSe_2-COOH film was resolved in real space with nanometric resolution using switching spectroscopy PFM (SS-PFM) (fig. S30). The selected areas exhibited standard 180° switching hysteresis loops and butterfly-shaped amplitude loops as a function of DC bias (V_{dc}) (Fig. 4, A and B). Ferroelectric domain switching was also observed (figs. S31 and S32), implying the nanoscale ferro- and piezoelectric properties of the PVDF-VSe_2-COOH film. The effective piezoelectric coefficient (d_{33}) was calculated to be 101.4 pm V^{-1} from the slope of the amplitude versus voltage curves, with resonance amplification eliminated through simple harmonic oscillator (SHO) parms in the DART panel.

To verify the calculated d_{33} value as discussed above, PFM amplitudes were measured under different AC voltages in both pure PVDF and PVDF-VSe_2-COOH film (fig. S33, A and B) (*48*), with corresponding amplitudes fitted linearly with the voltage (fig. S33C), confirming the piezoelectric property of the films. From the slopes of the curves, the d_{33} values of PVDF and PVDF-VSe_2-COOH films were determined to be 55.0 and 106.0 pm V^{-1}, respectively. Notably, the d_{33} of PVDF-VSe_2-COOH films was consistent with the value acquired from butterfly loops, affirming the accuracy of the measured piezoelectric coefficient. Furthermore, the d_{33} value of the PVDF-VSe_2-COOH film surpassed that of most previously reported polymer-based piezoelectric materials (fig. S33D and table S6).

The dielectric properties were further examined to analyze the ferroelectric characteristics (fig. S34). Unlike previously reported nanocomposite films, which generally suffer from leakage current issues due to the formation of extra conductive paths by the aggregated nanofillers with lower electrical resistivity than the insulating matrix, the PVDF-VSe_2-COOH film demonstrated improved performance. Although VSe_2 is metallic with excellent conductivity at the monolayer limit (*30*, *49*), the PVDF-VSe_2-COOH film displayed a dielectric loss comparable to that of pristine PVDF and maintained a low leakage current density of $< 2 \times 10^{-6}$ A cm^{-2}. We attributed these properties to the exceptional miscibility of VSe_2-COOH nanosheets within the PVDF matrix, as characterized and discussed previously.

The temperature-dependent dielectric constant was measured to assess ferroelectricity (Fig. 4C). The filled VSe_2-COOH nanosheets enhanced the composite's Curie temperature (above which the spontaneous polarization disappears), raising it to 156.9°C, because of their favorable crystallization effects toward the β phase and efficient interfacial interaction with the PVDF matrix. Additionally, we evaluated the piezoelectric voltage coefficient (g_{33}), a key figure of merit for sensing and energy harvesting applications in ferroic materials (*48*). The PVDF-VSe_2-COOH film exhibited a g_{33} of 1180.6×10^{-3} V m N^{-1}. It can be concluded that the integrated piezoelectric properties of our superlattice films surpass other piezoelectric soft materials, as evidenced by the comparison of critical parameters, including d_{33} and g_{33} (Fig. 4D and table S7).

VSe_2-COOH nanosheets exhibit intrinsic ferromagnetism at room temperature, making it a viable material for imparting ME properties to nanocomposite films. In contrast with the diamagnetism observed in pure PVDF (Fig. 4E), incorporating VSe_2-COOH nanosheets into the PVDF matrix resulted in typical magnetic hysteresis loops. As expected, the maximum magnetization (M_s) increases with the content of the VSe_2-COOH nanofiller (Fig. 4F). We also assessed the out-of-plane M-H loop of PVDF-VSe_2-COOH film, which exhibited a lower M_s compared with the in-plane M_s (fig. S35). Given that VSe_2 nanosheet features an easy magnetic axis in the in-plane direction (*28*), these results corroborated the in-plane orientation of VSe_2-COOH nanosheets in the composite films.

We further investigated the ME coupling between the ferroelectric and ferromagnetic phases through the flexoelectric effect (fig. S36). For comparison, we fabricated a similar VSe_2-COOH composite in a polyvinyl alcohol (PVA) matrix (a conventional polymer without piezoelectric property) using the same method. We then explored the impact of the flexoelectric effect on the M_s values of the PVDF-VSe_2-COOH and PVA-VSe_2-COOH films. Unlike the unchanged behavior observed in the PVA-VSe_2-COOH film, the PVDF-VSe_2-COOH film showed a decrease in M_s values as the degree of flexure increased, indicating a direct ME coupling effect in the PVDF-VSe_2-COOH film.

Theoretical studies

To elucidate the underlying mechanisms, theoretical analysis, simulations, and quantitative experiments were systematically conducted. These results highlight the critical role of hydrogen bonding in stabilizing the interface and aligning dipoles (figs. S37 and S38). The close contact

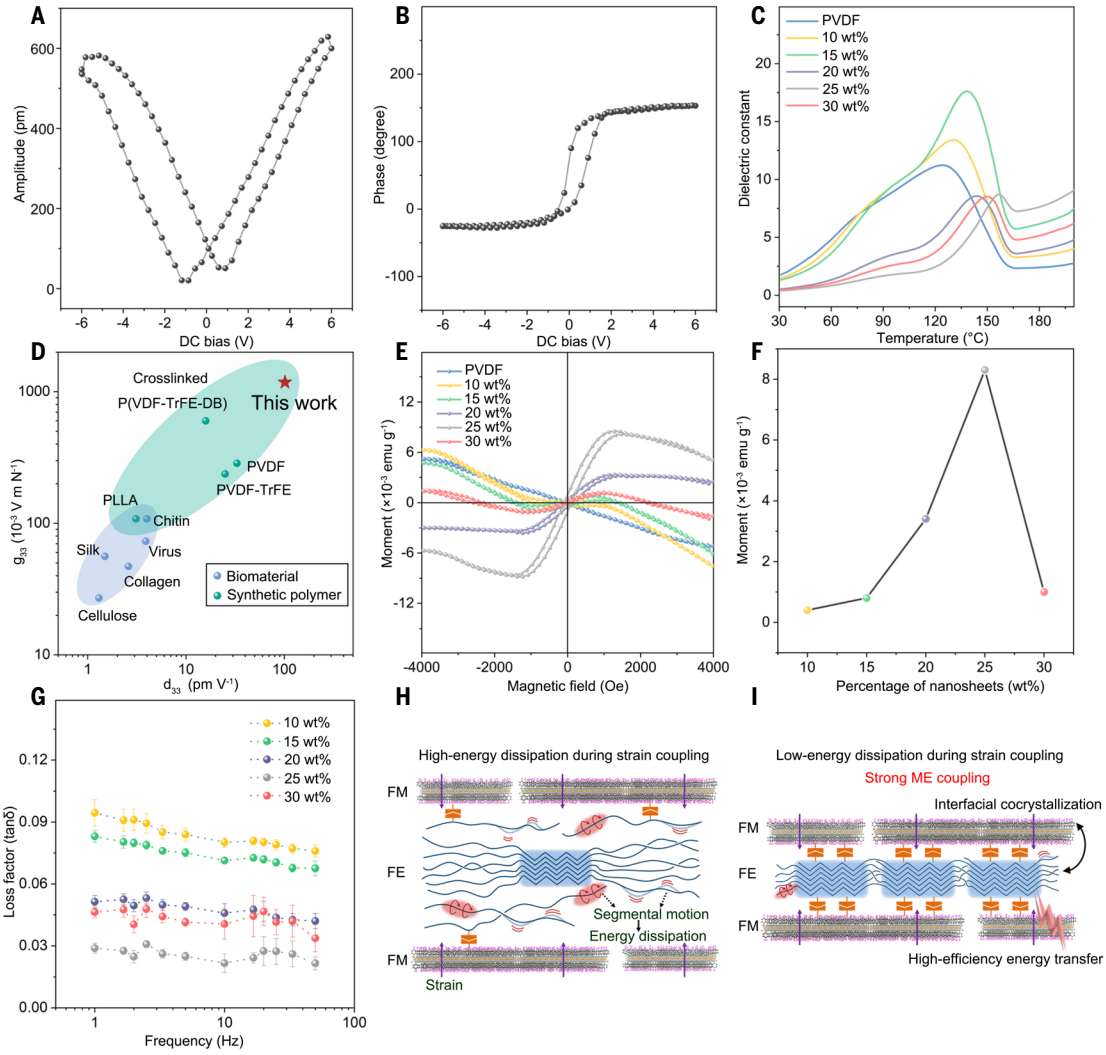


Fig. 4. Ferroic properties of the nanocomposites. (**A**) SS-PFM amplitude and (**B**) phase response of PVDF-VSe_2-COOH (25 wt %) superlattices, showing hysteresis loop behavior and polarization reversal. (**C**) Temperature-dependent changes in the dielectric constant for PVDF and PVDF-VSe_2-COOH superlattices with varying filler contents. (**D**) Comparison of piezoelectric voltage coefficient (g_{33}) as a function of piezoelectric coefficient (d_{33}) for various piezoelectric soft materials. (**E**) Magnetic hysteresis loops and (**F**) maximum magnetization of PVDF and PVDF-VSe_2-COOH superlattice film with varying filler contents in the in-plain direction. (**G**) Loss factor (tanδ) of PVDF-VSe_2-COOH films with varying filler contents. Schematic illustration of the mechanism of the magnetoelectric coupling process under (**H**) low and (**I**) high degrees of crystallinity, where "FM" and "FE" denote "ferromagnetic" and "ferroelectric," respectively.

between the ferroelectric and the ferromagnetic phases enabled efficient magnetoelectric conversion through strain-mediated coupling at the interface. Theoretical simulations further demonstrated that interfacial strain enhanced magnetoelectric coupling by breaking local symmetry, strengthening spin-orbital coupling, and delocalizing spin density, highlighting the importance of interfacial quality for efficient energy transfer (fig. S39).

However, in prior polymeric nanocomposites, issues such as wrinkles, defects, and viscoelastic losses drastically compromise the magnetoelectric effects. Our theoretical calculations further demonstrate that such defects suppressed local spin coherence and considerably weakened magnetoelectric coupling (fig. S40), leading to high energy dissipation and limited energy transfer (fig. S41). By contrast, our composite films feature a submolecular-flat interface between the ferroelectric and ferromagnetic phases that enabled robust strain coupling. This well-defined interface, achieved through interfacial cocrystallization, minimizes energy loss and supports highly efficient energy transfer (Fig. 4, G to I).

Under an alternating magnetic field, internal ferromagnetic nanosheets were predicted to experience dynamic strain, which is transferred across the interface to the ferroelectric phase. At low nanosheet content, the ferroelectric phase exhibits low crystallinity, with many polymer chains remaining mobile at the interface. These mobile chains dissipate mechanical energy during strain transfer, weakening the strain-mediated ME coupling. By contrast, when the nanosheet content reaches a critical threshold, the ferroelectric phase becomes highly crystalline, leading to interfacial cocrystallization. This ordered structure efficiently channels the strain from the nanosheets to the polar ferroelectric phase with minimal energy loss, facilitating high-efficiency energy transfer and achieving strong ME coupling.

Applications of magnetoelectric sensors

We investigated the mechanical-electrical response of the PVDF-VSe_2-COOH films to demonstrate their piezoelectric properties and potential applications in sensors and energy harvesters (fig. S42). As illustrated in fig. S43, the output voltages of a piezoelectric sensor were measured under varying forces and frequencies. At a constant frequency of 2 Hz, the PVDF-VSe_2-COOH–based device exhibited excellent linearity with applied forces ranging from 5 to 30 N, confirming its high sensitivity in piezoelectricity. Additionally, the PVDF-VSe_2-COOH film displayed

repeatable piezoelectric output voltages under different frequencies and loading forces in continuous operation, demonstrating a stable mechanical-electric response with a fast piezoelectric response rate.

To accurately quantify the response time of the PVDF-VSe_2-COOH film, we measured its voltage output with the widely used "switching polarity" test method (fig. S44, A and B). The identical magnitudes in reversed connection tests proved that the pulse signals were sourced from the piezoelectric effect (Fig. 5A and fig. S44C). The detected response time was approximately 1 ms, indicating a notable 10-fold improvement in response speed compared with conventional force sensors (Fig. 5B and table S8).

Given the high piezoelectric coefficient and rapid response speed of the PVDF-VSe_2-COOH film, we further explored its application as artificial skin for health and motion detection. As shown in figs. S45 and S46, it functions as a self-powered physiological sensor capable of monitoring physiological signals ranging from body movements to subtle deformations. Moreover, we demonstrated its potential for use in large-area sensor arrays and surveillance systems for underwater detection, because the device showed excellent and stable performance in detecting underwater ultrasound waves (fig. S47)

The direct ME coupling in PVDF-VSe_2-COOH film was used in a proof-of-concept wearable MC sensor. As schemed in Fig. 5C, the ME effect in PVDF-VSe_2-COOH film enabled direct coupling between magnetic fields and electrical capacitance. When exposed to an alternating magnetic (AC mode) field, the capacitance variations were readily detected with a portable inductance (L), capacitance (C), and resistance (LCR) meter. Notably, the PVDF-VSe_2-COOH film could be stacked into a multilayer configuration to enhance the signal-to-noise ratio, exhibiting quasi–layer-dependent enhancement behavior (Fig. 5D and fig. S48A).

MC measurement is a well-established method for characterizing the coupling between magnetic and electric polarization because the

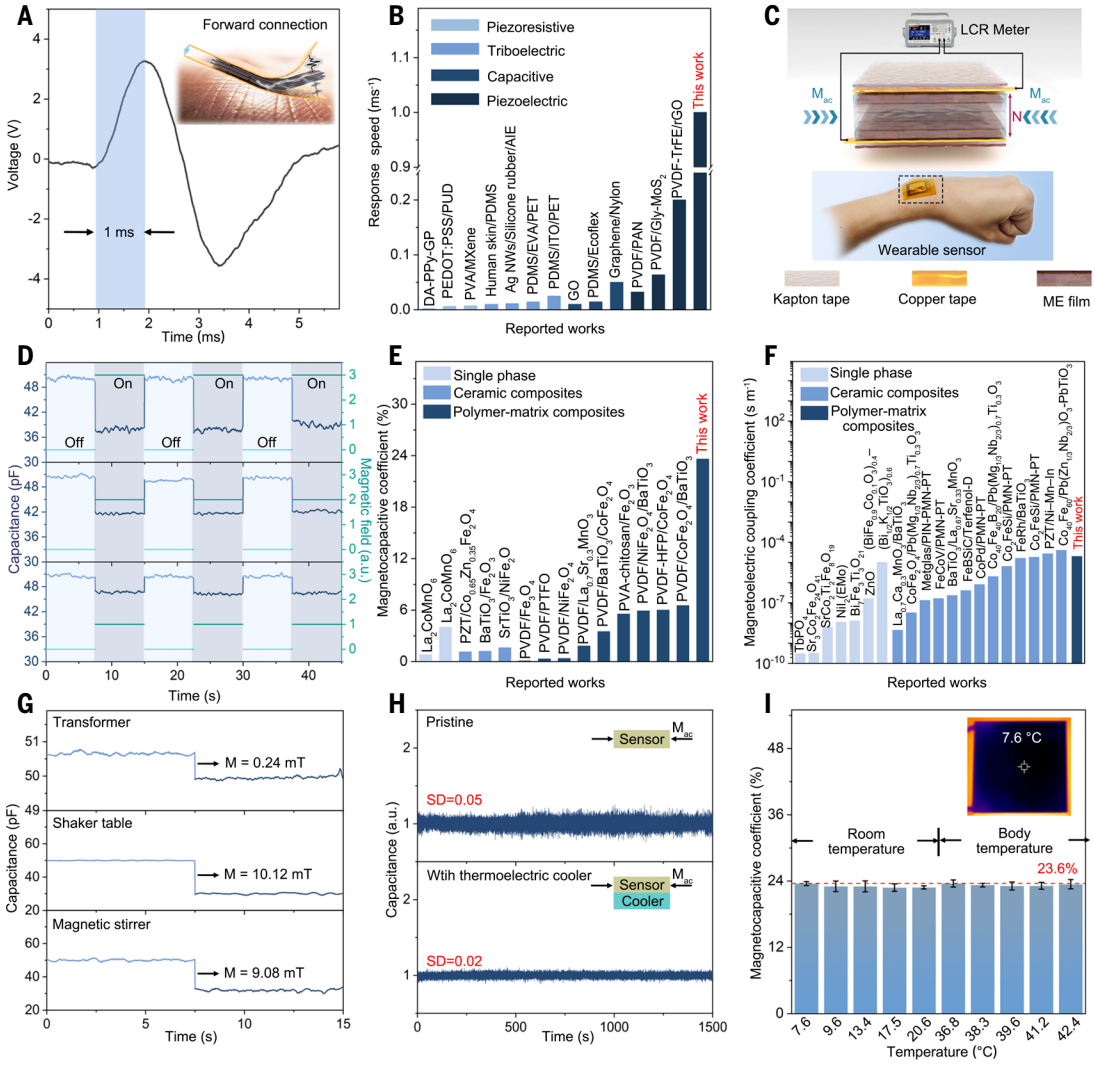


Fig. 5. Versatile applications of the magnetoelectric sensors. (**A**) Measured open-circuit voltage in the forward connection of the PVDF-VSe_2-COOH (25 wt %) film. The inset shows the schematic response of the magnetoelectric sensor under external fields. (**B**) The piezoelectric response speed of the as-prepared PVDF-VSe_2-COOH (25 wt %) film compared with other flexible force sensors, with response time (τ) converted to response speed (τ^{-1}) to intuitively illustrate piezoelectric efficiency. (**C**) Schematic illustration of the wearable magnetocapacitive sensor structure. (**D**) Capacitance variation of five-layer PVDF-VSe_2-COOH (25 wt %) films under different amplitudes of the AC magnetic field. "On" and "off" indicate the presence and absence of the magnetic field. Comparison of (**E**) magnetocapacitive coefficient and (**F**) magnetoelectric coupling coefficient (α) of the PVDF-VSe_2-COOH film with other benchmark magnetoelectric materials. (**G**) Magnetic field detection of a transformer, shaker table, and magnetic stirrer using the wearable magnetocapacitive sensor. The magnetic field was calculated from the corresponding capacitance change and standard curve. (**H**) Performance of the magnetoelectric sensor with or without thermoelectric cooler under an external magnetic field. (**I**) Magnetocapacitive coefficient measured at varying temperatures, with the inset showing the uniform temperature distribution of the thermoelectric device.

orientation of the dipoles is hindered by the generated piezoelectric charges as a result of strain effects at the interface (*1*, *50*). To quantitatively assess the ME coupling effect, we calculated the MC coefficient, defined as $MC = |(C_H\text{-}C_0)/C_0 \times 100\%|$, where C_H and C_0 are the capacitance measured with and without an applying magnetic field, respectively. As depicted in fig. S48B, the composite film exhibited an MC coefficient as high as 23.6%, versus typical values for ME materials of 6.5% (Fig. 5E) (*50*, *51*). We converted this value to a magnetoelectric coupling coefficient (α), which also compares favorably with the values from other studies, including with ceramic-based materials (Fig. 5F), showcasing its giant ME effect and highlighting the advantage of its flexibility. By contrast, control groups display negligible or inferior ME effects, emphasizing the essential roles of each component (fig. S48C).

More importantly, the flexible MC sensor can be worn on the wrist (Fig. 5C) to accurately detect magnetic fields from various sources, performing comparably to a standard gaussmeter (Fig. 5G and fig. S49, A and B). This capability highlights its potential for wearable electronics in applications such as magnetic resonance imaging (fig. S49C), robust sensing in diverse environments (fig. S50), and integration with other functional devices (Fig. 5, H and I).

Notably, the sensor demonstrates exceptional stability during long-term operation and under different chemical conditions. Integration with a thermoelectric cooler (*52*) enhances measurement stability, reducing the standard deviation from 0.05 to 0.02, maintaining a constant temperature, and enabling advanced sensor design with low Curie temperature components. The MC performance remains stable across varying temperatures, demonstrating reliable operation under both ambient and physiological conditions. Furthermore, the nanocomposite films demonstrate large-scale interlayer uniformity and interfacial cocrystallization quality (Fig. 1D, figs. S51 and S52), offering potential for environmentally sustainable, scalable production.

Conclusions

We developed an energy-efficient flexible ME polymer-inorganic sensor through interfacial cocrystallization-induced strong strain-coupling effect, composed of parallelly aligned ferromagnetic VSe_2-COOH monolayers and laminated ferroelectric PVDF nanocrystals in a layered configuration. The VSe_2-COOH nanofillers, characterized by atomic-scale thickness and robust 2D ferromagnetism, show miscible dispersion in the PVDF matrix with excellent interfacial matching behavior. Using a nanoconfined dewetting–induced ordered nanocrystallization protocol, in-plane stacked submolecular-flat VSe_2-COOH nanosheets and highly ordered crystalline PVDF laminates are readily achieved through shear flow, resulting in the formation of a ME superlattice film on a large scale. The fabricated nanocomposite films exhibit excellent flexibility, exceptional mechanical properties, and superior ME properties. Furthermore, they demonstrate versatile applications in wearable ME sensors, including an inspiring application as a MC sensor, offering high controllability and operability based on the collective ME effect. Our finding provides ME superlattice film, paving the way for versatile multifunction integration such as thermoelectric coolers in miniaturized wearable devices. These ME films hold promise for next-generation wearable electronics, and their seamless integration into thermoelectric devices enables enhanced thermal management in magnetoelectric sensor design.

REFERENCES AND NOTES

1. J. Ma, J. Hu, Z. Li, C.-W. Nan, *Adv. Mater.* **23**, 1062–1087 (2011).
2. W. Eerenstein, N. D. Mathur, J. F. Scott, *Nature* **442**, 759–765 (2006).
3. R. O. Cherifi *et al.*, *Nat. Mater.* **13**, 345–351 (2014).
4. T. Jungwirth, J. Wunderlich, K. Olejník, *Nat. Mater.* **11**, 382–390 (2012).
5. J. Hu, T. F. Rosenbaum, *Nat. Mater.* **7**, 697–700 (2008).
6. N. A. Spaldin, R. Ramesh, *Nat. Mater.* **18**, 203–212 (2019).
7. N. A. Hill, *J. Phys. Chem. B* **104**, 6694–6709 (2000).
8. J.-M. Hu, L.-Q. Chen, C.-W. Nan, *Adv. Mater.* **28**, 15–39 (2016).
9. H. Zheng *et al.*, *Science* **303**, 661–663 (2004).
10. X.-L. Liu *et al.*, *Adv. Mater.* **33**, e2004542 (2021).
11. H. Yang *et al.*, *Adv. Mater.* **36**, e2311996 (2024).
12. J. A. Mundy *et al.*, *Nature* **537**, 523–527 (2016).
13. A. K. Yadav *et al.*, *Nature* **530**, 198–201 (2016).
14. S. Valencia *et al.*, *Nat. Mater.* **10**, 753–758 (2011).
15. H. Watanabe, *Prog. Polym. Sci.* **24**, 1253–1403 (1999).
16. W. Eerenstein, M. Wiora, J. L. Prieto, J. F. Scott, N. D. Mathur, *Nat. Mater.* **6**, 348–351 (2007).
17. Y. Hernandez *et al.*, *Nat. Nanotechnol.* **3**, 563–568 (2008).
18. K. S. Novoselov, A. Mishchenko, A. Carvalho, A. H. Castro Neto, *Science* **353**, aac9439 (2016).
19. C. Tan, H. Zhang, *Chem. Soc. Rev.* **44**, 2713–2731 (2015).
20. M. Liu *et al.*, *Nature* **517**, 68–72 (2015).
21. K. Shehzad, Y. Xu, C. Gao, X. Duan, *Chem. Soc. Rev.* **45**, 5541–5588 (2016).
22. S. Stankovich *et al.*, *Nature* **442**, 282–286 (2006).
23. F. H. L. Koppens *et al.*, *Nat. Nanotechnol.* **9**, 780–793 (2014).
24. X. Xu, J. Chen, J. Zhou, B. Li, *Adv. Mater.* **30**, e1705544 (2018).
25. D. G. Papageorgiou, I. A. Kinloch, R. J. Young, *Prog. Mater. Sci.* **90**, 75–127 (2017).
26. C. Gong *et al.*, *Nature* **546**, 265–269 (2017).
27. B. Huang *et al.*, *Nature* **546**, 270–273 (2017).
28. M. Bonilla *et al.*, *Nat. Nanotechnol.* **13**, 289–293 (2018).
29. Y. Ma *et al.*, *ACS Nano* **6**, 1695–1701 (2012).
30. W. Yu *et al.*, *Adv. Mater.* **31**, e1903779 (2019).
31. Z. Zhang *et al.*, *Adv. Mater.* **29**, 1702359 (2017).
32. J. Li *et al.*, *Nat. Mater.* **20**, 181–187 (2021).
33. V. Nicolosi, M. Chhowalla, M. G. Kanatzidis, M. S. Strano, J. N. Coleman, *Science* **340**, 1226419 (2013).
34. X. Cai, Y. Luo, B. Liu, H.-M. Cheng, *Chem. Soc. Rev.* **47**, 6224–6266 (2018).
35. M. Garrido, A. Naranjo, E. M. Pérez, *Chem. Sci.* **15**, 3428–3445 (2024).
36. Q. Fu, X. Bao, *Chem. Soc. Rev.* **46**, 1842–1874 (2017).
37. Z. L. Cui, N. T. Hassankiadeh, Y. B. Zhuang, E. Drioli, Y. M. Lee, *Prog. Polym. Sci.* **51**, 94–126 (2015).
38. V. C. Tung, M. J. Allen, Y. Yang, R. B. Kaner, *Nat. Nanotechnol.* **4**, 25–29 (2009).
39. K. Maleski, V. N. Mochalin, Y. Gogotsi, *Chem. Mater.* **29**, 1632–1640 (2017).
40. S. W. Kong *et al.*, *Matter* **7**, – 2250–2264 (2024).
41. T. Zhou *et al.*, *ACS Nano* **16**, 12013–12023 (2022).
42. C. Zhao *et al.*, *Nature* **580**, 210–215 (2020).
43. S. Lin *et al.*, *Sci. Adv.* **5**, eaau8528 (2019).
44. C. Wang *et al.*, *Nature* **555**, 231–236 (2018).
45. J. Huang, J. Zhou, M. Liu, *JACS Au* **2**, 280–291 (2022).
46. Q. Q. Guo *et al.*, *Mater. Horiz.* **6**, 996–1004 (2019).
47. X. Huang, Y. Y. Wang, X. X. Zhang, *Nano Energy* **99**, 107379 (2022).
48. Z. Zhang *et al.*, *Nat. Commun.* **14**, 4094 (2023).
49. A. G. Kelly, D. O'Suilleabhain, C. Gabbett, J. N. Coleman, *Nat. Rev. Mater.* **7**, 217–234 (2022).
50. D. K. Rana *et al.*, *New J. Chem.* **43**, 3128–3138 (2019).
51. X. J. Lv, J. J. Liu, J. H. Zhao, M. K. Wang, Z. B. Pan, *J. Alloys Compd.* **918**, 165772 (2022).
52. D. Liu *et al.*, *Natl. Sci. Rev.* **12**, nwae448 (2024).

ACKNOWLEDGMENTS

We thank D. Wang (Institute of Chemistry, Chinese Academy of Sciences) for assistance with PFM experiments and L. Feng (Beihang University) for their support with magnetocapacitive sensor measurements. We thank the Analysis & Testing Center of Beihang University for the facilities and the scientific and technical assistance. **Funding:** This research was supported by the National Key Research and Development Project (2022YFA503000), the National Natural Science Foundation of China (22341301, 22272004, 52450001), the National Science Fund for Distinguished Young Scholars (52525101), the International Cooperation and Exchange of the National Natural Science Foundation of China (52411540237), the Tencent Xplorer Prize, and the project supported by the Space Application System of China Manned Space Program. **Author contributions:** Conceptualization: M. L., L.-D.Z., and J. Li; Funding acquisition: M. L., L.-D.Z., J. Li; Investigation: M. L., L.-D.Z., J. Li, J. Lu, T. Z., B. H., Y. H., W. W., Y. S., S. K., J.Hu., Y. R., B. Q., H. R., J. He; Methodology: M. L., L.-D.Z., J. Li, J. Lu, T. Z., B. H.; Project administration: M. L.; Supervision: M. L.; Visualization: M. L., J. Li, B. H.; Writing – original draft: B. H., J. Li; Writing – review & editing: M. L., L.-D.Z., J. Li, B. H. **Competing interests:** The authors declare that they have no competing interests. **Data and materials availability:** All data are available in the main text or supplementary materials.

License information: Copyright © 2025 the authors, some rights reserved; exclusive licensee American Association for the Advancement of Science. No claim to original US government works. https://www.science.org/about/science-licenses-journal-article-reuse

SUPPLEMENTARY MATERIALS

science.org/doi/10.1126/science.adt2741
Materials and Methods; Supplementary Text; Figs. S1 to S52; Tables S1 to S9; References (*53*–*155*)

Submitted 19 September 2024; resubmitted 29 April 2025; accepted 6 June 2025
10.1126/science.adt2741

METALLURGY

Three-dimensional nucleation and growth of deformation twins in magnesium

Sangwon Lee[1], Michael Pilipchuk[2], Can Yildirim[3], Duncan Greeley[4], Qianying Shi[5], Tracy D. Berman[5], Adam Creuziger[6], Evan Rust[6], Carsten Detlefs[3], Veera Sundararaghavan[2], John E. Allison[1,5], Ashley Bucsek[1,5]*

At two-thirds the weight of aluminum, magnesium alloys have the potential to reduce the fuel consumption of transportation vehicles. These advancements depend on our ability to optimize the desirable versus undesirable effects of deformation twins, which are three-dimensional (3D) microstructural domains that form under mechanical stresses. Previously only characterized through surface or thin-film measurements, we present 3D in situ characterization of deformation twinning inside an embedded grain over mesoscopic fields of view using dark-field x-ray microscopy supported by crystal plasticity finite element analysis. The results revealed the role of triple junctions on twin nucleation and the sequence and irregularity of twin growth and showed that twin-grain junctions, twin-twin junctions, and twin boundaries were the sites of localized dislocation accumulation.

The use of lighter structural components can substantially reduce the fuel consumption of gas-powered vehicles and lower the energy density needs of battery-powered vehicles. These compelling material needs drive much of the interest in magnesium alloys. Magnesium (Mg) is not only lightweight (weighing 30% less than aluminum) with high specific strength but also the eighth most common element in Earth's crust (*1*). In contrast to iron, aluminum, and titanium alloys, there are opportunities to extract Mg from seawater and to recycle or biodegrade Mg alloys, making Mg an environmentally attractive alternative to alloys used in the transportation sector. The mechanical behavior of Mg alloys, however, is complex. Mg and many of its alloys have a hexagonal close-packed crystal structure that causes strong plastic anisotropy and a limited number of dislocation slip systems, resulting in a propensity for deformation twinning (*2*). Deformation twins, which are three-dimensional (3D) microstructural domains that form under mechanical stresses, have competing impacts on mechanical behavior. Deformation twins can accommodate substantial plastic strain by enabling deformation along the c-axis of the crystal (*3*). However, deformation twins are often associated with crack initiation sites (*4*–*8*). Because of this dichotomy, understanding twin behavior is critical for understanding the plasticity, ductility, and failure mechanisms of Mg alloys.

Although atomistic modeling and transmission electron microscopy (EM) studies have provided insight into the atomic-scale nature of deformation twinning (*7*, *9*–*12*), recent studies have emphasized the importance of 3D characterization for a more comprehensive understanding of deformation twinning at the grain scale (*11*–*13*). For example, the conventional understanding of twin nucleation at the grain scale has relied largely on Schmid factors (*14*, *15*). Schmid factors are well-known parameters used to rank twin variants by quantifying how favorably specific crystallographic planes and directions are oriented for slip or twinning under an applied stress, based on the highest resolved shear stress on the twin plane in the twin shear direction. However, Lind *et al.* (*16*) used 3D high-energy diffraction microscopy (HEDM) to show that Schmid factors could not account for twin nucleation or variant selection behavior in pure zirconium, even when local grain orientations and stresses were included. Another HEDM study by Abdolvand *et al.* (*17*) found that the most favored (highest Schmid factor) twin variant contributed the most to the twin number fraction, but the contribution of other variants was relatively independent of the Schmid factor. In addition to twin nucleation, our understanding of twin propagation and growth has been limited by a lack of 3D in situ characterization capabilities. We used growth to denote a general increase in the size of the twin domain, propagation as the expansion of the twin domain along the twin shear or lateral directions, and thickening as the expansion along the twin plane normal direction. Liu *et al.* (*11*, *12*) noted that the irregular shapes of deformation twins and their growth behavior in different directions cannot be fully understood without 3D analysis. Their studies using statistical electron backscatter diffraction (EBSD) analysis and atomistic simulations suggest that the lateral expansion of twins is faster than their forward propagation. This anisotropic growth behavior underscores the importance of 3D analysis for a complete understanding of twin evolution.

We used dark-field x-ray microscopy (DFXM) to characterize 3D deformation twinning inside an embedded grain in a bulk, polycrystalline Mg-4Al alloy with submicrometer spatial resolution. The results revealed 3D twin growth behavior, showing that twins in 3D appeared as irregular ellipsoid shapes. In the early stage of growth, its shortest axis is in the twin plane normal k_1, the second longest axis is in the twin shear direction η_1, and the longest axis is in the twin lateral direction λ (a vector perpendicular to the twin plane normal and the shear direction, $\lambda = k_1 \times \eta_1$). We also observed that twins propagate along the lateral direction first (though not necessarily completing propagation), followed by propagation along the twin shear direction, and finally thickening in the twin plane normal direction. The results also showed that the intersection area between twin-grain junctions and triple junctions is maximized, suggesting preferential twin selection and nucleation based on the geometry of triple junctions. Finally, we used the high angular resolution of DFXM to reveal the local accumulation of geometrically necessary dislocations (GNDs) at twin-grain junctions, twin-twin junctions, and along twin planes.

Dark-field x-ray microscopy experiments

DFXM is an x-ray diffraction imaging technique that can be used to image subsurface grains with spatial resolutions as high as 60 nm and a field of view of ~125 × 125 μm^2 (*18*). With DFXM, an objective is aligned with a single Bragg reflection, and the reflection is then recorded on a far-field detector. The aperture of the objective serves to (i) magnify the reflection on the detector such that a real-space projection of the illuminated grain is visible, and (ii) filter reciprocal space such that the sample and/or objective require tilting for small variations in orientation or elastic strain. Because the imaging is performed in the diffraction condition over large working distances, DFXM can be used to map distortions in elastic strain and orientation with extremely high angular resolutions, on the order of 10^{-5} (i.e., 10 microstrains) and 0.001° (*19*), respectively. Together, these capabilities offer spatial resolutions approaching those of EM techniques with angular resolutions exceeding those of EM, but in 3D and over mesoscopic fields of view. We used in situ DFXM to measure the emergence and growth of twins and relate local orientation gradients to the accumulation of GNDs. The DFXM experiment was performed on beamline ID06-HXM at the European Synchrotron Radiation Facility

[1]Department of Mechanical Engineering, University of Michigan, Ann Arbor, MI, USA. [2]Department of Aerospace Engineering, University of Michigan, Ann Arbor, MI, USA. [3]European Synchrotron Radiation Facility, Grenoble Cedex, France. [4]Los Alamos National Laboratory, Los Alamos, NM, USA. [5]Department of Materials Science and Engineering, University of Michigan, Ann Arbor, MI, USA. [6]National Institute of Standards and Technology, Gaithersburg, MD, USA. *Corresponding author. Email: abucsek@umich.edu

(ESRF); this microscope now resides at their beamline ID03. The calculated spatial resolution of this experiment is 212 nm. The experimental setup is shown in Fig. 1A. The deformation twins were measured through diffraction contrast and identified from their twin plane normal direction. The relative misorientation of the parent grain was mapped by imaging the Bragg reflection while tilting the sample about two vectors perpendicular to the scattering vector (sample tilting angles α and β) and calculating the centroids of the resulting intensity distributions at each pixel (*19*–*24*).

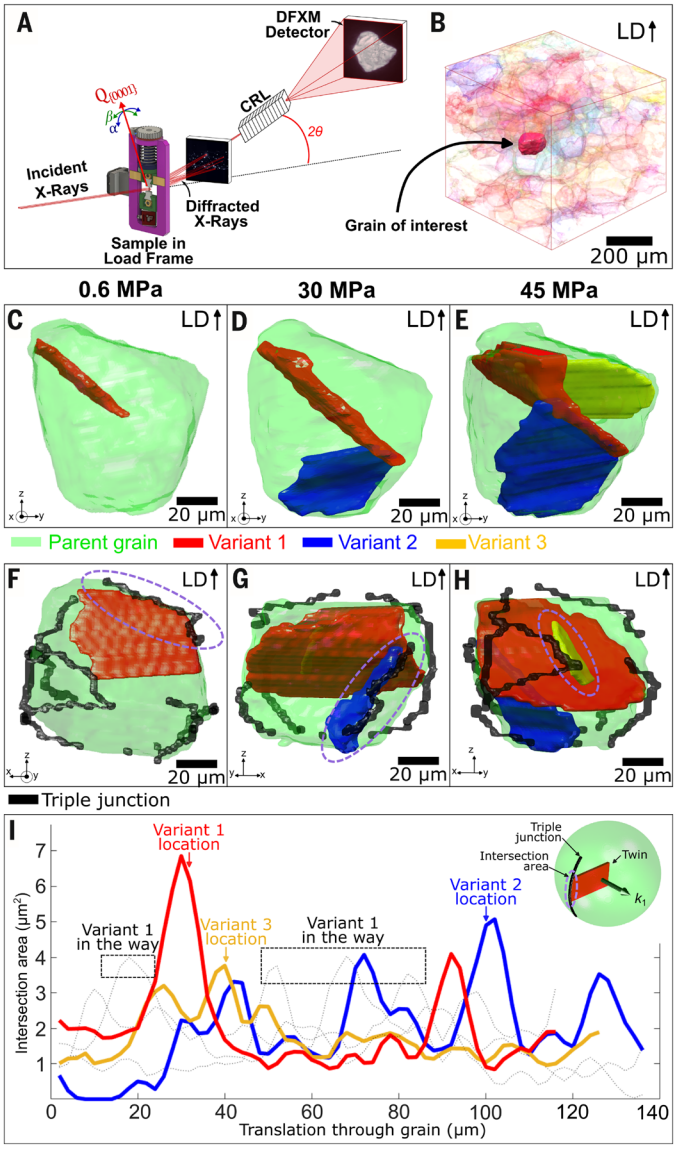


Fig. 1. In situ DFXM, 3D twin morphology, and triple junctions. (**A**) In situ DFXM technique. (**B**) Grain of interest inside the grain network. (**C** to **E**) The parent grain (50% transparency, green) and the three twins (opaque, red, blue, and yellow). Evolution of the twin morphology inside the parent grain relative to the loading direction (LD). (**F** to **H**) Triple junctions (opaque, black). The purple dashed lines highlight the intersection area between twin-grain junctions and triple junctions. (**I**) The intersection area between triple junctions and twins versus translation through the parent grain (along the twin plane normal direction k_1) calculated for each $\{10\bar{1}2\}$ twin variant. Arrows point to the locations where the three experimentally observed twins were located. Boxes point to regions where new twins could not form because the first twin variant (red) was already intersecting the triple junction line segment (i.e., was "in the way"). See movies S1 to S3 for full 3D characterization.

Uniaxial tensile loading was applied by using a custom miniature loading stage developed at the National Institute of Standards and Technology (NIST) with a mass of 240 g. The sample geometry is shown in fig. S1 and the loading stage is shown in fig. S4. The polycrystalline Mg-4Al alloy had an average grain size of 75 μm. Laboratory diffraction contrast tomography (labDCT) measurements were used to precharacterize the 3D grain map prior to the DFXM experiment using a Zeiss Xradia Versa 520 Micro-CT. To maximize the twinning volume fraction (fig. S3), we selected a grain that was oriented such that the basal plane was perpendicular to the loading direction (Fig. 1B). All six variants of the $\{10\bar{1}2\}$ extension twin system have twinning Schmid factors close to 0.5 (between 0.47 and 0.49). The neighboring grains had an average Schmid factor of 0.31 (fig. S6). The high likelihood for this grain to twin relative to its neighbors makes this grain ideal for observing twin initiation events (rather than twin transfer across grain boundaries), while still subject to network features such as triple junctions.

Twin nucleation

Figure 1, C to E, shows the three $\{10\bar{1}2\}$-type extension twins that formed during loading. The first twin that formed was a $(0\bar{1}12)[01\bar{1}1]$ twin (shown in red). This twin formed when the sample was mounted and preloaded to 0.6 MPa. The second twin, a $(\bar{1}102)[1\bar{1}01]$ twin (shown in blue), was not observed until the 30 MPa load step. The third twin, a $(\bar{1}012)[10\bar{1}1]$ twin (shown in yellow), was not observed until the 45 MPa load step. Although all six $\{10\bar{1}2\}$-type extension twin variants have high Schmid factors, these three variants had the lowest Schmid factors of the six variants (table S1), suggesting that there may be factors contributing to twin variant selection beyond the Schmid factor. Figure 1, F to H, shows the twin morphologies relative to triple junctions (shown in black) measured with labDCT. These results revealed that all three twins intersected triple junctions (see purple circles) and show that all three twin planes were geometrically aligned with triple junction segments—that is, each twin-grain junction line coincides with a segment of the triple junction line.

In Fig. 1I, we calculated how much area would be intersected between triple junctions and the twins for each of the six variants, had they nucleated anywhere in the grain. The results showed that the three twin variants that were experimentally observed corresponded to the three largest triple junction intersection areas. This result may suggest that variants that maximized triple junction intersection areas may form preferentially, which would favor twin variants with twin planes that are parallel to triple junction line segments. This idea may be explained by observations by Jiang *et al.* that multiple early-stage twin embryos can merge into a larger twin nucleus that subsequently grows (*10*). In other words, multiple twin nuclei may form along a triple junction and then merge, resulting in a twin domain that lies parallel to and intersects the triple junction.

In the metallurgy community, it is well known that triple junctions lead to stress concentrations, making them energetically favorable locations for twin nucleation (*25*–*27*). The effect of triple junctions on local stresses was investigated using the crystal plasticity finite element method (CPFEM) to simulate subgrain-scale stresses in the grain of interest and surrounding grains. The simulation volume consisted of the grain of interest and its first-order neighbors (fig. S8), and the simulations were performed without any instantiated twins and with plasticity "turned off," i.e., elastic deformation only. The results were used to understand the stress state before the formation of any twins, particularly at triple junctions. Figure 2, A to C, compares the stresses in voxels located near triple junctions with those located away from triple junctions, showing that voxels located near triple junctions exhibit higher stresses. Figure 2, D to F, shows only the stress values in voxels located near triple junctions, highlighting the relatively high local stresses at the triple junctions that are suspected to be the three twin nucleation sites.

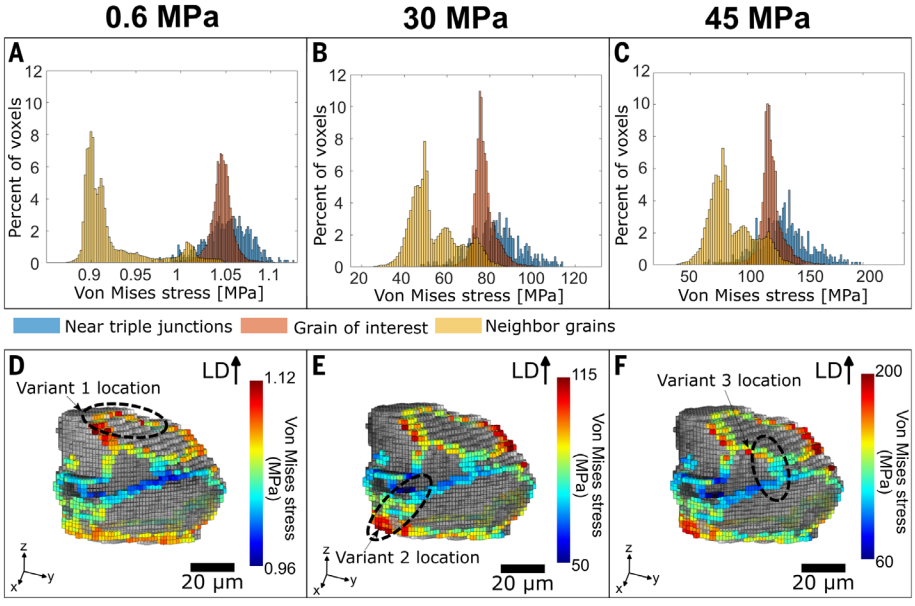


Fig. 2. Stress concentrations near triple junctions. Histograms of the simulated von Mises stress for voxels located near triple junctions (blue), inside the grain of interest (red), and inside neighboring grains (yellow) for macroscopic stresses of (**A**) 0.6 MPa, (**B**) 30 MPa, and (**C**) 45 MPa. Arrows point to locations where the three twins were experimentally observed in (**D**) variant 1 at 0.6 MPa, (**E**) variant 2 at 30 MPa, and (**F**) variant 3 at 45 MPa.

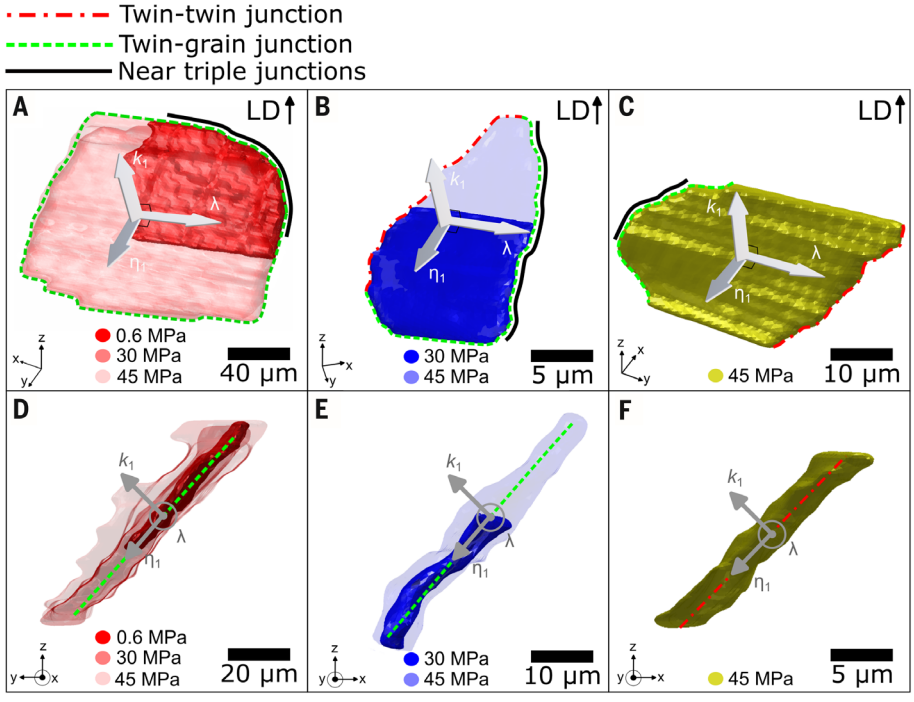


Fig. 3. 3D twin growth. Growth behavior of the three twins in (**A** to **C**) isometric viewing, and (**D** to **F**) with the viewing direction parallel to twin lateral vectors. The grain boundary is marked in (A) to (D) in green and the red twin is marked in (B), (C), and (F) in red. See movies S4 to S6 for full 3D characterization.

Twin growth

Figure 3 shows the growth behavior for the three twins. We observed that twins in 3D appear as irregular ellipsoid shapes, suggesting that growth is locally dominated. We observed that in the early stages of growth, the longest axis is in the lateral direction λ, the second longest axis is in the twin shear direction η_1, and shortest axis in the twin plane is in the normal direction k_1 (Fig. 3, A to F). We also observed that twins propagate along the lateral direction first, followed by propagation along the twin shear direction, and finally thicken in the twin plane normal direction. Last, we saw that growth in the lateral direction λ may become stunted until later stages of growth. These findings are detailed below.

At 0.6 MPa, the first (red) twin formed (Fig. 3, A and D) with its longest axis in the lateral direction λ. However, the twin had not yet completed propagation in the lateral direction λ; i.e., it had not yet reached the left grain boundary in Fig. 3A. Between 0.6 MPa and 30 MPa, it completed propagation in the lateral direction λ (touching the left grain boundary in Fig. 3A), as well as completing propagation in the twin shear direction η_1 (touching the top grain boundary in Fig. 3A). Between 30 and 45 MPa, the red twin substantially and irregularly thickens in the twin plane normal k_1 direction by ~5 μm. The observations are similar for the blue twin (Fig. 3, B and E), which was first observed at 30 MPa with its longest axis in the lateral direction λ. Between 30 and 45 MPa, the blue twin propagates in the twin shear direction η_1 to reach the grain/twin boundaries on top, and it thickens regularly in the twin plane normal k_1 direction. The yellow twin (Fig. 3, C and F) was not observed until 45 MPa, with its longest axis in the lateral direction λ.

Collectively, these results are consistent with Liu *et al.* (*11*), in which an ex situ EBSD statistical analysis on 2D twin shapes was used to also show that twins grow faster along the lateral direction λ than they do along the twin shear direction η_1 at the initial stages of twin growth. However, the observations corresponding to the red twin also suggest that propagation in the lateral direction λ can become stunted until the later stages of growth.

Finally, it is important to mention that the propensity to form a few twins that continue to grow with loading versus the propensity to nucleate more and more new twins of the same variant (which do not continue to grow) is alloy-specific. Mg-Al tends to do the former—i.e., nucleate a few twins that continue to grow with additional loading [e.g., (*28*)]. Mg-Y, on the other hand, tends to do the latter—i.e., nucleate more and more twins that do not continue to grow with additional loading.

Twins and dislocation accumulation

In addition to twin morphology (Fig. 4, A to C), in situ DFXM was used to spatially resolve local orientation gradients in the parent grain during deformation twinning. Figure 4 shows the evolution of intragranular misorientation (Fig. 4, D to F), kernel average misorientation (KAM) (Fig. 4, G to I), and GND density (Fig. 4, J to L). Intragranular misorientation refers to the misorientation of each voxel with respect to the grain average. KAM refers to the misorientation of each kernel with respect to its neighbor kernel (kernel size: 5 μm). The voxels in these visualizations

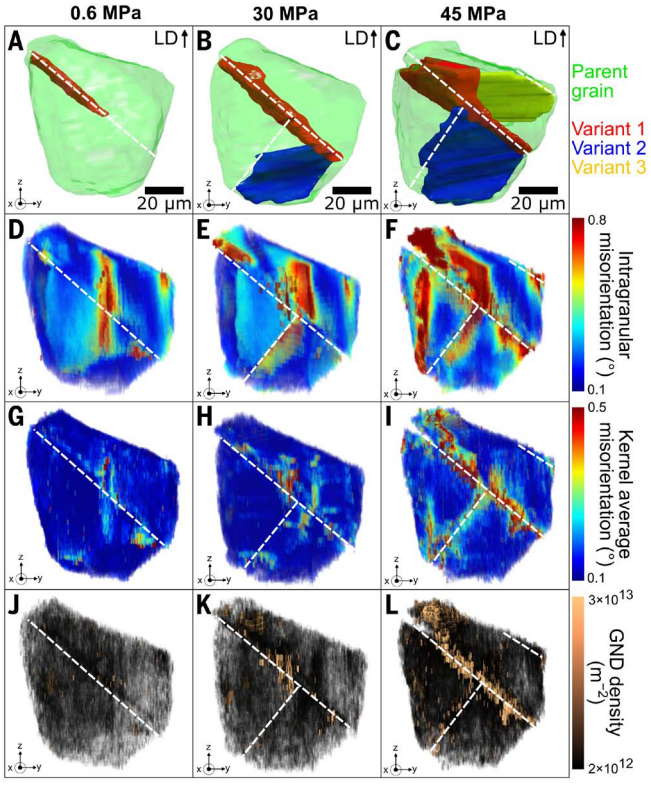


Fig. 4. Evolution of local orientation gradients and GND density near the grain exterior. (**A** to **C**) Evolution of the 3D twin morphology. (**D** to **F**) Intragranular misorientation with respect to the parent grain average. (**G** to **I**) KAM. (**J** to **L**) GND density inside the parent grain. White dashed lines indicate the locations of twin-grain junctions. See movie S7 for full 3D characterization.

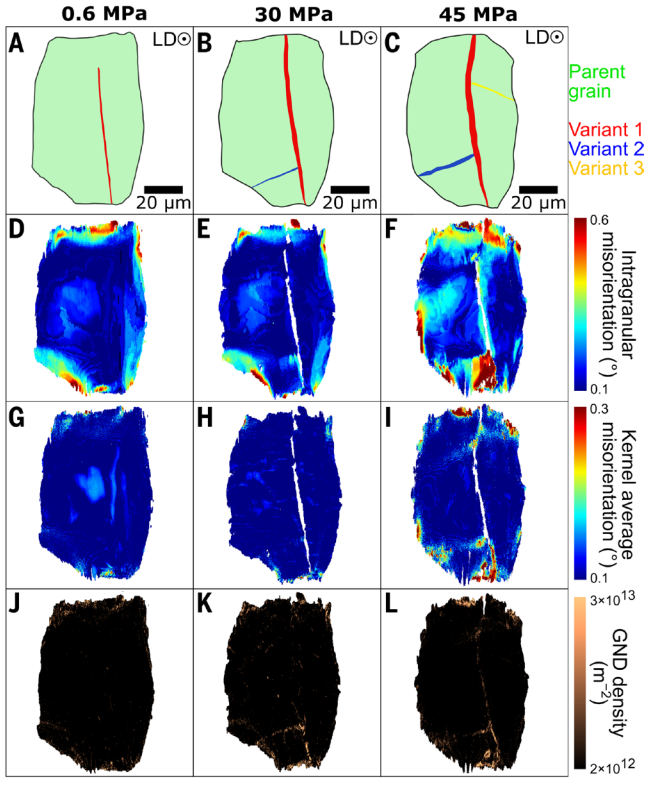


Fig. 5. Evolution of local orientation gradients and GND density in the grain interior. (**A** to **C**) Evolution of the twin morphology. (**D** to **F**) intragranular misorientation with respect to the parent grain average. (**G** to **I**) KAM. (**J** to **L**) GND density inside the parent grain. See movie S8 for full 2D characterization.

were opaque, so they only showed the orientation gradients near the grain boundaries. The dashed lines mark the locations of the twin-grain junctions. The results showed that twin-grain junctions were sites of large local orientation gradients and GND density accumulation, both of which increased with loading.

In the first measurement at 0.6 MPa (Fig. 4G), a faint line of high KAM can be seen along the red twin-grain junction. Between 0.6 to 30 MPa (Fig. 4H), and at 45 MPa (Fig. 4I), the KAM along this twin-grain junction increased from ~0.1° to 0.5°. The results were similar for the blue twin-grain junction, where a line of high KAM could be observed at 30 MPa (Fig. 4H). This line did not exist at 0.6 MPa when the blue twin-grain junction was not yet present, and it intensified between 30 MPa (Fig. 4G) and 45 MPa (Fig. 4I). These regions of high KAM translated to regions of high GND density accumulation (Fig. 4, J to L). Notice that the GND density was high at twin-grain junctions and low everywhere else, and that the GND density at the twin-grain junctions intensified as the macroscopic stress increased.

Figure 4 shows that twin-grain junctions are sites for dislocation accumulation, and this is the case for all of the twin-grain junctions regardless of the neighboring grain or how soft or hard it is. The reason that GNDs accumulate at twin-grain junctions can be understood from the following context: Twinning is a simple shear deformation applied along the twin plane in the twin shear direction. This deformation can be thought of as applied to the parent grain inside the twin domain. However, this deformation cannot be applied to the region of the parent grain that is connected to a grain boundary, as it is constrained by the neighboring grain (*29*). Thus, dislocation density accumulates at the twin-grain junction site in response to this strain incompatibility as a result of local stress concentrations and/or as a means of geometrical accommodation. This idea is further explored using CPFEM in the supplementary materials (fig. S10).

We also investigated whether GND density accumulated at other features, such as twin-twin junctions, twin boundaries, and triple junctions. Figure 5 shows how orientation gradients and GND density evolved inside the grain using a 2D "slice" of the grain (taken near the grain center; all slices can be seen in movie S8.) The intragranular misorientation results in Fig. 4, D to F show substantial intragranular misorientation near grain boundaries and along twin planes. However, the regions of high KAM (Fig. 4, J to L) and GND density (Fig. 4, J to L) were much more localized. High KAM/GND density can be seen where the twins impinge upon the grain boundaries and impinge upon each other. The highest KAM/GND density was observed at twin-grain junctions, with more moderate GND density accumulation at twin-twin junctions. KAM/GND density can also be seen accumulating along some twin boundaries. No substantial GND density was observed at triple junctions, except for the triple junction regions that also happened to be twin-grain junctions. Looking at the recent work of Li *et al.* (*30*), we note how similar our GND density observations are with their EBSD-based observations of total scalar disclination density at twin-grain junctions, twin-twin junctions, and along twin planes. The comparison suggests a possible connection between the orientation changes and stress fields caused by disclination formation at these boundaries and the accumulation of GNDs.

The measurements presented in Figs. 4 and 5 provide direct observations of how twins can lead to regions of high plastic deformation. This is potentially of importance for the following reasons: First, research that has shown that dislocations at twin-twin boundaries can hinder growth, as well as hinder detwinning (*9*, *31*); relatedly, research

has also shown that dislocations cause strain hardening due to the dislocation-twin boundary interactions during cyclic loading (*32*). Second, it is common to observe two twins connected across a grain boundary (*33*, *34*), suggesting either twin transfer or co-nucleation. In the case of twin transfer, it is understood to occur by way of a stress field on the other side of the grain boundary from the initial twin (*34*, *35*) (e.g., fig. S10). The dislocation accumulation that we observe near twin-grain junctions may be important for properly predicting these stress fields and, consequently, twin transfer. Finally, while many computational tools have been used to theorize the mechanisms behind twinning and crack initiation (e.g., *36*), a fundamental understanding based on experimental evidence is lacking. Strain localization by way of accumulation of plastic deformation is a necessary precedent to crack initiation in ductile materials (*37*). On the other hand, the stress relief and dislocation networks associated with twinning may retard crack propagation (*38*). Since GNDs are indicative of accumulation of plastic deformation, the dislocation accumulation that we consistently observe at twin-grain junctions as well as twin-twin junctions and along grain twin planes may be important for understanding crack initiation and propagation near twins. However, this connection requires further investigation.

Discussion

We present 3D in situ characterization of deformation twinning inside an embedded grain over mesoscopic fields of view using DFXM. The results confirm that twin growth behavior is locally dominated, leading to irregular 3D ellipsoidal shapes as previously suspected from EBSD measurements. We observed that twins propagate along the lateral direction λ first (though not necessarily completing propagation), followed by propagation along the twin shear direction η_1, and finally thickening in the twin plane normal direction k_1. As a result, in the early stage of growth, a twin's shortest axis is in the twin plane normal k_1, the second longest axis is in the twin shear direction η_1, and the longest axis is in the twin lateral direction λ. The results also revealed new observations regarding the 3D geometry of twins with respect to triple junctions, suggesting preferential twin selection and nucleation based on maximizing the intersection between twins and triple junctions. Finally, the results reveal that twin-grain junctions and, to a lesser extent, twin-twin junctions and along twin planes are the sites of localized GND accumulation. These 3D in situ observations offer new insights into deformation twinning and its relationship to nucleation, growth, and dislocations, contributing to a fundamental understanding of the complex micromechanical behavior of magnesium alloys and twinning materials in general. More broadly, this study highlights the importance of high-resolution 3D in situ characterization for understanding 3D deformation mechanisms and microstructure evolution.

REFERENCES AND NOTES

1. T. M. Pollock, *Science* **328**, 986–987 (2010).
2. I. J. Polmear, in *Light Alloys: From Traditional Alloys to Nanocrystals* (Elsevier, 2005), pp. 282–283.
3. J. W. Christian, S. Mahajan, *Prog. Mater. Sci.* **39**, 1–157 (1995).
4. N. S. Prasad, N. N. Kumar, R. Narasimhan, S. Suwas, *Acta Mater.* **94**, 281–293 (2015).
5. L. Li *et al.*, *Mater. Charact.* **179**, 111362 (2021).
6. M. Lentz, M. Risse, N. Schaefer, W. Reimers, I. Beyerlein, *Nat. Commun.* **7**, 11068 (2016).
7. B. Zhou *et al.*, *Int. J. Plast.* **128**, 102669 (2020).
8. K. Hazeli *et al.*, *Scr. Mater.* **100**, 9–12 (2015).
9. Q. Yu *et al.*, *Acta Mater.* **77**, 28–42 (2014).
10. L. Jiang *et al.*, *Nat. Commun.* **13**, 20 (2022).
11. Y. Liu *et al.*, *Nat. Commun.* **10**, 3308 (2019).
12. Y. Liu *et al.*, *Nat. Commun.* **7**, 11577 (2016).
13. M. Arul Kumar *et al.*, *Nat. Commun.* **9**, 4761 (2018).
14. E. Schmid, Yield point of crystals, critical shear stress lawin *Proceedings of the First International Congress for Applied Mechanics, Delft* (1924).
15. E. Schmid, W. Boas, *Plasticity of Crystals with Special Reference to Metals* (Chapman & Hall, 1968).
16. J. Lind *et al.*, *Acta Mater.* **76**, 213–220 (2014).
17. H. Abdolvand, M. Majkut, J. Oddershede, J. P. Wright, M. R. Daymond, *Acta Mater.* **93**, 246–255 (2015).
18. M. Carlsen, C. Detlefs, C. Yildirim, T. Ræder, H. Simons, *Acta Crystallogr. A Found. Adv.* **78**, 482–490 (2022).
19. H. Simons *et al.*, *Nat. Commun.* **6**, 6098 (2015).
20. M. Kutsal *et al.*, in *IOP Conference Series: Materials Science and Engineering* (IOP Publishing, 2019), vol. 580, p. 012007.
21. H. Simons, A. C. Jakobsen, S. R. Ahl, C. Detlefs, H. F. Poulsen, *MRS Bull.* **41**, 454–459 (2016).
22. H. F. Poulsen *et al.*, *J. Appl. Cryst.* **50**, 1441–1456 (2017).
23. A. Bucsek *et al.*, *Acta Mater.* **179**, 273–286 (2019).
24. S. Lee *et al.*, *Sci. Rep.* **14**, 6241 (2024).
25. J. M. Hestroffer *et al.*, *Acta Mater.* **249**, 118801 (2023).
26. S. Kobayashi, T. Inomata, H. Kobayashi, S. Tsurekawa, T. Watanabe, *J. Mater. Sci.* **43**, 3792–3799 (2008).
27. M. A. Kumar, I. J. Beyerlein, *J. Mater. Res.* **35**, 217–241 (2020).
28. Z. Chen, C. Torbet, J. Allison, *J. Miner. Met. Mater. Soc.* **74**, 2577–2591 (2022).
29. H. Zhi *et al.*, *Acta Mater.* **195**, 371–382 (2020).
30. H. Li *et al.*, *Acta Mater.* **281**, 120386 (2024).
31. Q. Yu, J. Wang, Y. Jiang, R. J. McCabe, C. N. Tomé, *Mater. Res. Lett.* **2**, 82–88 (2014).
32. Q. Yu, J. Wang, Y. Jiang, *J. Mater.* **2013**, 1–8 (2013).
33. M. A. Kumar, R. J. McCabe, V. Taupin, C. N. Tomé, L. Capolungo, *Mater. Charact.* **194**, 112457 (2022).
34. M. Arul Kumar, I. J. Beyerlein, R. J. McCabe, C. N. Tomé, *Nat. Commun.* **7**, 13826 (2016).
35. A. Khosravani *et al.*, *Acta Mater.* **100**, 202–214 (2015).
36. S. R. Yeratapally, M. G. Glavicic, M. Hardy, M. D. Sangid, *Acta Mater.* **107**, 152–167 (2016).
37. M. D. Sangid, *Int. J. Fatigue* **57**, 58–72 (2013).
38. J. Tian *et al.*, *Materials* **14**, 5217 (2021).
39. A. Bucsek, E. C. P. Valenzuela, J. Moya, S. Lee, Y. Jin, Understanding the role of recrystallized versus non-recrystallized grains during annealing in Mg alloys, ESRF (2025); https://doi.org/doi.org/10.15151/ESRF-ES-901214768.

ACKNOWLEDGMENTS

Funding: This work was funded by the following: U.S. Department of Energy Office of Basic Energy Sciences Division of Materials Science and Engineering Award DE-SC0008637 as part of the Center for Predictive Integrated Structural Materials Science (PRISMS) (to S.L., M.P., Q.S., D.G., T.D.B., V.S., J.E.A., and A.B.). **Author contributions:** Conceptualization: S.L. and A.B. Methodology: S.L., A.C., E.R., C.Y., C.D., and A.B. Visualization: S.L. Funding acquisition: J.E.A. and A.B. Supervision: A.B. Material preparation and pre-characterization: Q.S., T.D.B., and S.L. Simulations: M.P., D.G., and V.S. Experiments: S.L., C.Y., C.D., A.B., A.C., and E.R. Writing – original draft: S.L., and A.B. Writing – review & editing: S.L., C.Y., T.D.B., A.C., E.R., C.D., J.E.A., and A.B. **Competing interests:** Authors declare that they have no competing interests. **Data and materials availability:** All processed data are available to the public on the Materials Commons at https://doi.org/10.13011/m3-4hes-9d81. All raw data are available via the European Synchrotron Radiation Facility (ESRF) at https://doi.esrf.fr/10.15151/ESRF-ES-901214768 (*39*). Certain equipment, instruments, software, or materials are identified in this paper to specify the experimental procedure adequately. Such identification is not intended to imply recommendation or endorsement of any product or service by NIST, nor is it intended to imply that the materials or equipment identified are necessarily the best available for the purpose. **License information:** Copyright © 2025 the authors, some rights reserved; exclusive licensee American Association for the Advancement of Science. No claim to original US government works. https://www.science.org/content/page/science-licenses-journal-article-reuse

SUPPLEMENTARY MATERIALS

science.org/doi/10.1126/science.adv3460
Materials and Methods; Supplementary Text; Figs. S1 to S10; Table S1; References (*40*–*48*); Movies S1 to S9

Submitted 27 December 2024; accepted 16 June 2025

10.1126/science.adv3460

BIOMINERALS

Radular teeth matrix protein 1 directs iron oxide deposition in chiton teeth

Michiko Nemoto[1]*, Koki Okada[2], Haruka Akamine[2], Yuki Odagaki[2], Yuka Narahara[2], Kenji Okoshi[3], Kiori Obuse[1], David Kisailus[4,5], Hisao Moriya[1], Akira Satoh[6]

Nature builds multiscale mineral structures with impressive mechanical properties through spatially and temporally orchestrated organic-mineral assembly. One example of regulated mineralization is found in hypermineralized and ultrahard magnetic teeth of chiton, which grind on rock to feed on algae. At early stages of tooth formation, iron oxide deposition is controlled using a chiton-specific radular teeth matrix protein 1 (RTMP1), which is transported into teeth through microvilli. RTMP1 spatially and temporally guides and enhances mineralization on chitinous fibers within the tooth, providing a hard, tough, and strong architecture that enables the organism to perform repetitive abrasive events to survive.

Living organisms can synthesize biominerals with a variety of useful properties under physiological conditions. Several proteins have been reported to regulate the formation of biominerals, including those involved in the formation of mammalian bones and teeth (*1*, *2*), siliceous skeletons of sponges (*3*, *4*) and cell walls of diatoms (*5*, *6*), and calcium carbonate shells of mollusks (*7*). In addition to the well-studied Si- and Ca-based biominerals, a few organisms form magnetite (Fe_3O_4), an iron-based biomineral. Representative examples include magnetosomes produced by magnetotactic bacteria and the radular teeth of chitons. Magnetosome formation has been shown to be regulated by multiple proteins within precisely controlled intracellular vesicles (*8*, *9*). In contrast, the molecular mechanisms underlying the formation of radular teeth in chitons remain largely unknown. Chitons, mollusks found in rocky coastal areas, have a feeding organ called a radula and deposit magnetite on the cusps of their radular teeth (Fig. 1A). Chiton teeth were discovered by Lowenstam in 1962 as the first biologically formed magnetite (*10*). Chiton teeth exhibit greater wear resistance than zirconia (*11*). Chitons use these tough teeth to scrape algae and other organisms from rocks for food (*12*, *13*). As the magnetite-deposited cusps wear and fall off the anterior region of the radula during feeding, they are replaced by newly formed teeth advanced from the posterior. Teeth are continuously formed in the radular tissue, with those at different maturation stages present in one radula (Fig. 2A) (*14*). The formation of chiton teeth is regulated by the epithelial cells covering the teeth in a tissue called the radular sac. Tooth formation begins with the formation of a transparent tooth matrix composed of α-chitin and protein by odontoblast cells at the posterior end of the sac (Fig. 1B). Subsequently, mineral aggregates of weakly crystalline hydrated iron oxide (ferrihydrite) are deposited on the chitin fibers, resulting in reddish-brown teeth. The ferrihydrite then transforms to magnetite, resulting in black teeth (Fig. 2A).

We previously performed a transcriptomic analysis of the radular tissue of the gumboot chiton, *Cryptochiton stelleri*, and identified genes expressed in the radular tissue (*15*). Proteins extracted from mineralized cusps were compared with those extracted from base and radular membranes, and 22 proteins specific to mineralized cusps were identified (*15*, *16*). These proteins are believed to be important for iron oxide deposition on teeth, but their functions remain unclear.

RTMP1s are chiton-specific proteins

To identify proteins related to magnetite mineralization present across chiton species, we performed de novo assembly of transcriptomes of radular tissue from three chiton species, namely, *Acanthopleura japonica*, *Acanthochitona achates*, and *Placiphorella stimpsoni*, and performed cross-species comparisons with the previously analyzed transcriptomes of *C. stelleri* (Fig. 1, A and B, and table S1). A total of 9400 orthologous protein groups were found to be shared among the four chitons (Fig. 1C). Among them, homologs of 22 previously identified mineralized cusp–specific proteins in *C. stelleri* were found from the transcriptomes of the other three chiton species (Fig. 1D and table S2). Among the 22 mineralized cusp–specific proteins, radular teeth matrix protein 1 (RTMP1) shared no substantial homology with proteins from other organisms and was considered a chiton-specific protein. Additionally, a homolog of RTMP1 was found in the genome of the chiton *Acanthopleura granulata* (*17*). The RTMP1 homologs in *A. japonica*, *A. achates*, and *P. stimpsoni* were named AjRTMP1, AaRTMP1, and PsRTMP1, respectively (Fig. 1E). In this study, *C. stelleri* RTMP1, identified in a previous study (*15*), was renamed as CsRTMP1. Additionally, the term "RTMP1" is used collectively to refer to CsRTMP1 and all its homologs. All these sequences contain the predicted signal peptides and a high percentage of serine residues (>18.9%) (Fig. 1F). Sequence alignment revealed that the Gly-, Phe-, Trp-, and His-rich domains are conserved among CsRTMP1, AaRTMP1, and PsRTMP1 (Fig. 1E and fig. S1). AjRTMP1 does not contain Gly- or His-rich domains, but it does contain an Asp-rich domain. Among the previously predicted chitin-binding residues in CsRTMP1, only Trp is conserved in AjRTMP1, AaRTMP1, and PsRTMP1 (fig. S1). A single Trp conserved in four RTMP1s has been reported to play a key role in chitin binding in *Bacillus circulans* chitinase A1 (*18*). Sequence alignment revealed that the sequence similarity among CsRTMP1, AaRTMP1, and PsRTMP1 is 51.7 to 75.3%. Meanwhile, AjRTMP1 presents low sequence similarity (maximum: 35.8%) with the other three homologs (fig. S1). On the basis of structural prediction from the amino acid sequence, the N terminus of all RTMP1s has a region predicted to be disordered (Fig. 1G). Mass spectrometric analysis of proteins extracted from *C. stelleri* radular tissue confirmed that a serine residue in the SSSE motif of CsRTMP1 is phosphorylated (fig. S2). The SSSE motif of CsRTMP1, which was found to be phosphorylated, is present in all other homologs of the chiton species (fig. S1).

RTMP1 localizes to radular tissue and accumulates in tooth cusps

We examined AjRTMP1 protein expression in *A. japonica* radular tissue using an anti-AjRTMP1 antibody. In this analysis, the radular tissue was divided into three stages: stage 1 (eight or nine teeth), consisting of transparent teeth composed mainly of chitin; stage 2 (three to five teeth), consisting of teeth with a reddish-brown color due to ferrihydrite deposition; and stage 3 (10 teeth), where ferrihydrite transforms to magnetite, resulting in black teeth (Fig. 2, A and B). In stage 2, iron is deposited first at the junction zone of the cusps and bases and then at the leading edge of the cusps. We designated the first tooth where iron oxide deposition occurred at the leading edge as #0; designated less-mature teeth as #−1, #−2, and #−3; and designated more-mature

[1]Faculty of Environmental, Life, Natural Science and Technology, Okayama University, Okayama, Japan. [2]Graduate School of Environmental and Life Science, Okayama University, Okayama, Japan. [3]Department of Environmental Science, Faculty of Science, Toho University, Chiba, Japan. [4]Department of Materials Science and Engineering, University of California, Irvine, Irvine, CA, USA. [5]Materials and Manufacturing Technology Program, University of California, Irvine, Irvine, CA, USA. [6]Research Core for Interdisciplinary Sciences (RCIS), Okayama University, Okayama, Japan. ***Corresponding author. Email: mnemoto@okayama-u.ac.jp**

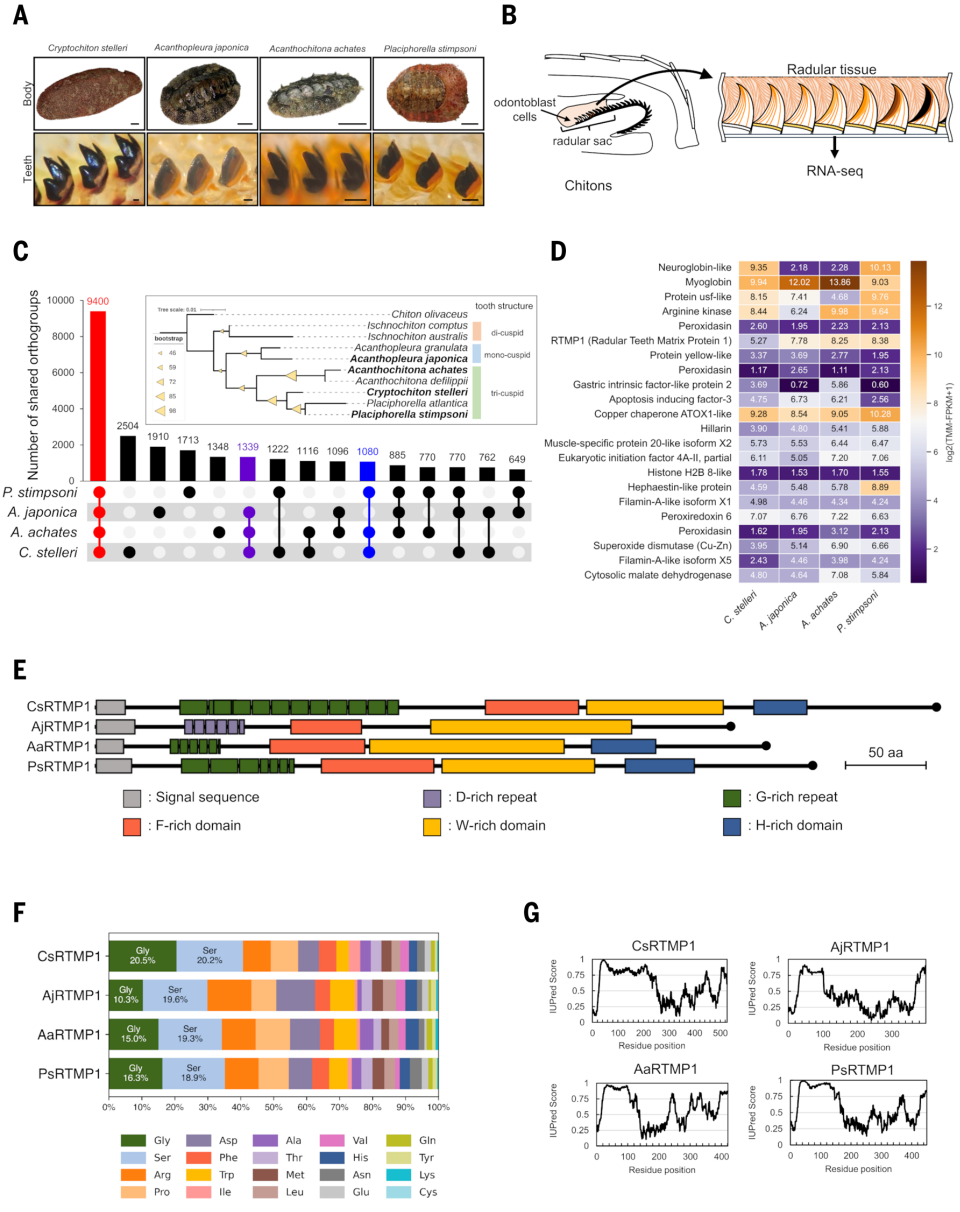


Fig. 1. A transcriptomic comparison of radular tissues revealed that RTMP1s are chiton-specific proteins. (**A**) Chitons used in this study. The upper images show the whole body, and the lower images show the teeth. Scale bars, 1 cm (top images) and 100 μm (bottom images). (**B**) Schematic of the RNA-seq experiments. (**C**) UpSet plot showing shared and unique orthologous protein groups (orthogroups) across four chiton species. The numbers at the top of the bars indicate the number of orthogroups shared among different chiton species. The shared orthogroups among all the chitons analyzed in this study are highlighted in red, those among herbivorous chitons are highlighted in purple, and those among chitons with tricuspid teeth are highlighted in blue. The inset shows a phylogenetic tree of cytochrome c oxidase subunit I (CO1) sequences of chitons. The species used in this study are shown in bold. Information on the tooth shape is shown on the right. (**D**) Heatmap showing the gene expression profiles of homologs of mineralized cusp–specific proteins, originally identified in *C. stelleri*, across four chiton species. (**E**) Schematic of the primary structures of RTMP1s. Single-letter abbreviations for the amino acid residues are as follows: A, Ala; C, Cys; D, Asp; E, Glu; F, Phe; G, Gly; H, His; I, Ile; K, Lys; L, Leu; M, Met; N, Asn; P, Pro; Q, Gln; R, Arg; S, Ser; T, Thr; V, Val; W, Trp; and Y, Tyr. aa, amino acids. (**F**) Comparison of the amino acid composition of RTMP1s. Amino acid compositions were determined on the basis of the full-length sequences, including their respective signal peptides. (**G**) Disordered region prediction for RTMP1s using IUPred.

teeth as #1, #2, and #3 (Fig. 2B). Proteins were extracted from epithelial cells at each stage, and Western blotting was performed. As a result, a band at ~43 kDa, which is the protein size expected from the amino acid sequence of AjRTMP1, was detected in stage 2 epithelial cells (Fig. 2, C and D). The results revealed that AjRTMP1 was most highly expressed in stage 2. This finding is consistent with the results of the quantitative polymerase chain reaction (qPCR) analysis of *C. stelleri*, which revealed that the CsRTMP1 gene had the highest expression in stage 2 (fig. S3). Western blotting was performed using proteins extracted from the mineralized cusps and the base plus radular membranes that support the cusps (Fig. 2B) (*16*). A band corresponding to AjRTMP1 was observed in the stage 3 mineralized cusp fraction (Fig. 2, C and D). The band size for AjRTMP1 observed in the cusp fraction was found to be slightly smaller than that in stage 2 epithelial cells (Fig. 2, C and D). These results indicate that AjRTMP1 is also a mineralized cusp–specific protein, similar to CsRTMP1, which was originally identified from *C. stelleri* radulae as a mineralized cusp–specific protein (*15*). Taken together, these results indicate that RTMP1s are expressed in stage 2 epithelial cells at the onset of iron oxide deposition and eventually localize to the cusps.

The timing and localization of RTMP1 expression

To elucidate the localization of AjRTMP1 in radular tissues, we performed immunofluorescence staining using an anti-AjRTMP1 antibody. Sections of *A. japonica* radular tissues were prepared and stained with an anti-AjRTMP1 antibody and Alexa Fluor 488–conjugated anti-rabbit immunoglobulin G (IgG). The results revealed that AjRTMP1 was initially expressed at teeth #–3 to #–2 and was expressed at the highest level at tooth #–1 (Fig. 2E). Furthermore, AjRTMP1 was confirmed to be localized at the leading edge of the tooth (Fig. 2E, white arrowhead). In the epithelial cells of teeth #–3 to #–1, AjRTMP1 was uniformly localized on both the leading edge and trailing edge of the tooth. In contrast, in the teeth following tooth #0, where iron oxide was deposited on the leading edge, AjRTMP1 was localized mainly to the epithelial cells of the trailing edge. These findings suggest that AjRTMP1 infiltrates from the trailing edge into the interior of teeth after iron oxide deposition on the leading edge. Brown ferritin granules were observed near tooth #0 and more-mature teeth (Fig. 2E). Iron ions coordinated and transported by ferritin may be deposited in the cusp because the timing of ferritin appearance in epithelial cells coincides with the timing of iron oxide deposition in the tooth cusp (*19*, *20*). On the basis of the above results, we propose the following hypothesis. In teeth #–3 to #–1, the organic template AjRTMP1 is transported and localized within the cusp. In tooth #0 and subsequent teeth, iron ions are released from ferritin and are likely coordinated with AjRTMP1, resulting in the deposition of iron oxide within the cusp. Immunostaining

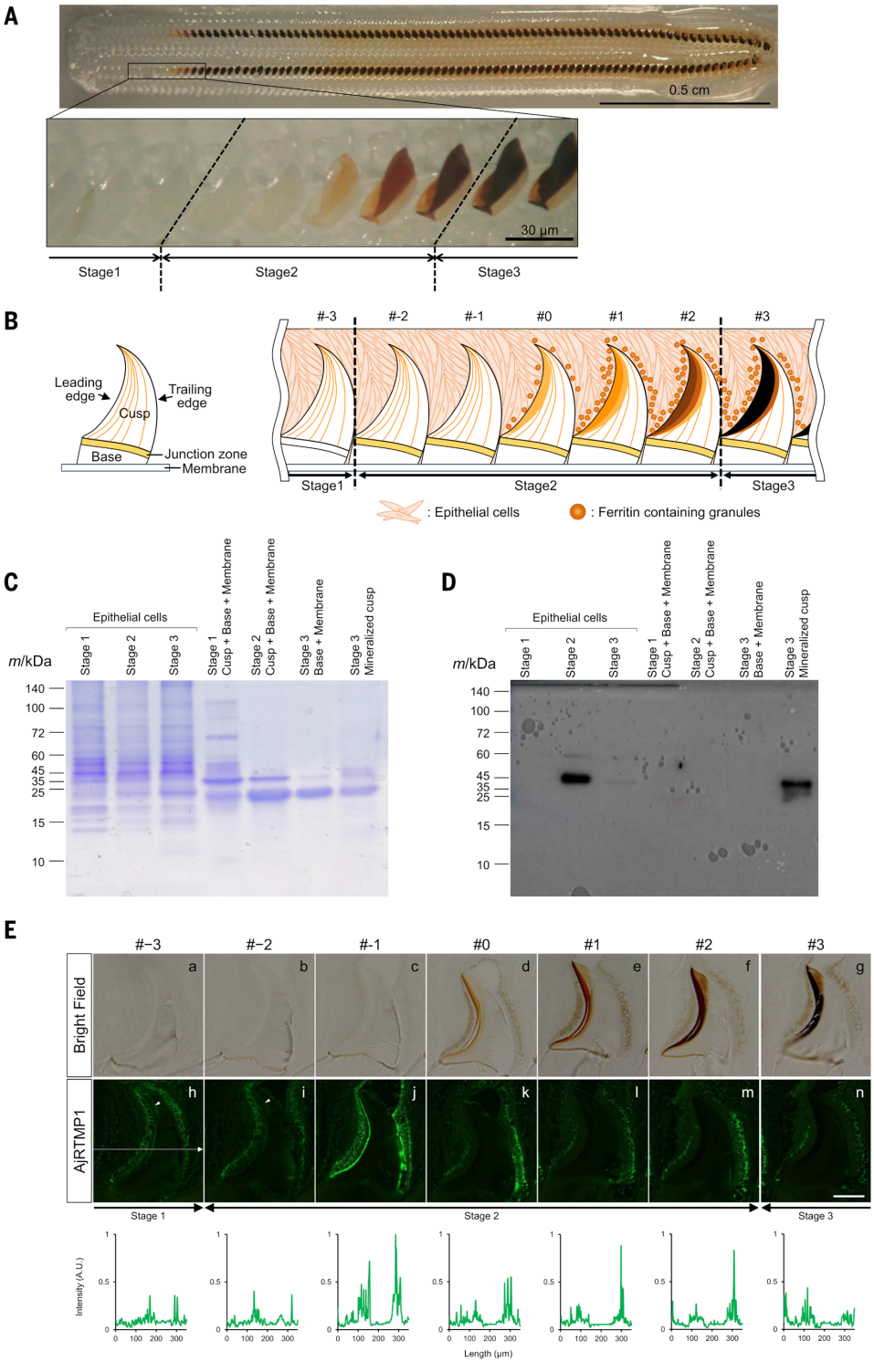


Fig. 2. Localization of AjRTMP1 during tooth maturation. (**A**) Radula of *A. japonica* with teeth in different stages of maturation. (**B**) Schematic representation of the radular tissue. The basal structure of the tooth (left), including the cusp, junction zone, base, and membrane, is composed primarily of α-chitin and proteins. (**C**) SDS-PAGE and (**D**) Western blot of proteins extracted from *A. japonica* radular tissue. Approximately 10 μg of protein extracted from epithelial cells at stages 1, 2, and 3, as well as proteins extracted from the base, membrane, and cusp after removal of epithelial cells, was subjected to tricine SDS-PAGE and stained with Coomassie brilliant blue (CBB). In stages 1 and 2, where the cusp was not fully mineralized, it was difficult to separate the cusp from the base plus membrane. Therefore, after removal of the epithelial cells, proteins were extracted together from the cusp plus base plus membrane and subjected to SDS-PAGE. Proteins fractionated by tricine SDS-PAGE were transferred to a polyvinylidene fluoride (PVDF) membrane, followed by immunoblotting with polyclonal anti-AjRTMP1 antibodies. (**E**) The 4-μm paraffin sections of *A. japonica* radular tissues were stained with an anti-AjRTMP1 antibody followed by Alexa Fluor 488–conjugated anti-rabbit IgG. The tooth with the earliest visible mineral deposition on the cusp was designated tooth #0. Teeth with up to three immature rows and up to three rows more mature than tooth #0 were analyzed. Bright-field (a to g) and fluorescence (h to n) images of (a and h) tooth #−3, (b and i) tooth #−2, (c and j) tooth #−1, (d and k) tooth #0, (e and l) tooth #1, (f and m) tooth #2, and (g and n) tooth #3. The graphs in the bottom panel are the fluorescence profiles of AjRTMP1 (green) along the direction of the arrow in the fluorescence image (h). For comparison of the changes in fluorescence intensity between the images, normalization was performed by dividing by the maximum brightness value across all images. The white arrowheads highlight the localization of AjRTMP1 within the teeth. Scale bar, 100 μm. A.U., arbitrary units.

using *C. stelleri* radular tissue sections and an anti-CsRTMP1 antibody confirmed that CsRTMP1, like AjRTMP1, is localized in the epithelial cells covering the teeth (fig. S4D). Unlike AjRTMP1, which was highly expressed around tooth #−1, the tooth just before the first iron oxide deposition, CsRTMP1 exhibited a more gradual expression at stage 2. Additionally, whereas AjRTMP1 was primarily localized on the leading edge of the tooth, CsRTMP1 was more diffusely distributed throughout the entire tooth. Furthermore, CsRTMP1 was observed to enter the tooth interior through the outer wall of the trailing edge (window), where iron oxide had not yet been deposited. The differences in the expression timing and localization of AjRTMP1 and CsRTMP1 are likely due to the distinct tooth structures of *A. japonica* (*Acanthopleura* type) and *C. stelleri* (*Cryptochiton* type) (fig. S4C) (*21*). No specific signal was detected in the radular tissues of either *A. japonica* or *C. stelleri* when immunostaining was performed without the primary antibody (fig. S5).

Transport of AjRTMP1 from epithelial cells to tooth cusps through microvilli

For a more detailed analysis of AjRTMP1 localization in epithelial cells, we performed multiplex staining of longitudinal and transverse tissue

sections using an anti-AjRTMP1 antibody together with Alexa Fluor 594–conjugated phalloidin and Hoechst, which stain filamentous actin (F-actin) and nuclei, respectively (Fig. 3A). AjRTMP1 was confirmed to be expressed in the columnar epithelial cells covering the teeth (Fig. 3B). The high density of actin near the cusps was suggested to be due to the microvilli covering the cusps (*19*). Furthermore, the fluorescence signal indicates that the localization of AjRTMP1 was stronger in the epithelial cells than in the cusps (Fig. 3B). To further elucidate the localization of AjRTMP1, we performed an analysis of sections with immunohistochemical staining using confocal laser scanning microscopy (Fig. 3, C and D). The results confirmed that AjRTMP1 is localized in a linear pattern adjacent to the cusp at both the tip and base of the F-actin filaments. We also confirmed that AjRTMP1 is localized between the F-actin filaments (Fig. 3C). Immunostaining and confocal

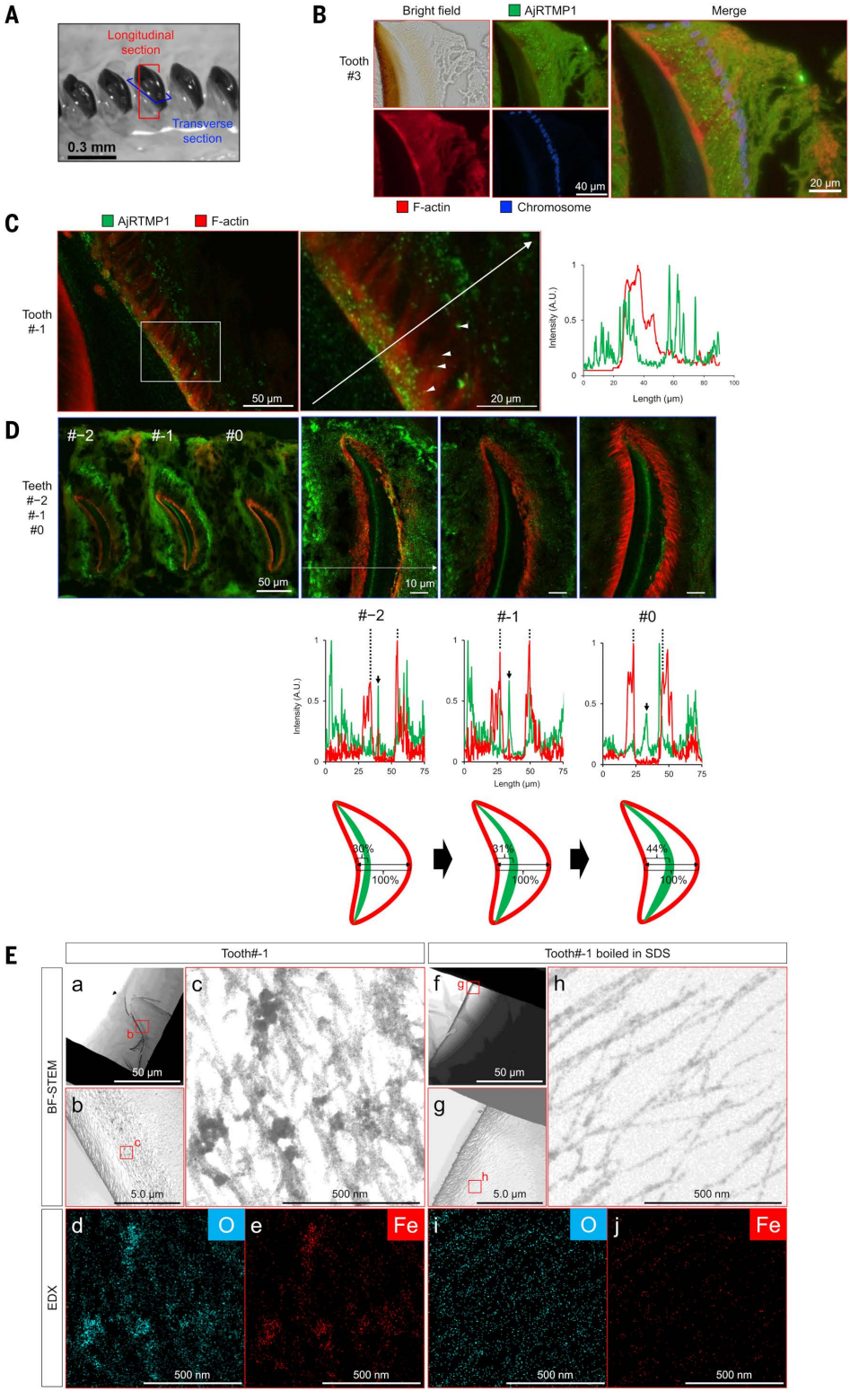


Fig. 3. Multiplex immunofluorescence staining was performed on sections of *A. japonica* radular tissue. (**A**) Longitudinal and transverse sections of *A. japonica* radular tissue were prepared and used for analysis. (**B**) The 4-μm paraffin sections of *A. japonica* radular tooth #3 were stained with anti-AjRTMP1 antibody followed by Alexa Fluor 488–conjugated anti-rabbit IgG. Chromosomes (blue) and F-actin (red) were counterstained with Hoechst 33342 and Alexa Fluor 594 phalloidin, respectively. (**C**) A 20-μm longitudinal cryosection of *A. japonica* radular tooth #−1 was stained with anti-AjRTMP1 (green) and Alexa Fluor 594 phalloidin (red) and analyzed using confocal microscopy. The graphs in the right panel are the fluorescence profiles of AjRTMP1 (green) and F-actin (red) along the direction of the arrow in the fluorescence image. AjRTMP1 signals localized between the F-actin filaments are indicated by white arrowheads. (**D**) A 20-μm transverse cryosection of *A. japonica* radular teeth #−2, #−1, and #0 was stained with anti-AjRTMP1 (green) and Alexa Fluor 594 phalloidin (red) and analyzed using confocal microscopy. The graphs in the bottom panel are the fluorescence profiles of AjRTMP1 (green) and F-actin (red) along the direction of the arrow in the fluorescence image. The lower schematic shows that as the tooth matures and mineralization occurs at the leading edge, the localization of AjRTMP1 shifts to the trailing edge. The peak indicated by the black dotted line was defined as the tooth surface, and the peak indicated by the black arrow was defined as the localization site of AjRTMP1. The relative position of AjRTMP1 within the tooth was then measured. (**E**) In vitro mineralization experiments using radular teeth extracted from *A. japonica*. After removal of the epithelial cells, tooth #−1 samples (a to e) and tooth #−1 samples boiled in SDS (f to j) were both left in $FeCl_3$ solution for 7 days and subsequently analyzed using TEM and EDX. (a to c and f to h) STEM bright-field images of radular teeth sections at the leading edge. (d and e) EDX mapping (O and Fe) from a region of (c). (i and j) EDX mapping (O and Fe) from a region of (h).

microscopy of transverse sections of radular tissue revealed that AjRTMP1 is localized within epithelial cells and at the leading edge inside the tooth cusps (Fig. 3D). Furthermore, before iron oxide deposition in the cusps, AjRTMP1 was observed to enter the interior of the cusps from both the leading and trailing edges (Fig. 3D). However, after iron oxide deposition in the cusps in tooth #0, AjRTMP1 was found to be localized in the epithelial cells at the trailing edge of the tooth (Fig. 3D). This suggests that in tooth #0 and subsequent teeth, AjRTMP1 enters the tooth from the trailing edge. This finding is consistent with the results from the immunohistochemical analysis of the longitudinal section in Fig. 2E. Furthermore, after iron oxide deposition occurs at the leading edge of the cusp, the localization of AjRTMP1 shifts slightly toward the trailing edge (Fig. 3D). These findings suggest that after iron oxide is formed at the leading edge with AjRTMP1 as a template, additional AjRTMP1 is transported into the immediate posterior region, where further mineral deposition occurs.

RTMP1 binds to ferric ions and directs the formation of iron oxide

The immunohistochemical staining results suggest that AjRTMP1 catalyzes the nucleation of iron oxide, guiding and enhancing the formation of iron oxide on chitin fibers. Therefore, iron oxide formation experiments were performed using tooth #−1, which presented the highest expression of AjRTMP1. After fresh radulae were extracted from the dissected specimens and epithelial cells were removed, the teeth were incubated in an aqueous ferric chloride ($FeCl_3$) solution, resulting in nanoparticle deposition on the chitin fibers of the leading edge where AjRTMP1 was localized (Fig. 3E). Energy-dispersive x-ray (EDX) analysis indicated that the nanoparticles formed on the chitin fibers consist of iron and oxygen. Conversely, samples treated with sodium dodecyl sulfate (SDS) to remove chitin-bound proteins showed a significant reduction in iron oxide particle deposition versus those without SDS treatment (Fig. 3E). These results suggest that the surfaces of chitin fibers within the tooth cusp are modified with protein prior to iron influx and act as a template for iron oxide deposition during iron release from ferritin.

To determine whether RTMP1 acts as an organic template to enhance iron oxide deposition, *Saccharomyces cerevisiae* was used to recombinantly express CsRTMP1, which was subsequently purified. CsRTMP1 without a signal sequence, which we named CsRTMP1 Δss, and CsRTMP1 without a G-rich repeat region, which we named CsRTMP1 ΔG, were expressed and purified as glutathione *S*-transferase (GST) fusion proteins (Fig. 4A and fig. S6). The results of chitin-binding assays using colloidal chitin revealed that the recombinant GST-CsRTMP1 ΔG protein was found in the chitin-binding fraction, similar to the chitin-binding protein wheat germ agglutinin (WGA) (Fig. 4B). These results showed that a domain of CsRTMP1 distinct from the G-rich repeat is responsible for chitin binding. In addition, the results of the iron binding assay using potassium ferrocyanide indicated that GST-CsRTMP1 Δss binds Fe^{3+}. The GST-CsRTMP1 ΔG protein showed attenuated iron-binding activity (Fig. 4C). To evaluate whether CsRTMP1 has iron oxide particle formation activity, we incubated recombinant GST-CsRTMP1 Δss with chitin nanofibers in an aqueous $FeCl_3$ solution (Fig. 4D). Results confirmed the formation of a brown precipitate in the presence of

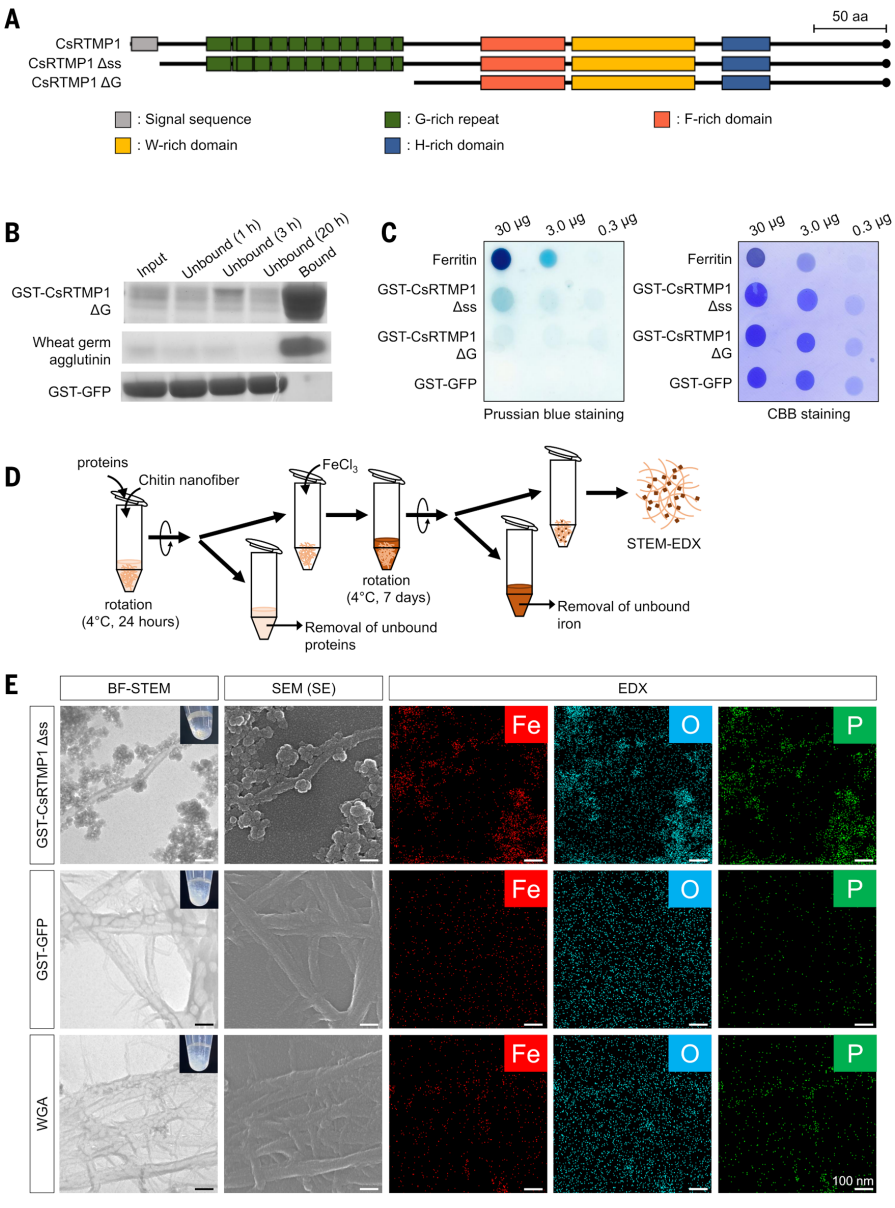


Fig. 4. The recombinant CsRTMP1 exhibited iron ion binding and iron oxide precipitation activity. (**A**) Schematic primary structures of CsRTMP1 and recombinantly expressed CsRTMP1 Δss and CsRTMP1 ΔG. (**B**) Chitin binding assay using recombinant GST-CsRTMP1 ΔG. Recombinant GST-CsRTMP1 ΔG was incubated with insoluble colloidal chitin. WGA and GST-GFP were used as controls. After incubation for 1, 3, and 20 hours, the supernatants (unbound fractions) obtained together with the pellets (bound fractions) obtained after 20 hours of incubation were collected and analyzed with the solubilized protein before mixing with colloidal chitin (input) by SDS-PAGE and stained with CBB. (**C**) Iron binding analysis of recombinant GST-CsRTMP1 Δss and GST-CsRTMP1 ΔG. Prussian blue (left) was used to detect Fe (III), and CBB (right) was used to stain the proteins. Equal amounts of ferritin and GST-GFP were used as controls. (**D**) Schematic diagram of the iron oxide formation experiment. (**E**) STEM bright-field images, SEM secondary electron images, and EDX maps (Fe, O, and P) of iron oxide nanoparticles formed on chitin nanofibers in the presence of GST-CsRTMP1 Δss. GST-GFP and WGA were used as controls. Scale bars, 100 nm.

GST-CsRTMP1 Δss (Fig. 4E). Scanning transmission electron microscopy (STEM) confirmed the formation of nanoparticles (~27 to 53 nm diameter) on the chitin fibers. The results of STEM-EDX mapping revealed the presence of iron and oxygen in the particle region, suggesting the formation of iron oxide particles on the chitin fibers. The results of the selected-area electron diffraction (SAED) analysis indicate that these iron- and oxygen-containing nanoparticles are amorphous and do not exhibit specific diffraction patterns characteristic of iron oxides such as ferrihydrite or magnetite (fig. S7). In the negative control experiment performed with GST–green fluorescent protein (GFP) and WGA, there are no observable particles on the chitin fibers, and there is a significant reduction of iron and oxygen, as indicated by EDX analyses (Fig. 4E).

To investigate the function of RTMP1 in vivo, we performed gene knockdown experiments using RNA interference in *A. japonica* (fig. S8A). Two days after the injection of double-stranded RNA (dsRNA) for the AjRTMP1 gene into the body cavity, the mRNA expression level of AjRTMP1 in the radular tissue was examined. Compared with the individuals injected with phosphate-buffered saline (PBS) or dsRNA for the GFP gene, the individuals injected with dsRNA for the AjRTMP1 gene presented ~69% lower mRNA expression levels (fig. S8B). Microscopic examination of the radular tissue sections revealed that in the individuals injected with dsRNA for GFP, as in wild-type individuals, iron was first deposited in tooth #0, followed by a clear progression of mineralization as maturation progressed, with the color gradually changing from light brown to dark brown and then to black. In contrast, in the individuals with decreased AjRTMP1 mRNA expression, after iron oxide was deposited in tooth #0, the next three teeth (#1, #2, and #3) did not show the same clear progression of mineralization as described above, and the change in saturation values indicating color change was minimal (fig. S8, C and D). These findings suggested that the reduction in AjRTMP1 expression prevented the progression of iron oxide deposition, resulting in the failure of gradual tooth maturation.

Discussion

The formation of amorphous iron oxide was observed in the presence of recombinant GST-CsRTMP1 Δss (Fig. 4E). These results suggest that RTMP1 bound to chitin may concentrate iron and reduce the energy barrier to heterogeneous nucleation of iron oxide–based nanoparticles on chitin fibers. However, the mineral formed in this study is an amorphous solid containing iron and oxygen, not ferrihydrite, the least metastable phase of iron oxide commonly observed to appear during the tooth formation stages of chitons (*14*, *22*). It remains unclear whether the transformation from amorphous mineral to ferrihydrite involves other processes (*23*, *24*), including kinetically controlled precursor addition or dehydration pathways, or whether the experimental conditions used in this study (e.g., precursor species and concentration, rate of precursor addition, local pH, ionic strength) do not fully replicate the biological conditions necessary for ferrihydrite formation.

The iron-binding activity of GST-CsRTMP1 ΔG was lower than that of GST-CsRTMP1 Δss, suggesting the importance of the G-rich repeat region in iron-binding activity (Fig. 4C). This G-rich repeat region is predicted to be disordered (Fig. 1G). We hypothesize that its extended, flexible conformation might provide more mineral ion binding sites than a tightly packed protein structure (*25*). In addition, we observed phosphorylation of the G-rich region of recombinant GST-CsRTMP1 Δss (table S3), suggesting a potential role of phosphate groups in the iron binding of this protein. Although the phosphorylation sites of the recombinant protein expressed in *S. cerevisiae* are different from those of native CsRTMP1 (fig. S2), phosphorylation itself may be important for iron binding. The presence of these charged motifs can enhance local supersaturation through electrostatic binding to iron species as well as through hydrogen bonding to hydrated iron species. The SSSE motif of native CsRTMP1, which was phosphorylated, contains the S-x-E motif, a known target sequence of Fam20C, a kinase reported to phosphorylate secreted proteins that regulate biomineralization (*26*). This suggests that CsRTMP1 may be phosphorylated by Fam20C. Furthermore, all RTMP1s, including CsRTMP1, have multiple S-x-E motifs, indicating that these motifs may also undergo phosphorylation. The importance of phosphate groups in binding to iron ions has been reported for other proteins (*27*). A previous amino acid analysis of the radular teeth of the chiton *Acanthopleura hirtosa* revealed relatively high levels of phosphoserine (*28*). Furthermore, recent EDX analysis of partially mineralized teeth suggested the presence of phosphorus coexisting with iron oxide (*22*).

The results of immunohistochemical staining showed that the fluorescence signal of AjRTMP1 was stronger inside the epithelial cells than in the cusps (Figs. 2E and 3, B and C). Like enamel matrix proteins (EMPs), RTMP1 may be compartmentalized in secretory vesicles within epithelial cells (*29*). The iron-free granules reported from previous transmission electron microscopy (TEM) observations of radular epithelial cells may be secretory vesicles that encapsulate RTMP1 (*19*). The protein band size of AjRTMP1 extracted from the cusp was smaller than that of AjRTMP1 within the epithelial cells (Fig. 2, C and D). Similarly, CsRTMP1 also exhibited different protein sizes between epithelial cells and the cusp (fig. S4, A and B). The smaller size of AjRTMP1 and CsRTMP1 proteins detected in the cusp compared with epithelial cells may result from posttranslational processing. While signal peptide cleavage could contribute to this difference, the extent of the observed size shift suggests that additional proteolytic digestion may occur, as is the case for other biomineralization-related proteins (*1*, *5*, *7*, *30*, *31*).

The amount of F-actin increased, and actin filamentation progressed as the tooth matured (Fig. 3D). Previous studies have reported an increase in the number and length of microvilli with tooth mineralization (*19*). Confocal microscopic analysis confirmed that AjRTMP1 was localized at the tips, bases, and interspaces of F-actin filaments (Fig. 3C). In ameloblasts involved in enamel formation, the F-actin network present at the apical surface has been reported to play a critical role in the transport of vesicles containing EMPs, such as amelogenin, and the secretion of EMPs. Moreover, a previous report showed that the F-actin network develops on the apical surface during EMP secretion and enamel formation (*32*). Like those in ameloblasts, the F-actin filaments between radular epithelial cells and cusps may serve as pathways or support the movement of secretory vesicles containing RTMP1 during transport.

On the basis of the above results, we propose a model in which RTMP1 regulates iron oxide deposition within chiton teeth (Fig. 5). First, RTMP1 expressed in radular epithelial cells is secreted extracellularly and binds to chitin fibers at the leading edge of the cusp interior (tooth #–3 to #–1). The specific binding of RTMP1 to chitin fibers at the leading edge of the cusp interior is regulated by an as yet unidentified mechanism. Iron ions released from ferritin, which is accumulated around the tooth, are deposited as ferrihydrite in the interior of the cusp through interactions with preexisting RTMP1 (tooth #0). RTMP1, which has an iron binding ability, may promote the formation of ferrihydrite by enhancing local supersaturation and lowering the activation energy barrier to nucleation of a metastable iron oxide. From tooth #0 and subsequently more mature teeth, the formation of iron oxide mineral on the leading edge effectively inhibits additional protein influx. Consequently, RTMP1 is continuously secreted from the cells at the trailing edge of the tooth into the interior of the cusp, where it binds to the chitin just behind the region where iron oxide has been deposited at the leading edge. Iron ions released from ferritin are then deposited, resulting in the layering of iron oxide in the interior of the tooth, from tooth #0 onward. As the tooth matures, the iron oxide initially deposited on the leading edge transforms to magnetite through an Fe(II)-induced solid-state phase transformation (*22*, *33*).

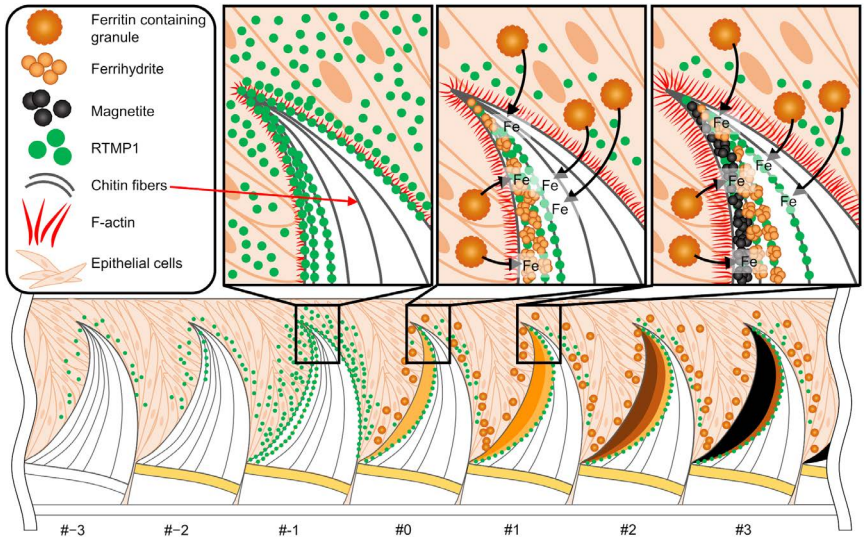


Fig. 5. Proposed model of iron oxide deposition on chiton teeth controlled by RTMP1. This schematic model is primarily based on the immunostaining results of AjRTMP1, with additional consideration of findings from in vitro experiments using CsRTMP1. The deposition of iron oxide in the tooth occurs through the following steps: (Step 1) RTMP1, which is expressed in radular epithelial cells, is secreted and attaches to chitin fibers at the leading edge of the cusp interior in teeth ranging from #–3 to #–1. (Step 2) At tooth #0, iron ions released from ferritin accumulated around the tooth interact with the preexisting RTMP1, leading to the deposition of ferrihydrite within the cusp interior. (Step 3) RTMP1 continues to be secreted from cells located at the trailing edge of the tooth, migrating into the cusp interior, where it binds to chitin just behind the region where iron oxide has already been deposited at the leading edge. The subsequent release of iron ions from ferritin facilitates the layering of iron oxide within the tooth interior (tooth #0 and beyond). (Step 4) As the tooth matures, the initially deposited iron oxide at the leading edge crystallizes into magnetite.

The molecular mechanisms governing iron oxide deposition in chiton teeth have remained elusive for decades. In this study, we identify RTMP1 as a key regulatory factor that binds to chitin, the structural framework of the tooth, and facilitates iron oxide nucleation. This protein plays an essential role in the bottom-up formation of ultrahard teeth composed of chitin and magnetite. Elucidating how chitons concentrate large quantities of iron—an element essential for life but toxic in excess—and deposit it as magnetite contributes to a deeper understanding of cellular iron metabolism.

REFERENCES AND NOTES

1. C. Du, G. Falini, S. Fermani, C. Abbott, J. Moradian-Oldak, *Science* **307**, 1450–1454 (2005).
2. G. He, T. Dahl, A. Veis, A. George, *Nat. Mater.* **2**, 552–558 (2003).
3. K. Shimizu *et al.*, *Nat. Commun.* **15**, 181 (2024).
4. J. N. Cha *et al.*, *Proc. Natl. Acad. Sci. U.S.A.* **96**, 361–365 (1999).
5. N. Kröger, R. Deutzmann, M. Sumper, *Science* **286**, 1129–1132 (1999).
6. A. Scheffel, N. Poulsen, S. Shian, N. Kröger, *Proc. Natl. Acad. Sci. U.S.A.* **108**, 3175–3180 (2011).
7. M. Suzuki *et al.*, *Science* **325**, 1388–1390 (2009).
8. R. Uebe, D. Schüler, *Nat. Rev. Microbiol.* **14**, 621–637 (2016).
9. A. Arakaki, J. Webb, T. Matsunaga, *J. Biol. Chem.* **278**, 8745–8750 (2003).
10. H. A. Lowenstam, *Geol. Soc. Am. Bull.* **73**, 435–438 (1962).
11. J. C. Weaver *et al.*, *Mater. Today* **13**, 42–52 (2010).
12. L. K. Grunenfelder *et al.*, *Adv. Funct. Mater.* **24**, 6093–6104 (2014).
13. W. Huang *et al.*, *Acc. Chem. Res.* **55**, 1360–1371 (2022).
14. Q. Wang *et al.*, *Adv. Funct. Mater.* **23**, 2908–2917 (2013).
15. M. Nemoto *et al.*, *Sci. Rep.* **9**, 856 (2019).
16. M. Nemoto *et al.*, *Proteomics* **12**, 2890–2894 (2012).
17. R. M. Varney, D. I. Speiser, C. McDougall, B. M. Degnan, K. M. Kocot, *Genome Biol. Evol.* **13**, evaa263 (2021).
18. S. Ferrandon, T. Sterzenbach, F. B. Mersha, M. Q. Xu, *Biochim. Biophys. Acta* **1621**, 31–40 (2003).
19. J. A. Shaw *et al.*, *Microsc. Microanal.* **15**, 154–165 (2009).
20. M. H. Nesson, H. A. Lowenstam, in *Magnetite Biomineralization and Magnetoreception in Organisms: A New Biomagnetism*, J. L. Kirschvink, D. S. Jones, B. J. MacFadden, Eds., vol. 5 of *Topics in Geobiology* (Springer US, 1985), pp. 333–363.
21. D. Joester, L. R. Brooker, in *Iron Oxides: From Nature to Applications*, D. Faivre, Ed. (Wiley-VCH, 2016), pp. 177–206.
22. T. Wang *et al.*, *Small Struct.* **3**, 2100202 (2022).
23. D. Faivre, T. U. Godec, *Angew. Chem. Int. Ed.* **54**, 4728–4747 (2015).
24. J. Baumgartner *et al.*, *Proc. Natl. Acad. Sci. U.S.A.* **110**, 14883–14888 (2013).
25. M. Wojtas, P. Dobryszycki, A. Ożyhar, in *Advanced Topics in Biomineralization*, J. Seto, Ed. (InTech, 2012), pp. 3–32.
26. V. S. Tagliabracci *et al.*, *Science* **336**, 1150–1153 (2012).
27. O. Castellani, C. Guérin-Dubiard, E. David-Briand, M. Anton, *Food Chem.* **85**, 569–577 (2004).
28. L. A. Evans, D. J. Macey, J. Webb, *Mar. Biol.* **109**, 281–286 (1991).
29. M. Pandya, T. G. H. Diekwisch, *J. Struct. Biol.* **213**, 107809 (2021).
30. C. Qin *et al.*, *J. Biol. Chem.* **278**, 34700–34708 (2003).
31. K. Shimizu, J. Cha, G. D. Stucky, D. E. Morse, *Proc. Natl. Acad. Sci. U.S.A.* **95**, 6234–6238 (1998).
32. Y. Zhang *et al.*, *BMC Biol.* **17**, 104 (2019).
33. E. Tronc, P. Belleville, J. P. Jolivet, J. Livage, *Langmuir* **8**, 313–319 (1992).

ACKNOWLEDGMENTS

We thank S. Hamano of the Akkeshi Marine Station, Field Science Center for Northern Biosphere, Hokkaido University, and W. Godo and K. Saito of the Ushimado Marine Institute, Okayama University, for their assistance in collecting live specimens of chitons. We also thank M. Owada of the Faculty of Science, Department of Biological Sciences, Kanagawa University, for helpful advice regarding the identification of the chiton species used in this study. We are grateful to M. Monobe and T. Tsukano at the Central Research Laboratory of Okayama University for their technical support in preparing paraffin-embedded and epoxy resin-embedded ultrathin sections. We thank T. Shiokawa and H. Tada at the Division of Instrumental Analysis for their assistance with the liquid chromatography–tandem mass spectrometry measurements and I. Nakamura of Okayama University for help with sample preparation for these measurements. Special thanks to C. Nakano at the Organization for Research Strategy and Development, Okayama University, for technical support with STEM-EDX analysis. We also thank S. Ifuku of Kyoto University for providing marine nanofibers and T. Nitoda of Okayama University for providing colloidal chitin. We thank Y. Takemoto of Okayama University for technical support with SAED analysis. We appreciate the insightful discussions with K. Aoki of Okayama University of Science, H. Yamada of Okayama University, J. A. Shaw of the University of Western Australia, M. Suzuki of the University of Tokyo, and K. Seki of Shiretoko Diving Service. Computations were partially performed on the NIG supercomputer at the ROIS National Institute of Genetics. We also thank American Journal Experts (AJE) for their assistance with language editing. **Funding:** Ministry of Education, Culture, Sports, Science, and Technology (MEXT Japan) KAKENHI 21K05781 (M.N.); Ministry of Education, Culture, Sports, Science, and Technology (MEXT Japan) KAKENHI 22H04812 (M.N.); Japan Science and Technology Agency (JST) Fusion Oriented REsearch for disruptive Science and Technology (FOREST) JPMJFR210E (M.N.); JGC Saneyoshi Scholarship Foundation (M.N.); Kato Memorial Bioscience Foundation (M.N.); Air Force Office of Scientific Research, FA9550-20-1-0292 (D.K.); Air Force Office of Scientific Research, FA9550-23-1-0647 (D.K.); Army Research Office, W911NF-20-1-0201 (D.K.). **Author contributions:** Conceptualization: M.N., K.Oka., D.K.; Funding acquisition: M.N., D.K.; Investigation: M.N., K.Oka., H.A., Y.O., Y.N., K.Oko., K.Ob., D.K., H.M., A.S.; Software: K.Ob.; Supervision: M.N.; Writing – original draft: M.N., K.Oka.; Writing – review & editing: M.N., K.Oka., K.Oko., K.Ob., D.K., H.M., A.S. **Competing interests:** The authors declare that they have no competing interests. **Data and materials availability:** RNA sequencing (RNA-seq) data have been deposited in the DNA Data Bank of Japan (DDBJ) Sequence Read Archive under accession numbers DRR598739, DRR598778, and DRR598779. RNA-seq data of *C. stelleri* obtained in our previous study (*15*) were used in this study (accession number DRA007106). CO1 sequences of *Chiton olivaceus* (XBY88089.1), *Acanthopleura granulate* (QXE46576.1), *A. japonica* (*Liolophura japonica*) (BDO47095.1), *Ischnochiton australis* (UEF90774.1), *Ischnochiton comptus* (BAV14531.1), *A. achates* (BDO47092.1), *Acanthochitona defilippii* (UGZ24807.1), *C. stelleri* (BDO47091.1), *Placiphorella atlantica* (ADH41916.1), and *P. stimpsoni* (AXG25339.1) were used for the phylogenetic analyses. **License information:** Copyright © 2025 the authors, some rights reserved; exclusive licensee American Association for the Advancement of Science. No claim to original US government works. https://www.science.org/about/science-licenses-journal-article-reuse

SUPPLEMENTARY MATERIALS

science.org/doi/10.1126/science.adu0043
Materials and Methods; Figs. S1 to S8; Tables S1 to S5; References (*34*–*57*); MDAR Reproducibility Checklist

Submitted 4 November 2024; accepted 12 June 2025

10.1126/science.adu0043

OPTOELECTRONICS

Single-photon detection enabled by negative differential conductivity in moiré superlattices

Krystian Nowakowski[1]†, Hitesh Agarwal[1]†, Sergey Slizovskiy[2], Robin Smeyers[3], Xueqiao Wang[4], Zhiren Zheng[4], Julien Barrier[1], David Barcons Ruiz[1], Geng Li[1], Riccardo Bertini[1], Matteo Ceccanti[1], Iacopo Torre[1,5], Bert Jorissen[3], Antoine Reserbat-Plantey[1,6], Kenji Watanabe[7], Takashi Taniguchi[8], Lucian Covaci[3], Milorad V. Milošević[3], Vladimir Fal'ko[2], Pablo Jarillo-Herrero[4], Roshan Krishna Kumar[1,9]*, Frank H. L. Koppens[1,10]*

Detecting individual light quanta is essential for quantum information, space exploration, advanced machine vision, and fundamental science. In this work, we introduce a single-photon detection mechanism using highly photosensitive nonequilibrium electron phases in moiré materials. Using tunable bands in bilayer graphene/hexagonal boron nitride superlattices, we engineer negative differential conductance and a sensitive bistable state capable of detecting single photons. Operating in this regime, we demonstrate single-photon counting at mid-infrared (11.3 micrometers) and visible wavelengths (675 nanometers) and temperatures up to 25 kelvin. This detector offers prospects for broadband, high-temperature quantum technologies with complementary metal-oxide semiconductor compatibility and seamless integration into photonic-integrated circuits. Our analysis suggests that the underlying mechanism originates from superlattice-induced negative differential velocity.

Single-photon detectors (SPDs) play a crucial role in modern optoelectronics (*1*–*3*), with the demands for long-wavelength and high-temperature capabilities growing rapidly. The state-of-the-art devices based on single-photon avalanche diodes (SPADs), superconducting nanowire single-photon detectors (SNSPDs), and transition edge sensors (TESs) (*1*, *4*, *5*) exhibit high performance but are limited by their wavelength and temperature operating ranges. In SPADs, their semiconductor bandgaps impose sharp cutoffs that require complex up-conversion techniques for longer wavelengths (*6*, *7*). SNSPDs can extend their range to mid-infrared (mid-IR) wavelengths but only using low–critical temperature (T_c) materials below 1 K (*8*–*11*) because their intrinsic superconducting gap makes high-temperature (*12*–*14*) and long-wavelength operation mutually exclusive (*8*–*11*, *15*). Hence, disruptive progress requires devices operating under fundamentally distinct principles.

Two-dimensional (2D) materials are well suited for sensitive photodetection owing to their intrinsically low heat capacities (*16*), which enable substantial photon-induced temperature changes even from small amounts of energy (*17*–*22*). Moiré superlattices represent a new era in 2D materials engineering with their correlated electron phases and tunable infrared bandgaps offering exciting prospects for photodetection (*23*–*25*). Additionally, the large lattice constant imposes peculiar quantum properties under high electric fields, in which carriers can be accelerated to their band velocity limit or even spontaneously created, inducing an electron-hole plasma (*26*) (Fig. 1A). Because of the small superlattice Brillouin zone, carriers may even be decelerated by electric fields, attaining a negative velocity. High-field phenomena in superlattices produce distinct nonlinear electrical responses that underpin some of the most groundbreaking optoelectronic devices to date (*27*), but they remain little explored in moiré materials.

In this work, we leverage the high-field properties of moiré superlattices to develop a so-far unexplored mechanism for single-photon detection with larger operating temperatures and wavelength range. By engineering their nonequilibrium electron phases (*26*) using the tunable band structure of bilayer graphene (BLG), we reveal a regime of in-plane negative differential conductance (NDC), which makes the system capable of detecting single light quanta over a broad wavelength range. Our analysis suggests that the NDC originates from particle acceleration into regions of the Brillouin zone with negative velocity (shaded red in Fig. 1A), effectively deaccelerating charge carriers (*28*, *29*). The operation principle of our moiré single-photon detectors (MSPDs) bears strong similarities to that of SNSPDs (*1*, *2*), leveraging a sharp critical current behavior with exceptional photosensitivity, whereas the distinct underlying physical mechanism enables higher operating temperatures (>20 K) and long-wavelength capabilities (*4*) (>10 μm, <109 meV) owing to the low-energy bandgaps intrinsic to moiré BLG under a moderate displacement field.

High-field transport in moiré superlattices

We studied two moiré-based superlattice devices ($DBLG_A$ and $DBLG_B$), consisting of BLG aligned to hexagonal boron nitride (hBN), that showed similar behaviors, including sensitivity to single photons (for fabrication details and transport characterization, see materials and methods and supplementary text, section S1). Figure 1B plots the resistivity measured as a function of the gate voltage (V_G) and filling factor (ν), exhibiting features expected for BLG aligned to hBN, including a peaked response at neutrality point and additional peaks for hole and electron doping indicating the band edges (*30*). Figure 1C plots the current-voltage (IV) characteristics of $DBLG_A$ extending to high bias. It reveals strong nonlinearities and a critical current behavior (*26*) appearing as peaks in the differential resistance (dV/dI). The low-resistance state is described by the Drude conductivity, with a current-saturating regime occurring at higher bias. At the critical current (I_C), the strong electric field triggers Schwinger-like particle production (*26*), creating a highly dissipative electron-hole plasma (Fig. 1A).

Notably, the nonlinearities are extremely sharp at negative current densities, indicated by the large peaks in dV/dI and discontinuities in the simultaneously measured four-probe DC voltage (Fig. 1C). This is unexpected because it resembles a phase transition, which contrasts with previous observations that the evolution is smooth (*26*). The origin of this anomalous behavior is revealed when, instead of using a current source, we switch to biasing our sample using a voltage source. Figure 1D plots the two-probe IV characteristics in the vicinity of the transition. Notably, at $V_{bias} = -1.42$ V, we observe NDC, when the current starts to decrease upon increasing the bias voltage. NDC extends over a small voltage range after the critical current I_C, beyond which the current increases again with a larger differential resistivity. This explains why the transition appears sharp in the current-biased scheme (Fig. 1B). The large resistor placed in series imposes a horizontal load line that masks the NDC region and forces the current to jump to the next stable point, creating discontinuities in the IV characteristics (supplementary text, section S2). Figure 1E plots the two-probe IV characteristics when a load resistor of 200 kilohms is placed

[1]ICFO - Institut de Ciències Fotòniques, The Barcelona Institute of Science and Technology, Castelldefels (Barcelona), Spain. [2]Department of Physics and Astronomy, The University of Manchester, Manchester, UK. [3]Department of Physics and NANOlab Center of Excellence, University of Antwerp, Antwerp, Belgium. [4]Department of Physics, Massachusetts Institute of Technology, Cambridge, MA, USA. [5]Department of Physics, Universitat Politècnica de Catalunya - BarcelonaTech (UPC), Campus Nord, Barcelona, Spain. [6]Université Côte d'Azur, CNRS, CRHEA, Valbonne, France. [7]Research Center for Functional Materials, National Institute for Materials Science, Tsukuba, Japan. [8]International Center for Materials Nanoarchitectonics, National Institute for Materials Science, Tsukuba, Japan. [9]Catalan Institute of Nanoscience and Nanotechnology (ICN2), CSIC and BIST, Barcelona, Spain. [10]ICREA - Institucio Catalana de Recerca i Estudis Avancats, Barcelona, Spain. ***Corresponding author. Email: roshan.krishnakumar@icfo.eu (R.K.K.); frank.koppens@icfo.eu (F.H.L.K.)** †These authors contributed equally to this work.

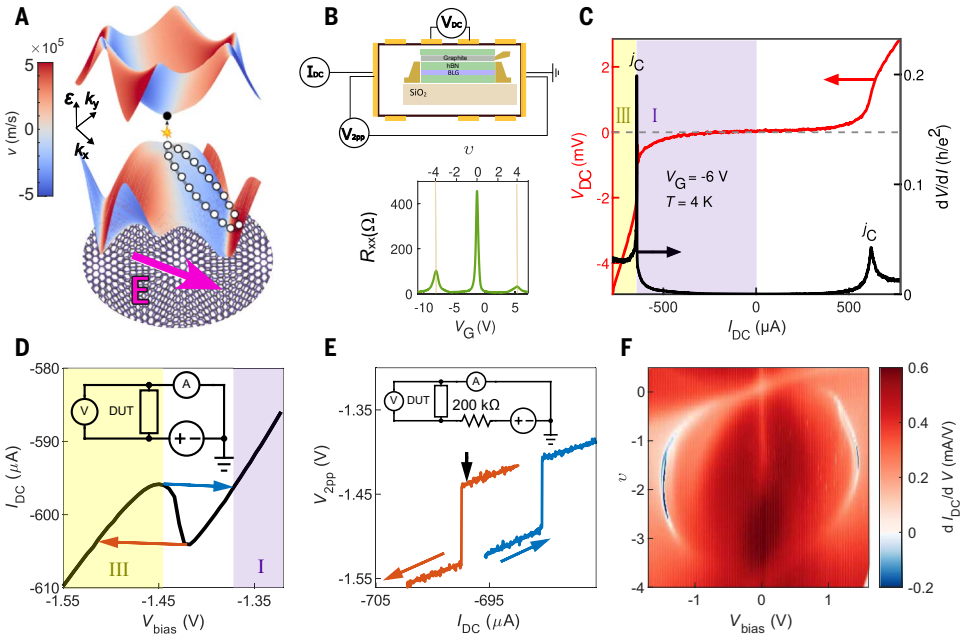


Fig. 1. High-field experiments in moiré superlattices. (**A**) Conduction and valence bands of BLG/hBN superlattice calculated for $D = 0.1$ V/nm (supplementary text, section S8), plotted within the superlattice Brillouin zone. Color shading corresponds to the velocity of holes (open circles) or electrons (filled circles) in the direction of the electric field (pink arrow). With strong electric fields, Schwinger-like transitions are triggered, creating electron-hole pairs. If the gap is sufficiently large to suppress Schwinger-like transitions, carriers may drift into negative-velocity states (red regions). (**B**) (Top) Measurement schematic sketched on a top-down view of the Hall bar mesa. The inset illustrates the heterostructure. (Bottom) Longitudinal resistance measured as a function of gate voltage (V_G) determined from $V_{DC}/I_{DC} = 100$ nA. The top axis depicts filling factor (n). (**C**) IV characteristics measured in $DBLG_A$. The left axis plots four-probe voltage (V_{DC}, in red) measured at fixed doping around half filling of the superlattice Brillouin zone ($\upsilon \approx 2$) as a function of current (I_{DC}). The right axis plots the corresponding differential resistivity dV/dI. (**D**) Current (I_{DC}) plotted as a function of the voltage bias (V_{bias}) close to the high-field transition. (Inset) Circuit schematic. DUT, device under test. (**E**) Two-point-probe voltage drop (V_{2pp}) versus applied current bias, zoomed in on the transition region. Orange and blue solid lines plot forward and backward sweeps, respectively. (Inset) Circuit schematic. (**F**) Differential conductivity (dI_{DC}/dV_{bias}) as a function of filling factor (υ) and V_{bias}. All measurements were performed at $T = 4$ K.

in series. The voltage jumps abruptly at I_C, and hysteresis in the current sweep direction is observed, which is characteristic of a bistable system. The load resistor essentially allows us to engineer a bistability from NDC. Figure 1F plots the differential conductivity dI/dV as a function of filling and voltage bias, where NDC (blue regions) appears over a broad parameter space, tracing a ringlike structure characteristic of out-of-equilibrium criticalities in moiré superlattices (*26*, *31*). Although there is some asymmetry in the IV characteristics originating from self-gating (supplementary text, section S3), the NDC appears for both negative and positive bias. This highlights the robust nature of the NDC and its connection to nonequilibrium electron phases (Fig. 1A), which will be addressed later.

Single-photon detection with field-induced bistabilities

The jumps in the IV characteristics close to I_C form the core ingredients required for sensitive photodetection. When biasing close to I_C (black arrow in Fig. 1E), we find that the system stochastically switches from the metallic to the electron-hole plasma state. This is shown in Fig. 2A, which plots the two-probe voltage drop recorded over time (t), when the system spontaneously jumps to a high resistance state at $t = 211$ ms. To restore the system, we apply resetting voltage pulses, with reset frequencies reaching up to 38 kHz depending on the measurement conditions. We attribute the observed jumps to the electrical noise and thermal radiation in the system, which demonstrates the extreme sensitivity of the bistability. Led by this result, we record similar time traces under mid-IR illumination (11.32 μm). Notably, we observe many more switching events (Fig. 2B), which demonstrates that light increases the count rate (Γ). Figure 2C plots Γ as a function of I_{DC} near the transition for different illumination intensities, revealing two fundamental characteristics. First, Γ increases exponentially as I_{DC} approaches the transition (see supplementary text, section S16, for a detailed analysis). Second, close to I_C, Γ increases linearly with power (P) and exhibits superlinear behavior when biased further from the transition (Fig. 2D). Both observations bear strong similarities with the operation of SNSPDs. The former indicates the probabilistic nature of switching events (*32*, *33*), whereas the latter provides the first indication of single-photon detection, where the number of switching events is directly proportional to the photon flux (*34*). More generally, the exponent in the P dependence $\Gamma \propto P^x$ is characteristic of the number of photons necessary for triggering a switch and increases further away from the critical bias. This is evidenced in our data by a range of biases showing $x = 1$, whereas those further away from the I_c tend toward $x = 2$ (Fig. 2D).

The observation of linear P dependence of Γ (Fig. 2D) points toward the detection of single photons. However, the presence of switching in the dark (Fig. 2A) brings into consideration the effect of light-induced heating. To disentangle the different contributions, we measure the temperature dependence of Γ. Figure 2E plots Γ as a function of I_{DC} and temperature (T) in the dark, whereas Fig. 2F plots Γ as a function of I_{DC} and P. The dark red regions mark the count rate equal to the reset frequency ($\Gamma = f_{reset} = 38.133$ kHz), indicating detector saturation. The two maps are markedly different. In Fig. 2E, the saturation region shifts to lower current densities with temperature. We attribute this behavior to a global shift in the critical current as temperature increases, a trend characteristic of the NDC in our samples, as will be shown later. By contrast, the $\Gamma = f_{reset}$ region does not shift but rather broadens with increasing P. The critical current remains the same, but the onset of switching occurs for a bias further from the transition. Moreover, analysis of the $\Gamma(I_{DC})$ dependencies (supplementary text, section S16) shows that they are strongly modified when changing P, whereas they remain unchanged with variations in temperature. A detailed analysis of the temperature dependence of the dark count rate (supplementary text, section S16) reveals further differences. It increases exponentially with temperature, exhibiting activated behavior, in contrast to the linear response observed in the power dependence (Fig. 2D). These differences suggest that mid-IR sensitivity arises from direct photon absorption rather than global sample heating.

Without using a single-photon emitter, an alternative proof for single-photon detection involves analyzing the switching statistics of the detector and correlating it with the emission statistics of a dim coherent source (*35*). In the mid-IR, such measurements are challenging in free-space coupling schemes because background radiation dominates our dark counts and mixes with the statistical analysis (supplementary text, section S5). Therefore, to characterize the underlying mechanism, we performed measurements using visible light

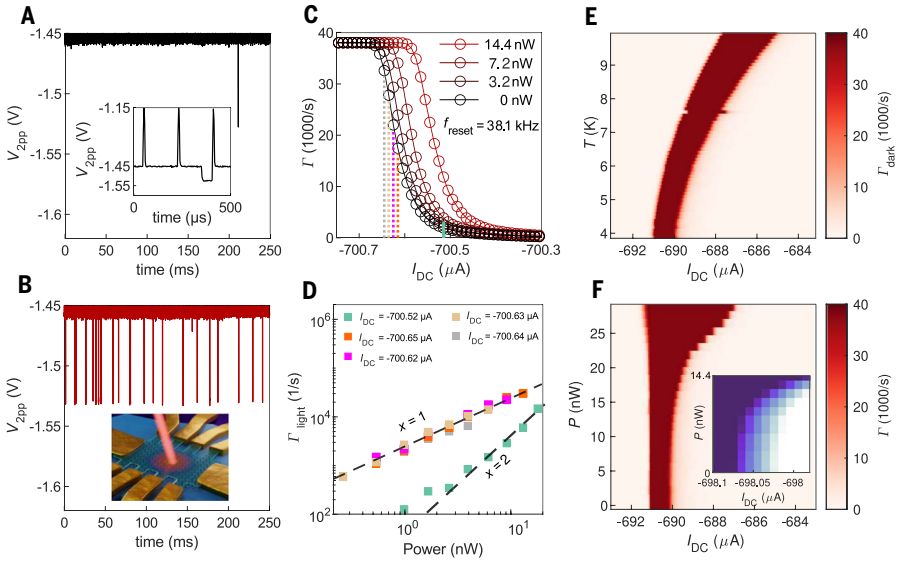


Fig. 2. Single-photon counting at mid-IR frequencies. (**A**) Two-probe voltage (V_{2pp}) plotted as a function of time (milliseconds) when current-biased close to the critical current I_C. The reset frequency $f_{reset} = 5.6$ kHz. We apply voltage pulses at frequency of $f_{reset} = 5.6$ kHz to reset the system. (Inset) Zoom of main panel displaying three reset pulses and one click. (**B**) Same as (A) but under mid-IR illumination. $I_{DC} = -701.2$ μA, $\lambda = 11.32$ μm, $P = 4.8$ nW, $f_{reset} = 5.6$ kHz, filling factor (n) = −2. (Inset) Schematic of device and photocurrent experiment. (**C**) Count rate (Γ) plotted as a function of bias current (I_{DC}) for different powers (P) (black to red). $f_{reset} = 38$ kHz. (**D**) Count rate only due to light, $\Gamma_{light} = \Gamma - \Gamma_{dark}$, plotted as a function of P for different I_{DC}. Filled squares are experimental data points, with colors corresponding to the bias levels marked with dashed lines in (C). The dashed lines mark dependencies $\Gamma \sim P^x$ for $x = 1$ and 2. (**E**) $\Gamma(I_{DC},T)$ measured in the dark. (**F**) $\Gamma(I_{DC},P)$ measured at $\lambda = 11.32$ μm. $f_{reset} = 38$ kHz. (Inset) Same as (F), but measured in a lower-noise configuration, focusing on the low-power regime. We note the doping level in (E) and (F) was slightly different from the measurements in (C), which accounts for slight differences in I_c between these measurements. The P values reported in all panels refer to absorbed powers and are calculated using rigorous coupled wave analysis method (supplementary text, section S19) to be 4%. All measurements were performed at 4 K except (E).

(675 nm), where background mid-IR radiation was heavily filtered using a quartz window (materials and methods). Additionally, the shorter wavelength enables spatially resolved measurements, providing further fundamental insights into the detector operation. For spatially resolved measurements, we use an alternative measurement scheme that yields a quantity Γ_{arb} proportional to Γ (supplementary text, section S4). Figure 3A plots Γ_{arb} as a function of position (X,Y) of the beam, with the device outline overlaid; the device mesa is mapped out by tracking the zero-bias photocurrent originating from contact regions (supplementary text, section S4). Unexpectedly, it shows that Γ_{arb} is maximum in a narrow strip of the device (see further discussion below). Parking the laser there, we studied the dependence of Γ on I_{DC} and laser power P (Fig. 3B), revealing a similar behavior to the mid-IR case (Fig. 2B); note that the count rate is less than that in mid-IR experiments only because we used a lower reset frequency for these measurements (5.6 kHz) and does not reflect spectral dependencies. Fixing I_{DC}, we performed statistical measurements of the switching events. Coherent sources emit photons according to a Poissonian distribution (*36*), and observing that distribution reflected in the count statistics is a commonly accepted benchmark of single-photon detection (*2*, *5*, *19*, *35*). Figure 3C plots histograms of the counts recorded in 235-ms time bins, demonstrating that they obey Poissonian statistics (pink lines) for finite P. Figure 3D shows that the histograms satisfy the relation variance = mean, characteristic of Poissonian distribution, for the entire dynamic range of the detector. These results demonstrate that our device can detect single photons. Although the statistical measurements for mid-IR require more controlled experimental conditions, the stochastic switching behavior, linear power dependence, and exclusion of laser-induced heating (Fig. 2) provide sufficient evidence for the mid-IR capabilities of our detector.

Origin of NDC

The data above provide exciting prospects for single-photon detection. The first step toward finding the design principles necessary for the development of MSPDs is understanding the mechanism of NDC. This phenomenon is characteristic of superlattice structures (*37*) and, broadly, can be split into two classes. First, the regime of sequential tunneling in weakly coupled superlattices, also known as electric-field localization, which occurs when the voltage drop (V_{SL}) per superlattice period (a) exceeds the minibandwidth (*38*) (W): $V_{SL}/a > W$. The second class refers to the Esaki-Tsu negative differential velocity (NDV) in strongly coupled superlattices (*28*, *29*), where carriers are accelerated to negative velocity states at the inflection points of the Brillouin zone (supplementary text, section S6). Although these peculiar quantum effects are not accessible in normal metals, the superlattice imposes a small Brillouin zone (0.01% of the size of that in regular crystals), which makes such phenomena readily accessible in moderate electric fields. Electric-field localization is more common in narrow-bandwidth materials (*38*), in which the condition $V_{SL}/a > W$ is easier to satisfy, whereas NDV pertains to wider bands. Although our moiré system resembles strongly coupled superlattices, disentangling these two mechanisms is challenging owing to the uncertainties in the material parameters and electric-field distributions in our devices. Nonetheless, they can be distinguished on the basis of the dependence of NDC on W (*29*). Specifically, the threshold for electric-field localization increases linearly with W, whereas the threshold for NDV is generally independent of W. In our moiré heterostructures using BLG, we can in situ tune W using displacement fields (*39*) and hence study the dependence of the critical field (E_C) on W. For this purpose, we turn to the second device with two electrical gates, the $DBLG_B$.

Because in $DBLG_B$, the NDC is localized to one side of the device (supplementary text, section S11), it is masked by parallel non-NDC channels. Hence, to track the NDC response, we measure the four-probe voltage (V_{4pp}) in the region where bistabilities were observed (supplementary text, sections S10 and S11). The inset of Fig. 4A plots the V_{4pp} as a function of the source voltage in $DBLG_B$ for different displacement fields (D) close to I_C. By increasing D, we observe that the NDC region becomes more pronounced, but its critical voltage (V_C) remains little influenced. At the same time, the measurements of the critical current (supplementary text, section S10) show a decrease in I_C by 50% for the largest D, providing experimental evidence for reducing W (i.e., band flattening) with D. Figure 4A plots V_C as a function of W, where the D-dependent W is obtained from calculations (supplementary text, section S8). The red dashed line plots the critical voltage expected for electric-field localization. Our experiment clearly does not follow this trend, and the measured V_C is mostly independent of $W(D)$, which suggests that the observed NDC originates from NDV rather than sequential tunneling.

Guided by these insights, we performed Boltzmann transport simulations of electron transport in realistic band structures (supplementary text, section S7) to obtain IV characteristics in the high-field regime.

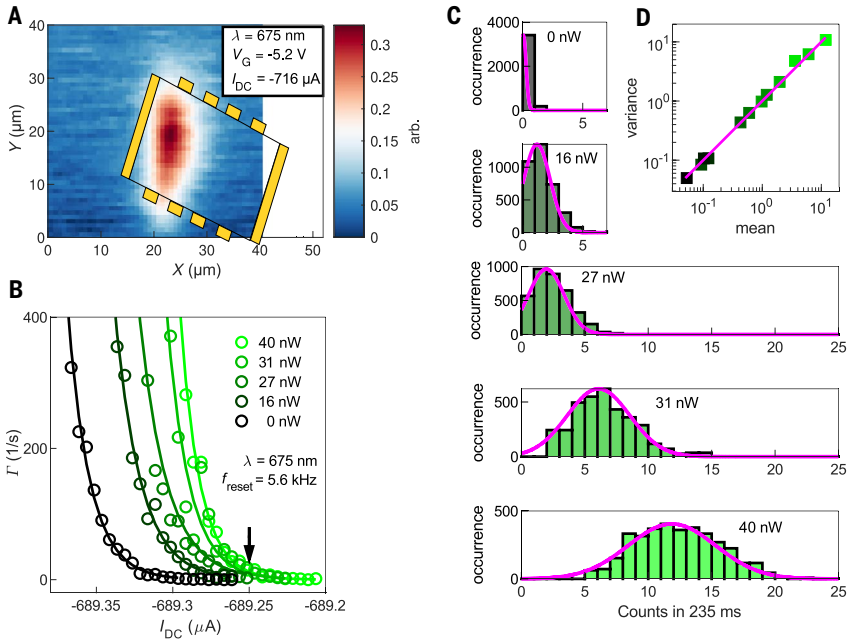


Fig. 3. Spatial and statistical measurements of switching events using visible light. (**A**) Measurements of Γ_{arb} as a function of spatial position (X,Y) in the two-point-probe geometry ($V_{2\text{-probe}}$). The scale bar marks the relative values of Γ_{arb} (see supplementary text, section S4, for details on the measurement scheme). The device mesa and measurement contacts are sketched in black and gold, respectively. (**B**) Γ as a function of I_{DC} plotted for different powers (P) (black to green). The solid lines plot exponential fits. The reset pulse frequency is 5.6 kHz (lower than in Fig. 2), and the plot is truncated at $\Gamma = 400$ to better see the features at low Γ values. The displayed P are corrected for BLG absorption (2% at $\lambda = 675$ nm; supplementary text, section S19). (**C**) Histograms presenting the statistical distribution of count number registered in a 235-ms time bin for different illumination P, recorded for the bias value marked by the black arrow in (B). The distributions follow Poissonian statistics (pink solid lines). (**D**) Variance plotted as a function of mean calculated from the histograms measured for 12 different P values. The color scale corresponds to the main different P presented in (B). The solid purple line plots the variance = mean line, indicating a Poissonian distribution. All measurements were performed at $T = 4$ K.

these transitions, allowing the carriers to continue accelerating within their bands and to reach the NDV regime. This explains why in $DBLG_B$, the NDV appears only when gapping the charge neutrality point strongly with displacement fields (Fig. 4A, inset) and provides evidence for the requirement of a gapped state. The interplay of NDV with Schwinger-Zener transitions may also explain the doping dependence of the NDC regime, appearing only for the highest doping in the middle of the bands. However, a complete understanding requires considering a two-band model.

Further understanding of the measured NDC can be obtained from our spatially resolved measurements (Fig. 3A and supplementary text, section S11), which show photoactivity only in a narrow strip of the device, which suggests that the NDC is localized to a small domain within the sample. The local nature of the effect is further confirmed through transport measurements performed between different contact pairs, where NDC can only be observed if the current path crosses this region of the device (supplementary text, section S12). We also note that the photoactivity remains fixed to this region for all gate voltages and bias currents and directions (supplementary text, section S17), suggesting that the domain is not field induced but rather structural in origin. The spatial dependence hence likely reflects local regions of favorable stacking arrangements, which can vary substantially in moiré materials (*39*, *41*). Although the domain in $DBLG_A$ appeared close to current injectors, the count rate was seemingly independent of the polarization of light (supplementary text, section S14), suggesting that the effect originates from the bulk rather than metallic contacts. Moreover, similar localized regions observed in $DBLG_B$ were found in the center of the device, micrometers away from the current injectors, which provides stronger evidence for domain structures in the bulk of the device (supplementary text, section S11).

The green curve in Fig. 4B shows the calculated current density as a function of E field at a fixed doping density. It shows that carriers' drift velocity first increases before reaching the critical field, at which it begins to drop. To visualize the microscopic origin of the NDV, we plot the distributions of carriers for zero bias (Fig. 4D, left), at E_C (Fig. 4D, middle), and in the NDC regime (Fig. 4D, right), with arrows representing the contribution of individual states to the total current. At zero bias, the carriers are evenly distributed around the Brillouin zone and the total current is zero. As E increases, the carrier distribution shifts and the current grows until, around E_C, more and more carriers start to enter the regions with negative velocity (arrows pointing in the direction opposite to the applied field). Figure 4C plots the calculated critical current I_C at which NDC onsets, compared with that extracted from our experiment (Fig. 1E) as a function of doping. Without any fitting parameters, the experiment and calculations agree within an order of magnitude. Moreover, the calculations capture the filling dependence with the largest critical current peaking at $\nu = \pm 2$. This is attributed to the presence of van Hove singularities at $\nu = \pm 2$ for which the free carrier density is largest and the current is maximum. Beyond E_C, the green line in Fig. 4B deviates importantly from the experiment. This is unsurprising because the calculations do not consider interband transitions (*40*) to neighboring bands, which are responsible for the continued growth of the current beyond the NDC regime (*26*) and were found to dominate in previous high-field transport studies in moiré superlattices without a gap at charge neutrality. However, our BLG/hBN superlattices exhibit a gapped band structure. If sufficiently large, the gap suppresses

Although the lowest-lying bands are easily gapped with displacement fields, they remain mixed with remote bands for most stacking configurations, and hence Schwinger transitions are still expected to dominate. However, there exist a few stackings resulting in a gap between the lowest-lying and remote bands (supplementary text, section S8). Statistically, they are far less common but may be found in the large devices used in this study. Transport measurements in the linear response regime showed varying behaviors between different contact pairs, including signatures of supermoiré lattices (*42*, *43*), providing strong evidence for spatial variations in stacking (supplementary text, section S1). This explanation also clarifies why our NDC is seemingly tied to the Schwinger criticalities (Fig. 1F). A simple circuit model (supplementary text, section S13) demonstrates how the regions without this stacking-induced gap, where Schwinger criticalities dominate (pink curve in Fig. 4B), influence the IV characteristics of the entire device when connected in series with the NDC region. This results in a compression of the NDC region and the combined IV characteristics (black curve in Fig. 4B) that resemble the experimentally measured data (Fig. 1D). Consequently, the measured NDC appears only for a narrow bias range as a result of interplay between the two regions.

Single-photon detection mechanism

Our detector integrates engineered light-sensitive bistabilities with the broadband mid-IR absorption inherent to BLG (*44*). The switching mechanism shares similarities with both Geiger-mode operation in resonant tunneling diodes (*45*) and SNSPDs, where the system transitions

between conductive electron phases (Fig. 1A). Phenomenologically, the switching is triggered by a photon-induced current or voltage, which drives the system into the unstable NDC region, initiating the switch. Given that our electron system is metallic, photoexcited carriers likely perturb the local current distribution, leading to the formation of a localized hotspot with a reduced critical current. This hotspot expands, eventually exceeding the threshold for switching. This interpretation is supported by the strong temperature dependence of the globally measured critical current (Fig. 2E).

The underlying microscopic process remains an open question, particularly in understanding how a single photon generates a sufficiently large photocurrent to trigger the global switching event. This typically requires some form of gain or carrier multiplication. Photoconductive gain may play a role in amplifying the current generated by a single photon, if electron-hole lifetimes invoke the asymmetries intrinsic to the hBN/graphene superlattice (*30*, *46*). Alternatively, our findings indicate that the photoactive region is spatially confined, possibly exhibiting high-field domains that may enable carrier multiplication through impact ionization (*47*), assisting hotspot formation. Further experimental work is required to fully elucidate the microscopic processes governing single-photon switching in this system.

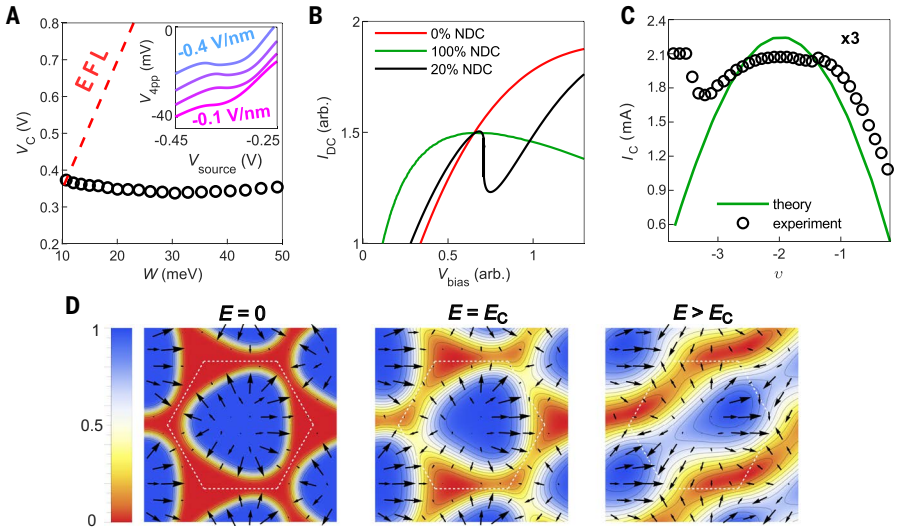


Fig. 4. Displacement field dependence of NDC and modeling negative velocity. (**A**) Critical voltage (V_C) as a function of bandwidth (W). (Inset) Four-probe voltage V_{4pp} as a function of voltage bias V_{source}, measured for different displacement fields (D). V_c in the main panel was obtained from analyzing this trend (see supplementary text, sections S8 and S10, for details on V_c and W extraction). EFL, electric field localization. (**B**) The two-region model shows how the NDC (green) and non-NDC (pink) regions connected in series can result in different IV characteristics (black), depending on the relative contribution of the two regions (see supplementary text, section S13, for details). (**C**) Critical current (I_C) as a function of doping. Green line is calculated for BLG/hBN superlattice considering the carrier dynamics within the lowest-lying band. Open circles plot experimental data of $DBLG_A$, scaled by a factor of 3. Extraction of I_C from experiment is unreliable for $\nu < -3$ due to low signal (see Fig. 1F). (**D**) Carrier distributions within a single Brillouin zone (white dashed hexagon) for electric fields below, at, and above critical field E_C, obtained from the same model as the green curves in (B) and (C). The color scale plots probability of occupation, and the black arrow direction and magnitude plots the relative direction and amplitude of group velocity of those carriers in the direction of the applied field.

Discussion

The distinct underlying physics of our MSPDs means that they are not constrained to the same operating conditions as SNSPDs. Their operating temperatures are instead limited by the robustness of NDC and the accompanying bistabilities. Figure 5A plots IV characteristics for increasing temperatures, showing that the NDC persists up to around 30 K. Figure 5B plots Γ as a function of Γ_{dark} for temperatures up to 25 K and under mid-IR illumination, where larger Γ_{dark} indicates larger bias currents closer to the transition. For all T, we find light-induced switching with little deterioration in detector performance up to 20 K. Figure 5 demonstrates the higher T capabilities of our MSPDs, which may be pushed to even higher T through engineering the superlattice minibands.

We developed a platform for single-photon detection based on nonequilibrium electron phases in moiré superlattices with tunable band structures. In our unoptimized devices and measurement protocols, we demonstrate a distinctive combination of detection capabilities, including single-photon sensitivity extending to mid-IR wavelengths (>10 μm), fast response (>38 kHz, setup limited), and high-temperature operation (25 K). Although our demonstrated detector operation was limited to the probabilistic regime (*32*, *33*) with inherently low efficiencies, the exponential dependence of the count rate on bias current suggests that high detector efficiencies are attainable if dark counts are reduced and the reset rate can be increased. To achieve this, fiber-coupled device packages may be engineered with sharp band pass filters to suppress background photons (*48*). Similarly, the 38-kHz speed and the detection range that we report represent lower bounds, limited by our experimental setup (supplementary text, section S15).

Now that the proof-of-concept device has been demonstrated, there are a myriad of future directions to explore. At the material level, engineering the NDV and nonequilibrium electron phases through moiré heterostructure engineering is crucial to achieving high performance. This could lower critical currents and accompanying shot noise, expand the photoactive region, and potentially increase sensitivity for longer wavelengths. In this regard, other moiré systems or van der Waals superlattice structures may also be explored and may even be better suited for observing NDC. For example, we also observed high-field induced bistabilities in magic-angle twisted BLG (*49*, *50*) (supplementary text, section S18), showing that the NDC is commonplace to different moiré materials. At the device level, the geometry of the mesa can also be improved substantially. Large current injectors help to minimize joule heating effects, which may smear the NDC, and narrower channels can lower the critical current. The latter is analogous to the behavior of SNSPDs that use nanowire structure for enhancing internal quantum efficiency. From the measurement side, improving optical coupling and devising automatic resetting schemes will enable much faster and sensitive operation, approaching and potentially surpassing that of SNSPDs, which are limited by kinetic inductance.

Our work introduces a class of compact, broadband, and complementary metal-oxide semiconductor (CMOS)–compatible SPDs, with potential applications ranging from astrophysics to light detection and ranging (LIDAR), molecular spectroscopy, and quantum technologies (*3*, *4*). Although our detection mechanism is specific to the high-field properties of moiré superlattices, we note that alternative NDC-based devices may also be explored, combining the capability to engineer sensitive bistabilities with resonances at mid-IR wavelengths. Given BLG's intrinsically large long-wavelength response, our devices may even have potential for photodetection in the terahertz regime (*30*, *44*). Simultaneously, the manifestation of NDC opens new avenues for high-field experiments in moiré heterostructures. Our observation of NDV represents an important milestone toward realizing Bloch oscillations in 2D solid-state systems, where several intriguing phenomena (*51*) and

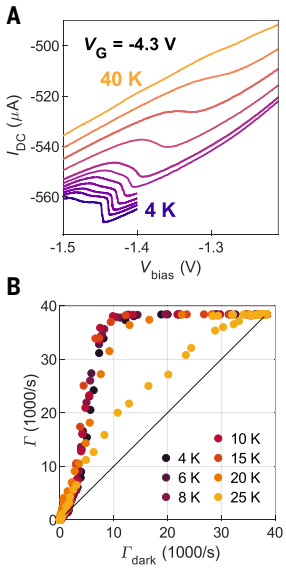


Fig. 5. High-temperature performance. (**A**) IV curves showing NDC as a function of temperature. The NDC region shifts to lower bias and flattens with increasing temperature, and the NDC survives up to around 30 K. (**B**) Correlation plot relating Γ to Γ_{dark} for a few different temperatures. Every trace is in fact a bias sweep, but this way of plotting the data allows for a direct comparison between different temperatures because changing the temperature moves the optimal operating bias point. The detector performance stays unchanged up to around 20 K.

potential device technologies reside, including high-frequency oscillators (*52*), multivalued logic (*53*), and compact terahertz emitters.

REFERENCES AND NOTES

1. I. Esmaeil Zadeh *et al.*, *Appl. Phys. Lett.* **118**, 190502 (2021).
2. R. H. Hadfield, *Nat. Photonics* **3**, 696–705 (2009).
3. E. Pelucchi *et al.*, *Nat. Rev. Phys.* **4**, 194–208 (2021).
4. S. Dello Russo *et al.*, *Photonics* **9**, 470 (2022).
5. D. V. Morozov, A. Casaburi, R. H. Hadfield, *Contemp. Phys.* **62**, 69–91 (2021).
6. J. S. Dam, P. Tidemand-Lichtenberg, C. Pedersen, *Nat. Photonics* **6**, 788–793 (2012).
7. M. Widarsson *et al.*, *Appl. Opt.* **59**, 2365–2369 (2020).
8. H. Shibata, *IEICE Trans. Electron.* **E104.C**, 429–434 (2021).
9. M. Colangelo *et al.*, *Nano Lett.* **22**, 5667–5673 (2022).
10. V. B. Verma *et al.*, *APL Photonics* **6**, 056101 (2021).
11. G. G. Taylor *et al.*, *Optica* **10**, 1672–1678 (2023).
12. I. Charaev *et al.*, *Nat. Nanotechnol.* **18**, 343–349 (2023).
13. R. L. Merino *et al.*, *2D Mater.* **10**, 021001 (2023).
14. I. Charaev *et al.*, *Nat. Commun.* **15**, 3973 (2024).
15. F. Marsili *et al.*, *Nano Lett.* **12**, 4799–4804 (2012).
16. M. A. Aamir *et al.*, *Nano Lett.* **21**, 5330–5337 (2021).
17. D. K. Efetov *et al.*, *Nat. Nanotechnol.* **13**, 797–801 (2018).
18. J. Yan *et al.*, *Nat. Nanotechnol.* **7**, 472–478 (2012).
19. E. D. Walsh *et al.*, *Science* **372**, 409–412 (2021).
20. P. Seifert *et al.*, *Nano Lett.* **20**, 3459–3464 (2020).
21. G. Di Battista *et al.*, *Nano Lett.* **22**, 6465–6470 (2022).
22. B. Huang *et al.*, arXiv:2410.22433 [cond-mat.mes-hall] (2024).
23. B. Deng *et al.*, *Nat. Photonics* **14**, 549–553 (2020).
24. C. Ma *et al.*, *Nature* **604**, 266–272 (2022).
25. G. Di Battista *et al.*, *Sci. Adv.* **10**, eadp3725 (2024).
26. A. I. Berdyugin *et al.*, *Science* **375**, 430–433 (2022).
27. J. Faist *et al.*, *Science* **264**, 553–556 (1994).
28. L. Esaki, R. Tsu, *IBM J. Res. Develop.* **14**, 61–65 (1970).
29. A. Sibille, J. F. Palmier, H. Wang, F. Mollot, *Phys. Rev. Lett.* **64**, 52–55 (1990).
30. A. L. Shilov *et al.*, *ACS Nano* **18**, 11769–11777 (2024).
31. H. Tian *et al.*, *Nature* **614**, 440–444 (2023).
32. A. Engel, J. J. Renema, K. Il'in, A. Semenov, *Supercond. Sci. Technol.* **28**, 114003 (2015).
33. A. D. Semenov, *Supercond. Sci. Technol.* **34**, 054002 (2021).
34. G. N. Gol'tsman *et al.*, *Appl. Phys. Lett.* **79**, 705–707 (2001).
35. C. J. Chunnilall, I. P. Degiovanni, S. Kück, I. Müller, A. G. Sinclair, *Opt. Eng.* **53**, 081910 (2014).
36. J. W. Goodman, *Statistical Optics* (Wiley, 2015).
37. K. Leo, *High-Field Transport in Semiconductor Superlattices* (Springer, 2003).
38. L. Esaki, L. L. Chang, *Phys. Rev. Lett.* **33**, 495–498 (1974).
39. R. Smeyers, M. V Milošević, L. Covaci, *Nanoscale* **15**, 4561–4569 (2023).
40. C. Zener, *Proc. R. Soc. Lond. A* **145**, 523–529 (1934).
41. D. Beitner *et al.*, *Nano Lett.* **23**, 10758–10764 (2023).
42. L. Wang *et al.*, *Nano Lett.* **19**, 2371–2376 (2019).
43. Z. Wang *et al.*, *Sci. Adv.* **5**, eaay8897 (2019).
44. H. Agarwal *et al.*, *Nat. Photon.* **17**, 1047–1053 (2023).
45. A. Pfenning *et al.*, *Nanomaterials* **12**, 2358 (2022).
46. J. R. Wallbank *et al.*, *Nat. Phys.* **15**, 32–36 (2019).
47. P. P. Bohn, G. J. Herskowitz, *IEEE Trans. Electron Dev.* **19**, 14–21 (1972).
48. Y. Pan *et al.*, *Opt. Express* **30**, 40044–40052 (2022).
49. Y. Cao *et al.*, *Nature* **556**, 43–50 (2018).
50. Y. Cao *et al.*, *Nature* **556**, 80–84 (2018).
51. A. Fahimniya, Z. Dong, E. I. Kiselev, L. Levitov, *Phys. Rev. Lett.* **126**, 256803 (2021).
52. P. R. Berger, A. Ramesh, in *Comprehensive Semiconductor Science and Technology*, P. Bhattacharya, R. Fornari, H. Kamimura, Eds. (Elsevier, 2011), pp. 176–241.
53. B. Murugan, S. Y. Lee, *Carbon Lett.* **33**, 59–76 (2023).
54. K. Nowakowski, Data for "Single-photon detection enabled by negative differential conductance in moiré superlattices" Figures 1-2, data set, Zenodo (2025). https://doi.org/10.5281/zenodo.15577516.
55. K. Nowakowski, Data for "Single-photon detection enabled by negative differential conductance in moiré superlattices" Figures 3-5, data set, Zenodo (2025). https://doi.org/10.5281/zenodo.15600319.

ACKNOWLEDGMENTS

We thank I. Charaev for in-depth technical advice and for reviewing the manuscript. We also thank G. Scalari, J. Faist, and L. Levitov for helpful discussions. **Funding:** P.J.-H. acknowledges support by Air Force Office of Scientific Research (AFOSR) grant FA9550-21-1-0319, the Gordon and Betty Moore Foundation's EPiQS Initiative through grant GBMF9463, the Ramon Areces Foundation, and the ICFO Distinguished Visiting Professor program. We also acknowledge support from Fundació Cellex for funding P.J.-H.'s sabbatical. F.H.L.K. acknowledges support from the ERC TOPONANOP (726001), the government of Spain [PID2022-141081NB-I00; Severo Ochoa CEX2019-000910-S (MCIN/ AEI/10.13039/501100011033); and PCI2021-122020-2A funded by MCIN/AEI/10.13039/501100011033], the "European Union NextGenerationEU/PRTR" (PRTR-C17.I1), Fundació Cellex, Fundació Mir-Puig, and Generalitat de Catalunya (CERCA, AGAUR, 2021 SGR 01443). Furthermore, the research leading to these results received funding from the European Union's Horizon 2020 under grant agreement nos. 881603 (Graphene flagship Core3) and 820378 (Quantum flagship). This material is based on work supported by the AFOSR under award no. FA8655-23-1-7047. Any opinions, findings, and conclusions or recommendations expressed in this material are those of the author(s) and do not necessarily reflect the views of the US Air Force. J.B. acknowledges support from the European Union's Horizon Europe program under grant agreement 101105218. R.S., B.J., M.V.M., and L.C. acknowledge support from Research Foundation–Flanders (FWO) research projects G0A5921N and 11E5821N. H.A., K.N., and R.B. acknowledge funding from the European Union's Horizon 2020 research and innovation program under Marie Skłodowska-Curie grant agreement nos. 665884, 713729, and 847517, respectively. V.F. and S.S. acknowledge support from EPSRC grants EP/S019367/1, EP/P026850/1, and EP/N010345/1 and British Council project 1185409051. D.B.R. acknowledges funding from the Secretaria d'Universitats i Recerca del Departament d'Empresa i Coneixement de la Generalitat de Catalunya as well as the European Social Fund (L'FSE inverteix en el teu futur)–FEDER. R.K.K. acknowledges funding by MCIN/AEI/10.13039/501100011033; by the "European Union NextGenerationEU/PRTR" PCI2021-122020-2A within the FLAG-ERA grant (PhotoTBG); by ICFO, RWTH Aachen, and the Department of Physics of ETHZ; and from the Ramon y Cajal grant RYC2022-036118-I, funded by MICIU/AEI/10.13039/501100011033 and by "ESF+." **Author contributions:** Conceptualization: K.N., H.A., R.K.K., F.H.L.K.; Funding acquisition: F.H.L.K., R.K.K., P.J.-H., V.F., M.V.M.; Investigation: K.N., H.A., S.S., R.S., X.W., Z.Z., J.B., D.B.R., G.L., R.B., M.C., I.T., B.J., K.W., T.T., R.K.K.; Methodology: K.N., H.A., S.S., R.S., A.R.-P., R.K.K., F.H.L.K.; Project administration: R.K.K.; Supervision: R.K.K., F.H.L.K., P.J.-H., L.C., M.V.M., V.F.; Visualization: K.N., S.S., R.K.K., F.H.L.K.; Writing – original draft: K.N., R.K.K., F.H.L.K.; Writing – review & editing: All authors. **Competing interests:** The authors declare that they have no competing interests. **Data and materials availability:** All data are available in the main text or the supplementary materials. The raw data for main text figures and scripts are uploaded to Zenodo (*54*,*55*). The hBN used in this work is available from K.W. and T.T. under a material transfer agreement with the National Institute for Materials Science (NIMS). **License information:** Copyright © 2025 the authors, some rights reserved; exclusive licensee American Association for the Advancement of Science. No claim to original US government works. https://www.science.org/about/science-licenses-journal-article-reuse. This research was funded in whole or in part by the Engineering and Physical Sciences Research Council (EP/S019367/1, EP/P026850/1, and EP/N010345/1), a cOAlition S organization, and by the European Research Council (TOPONANOP, 726001); as required, the author will make the Author Accepted Manuscript (AAM) version available under a CC BY public copyright license.

SUPPLEMENTARY MATERIALS

science.org/doi/10.1126/science.adu5329
Materials and Methods; Supplementary Text; Figs. S1 to S19; References (*56*–*76*)

Submitted 13 November 2024; accepted 18 June 2025

10.1126/science.adu5329

CHEMICAL PHYSICS

Imaging collective quantum fluctuations of the structure of a complex molecule

Benoît Richard[1,2,3], Rebecca Boll[4]*, Sourav Banerjee[1], Julia M. Schäfer[1,5], Zoltan Jurek[1], Gregor Kastirke[6,7], Kilian Fehre[6], Markus S. Schöffler[6], Nils Anders[6], Thomas M. Baumann[4], Sebastian Eckart[6], Benjamin Erk[8], Alberto De Fanis[4], Reinhard Dörner[6,7], Sven Grundmann[6], Patrik Grychtol[4], Max Hofmann[6], Markus Ilchen[1,2,4], Max Kircher[6], Katharina Kubicek[2,3,4], Maksim Kunitski[6], Xiang Li[9,10], Tommaso Mazza[4], Severin Meister[11], Niklas Melzer[6], Jacobo Montano[4], Valerija Music[4,12], Yevheniy Ovcharenko[4], Christopher Passow[8], Andreas Pier[6], Nils Rennhack[4], Jonas Rist[6], Daniel E. Rivas[4], Daniel Rolles[9], Ilme Schlichting[13], Lothar Ph. H. Schmidt[6], Philipp Schmidt[4,12], Daniel Trabert[6], Florian Trinter[6,14], Rene Wagner[4], Peter Walter[10], Pawel Ziolkowski[4], Artem Rudenko[9], Michael Meyer[3,4], Robin Santra[1,2,3,5], Ludger Inhester[1,3]*, Till Jahnke[4,11]*

Because of the Heisenberg uncertainty principle, the structure of a molecule fluctuates about its mean geometry, even in the ground state. Observing this fundamental quantum effect experimentally—particularly, revealing the collective nature of the structural quantum fluctuations—remains an unmet challenge for complex molecules. In this work, we achieved this for an 11-atom molecule by inducing its Coulomb explosion with an x-ray free-electron laser. We show that the structural fluctuations manifest themselves in correlated variations of ion momenta obtained through coincident detection of the atomic fragments from individual molecules. Our analysis scheme allows extracting these variations, despite our measurements covering only a fraction of the full 33-dimensional momentum space, thereby establishing a general approach for extracting information on high-dimensional structural dynamics using Coulomb explosion.

Near absolute zero temperature, matter exhibits structural fluctuations that are fully absent in a classical description and that can substantially affect its properties. These quantum fluctuations, termed ground-state structural fluctuations (GSFs) (or zero-point fluctuations), arise from the vibrational wave function of the system and play a key role in many phenomena: at high pressure, causing various types of quantum phase transitions (*1*, *2*), for example, to a symmetric phase of ice (*3*) or an antiferroelectric phase of anhydrous sodium hydroxide (*4*); inhibiting or promoting glass transitions (*5*); imposing structural changes that lead to superconductivity at high temperatures (*6*); suppressing the formation of charge density wave phases in layered transition-metal dichalcogenides (*7*); strengthening or weakening hydrogen bonds (*8*); or influencing cross sections of chemical reactions (*9*).

GSFs are complex, as the atoms of bound systems fluctuate in a concerted manner following specific collective patterns. This intricate behavior emerges already in individual molecules: Their structural properties are determined by their respective ground-state potential energy surfaces, which are many-body potentials that are challenging to visualize and characterize. Although the equilibrium structure of a molecule corresponds to the global minimum on its potential energy surface, its structure is, in reality, fuzzy, as the aforementioned quantum fluctuations explore the potential energy landscape. Matching the high dimensionality of the potential energy surface, these fluctuations involve many different degrees of freedom, which results in their strongly collective nature. In this work, we demonstrate that this collective nature of structural quantum fluctuations in complex molecules can be directly observed.

Indirect evidence for this quantum phenomenon was found already 100 years ago, when Robert S. Mulliken compared energy levels of different isotopologues (*10*). By now, the measurement of discrete molecular energy levels and the identification of zero-point energies are routine (*11*). However, typically, one only measures the consequences of the ground-state quantum fluctuations on molecular energy levels but cannot observe the underlying structural manifestation of these fluctuations, and the relevance of GSFs is usually inferred from theoretical modeling (*3*–*7*). To experimentally image the GSFs themselves and obtain critical insight into collective quantum phenomena, such as the ones mentioned above, it is necessary to target individual molecules to access their entire high-dimensional phase space and thus the structural dependencies among the atoms constituting the molecules. This is out of reach for traditional imaging techniques, such as crystallography, because those sample ensembles of molecules and thus inherently only provide information about the average structure.

By contrast, Coulomb explosion imaging (CEI) is a method that is distinctly suited to performing the required single-molecule measurements. In CEI, a molecule fragments violently owing to the Coulomb repulsion following a rapid charge-up. In the ideal case, the molecule is fully fragmented into atomic ions on a short timescale, and the information on its initial geometry is retrieved by analyzing the momenta of the fragment ions. The charge required to trigger an effective fragmentation was first generated by passing molecular ions through a thin foil (stripping off electrons) (*12*) and, later, by using femtosecond laser pulses (*13*–*20*), synchrotron light (*21*–*24*), or intense (x-ray) free-electron laser pulses (*25*–*30*). Previous experiments were able to highlight structural fluctuations of small, symmetric molecules using CEI, including the correlations between atoms necessary to probe the GSFs. For example, CO_2 molecules, whose nominal ground-state geometry is linear, were found to deviate from linearity most of the time (*22*), and deuterated methane (CD_4), highly symmetric in its equilibrium state, is in fact asymmetric and even chiral owing to its structural fluctuations (*31*). These previous works relied on obtaining the full N-body distribution of ions (where N represents the number of ions) by the measurement of all (or all but one) ions in coincidence. Such a complete measurement is impossible for complex molecules because of the finite detection efficiency of the ion detectors, limiting previous results to small molecules. In this work, we overcome this barrier, opening the possibility to apply the method to a much larger class of complex and extended molecules. We show that, by using intense, femtosecond x-ray pulses and an elaborate analysis of only a subset of the fragment ions detected in coincidence, the full dimensionality of the structural fluctuations and their intramolecular correlations can be probed, which goes far beyond the visualization of independent fragments in the molecular frame presented in our previous work (*30*). In particular, it allowed us to identify fingerprints of specific ground-state normal modes (NMs) in our data through correlated fluctuations involving more than five atoms. This result constitutes an important advance toward measuring the collective fluctuations of atoms in molecules.

[1]Center for Free-Electron Laser Science CFEL, Deutsches Elektronen-Synchrotron DESY, Hamburg, Germany. [2]Department of Physics, University of Hamburg, Hamburg, Germany. [3]The Hamburg Centre for Ultrafast Imaging, Hamburg, Germany. [4]European XFEL, Schenefeld, Germany. [5]Department of Chemistry, University of Hamburg, Hamburg, Germany. [6]Institut für Kernphysik, Goethe-Universität Frankfurt, Frankfurt am Main, Germany. [7]Helmholtz Forschungs-akademie Hessen für FAIR (HFHF) GSI Helmholtzzentrum für Schwerionenforschung Campus Frankfurt, Frankfurt am Main, Germany. [8]Deutsches Elektronen-Synchrotron DESY, Hamburg, Germany. [9]J. R. Macdonald Laboratory, Department of Physics, Kansas State University, Manhattan, KS, USA. [10]SLAC National Accelerator Laboratory, Menlo Park, CA, USA. [11]Max-Planck-Institut für Kernphysik, Heidelberg, Germany. [12] Institut für Physik und CINSaT, Universität Kassel, Kassel, Germany. [13]Max-Planck-Institut für medizinische Forschung, Heidelberg, Germany. [14]Molecular Physics, Fritz-Haber-Institut der Max-Planck-Gesellschaft, Berlin, Germany.
***Corresponding author. Email: rebecca.boll@xfel.eu (R.B.); ludger.inhester@cfel.de (L.I.); till.jahnke@xfel.eu (T.J.)**

Coulomb explosion of individual 2-iodopyridine molecules (C_5H_4NI; see equilibrium geometry in Fig. 1) was induced by intense, femtosecond soft x-ray pulses from the European X-ray Free-Electron Laser (EuXFEL). A COLTRIMS reaction microscope (*32*, *33*) available at the Small Quantum Systems (SQS) instrument was used to image the three-dimensional momenta of the emitted fragment ions in coincidence. More details on the experiment are given in the supplementary materials (SM) section S1 and in our earlier paper (*30*). The x-ray fluence at SQS is sufficiently high to trigger a full Coulomb explosion of the molecule, dissociating it into atomic fragments, and the repetition rate is high enough to detect many atomic fragments in coincidence. This provides a wealth of in-depth information, as will become evident in the following. Owing to the finite ion detection efficiency in the experiment, the recorded multi-dimensional data are typically incomplete, which poses a fundamental analysis challenge (*34*, *35*). We have overcome this problem for an N-atom molecule (here, $N = 11$ atoms) by reconstructing the full N-fold coincidence information from sets of coincident measurements of n ions ($n < N$), with a sophisticated data analysis technique fitting a multivariate distribution to the measured data.

Figure 1 shows the experimental results of Coulomb explosion imaging of iodopyridine molecules. Here and in the following, we focus on a specific coincidence channel where an I^{4+} ion, an N^{2+} ion, and at least one C^{2+} ion and one H^+ ion were measured in coincidence. Figure 1, A to D, depicts the carbon and hydrogen ions' three-dimensional momentum distributions projected onto two different planes in the molecular recoil frame. The emission direction of the iodine ion defines the z axis and spans the xz plane together with the emission direction of the nitrogen ion. All ion momenta have been normalized such that, for each coincident measurement, the magnitude of the iodine momentum equals one. The projections on the xz plane (Fig. 1, A and C) clearly resemble the molecular structure, as reported earlier (*30*). The projections on the yz plane (Fig. 1, B and D) reveal that, notably, many ions were emitted with substantial out-of-plane momentum, despite the planar equilibrium geometry of the molecule. To further study this feature, we switched to spherical coordinates, sketched in Fig. 1E, resulting in the angular emission distribution of the carbon ions (Fig. 1F). The four pronounced peaks correspond to the C3, C4, C5, and C6 carbon ions (see fig. S9 for a sketch of the molecule with full labeling). The C2 ion has comparatively low momentum (Fig. 1A) and lies close to the origin of the spherical coordinate system; thus, it appears as a broad feature in Fig. 1F, overlapping partially with the peaks for the C4 and C5 carbon ions. This angular representation of the coincidence data allows visualizing the dependence between the carbon and hydrogen out-of-plane momenta: The panels in Fig. 1G depict carbon ion angular emission distributions corresponding to specific emission directions of the H3 hydrogen ion (marked with boxes in Fig. 1D). If the H3 ion was emitted within the molecular plane (middle, Fig. 1G), then the carbon ions were on average also emitted in plane. If the H3 ion was either emitted upward (top, Fig. 1G) or downward (bottom, Fig. 1G) with respect to the molecular plane, the carbon angular distribution became tilted, with C3 and C4 being emitted in the same direction as H3, and C6 in the opposite direction. C5 remained centered in plane. The full dependence between the H3 emission direction and the out-of-plane emission angle of C3 to C6 is summarized in Fig. 1H, where we depict the mean emission angle θ of these carbon ions as a function of the out-of-plane momentum of the H3 proton. Similar correlations also exist for other hydrogen ions (SM section S2, where we extracted the full correlated behavior for all hydrogen and carbon ion pairs).

Origin of out-of-plane fluctuations

The experimental results presented in Fig. 1 show the rich information content available in such multidimensional data sets. In this section, we will demonstrate that the observed momentum fluctuations

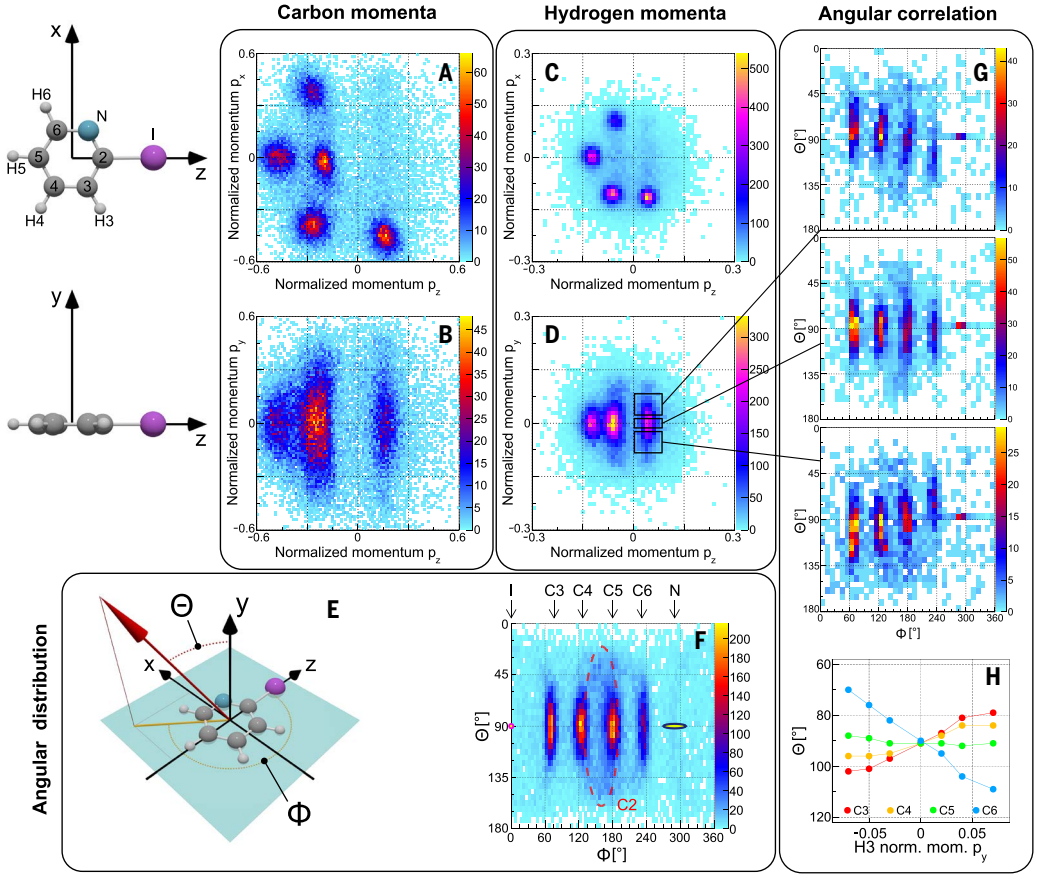


Fig. 1. Correlated out-of-plane fluctuations probed by Coulomb explosion. The sketches on the left depict the ground-state equilibrium geometry of iodopyridine and the recoil frame, for reference. (**A** to **D**) Newton diagrams of ion momenta, depicting the C^{2+} [(A) and (B)] and H^+ ions [(C) and (D)] in the molecular frame. All momenta are normalized relative to the momentum of the I^{4+} ion. (**E**) Definition of the spherical coordinates used. (**F**) Angular emission distributions of the carbon ions in the coordinates defined in (E). (**G**) Angular emission distributions of the carbon ions when restricted to different emission directions of the H3 proton. (**H**) Angular emission dependence between H3 and C3 to C6. The error bars are smaller than the symbols. The plotted data contain fourfold ion coincidence events, including I^{4+}, N^{2+}, C^{2+}, and H^+.

directly reflect quantum fluctuations present in the molecule in its vibrational ground state. Because the equilibrium geometry of iodopyridine is planar, the contributions of the quantum fluctuations can be expected to be particularly clear in the out-of-plane momenta, and we found that, indeed, initial out-of-plane GSFs are reflected in the final momenta after Coulomb explosion. In-plane momenta, by contrast, are more strongly impacted by additional variations in the mutual ion interaction during the explosion dynamics caused by variations in the timing of individual ionization events.

To elucidate how GSFs relate to the observed fluctuations in the measured ion momenta, we performed a simulation of the x-ray–induced ionization and the subsequent Coulomb explosion of the molecule. To this end, we utilized the XMDYN package (*36*) in combination with the reactive force field method (*37*, *38*) implemented in PuReMD (*39*). We used an ensemble of initial atomic positions and velocities that samples the corresponding vibrational ground-state Wigner distribution (see SM section S3 for further details on the simulation). In Fig. 2, we examine the out-of-plane behavior as predicted by our simulation and compare the simulation results to the momenta observed in the experiment as well as to the magnitude of the quantum fluctuations. Fig. 2, A to D, and shows the out-of-plane Newton diagrams for protons and carbon ions. The simulations took into consideration GSFs. The predicted momentum distributions after the Coulomb explosion are in good agreement with the measured data. The impact of the GSFs becomes evident by comparison with Fig. 2, E and F, which depicts simulation results where GSFs have been neglected (see SM section S3.4 for a quantitative comparison). In this case, out-of-plane momenta can only be caused by the recoil from the electrons emitted during the charge-up, which has a comparatively minor effect. The GSFs themselves are depicted in Fig. 2, G to J, showing the out-of-plane momentum and position distribution in the initial, neutral equilibrium state. As can be seen, the initial-state momentum fluctuations (Fig. 2, G and H) are much smaller than the variations in the final momenta after the Coulomb explosion (Fig. 2, A and B). The position fluctuations are depicted in Fig. 2, I and J (for hydrogen and carbon atoms, respectively).

Momentum-space reconstruction and correlation analysis

To access the correlations among the momenta in the final state, we must determine the full 33-dimensional momentum distribution of all 11 ionic fragments of the Coulomb-exploded molecule. To do so, we need to overcome three challenges. (i) Although the mass-to-charge ratio of each detected ion is measured in the experiment, its initial position within the molecule is unknown (for those cases where multiple atoms of the same element are present, carbon and hydrogen atoms for iodopyridine). (ii) The orientation of each molecule in the laboratory frame is random and unknown. Therefore, the molecular frame has to be determined based on the recorded ion momenta. In Fig. 1, for example, we used the recoil frame defined by the iodine and nitrogen ions (see SM section S5). (iii) Only a subset of all ions created by the x-ray pulse is detected. In this work, relevant statistics could be achieved for up to seven ions in coincidence (SM section 1.7) owing to the typical detection efficiency of ~60% per ion. We overcame these problems and recovered the momentum distribution in its full dimensionality by fitting a 33-dimensional Gaussian distribution to the measured data that involved four or more ions detected in coincidence. To make the fit independent of the initial (laboratory-frame) orientation of the molecule, we used scalar products between the measured momenta as internal coordinates. In this way, we avoided any bias from choosing specific ion momenta to define the molecular frame. The Gaussian distribution was then fitted by matching the statistical moments of the distribution of the scalar products, a procedure that is not biased by undetected ions and was performed in a manner that does not rely on the (unknown) identity of each ion. More details on the fitting procedure can be found in the SM (section S7).

We performed dimensional reduction of the resulting momentum distribution by principal component analysis (PCA) (*40*, *41*) based on the fitted Gaussian model (see SM section S8.3). Heavy atoms stay longer in the repulsive Coulomb potential and acquire, in general, both a larger momentum and a larger variance in their momentum. Therefore, to compare light and heavy atoms on a more equal footing, we performed the fit on the momenta weighted by the inverse square root of the ion mass, as commonly done in normal-mode analysis. The resulting principal components (PCs) of the weighted momenta are collective, 33-dimensional vectors that describe the dominant variations in the final ion momenta.

The four dominant out-of-plane PCs extracted from the experimental data are shown in Fig. 3, A to D, together with their explained variance σ^2. The corresponding PCs obtained from the simulation, using the same procedure, are depicted in Fig. 3, E to H. The order of the simulation components has been altered to facilitate the comparison.

The similarity of the PCs may be further characterized by the mutual overlaps S (defined as the absolute value of their scalar product) provided in between the respective pairs of PCs. Apart from the somewhat different values in the explained variances, the PCs extracted from the simulation data show strong similarity (overlap between 0.66 and 0.97) with the respective experimental PCs, indicating that the collective momentum fluctuations found in the experiment are in agreement with those obtained from the simulation.

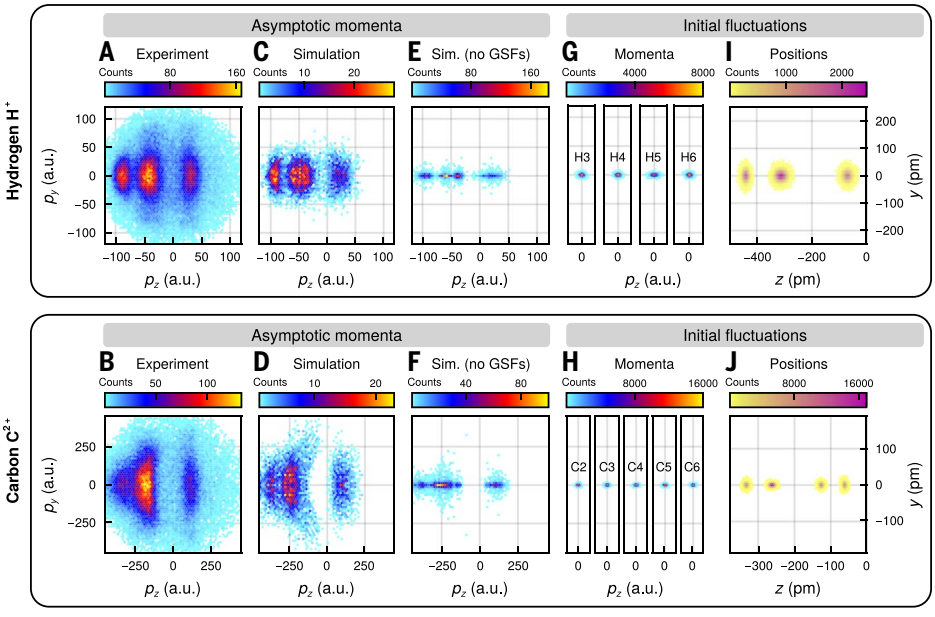


Fig. 2. Out-of-plane momenta of the hydrogen and carbon ions from experiment and simulation. (**A** and **B**) Experiment. (**C** and **D**) Simulation with initial conditions from the ground-state Wigner distribution. (**E** and **F**) Simulation with the initial geometry restricted to the equilibrium geometry. (**G** to **J**) Initial-state momentum and position fluctuations as sampled from the Wigner distribution. The (0,0) position is the center of mass of the molecule. a.u., atomic units. All data are for the I^{4+}, N^{2+}, C^{2+}, H^+ coincidence channel.

Fingerprints of collective ground-state fluctuations

The good agreement with the simulation results allowed us to directly relate the observed correlated behavior of the ions in the momentum space data (Fig. 3) to the collective nature of quantum fluctuations in the molecular ground state. To that end, we inspected the GSF along individual NM coordinates before the molecule interacts with the x-ray pulse and determined the contribution of the GSF along each NM to the variance in the final momenta along a given PC (SM section S9).

For the three dominant out-of-plane PCs displayed in Fig. 4, A, E, and I, the mode contributions are shown in Fig. 4, B, F, and J, respectively. The analysis for the other dominant modes is given in the SM (section S9). Figure 4, C, D, G, H, K, and L, shows the two NMs with the highest contribution to the respective PCs. Each of the three PCs can be associated with few NMs. PC 1 is dominated by the variance of the C2 ion, resulting from a near collision between this carbon ion and the iodine atom, as described in our previous works (*30*, *40*). Accordingly, PC 1 is promoted by NMs where the C2 atom strongly shifts out of plane, such as the NMs at 16.5 (Fig. 4C) and 27.1 THz (Fig. 4D). In the other cases, the connection between the NMs and the PCs is directly visually evident. For example, the displacement of atoms along the NMs at 26.1 (Fig. 4G) and 36.3 THz (Fig. 4H) corresponds to a similar pattern of correlated variations in the atomic CEI momenta along PC 2 (Fig. 4E). In the explosion, some of the collective out-of-plane patterns inherent in the GSFs were amplified and, thus, transferred into similar momentum patterns. This visual similarity is, however, lower when looking at the hydrogen atoms, as the contributions from the NMs are opposite and can cancel out. Similar observations can be made for PC 3 (Fig. 4I): There is a low-frequency mode (14.4 THz) and a high-frequency mode (34.9 THz), both having a matching carbon pattern with PC 3 but different contributions for the hydrogen atoms.

Figure 4 establishes that the correlated fluctuations occurring in the measured momenta can indeed be traced back to the effect of collective quantum fluctuations along individual NMs. The measured ion momenta thus provide access to the collective structural fluctuations present in the ground state of the molecule. Further analysis provided in the SM (section S11) also demonstrates that the patterns highlighted in Fig. 1 are associated primarily with the GSFs along the NMs with frequencies of 16.5 and 36.3 THz, respectively. Furthermore, our simulation results indicate that such a clear mapping between initial-state quantum fluctuations and final-state CEI momentum distributions is only possible for the out-of plane momenta, when several dominating modes are considered. Variations of in-plane momenta, by contrast, can only partially be associated with GSFs, demonstrating that they are much more influenced by the additional contributions imprinted on the explosion dynamics due to variations in the ionization dynamics and the strong nonlinear interaction among the ions during the charge-up and the explosion. These effects could, in the future, be partially overcome

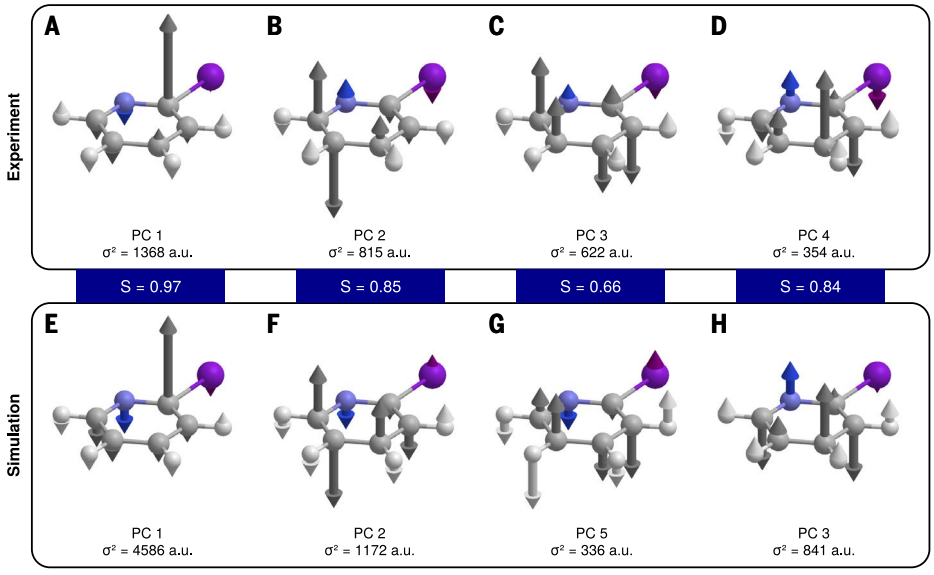


Fig. 3. Dominant out-of-plane PCs of the distribution of asymptotic momenta. (**A** to **D**) Reconstructed from the experimental data using the fitting algorithm described in the text. (**E** to **H**) Reconstructed from the XMDYN simulation data. σ^2 is the variance associated with each PC (explained variance). For a better comparison with those above, we changed the order of the simulation PCs in (G) and (H). The blue boxes show the mutual overlap *S* between the two linked PCs, computed as their scalar product (maximum 1 for identical PCs).

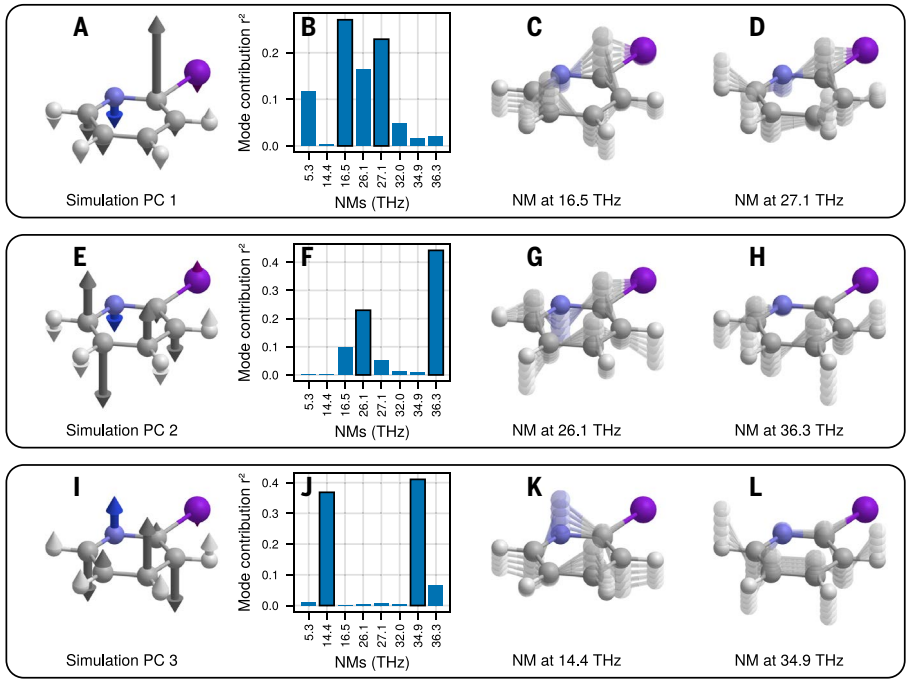


Fig. 4. Mapping of the PCs to the NMs. (**A**, **E**, and **I**) Out-of-plane-momentum PCs computed from the simulation. (**B**, **F**, and **J**) Mode contributions r_{ij}^2 to the respective momentum PCs from each NM. The two leading contributions are highlighted, and the corresponding NMs are shown in the next panels. (**C**, **D**, **G**, **H**, **K**, and **L**) NMs with the dominant contribution. To improve the visibility of the collective motion of hydrogen and heavier atoms, the NMs are shown through position variations that are weighted by the inverse square root of the atom mass. For the absolute scale of the GSFs, see table S1 and fig. S9.

by reducing the fluctuations in the ionization dynamics through shorter x-ray pulses and targeting even higher ion charge states. Along the same line, it should be noted that a clear correspondence of the experimental data with the simulated explosion dynamics could only be reached when utilizing coincidence events with sufficiently high charge. Coincidence datasets consisting of singly charged ions are considerably impacted by the influence of chemical bonding during the explosion, such that discrepancies to the Coulomb explosion simulation appear (SM section S10). Only the high x-ray fluence available at the SQS instrument of the EuXFEL produced such a high charge in the molecule that a direct connection between the CEI data and GSFs could be demonstrated in this experiment.

Conclusions

We measured fingerprints of the ground-state fluctuations in a complex molecule that originate from the Heisenberg uncertainty principle. The fingerprints emerge as collective features in the momenta of the ions generated in an x-ray free-electron laser–induced Coulomb explosion. This achievement was made possible through an advanced analysis technique that turns Coulomb explosion imaging into a powerful tool for measuring highly collective structural fluctuations that are inaccessible to any ensemble-averaging imaging method. Our analysis demonstrated that the variances present in incomplete coincidence sets are sufficient to construct a Gaussian model for the full-dimensional data, thereby also capturing collective features. Thanks to refined simulations of the Coulomb explosion, the measured momentum variances could be linked to ground-state fluctuations along individual NMs that exhibit correlations among multiple atoms. Our work thereby shows that it is possible to probe high-dimensional potential energy surfaces by observing the spontaneous structural fluctuations that molecules undergo due to quantum effects. Thanks to its ability to address highly collective effects and delocalized systems, our work also opens up new avenues to explore chemical dynamics, where the nuclear wave packet tends to spread and split over different reaction pathways. The visualization of the collective motion of the atoms rather than only the centroid of their distribution, as is the case for many other experimental methods, offers incomparably more detailed insight into the time evolution of molecular systems. In the future, one might even be able to simultaneously track electronic degrees of freedom by measuring, in addition, emitted electrons in coincidence with the fragment ions. Recent advances in the generation of more-intense, few- to subfemtosecond x-ray pulses (*42*–*44*) further facilitate rapid and complete charge-up and fragmentation of larger systems and, thus, put the long-awaited goal to image evolving wave packets in complex polyatomic systems within reach of the method presented in this work.

REFERENCES AND NOTES

1. T. Vojta, *Rep. Prog. Phys.* **66**, 2069 (2003).
2. S. Sachdev, *Quantum Phase Transitions* (Cambridge Univ. Press, ed. 2, 2011).
3. M. Benoit, D. Marx, M. Parrinello, *Nature* **392**, 258–261 (1998).
4. S. Schaack *et al.*, *Phys. Rev. Lett.* **131**, 126101 (2023).
5. T. E. Markland *et al.*, *Nat. Phys.* **7**, 134–137 (2011).
6. I. Errea *et al.*, *Nature* **578**, 66–69 (2020).
7. Y. Zheng *et al.*, *Nano Lett.* **22**, 1858–1865 (2022).
8. X.-Z. Li, B. Walker, A. Michaelides, *Proc. Natl. Acad. Sci. U.S.A.* **108**, 6369–6373 (2011).
9. B. Csorba, P. Szabó, S. Góger, G. Lendvay, *J. Phys. Chem. A* **125**, 8386–8396 (2021).
10. R. S. Mulliken, *Nature* **114**, 349–350 (1924).
11. D. A. McQuarrie, J. D. Simon, *Physical Chemistry: A Molecular Approach* (Univ. Science Books, 1997).
12. Z. Vager, R. Naaman, E. P. Kanter, *Science* **244**, 426–431 (1989).
13. H. Stapelfeldt, E. Constant, H. Sakai, P. B. Corkum, *Phys. Rev. A* **58**, 426 (1998).
14. F. Légaré *et al.*, *Phys. Rev. A* **71**, 013415 (2005).
15. A. Hishikawa, A. Matsuda, M. Fushitani, E. J. Takahashi, *Phys. Rev. Lett.* **99**, 258302 (2007).
16. C. B. Madsen *et al.*, *J. Chem. Phys.* **130**, 234310 (2009).
17. T. Endo *et al.*, *Science* **370**, 1072–1077 (2020).
18. S. Bhattacharyya *et al.*, *J. Phys. Chem. Lett.* **13**, 5845–5853 (2022).
19. A. J. Howard *et al.*, *Commun. Chem.* **6**, 81 (2023).
20. H. V. S. Lam *et al.*, *Phys. Rev. Lett.* **132**, 123201 (2024).
21. Y. Muramatsu *et al.*, *Phys. Rev. Lett.* **88**, 133002 (2002).
22. N. Saito *et al.*, *J. Electron Spectrosc. Relat. Phenom.* **141**, 183–193 (2004).
23. U. Ablikim *et al.*, *Sci. Rep.* **6**, 38202 (2016).
24. M. Pitzer *et al.*, *ChemPhysChem* **17**, 2465–2472 (2016).
25. Y. H. Jiang *et al.*, *Phys. Rev. Lett.* **105**, 263002 (2010).
26. K. Amini *et al.*, *J. Chem. Phys.* **147**, 013933 (2017).
27. F. Allum *et al.*, *J. Chem. Phys.* **149**, 204313 (2018).
28. E. Kukk *et al.*, *Phys. Rev. A* **99**, 023411 (2019).
29. T. Jahnke *et al.*, *Phys. Rev. X* **11**, 041044 (2021).
30. R. Boll *et al.*, *Nat. Phys.* **18**, 423–428 (2022).
31. T. Kitamura, T. Nishide, H. Shiromaru, Y. Achiba, N. Kobayashi, *J. Chem. Phys.* **115**, 5–6 (2001).
32. J. Ullrich *et al.*, *Rep. Prog. Phys.* **66**, 1463 (2003).
33. T. Jahnke *et al.*, *J. Electron Spectrosc. Relat. Phenom.* **141**, 229–238 (2004).
34. C. Vallance, D. Heathcote, J. W. L. Lee, *J. Phys. Chem. A* **125**, 1117–1133 (2021).
35. X. Li *et al.*, *Chin. Phys. B* **31**, 103304 (2022).
36. Z. Jurek, S.-K. Son, B. Ziaja, R. Santra, *J. Appl. Cryst.* **49**, 1048–1056 (2016).
37. A. C. T. van Duin, S. Dasgupta, F. Lorant, W. A. Goddard, *J. Phys. Chem. A* **105**, 9396–9409 (2001).
38. M. F. Russo Jr., A. C. T. van Duin, *Nucl. Instrum. Methods Phys. Res. B* **269**, 1549–1554 (2011).
39. H. M. Aktulga, S. A. Pandit, A. C. T. van Duin, A. Y. Grama, *SIAM J. Sci. Comput.* **34**, C1–C23 (2012).
40. B. Richard, J. M. Schäfer, Z. Jurek, R. Santra, L. Inhester, *J. Phys. B: At. Mol. Opt. Phys.* **54**, 194001 (2021).
41. I. T. Jolliffe, J. Cadima, *Philos. Trans. A Math. Phys. Eng. Sci.* **374**, 20150202 (2016).
42. S. Huang *et al.*, *Phys. Rev. Lett.* **119**, 154801 (2017).
43. J. Duris *et al.*, *Nat. Photonics* **14**, 30–36 (2020).
44. A. Trebushinin *et al.*, *Photonics* **10**, 131 (2023).
45. R. Boll, Tracing electron rearrangement upon absorption of very intense X-ray pulses, European XFEL Database (2019); https://doi.org/10.22003/xfel.eu-data-002159-00.
46. B. Richard, S. Banerjee, Z. Jurek, R. Santra, L. Inhester, Simulation and reconstruction of the final momenta generated in the Coulomb explosion of iodopyridine, University of Hamburg research data repository (FDR-UHH) (2025); https://doi.org/10.25592/uhhfdm.16697.

ACKNOWLEDGMENTS

L.I. acknowledges discussion with S. Trippel and I. Vinklárek about supersonic molecular beams. We also acknowledge European XFEL in Schenefeld, Germany, for the provision of XFEL beam time at the SQS instrument and thank the staff for their assistance. **Funding:** B.R., R.S., M.I., J.M.S, B.E, and L.I. acknowledge support from DESY (Hamburg, Germany), a member of the Helmholtz Association (HGF). B.R., R.S., M.I., K.K., and L.I. acknowledge support from the Cluster of Excellence "CUI: Advanced Imaging of Matter" of the Deutsche Forschungsgemeinschaft (DFG) - EXC 2056 - project no. 390715994, and K.K. in addition acknowledges the program "Sachbeihilfe" project no. 497431350 (KU 4184/1-1). F.T. acknowledges funding by the Deutsche Forschungsgemeinschaft (DFG, German Research Foundation) project no. 509471550, Emmy Noether Programme. The reaction microscope and its implementation at SQS were funded by the Bundesministerium für Bildung und Forschung (BMBF). R.D., K.F., S.G., M.H., M.I., and M.S.S. acknowledge support from DFG through Sonderforschungsbereich 1319 (ELCH). G.K. acknowledges funding by Helmholtz Forschungsakademie Hessen für FAIR (HFHF). D.R., X.L., and A.R. are supported by the Chemical Sciences, Geosciences, and Biosciences Division, Office of Basic Energy Sciences, Office of Science, US Department of Energy, grant no. DE-FG02-86ER13491. M.I. acknowledges support by the BMBF within grant 13K22CHA. V.M. acknowledges funding from the Volkswagen Foundation for a Peter Paul Ewald fellowship. **Author contributions:** T.J. originated the project's idea and analyzed the experimental data. L.I. initiated the advanced analysis methodology. R.B. was principal investigator of the experiment. B.R. wrote the code, ran the simulations, and performed the fitting of the data with input from J.M.S., Z.J., R.S., and L.I. S.B. and Z.J. performed the adjustments of the force field parameters. The experiment was carried out by R.B., J.M.S., K.F., M.S.S., S.E., B.E., M.I., K.K., X.L., T.M., C.P., D.E.R., D.R., J.M.S., L.P.H.S., F.T., P.W., M.M., and T.J. after the experiment was previously prepared and commissioned by G.K., N.A., T.M.B., A.D.F., S.G., P.G., M.H., M.Ki., M.Ku., S.M., N.M., J.M., V.M., Y.O., A.P., N.R., J.R., A.R., I.S., L.P.H.S., D.T., R.W., and P.Z. The SQS reaction microscope (REMI) endstation was designed and built by G.K., T.J., M.S.S., R.D., and L.P.H.S., with contributions from the whole University of Frankfurt group. B.R., T.J., R.B., R.S., and L.I. wrote the manuscript after in-depth discussions with M.M. and D.R. and with input from all the authors. **Competing interests:** The authors declare that they have no competing interests. **Data and materials availability:** The data recorded during the experiment are available in the European XFEL database under proposal no. 002159 (*45*). The simulation data and the result of the reconstructions are available at the research data repository of the University of Hamburg (*46*).

License information: Copyright © 2025 the authors, some rights reserved; exclusive licensee American Association for the Advancement of Science. No claim to original US government works. https://www.science.org/about/science-licenses-journal-article-reuse

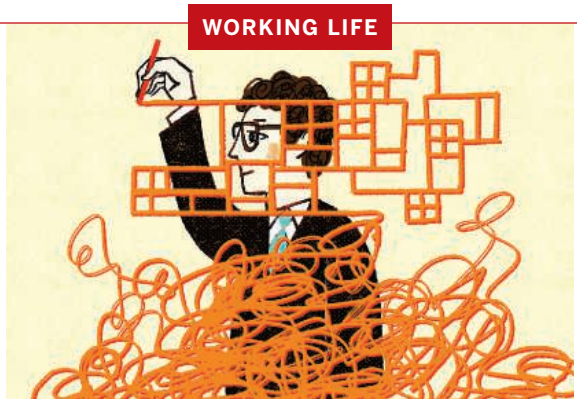
SUPPLEMENTARY MATERIALS

science.org/doi/10.1126/science.adu2637
Supplementary Text; Figs. S1 to S18; Tables S1 and S2; References *(47–65)*

Submitted 4 November 2024; accepted 10 June 2025

10.1126/science.adu2637

Check for



How a diagnosis altered my path

Matteo De Vuyst

My hands trembled as I held a lukewarm cup of coffee, scanning the packed conference room. It was the end of my first year as a Ph.D. student, and the biggest meeting I'd attended so far. I stood alone, watching the crowd. I longed to join in, but every attempt felt like hitting an invisible wall. Conversations moved too fast to follow. After a few awkward nods and half-finished sentences, I gave up and retreated to a corner in silence. That evening, in my hotel room, I wondered: "Why did something so simple feel so hard? Is there even a place for me in academia?" It was a familiar feeling. But only much later, after an unexpected diagnosis, did I understand why I felt so out of sync, and start to imagine a different way forward.

I'd worked hard to get here. As an undergraduate, I lived like a hermit, studying nonstop to earn the grades I needed. I enjoyed solving problems and working through data. The intellectual side of academia suited me. But I struggled with the social side—the conferences, meetings, hallway conversations. In grad school, the demands only intensified: Networking was no longer optional, group discussions required quick responses, and visibility mattered. Nonetheless, I pushed on. For a while, small successes kept me going: positive feedback, publications, and even a prestigious fellowship. I figured I needed more practice, more exposure, more effort. But beneath the surface, cracks were beginning to form.

By my third year, I hit a wall. Research still offered comfort, but the relentless social difficulties left me too depleted to focus. Success seemed to depend on skills I struggled to master. I spent hours frozen at my desk, overwhelmed with anxiety. Over time, exhaustion eroded my confidence and motivation, and I withdrew from colleagues, friends, even my research. I carried this weight alone, afraid that speaking up would confirm my worst fear: that I didn't belong.

Eventually, the stress became unmanageable. I stepped away from my Ph.D. to seek professional help. That decision led to an 8-week hospitalization and a 6-month leave, a break in my academic journey that I could never have imagined. Initially, I saw it as a personal failure. But with time and space to reflect, my perspective began to shift and I realized how much energy I'd spent trying to navigate a world that didn't quite fit me.

When a psychiatrist asked me whether I'd ever considered that I might be autistic, I was stunned. But as I started reading, it began to make sense: the social struggles, the sensory overload, the need for clear structure. A few months later, I received an official autism diagnosis. Finally, I had an explanation. Still, one question remained: Could I continue in academia? The thought of returning felt daunting. But I wasn't ready to give up.

Instead, I began to make subtle yet meaningful adjustments. Many emerged through trial and error, guided by reading and learning from other neurodivergent researchers. I began to schedule recovery time after work and started to wear noise-canceling headphones to manage sensory input. To create structure and make progress tangible, I broke down larger tasks into smaller ones and tracked them visually with hand-drawn graphs. I abandoned behaviors, such as forcing myself to follow conventional work routines, that only increased my stress. Slowly, I discovered what helped, and built a rhythm that feels sustainable.

These adjustments haven't solved everything. Now, in the fourth year of my Ph.D., I still leave some meetings feeling invisible, and old doubts occasionally resurface. However, I've learned to meet them with understanding rather than harsh self-judgment. My struggles aren't signs of incompetence, they're reminders that academia wasn't designed for people wired like me.

The most significant change hasn't been to my workload or environment, but to the connection with myself. The traits I once tried to suppress shape how I think, work, and move through the world. I've stopped believing I need to blend in to belong. Instead of trying to squeeze myself into a space, I'm gently reshaping it to fit me. □

Matteo De Vuyst is a Ph.D. student at Ghent University. Do you have an interesting career story to share? Send it to SciCareerEditor@aaas.org.



Evosep Eno

Evosep, a global leader in proteomics solutions, is proud to announce the launch of the Evosep Eno™, a robust, high-throughput separation tool preparing for next generation workflow integration for LC-MS based proteomics. This new platform will significantly enhance the company's ability to advance the use of LC-MS based proteomics as a vital tool for the pharmaceutical and biotech industries. Introducing Evosep Eno: a key component of the next generation in LC-MS based proteomics workflows. The Evosep Eno represents a significant leap forward in proteomics technology. Designed to drive the capabilities of next generation LC-MS based proteomics, the Evosep Eno offers unparalleled standardization, performance, reliability, and ease-of-use. This new platform will enable our customers to significantly speed up drug discovery and translational research programs, while enhancing researchers' capabilities to gain deeper insights into the proteome quickly and accurately. Key features and benefits of Evosep Eno are a 40% improved performance while increasing accuracy and precision in protein quantification. This ensures reliable and reproducible results for drug discovery and translational research. More than 2000 proteins per minute at 500 samples per day enables unmatched throughput for large-scale studies, accelerating biomarker discovery and clinical research without compromising data quality. Industry-leading system-to-system and lab-to-lab reproducibility. Consistent results across different systems and locations provide trustworthy data for multi-site studies, supporting academic research centers, drug developers, and contract research organizations. Standardized workflows with integrated consumable solutions simplify and streamline processes, increasing efficiency and reducing errors.

Evosep

For info: + 45 26 33 20 21
www.evosep.com

eProtein Discovery system

Nuclera's mission is to accelerate discovery by enabling rapid, easy access to functional proteins essential for drug discovery research. The company's eProtein Discovery™ benchtop system accelerates protein expression and purification optimization in research labs. Applying digital microfluidics alongside in situ protein detection assays and cell-free protein synthesis, eProtein Discovery enables rapid, scalable access to high-quality proteins, supporting both cell-free and cell-based expression methods. The system significantly reduces time and cost of these processes by automating construct screening, protein scale-up, and producing purified proteins for downstream functional testing in under 48 hours. The system accelerates workflows, achieving results in days rather than the months required by traditional cell-based methods. Nuclera has added a new membrane protein workflow to its system. This expanded capability enables the expression, purification and stabilization of challenging membrane proteins, which are often key targets in therapeutic development. Using cell-free protein synthesis, digital microfluidics, and optimized additive screening, eProtein Discovery can express and purify functional, correctly folded membrane proteins, in 48 hours. Membrane proteins play vital roles in regulating cellular processes and many are implicated in the development and progression of disease. 60% of FDA-approved drugs target membrane proteins yet the extraction and stabilization of these structurally complex proteins remains challenging due to their intrinsic hydrophobic nature. Nuclera demonstrated the capabilities of eProtein Discovery to produce membrane proteins by synthesizing MsbA (a membrane transporter) and ZMPSTE24 (an integral membrane protein). In 24 hours, eProtein Discovery evaluated different expression and purification conditions, including assessing the effects of using nanodiscs, lipids, and detergents, to identify the optimal conditions for producing soluble, stable MsbA and ZMPSTE24. Scale-up production of these membrane proteins was achieved within 48 hours, enabling rapid functional evaluation. MsbA and ZMPSTE24 generated using eProtein Discovery had high-yield, were functionally active, and compatible with cryo-electron microscopy (cryo-EM). Existing eProtein Discovery users can access this new membrane protein production capability through a software update.

Nuclera

For info: +44 1223 625095
www.nuclera.com

EvoLiver Test

Mursla Bio, a leader in extracellular vesicle (EV) science on a mission to significantly improve cancer outcomes for at-risk patients through the power of dynamic biopsy technology, today announced that the US Food and Drug Administration (FDA) has granted Breakthrough Device designation to its lead product, EvoLiver™. The designation recognizes the potential of the company's dynamic biopsy-based blood test, EvoLiver, which is enabled by a novel platform based on organ-specific EVs for the surveillance of hepatocellular carcinoma (HCC), the most common form of primary liver cancer, in high-risk cirrhotic patients. The FDA's Breakthrough Device designation is awarded to medical technologies that offer more effective diagnosis of life-threatening or irreversibly debilitating diseases and that represent a breakthrough over existing solutions. The designation enables an accelerated regulatory pathway, including priority review and closer collaboration with the FDA, which ultimately supports broader market reach and commercial adoption. HCC is the fastest-growing cause of cancer-related deaths. Although clinical guidelines recommend routine surveillance for high-risk individuals, adherence to these programs remains low, and the standard-of-care method, based on ultrasound, has limited sensitivity, particularly for detecting small tumors and in overweight patients. Together, these challenges contribute to late diagnoses, poor patient outcomes, and escalating healthcare costs. Mursla Bio's dynamic biopsy technology combines the accuracy and disease sub-typing capabilities of tissue biopsies with the ease of liquid biopsy sample collection, providing a non-invasive intervention with comprehensive biological insights. This is made possible by advanced EV science and an innovative extracellular omics approach, supported by Mursla Bio's technologies. These technologies include organ-specific EV isolation from biofluids for precise targeting, an AI-enabled multi-omics workflow for disease biomarker identification, and a scalable assay platform using optimal biomarkers for clinical use.

Mursla Bio is advancing regulatory compliance for EvoLiver as a Laboratory Developed Test (LDT) in preparation for its upcoming product launch, while also laying the groundwork for future FDA approval through the Premarket Approval (PMA) pathway to enable broader clinical and commercial scale-up.

Mursla Bio

For info: +44 (0) 1223 928 141
www.mursla.com

Electronically submit your new product description or product literature information! Go to www.science.org/about/new-products-section for more information.

Newly offered instrumentation, apparatus, and laboratory materials of interest to researchers in all disciplines in academic, industrial, and governmental organizations are featured in this space. Emphasis is given to purpose, chief characteristics, and availability of products and materials. Endorsement by *Science* or AAAS of any products or materials mentioned is not implied. Additional information may be obtained from the manufacturer or supplier.